

# THIS WEEK

## EDITORIALS

**WORLD VIEW** Religion can trump science in tackling unknowns **p.431**

**ZOOLOGY** The zebra virus that killed Jerka the polar bear **p.432**



**GREENLAND** Ice sheet set for widespread surface melt this decade **p.433**

## Social dimensions to biodiversity

*The international body set up to address the loss of biodiversity must take account of more than just science if it is to fulfil its mission.*

In a Comment article on page 454 of this issue, a group of researchers writing about the future direction of the Intergovernmental Platform on Biodiversity and Ecosystem Services (IPBES) note that the organization is “promoting a predominantly science-based understanding of biodiversity”.

This is to be expected, you probably think. *Nature*, after all, is the international weekly journal of science. Science-based understanding is what *Nature* does.

Yet, that line from the Comment is not an endorsement of that ‘science-based’ approach. It is a criticism. In the same article the authors dismiss a reliance on peer-reviewed science as “tunnel vision” and argue that “knowledge that has been standardized and scientifically validated” is insufficient to set useful policy. Above all, they insist, the IPBES must take a different approach from that of the Intergovernmental Panel on Climate Change (IPCC). The desire of the IPCC to produce standardized assessments (it is now working on its fifth) has limited its success, the authors argue, because it has “overshadowed arguably more important tasks: synthesizing wider perspectives about changing climates and spurring action by multiple policy actors”.

This provocative stance raises many questions. First of all, is the criticism of the IPCC fair? The answer is yes and no. That body is set up to draw fire from all sides — the more so because of its clumsy handling of claimed mistakes and the waning of political support for policies to restrict greenhouse-gas emissions. Yet critics of the IPCC too often overlook its heterogeneous nature: goals and practices vary

across the three separate working groups, so much so that some have argued convincingly that the IPCC should release not a combined report but three distinct ones. The political clout of speaking with one voice is greater, but a larger target is also easier to hit.

Hostility towards the IPCC’s perceived approach perhaps flows in part from how climate change is often presented: as a problem to solve; as something large and external to tackle; and so as something for science to quantify. But it can be viewed instead as a consequence of millions, if not billions, of separate decisions by individuals.

Here, there probably are lessons for the IPBES. If people are seen as major contributors to the problems of climate change and loss of biodiversity, then people’s behaviour and attitudes must be a major part of the solutions. That view makes both the problem and the solution more fuzzy and less susceptible to standardization, but it perhaps also makes the problem more realistic and the solution more practicable.

Discussion of values, stakeholders, community partners and engagement — the language of the social sciences — can make some traditional scientists uncomfortable. So what does this approach mean in practical terms for the IPBES? On one level, as the Comment authors suggest, the answer could be as simple as broadening the criteria of what counts as admissible material — learning to value local knowledge and expertise. The challenge of protecting biodiversity from a cumulative death by thousands and thousands of cuts is surely a good place to test this approach. One size cannot fit all. And it does not need to. ■

## The name game

*Nomenclature rules can disrupt planetary scientists’ fun, but they serve a purpose.*

After the Soviet spacecraft Luna 3 retrieved the first pictures from the far side of the Moon in 1959, the justifiably proud Soviets started to call one of the lunar lava plains Mare Moscoviense, after their capital. The move seemed to defy a decades-old tradition that such maria are named after mental states (Tranquillitatis, for example, or Serenitatis), or words for water. At the 1961 meeting of the International Astronomical Union (IAU), French astronomer Audouin Dollfus was able to restore tranquillity in the astronomical community with a serene move. Moscoviense worked as a name, he said, because Moscow is, in fact, a “state of mind”.

To avoid further disputes as proud pioneers sought to thank benefactors, curry favour or merely indulge themselves, the IAU went on to establish working groups to set rules and conventions for nomenclature.

Procedures now make sure that mountains on Mercury are named with words for ‘hot’ in various languages, canyons on Venus christened after goddesses and small craters on Mars twinned with villages on Earth. Just last month, a 39-kilometre-wide Martian crater was named Moanda, after a town in Gabon.

However, as the News story on page 442 makes clear, those who seek to explore often remain (pleasingly) reluctant to follow the rules. The disputes are minor, but it is no surprise that those scientists working on NASA missions to Mars and Vesta, flushed with discovery, are annoyed by the apparently hidebound rules of the IAU. The row over Vesta centres, quite literally, not on a name but on issues of how to apply systems of longitude and latitude and mapping coordinates. On Mars, NASA researchers have taken to calling a prominent mountain that will be tackled by their Curiosity rover Mount Sharp, after a late colleague, rather than using the official title, Aeolis Mons.

Still, rules are rules. What’s in a name? Quite a lot, actually. Think how it would have been had the namers of planets not yielded to tradition. After discovering Uranus in 1781, astronomer William Herschel wanted to name the planet after George III, the king of Great Britain. And what a loss that would have been to generations of sniggering schoolchildren. ■



## Sometimes science must give way to religion

*The Higgs boson, and its role in providing a rational explanation for the Universe, is only part of the story, says Daniel Sarewitz.*

Visitors to the Angkor temples in Cambodia can find themselves overwhelmed with awe. When I visited the temples last month, I found myself pondering the Higgs boson — and the similarities between religion and science.

The Higgs, of course, has been labelled the ‘god particle’ because it accounts for the existence of mass in the Universe. But the term (coined by physics Nobel laureate Leon Lederman, perhaps to the regret of some of his colleagues) also signals the ambition of science, or at least of certain branches of physics, to probe the origins and meaning of existence itself — which, to some, is the job of religion. Science may seek a theoretically and empirically sound explanation of such origins and religion may not. But this distinction is less clear than it seems.

The wonder invoked by the Angkor temples is not an accident or a modern conceit. It flows, at least in part, from the intention of those who designed the temples. “In each of the Angkor monuments,” the architect Maurice Glaize explained in his exhaustive 1944 guide to the temples, “a preoccupation with symbolic order seeks to create a representation of the universe in reduction ... realising a kind of correctly ordered model”. The overwhelming scale of the temples, their architectural complexity, intricate and evocative ornamentation and natural setting combine to form a powerful sense of mystery and transcendence, of the fertility of the human imagination and ambition in a Universe whose enormity and logic evade comprehension.

Science is supposed to challenge this type of quasi-mystical subjective experience, to provide an antidote to it. The Higgs discovery, elucidating the constituents of existence itself, is even presented as a giant step towards the ultimate cure: a rational explanation for the Universe. That such scientific understanding provides a challenge to religion is an idea commonly heard from defenders of science, especially those in more militant atheist garb. Yet scientists who occupy that ground are often too slow to recognize the irrational bases of their own beliefs, and too quick to draw a line between the scientific and the irrational. Take, for example, how we come to know what science discovers. Most people, including most scientists, can acquire knowledge of the Higgs only through the metaphors and analogies that physicists and science writers use to try to explain phenomena that can only truly be characterized mathematically.

Here’s *The New York Times*: “The Higgs boson is the only manifestation of an invisible force field, a cosmic molasses that permeates space and imbues elementary particles with mass ... Without the Higgs field, as it is known, or something like it, all elementary forms of matter would zoom around at the speed

of light, flowing through our hands like moonlight.” Fair enough. But why “a cosmic molasses” and not, say, a “sea of milk”? The latter is the common translation of an episode in Hindu cosmology, represented on a spectacular bas-relief panel at Angkor Wat showing armies of gods and demons churning the “sea of milk” to produce an elixir of immortality.

If you find the idea of a cosmic molasses that imparts mass to invisible elementary particles more convincing than a sea of milk that imparts immortality to the Hindu gods, then surely it’s not because one image is inherently more credible and more ‘scientific’ than the other. Both images sound a bit ridiculous. But people raised to believe that physicists are more reliable than Hindu priests will prefer molasses to milk. For those who cannot follow the mathematics, belief in the Higgs is an act of faith, not of rationality.

Science advocates have been keen to claim that the Higgs discovery is important for everyone. Yet in practical terms, the Higgs is an incomprehensible abstraction, a partial solution to an extraordinarily rarified and perhaps always-incomplete intellectual puzzle.

By contrast, the Angkor temples demonstrate how religion can offer an authentic personal encounter with the unknown. At Angkor, the genius of a long-vanished civilization, expressed across the centuries through its monuments, allows visitors to connect with things that lie beyond their knowing in a way that no journalistic or popular scientific account of the Higgs boson can. Put another way, if, in a thousand years, someone visited the ruins of the Large Hadron Collider, where the Higgs experiment was conducted, it is doubtful that they would get from the relics of the detectors and superconducting magnets a sense of the subatomic

world that its scientists say it revealed.

Why does this matter? Challenges to the cultural and political authority of science continue to rise from both ideological and religious directions. It is tempting to dismiss these as manifestations of ignorance or scientific illiteracy. But I believe instead that they help to show us why it will always be necessary to have ways of understanding our world beyond the scientifically rational.

I am an atheist, and I fully recognize science’s indispensable role in advancing human prospects in ways both abstract and tangible. Yet, whereas the Higgs discovery gives me no access to insight about the mystery of existence, a walk through the magnificent temples of Angkor offers a glimpse of the unknowable and the inexplicable beyond the world of our experience. ■

**Daniel Sarewitz** is co-director of the Consortium for Science, Policy and Outcomes at Arizona State University, and is based in Washington DC. e-mail: [daniel.sarewitz@asu.edu](mailto:daniel.sarewitz@asu.edu)

FOR THOSE WHO  
CANNOT FOLLOW THE  
**MATHEMATICS,**  
BELIEF IN THE  
HIGGS IS AN ACT  
OF FAITH, NOT OF  
**RATIONALITY.**

➔ **NATURE.COM**  
Discuss this article  
online at:  
[go.nature.com/oari6p](http://go.nature.com/oari6p)

# RESEARCH HIGHLIGHTS

Selections from the  
scientific literature

## MICROBIOLOGY

### Cigarette smoke boosts biofilms

Components of cigarette smoke can cause bacteria in the nose to increase their production of biofilms — sticky structures that help the microorganisms to establish an infection.

Cigarette smoke is known to impair the immune system and to irritate the lining of the lungs. Adam Ratner and his team at Columbia University, New York, exposed *Staphylococcus aureus* to cigarette smoke and found that some of the toxic molecules in smoke switched on biofilm-forming signalling pathways. The smoke also boosted bacterial adherence to cultures of the cells that line the lungs.

The findings offer another explanation for why smokers and those exposed to second-hand smoke are prone to respiratory infections.

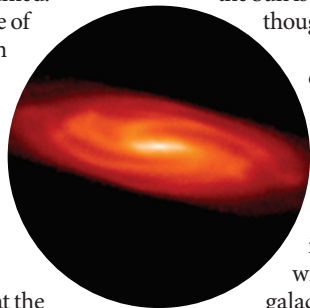
*Infect. Immun.* <http://dx.doi.org/10.1128/IAI.00689-12> (2012)

## ASTRONOMY

### Dark matter hugs the Sun

Dark matter constitutes roughly 85% of all matter in the Universe, and there may be more of it near the Sun than previously assumed.

The presence of dark matter can be inferred from its gravitational effect on the rotation of the Milky Way and other groups of stars. Silvia Garbari at the University of Zurich in Switzerland and her team have developed a dynamic model of the Milky Way (pictured)



that focuses on the motion of about 2,000 stars local to the Sun. Their model suggests that the density of dark matter near the Sun is higher than had been thought.

This result is at odds with the prevailing view that a spherical halo of dark matter surrounds the Galaxy. The result is instead consistent with a less spherical galactic halo or with a local disc of dark matter.

*Mon. Not. R. Astron. Soc.* <http://dx.doi.org/10.1111/j.1365-2966.2012.21608.x> (2012)



B. SCHEER/ZOO WUPPERTAL

## ANIMAL HEALTH

### The spread of herpes in zoos

The death in 2010 of Jerka, a polar bear at a zoo in Germany, has been blamed on a herpes virus that originated in zebras.

By sequencing and analysing viral genetic material from Jerka (pictured) and other polar bears, Alex Greenwood at the Leibniz Institute for Zoo and Wildlife Research in Berlin and his team identified the polar bear virus as being similar to the zebra EHV1 herpes strain. However, the virus that was found in the polar bears was a recombinant strain, which could explain how it was able to

jump between species. Rodents moving freely between enclosures containing zebras and polar bears might have acted as vehicles for the recombinant viruses.

Because not all the infected polar bears showed symptoms, the team warns that disease outbreaks in zoos ought to be monitored more carefully to track pathogen spread and to prevent other animals from suffering Jerka's fate.

*Curr. Biol.* <http://dx.doi.org/10.1016/j.cub.2012.07.035> (2012)

## REPRODUCTIVE BIOLOGY

### Molecule blocks sperm production

A small molecule that reversibly lowered sperm count and rendered sperm immobile in male mice has potential as a male contraceptive.

Martin Matzuk at Baylor College of Medicine in Houston, Texas, James Bradner at the Dana-Farber Cancer Institute in Boston, Massachusetts, and their colleagues show that the molecule, JQ1, binds to a protein called BRDT. This

protein is found only in the testes, where it is required for sperm generation. Male mice injected with JQ1 continued to mate normally with females, but they showed shrunken testes and decreased sperm count, and sired no offspring. Within four months of the treatment being stopped, the male mice could impregnate females.

The molecule could be part of a new class of contraceptive drugs that specifically target male sex cells, the authors suggest.

*Cell* 150, 673–684 (2012)  
For a longer story on this research, see <http://go.nature.com/sd4sko>



## MICROBIOLOGY

## Inflamed guts boost bad bacteria

Inflammatory bowel disease increases the risk of colorectal cancer — possibly because gut inflammation promotes the growth of a bacterial strain that produces a DNA-damaging toxin.

Christian Jobin of the University of North Carolina at Chapel Hill and his team exposed mice suffering from gut inflammation, or colitis, to gut bacteria and to a carcinogen. Animals that had been colonized with the *Escherichia coli* strain NC101 were much more likely to develop colorectal cancer than those that had been colonized with another human gut bacterium. However, in the absence of inflammation, mice were able to protect themselves from the *E. coli* strain's harmful effects. The researchers pinpointed a small region of DNA in *E. coli* NC101 that encodes a DNA-damaging toxin. *E. coli* lacking this toxin induced intestinal inflammation but not cancer. *Science* <http://dx.doi.org/10.1126/science.1224820> (2012)

For a longer story on this research, see <http://go.nature.com/tx21ez>

## NEUROBIOLOGY

## Flushing proteins from the brain

To rid itself of extracellular proteins, the brain relies on water transport by cells called astrocytes and on the flow of cerebrospinal fluid. This fluid was thought mainly to provide mechanical and immunological protection to the brain.

Jeffrey Iliff and Maiken Nedergaard at the University of Rochester Medical Center in New York and their teams tracked fluorescently labelled molecules as they moved through the brain. The proteins — including amyloid beta, thought to be pathogenic in Alzheimer's disease — were

transferred into cerebrospinal fluid. This, the authors report, flows into the brain through the spaces surrounding arteries, and out by means of the spaces around veins. The blood vessels were surrounded by projections from astrocytes. In mice lacking a protein that transports water across the astrocyte cell membrane, 70% fewer molecules were cleared from the brain than in normal animals.

Understanding this clearance system could help to explain how some neurodegenerative diseases develop, the researchers suggest.

*Sci. Transl. Med.* 4, 147ra111 (2012)

## INFORMATION TECHNOLOGY

## Textbook encoded in DNA

A 5.27-megabit book containing more than 53,000 words, 11 digital images and a computer program has been encoded in DNA — the largest amount of non-biological data yet stored in this way.

Sriram Kosuri at Harvard's Wyss Institute in Boston, Massachusetts, and his colleagues created nearly 55,000 different short DNA strands, or oligonucleotides, each containing 159 nucleotides. Of these, 96 represent data in the form of 1's and 0's, 19 show how the oligonucleotides should be ordered, and 44 facilitate sequencing. The researchers designed their system such that the DNA's A and C bases represent 0, with G and T corresponding to 1. Sequencing the DNA molecules allows the data to be decoded.

The technology, although currently too costly for routine use, stores information more densely than is possible with conventional devices.

*Science* <http://dx.doi.org/10.1126/science.1226355> (2012)

For a longer story on this research, see <http://go.nature.com/i56h26>

## COMMUNITY CHOICE

The most viewed papers in science

## MATERIALS

## Graphene, heal thyself



Graphene, atom-thick sheets of carbon, has a multitude of unusual properties, and self-healing can now be added to the list.

Quentin Ramasse of the SuperSTEM Laboratory in Daresbury, UK, and his colleagues deposited metals on sheets of graphene and then scanned the sheets using an electron microscope. The metals catalysed the breaking of carbon bonds, making holes in the carbon's honeycomb structure. When the supply of catalysts had been exhausted, the graphene healed itself. In the presence of other hydrocarbons, the graphene sheet filled its gaps with variably sized rings of additional carbon atoms. However, if no hydrocarbons were present, the carbon atoms rearranged themselves into their original two-dimensional hexagonal structure.

Researchers hope that the 'reknitting' process can be used to help control nanometre-scale etching of graphene.

*Nano. Lett.* 12, 3936–3940 (2012)



A. COOPER/R. HARDING

## CLIMATE SCIENCE

## Melting triggers more melting

The whole of Greenland's ice sheet is likely to experience some degree of melting over the next decade.

Jason Box at the Ohio State University in Columbus and his team combined satellite measurements of surface albedo — how much sunlight the ground reflects — with models of surface air temperature and solar radiation hitting the surface for the past 12 summers. The researchers found that positive albedo feedback — whereby melting ice reduces surface reflectivity, leading to faster melting — has doubled the ice sheet's surface melt rate since 2000.

The authors identified three ways in which recent

warm summers could have contributed to the reduced albedo: surface heating due to unusually warm air currents creates larger snow grains that reflect less sunlight; less cloudy skies increase direct heating from sunlight; and reduced summer snowfall results in a darker surface.

Another warm decade could mean that Greenland will absorb instead of resist the heat from 24-hour sunlight, leading to expansion of the melt area to encompass the entire ice sheet. This process has already begun, with an estimated 97% of Greenland's ice sheet having shown surface melting by mid-July of this year.

*Cryosphere* 6, 821–839 (2012)

➔ **NATURE.COM**

For the latest research published by Nature visit:

[www.nature.com/latestresearch](http://www.nature.com/latestresearch)



# SEVEN DAYS

The news in brief

## POLICY

### Gene patent boost

For the second time, the US legal system has upheld the biotechnology industry's ability to patent genes. A lawsuit against Myriad Genetics of Salt Lake City, Utah, asserted that some of the firm's patents for genes (associated with breast cancer) should be invalidated because they refer to DNA that is a product of nature, and so not patentable under US law. But in a 2:1 decision on 16 August, a US appeals court ruled that Myriad's isolated DNA sequences represented a "nonnaturally occurring composition of matter", and so could be patented. The decision was similar to an earlier ruling in July 2011, before the case was reopened. See [go.nature.com/cvhlvrl](http://go.nature.com/cvhlvrl) for more.

### Tobacco control

The Australian government's world-first plan to strip logos and branding from cigarette packets has survived a legal fight from tobacco companies, which claimed the law would breach Australia's constitution. The nation's highest court dismissed that challenge on 15 August. From 1 December, tobacco products will be sold in plain olive-green packets with large graphic health warnings. The World Health Organization urged other countries to follow Australia, stating that with the legal victory, "public health enters a brave new world of tobacco control".

### Telescope sale

A panel of astronomers has advised the US National Science Foundation (NSF) to divest itself of six telescopes by 2017 so that the agency can pay for future facilities, such as the planned Large

Synoptic Survey Telescope in Chile. Responding to the report, released on 16 August, NSF astronomy division director James Ulvestad said that he would try to find new operators for the telescopes in the next 18 months, before the agency begins to consider closing the facilities. See page 440 for more.

### Online disclosure

US president Barack Obama on 16 August approved a month's delay to a financial disclosure bill that some US government scientists are fiercely resisting. The STOCK Act requires senior government officials to post financial information online in order to make transparent

any conflicts of interest. It was to come into force from 31 August, but has attracted widespread criticism from some federal employees who argued that making details so readily available would be a threat to national security. The legislation is now to be implemented from 30 September, although federal employees, including researchers at the National Institutes of Health, launched a lawsuit on 2 August to try to stop it taking effect.

### Heliophysics plan

The next decade of US solar-physics research should concentrate on small- and medium-scale research missions, including examining

largest in terms of capacity. It is one of a series of dams planned for the Xingu River, a tributary of the Amazon in the state of Pará. The latest court order — which halts work pending a hearing for indigenous groups to voice their opposition — follows several lawsuits, rulings and appeals that have seen work on the dam stop and start.



EVARISTO SALAS/GETTY

## Amazon's giant dam halted again

A federal court in Brasília ordered the suspension of work on Brazil's enormous Belo Monte dam on 13 August, citing the need for further consultation with indigenous people in the region. At an estimated cost of US\$13 billion, the 11-gigawatt hydroelectric project (pictured, under construction) would be the world's third

the effects of space weather on Earth activities, says a report released on 15 August by the US National Academies in Washington DC. "We're bringing this a lot closer to home, with a lot more focus on the near-Earth end," explains Dan Baker, head of the Laboratory for Atmospheric and Space Physics at the University of Colorado Boulder, who chaired the heliophysics decadal survey. See [go.nature.com/vtioeg](http://go.nature.com/vtioeg) for more.

### Materials 2022

The US National Science Foundation (NSF) should expand its investment in innovative instrumentation that could serve a large

number of researchers, such as advanced nuclear magnetic resonance spectrometers and electron microscopes, according to an advisory report on materials science released on 16 August. The report was written by the Materials 2022 panel, which was convened last year after a separate NSF report raised concerns about investment in medium-sized (US\$0.1 million to \$10 million) facilities. See [go.nature.com/t6ayqu](http://go.nature.com/t6ayqu) for more.

## EVENTS

## West Nile virus

The city of Dallas, Texas, declared a state of emergency on 15 August, following ten deaths from West Nile virus in Dallas County over the past month. By that date, 693 cases of the disease, and 26 deaths, had been reported in the United States this year. The country is hit by West Nile virus every year, but this year's cases represent the highest number reported by mid-August since the virus was first detected in the country in 1999, according to the US Centers for Disease Control and Prevention in Atlanta, Georgia.

## Mars laser

NASA's Mars Curiosity rover tested out the laser on its ChemCam instrument on 19 August, firing 30 pulses



in 10 seconds at a fist-sized rock nicknamed Coronation (pictured), and recording the spectra of the induced sparks. It was one of the final instrument checks before the rover takes its first drive, in which it will head about 400 metres east-southeast to an intriguing spot where three kinds of terrain meet. The target area, dubbed Glenelg, was picked on 17 August. See [go.nature.com/qeuxhl](http://go.nature.com/qeuxhl) for more.

## Hypersonic flight

An experimental aircraft designed to fly at six times the speed of sound (Mach 6) broke apart in the air before it could begin a five-minute test flight on 15 August. The X-51A Waverider, a hypersonic jet, failed because of a faulty control fin about 15 seconds into its flight, the US Air Force said. Four X-51 aircraft have been built — one reaching Mach 5 for three minutes in 2010 — but the Air Force now has only one left.

## RESEARCH

## Forest emissions

As a result of Brazil's crackdown on deforestation, annual carbon dioxide emissions from forest clearance in the Brazilian Amazon dropped by roughly 57%, from 986 million to 420 million tonnes between 2004 and 2011, according to an analysis released on 13 August by Brazil's National Institute for Space Research. Emissions have not fallen as fast as deforestation (which plummeted by 77% over the same period), because carbon does not instantly move from soils and plants to the atmosphere, and because remaining deforestation is moving to denser forest that stores more carbon.

## Next Mars mission

NASA will be landing on Mars again. On 20 August, the agency announced that it had given the go-ahead to a mission that in 2016 would land near the equator of Mars to listen to the tremors rumbling through the planet's interior. The US\$425-million mission, called InSight (Interior Exploration using Seismic Investigations, Geodesy and Heat Transport) could expect to hear quakes as large as magnitude 5 in its two-year mission. It was chosen over two other mission

## COMING UP

### 27 AUGUST

The US Food and Drug Administration decides whether to approve Quad, a pill that combines four drugs in one to treat HIV. The pill was developed by Gilead Sciences of Foster City, California, which hopes to maintain income after a key component of its 3-in-1 pill Atripla comes off patent next year (see *Nature* 488, 267; 2012).

### 30 AUGUST

The twin spacecraft in NASA's Moon-mapping GRAIL mission, which powered down in May, switch on again for an extended science mission. They will halve their distance to the Moon's surface to examine its gravity field (at an average altitude of 23 kilometres).

candidates: one to float on a hydrocarbon sea of Saturn's moon Titan, and the other to land on a comet. See [go.nature.com/fhkyvg](http://go.nature.com/fhkyvg) for more.

## NASA contract

Hot on the heels of the Curiosity rover's landing on Mars, NASA announced on 17 August that the California Institute of Technology (Caltech) in Pasadena will continue to run the Jet Propulsion Laboratory (JPL), where the rover was built, for the next five years. The contract to manage the JPL is worth US\$8.5 billion; the current deal was set to expire on 30 September. US federal contracting rules require that contracts are put up for open competition every five years, although the JPL has been run for NASA by Caltech consistently since 1958.

► **NATURE.COM**

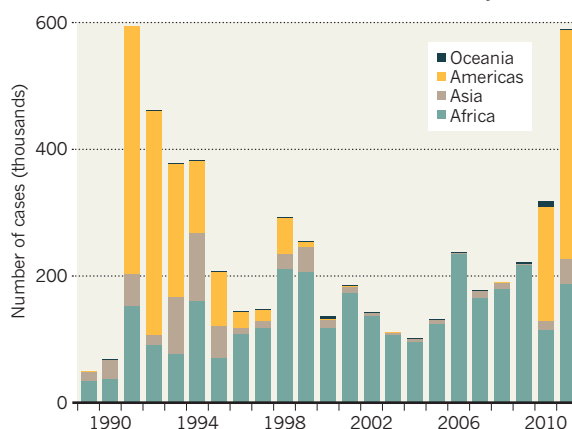
For daily news updates see:  
[www.nature.com/news](http://www.nature.com/news)

## TREND WATCH

An outbreak of cholera that started in Haiti in October 2010 lay behind the surge in worldwide cholera cases in 2011. The reported total of some 600,000 cases — thought to greatly under-represent the true number — was a two-decade high (see chart). By mid-August this year, Haiti's outbreak had calmed to fewer than 100 new cases a day. But Sierra Leone is seeing its biggest outbreak since 1996, with more than 10,000 cases and 180 deaths by 15 August. Its government has declared a state of emergency.

## WORLDWIDE CHOLERA CASES SURGE

Haiti's cholera crisis saw cases in 2011 rise 85% above the year before.





# NEWS IN FOCUS

**GENOMICS** Sequencing gives older fathers pause for thought **p.439**

**US ELECTION** What Paul Ryan could mean for the future of science **p.441**

**PLANETARY SCIENCE** Mission teams fight over names and numbers **p.442**



**PROFILE** Yoshiki Sasai reveals the art of growing eyes **p.444**

H. HOAG



The isolated Experimental Lakes Area has been the site of landmark experiments on the sources and effects of pollution.

## ENVIRONMENTAL SCIENCE

# Test lakes face closure

*Slashed funding threatens Canada's unique freshwater study site.*

BY HANNAH HOAG

Lake 239 looks inviting. Pines and spruce fringe the shoreline and waves lap against outcrops of weathered granite. But on this hot August afternoon in northwestern Ontario (see 'Water works'), one feature stands out. At the far end of the 800-metre-long lake, a series of plastic-walled columns descend from a floating dock to the muddy bottom about 2 metres down. They are the sign that the lake's placid setting disguises an experiment in controlled environmental abuse.

Jennifer Vincent, a graduate student at Trent University in Peterborough, Ontario, kneels by one of the columns and empties a vial of silver nanoparticles into it. An iridescent purple cloud blooms in the water for a moment before the

metal particles are mixed and disperse. These experiments are the first stage of a three-year, Can\$720,000 (US\$728,000) project to understand the biological effects of 'nanosilver' — an antibacterial agent commonly added to commercial products — and its possible effect on the environment. Previous work has shown that the chemical alters bacterial-community structure, affects algae and may change phosphorus cycling. Next year, the project intends to add nanosilver to an entire lake (Lake 222) and measure its effects across the ecosystem.

With 58 such lakes serving as sites for a broad range of studies, the Experimental Lakes Area (ELA) is unique in the world. "I don't

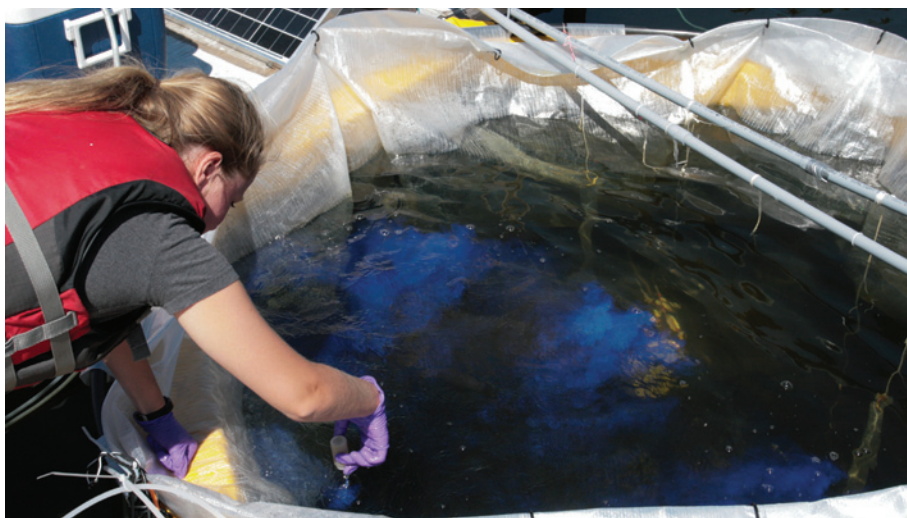
take it lightly that you're basically poisoning a lake," says Chris Metcalfe, an environmental toxicologist from Trent University, and a leader on the project. But at the ELA, he adds, "you can graphically demonstrate what goes on in a whole lake ecosystem."

Yet the ELA project, with its laboratory buildings, residences and workshops, may soon disappear. Earlier this year, Canada announced that it would cease funding the ELA after March 2013, a development that dismayed scientists who have made use of the 44-year-old facility for investigations ranging from chemical contamination to the effects of climate change.

The decision was unexpected. On 17 May, ELA employees at the Freshwater Institute in Winnipeg, were called to an emergency meeting, where they were told that the ►

► **NATURE.COM**  
For more on  
environmental cuts  
in Canada see:  
[go.nature.com/717wpa](http://go.nature.com/717wpa)





A three-year experiment to monitor the environmental effects of nanosilver particles faces cancellation.

► government was no longer interested in experiments requiring whole-lake manipulation. The 17 ELA staff at the institute, including four scientists, who are employed by the Department of Fisheries and Oceans (DFO), were told that their positions will be axed as of April 2013.

### LAKES WITH A HISTORY

Critics charge that the move reflects a broader hostility towards environmental science within the federal government. But Dave Gillis, director-general for ecosystem science at the DFO, maintains that the decision to cut the ELA's funding came down to priorities for spending at a time of fiscal restraint. In the federal government's budget released in March 2012 all departments faced reductions. The DFO's base budget of Can\$1.36 billion will drop by 5.8% (Can\$79.3 million) by 2015. ELA supporters argue that the facility's small budget and high scientific value should prevent it from being a casualty. Its annual operating costs run to Can\$600,000, half of which is covered by Environment Canada, a separate department of the government, which has also cancelled its funding. Another Can\$1.2 million to 1.5 million from the DFO covers salaries.

The origin of the ELA dates back to the 1960s, when blooms of blue-green algae covered Lake Erie, and commercial and sport fish started to die off. Two enterprising scientists — Wally Johnson, the first director of the Freshwater Institute, and Ronald Hayes, chairman of the Fisheries Research Board of Canada (a precursor to the DFO) — told the Canadian and Ontario governments that they might be able to make sense of the problem if they could deliberately pollute a whole lake with fertilizer, thought to be the driver of the algal overgrowth that was starving Lake Erie of oxygen. In 1969, they got their wish, and began the experimental enrichment of Lake 227, one of several small, isolated lakes in an area that is underlain with impermeable bedrock that

effectively contains the water and pollutants.

The study continued until the mid-1970s, and eventually included seven lakes. The most striking results emerged from Lake 226, where the researchers raised a plastic curtain across the narrow waist of the double-lobed lake and began adding carbon and nitrogen to one side and carbon, nitrogen and phosphorus to the other. The phosphorus side developed such a blanket of blue-green algae that it turned a stomach-churning chartreuse colour. "Those lake experiments are pretty well the thing that convinced politicians that we needed to control phosphate in detergents and sewage," says David Schindler, an ecologist at the University of Alberta, Edmonton, and one of the ELA's founding scientists. Canada and several US states have since banned phosphates from laundry and dishwasher detergents.

Since then, ELA scientists have dripped pollutants such as mercury, synthetic oestrogen and sulphuric acid into the lakes to explore their chemical impacts. They've built dams, constructed fish farms and drained wetlands to study the environmental outcomes of reservoir construction, aquaculture and climate change. The results have guided lawmakers in Canada and the United States to regulate sulphur dioxide and mercury emissions. "It's easy for regulatory agencies to dismiss research done in a lab, but it's less easy to dismiss work

done in whole lakes," says Metcalfe. "People sit up and take notice."

These studies are now in jeopardy. This autumn, ELA scientists had planned to launch the second phase of an experiment designed to explore the ecological impact of transgenic fish, which might be used in future aquaculture. Domestic fish dosed with growth hormones would have served as proxies for the fast-growing transgenic varieties in experiments designed to study the effects of an accidental escape. Following this, the plan was to carry out a controlled release of transgenic fish by 2015. "The government should have a group of people to do the science that provides the evidence to direct environmental policy," says a DFO researcher, who asked to remain anonymous.

The timing of the announcement has ELA researchers confused. Several ELA projects received internal grants shortly before the defunding announcement. And the ELA's new Can\$850,000 fish biology laboratory — paid for by the federal government — has been open for just one field season.

Gillis, charged with finding a new benefactor, sets his sights on the universities. The DFO has said that it believes universities are better suited to conduct whole-lake ecosystem research. George Dixon, an aquatic toxicologist and vice-president for research at the University of Waterloo, Ontario, took part in discussions with the DFO in June. He says that the universities are cataloguing ELA research projects and sourcing budget details. "What will we use it for and how do we go about paying for it? We have to be very sure that we are going to get benefits in the future," he says. A meeting with the DFO will take place in September.

Many doubt that a new operator will be in place by next April, when the government funding expires — and some are dubious that one will be found at all. "Where's the money going to come from? Universities are barely getting by," says John Smol, a limnologist at Queen's University in Kingston, Ontario.

Another complication is that any new operator of the ELA could be liable for cleaning up the site. Legal documents show that any remediation, as well as the eventual rehabilitation of the lakes, watersheds, streams and land, is currently the responsibility of the federal government. Gillis says that the DFO has no estimate for that work. Diane Orihel, a graduate student in ecology at the University of Alberta, and the leader of a coalition to save the ELA, says that her research points towards a bill of tens of millions of dollars. "In terms of liability, universities are not interested in that," says Dixon.

Over coffee in the ELA lounge, Metcalfe says that he doesn't know if he should prepare Lake 222 for next summer's experiments. Yet he remains optimistic. "My hope is that there will be some sort of compromise between government agencies, universities and foundations," he says. ■



## GENETICS

# Fathers bequeath more mutations as they age

Genome study may explain links between paternal age and conditions such as autism.

BY EWEN CALLAWAY

In the 1930s, the pioneering geneticist J. B. S. Haldane noticed a peculiar inheritance pattern in families with long histories of haemophilia. The faulty mutation responsible for the blood-clotting disorder tended to arise on the X chromosomes that fathers passed to their daughters, rather than on those that mothers passed down. Haldane subsequently proposed<sup>1</sup> that children inherit more mutations from their fathers than their mothers, although he acknowledged that “it is difficult to see how this could be proved or disproved for many years to come”.

That year has finally arrived: whole-genome sequencing of dozens of Icelandic families has at last provided the evidence that eluded Haldane. Moreover, a study published in *Nature* finds that the age at which a father sires children determines how many mutations those offspring inherit<sup>2</sup>. By starting families in their thirties, forties and beyond, men could be increasing the chances that their children will develop autism, schizophrenia and other diseases often linked to new mutations. “The older we are as fathers, the more likely we will pass on our mutations,” says lead author Kári Stefánsson, chief executive of deCODE Genetics in Reykjavik. “The more mutations we pass on, the more likely that one of them is going to be deleterious.”

Haldane, working years before the structure of DNA was determined, was also correct about why fathers pass on more mutations. Sperm is continually being generated by dividing precursor cells, which acquire new mutations with each division. By contrast, women are born with their lifelong complement of egg cells.

Stefánsson, whose company maintains genetic information on most Icelanders, compared the whole-genome sequences of 78 trios of a mother, father and child. The team searched for mutations in the child that were not present in either parent and that must therefore have arisen spontaneously in the egg, sperm or embryo. The paper reports the largest such study of nuclear families so far.

Fathers passed on nearly four times as



Older fathers' sperm have more mutations — as do their children.

many new mutations as mothers: on average, 55 versus 14. The father's age also accounted for nearly all of the variation in the number of new mutations in a child's genome, with the number of new mutations being passed on rising exponentially with paternal age. A 36-year-old will pass on twice as many mutations to his child as a man of 20, and a 70-year-old eight times as many, Stefánsson's team estimates.

The researchers estimate that an Icelandic child born in 2011 will harbour 70 new mutations, compared with 60 for a child born in 1980; the average age of fatherhood rose from 28 to 33 over that time.

Most such mutations are harmless, but Stefánsson's team identified some that studies have linked to conditions such as autism and schizophrenia. The study does not prove that older fathers are more likely than younger ones to pass on disease-associated or other deleterious genes, but that is the strong implication,

Stefánsson and other geneticists say.

Previous studies have shown that a child's risk of being diagnosed with autism increases with the father's age. And a trio of papers<sup>3–5</sup> published this year identified dozens of new mutations implicated in autism and found that the mutations were four times more likely to originate on the father's side than the mother's.

The results might help to explain the apparent rise in autism spectrum disorder: this year, the US Centers for Disease Control and Prevention in Atlanta, Georgia, reported that one in every 88 American children has now been diagnosed with autism spectrum disorder, a 78% increase since 2007. Better and more inclusive autism diagnoses explain some of this increase, but new mutations are probably also a factor, says Daniel Geschwind, a neurobiologist at the University of California, Los Angeles. “I think we will find, in places where there are really old dads, higher prevalence of autism.”

However, Mark Daly, a geneticist at Massachusetts General Hospital in Boston who studies autism, says that increasing paternal age is unlikely to account for all of the rise in autism prevalence. He notes that autism is highly heritable, but that most cases are not caused by a single new mutation — so there must be predisposing factors that are inherited from parents but are distinct from the new mutations occurring in sperm.

Historical evidence suggests that older fathers are unlikely to augur a genetic meltdown. Throughout the seventeenth and eighteenth centuries, Icelandic men fathered children at much higher ages than they do today, averaging between 34 and 38. Moreover, genetic mutations are the basis for natural selection, Stefánsson points out. “You could argue what is bad for the next generation is good for the future of our species,” he says. ■

SEE NEWS AND VIEWS, P467 AND ARTICLE, P471

➔ **NATURE.COM**  
Hear more about  
this research on the  
Nature Podcast:  
[go.nature.com/lq2dhy](http://go.nature.com/lq2dhy)

1. Haldane, J. B. S. *Ann. Eugen.* **13**, 262–271 (1947).
2. Kong, A. *et al. Nature* **488**, 471–475 (2012).
3. Sanders, S. J. *et al. Nature* **485**, 237–241 (2012).
4. O’Roak, B. J. *et al. Nature* **485**, 246–250 (2012).
5. Neale, B. M. *et al. Nature* **485**, 242–245 (2012).

V. PEÑAFIEL/FUCKR/GETTY





Supporters say they will fight to make sure that the Sun doesn't set on the Green Bank Telescope.

## ASTRONOMY

# US telescopes face up to agency cuts

*Six observatories run by the National Science Foundation should be jettisoned in favour of new facilities, says panel.*

BY ERIC HAND

When the economist Joseph Schumpeter coined the term creative destruction, he wasn't talking about telescopes. But it is a process that the US National Science Foundation (NSF) will soon be familiar with, as it seeks to shed obligations to existing astronomical observatories to make way for new ones.

On 16 August, a panel of external scientists — charged with balancing the NSF astronomy division's facilities portfolio in the face of a tougher budget climate — released its report at a meeting at the agency's headquarters in Arlington, Virginia. Its recommendations amount to a dramatic divestment of assets, including six NSF observatories, by 2017.

Four of the telescopes sit atop Kitt Peak in Arizona: the 4-metre Mayall Telescope; the 3.5-metre Wisconsin–Indiana–Yale–National Optical Astronomy Observatory (NOAO) Telescope, or WIYN; a separate 2.1-metre telescope; and the 1.6-metre McMath–Pierce Solar Telescope. The other two are radio observatories: the 110-metre Green Bank Telescope in West Virginia, the world's largest steerable dish antenna; and the Very Long Baseline Array (VLBA), a collection of ten dishes in various locations. James Ulvestad, director of the NSF's

Division of Astronomical Sciences, hopes to find new operators for the telescopes within 18 months. Only after that would the agency begin to consider closure or mothballing.

The recommendation is aimed at freeing up the US\$20 million that is currently spent on running the facilities — an amount drawn directly from the budget of the NSF astronomy division — and which creates a strain on grant programmes. “That pressure is quite real,” says Daniel Eisenstein, an astronomer at Harvard University in Cambridge, Massachusetts, and chairman of the portfolio-review panel.

Another strong motivator was the need to preserve support for two future survey telescopes in Chile: the 8-metre optical Large Synoptic Survey Telescope and the Cerro Chajnantor Atacama Telescope, a 25-metre submillimetre-range telescope. “Unless you do this trimming, you can't do new things,” says Michael Turner, director of the Kavli Institute for Cosmological Physics at the University of Chicago in Illinois.

But the loss of publicly funded telescopes means that it will be tougher for astronomers who are affiliated with universities that don't have access to other observatory facilities. For example, the Mayall telescope currently offers 300 nights a year of public-access time. “It's not good for the have-nots,” says David Silva,

director of the NOAO in Tucson, Arizona.

Silva was already in the process of courting a new partner for the Mayall telescope. The US Department of Energy is considering whether to build a special instrument, called BigBOSS, that would allow the Mayall to observe 20 million galaxies in the hunt for dark energy, which is speeding up the expansion of the Universe. BigBOSS principal investigator David Schlegel, of Lawrence Berkeley National Laboratory in California, was hoping to rally the energy department's support for the instrument while the NOAO continued to pay for operations. He says that if the department were to become the sole operator of the telescope, BigBOSS could complete its survey in three-and-a-half years rather than five, because the Mayall would no longer have to allocate time to other projects. Paying a few million dollars a year in operations costs would be offset by performing the survey more quickly, he says.

Silva notes that finding operators for the other telescopes on Kitt Peak will be more difficult. Small and state-funded universities are as cash-strapped as the government, he says, and private universities with deeper pockets are trying to raise money to help to fund new 30-metre-scale telescopes.

Anthony Beasley, director of the National Radio Astronomy Observatory (NRAO) in Charlottesville, Virginia, says that a move by the NSF towards total divestment could damage the NRAO's efforts to find partial support for its facilities among new partners. “They've kind of stuck a spear in our side,” he says. He notes that, of the \$5.5 million in annual operating costs for the VLBA, \$2 million already comes from foreign partners. New ones may be reluctant to join if they know that the NSF wants to divest of the facility completely, he argues.

Beasley says that he is most surprised by the decision to target the recently refurbished Green Bank Telescope, which was reopened in 2000. Others doubt whether the NSF could ever shut down the observatory, which has strong support from Senator Jay Rockefeller (Democrat, West Virginia), who also chairs the Senate committee on commerce, science and transportation. In a statement, Rockefeller said: “The needs for this observatory are clear and I will work to make sure it remains open.”

The portfolio-review panel worked with two budget scenarios: one in which future budgets would remain relatively flat, and another that was far gloomier, with a 20% drop by mid-decade from 2011 fiscal year levels. The panel recommended that the NSF should divest of the six facilities under both scenarios. Under the more optimistic scenario, it said, money saved from divestment should be used to augment research-grant budgets. Given the short-term vagaries of the budget and the difficulties of making long-term decisions on facilities, planning for cuts is probably wise, says Turner. “Predicting budgets is harder than predicting the future of the Universe,” he notes. ■

H. MORTON/AU/NRAO



## US ELECTION

# Republican spending plan casts shadow on science

*Romney's running mate, Paul Ryan, wants to curb expenditure on non-defence research.*

BY AMY MAXMEN

When the spotlight falls on Tampa, Florida, next week for the US Republican National Convention, science will not be an obvious part of the agenda. Delegates can expect to hear about the need to cut the federal deficit, reduce spending and limit government — all key positions for the fiscally conservative party and for Mitt Romney, who will be nominated as its presidential candidate at the convention.

The Republicans' economic message is familiar, but some research advocates warn that if Romney wins the general election on 6 November, it could translate into a pronounced shift in the US government's approach to science. They fear the party will reduce the overall budget for research, shift its emphasis, and target regulations it sees as hampering economic growth.

"In general, conservatives believe that society has been over-regulated and that there are areas to be cut back in order to be improved," says Kenneth Green, a fiscally conservative resident scholar at the American Enterprise Institute, a think tank in Washington DC.

Romney's choice of Wisconsin congressman Paul Ryan as his running mate is the latest sign that the party is ready to push for big changes. As chairman of the House of Representatives budget committee in the current Congress, Ryan has crafted a federal spending plan that contrasts sharply with that of President Barack Obama, whose budget requests have largely maintained science and technology funding as an economic investment.

If carried out, Ryan's plan could cut spending on non-defence-related research and development by 5%, or \$3.2 billion, below the President's 2013 request, according to the American Association for the Advancement of Science.



Paul Ryan aims to limit government's reach.

Over the long term, Ryan's small-government approach would shrink funding for research and development to historically small sizes.

Ryan's spending caps would also represent a change in emphasis in the type of science that is supported. Although Ryan's economic plan voices support for "basic research and development", it would pare back spending in applied research and projects "best left to the private sector". Science advocates worry that this might include research such as clinical trials sponsored by the National Institutes of Health for therapies from which the drug industry would be unlikely to profit. Ryan's budget proposals have won the support of the Republican-led House, but they have been blocked by the Senate, where Democrats hold a slim majority.

"We are glad that Congressman Ryan and Governor Romney have acknowledged the importance of funding basic research as a core government function, but we are extremely concerned that Ryan's budget appears to reflect the opposite," says Mary Woolley, president of

Research!America, a science-advocacy group based in Alexandria, Virginia.

"Governor Romney understands that innovation is crucial to our prosperity," a campaign spokeswoman told *Nature*. She also noted that Romney has emphasized the need to attract and retain people with advanced degrees in science-related disciplines by expanding the availability of visas for skilled immigrants.

In selecting Ryan as his running mate, Romney has shifted his campaign towards those in his party who support limiting the government's reach. For example, even among his Republican colleagues in the House, Ryan stands out in his opposition to environmental regulation. According to the League of Conservation Voters, an environmental-advocacy group based in Washington DC, Ryan was among the 16 of 242 House Republicans who voted against almost all of the environmental actions that the league considered priorities in 2011. In addition to opposing funding for the listing of plants and animals under the Endangered Species Act and Obama's push for the development of alternative-energy technologies, Ryan, through his budget plan, takes aim at the Environmental Protection Agency for its measures to regulate carbon emissions.

Ryan has also taken a hard line on the US Food and Drug Administration (FDA) — for example, by voting against a food-safety bill that expands the agency's role in detecting food contaminated by pathogens such as *Salmonella*. He also voted to exempt tobacco products from the agency's oversight and to repeal legislation appropriating funds for preventive-health programmes.

"If the way to show your cred is by attacking regulation, that's not a good outcome for science agencies," says William Hubbard, a former FDA associate commissioner. ■



## NEWS

- Nerve-growth protein linked to ovulation [go.nature.com/9zk9yz](http://go.nature.com/9zk9yz)
- Dextrous four-fingered robot manages to replace batteries in a torch [go.nature.com/qgoffk](http://go.nature.com/qgoffk)
- Photosynthesis-like process found in insects [go.nature.com/bq783q](http://go.nature.com/bq783q)

## VIDEO



Curiosity rover takes its first look at Mars [go.nature.com/qeuxhl](http://go.nature.com/qeuxhl)

## BLOG

- Blood cells converted into chemical sensors [go.nature.com/dxjvtj](http://go.nature.com/dxjvtj)
- 'Virus-like' nanoparticle built to target tumours [go.nature.com/gzcez2](http://go.nature.com/gzcez2)
- D-Wave quantum computer solves protein-folding problem [go.nature.com/ggaajh](http://go.nature.com/ggaajh)



Features on Vesta can be located using two coordinate systems — the subject of scientific wrangling.

## PLANETARY SCIENCE

# Space missions trigger map wars

*Planetary explorers rebel against nomenclature protocols.*

BY ERIC HAND

When NASA's Dawn spacecraft departs from Vesta on 26 August, it will have mapped the second-most-massive object in the Solar System's asteroid belt in unprecedented detail, revealing a diverse, planet-like body with sheer cliffs and deep craters.

But don't ask for the latitude and longitude of those features. The mission team is embroiled in a dispute with the International Astronomical Union (IAU) in Paris over which coordinate system to use, and where to place the prime meridian from which longitude will be measured. At the moment, the groups each have their own meridians, separated by 155°: nearly half a world. "It's an untenable

situation to have an outside group that has no ownership, no belonging to the project, impose arbitrary things," says Chris Russell, Dawn's principal investigator and a planetary scientist at the University of California, Los Angeles.

Brent Archinal, chairman of the IAU working group responsible for coordinate systems, says that the Dawn team is welcome to use an alternate system for its own purposes. "That's not what's happening. They're saying theirs is the only system," says Archinal, a geodesist at the US Geological Survey in Flagstaff, Arizona.

The feud shows how the conquering instinct of a mission team sometimes falls foul of rules established by the IAU, which emerged as the arbiter of planetary names and coordinate systems during the early years of space exploration. Back then, standardization helped to

prevent the Solar System from being plastered with conflicting sets of names used by Soviet and US scientists. These days, the tensions are less nationalistic and more interdisciplinary: a dust-up between the geologists who tend to lead planetary missions and the astronomers who comprise much of the IAU. "Why should I let astronomers name things just because they're on another planet?" asks Mike Malin, a geologist and principal investigator for the mast camera on NASA's Curiosity rover mission, which has generated its own conflict with the IAU over the naming of a feature at its Martian landing site. "It's anachronistic," adds Malin.

The IAU's coordinate system for Vesta is based on observations from NASA's Hubble Space Telescope. It was published<sup>1</sup> in 1997, and puts the prime meridian at the centre of Olbers Regio, a dark, circular region 200 kilometres across.

After Dawn began orbiting Vesta in July 2011, the mission team found that the rotational pole in the IAU's system was off by as much as 10°. The team established its own coordinate system, which not only corrected the pole, but also focused the prime meridian on Claudia, a 700-metre crater. The Dawn team says that Claudia can be defined much more precisely than Olbers, and that its system produces more logical mapping quadrangles. NASA has released images that refer to the Claudia system, and the Dawn team has published papers using it, including a suite of articles<sup>2-7</sup> that appeared in *Science* in May.

The Claudia system is not acceptable to the IAU, which states in its guidelines<sup>8</sup> that changes to any established coordinate system should be avoided unless there has been a loss or change to the meridian-defining feature. But Russell says that the Dawn team will continue to publish using Claudia: "We cannot afford to change to a new coordinate system."

Michael A'Hearn, a planetary scientist at the University of Maryland in College Park, is trying to find a compromise. A member of the IAU working group, A'Hearn is also in charge of the part of the NASA database that will host Dawn data for the public — and he says that the data must use an IAU-sanctioned coordinate system. He suggests rotating the Claudia system by 155°, to put the prime meridian within one degree of the centre of Olbers Regio. That would preserve the pole correction but keep the meridian close enough to Olbers to satisfy the IAU rules.

Mark Sykes, director of the Planetary Science Institute in Tucson, Arizona, and a co-investigator on Dawn, says that the entire episode is silly and counterproductive: "Now we're going to have three systems in the literature." But he is not too surprised.

"When an organization sets itself up as the holy mother church," he says, "you're always going to get heretics."

**NATURE.COM**  
For ongoing coverage of the Curiosity mission, see: [nature.com/curiosity](http://nature.com/curiosity)



Such disputes are unlikely to hinder science in the long run, but they can sow short-term confusion. Mars, which has been visited more than any other Solar System body in the past two decades, offers several examples. The latest concerns Curiosity, which touched down on 6 August.

The rover's chief target is a 5.5-kilometre-tall mountain in the middle of Gale crater<sup>9</sup>. Early this year, the mission's science team asked the IAU to name the feature Mount Sharp, after Robert Sharp, a planetary geologist at the California Institute of Technology (Caltech) in Pasadena, who died in 2004. But that fell foul of the IAU rule book. Brad Smith, a retired astronomer and chairman of the IAU's Mars task group, points out that large features such as mountains must be named in Latin, after nearby light and dark features discerned on Mars by nineteenth-century astronomers. In May, the mountain was granted such a name: Aeolis Mons. (Craters can be named after people, however, so Sharp got a 152-kilometre crater just west of Gale.)

But the NASA team has been referring to the mound as Mount Sharp in public discussions and press releases. Curiosity project scientist John Grotzinger, a Caltech geologist, says he is "not trying to break the law" — rather, he wanted a user-friendly name similar to that of Mars's Columbia Hills, which were named to commemorate the 2003 space-shuttle disaster soon after they were discovered by NASA's Spirit rover in 2004. Smith says that the hills are big enough to get an official name, but none was ever requested, so the informal name stuck.

In future, says Grotzinger, the Curiosity team will use Aeolis Mons on official maps, and will indicate in publications that Mount Sharp is an informal name.

That is fine with Smith, who points out that the Curiosity team can do whatever it wants in an unofficial capacity. "There's perhaps more drama being made about all this by the media than meets reality," he says. ■

1. Thomas, P. C. *et al.* *Icarus* **128**, 88–94 (1997).
2. Russell, C. T. *et al.* *Science* **336**, 684–686 (2012).
3. Jaumann, R. *et al.* *Science* **336**, 687–690 (2012).
4. Marchi, S. *et al.* *Science* **336**, 690–694 (2012).
5. Schenk, P. *et al.* *Science* **336**, 694–697 (2012).
6. De Sanctis, M. C. *et al.* *Science* **336**, 697–700 (2012).
7. Reddy, V. *et al.* *Science* **336**, 700–704 (2012).
8. Archinal, B. A. *et al.* *Celest. Mech. Dyn. Astr.* **109**, 101–135 (2011).
9. Hand, E. *Nature* **488**, 262–263 (2012).

## POLICY

# Companies set to fight food-label plan

*California's Proposition 37 would add labels to all foods made from genetically modified crops.*

BY MONYA BAKER

A battle over genetically modified (GM) foods in California is turning into an expensive war. Agribusinesses and food manufacturers last week pledged US\$13 million to the campaign against a proposition that would require food to carry labels noting its GM content.

The money swells the opponents' coffers to \$25 million, promising months of campaigning before the public vote on the proposal in November. Supporters of Proposition 37, including organic farmers and environmentalists, have so far raised less than \$2.5 million.

Those in favour of labelling argue that the public has the right to know what is in their food, citing food-safety concerns and a general mistrust of corporate interests in agriculture. Opponents say that the labels will be perceived as warnings, stoking consumer hostility to genetic engineering. They also argue that the move would raise food costs, and expose grocers, farmers and food manufacturers to frivolous lawsuits for incorrect labelling.

Similar labelling proposals have failed in other states, but a victory in California could set a national precedent. "If the ballot initiative passes, it would mark a turning point for public activism in the United States," says Charles Benbrook, chief science consultant at the Organic Center, an organic farming advocacy group in Troy, Oregon.

Labelling would certainly have far-reaching consequences: around 94% of the soya beans and 88% of the maize (corn) grown in the United States is genetically engineered to resist herbicides, insect pests or both, according to the US Department of Agriculture. The plan could affect tens of thousands of brand-name products, and food manufacturers Coca-Cola, PepsiCo and Nestlé have each contributed more than \$1 million to the campaign; meanwhile, agribusinesses DuPont and Monsanto have chipped in more than \$4 million apiece.

The labels would not reflect how the crops have been modified, or the quantity of GM ingredients in a food.

➔ **NATURE.COM**  
Can science feed the world?

[go.nature.com/vt3rqo](http://go.nature.com/vt3rqo)

Meat from animals fed on GM crops would not need to be labelled.

Bob Goldberg, a plant

geneticist at the University of California, Los Angeles, says the proposition is "anti-science", and could discourage research to develop drought-tolerant crops and more nutritious foods. Studies by the US National Academies<sup>1</sup> and Britain's Royal Society of Medicine<sup>2</sup> found no evidence that biotech crops are unsafe to eat. And, in June, the American Medical Association said that there was no scientific reason to label GM foods, but recommended that long-term studies should be vigilant for any health effects. Benbrook says that, far from being anti-science, the labelling could support health studies by helping to track people's food choices.

Pro-GM plant scientists also point out that the crops can benefit the environment by enabling farmers to use less-toxic herbicides and reduce insecticide use. But proponents of labels say that these benefits are temporary, and point to studies showing that weeds and insects have evolved resistance to the modified crops<sup>3</sup>. Seed companies can counter this by engineering new crops that are resistant to additional herbicides — such as a new soya bean developed by Dow AgroSciences of Indianapolis, Indiana — something that Benbrook argues will actually increase herbicide use.

In a poll earlier this month, 69% of Californians supported the proposition, and a national survey by Thomson Reuters in 2010 found that 93% of respondents wanted labels. But opinions can change: earlier this year, a cigarette tax that would have funded disease research was narrowly defeated at the ballot after 67% of voters initially supported it. That change of heart coincided with the cigarette lobby spending an estimated \$50 million on campaigning. Benbrook predicts that even more money will be thrown at the anti-GM-labelling campaign. ■

1. National Research Council *Safety of Genetically Engineered Foods* (National Academies Press, 2004).
2. Key, S. *et al.* *J. R. Soc. Med.* **101**, 290–298 (2008).
3. Mortensen, D. A. *et al.* *BioScience* **62**, 75–84 (2012).

## CORRECTION

The News story 'Heatwaves blamed on global warming' (*Nature* **488**, 143–144; 2012) should have said that the paper by Trenberth's team will appear in the *Journal of Geophysical Research*.





# THE BRAINMAKER

BY DAVID CYRANOSKI

*With his knack for knowing what stem cells want, Yoshiki Sasai has grown an eye and parts of a brain in a dish.*

**I**n December 2010, Robin Ali became suddenly excited by the usually mundane task of reviewing a scientific paper. “I was running around my room, waving the manuscript,” he recalls. The paper described how a clump of embryonic stem cells had grown into a rounded goblet of retinal tissue. The structure, called an optic cup, forms the back of the eye in a growing embryo. But this one was in a dish, and videos accompanying the paper showed the structure slowly sprouting and blossoming. For Ali, an ophthalmologist at University College London who has devoted two decades to repairing vision, the implications were immediate. “It was clear to me it was a landmark paper,” he says. “He has transformed the field.”

‘He’ is Yoshiki Sasai, a stem-cell biologist at the RIKEN Center for Developmental Biology in Kobe, Japan. Sasai has impressed many researchers with his green-fingered talent for

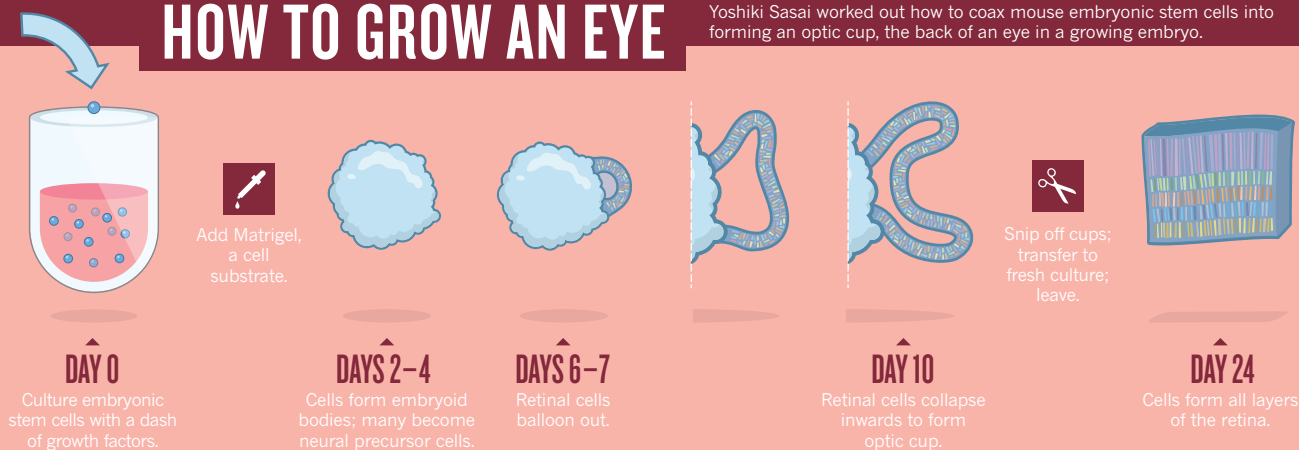
coaxing neural stem cells to grow into elaborate structures. As well as the optic cup<sup>1</sup>, he has cultivated the delicate tissue layers of the cerebral cortex<sup>2</sup> and a rudimentary, hormone-making pituitary gland<sup>3</sup>. He is now well on the way to growing a cerebellum<sup>4</sup> — the brain structure that coordinates movement and balance. “These papers make for the most addictive series of stem-cell papers in recent years,” says Luc Leyns, a stem-cell scientist at the Free University of Brussels.

Sasai’s work is more than tissue engineering: it tackles questions that have puzzled developmental biologists for decades. How do the proliferating stem cells of an embryo organize themselves seamlessly into the complex structures of the body and brain? And is tissue formation driven by a genetic program intrinsic to cells, or shaped by external cues from neighbouring tissues? By combining intuition with patient trial and error, Sasai has found that it takes a delicate

HANS SAUTTER

# HOW TO GROW AN EYE

Yoshiki Sasai worked out how to coax mouse embryonic stem cells into forming an optic cup, the back of an eye in a growing embryo.



balance of both: he concocts controlled environments that feed cells physical and chemical signals, but also gives them free rein to ‘do their thing’ and organize themselves into issues. He sometimes refers to himself as a Japanese matchmaker who knows that, having been brought together, two strangers need to be left alone. “They know what to do,” he says. “They interact in a delicate manner, and if the external cues are too strong, it will override the internal ones.”

Sasai’s work could find medical applications. Recapitulating embryonic development in three dimensions, it turns out, generates clinically useful cells such as photoreceptors more abundantly and efficiently than two-dimensional culture can, and houses them in an architecture that mirrors that of the human body. Sasai and his collaborators are now racing to implant lab-grown retinas into mice, monkeys and humans. The way Sasai sees it, maturing stem cells in two-dimensional culture may lead to ‘next generation’ therapy — but his methods will lead to ‘next, next generation’ therapy.

## SELF-DETERMINED

A bit stiff in movement and reserved in manner, Sasai nevertheless puts on a theatrical show with a cocktail shaker at parties held by his institute after international symposia. “My second job is bartender,” he says, without a trace of a smile. It is, however, the cocktails he mixes in 96-well culture plates that have earned him scientific acclaim.

Like many members of his family, Sasai studied medicine. But he soon became frustrated by the lack of basic understanding in the field, especially when it came to neurological conditions. “Without knowing the brain, a doctor cannot do much for the patient and therapeutics will always be superficial,” he recalls thinking. There seemed no better way to know the brain than to study how it emerges and folds in the embryo. “It’s complex and usually complex systems are messy,” says Sasai. “But it’s one of the most ordered.” He wanted to know how this elaborate system was controlled.

One piece of the puzzle was well known: the Spemann organizer, a node in vertebrate embryos that induces surrounding cells to become neural tissue. How the organizer works had been a mystery since its discovery in 1924; to find out, Sasai accepted a postdoctoral position at the University of California, Los Angeles. The post got off to a difficult start when Sasai was robbed of his money and passports at the airport on his way to California. But his scientific efforts were soon rewarded. “He replaced the passports

and within a month produced the clones that gave us the famous gene *chordin*,” says his supervisor, developmental biologist Eddy De Robertis.

Sasai and his colleagues discovered that the chordin protein is a key developmental signal released by the Spemann organizer<sup>5</sup>. Rather than pushing nearby cells to become neurons, they found, chordin blocks signals that would turn them into other cell types<sup>6,7</sup>. The work helped to establish the default model of neural induction: the idea that, without other signals, embryonic cells will follow an internal program to become neural cells.

By the late 1990s, embryonic-stem-cell scientists were also looking at these signals. They wanted to turn stem cells into mature cell types — particularly neurons — that might lead to therapies. The problem, says Sasai, is that scientists generally “push too hard and perturb the system”. Sasai knew that in the embryo, subtracting signals from the system is what counts, not perturbing it. “We tried to minimize external cues,” he says.

Sasai built an experimental system around that philosophy. He threw out the serum usually added to growing embryonic stem cells, which contains a brew of uncharacterized growth factors and other signalling molecules. He also removed physical cues, such as contact with the plastic surfaces of a culture dish, by allowing embryonic stem cells to spontaneously form floating aggregates known as embryoid bodies. “If they’re attached, they’re like prisoners and can’t act out their own desires,” he says. Keeping the cells alive without these support systems was a challenge but, five years of careful experimentation later, Sasai published<sup>8</sup> and later patented his serum-free embryoid body culture — a pared-down life-support system with just the right mixture of ingredients for cells to survive. It would go on to form the heart of his brain-tissue factory.

## TAILOR-MADE

Embryoid bodies in Sasai’s system quickly become what he calls “brain balls” — populated with neural precursor cells. Sasai found that balls left entirely alone give rise to cells like those in the developing brain region called the hypothalamus<sup>9</sup>, but those given just a whiff of growth factors start differentiating into cerebral-cortex cells<sup>2</sup>. And when Sasai cultured the cells for about two weeks, he got a surprise: the cortical cells spontaneously started to form a layered structure that ended up strikingly similar to the cortex of a 15-day-old mouse. When transplanted into the brain of a newborn mouse, the structure survived. “That’s what we do,” says Sasai. “We set up the permissive conditions, selecting

“IN ENGLISH WHEN YOU ARE SURPRISED, YOU SAY ‘EYE POPPING’ — SO WE REALLY THOUGHT THIS WAS EYE-POPPING.”

**NATURE.COM**  
To watch a movie of optic cups growing, visit:  
[go.nature.com/xvbw7](http://go.nature.com/xvbw7)



“WE SET UP THE PERMISSIVE CONDITIONS. BUT AFTER THAT WE DON'T DO ANYTHING. KEEP THEM GROWING AND LET THEM DO THEIR JOB.”

the right medium and cell number. But after that we don't do anything. Keep them growing and let them do their job.”

The lab-grown cortex wasn't perfect, however: it had only four of the cerebral cortex's six cell layers, for example. Sasai thought that a retina — a layered tissue that sprouts from the embryonic brain and contains light-sensing photoreceptors — might be easier to grow. The retina is thinner than the cortex, forms earlier in embryo development and doesn't require a complex vascular system.

To adapt his system to a different type of tissue, Sasai makes minute changes to the culture conditions that nudge the cells down a developmental path. He genetically engineers fluorescent ‘reporter’ genes into the stem cells so that they are expressed when the cells differentiate into the desired type — in this case, retinal precursor cells — and reveal whether the system is working. “Our success depends on knowing how slight modifications can lead to dramatic change,” he says.

All it took to grow a retina, it turned out, were a few tweaks, such as a reduction in the concentration of growth factors and the addition of a standard cell-culture ingredient called Matrigel. The result closely mimics eye development in the embryo (see ‘How to grow an eye’). By the sixth day in culture, the brain balls start sprouting balloon-like growths of retinal cells, which then collapse in on themselves to make the double-walled optic cups. Sasai's team snip them off — “like taking an apple from a tree,” says Sasai — transfer them to a different culture and let them be. Two weeks later, the cups have formed all six layers of the retina, an architecture that resembles the eye of an 8-day-old mouse (which, at that age, is still blind). That the cells could drive themselves through this dramatic biomechanical process without surrounding tissues to support them<sup>1</sup> stunned Sasai as much as anyone else. “When I saw it, I thought, ‘Oh my god.’ Shape, topology and size are all recapitulated,” he says. Carefully explaining the pun to come, he adds: “In English, when you are surprised, you say ‘eye-popping’ — so we really thought this was eye-popping.”

Reproducing the results with human cells was the obvious, but not simple, next step. Peter Coffey, an ophthalmologist and neuroscientist at University College London, tried following Sasai's recipe to grow optic cups with human cells, and, as Coffey puts it, “failed catastrophically”. Sasai, who reported<sup>10</sup> this year that he had accomplished the feat, says that it took careful tweaks to accommodate the sensitivities of human embryonic stem cells. Because these cells grow three times slower than those from mice, for example, Sasai had to start with of 9,000 cells instead of 3,000. Coffey says that his experience made him realize how much expertise has been built up in Sasai's lab. “They've been doing it a long time. Good on 'em,” he says, with an air of good-natured jealousy.

## ALL EYES

All this will not create eyes that can be plugged into an eye socket like a light bulb into a lamp. Even if Sasai could get his optic cups to develop into mature retinas, researchers have little idea about how to wire a transplanted retina up to the brain.

What the work does offer is a potentially abundant source of pure, dense, well-organized photoreceptors, the developmental stage of which can be precisely selected — something that has been difficult to achieve in standard two-dimensional culture. Eventually, Sasai hopes, his optic cups will provide sheets of photoreceptors that can be inserted into a retina damaged by conditions such as retinitis pigmentosa or macular degeneration. Sasai demonstrates the procedure by grabbing a stack of papers to stand in for the retinal layers and then slipping one sheet between the others.

But linking the transplanted photoreceptors with the rest of the retina and with the brain will not be easy, as researchers working on eye stem-cell technologies have found. Robert Lanza, chief scientific officer of the stem-cell therapy company Advanced Cell Technology in Santa Monica, California, is sceptical. “I don't think we're anywhere near when we get those cells to connect up in any meaningful way,” he says.

Ali is more hopeful. In April, his team reported<sup>11</sup> that it had improved the vision of partially blind mice using transplants of photoreceptor precursor cells taken from mice a few days old. Ali and another of Sasai's collaborators, Masayo Takahashi at the RIKEN Center for Developmental Biology, are starting to extract sheets of photoreceptors that have been grown using Sasai's methods and transplant them into mice; Takahashi plans to transplant them into monkeys by the end of the year. Both are cagey about their early results, but Takahashi says that in mice, the transplanted photoreceptors “survived well”.

## HORMONAL CHALLENGE

Sasai has set his sights on more complex neural tissues. Last November, he reported<sup>3</sup> the formation of a part of the pituitary gland — his “most complicated” tissue yet. In the embryo, the pituitary gland arises when two different tissues integrate to form a pouchlike structure. Sasai managed to recapitulate this *in vitro* partly by starting out with more than three times more embryonic stem cells than he had used to grow a mouse retina; the adjustment seems to increase the levels of signals that the cells exchange. When transplanted into mice in which the pituitary glands had been knocked out, the rudimentary organs restored the endocrine system and saved the mice. This work, too, might eventually provide a supply of pure, specialized cells, which could be used to treat endocrine disorders.

Sasai hopes to improve on his early efforts by growing a better pituitary gland, equipped with a blood supply; a cerebral cortex with all six layers of tissue; and photoreceptors mature enough to detect light. But his next major task is to culture a cerebellum, which will involve growing and integrating three tissues of different embryonic origins. The matchmaker is already at work, trying to conjure up the right atmosphere. “When a boy meets a girl, they start their own story — but not in a large auditorium full of people,” he says. “You need to put them on a beach or in a disco. Our system is simply going to create this environment.”

What Sasai plans to take on after the cerebellum is a secret, but he hopes eventually to encompass the whole brain. He does not mean building one — that would be enormously difficult and ethically fraught. Instead, he wants to work out how brain parts, with their remarkable capacity for autonomous growth and organization, combine and fold into a structure of such tremendous complexity.

“I don't want to be a parts-maker, making more and more tissues,” says Sasai. “I always want something conceptually different.” ■

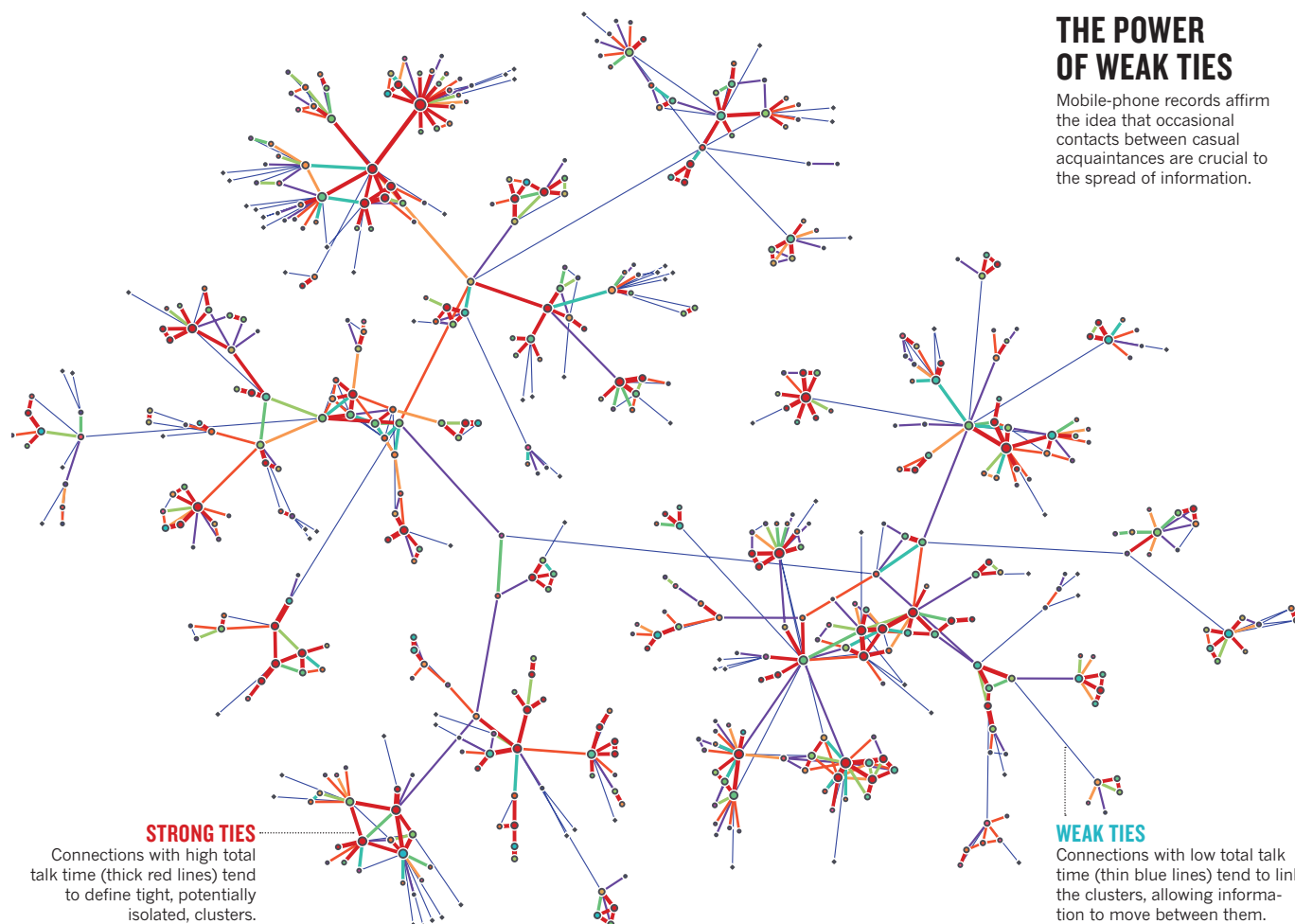
David Cyranoski is Nature's Asia-Pacific correspondent.

1. Eiraku, M. *et al. Nature* **472**, 51–56 (2011).
2. Eiraku, M. *et al. Cell Stem Cell* **3**, 519–532 (2008).
3. Suga, H. *et al. Nature* **480**, 57–62 (2011).
4. Muguruma, K. *et al. Nature Neurosci.* **13**, 1171–1180 (2010).
5. Sasai, Y. *et al. Cell* **79**, 779–790 (1994).
6. Piccolo, S., Sasai, Y., Lu, B. & De Robertis, E. M. *Cell* **86**, 589–598 (1996).
7. Sasai, Y., Lu, B., Steinbeisser, H. & De Robertis, E. M. *Nature* **376**, 333–336 (1995).
8. Watanabe, K. *et al. Nature Neurosci.* **8**, 288–296 (2005).
9. Wataya, T. *et al. Proc. Natl Acad. Sci. USA* **105**, 11796–11801 (2008).
10. Nakano, T. *et al. Cell Stem Cell* **10**, 771–785 (2012).
11. Pearson, R. A. *et al. Nature* **485**, 99–103 (2012).



## THE POWER OF WEAK TIES

Mobile-phone records affirm the idea that occasional contacts between casual acquaintances are crucial to the spread of information.



# MAKING THE LINKS

FROM E-MAILS TO SOCIAL NETWORKS, THE DIGITAL TRACES LEFT BY LIFE IN THE MODERN WORLD ARE TRANSFORMING SOCIAL SCIENCE.

BY JIM GILES

**J**on Kleinberg's early work was not for the mathematically faint of heart. His first publication<sup>1</sup>, in 1992, was a computer-science paper with contents as dense as its title: 'On dynamic Voronoi diagrams and the minimum Hausdorff distance for point sets under Euclidean motion in the plane'.

That was before the World-Wide Web exploded across the planet, driven by millions of individual users making independent decisions about who and what to link to. And it

was before Kleinberg began to study the vast array of digital by-products generated by life in the modern world, from e-mails, mobile phone calls and credit-card purchases to Internet searches and social networks. Today, as a computer scientist at Cornell University in Ithaca, New York, Kleinberg uses these data to write papers such as 'How bad is forming your own opinion?'<sup>2</sup> and 'You had me at hello: how phrasing affects memorability'<sup>3</sup> — titles that would be at home in a social-science journal.

"I realized that computer science is not just about technology," he explains. "It is also a human topic."

Kleinberg is not alone. The emerging field of computational social science is attracting mathematically inclined scientists in ever-increasing numbers. This, in turn, is spurring the creation of academic departments

and prompting companies such as the social-network giant Facebook, based in Menlo Park, California, to establish research teams to understand the structure of their networks and how information spreads across them.

"It's been really transformative," says Michael Macy, a social scientist at Cornell and one of 15 co-authors of a 2009 manifesto<sup>4</sup> seeking to raise the profile of the new discipline. "We were limited before to surveys, which are retrospective, and lab experiments, which are almost always done on small numbers of college sophomores." Now, he says, the digital data-streams promise a portrait of individual and group behaviour at unprecedented scales and levels of detail. They also offer plenty of challenges — notably privacy issues, and the problem that the data sets may not truly be reflective of the population at large.

Nonetheless, says Macy, "I liken the opportunities to the changes in physics brought about by the particle accelerator, and in neuroscience by functional magnetic resonance imaging".

## SOCIAL CALLS

An early example of large-scale digital data being used on a social-science issue was a study in 2002 by Kleinberg and David Liben-Nowell, a computer scientist at Carleton College in Northfield, Minnesota. They looked at a mechanism that social scientists believed helped drive the formation of personal relationships: people tend to become friends with the friends of their friends. Although well established, the idea had never been tested on networks of more than a few tens or hundreds of people.

Kleinberg and Liben-Nowell studied the relationships formed in scientific collaborations. They looked at the thousands of physicists who uploaded papers to the arXiv preprint server during 1994–96. By writing software to automatically extract names from the papers, the pair built up a digital network several orders of magnitude larger than any that had been examined before, with each link representing two researchers who had collaborated. By following how the network changed over time, the researchers identified several measures of closeness among the researchers that could be used to forecast future collaborations<sup>5</sup>.

As expected, the results showed that new collaborations tended to spring from researchers whose spheres of existing collaborators overlapped — the research analogue of 'friends of friends'. But the mathematical sophistication of the predictions has allowed them to be used on even larger networks. Kleinberg's former PhD student, Lars Backstrom, also worked on the connection-prediction problem — experience that he

has put to good use now that he works at Facebook, where he designed the social network's current friend-recommendation system.

Another long-standing social-science idea affirmed by computational researchers is the importance of 'weak ties' — relationships with distant acquaintances who are encountered relatively rarely. In 1973, Mark Granovetter, a social scientist now at Stanford University in Stanford, California, argued that weak ties form bridges between social cliques and so are important to the spread of information and to economic mobility<sup>6</sup>. In the pre-digital era it was almost impossible to verify his ideas at scale. But in 2007, a team led by Jukka-Pekka Onnela, a network scientist now at Harvard University in Cambridge, Massachusetts, used data on 4 million mobile-phone users to confirm that weak ties do indeed act as societal bridges<sup>7</sup> (see 'The power of weak ties').

In 2010, a second group, which included Macy, showed that Granovetter was also right about the connection between economic mobility and weak ties. Using data from

65 million landlines and mobile phones in the United Kingdom, together with national census data, they revealed a powerful correlation between the diversity of individuals' relationships and economic development: the richer and more varied their connections, the richer their communities<sup>8</sup> (see 'The economic link'). "We didn't imagine in the 1970s that we could work with data on this scale," says Granovetter.

## INFECTIOUS IDEAS

In some instances, big data have showed that long-standing ideas are wrong. This year, Kleinberg and his colleagues used data from the roughly 900 million users of Facebook to study contagion in social networks — a process that describes the spread of ideas such as fads, political opinions, new technologies and financial decisions. Almost all theories had assumed that the process mirrors viral contagion: the chance of a person adopting a new idea increases with the number of believers to which he or she is exposed.

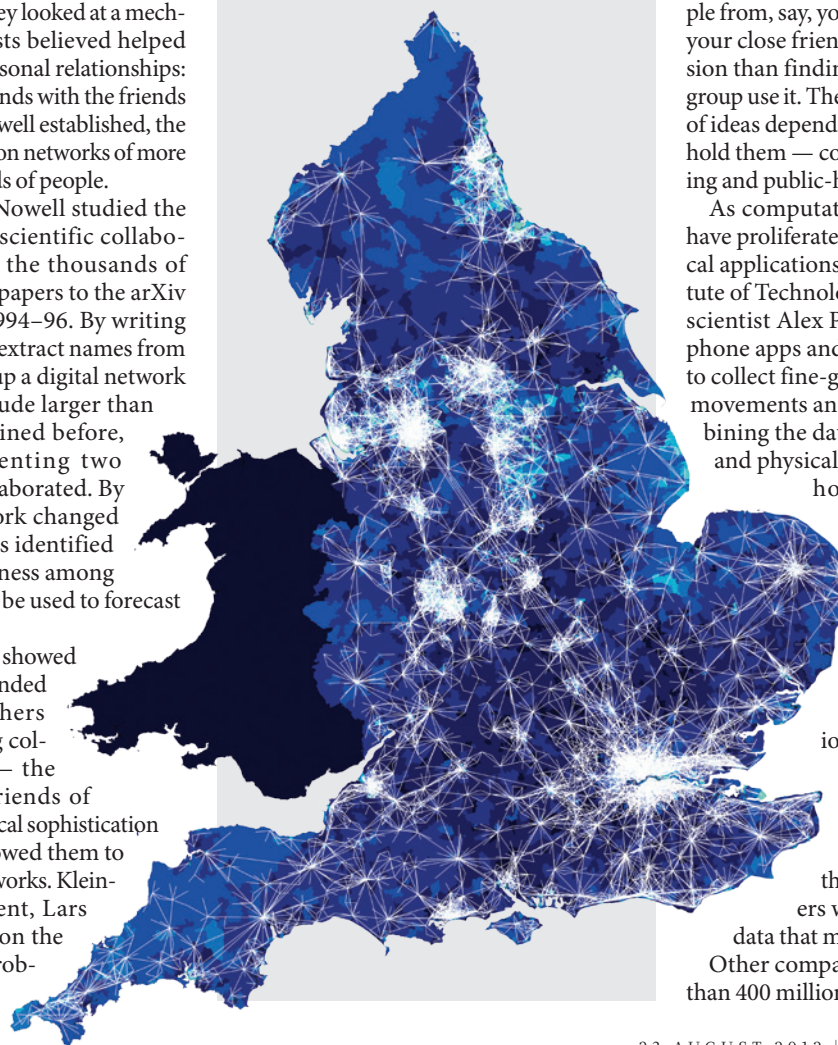
Kleinberg's student Johan Ugander found that there is more to it than that: people's decision to join Facebook varies not with the total number of friends who are already using the site, but with the number of distinct social groups those friends occupy<sup>9</sup>. In other words, finding that Facebook is being used by people from, say, your work, your sports club and your close friends makes more of an impression than finding that friends from only one group use it. The conclusion — that the spread of ideas depends on the variety of people that hold them — could be important for marketing and public-health campaigns.

As computational social-science studies have proliferated, so have ideas about practical applications. At the Massachusetts Institute of Technology in Cambridge, computer scientist Alex Pentland's group uses smartphone apps and wearable recording devices to collect fine-grained data on subjects' daily movements and communications. By combining the data with surveys of emotional and physical health, the team has learned

how to spot the emergence of health problems such as depression<sup>10</sup>. "We see groups that never call out," says Pentland. "Being able to see isolation is really important when it comes to reaching people who need to be reached." Ginger.io, a spin-off company in Cambridge, Massachusetts, led by Pentland's former student Anmol Madan, is now developing a smartphone app that notifies health-care providers when it spots a pattern in the data that may indicate a health problem. Other companies are exploiting the more than 400 million messages that are sent every

## THE ECONOMIC LINK

British telephone records show that England's communication diversity (white links) correlates strongly with higher economic prosperity (light blue).





day on Twitter. Several research groups have developed software to analyse the sentiments expressed in tweets to predict real-world outcomes such as box-office revenues for films or election results<sup>11</sup>. Although the accuracy of such predictions is still a matter of debate<sup>12</sup>, Twitter began in August to post a daily political index for the US presidential election based on just such methods (election.twitter.com). At Indiana University in Bloomington, meanwhile, Johan Bollen and his colleagues have used similar software to search for correlations between public mood, as expressed on Twitter, and stock-

Granovetter has a more philosophical reservation about the influx of big data into his field. He says he is "very interested" in the new methods, but fears that the focus on data detracts from the need to get a better theoretical grasp on social systems. "Even the very best of these computational articles are largely focused on existing theories," he says. "That's valuable, but it is only one piece of what needs to be done." Granovetter's weak-ties paper<sup>6</sup>, for example, remains highly cited almost 40 years later. Yet it was

meetings with graduate students in computer science and sociology. "It was abundantly clear that these two groups could really use each other: the computer-science students had much better methodological chops than their sociology counterparts, but the sociologists had much more interesting questions," he says. "And yet they'd never heard of each other, nor had it ever occurred to any of them to walk over to the other's department."

Many researchers remain unaware of the power of the new data, agrees Harvard social scientist David Lazar, lead author on the 2009 manifesto. Little data-driven work is making it into top social-science journals. And computer-science conferences that focus on social issues, such as the Conference on Weblogs and Social Media, held in Dublin in June, attract few social scientists.

Nonetheless, says Lazar, with landmark papers appearing in leading journals and data sets on societal-wide behaviours available for the first time, those barriers are steadily breaking down. "The changes are more in front of us than behind us," he says.

Certainly that is Kleinberg's perception. "I think of myself as a computer scientist who is interested in social questions," he says. "But these boundaries are becoming hard to discern." ■

Jim Giles is a freelance writer in San Francisco.

"WE DIDN'T IMAGINE IN THE 1970s THAT WE COULD WORK WITH DATA ON THIS SCALE."

market fluctuations<sup>13</sup>. Their results have been powerful enough for Derwent Capital, a London-based investment firm, to license Bollen's techniques.

#### MESSAGE RECEIVED

When such Twitter-based polls began to appear around two years ago, critics wondered whether the service's relative popularity among specific demographic groups, such as young people, would skew the results. A similar debate revolves around all of the new data sets. Facebook, for example, now has close to a billion users, yet young people are still overrepresented among them. There are also differences between online and real-world communication, and it is not clear whether results from one sphere will apply in the other. "We often extrapolate from how one technology is used by one group to how humans in general interact," notes Samuel Arbesman, a network scientist at Harvard University. But that, he says, "might not necessarily be reasonable".

Proponents counter that these are not new problems. Almost all survey data contain some amount of demographic skew, and social scientists have developed a variety of weighting methods to redress the balance. If the bias in a particular data set, such as an excess of one group or another on Facebook, is understood, the results can be adjusted to account for it.

Services such as Facebook and Twitter are also becoming increasingly widely used, reducing the bias. And even if the bias remains, it is arguably less severe than that in other data sets such as those for psychology and human behaviour, where most work is done on university students from Western, educated, industrialized, rich and democratic societies (often denoted WEIRD).

"more or less data-free," he says. "It didn't result from data analyses, it resulted from thinking about other studies. That is a separate activity and we need to have people doing that."

The new breed of social scientists are also wrestling with the issue of data access. "Many of the emerging 'big data' come from private sources that are inaccessible to other researchers," Bernardo Huberman, a computer scientist at HP Labs in Palo Alto, wrote in February<sup>14</sup>. "The data source may be hidden, compounding problems of verification, as well as concerns about the generality of the results."

A prime example is Facebook's in-house research team, which routinely uses data about the interactions among the network's 900 million users for its own studies, including a re-evaluation of the famous claim that any two people on Earth are just six introductions apart. (It puts the figure at five<sup>15</sup>.) But the group publishes only the conclusions, not the raw data, in part because of privacy concerns. In July, Facebook announced that it was exploring a plan that would give external researchers the chance to check the in-house group's published conclusions against aggregated, anonymized data — but only for a limited time, and only if the outsiders first travelled to Facebook headquarters<sup>16</sup>.

In the short term, computational social scientists are more concerned about cultural problems in their discipline. Several institutions, including Harvard, have created programmes in the new field, but the power of academic boundaries is such that there is often little traffic between different departments. At Columbia University in New York, social scientist and network theorist Duncan Watts recalls a recent scheduling error that forced him to combine

1. Huttenlocher, D. P., Kadem, K. & Kleinberg, J. M. *Proc. 8th Annu. Symp. on Computational Geometry* 110–119 (1992).
2. Bindel, D., Kleinberg, J. & Oren, S. *Proc. IEEE 52nd Annu. Symp. Foundations of Computer Science* 57–66 (2011).
3. Danescu-Niculescu-Mizil, C., Cheng, J., Kleinberg, J. & Lee, L. *Proc. 50th Annu. Meeting Assoc. Computational Linguistics* (in the press); Preprint at <http://arxiv.org/abs/1203.6360>.
4. Lazar, D. et al. *Science* **323**, 721–723 (2009).
5. Liben-Nowell, D. & Kleinberg, J. *J. Am. Soc. Inf. Sci. Technol.* **58**, 1019–1031 (2007).
6. Granovetter, M. S. *Am. J. Sociol.* **78**, 1360–1380 (1973).
7. Onnela, J.-P. et al. *Proc. Natl Acad. Sci. USA* **104**, 7332–7336 (2007).
8. Eagle, N., Macy, M. & Claxton, R. *Science* **328**, 1029–1031 (2010).
9. Ugander, J., Backstrom, L., Marlow, C. & Kleinberg, J. *Proc. Natl Acad. Sci. USA* **109**, 5962–5966 (2012).
10. Madan, A., Cebrian, M., Moturu, S., Farrahi, K. & Pentland, S. *IEEE Pervasive Computing* <http://dx.doi.org/10.1109/MPRV.2011.79> (2011).
11. Asur, S. & Huberman, B. A. *Proc. 2010 IEEE/WIC/ACM Int. Conf. Web Intelligence and Intelligent Agent Technology* Vol. 1, 492–499 (2010).
12. Gayo-Avello, D., Metaxas, P. T. & Mustafaraj, E. *Proc. Fifth Int. AAAI Conf. on Weblogs and Social Media* 490–493 (2011).
13. Bollen, J. & Mao, H. *IEEE Computer* **44**(10), 91–94 (2011).
14. Huberman, B. A. *Nature* **482**, 308 (2012).
15. Backstrom, L., Boldi, P., Rosa, M., Ugander, J. & Vigna, S. Preprint at <http://arxiv.org/abs/1111.4570> (2011).
16. Corbyn, Z. *Nature* <http://dx.doi.org/10.1038/nature.2012.11064> (2012).

# COMMENT

**CONSERVATION** Advice for biodiversity body from the IPCC **p.454**



**EXHIBITIONS** Works by Damian Hirst and Gunther von Hagens compared **p.456**

**MUSIC** Darwinian algorithm composes plausible orchestral works **p.458**

**OBITUARY** Sally Ride, first US woman in space, remembered **p.460**

ESA/MEDIA/LAB



Europe's ExoMars mission aims to land a rover on Mars in 2018 to search for traces of life.

## When international partnerships go wrong

David Southwood draws lessons from a crisis-ridden year for European cooperation in space.

**T**he recent discovery of the Higgs boson by CERN, the European Organization for Nuclear Research made up of 20 member states, shows how international cooperation can lead to success in science that is otherwise unachievable.

But there are challenges in working across borders. As the current crisis with the euro illustrates, political and financial problems hit some partners harder than others. In my final year as director of Science and Robotic Exploration at the European Space Agency (ESA) in 2011, I had to face withdrawal of

US funds from two major joint missions, the James Webb Space Telescope (JWST) and a planned mission to Jupiter. My successor, Alvaro Giménez, has already had worse: withdrawal of the United States from ExoMars, a Mars exploration programme.

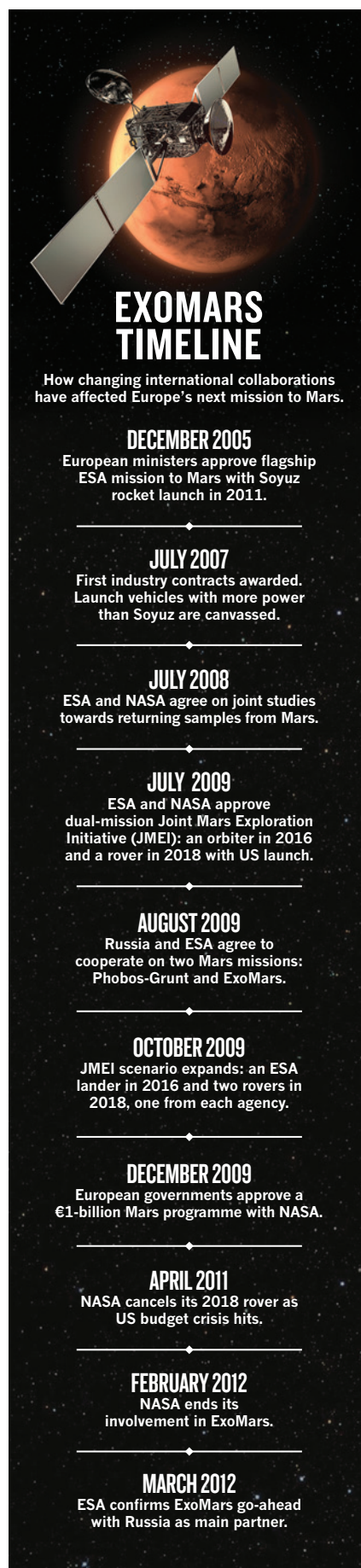
All three cases played out differently. Each project holds lessons for managing future collaborations, such as understanding partners' motivations for joining, overseeing

projects while bearing in mind the possible withdrawal of players and curbing mission creep. Although it was the United States that withdrew as a major partner in the cases I mention, the lessons are general and will become increasingly important with the rise of large international collaborations involving new players such as China, India and Russia.

The nature of sovereign governments means that rarely is an international agreement to cooperate completely legally binding. A sense of solidarity among partners usually motivates them to remain ►

**► NATURE.COM**  
For more on  
NASA's Mars rover,  
Curiosity, see:  
[nature.com/curiosity](http://nature.com/curiosity)





► committed, as with the JWST, for example. Cooperation between Europe and the United States on this infrared successor to the Hubble Space Telescope began in 2002. Europe agreed to provide the mid-infrared instrument, the near-infrared spectrograph and an Ariane rocket as the launcher. The United States would provide the spacecraft and its operations, another instrument and the complex deployable telescope. The European instruments are now ready, but the US side has seen financial over-runs and delays. Launch is now expected in 2018, seven years later than planned.

In July 2011, after further escalations in budget requests for the JWST, a US House of Representatives committee recommended cancelling the observatory. The Europeans found themselves in the uncomfortable position of having spent well over €100 million (US\$123 million) with the possibility of no flight, and having no direct influence other than moral pressure. In the end, deliberations between the White House, Congress and NASA — helped by diplomatic and political pressure from Europe — led to the project's reprieve.

### JUMPING SHIP

In February last year, the United States pulled out of a joint Jupiter mission, leaving Europe to go it alone. The mission was the front-runner in a group of similar projects under deliberation by the ESA science-advisory groups. Fortunately, Europe had spent only around €5 million on it. Because more missions enter the study phase than actually fly, this was not a disaster. But, without the certainty of US involvement, long-term planning by the Europeans was thrown into disarray. There were no alternative proposals involving only Europe.

The Europeans bounced back by resetting the clock for entries to the competition, and by rethinking and reconstructing several missions with reduced goals. A final ESA go-ahead for the Jupiter mission came in May 2012. Costing €830 million, the planned Jupiter Icy Moons Explorer (JUICE) aims to fly past Europa and Callisto and then orbit Ganymede and study its subsurface ocean in 2030. US scientists are anxious to get back on board, and NASA has just found US\$100 million to secure some participation.

ExoMars, a €1-billion mission for Europe alone, is a different story. This February, the United States pulled out, leaving Europe with a funding gap of up to €250 million and having already spent more than €100 million. Given the committed industrial contracts, cancellation would cost up to €400 million.

The flagship mission to send an orbiter and rover to Mars by 2018 started with purely European ambitions in 2005 — to develop regional expertise in exploration technologies and to apply methods to search

for life on the red planet. In this case, the US withdrawal has clearly damaged Europe's position, although not all the fault lies with the United States, which stepped in to help only in 2009 (see 'ExoMars timeline').

### MISSION CREEP

Pulling together resources for a large programme is a long, difficult job with numerous pitfalls. Projects start by consensus-building. Compromise is the order of the day and so the first danger emerges: features are added to win further support from participating countries. ExoMars was vulnerable from the start. With participation optional for ESA member states, and no formula to determine their share, each wanted an assured niche role before they committed.

So the ExoMars programme grew. Expanding the scope improved the mission from a scientific and technical perspective, but it became unwieldy and unaffordable. The added complexity increased the risk that some components would not work or might not be on time and budget. Vocal optimists dissuaded the prudent managers who wanted to drop modules to get more done. Instead, ESA sought new partners.

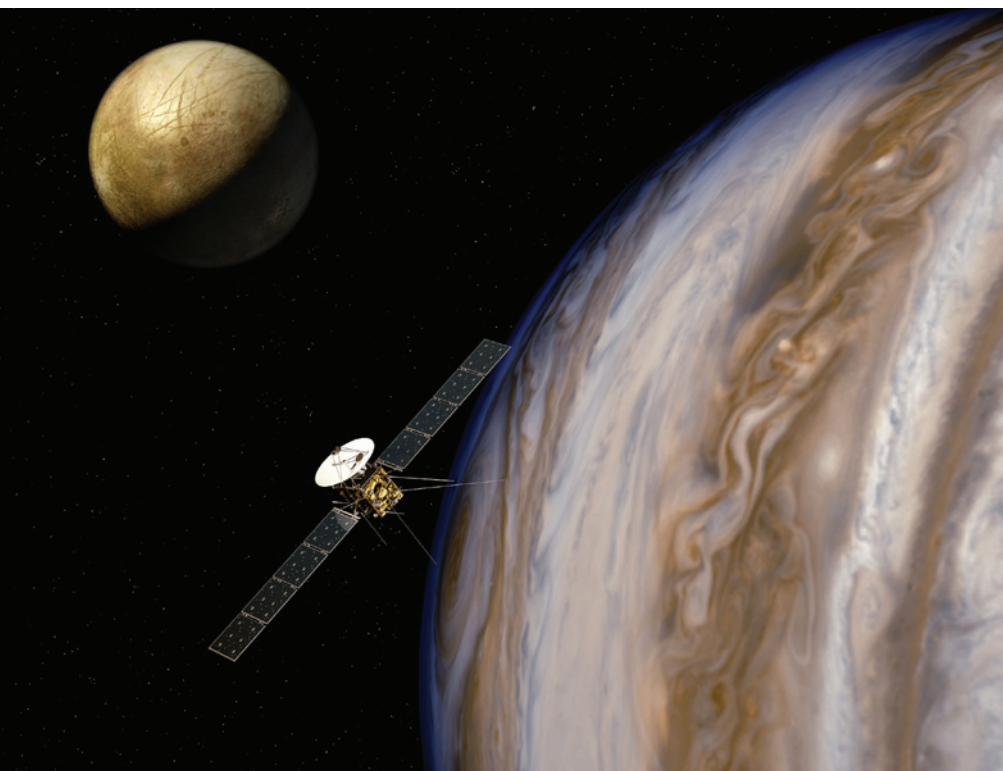
The United States and Russia were approached but didn't sign up, partly because of Europe's need to stick to promises already made within the original European consortium and because there was no joint goal for the potential partner to share.

In 2008, I inherited the programme from another directorate. I went back to talk to NASA. The long-term goal of robotic exploration of Mars, as underscored a few years later by the 2011 US National Academy of Sciences decadal survey, is to return samples. That will be expensive and cannot be achieved by the United States alone. My NASA counterpart, Ed Weiler, and I agreed that cooperation would be inevitable at some point in the next decade. Once this was accepted, it was rational to start working together as early as possible.

The design of ExoMars was modified to suit common European and US goals and to allow sample return. It seemed a win-win arrangement: ExoMars was able to continue, and the prospect of sample return from Mars moved closer for both US and European scientists. I felt confident as the European side of ExoMars moved into the development phase in early 2011. No one foresaw that the US priority for a joint Mars programme would founder as soon as the next annual budget cycle.

Although such let-downs are mercifully rare, a similar thing happened around 30 years ago in the first months of President Ronald Reagan's administration. NASA, faced with a funding crisis, was forced to choose between the Hubble Space Telescope, the Galileo Jupiter orbiter and the International

ESA



The European Space Agency intends its Jupiter Icy Moons Explorer to reach Ganymede in 2030.

ESA/AOES

Solar Polar Mission. It withdrew from the last. Reluctantly, Europe assumed the lead in a reduced solar mission, renamed Ulysses. The spacecraft was enormously successful, making three polar orbits of the Sun and operating for 18 years before being switched off in 2009.

Ulysses marked a watershed: the first mission in which Europe led and the United States followed. Many more have been launched since — including the Cluster satellite constellation that mapped the electrical current systems of Earth's magnetosphere and the Herschel infrared observatory. The ESA Jupiter moon mission follows the Ulysses model of downscaling and going it alone.

The solution for ExoMars seems to mark another watershed: Europe has alternative partners. ESA has turned to Russia to make up the deficit left by the United States. It is not the first time that these nations have collaborated in space, but it is the most ambitious project proposed so far. Space scientists should wish the venture well, because the future is likely to hold an increasingly varied pattern of international partners. In recent years, Europe has undertaken joint space-science projects with China and India, and has begun a large cooperation with Japan on BepiColombo, a mission involving two Mercury orbiters.

### VALUABLE LESSONS

Five lessons can be drawn from this crisis-ridden year for national space administrators (see 'Steps to success').

First, it is important to understand each

partner's motivation for joining a mission. Cooperation cannot be relied on when partners' agendas are incompatible. If a programme is intended mainly to display one group's capability, as with the original plans for ExoMars, then that group must be prepared to go it alone. Mutual goals — such as a collective priority for sample return — can encourage others to get on board.

Second, cooperation means that consensus and compromise rule, and that leads to growth. Multi-partner missions rarely shrink. Moreover, no interested party will voluntarily descope and lessen their project's priority once the programme starts. Be prepared to cancel modules in the preparatory phases if demands keep increasing and resources are spread too thin.

Delay and reflection can lead to a rebirth

### COLLABORATION

#### Steps to success

- Understand each partner's motivation.
- Be willing to drop features to assure completion.
- Keep contributions modular to reduce risk if one fails.
- Be prepared for international agreements to be broken.
- Argue the political case for collaboration in difficult times.

of a more effective mission. The European GAIA mission to map and track the stars in the Galaxy, scheduled for launch next year, was targeted for cancellation because of a financial crisis in 2001, shortly after my appointment at ESA. A major descoping took place but the programme survived. I am sure it will be a success.

Third, one needs to ensure that managerial risk inside programmes is minimized by making partners' contributions as modular as possible. If one part fails, it need not hinder the whole. Efficiency gains follow, and the programme retains the potential to change partners. Of course, discrepancies in schedule-keeping will leave open the situation where one partner moves ahead of the other (as with the JWST), but the modular approach avoids many potential log-jams.

Fourth, be aware that even the most thoroughly crafted agreements between nations can be broken. It seemed unthinkable that NASA would drop a Mars sample-return mission deemed as a first priority in the decadal review, but it happened. Managers must always consider the possibility of cooperation breakdown as a risk. If such a breakdown does occur, the final levers are those of diplomacy and political persuasion by national administrations, together with moral pressure from the scientific community.

Fifth, in difficult times, space scientists need to know the virtues of collaboration and be prepared to deploy those arguments through whatever channel. In my opinion, cooperation goes beyond simple economics — it breaks down cultural differences, builds mutual trust, opens up scientific potential worldwide and conveys inspiration globally, and thereby benefits all humanity. The damage done by breaking understandings, however technically legal, is to be avoided for all these reasons.

In the end, the economic advantages of international cooperation manifestly outweigh the increased risks. In many cases, such as with the JWST and European exploration of Mars, there is no alternative. Large international partnerships are becoming the norm in other fields, from the Square Kilometre Array telescope to be built in Australia and South Africa, to ITER, the international nuclear-fusion project under construction in France. Pooling resources creates facilities that could not otherwise be built. Learning from what has gone wrong in the past is vital if these consortia are to be successful. ■

**David Southwood** is senior research investigator in physics at Imperial College London, president of the Royal Astronomical Society and a steering-board member of the UK Space Agency. He was director of science and robotic exploration at the European Space Agency in 2001–11.  
e-mail: d.southwood@imperial.ac.uk





ILLUSTRATION: MARTIN O'NEILL; PHOTOS: OWAKI/KULLA/CORBIS; M. WESSON/ALAMY; ITANISTOCK/ALAMY; JOANNA T/ALAMY; B.A.E. INC./ALAMY; JOKMEDIA/ISTOCKPHOTO

# Listen to the voices of experience

The intergovernmental body for biodiversity must draw on a much broader range of knowledge and stakeholders than the IPCC, say **Esther Turnhout** and colleagues.

In April this year, the Intergovernmental Platform on Biodiversity and Ecosystem Services (IPBES) was born in Panama City. It hopes to gain similar global scientific authority and policy influence for biodiversity to what the Intergovernmental Panel on Climate Change (IPCC) has for climate change — although not the same opposition and controversies.

Decisions have been made about the platform's functions and guiding principles. But many important issues regarding funding, expertise and institutional design are yet to be resolved. The interim secretariat has invited input into the drafting of a work programme as well as nominations for a multidisciplinary expert panel.

The IPBES's next plenary meeting is in early 2013. A window of opportunity therefore remains for it to learn from more than 20 years of IPCC experience, to better marry legitimacy and effectiveness. Here's how.

The IPCC focused on producing standardized assessments, with one view of what

counts as relevant and valid knowledge for climate change: peer-reviewed science. This approach overshadowed arguably more important tasks: synthesizing wider perspectives about changing climates and spurring action by multiple policy actors.

The IPBES must not adopt such tunnel vision. Simply generating and communicating scientific knowledge is not sufficient to combat biodiversity loss. Current IPBES documentation, such as the provisional work programme and technical background documents, suggests that the platform aims to serve as a clearing house that guarantees the global availability of all biodiversity knowledge that has been standardized and scientifically validated.

This IPCC-like focus might be attractive to 'elite actors', from natural scientists to national governments, but it omits many other important stakeholders and knowledge-holders, including indigenous people, businesses, farmers, community partnerships and fishers. What counts as

legitimate knowledge, and how it is generated, influences its practical effectiveness.

The knowledge of traditional and 'ordinary' citizens might not meet scientific criteria or be amenable to standardization, but ignoring or misappropriating such experience, undermines the possibilities for innovation<sup>1</sup>. For example, Jan Douwe van der Ploeg, an anthropologist at Wageningen University in the Netherlands, has shown how the agricultural revolution endangered the livelihoods of Andean hill farmers when the miracle crops did not deliver, and de-skilled them because it over-rode their local knowledge, which had led to sustainable yields for generations<sup>2</sup>.

## MEETING OF MINDS

Scientific and experience-based knowledge can come together. A good example is an initiative by the Natural History Museum in London in which fly-fishers' expertise has made official water-monitoring schemes more realistic and robust<sup>3</sup>. Another example is from India, where incorporating local

knowledge in scientific censuses improved tiger management<sup>4</sup>.

Admittedly, different types of information require different processes of validation. So the IPBES expert panel must design and use appropriate review protocols. These could involve the recruitment of multiple peer communities, including specialist citizens, biodiversity practitioners and place-based experts, to assess the credibility, quality and practical relevance of knowledge.

An important step in this direction is the development of experimental partnerships with established and trusted organizations such as natural history museums, zoos and botanical gardens. Many of these organizations are becoming places that bring together research and public engagement, often through citizen science. The Berlin Museum for Natural History was recently awarded a grant by the German Federal Cultural Foundation to work on the role of natural history museums in IPBES and in global biodiversity governance. At the conference of the parties to the UN Convention on Biological Diversity in Nagoya, Japan, in 2010, such organizations were mentioned as important nexus of practical knowledge and local action through which biodiversity awareness could be heightened.

### CHECK THE LABEL

There is no single scientific definition of biodiversity<sup>5</sup>, nor is there one that does justice to the many ways of living with and knowing nature that human cultures have developed. The IPBES has not taken adequate notice of this and is promoting a predominantly science-based understanding of biodiversity, with ecosystem services taking centre stage.

This focus reduces biodiversity to an object of exploitation and runs the risk of

bringing it even further into a system of market exchange<sup>6</sup>. Although the concept of ecosystem services prompts private-sector and governmental responses in the developed world, it alienates important political actors. Objectors include Bolivian, Ecuadorian and Cuban delegates at IPBES meetings, and other developing countries at the Convention on Biological Diversity. Moreover, scientists from several disciplines question the benefits of the ecosystem-services approach<sup>7</sup>.

We ask that the IPBES respect the manifold meanings biodiversity has for people. Monetary, aesthetic and sacred values should be given equal prominence in policy discussions of what biodiversity and ecosystems offer to humans, for example.

The IPCC claims to be both policy-relevant and policy-neutral. But the IPCC's knowledge is not equally relevant for all actors, so it cannot claim to be entirely neutral. Different policy-makers want and need different things, so any one framing of a problem — be it scientific, economic or ethical — signals who will act and how<sup>8</sup>. For example, by promoting 'global temperature' as the standardized unit to express the problem of global-warming, the IPCC deems only certain types of action relevant, whether it be mitigating climate change or manipulating the stratosphere. Such standardization is good for modellers and funders, but it has failed to inform effective, diverse and local adaptation and mitigation policies and practices.

Another reason why climate policies have been hard to enact is the IPCC's implicit assumption that the key actors will assent to top-down knowledge and that national and global institutions are synonymous with 'the policy world'. Legislation is essential, but for global issues such as climate and biodiversity

it is not sufficient<sup>9</sup>.

Ending practices that destroy biodiversity — such as uncontrolled mono-crop agriculture or large-scale deforestation — requires diverse and locally appropriate actions. The IPBES must therefore forge productive and trusted connections between organized global knowledge and the many biodiversity actors operating at multiple levels and scales. It should draw inspiration from existing research-practice networks, such as community forestry partnerships and the Agreco network developed by local agriculturalists in Santa Catarina, Brazil. Working with the Federal University of Santa Catarina, Agreco transformed its chemicals-intensive tobacco farms into a more biodiverse and multifunctional agricultural economy and society and now also produces grains, fruits and honey<sup>10</sup>.

### STEPS TO SUCCESS

The IPBES will be deemed successful if it manages to increase the available range of policy interventions, based on a broad set of relevant ecological knowledge, to slow biodiversity loss at all scales. We believe that the IPBES can achieve this and need not become just another remote and disconnected international body, if it follows our nine recommendations (see 'Rules of engagement for the IPBES'). Although perhaps uncomfortable and unpredictable, the open and experimental approach we outline is necessary for meeting the momentous challenge of biodiversity loss. ■

**Esther Turnhout** is in the Forest and Nature Conservation Policy Group, Wageningen University, the Netherlands. **Bob Bloomfield** is at Science in Society, The Natural History Museum, London, UK. **Mike Hulme** is in the Science, Society and Sustainability Group, School of Environmental Sciences, University of East Anglia, Norwich, UK. **Johannes Vogel** is director-general of the Museum für Naturkunde, Berlin, Germany. **Brian Wynne** is at the UK ESRC Centre for Economic and Social Aspects of Genomics, Cesagen, Lancaster University, UK. e-mail: [esther.turnhout@wur.nl](mailto:esther.turnhout@wur.nl)

## BIODIVERSITY

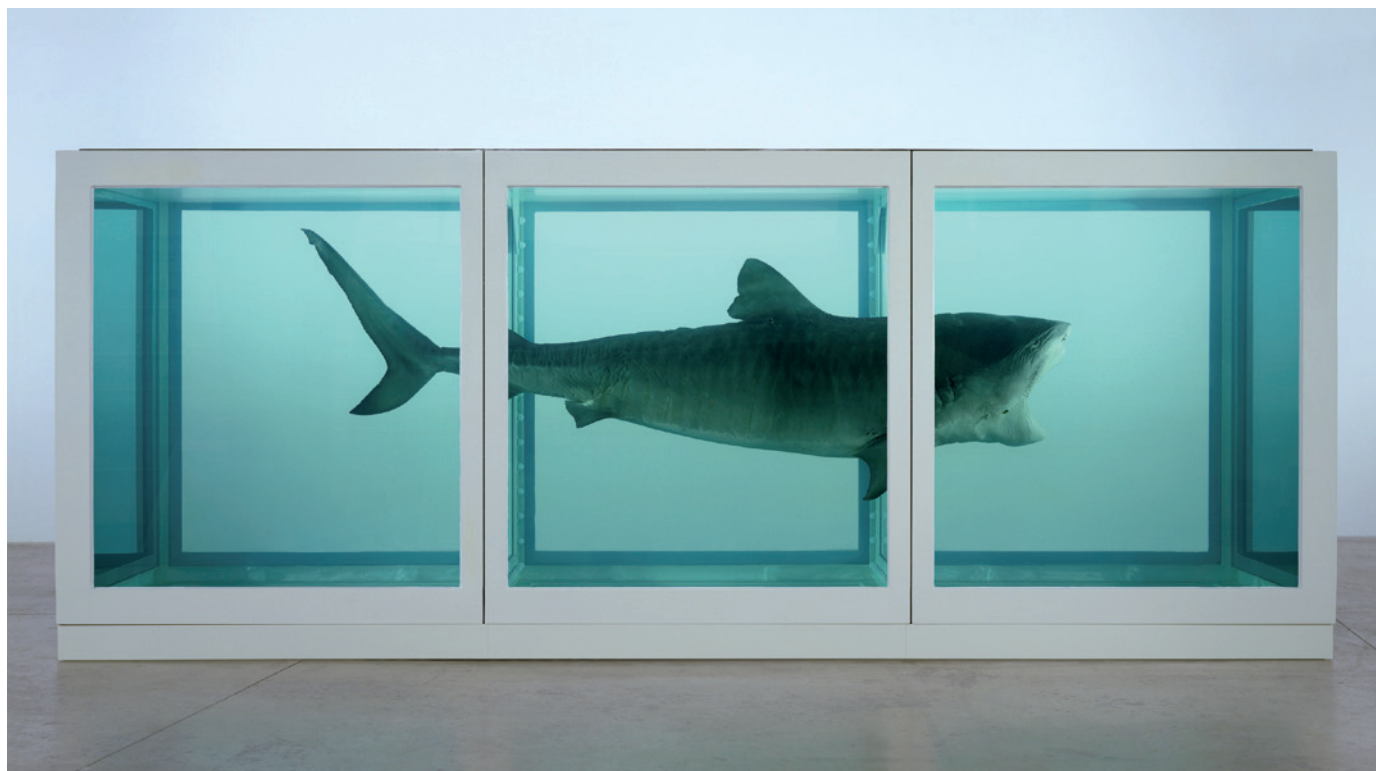
### Rules of engagement for the IPBES

1. Operate not as a centralized global organization, but as global coordinator of a distributed network that can be sensitive to local knowledge, needs and conditions.
2. Address all mandated functions simultaneously and in a balanced way so that non-elite actors are not placed in an end-of-pipe position.
3. Facilitate broad discussion of the terms and methodologies used to define, understand, assess and conserve biodiversity; and be explicit about contested assumptions.
4. Ensure diverse representation in activities and decisions. Expert panel should include natural scientists, social scientists, humanities researchers, biodiversity practitioners and indigenous-knowledge

- networks, with accreditation criteria and selection processes made public.
5. Experiment with ways to validate and maintain quality control, such as sensible narratives and citizen panels.
  6. Embrace dissenting views and perspectives to build trust among represented parties — for example, through minority reporting instead of pursuing consensus.
  7. Work with trusted civic organizations and networks at the interface of science, citizens, business and culture.
  8. Have rolling and overlapping timetables for different products, rather than delivering a single 'big-bang report' every six years.
  9. Reflect regularly to identify areas for improvement.

1. Agrawal, A. *Dev. Change* **26**, 413–439 (1995).
2. van der Ploeg, J. D. in *An Anthropological Critique of Development: The Growth of Ignorance* (ed. Hobart, M.) 209–227 (Routledge, 1993).
3. Waterton, C. *Salmo Trutta* **6**, 56–58 (2003).
4. Karanth, K. U. et al. *Anim. Conserv.* **6**, 141–146 (2003).
5. Royal Society *Measuring biodiversity for conservation* (Royal Society, 2003).
6. Hayden, C. *When Nature Goes Public: The Making and Unmaking of Bioprospecting in Mexico* (Princeton Univ. Press, 2003).
7. Walker, S. et al. *Conserv. Lett.* **2**, 149–157 (2009).
8. Wynne, B. in *Environmental Threats: Perception, Analysis and Management* (ed. Brown, J.) 233–247 (Frances Pinter, 1989).
9. William, W. B. *Iowa Law Rev.* **89**, 3–53 (2003).
10. Pinheiro, S. in *The Earthscan Reader in Sustainable Agriculture* (ed. Pretty J.) 352–361 (Earthscan, 2009).





D. HIRST/SCIENCE LTD/DACS/PRUDENCE CUMING ASSOCIATES

In *The Physical Impossibility of Death in the Mind of Someone Living*, artist Damien Hirst makes no attempt to romanticize death.

## ANATOMY

# Flayed, pickled, plastinated

Ewen Callaway discovers compelling cross-currents in two very different displays of dead animals exhibited just a few kilometres apart.

A horse's head is sliced lengthwise into three sections and splayed a few centimetres apart. In another gallery, a 2-metre skinned shark hovers, its red blood vessels aglow. Each is the work of a controversial iconoclast, made rich by his grotesque creations.

I am, of course, describing anatomist Gunther von Hagens' thrilling exhibition at London's Natural History Museum (NHM), a menagerie given the same patented plastination treatments as his blockbuster *Body Worlds*. The show might spark envy from the British artist Damien Hirst, no stranger to dead fauna. His career retrospective is showing a few kilometres away at Tate Modern.

Von Hagens is at pains to define himself as a scientist, albeit one "with a sense of aesthetics". His *Animals Inside Out* is a collaboration between NHM and von Hagens' Institute for Plastination in Heidelberg, Germany (a branch in Dalian, China, is devoted to animal preparations). The show opens with a tribute to Richard Owen, the comparative anatomist who founded the NHM

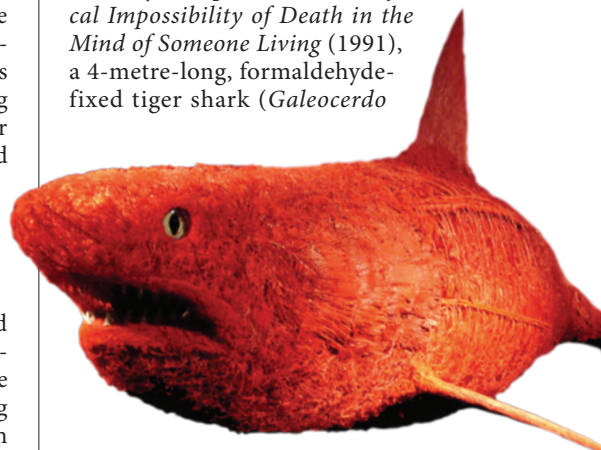
and coined the term homology to refer to structures with common evolutionary origins, such as wings and arms.

It can be easy to see anatomy as art here. Cross-section slices of a crocodile, needlefish and other animals are mounted like paintings — but labelled like anatomy diagrams. The (more or less) whole animals are often artfully posed. A cat, with skin, muscles and two legs removed, lies on its side as if playing with a ball of yarn — and offering a view of its chest cavity. The stances of a pair of reindeer — one with legs outstretched as if mid-leap, the other poised as if about to jump — highlight the animals' musculature.

Von Hagens' most stunning treatments strip away skin, muscle and organs, leaving only vasculature, injected with coloured resin. Two horse heads, so thick with capillaries that they seem made of red foam, are placed opposite one another as if guarding the exhibition. A tiny piglet and a lamb, both 'peeled', stand face-to-face as if at a morbid petting zoo. The shark has a sinister grin as

it hovers above its large liver, which helps to keep it buoyant. My only quibble is that no species names are given for the animals — an odd decision at a museum that is a testament to Linnaean nomenclature.

Many of Hirst's best-known pieces are tame by comparison. *The Physical Impossibility of Death in the Mind of Someone Living* (1991), a 4-metre-long, formaldehyde-fixed tiger shark (*Galeocerdo*



Gunther Von Hagens' shark hovers, its red blood vessels aglow.

**Animals Inside Out**

Natural History Museum, London.  
Until 16 September 2012, then on tour.

**Damien Hirst**

Tate Modern, London.  
Until 9 September 2012.

cuvier), floats in its vitrine with skin like rumpled denim, misshapen fins and a gaping mouth revealing rounded, un-razor-like teeth. The iconic *Mother and Child Divided* (1993) features a cow and calf, each halved lengthways, hovering in four formalin-filled glass cases. The work bears a fleeting similarity to von Hagens' creations until you walk between the split carcasses. Instead of brilliant reds and purples, the wilted organs are a dull grey.

It is tempting to say that the British artist could learn a thing or two from the idiosyncratic German about preserving animals, but that would miss the point of these particular pieces: that death is ugly, awful, inevitable, and to doll it up is misguided.

In Hirst's hands death can also be beautiful. Butterfly wings have never been used to greater effect than in *Doorways to the Kingdom of Heaven* (2007), a triptych resembling a cathedral's stained-glass windows. *In and Out of Love* (1991) is a bright, humid room filled with hundreds of fluttering butterflies. As I watch, one seems dead, until a museum employee picks it up and lays it in a bowl of cut-up fruit. It lives!

Hirst isn't all about animals. Pills, cigarettes and jewels are major motifs in his art, and the exhibition's chronological presentation traces how his use of these objects has evolved. A single cabinet of pharmaceuticals and surgical equipment (*Sinner*, 1988) morphs into a room-sized pharmacopoeia (*Pharmacy*) four years later. By 2000, *Trinity — Pharmacology, Physiology, Pathology* is a room jammed with cabinets of gleaming silver surgical equipment, drug packaging and anatomy models.

But, a science-minded reader might ask, is it art? Here, intention and context are everything. Hirst's animals and objects are art because he says they are, and galleries such as the Tate Modern agree. Von Hagens, who purposefully chose the NHM as his venue, summed up his position in a 2007 interview: "I don't do Damien Hirst," he said. "I am an anatomist, not an artist." Von Hagens' dead animals look prettier than most of Hirst's, but that is the point. ■

**Ewen Callaway** is a news reporter for *Nature* in London.

## FICTION

# New moral arbiters

**Jennifer Rohn** enjoys an epic novel about scientists, the media, ethics and society.

**J**ames Meek's novel about scientists and society, *The Heart Broke In*, tackles a big question: what does the rise of secularism in much of the West mean for ethical codes?

Some stories might suggest that rationalism should provide some kind of model. But Meek uses nuanced debate to build towards a very different climax. His mouthpieces are Bec, a malaria researcher; her computational-biologist lover, Alex; Bec's misbehaving ex-rock-star brother, Ritchie; and their friends, family and lovers. Meek, a former science correspondent for *The Guardian* newspaper, deftly handles the complex, day-to-day issues that scientists grapple with: the ethics of research; interaction with society; lab politics; and the struggle to make a mark in a difficult profession. *The Heart Broke In* is a realistic slice of life at the bench, reflecting both the admirable and the unflattering qualities of scientists.

Meek uses Alex's Uncle Harry, a militant atheist and famous cancer researcher, to explore whether science can replace God. Harry boasts of besting God by saving lives with his niche cure for one rare form of cancer, but develops a different type of tumour himself. Science can neither save him nor help him to accept the end of his existence.

In another plot strand, Bec romantically spurns Val, a militant Christian and the editor of a prominent newspaper. Val labels her an intellectual obsessive cut off from ordinary life, and tries to exact revenge by destroying her public reputation using the media weapons at his disposal.

Somewhere in the middle, Bec and Alex flounder. Bec is so devoted to her science that she allows herself to be parasitized by an African worm to study its protective effects against malaria. Alex is a dreamer whose hyped *Nature* paper on a 'treatment' for ageing ("SCIENTIST FINDS FOUNTAIN OF YOUTH!"), shrills the headline in Val's paper) transforms him into an unproductive media darling. In danger of becoming a one-hit wonder like Harry, Alex starts to realize that this might be the normal progression of a 'successful' scientific career — a suspicion confirmed when he interviews the brightest

minds in his field for a documentary. All typecast by one big breakthrough, they have spent the rest of their lives trying to recapture the glory, to little avail.

As their personal problems mount, the scientists emerge as refreshingly three-dimensional in a way rarely seen in fiction. Yet Meek also plays with the one-dimensional view of scientists so often taken by the media.

Val, for instance, sees scientists as arrogant, atheistic meddlers. Ritchie is conflicted: expressing surprise that scientists could actually be well dressed or have friends, while also holding up Bec and Alex as the paragons he will never be. Then, when the pair grow more famous than he is, he describes them sarcastically as white-coated secular saints. Bec's mother, meanwhile, fears her daughter's disapproval of her bizarre diets, and marvels that scientists get anywhere when they are "closed to new ideas".

Even the scientists flirt with stereotypes. Bec, for instance, berates herself because she can't recall how many times she had sex with Val — the kind of thing, she feels, that a scientist should be able to monitor. And Harry regales the young Alex with mythical descriptions of his work, from battles and breakthroughs to silver bullets and holy grails. Part of Alex's growth as a character is realizing that his profession isn't nearly as heroic as Harry makes out.

*The Heart Broke In* ends with almost everyone receiving their comeuppance. In the absence of a viable moral code, good and bad are enforced by naming and shaming in the press and social media — not by the desire to do no wrong, but by the imperative not to get caught. Science and religion have had their day, it says: the media, old and new, are the higher powers, with the ability to create and destroy reputations in predictable cycles. ■

**Jennifer Rohn** is a cell biologist at University College London and the editor of *LabLit.com*. Her most recent novel is *The Honest Look*. e-mail: [jenny@lablit.com](mailto:jenny@lablit.com)



**The Heart Broke In**  
JAMES MECK  
Canongate/  
Farrar, Straus and  
Giroux: 2012.  
551 pp./416 pp.  
£17.99/\$28

*In the absence of a viable moral code, good and bad are enforced by naming and shaming in the press.*



## COMPUTER SCIENCE

# Algorithmic rapture

**Philip Ball** listens in on an album of evolved music composed by the Darwinian computer program Iamus.

If a computer can produce an artwork that moves us, does it take artificial intelligence beyond an important threshold? That is one of the questions raised by Iamus, an algorithm that composes music from scratch, developed by Francisco Vico and his colleagues at the University of Malaga in Spain.

*Iamus*, an album of compositions by the algorithm — including two orchestral pieces played by the London Symphony Orchestra — comes out on 1 September. A live performance of several Iamus pieces was broadcast in July to commemorate the centenary of the birth of British computing pioneer Alan Turing.

The recordings, scored for a variety of chamber and orchestral ensembles, are at the very least musically 'plausible', and some listeners have found them stimulating, both intellectually and expressively. They should provoke lively discussion.

Composers, most notably the experimentalist Iannis Xenakis, have been using computers to make music since the 1960s. And there is nothing especially new about an algorithmic approach to composition: the rule-bound, even formulaic, nature of most music lends itself to that. A program called CHORAL, devised in the 1980s by computer scientist Kemal Ebcioglu to harmonize chorales in the style of Johann Sebastian Bach, drew on principles of harmony and melody observed by Bach himself.

Computer scientists have also succeeded in making programs that learn from human examples. Even their creators admitted that early improvisational algorithms such as GenBebop, created in the early 1990s by cognitive scientists Lee Spector and Adam Alpern to produce jazz solos in the style of Charlie Parker, gave indifferent results. The Continuator program, devised a decade later by François Pachet at the Sony Computer Science Laboratory in Paris, is much more convincing, particularly when it elaborates on improvisations by a human pianist.

It is quite another matter, however, for a computer to come up with captivating music without relying on human input for the raw ideas. Before now, such efforts have often sounded like pastiche, using clichéd harmonic progressions and melodic structures.

This is where Iamus's creators claim to have something new. The algorithm is inspired by Darwinian evolution. It is named after an ancient Greek hero, son of the god

Apollo, who could understand the language of birds. The computer generates very simple 'musical genomes' — little motifs that are evolved, mutated and elaborated until they acquire genuine musical content and interest. Genetic and evolutionary algorithms



Iamus awaits performers and audience to begin making music in Sala María Cristina, Spain.

for making music have been seen before, but Iamus's approach of unfolding complex structure from a mutable core has enabled the kind of dramatic invention found in biological evolution. The music is far more than just a succession of transparent variations.

The recorded pieces are all in a modernist classical style — full of dissonance, but with hints of harmony and rich textures that are reminiscent of works by, for example, György Ligeti and Krzysztof Penderecki. However, the same approach can be used for other idioms, and Vico and his colleagues say that similar algorithms could generate music for commercial purposes.

The willingness of professionals to perform the works marks Iamus as unique. Lennox Mackenzie, chairman of the London Symphony Orchestra, was impressed with what the algorithm had achieved, although he felt that its scores still fell short of good human compositions. The music struck him as "going nowhere" — a complaint often made of other modernist works — yet ultimately achieving

an "epic" quality. Many other musicians were pleasantly surprised by the material, and found some of it genuinely expressive.

**Iamus**  
IAMUS  
MELOMICS RECORDS:  
2012. €14.95

Which brings us back to the initial question. If Iamus can simulate (and thus stimulate) emotionality, is it not merely 'thinking' in the limited sense meant by Turing when he proposed a test for artificial intelligence, but also displaying human characteristics?

Here we should heed studies of music cognition, which have shown that emotion in music is not some deeply mysterious process, but has its own rules and regularities, as discussed by psychologist John Sloboda in his books *The Musical Mind* (Clarendon, 1985) and *Music and Emotion* (co-edited with Patrik Juslin; Oxford University Press, 2001). For example, certain musical structures, including judicious injections of dissonance or 'false trails' that create and then confound expectation, can elicit emotions quite reliably — as anyone whose feelings have been manipulated by formulaic film scores can attest.

What is more, the involvement of human performers is vital. The same notes can be performed drily and without engagement or with heart-rending fervour. Good performers achieve expression with a wide range of techniques, such as subtle distortions of tempo, intonation and timbre.

Iamus's work might therefore be considered to demonstrate the role of performer and audience in 'making music'. It does not deny the sensitivity and skill of the greatest composers to say that a composition becomes music in the mind of the listener only through the interaction of the composer's and the performer's choices with the wealth of learning and association that even allegedly unskilled listeners possess.

This consideration ought to diminish a widespread prejudice against computer-composed music that has been evident in the critical responses to Iamus so far. Neuroscientists Stefan Koelsch and Nikolaus Steinbeis have shown that part of this prejudice is unconscious: the same piece of music may or may not activate parts of the brain associated with ascribing intention to others, depending on whether listeners have been told that the piece was composed by a human or by a computer (N. Steinbeis and S. Koelsch *Cerebral Cortex* 19, 619–623; 2009).

Human performance of computer-made music might at least partly override this obstacle to emotional engagement. We should also celebrate the way that Iamus, far from threatening humanity's supposedly unique claim to creativity, can put the audience back in the picture as a participant in the creative act. ■

**Philip Ball** is a writer based in London and Author of *The Music Instinct*.  
e-mail: p.ball@btinternet.com

J. DRAGON

# Correspondence

## Some facts about Ye Shiwen's swim

We write on behalf of the Chinese Biological Investigators Society, a professional organization of overseas and native Chinese scientists ([www.cbisociety.org](http://www.cbisociety.org)), to express our concern over your online News 'Explainer' about the performance of Ye Shiwen, a 16-year-old Chinese swimmer who won gold medals in the 200- and 400-metre individual medley during the London 2012 Olympics (<http://doi.org/h55>; 2012). We feel strongly that you overlooked some important facts.

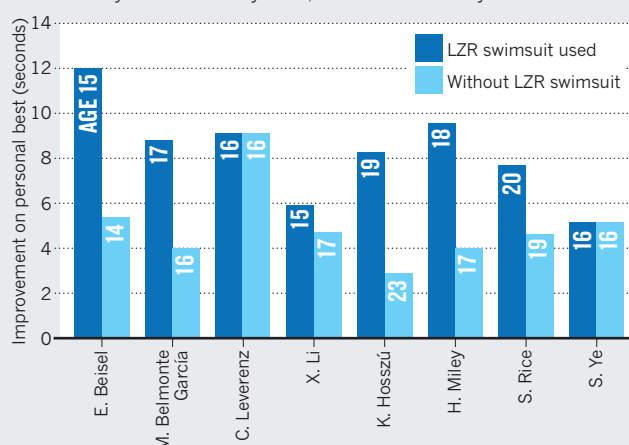
You join in the widespread speculation that Ye's performance was anomalous, in which it has generally been implied that no one else has accomplished such a feat before without the aid of performance-enhancing drugs — a premise that, in our view, stems from data cherry-picked to support an unfounded accusation.

You indicate that Ye's 400-metre performance was about 7 seconds faster than a time she set at a major meet a year earlier. Ye's personal best was actually set in 2010, when she was 14 years old. She improved her performance at the Olympics final by 5 s over her earlier personal best — a feat that is not anomalous, but is expected for elite swimmers of Ye's age as they grow bigger and stronger.

There are many examples of elite swimmers who showed a significant improvement at a young age. For example, Australian swimmer Ian Thorpe took 5 s off his 400-metre freestyle time between the ages of 15 and 16, and UK swimmer Adrian Moorhouse, Seoul Olympics gold medallist in 1988, improved by 4 s in the 200-metre breaststroke aged 17. The same happened to the other seven finalists in the 2012 Olympics women's 400-metre medley (see 'Young swimmers' improvements'). Also, Rūta Meilutytė, a 15-year-old Lithuanian swimmer,

### YOUNG SWIMMERS' IMPROVEMENTS

Improved performances in young swimmers are not rare — all eight finalists in the women's 400-metre individual medley at the 2012 Olympics showed performance leaps at an early age. Streamlined LZR swimsuits were used from February 2008 to January 2010, but were not worn by Ye Shiwen.



improved her personal best by more than 4% in the 100-metre breaststroke, compared with Ye's improvement of 2% in the 400-metre medley.

You say that Ye "raised eyebrows" by her showing in the last 50 metres of the race, noting that she swam faster than US swimmer Ryan Lochte when he won gold in the men's 400-metre medley, the second-fastest time ever for that event. What you do not mention is that Ye was actually more than 23 s slower over 400 metres than Lochte, an eternity for elite swimmers at this distance.

In fact, the time for Lochte's last 50 metres is nowhere near the second-fastest ever for that event: several other swimmers in the same men's final were faster than he was and faster than Ye. Lochte ranked only fifth in the last 50 metres, at 29.1 s, which was significantly slower than Japan's Yuya Horiata (27.87 s) and three other swimmers competing in the same event. Ye's time was 28.93 s.

All of this information is available on the Internet. It is unfortunate that *Nature* seems to have put a stamp of scientific approval on the Western media's unsubstantiated speculation that Ye's feat is humanly impossible

without the aid of performance-enhancing drugs.

We emphasize that our data serve only to provide a more complete backdrop to Ye's achievement, and not to negate her spectacular performance in winning two golds and shattering the world record.

**Weimin Zhong** Yale University, New Haven, Connecticut, USA.

**Hao Wu** Children's Hospital Boston, Harvard Medical School, Boston, Massachusetts, USA.

**Linheng Li** Stowers Institute for Medical Research, Kansas City, Missouri, USA.

## Stricter management of organ transplants

Organ trafficking and the reported manipulation of data from patients on waiting lists (see A. Ginzel, M. Kraushaar and S. Winter *Der Spiegel*, 30 July 2012) are putting organ transplantation at risk by encouraging public distrust and threatening to reduce organ donation.

As former president of the European Group for Blood and Marrow Transplantation and of the foundation Swiss Blood Stem Cells, I suggest

that haematopoietic stem-cell transplantation can offer lessons in stricter control of organ transplants and in promoting global cooperation.

The Worldwide Network for Blood and Marrow Transplantation ([www.wbmt.org](http://www.wbmt.org)) has 20 million volunteer stem-cell donors, whose human leukocyte antigens (HLAs) have been typed to allow matching. Donors are selected only for matching with individual recipients and are protected and followed up according to standardized rules (J. P. Halter *et al. Bone Marrow Transpl.* <http://doi.org/h54>; 2012).

An accreditation system that ensures uniform quality of products and processes operates under identical regulations in Europe, the United States and Canada (see [www.jacie.org](http://www.jacie.org) and [www.factwebsite.org](http://www.factwebsite.org)), with health-care providers and payers increasingly demanding this accreditation as a condition for reimbursement. Internal and external audits of processes, together with standardized reporting to national and international data registries, are requisite.

Solid-organ transplantation would also benefit from a global quality-management system and from national networks of living HLA- and blood-typed volunteer donors. Although it will be hard to stamp out fraud altogether, professional oversight of activities would safeguard the interests of prospective donors and encourage more to register (A. Rios *et al. Transplant Proc.* **44**, 1489–1492; 2012).

**Alois Gratwohl** University of Basel, Switzerland.  
[alois.gratwohl@unibas.ch](mailto:alois.gratwohl@unibas.ch)

### CONTRIBUTIONS

Correspondence may be sent to [correspondence@nature.com](mailto:correspondence@nature.com) after consulting the author guidelines at <http://go.nature.com/cmchno>.



# Sally Ride

## (1951–2012)

Physicist, education advocate and first US woman in space.

“We talk about women breaking through the glass ceiling, but Sally broke through the atmosphere,” a colleague once said of Sally Ride, the first US woman to fly to space. Rather than coasting on that success, the enigmatic Ride led several more lives — as a physicist, investigator of the *Challenger* and *Columbia* shuttle disasters and tireless advocate for science education — gaining the respect and affection of her colleagues along the way.

Ride, who died from pancreatic cancer on 23 July aged 61, was born in Encino, California. Science and mathematics came easily to her, and when she entered Swarthmore College in Pennsylvania, she studied physics. After a year and a half, she dropped out to try her hand at another early passion: tennis. Wimbledon champion Billie Jean King thought she had the chops to make it in professional tennis, but Ride said in a 2006 interview that she had disagreed after taking “a long, hard look” at her forehead.

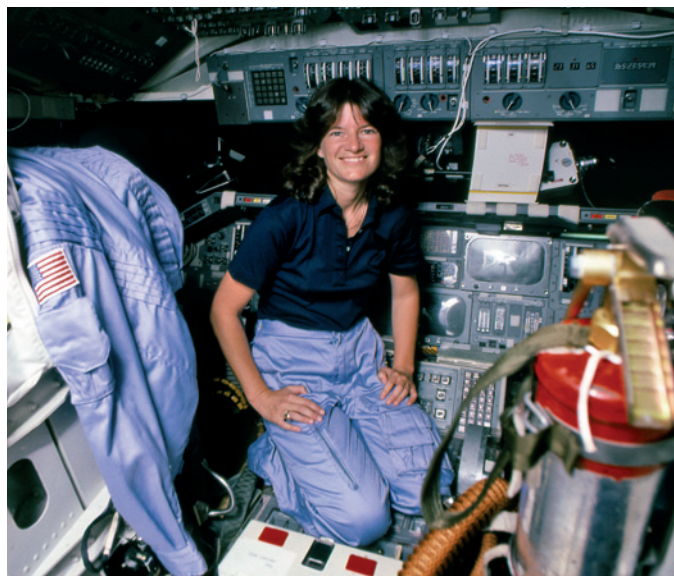
Ride returned to college and took degrees in physics and English from Stanford University in California. She went on to earn a PhD for her research on the absorption of X-rays by interstellar gas. As a graduate student, Ride spotted an advert in the student newspaper announcing that NASA was looking for new astronauts. “The moment I saw that, I knew that that’s what I wanted to do,” she told an interviewer.

Ride beat some 8,000 other applicants to become one of 35 members of the astronaut class of 1978, which included 6 women. The women generated tremendous media attention — and tiresome ribbing from some male colleagues. The women wanted to be accepted for their professional skills; instead, journalists asked them who would do the cooking on the shuttle. Ride found the attention dispiriting. “It’s too bad our society isn’t further along,” she said at a NASA news conference.

Bob Crippen, who piloted the first space shuttle flight in 1981, asked to have Ride aboard his next mission in 1983. She and astronaut John Fabian would operate the shuttle’s 15-metre-long robotic arm, using it for the first time to deploy and retrieve a satellite. Ride’s ability to stay calm under

pressure — a skill her sister, Bear, has attributed to her tennis days — led Crippen to make her flight engineer for the mission. “I never saw Sally flustered,” he says.

Ride’s first flight, on 18 June 1983, went nearly flawlessly, and she marvelled at the view of our planet and its thin, blue



atmosphere. “It’s so clear from that perspective how fragile our existence is,” she said later. “It makes you appreciate how important it is to take care of that atmosphere.”

Crippen was offered two flights for the next year, and he accepted the second only on the condition that Ride would be on the crew — he trusted her to stand in as commander during practices while he was away training for the first mission. That flight, in 1984, was Ride’s last.

She would later put her experience at NASA to use in investigating both the *Challenger* and *Columbia* disasters. She advised the agency on what direction it should take, authoring a report in 1987 that highlighted the importance of studying the Earth from space. “That has turned out to be one of the most important things the agency has done in the last 25 years,” says Roger Launius, a historian at the Smithsonian National Air and Space Museum in Washington DC. Instruments on NASA satellites confirmed the existence of the polar ozone holes, made the first global measurements of atmospheric aerosols and have monitored ice-sheet melting and rising sea levels.

Ride was not one to pull punches. Serving on a NASA review committee in 2009, she announced bluntly at a public meeting that the agency simply did not have enough money to undertake a new human space-flight programme. The audience listened intently — she had tremendous credibility, recalls

fellow committee member Wanda Austin, president and chief executive of The Aerospace Corporation in El Segundo, California. But Ride never let the attention go to her head. “She was just like your sister,” Austin says.

Ride left NASA in 1987 and returned to academia, heading back to Stanford and then to the University of California, San Diego (UCSD). There, she studied how free-electron lasers could be made to produce X-rays similar to those generated when the solar wind slams into comets or planets. She also worked on Urey, an instrument intended to look for signs of life on Mars. When NASA did not fund it, she comforted her colleagues.

Students’ evaluations of Ride’s classes at UCSD were typically 98–100% positive. In 2001, she founded the company Sally Ride Science, based in San Diego, to encourage middle-school students — and especially girls — to pursue science careers. The organization, which she ran with her partner, Tam O’Shaughnessy, enabled students to take images of Earth and the Moon using remote-controlled cameras aboard the International Space Station and NASA’s Gravity Recovery and Interior Laboratory.

Ride never sought the limelight and revealed little about her personal life. “She had no need or desire to get rich on being Sally Ride,” says Jeffrey Hoffman, a member of Ride’s astronaut class, who now teaches astronautics at the Massachusetts Institute of Technology in Cambridge. “She didn’t use her fame as a stepping stone to a big ego trip.”

That this natural introvert withstood the glare of celebrity with such dignity and grace makes her accomplishments even more inspiring. ■

Maggie McKee is a journalist based in Boston, Massachusetts, USA.  
e-mail: [maggieqmckee@gmail.com](mailto:maggieqmckee@gmail.com)

HARRY BENSON/CONTOUR BY GETTY IMAGES

# CAREERS

**TURNING POINT** Two awards ease the way for population geneticist **p.547**

**CAREER TOOLKIT** Expert advice on scientific career fundamentals [go.nature.com/mfgmok](http://go.nature.com/mfgmok)

**NATUREJOBS** For the latest career listings and advice [www.naturejobs.com](http://www.naturejobs.com)



## CAREER DEVELOPMENT

# What's your type?

*Personality and vocation tests can help researchers to improve their 'soft skills' and find careers that suit them.*

BY CORIE LOK

When physicist David Dean joined the Oak Ridge National Laboratory in Tennessee in 1995, he says, he was a "typical theory guy": a staff scientist focused on research. About ten years later, as head of the nuclear-theory research group, he joined an in-house leadership-development programme that involved extensive personality

tests meant to get trainees thinking about their leadership potential, and what skills they needed to work on. The tests, along with one-on-one sessions with a psychologist and a human-resources professional who helped to interpret the results, showed Dean that he had a 'collaborative' leadership style. But they also taught him that sometimes he needed to be a more 'directive' leader — to be more assertive and to make executive decisions more readily.

Knowing about different leadership styles and when to implement them was useful and relevant as Dean took on a post first as a strategic planner for the director's office at Oak Ridge, then as a senior science adviser for the US Department of Energy. And, in July last year, the techniques he learned helped Dean to win the post of head of the physics division at Oak Ridge. The tests and the training augmented his leadership skills, says Dean. "It takes a certain personality to do these jobs."

Early- and mid-career scientists use personality tests in settings from career-counselling and human-resources offices in academia and businesses to training workshops at the US National Institutes of Health (NIH). Tests such as the Myers-Briggs Type Indicator assess how people tend to behave in certain situations, focusing on personality traits such as extroversion and agreeableness (see 'Type by type').

Assessments can also show people how they might differ from their colleagues in terms of, for example, communication style, approach to the workplace, interactions with workmates and conflict resolution. Armed with this information, scientists can manage their own behaviour to avoid misunderstandings, improve their communication and leadership skills, troubleshoot personality clashes, make teamwork function more smoothly and, like Dean, take their careers to the next level. "An awareness of your type can give you insight into your strengths and liabilities, and the ways you can grow as a scientist, as a member of a team, a member of society and a member of a household," says Sharon Milgram, director of the NIH's Office of Intramural Training and Education in Bethesda, Maryland.

## INTEGRAL TRAITS

The Myers-Briggs assessment is probably the personality test most widely used by scientists and the general public, says John Lounsbury, a psychologist at the University of Tennessee in Knoxville who has conducted personality tests on Oak Ridge scientists. He and other academic psychologists say that Myers-Briggs is overly simplistic and misses out a few key traits, and that better tests exist. However, it remains popular because it is easy to understand, many people have been trained to administer it and there is a large body of interpretive books, websites and other materials that further boost awareness of the test. It assesses people on eight different personality traits, grouped into four dichotomies, so that a person is designated as introvert (I) or ►



► extrovert (E); sensing (S) or intuition (N); thinking (T) or feeling (F); and judging (J) or perception (P). The result is 16 possible combinations of personality type, such as INTJ, that can help to explain how people approach different aspects of their lives.

The big benefit of the Myers-Briggs assessment is that it shows test-takers how they differ from others in their personalities and approaches, says Milgram. “For many people, it is a validation of the fact that people can bring different styles and approaches to work and still be successful,” she says. For the past couple of years, Milgram’s office at the NIH has run training and orientation programmes including the Myers-Briggs assessment for students, postdocs, staff scientists and principal investigators.

One set of Myers-Briggs traits that is particularly relevant to scientists is the sensing versus intuition axis. ‘Sensing’ people tend to focus on details and proceed through work step by step, whereas those designated ‘intuition’ look at the big picture and are less detail-oriented. “Good scientists need to be able to operate out of both worlds,” says Bill Lindstaedt, director of



**“Myers-Briggs results provide just one window through which you can look at your overall capabilities.”**

Bill Lindstaedt

the Office of Career and Professional Development at the University of California, San Francisco (UCSF), where he administers tests including the Myers-Briggs (see ‘Interests before indicators’). No one can change whether they are inherently S or N, but with proper interpretation from a trained person such as a psychologist or career counsellor, personality assessments can suggest ways in which people can adjust and manage their behaviour to better understand and work with different personalities. For example, a big-picture thinker might need to sharpen their focus on the minutiae of a project or experiment when giving directions to a detail-oriented person. People can modulate their behaviour, develop skills or hire people who will complement their way of working to make sure that their team can move between the two modes, says Lindstaedt.

#### IN AND OUT

Another pair of traits that can come into play in the lab, especially in meetings, is introversion versus extroversion. For example, extroverts tend to talk aloud as they think, whereas introverts prefer to formulate their thoughts before voicing them. Milgram says that she is trying to alter her own extroverted behaviour by being less talkative in meetings and giving introverts in the room a chance to process before they speak.

Melissa Wong, a graduate student in virology and immunology at the UCSF who took the Myers-Briggs as part of an internship programme exploring non-academic scientific careers, was struck by how the E–I difference can underlie misunderstandings in the lab.

For example, extroverts may think that introverts aren’t bright enough to speak up right away, and introverts may think that extroverts speak without substance. “I work with both of those types of personalities, and I think there’s a lot of miscommunication,” says Wong.



**“The worksheet helped me to realize what’s most important in a work environment.”**

Melissa Wong

Becca Stoloff, a graduate student in neuroscience at the University of California, Berkeley, is considering embarking on a teaching career. She says that the Myers-Briggs confirmed that she had the personality of a mentor; this autumn, she will teach maths

at a private school for a semester as part of her career exploration.

Individual scientists and labs are even starting to use Myers-Briggs outside training programmes. Milgram says that postdocs and students on the NIH’s Bethesda campus are requesting Myers-Briggs workshops for labs and retreats. And in one developmental-biology lab at the University of Missouri in Columbia, the students have all taken the assessment; their four-letter personality types and a few words of description are posted on a chart next to the door. Lab leader Dawn Cornelison says that she first took the test as part of a lab-management

## CAREER FOCUS

### *Interests before indicators*

For young scientists trying to decide what type of career to pursue, vocational-interest inventories might be more useful than personality tests. Inventories gauge activities that a person enjoys and suggest possible occupations on the basis of careers undertaken by people with similar interests. Most of these tests can be taken through career-counselling or human-resources offices, or through private practices; some of them are available online.

Early-career researchers should also keep in mind, however, that most such inventories cover a vast range of occupations and don’t focus solely on science. To fill this gap, Bill Lindstaedt, head of the careers office at the University of California, San Francisco (UCSF), collaborated on developing an assessment tailored to young researchers with advanced degrees who are interested in scientific careers outside of academia. The Career Assessment Worksheet asks

graduate students to evaluate and prioritize their skills and interests, as well as the things that matter to them most at work. Students receive a list of 60 careers ranging from science-policy adviser to patent attorney, along with information about those careers. The students narrow down the list of possibilities by eliminating the careers that don’t match their interests, skills and values.

The assessment exercise has proved effective. “That worksheet helped me realize what’s most important to me in a work environment,” says Melissa Wong, a UCSF graduate student in virology and immunology. She took the assessment this year as part of a university-run internship programme that helps students to explore science careers outside academia.

Wong already knew that academia wasn’t for her when she entered the programme, but she wanted to stay close to science and thought that she might do bench research at

a biotechnology firm. Then she completed the Career Assessment Worksheet, and realized that she wanted teamwork to be part of her job. After reading about the biotechnology industry, and meeting and speaking to several professionals in the field, Wong is now considering careers in regulatory affairs and business development.

At the end of the internship programme, Wong took the Myers-Briggs Type Indicator personality test. Lindstaedt gets the students to take the Career Assessment Worksheet first because he finds that it provides a more direct connection to possible career choices than the Myers-Briggs test does. “My skills, values and interests can more clearly point to a certain career path than my Myers-Briggs type,” says Lindstaedt. “The Myers-Briggs is more useful for people, once they get into a job, to identify strengths and potential blind spots for success.” **C.L.**

## TOOLS AND TESTS

## Type by type

**Myers-Briggs Type Indicator** Widely used test. Classifies personalities into 16 categories on the basis of the traits of extrovert and introvert, sensing and intuition, thinking and feeling, and judging and perception.

**NEO Personality Inventory** Based on the 'Big 5' model of traits — neuroticism, extroversion, openness to experience, agreeableness and conscientiousness. Used mostly in psychology research.

**Hogan Personality Inventory** Also based on the Big 5 model. Used mainly for career development and hiring.

**Strong Interest Inventory** Assesses interests and working styles, and compares them to the interests of people in a range of vocations. Used mostly by undergraduate students seeking advice on career choices. **C.L.**

'boot camp' for new faculty members offered by the US Society for Developmental Biology in Bethesda. When she told her students about it, they became interested, took the test and asked students joining the lab to take it as well. The assessment has become part of the culture of the Cornelison lab. "It's like a getting-to-know-you game," says Cornelison: it breaks the ice and helps new students to integrate rapidly into the lab.

## PRESCRIPTION PRECAUTION

People who administer personality assessments are quick to point out that they are not meant to be deterministic or prescriptive. The results should not be used to pigeonhole someone, or to tell them what kind of job they should have or whether they can succeed at it. The assessments do provide some insight into what kind of person the test-taker is, but only as one data point to be used in overall career guidance and development. "Myers-Briggs results provide just one window through which you can look at your overall capabilities," says Lindstaedt.

Milgram emphasizes that there is no 'right' or 'wrong' personality type in science. No one needs to change their personality to be an excellent scientist. "It's about how you manage your behaviour," she says. ■

**Corie Lok** is the editor of *Nature's Research Highlights*.

# TURNING POINT

## Sohini Ramachandran

*Sohini Ramachandran, a population geneticist at Brown University in Providence, Rhode Island, received two high-profile awards this year. In June, she was named a Pew Scholar in Biomedical Sciences by the Pew Charitable Trusts, based in Philadelphia, Pennsylvania; and in February, she received a fellowship from the Alfred P. Sloan Foundation in New York. She plans to use the grants to distinguish herself in a fast-moving field.*

### How did you realize you wanted to combine maths and biology?

It began when I was in high school. Marcus Feldman, an evolutionary biologist at Stanford University in California, let me do a project in his lab so that I could enter what is now the Intel Science Talent Search, a pre-university research competition. I studied genetic variation in *Arabidopsis thaliana*, the plant equivalent of the lab rat, and found that the species moved into the Americas 30,000 years ago, at the same time as humans. I got fourth place. Later, as a computational-science undergraduate at Stanford, I attended a lecture by Feldman in which he estimated the number of females missing from China's population as a result of the one-child law. I realized how incredible it was that we could use maths to learn so much about human behaviour. I have since used genomics to study topics from historical patterns of human migration to whether genetic variation accounts for differences in cancer-treatment outcomes.

### What was your first difficult career decision?

Whether to stay at Stanford for my graduate research. Everyone told me to go somewhere else to get broader experience, but I stayed and Feldman became my PhD adviser. I wanted to stay with him because he had a strong history of training students who go on to get tenure-track jobs and make an impact on the field.

### How did you come to work at Brown?

I was lucky enough to have multiple offers, but my husband needed an academic post nearby, which can take a lot of time to work out. I found that this two-body problem has become so common that administrators expect it. My husband is a historian, and Brown came up with the best offer — a multi-year, non-tenure-track position. We had been living in different states since we met, so being at the same institution for the first time was important to us.

### What is your current biggest career challenge?

Being a junior faculty member in human population genomics. The field is much more



S. EVENS

competitive than it used to be. All the data are coming from large consortia, such as the 1000 Genomes Project Consortium. Junior people just starting to establish their research credentials can have difficulty joining such consortia. I have always worked on publicly available data, so the biggest change to my research programme is trying to differentiate my work by generating new whole-genome and exome data and analytical methods. My two latest funding sources are very helpful because this work is expensive. Building collaborations is a new frontier for me, but I am finding colleagues at Brown — from anthropologists to clinicians — who have unique data sets to which I can apply my methods.

### Did you have female role models in academia?

Yes, my mother and sister. My parents are statisticians at California State University in Sacramento, and my older sister is a pathologist at the University of California, San Francisco. They had a huge influence on me while I was growing up and as I got into applied maths. As a result, I didn't think about gender or the fact that there were few women in my classes.

### Do young women seek you out as a mentor?

I get a lot of interest from both female and international students, and I mentor a number of undergraduate women. I understand that it can be difficult to pursue a career path without role models, and I am glad if I can provide an example for someone. Mentoring is a huge part of why I want to be a professor, and of what I plan to do in future. ■

INTERVIEW BY VIRGINIA GEWIN



# THE WRITE RULES

*Character development.*

BY FREYA MORRIS

Nari stared at the brass knob. She had already tried to open the wooden door by flicking her head to one side, but it didn't work. She went through troubleshooting but found nothing; according to the system, the door wasn't there. She'd heard about lost doors: forgotten, not converted, hiding some unknown treasure. A smile filled her cheeks. Grasping the cold handle, she rattled and pushed against it until the door finally opened. The room inside glowed. Not the fluorescent white she was used to, but a dull, dim brown-yellow, filled with shadows. A familiar but forgotten smell submerged her, reminiscent of a damp cave.

An old man sat at a desk, surrounded by cream-coloured, wafer-thin piles. Wrinkles entrenched his skin like cracked soil. He looked up at her with bold eyes. A cotton-white beard framed his open mouth. The white light behind her bleached his face. His hand hung in the air, frozen in a pinching motion that Nari hadn't seen before, his fingers arranged like a tulip, gripping a tubular black stick.

Nari pressed her tongue on the inside of her cheek, activating her screen. A translucent menu rose in front of her. She selected the camera with her eyes, zoomed in on his hand and winked, taking the picture. She flicked the frozen image onto the Internet and cross-referenced it. Nothing matched.

The screen went blank. Then a single word appeared: *writing*.

Her heart pounded against her ribs. Her tongue stumbled around in her mouth in a bid to turn it off. But she was too late. They would have seen it too. And they would soon be on their way.

"I'm so sorry," she blurted. "I didn't know what it was."

The old man put his head into his hands and then looked back up at her. "Quick, come here."

"What? Why?"

"We have about 20 minutes," he said, rearranging some white sheets in front of him. "I'm going to teach you how to write."

"Why?"

"For the same reason we still walk." With his palms on the table, he heaved himself up and shuffled towards her.

"But ... but it's illegal for a reason."

"Yes, but is it the right one?"

"Well it saves trees ... somehow. And the planet."



He laughed, a sound like sandpaper on wood. Nari wasn't sure how it saved trees and the planet. It was something she had been told by her parents when she was a child. Everyone was taught this. You would be punished if you ever questioned it. Punished, even if you tried to draw a single line in the sand.

"They are good aren't they?" He pointed his index finger up, holding her gaze. "But to write, is to be free."

She shook her head. "But dictation is free too."

"My dear, the cost is not tangible. When you commit a thought, dictate it, it's monitored, it's used. Even if you don't save it, they do. It's like a firework, leaving trails of light in the system. Writing was banned because it couldn't be controlled. It can't be traced. Don't you see? Writing is free, it's art, it's uncensored, you don't need a screen or a piece of software." His eyes were alight, sparkling.

"But if it's not on the system then you can't do anything with it. No one would see it. What's the point?"

"What's the point?!" He sniffed. "You'll see. Now, look, we don't have much time."

He pulled her around the desk, sat her down and placed the tubular stick in her hand.

"What's this?"

"It's charcoal."

With his leathery fingers he moulded her hand around it and pressed it down onto the white sheet in front of her.

"Is this ... pa ..."

➔ **NATURE.COM**

Follow Futures on

Facebook at:

[go.nature.com/mtoodm](http://go.nature.com/mtoodm)

"Paper, yes. Now, keep these three fingers here in place and push down."

Guided by the old man, Nari dragged a straight line across the page. The vibrations soared up through the stick into her fingers and up her skin.

"Good. Good. Now I want you to write your name."

"But it keeps slipping."

The old man plucked the charcoal from her hand. His fingers danced over the white sheet, marking out a word: 'John'.

"That's my name."

"Really? Jo-han"

"John."

"I've never heard that name before."

"I come from a long line of traditionalists."

He smiled.

Nari grinned back. She closed her eyes and pictured her name. First, she dragged out a squiggly and large 'N', followed by a smaller 'a', which was the hardest, and then an 'r' and an 'i'. She lifted her hand up to see her name carved in squiggles on the pure white sheet.

"I did it!" She laughed. "I did it. It's beautiful."

It was as if she had been cemented; as if she suddenly existed. To see it tangibly, like that. She traced her name with her finger, stroking it carefully. She could see her curly hair in the 'a', her ambitions in the 'N' far overshadowing the rest, and the watchful 'i' of her father, alien and out of place.

"Can I do pictures like this?"

"Of course. Before screens, art was done by hand. It was skill, not concept."

"But what if I get caught?"

He winked at her. "It'll be worth it."

There was a loud bang. Nari leapt from her chair, throwing the stick aside. The light in the room had dimmed; a shadow stood in the doorway. In slow motion, the shadow came towards them and grabbed John's arm.

"You are partaking in an illegal activity ..."

"Me? No. I wouldn't dare."

"Writing is an illegal activity, punishable by death."

"He wasn't doing anything, were you?"

Nari cried, campaigning for John's words.

He leaned close to her ear. "Better to be free in death, than imprisoned in life."

He lifted up his palms, marked with black smudges, in surrender, and smiled as he was led from the room, which moments before hadn't existed. ■

**Freya Morris** is a communications officer at the University of Bristol, UK, who by night dreams of being a scientist. This involves sneaking into lectures and delving into Nature.

JACEY

## Is BID required for NOD signalling?

ARISING FROM G. Yeretssian *et al.* *Nature* **474**, 96–99 (2011).

Innate immune signalling mediated by the nucleotide-binding and oligomerization domain (NOD) receptors for pathogen-associated constituents regulates the response to intracellular peptidoglycans present in Gram-negative and Gram-positive bacteria. Recently, Yeretssian *et al.*<sup>1</sup> reported that the pro-apoptotic BH3-only BCL2 family member BID is essential for NOD-mediated immune signalling. This was on the basis of their finding that bone marrow-derived macrophages (BMDMs) from *Bid*<sup>-/-</sup> mice failed to activate NF- $\kappa$ B and extracellular signal-regulated kinase (ERK), and were unable to secrete inflammatory cytokines after stimulation with NOD ligands, and that BID-deficient mice were also defective in mounting a cytokine response to *in vivo* challenge with NOD ligands. Using the same strain of *Bid*<sup>-/-</sup> mice used by Yeretssian *et al.*<sup>1</sup>, we found that the mice responded like wild-type mice to NOD ligands, and that the levels of NF- $\kappa$ B or ERK activation and cytokine secretion from *Bid*<sup>-/-</sup> BMDMs were indistinguishable from the wild-type response. We therefore propose that the non-apoptotic role of BID in inflammation and innate immunity should be reassessed.

We are investigating NOD signalling, and because the BID-deficient mice that were reported to have such marked defects in this process<sup>1</sup> were generated by us<sup>2</sup>, we attempted to verify the key findings of Yeretssian *et al.*<sup>1</sup>. However, when we treated wild-type and *Bid*<sup>-/-</sup> mice with either tripeptide L-Ala- $\gamma$ -D-Glu-meso-diaminopileic acid ( $\gamma$ Tri-DAP) or muramyl dipeptide (MDP) to activate NOD signalling and measured 23 chemokines and cytokines by multiplex analysis, we found that the two sets of mice responded indistinguishably. Injection of MDP caused a reproducible and comparable increase in the levels of the cytokines and chemokines interleukin (IL)-6, keratinocyte-derived chemokine (KC), granulocyte colony-stimulating factor (G-CSF) and monocyte chemoattractant protein-1 (MCP-1) in the serum of both wild-type and *Bid*<sup>-/-</sup> mice (Fig. 1a and data not shown). By contrast, and as expected<sup>3</sup>, no increase in these cytokines or chemokines was seen in MDP-injected *Ripk2*<sup>-/-</sup> mice (Fig. 1a). A comparable increase in nine cytokines and chemokines in the sera of wild-type and *Bid*<sup>-/-</sup> mice was also seen after challenge with  $\gamma$ Tri-DAP (Fig. 1b and data not shown). In mice of all three genotypes (wild-type, *Bid*<sup>-/-</sup> and *Ripk2*<sup>-/-</sup>), the serum levels of these cytokines and chemokines were barely detectable (and not significantly different from each other) before challenge (Fig. 1a, b).

To understand the discrepancy between our results and those of Yeretssian *et al.*<sup>1</sup>, we generated BMDMs from wild-type, *Bid*<sup>-/-</sup> and *Ripk2*<sup>-/-</sup> mice and activated NOD signalling in these cells *in vitro* by two separate methods. In the first method, we transfected MDP with DOTAP using a protocol supplied by Yeretssian *et al.* in which MDP is transfected into BMDMs in the absence of serum in the tissue culture media<sup>1</sup> (Fig. 1c, left). In the second, established protocol, cells are first primed with interferon (IFN)- $\gamma$  and then treated with MDP or DAP<sup>4</sup> (Fig. 1c, right), thereby avoiding any potential complications that might arise owing to a particular transfection protocol. Independent of the method used, we observed comparable levels of IL-6 secretion in *Bid*<sup>-/-</sup> and wild-type BMDMs, whereas *Ripk2*<sup>-/-</sup> cells were unresponsive to any of the MDP treatments.

We also performed western blot analysis to evaluate activation of NF- $\kappa$ B and ERK signalling; pathways that were reported by Yeretssian *et al.*<sup>1</sup> to be completely defective in *Bid*<sup>-/-</sup> BMDMs. By contrast, using four different protocols for NOD activation—DOTAP transfection without serum in the tissue culture media, identical to Yeretssian *et al.*<sup>1</sup> (Fig. 1d, left), a DOTAP transfection protocol with serum in the

media (see Appendix Fig. 1b), IFN- $\gamma$  priming (Fig. 1d, right, and Appendix Fig. 1a), and another lipidated-MDP protocol (see Appendix Fig. 1c)—we found normal levels of NF- $\kappa$ B activation (reflected by loss of I $\kappa$ B- $\alpha$  after 30 and 60 min of stimulation and

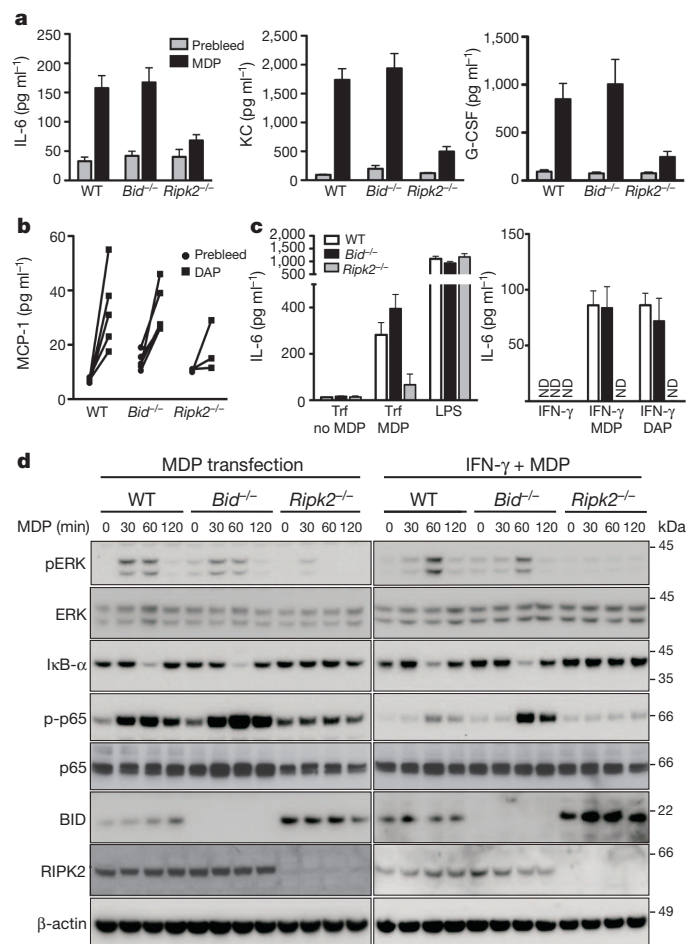


**Figure 1 | BID is dispensable for NOD signalling.** **a**, Wild-type (WT;  $n = 10$ ), *Bid*<sup>-/-</sup> ( $n = 9$ ) and *Ripk2*<sup>-/-</sup> mice ( $n = 7$ ) were injected with MDP and killed after 4 h. Levels of IL-6, KC and G-CSF were measured by Multiplex analysis in these serum samples and also in bleeds taken from the same animals before challenge. **b**, Wild-type ( $n = 5$ ), *Bid*<sup>-/-</sup> ( $n = 5$ ) and *Ripk2*<sup>-/-</sup> ( $n = 3$ ) mice were injected with  $\gamma$ Tri-DAP for 2 h, and serum levels of MCP-1 before and after the treatment were measured by Multiplex analysis. **c**, BMDMs from wild-type, *Bid*<sup>-/-</sup> and *Ripk2*<sup>-/-</sup> mice were mock transfected (trf), transfected with MDP, treated with lipopolysaccharide (LPS; left) or stimulated with IFN- $\gamma$ , IFN- $\gamma$  plus MDP or IFN- $\gamma$  plus DAP (right). Twenty hours after stimulation, the levels of IL-6 in the supernatant were assessed by ELISA. Error bars denote s.e.m.;  $n = 3$ ; ND, not detected. One representative experiment of at least three repeats is shown. **d**, BMDMs from wild-type, *Bid*<sup>-/-</sup> and *Ripk2*<sup>-/-</sup> mice were either transfected with MDP using DOTAP reagent or stimulated for the indicated times with IFN- $\gamma$  plus MDP. Lysates were tested for ERK phosphorylation (pERK; a marker of ERK activation), I $\kappa$ B- $\alpha$  disappearance and p65 phosphorylation (p-p65; both markers of NF- $\kappa$ B activation) by western blotting. Probing for BID and RIPK2 (also known as RIP2) confirmed the mouse genotyping, and  $\beta$ -actin was used as a loading control. One representative experiment of at least three repeats is shown.



by p65 phosphorylation) and ERK phosphorylation (indicative of activation of this kinase) in BID-deficient BMDMs (Fig. 1d and Appendix).

Our data demonstrate a robust cytokine response in wild-type and *Bid*<sup>-/-</sup> mice *in vivo* and in cultured BMDMs from these animals using the same commercial NOD-activating reagents at the same doses, the same experimental protocols, and the same strain of BID-deficient mice that were used by Yeretssian *et al.*<sup>1</sup>. The profound reduction of NOD responses in RIPK2-deficient mice indicates that the methods we used efficiently and specifically stimulated NOD signalling. The reasons for the discrepancies in our findings and those of Yeretssian *et al.*<sup>1</sup> are unclear, but our results indicate that BID, which is crucial for death receptor-induced apoptosis in so-called type 2 cells (for example, hepatocytes and pancreatic  $\beta$  cells<sup>2,5-7</sup>), is not essential for NOD signalling.

## Methods

*Bid*<sup>-/-</sup> mice were generated using C57BL/6-derived embryonic stem cells<sup>7</sup> and *Ripk2*<sup>-/-</sup> mice were a gift from R. Flavell<sup>3</sup>. Prebleeds were collected retro-orbitally and, at culling, blood was collected by cardiac puncture. MDP (100  $\mu$ g, 500  $\mu$ l per mouse, Bachem or Invivogen,) or  $\gamma$ Tri-DAP (2 mg kg<sup>-1</sup>, Anaspec) were injected intraperitoneally and serum was collected 4 or 2 h after injection, respectively. The levels of 23 cytokines and chemokines were measured by multiplex analysis (Biorad). BMDMs from wild-type, *Bid*<sup>-/-</sup> or *Ripk2*<sup>-/-</sup> mice were transfected with 100  $\mu$ g ml<sup>-1</sup> MDP using DOTAP transfection reagent (Roche), or primed for 2 h with murine IFN- $\gamma$  (10 ng ml<sup>-1</sup>, R&D Systems) before the addition of MDP (10  $\mu$ g ml<sup>-1</sup>, Bachem), DAP (10  $\mu$ g ml<sup>-1</sup>, Invivogen) or L-18 MDP (200 ng ml<sup>-1</sup>, Invivogen) was added to the BMDMs without priming. Levels of IL-6 in the supernatant of BMDMs were measured by ELISA (ebioscience) 20 h after stimulation. Lysates of cells were run on SDS-PAGE gradient gels, transferred to polyvinylidene difluoride (PVDF) membrane and blotted with antibodies against total ERK, phospho-ERK, phospho-p65, I $\kappa$ B- $\alpha$

(Cell Signaling), BID (gift from D. Huang), RIPK2, total p65 (Santa Cruz) and  $\beta$ -actin (Sigma). All experiments were performed double-blinded, and in the case of Fig. 1d and Appendix Fig. 1, sample identity was revealed only before loading SDS-PAGE gels.

Ueli Nachbur<sup>1,2</sup>, James E. Vince<sup>1,2</sup>, Lorraine A. O'Reilly<sup>1,2</sup>,  
Andreas Strasser<sup>1,2</sup> & John Silke<sup>1,2</sup>

<sup>1</sup>The Walter and Eliza Hall Institute, 1G Royal Parade, Parkville, Victoria 3052, Melbourne, Australia.

<sup>2</sup>Department of Medical Biology, University of Melbourne, Melbourne, Victoria 3010, Australia.

email: j.silke@latrobe.edu.au

Received 21 September 2011; accepted 25 May 2012.

1. Yeretssian, G. *et al.* Non-apoptotic role of BID in inflammation and innate immunity. *Nature* **474**, 96–99 (2011).
2. Kaufmann, T., Gugasyan, R., Gerondakis, S., Dixit, V. M. & Strasser, A. Loss of the BH3-only protein Bid does not rescue RelA-deficient embryos from TNF-R1-mediated fatal hepatocyte destruction. *Cell Death Differ.* **14**, 637–639 (2007).
3. Kobayashi, K. *et al.* RICK/Rip2/CARDIAK mediates signalling for receptors of the innate and adaptive immune systems. *Nature* **416**, 194–199 (2002).
4. Saiki, I. & Fidler, I. J. Synergistic activation by recombinant mouse interferon-gamma and muramyl dipeptide of tumoricidal properties in mouse macrophages. *J. Immunol.* **135**, 684–688 (1985).
5. Yin, X. M. *et al.* Bid-deficient mice are resistant to Fas-induced hepatocellular apoptosis. *Nature* **400**, 886–891 (1999).
6. Jost, P. J. *et al.* XIAP discriminates between type I and type II FAS-induced apoptosis. *Nature* **460**, 1035–1039 (2009).
7. Kaufmann, T. *et al.* The BH3-only protein bid is dispensable for DNA damage- and replicative stress-induced apoptosis or cell-cycle arrest. *Cell* **129**, 423–433 (2007).

Competing Financial Interests Declared none.

doi:10.1038/nature11366

## APPENDIX

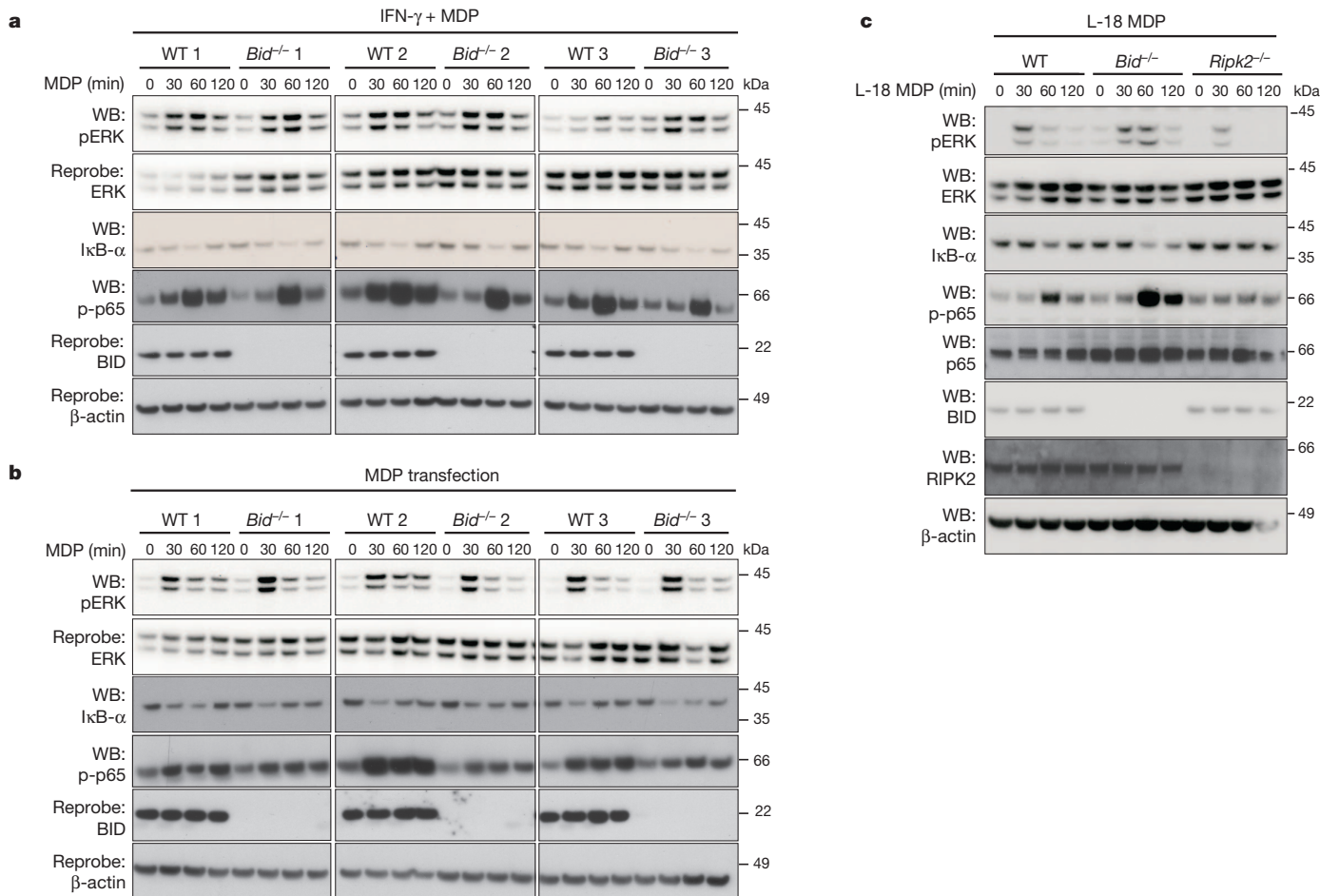


**Figure 1** | *Bid*<sup>-/-</sup> BMDMs respond like wild-type BMDMs to various NOD-stimulating protocols. **a**, BMDMs from three wild-type (WT) and three *Bid*<sup>-/-</sup> mice were primed with IFN- $\gamma$  (10 ng ml<sup>-1</sup>) for 2 h before the addition of MDP (10  $\mu$ g ml<sup>-1</sup>) for the indicated times. Lysates from the BMDMs were separated on SDS-PAGE gradient gels. The pairing of wild-type and knockout BMDMs was random, and samples were run on the same gel and probed at the same time with the indicated antibodies. Gel fragments are shown so that the marked up molecular mass ladder, run between each pair of BMDMs, could be removed. Lysates were tested for ERK phosphorylation, disappearance of I $\kappa$ B- $\alpha$  and p65 phosphorylation by western blotting. Probing for BID confirmed the genotype, and  $\beta$ -actin was used as a loading control. **b**, The same BMDMs as in **a** were transfected with MDP (100  $\mu$ g ml<sup>-1</sup>) using DOTAP transfection closely matching the protocol used by Yeretssian *et al.*<sup>1</sup> except that BMDMs were maintained in serum containing medium for the duration of the transfection

and experiment. Lysates, run in the same order as in **a**, from the indicated time points after transfection were tested for ERK and NF- $\kappa$ B activation using the same antibodies as in **a**. *Bid*<sup>-/-</sup> BMDMs activated both ERK and NF- $\kappa$ B in the same manner as wild-type cells. It is noteworthy that wild-type sample two (WT 2) shows increased p65 phosphorylation compared with all other BMDMs, independent of the mode of MDP stimulation used (IFN- $\gamma$  priming or DOTAP transfection). **c**, A fresh batch of BMDMs from wild-type, *Bid*<sup>-/-</sup> and *Ripk2*<sup>-/-</sup> mice was treated with L-18 MDP (200 ng ml<sup>-1</sup>), a lipidated form of MDP that is cell permeable and therefore circumvents either IFN- $\gamma$  priming or MDP transfection. Lysates from the indicated time points were tested for ERK and NF- $\kappa$ B activation using the same antibodies as in Fig. 1d. As with the other protocols *Bid*<sup>-/-</sup> BMDMs activated ERK and NF- $\kappa$ B activation in a similar manner to wild-type BMDMs, whereas *Ripk2*<sup>-/-</sup> BMDMs were defective.

Yeretssian *et al.* reply

REPLYING TO U. Nachbur, J. E. Vince, L. A. O'Reilly, A. Strasser & J. Silke *Nature* **488**, <http://dx.doi.org/10.1038/nature11366> (2012).

Nucleotide-binding and oligomerization domain (NOD) receptors are cytosolic sensors of microbe-associated molecular patterns (MAMPs). Like other members of the BCL2 family of proteins (such as BCL2 and BCL-X<sub>L</sub>), BID has a role in inflammation and innate immunity<sup>2,3</sup>. Its association with the NOD signalosome showed it to be an important player in the pathway. Furthermore, a recent report demonstrated unequivocal and direct binding of BID to purified NOD1 protein<sup>4</sup>. Although Nachbur *et al.*<sup>5</sup> question whether BID is

essential for NOD signalling, they show no clear evidence to the contrary. Instead, they provided three data sets, and an analysis of these data sets is presented in Fig. 1 and Appendix Fig. 1 (ref. 5). Although there was considerable variability in the results from these independently performed experiments (also apparent in the data presented in their Comment), overall the data support the findings in our Letter<sup>6</sup> that BID contributes to the NOD-mediated response. A challenge to our conclusions was based on the claim that BID deficiency



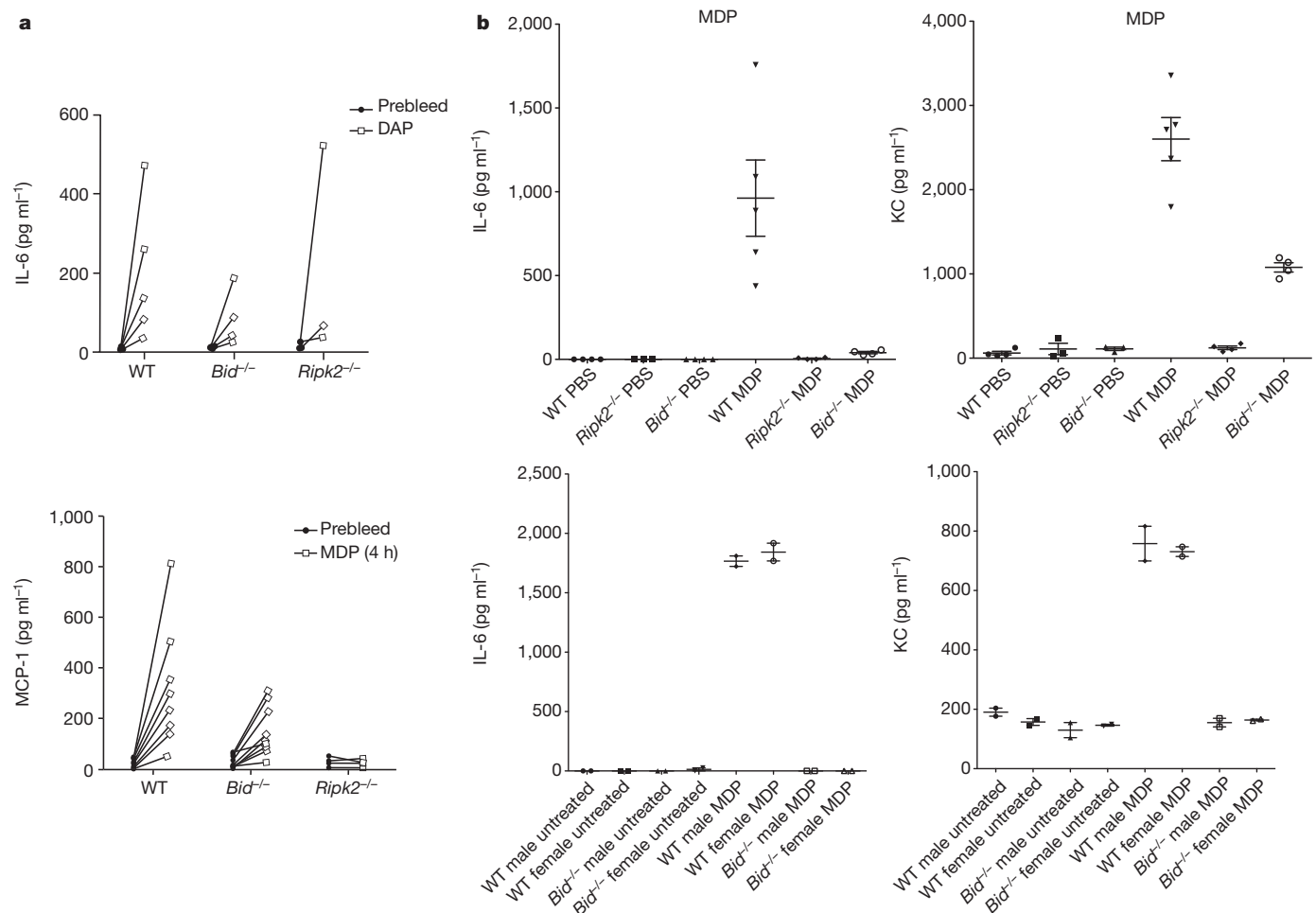


**Figure 1 | Defect in NOD-mediated cytokine induction in the absence of BID.** **a**, Results by Nachbur *et al.* from data set 1. **b**, Independent repeat of experiments (in ref. 3). Top, PBS or MDP (25 mg kg<sup>-1</sup>) was injected intraperitoneally for 4 h before blood collection by heart puncture. Four to five

male mice of each genotype at 6–8 weeks of age were used. Cytokine levels were determined by ELISA. Bottom, macrophages were transfected with DOTAP and MDP for 18 h, supernatants were collected and cytokine levels were determined by ELISA. We did not observe a gender difference in the response.

does not affect NOD signalling. Data in Appendix Fig. 1a and b (ref. 5) support our conclusions and show a role for BID in NF- $\kappa$ B activation (decreased p65 phosphorylation). By contrast, a third set of immunoblots shows the opposite effect, in which BID seems to be a negative regulator of NF- $\kappa$ B signalling (increased p65 phosphorylation in *Bid*<sup>-/-</sup> cells; Fig. 1 from ref. 5). The basis for these incoherent and non-reproducible results is unclear but suggests technical caveats. For instance, it is surprising to see p65 phosphorylation in *Ripk2*<sup>-/-</sup> cells (Fig. 1c in ref. 5).

Similarly, the effect of BID on ERK activation was highly variable and difficult to assess owing to uneven levels of total ERK (Appendix Fig. 1a from ref. 5). It is important to note that in contrast to wild-type or *Ripk2*<sup>-/-</sup> cells, *Bid*<sup>-/-</sup> cells showed increased ERK phosphorylation at the steady state (Nachbur *et al.*<sup>5</sup> Fig. 1d), suggestive of a potential MAMP contamination in culture. However, despite this apparent pERK signal at time 0, ERK phosphorylation is induced to a lesser extent in *Bid*<sup>-/-</sup> cells than in wild-type bone marrow-derived macrophages (BMDMs) after muramyl dipeptide (MDP) treatment. Of note, the extent of BID expression in wild-type versus *Ripk2*<sup>-/-</sup> cells was also notably different across experiments (compare Nachbur *et al.*<sup>5</sup> Fig. 1d with Appendix Fig. 1c). *In vivo* cytokine production in response to NOD agonists was equally variable across experiments and among mice from the same genotype. For instance, in contrast to Fig. 1a and b, the first data set by Nachbur *et al.*<sup>5</sup> showed decreased interleukin (IL)-6

and monocyte chemoattractant protein-1 (MCP-1) secretion after diaminopipelic acid (DAP) and MDP injection, respectively, in *Bid*<sup>-/-</sup> mice compared with wild-type animals (Fig. 1a). Altogether, it is difficult to draw any conclusions based on the divergent data presented by Nachbur *et al.* Although the extent to which BID is required for NOD signalling may vary with cellular context and with environmental (for example, microbiota) and disease conditions, our conclusion that BID contributes to NOD-mediated responses is reproducible and has been repeated independently (Fig. 1b). Thus, the controversy seems to be more semantic, than substantive.

**Garabet Yeretssian<sup>1</sup>, Ricardo G. Correa<sup>2</sup>, Karine Doiron<sup>1</sup>, Patrick Fitzgerald<sup>3</sup>, Christopher P. Dillon<sup>3</sup>, Douglas R. Green<sup>3</sup>, John C. Reed<sup>2</sup> & Maya Saleh<sup>1</sup>**

<sup>1</sup>Department of Medicine, McGill University, Montreal, Quebec H3G 0B1, Canada.

email: maya.saleh@mcgill.ca

<sup>2</sup>Sanford-Burnham Medical Research Institute, La Jolla, California 92037, USA.

<sup>3</sup>St. Jude Children's Research Hospital, Memphis, Tennessee 38105, USA.

1. Bruey, J. M. *et al.* Bcl-2 and Bcl-X<sub>L</sub> regulate proinflammatory caspase-1 activation by interaction with NALP1. *Cell* **129**, 45–56 (2007).

# BRIEF COMMUNICATIONS ARISING

---

2. Luo, W. *et al.* Bid mediates anti-apoptotic COX-2 induction through the IKK $\beta$ /NF $\kappa$ B pathway due to 5-MCDE exposure. *Curr. Cancer Drug Targets* **10**, 96–106 (2010).
3. Yeretssian, G. *et al.* Non-apoptotic role of BID in inflammation and innate immunity. *Nature* **474**, 96–99 (2011).
4. Askari, N. *et al.* Expression, purification, and characterization of recombinant NOD1 (NLRC1): A NLR family member. *J. Biotechnol.* **157**, 75–81 (2012).
5. Nachbur, U., Vince, J. E., O'Reilly, L. A., Strasser, A. & Silke, J. Is BID required for NOD signalling? *Nature* **488**, <http://dx.doi.org/10.1038/nature11366> (2012).
6. Yeretssian, G. *et al.* Non-apoptotic role of BID in inflammation and innate immunity. *Nature* **474**, 96–99 (2011).

doi:10.1038/nature11367



## FORUM: Cancer

# Resolving the stem-cell debate

New research backs the contentious idea that solid tumours are not masses of equivalent cells, but instead contain cancer stem cells that support tumour maintenance. Here, two experts provide complementary views on the findings and on the implications for potential therapies. **SEE LETTERS P.522 & P.527**

### THE PAPERS IN BRIEF

- Evidence that cancer stem cells spawn more highly differentiated (non-stem) cells in solid tumours has relied almost entirely on analyses of tumours formed by human cancer cells injected into mice that have compromised immune systems.
- Chen *et al.*<sup>1</sup> (page 522) and Driessens *et al.*<sup>2</sup> (page 527), together with Schepers *et al.*<sup>3</sup> (writing in *Science*), traced individual cells in intact tumours as the tumours developed

from non-cancerous cells in mice\*.

- The studies identify specific cell subsets that act as cancer stem cells in brain, skin and intestinal tumours, with one of the reports<sup>1</sup> indicating that targeting such cells may improve therapeutic outcome.
- The papers also describe how different cell subpopulations emerge and evolve as a tumour grows and in response to anticancer treatment.

## Meet the parents

RICHARD J. GILBERTSON

Despite decades of research, one-third of patients with cancer die within five years of diagnosis. Therefore, it is not surprising that any concepts offering a sea change in the way we think about and treat cancer garner enormous attention and resources. One such concept is the cancer stem cell (CSC) hypothesis, which suggests that cancers are organized into aberrant cell hierarchies in which 'differentiated' daughter cells that have limited capacity to proliferate are produced by a subset of parent CSCs that replicate indefinitely (Fig. 1).

Until now, evidence for the existence of CSCs has been controversial, but the hypothesis is extremely attractive because it provides a conceptual framework on which new therapeutic approaches could be built: any drug capable of killing CSCs would, in theory, be curative. Now, three independent studies of mouse models of brain<sup>1</sup>, skin<sup>2</sup> and intestinal<sup>3</sup> tumours provide the first evidence that CSCs do exist and arise *de novo* during tumour formation in intact organs.

Lineage tracing is a technique that allows permanent *in vivo* fluorescent marking of stem cells and their progeny. This method has been used previously<sup>4</sup> to identify intestinal stem

cells, which give rise to the various cell types that make up intestinal epithelial tissue in mice. The same study also revealed that when a gene encoding the protein APC is deleted, these stem cells generate benign tumours (intestinal adenomas).

To test whether the tumours were maintained by CSCs, Schepers *et al.*<sup>3</sup> used a lineage-tracing strategy involving intestinal stem cells in which APC had been knocked out, so that cells randomly adopted one of four fluorescent tagging colours when the mice were given a low dose of the drug tamoxifen. Initial tamoxifen dosing often generated single-colour 'clonal' adenomas, indicating that they typically originated from single intestinal stem cells. Remarkably, a subsequent dose of tamoxifen switched the colour of individual cells in the adenomas, and the progeny of these newly coloured cells (which included differentiated tumour cells) went on to populate the tumour, pinpointing their parents as CSCs.

Similar observations were made by Driessens *et al.*<sup>2</sup> in a mouse model of a benign skin tumour (papilloma). Using lineage tracing of individual papilloma cells, the authors observed great variability in the cells' proliferative potential, with only 20% of them being able to generate daughters that populated large swathes of tumour.

The studies by Schepers *et al.* and Driessens

*et al.* provide elegant demonstrations of stem-cell activity in intact tumours. But adenomas and papillomas are benign tumours, not cancers. The cells in these tumours are organized in much the same way as the corresponding normal tissue, and so it is not surprising that these benign tumours contain cell hierarchies that approximate to normality.

A key question, therefore, is whether cell hierarchies driven by CSCs exist in the invasive malignant tumours that kill patients. With this in mind, Driessens *et al.* also analysed a mouse model of squamous skin cancer. The researchers found that, in comparison with papillomas, the malignant tumours contained much higher numbers of long-term replicating cancer cells that showed little evidence of cell differentiation. This raises the possibility that cancers slip from hierarchical organization into relative anarchy as they progress from the benign to the malignant state.

So what is the evidence that malignant tumours contain CSCs? Chen *et al.*<sup>1</sup> provide compelling data that glioblastomas (the deadliest brain tumours) are organized hierarchically. Using a clever combination of 'suicide-gene' technology that selectively killed glioblastoma CSCs, and antitumour drugs that eliminate the bulk of dividing cancer cells, they show that CSCs repopulate the cancer when the bulk of the tumour is wiped out by anticancer drugs (Fig. 1a). Targeting both CSCs and their daughter cells with a combination of suicide-gene targeting and anticancer drugs, the authors dramatically impeded the growth of glioblastomas *in vivo*.

The three papers represent an important new chapter in the debate over CSCs. They introduce us for the first time to these cells in their native habitats and provide the first hard evidence that such cells are a legitimate therapeutic target. The next steps will include determining how well mouse CSCs recapitulate their human counterparts, and how best to destroy these for the benefit of patients.

Richard J. Gilbertson is at the Comprehensive Cancer Center, St. Jude Children's Research Hospital, Memphis, Tennessee 38105-3678, USA.  
e-mail: richard.gilbertson@stjude.org

\*This article and the papers under discussion<sup>1-3</sup> were published online on 1 August 2012.

# Stemming tumour evolution

TREVOR A. GRAHAM

Cancer formation is an evolutionary process: repeated rounds of mutation and selection lead to outgrowth of the fittest mutant clones and transform normal healthy cells into cancer cells<sup>5</sup>. The identification of CSCs as a restricted population of cells responsible for the maintenance of tumours suggests that these are the cells that have the inherent ability to propagate mutations throughout a tumour and to drive cancer evolution: CSCs are the 'movers and shakers' of carcinogenesis. Selective killing of such cells is therefore an appealing therapeutic prospect. Indeed, Chen *et al.*<sup>1</sup> observed a near-twofold reduction in the density of brain tumours in mice when they combined standard anticancer drugs with selective killing of CSCs, compared with standard agents alone.

But should the primary goal of cancer therapy now be to kill the CSC 'root' of the tumour? This is akin to asking if we may safely ignore the non-stem-cell population of tumour cells. It is conceivable that selected mutations in non-stem cells will cause them to revert to a stem-cell-like state and so contribute to tumour evolution. Furthermore, non-stem cells in tumours may revert to such a stem-cell-like state even in the absence of mutation<sup>6</sup>. If that is the case, then selectively killing a

**"The results place competition between tumour cells at the centre of cancer evolution."**

CSC population may vacate a niche within the tumour, opening it up to occupancy by a rival population of cells. Trying instead to limit 'stemness' — perhaps by modifying the microenvironment that supports

stem cells in tumours<sup>7</sup> — may prove a more effective therapeutic strategy than simply eradicating CSCs.

Driessens *et al.* and Chen *et al.* show that the cellular organization of the early (pre-cancer) skin and intestinal tumours are caricatures of their normal organs, and are composed of both stem cells and non-stem cells. The presence of non-stem cells may represent a brake on tumour evolution: such cells not only consume the limited resources available, but also may be evolutionary dead ends, in the sense that (unlike the stem cells) they have only limited potential for growth. Interestingly, Driessens *et al.* observed that progression to cancer in benign skin tumours was associated with an expansion of the CSC population and a decrease in the production of non-stem cells. This suggests that tumour evolution enriches the CSC population.

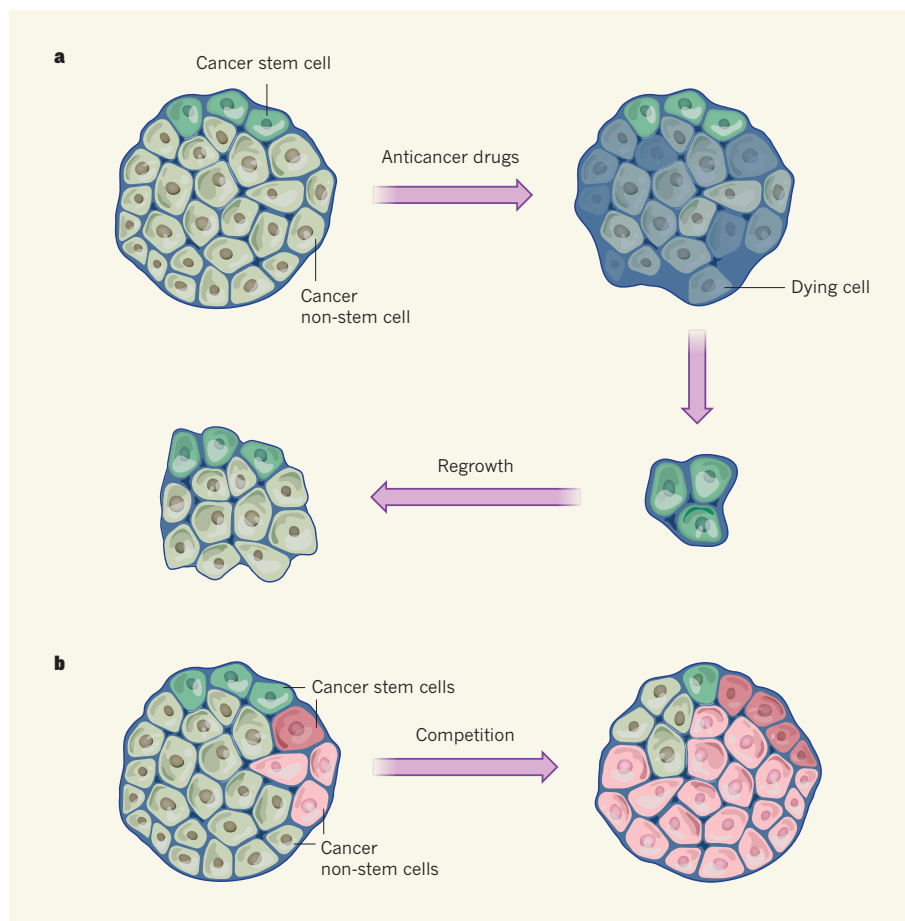


**Figure 1 | Not all cells in a tumour are equal.** Chen *et al.*<sup>1</sup>, Driessens *et al.*<sup>2</sup> and Schepers *et al.*<sup>3</sup> show that brain, skin and intestinal tumours include cancer stem cells (CSCs) that self-renew and that produce other, more-differentiated (non-stem) cells that constitute the bulk of the tumour-cell population. **a**, Chen and colleagues' results indicate that, although current anticancer drugs can wipe out most of the dividing non-stem cells, surviving CSCs can repopulate the tumour. Therefore, targeting both CSCs and the dividing cells would be required for complete tumour eradication. **b**, Driessens *et al.* report that CSCs continuously compete with each other for a place in the tumour, and that the winners' daughter cells predominate. Red and green colours indicate different clonal populations, each one originally derived from an individual CSC.

Thus, designing therapies that prevent increases in stemness may be a means to restrict tumour progression to cancer.

A common model of cancer evolution involves sequential waves of clonal expansion, each triggered by a new mutation<sup>5</sup>. Remarkably, Driessens and colleagues' results are at odds with this model. The authors found neutral competition between CSCs; that is, every CSC within a tumour is equally likely to clonally expand or die off, probably even in the absence of new mutations (Fig. 1b). Their observations suggest that clonal expansion is a continuous process in tumours, not a rarity driven by a new, selectively advantageous mutation. And the results place competition between tumour cells at the centre of cancer evolution. In this context, mutations that simply drive proliferation may be of less importance than previously thought, whereas mutations that slightly tip the balance of competition to favour one CSC over another — perhaps by improving survival, promoting self-renewal or monopolizing limited

resources — might be the ones that are highly selected in tumours.

The main take-home message from the three studies is that cells are organized hierarchically within tumours; all tumour cells are not equal. Understanding how these cellular hierarchies shape carcinogenesis, and exploiting them to change the course of tumour evolution, holds promise for effective treatment. ■

**Trevor A. Graham** is at the Centre for Evolution and Cancer, University of California, San Francisco, San Francisco, California 94143-1351, USA.  
e-mail: trevor.graham@ucsfmedctr.org

1. Chen, J. *et al.* *Nature* **488**, 522–526 (2012).
2. Driessens, G., Beck, B., Caauwe, A., Simons, B. D. & Blanpain, C. *Nature* **488**, 527–530 (2012).
3. Schepers, A. G. *et al.* *Science* **337**, 730–735 (2012).
4. Barker, N. *et al.* *Nature* **457**, 608–611 (2009).
5. Greaves, M. & Maley, C. C. *Nature* **481**, 306–313 (2012).
6. Gupta, P. B. *et al.* *Cell* **146**, 633–644 (2011).
7. Medema, J. P. & Vermeulen, L. *Nature* **474**, 318–326 (2011).



# Electrons in perfect drag

A neat experiment shows that if a current is sent through one of two adjacent conducting layers placed in a strong magnetic field, a quantum effect generates an exactly equal but opposite current in the other layer. [SEE LETTER P.481](#)

STEVEN M. GIRVIN

In a superconductor, electrons travel in pairs and can flow past obstacles without resistance. On page 481 of this issue, Nandi *et al.*<sup>1</sup> demonstrate the existence of a strange analogue of this electronic behaviour in a system of two adjacent conducting layers in which the pairing is instead between an electron in one layer and the absence of an electron in the other layer. This strange form of pairing causes the current in the system to flow without dissipation, as long as the separate currents in each layer are exactly equal in magnitude and opposite in direction. As the physicist Isidor Isaac Rabi once remarked when confronted with an unexpected item from the menu of the delicatessen that is our Universe, “Who ordered that?”

The ‘fluid’ model of electricity, developed in the eighteenth century by Benjamin Franklin and others, postulates that electrical charge is a continuous quantity associated with an excess or deficit in the density of some mysterious fluid that smoothly pervades the Universe. This model is perfectly adequate for many practical purposes, but in 1897, J. J. Thomson discovered the electron and concluded that electrical charge is quantized — it occurs in tiny but discrete units carried by elementary particles.

The discreteness of charge is responsible for a phenomenon known as Coulomb drag. To understand what this is, consider two thin metal layers that are separated by an electrically

insulating barrier but that are so close to each other that the distance between them (about 10 nanometres) is comparable to the distance between individual electrons within each layer (Fig. 1). The electrons in each layer therefore ‘see’ the graininess of the charge density of the electrons in the other layer. Because of their mutual Coulomb force, electrons in each layer can collide with each other. These collisions cause electrons flowing in one layer (the drive current) to ‘drag’ the electrons in the other layer, producing a drag current that flows in the same direction as the drive current. An analogous phenomenon occurs when a piece of sandpaper is pushed past another piece: the discrete grains of sand in each sheet produce a mutual friction that drags the second sheet along in the same direction as the first.

In typical circumstances, the drag current does indeed flow in the same direction as the drive current, but it is much smaller and vanishes as the temperature approaches absolute zero. This is because the mutual drag friction between electron layers is far smaller than the internal friction — that is, the ordinary electrical resistance resulting from the collisions of the electrons with ever-present impurity atoms in each layer. The smallness of the mutual friction is due in part to the fact that, in ordinary metals, the electrons are whizzing about at 1% of the speed of light and don’t spend much time near each other during collisions. The disappearance of the drag current at zero temperature is caused by a quantum effect

associated with the Pauli exclusion principle, which states that two electrons cannot occupy the same quantum state.

In Nandi and colleagues’ experiment, the application of a strong magnetic field perpendicular to the two adjacent conducting layers puts the system in the quantum Hall regime, in which the electrons are forced into small, quantized, circular orbits whose centres drift only slowly. This effectively nullifies the electrons’ kinetic energy, leaving the Coulomb interactions to dominate the physics of the system. The microscopic electronic motion in the two layers can thus become strongly correlated, markedly increasing the Coulomb drag current.

It thus seems plausible that the drag current in Nandi and colleagues’ experiment could be large, and might even equal the drive current in magnitude. And this is indeed what the authors observe: they detect a drag current that is precisely as large as the drive current. However, the two currents flow in opposite directions. How can that be?

It turns out that our simple sandpaper analogy fails because of quantum effects. The Coulomb interaction energy is lowered if an electron in one layer is paired with a hole (an absence of an electron) in the other layer. The Coulomb attraction between the opposite charges of the electron and the hole produces a quantum-mechanical bound state called an exciton<sup>2</sup>. An exciton is rather like a hydrogen atom, with the hole replacing the positive charge of the proton. Clearly, when hydrogen atoms move there is no electrical current because the atoms are charge neutral. The same is true here. If all the electrons are bound up in neutral excitons, the sum of the currents in the two layers is zero — no matter which way the excitons are moving.

The story is a bit more subtle than this, however. There are actually two exciton states, denoted ‘up’ and ‘down’ according to which layer contains the electron. Quantum mechanically, even if electrons can never tunnel through the insulating barrier to change layers, the two exciton possibilities ‘know’ about each other, and the lowest-energy exciton state is a quantum superposition of both up and down states at the same time. This superposition can be thought of in chemical-bonding terms as an orbital hybridization in which there is uncertainty about which layer the electron is in.

Crucially, the quantum states of the excitons carrying a current consist of a quantum superposition of an up exciton moving, say, to the left, and a down exciton moving to the right. Although there is still uncertainty about which layer the electron is in, we know that if it is in the upper layer it is moving to the left, and if it is in the lower layer it is moving to the right. As a result, the currents in the two layers are exactly equal in magnitude but opposite in direction. Furthermore, much as in a

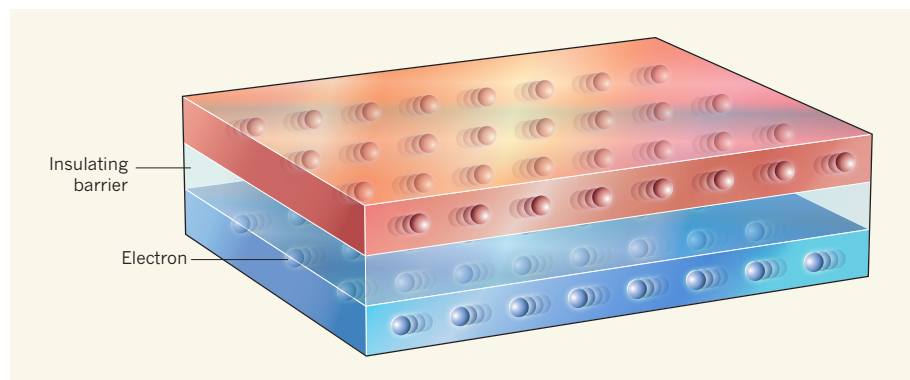


**Figure 1 | Against the current.** Nandi and colleagues’ system<sup>1</sup> consists of two closely spaced layers of electrons separated by an electrically insulating barrier. The authors show that, by applying a strong magnetic field, the system can be brought into a regime in which the current of electrons in one layer drives the electrons in the other layer to flow in a current that has the same magnitude as the drive current, but the opposite direction. Layer thickness and separation, and the spacing between electrons in each layer, are all about 10 nanometres.

superconductor, the two currents flow without dissipation. The system prefers to be in this dissipationless state, and so if a current is sent through the drive layer, an exactly equal and opposite drag current automatically appears in the other layer.

Nandi and colleagues' experiment dramatically shows this novel effect of quantum superposition. Although practical applications of the phenomenon are unlikely, it does provide an example of quantum physics that allows the production of something previously

considered impossible — namely, an electrical transformer (a device that boosts or reduces voltage) that works with unidirectional (d.c.) current instead of requiring periodically reversing (a.c.) current<sup>3</sup>.

Finally, if the currents in the two layers are in the form of opposite-handed whirlpools (vortices), something even more bizarre is believed to occur. According to theory<sup>4</sup>, a new elementary particle emerges — one that has a fractional charge, equal to half that of an electron. But that is a tale for another time. ■

**Steven M. Girvin** is in the Department of Physics, Yale University, New Haven, Connecticut 06520–8120, USA.  
e-mail: [steven.girvin@yale.edu](mailto:steven.girvin@yale.edu)

1. Nandi, D., Finck, A. D. K., Eisenstein, J. P., Pfeiffer, L. N. & West, K. W. *Nature* **488**, 481–484 (2012).
2. Eisenstein, J. P. & MacDonald, A. H. *Nature* **432**, 691–694 (2004).
3. Halperin, B. I., Stern, A. & Girvin, S. M. *Phys. Rev. B* **67**, 235313 (2003).
4. Moon, K. *et al.* *Phys. Rev. B* **51**, 5138–5170 (1995).

## TISSUE ENGINEERING

# Blood vessels on a chip

**To understand how blood vessels form and function, scientists require reproducible systems that mimic living tissues. An innovative approach based on microfabricated vessels provides a key step towards this goal.**

CLAUDIO FRANCO & HOLGER GERHARDT

**T**he establishment of blood-vessel networks is a matter of life and death for tissues and organisms. Failure to form a functional vascular network causes early death of embryos, and dysfunction of endothelial cells (which line the inside of blood vessels) contributes to many diseases, including stroke, thrombosis and atherosclerosis<sup>1</sup>. Therefore, substantial resources are being directed towards research into the cellular, molecular and physical factors that regulate the formation, stability and functional responses of the vasculature. Writing in *Proceedings of the National Academy of Sciences*, Zheng *et al.*<sup>2</sup> describe how they created living, three-dimensional microvascular networks that recapitulate some of the functions that are typical of blood vessels.

Animal models take centre stage in the study of many aspects of blood vessels, such as genetic regulation, developmental patterning and diseases. But *in vitro* culture of tissues and vascular cells provides the basis for our understanding of other aspects, such as endothelial cell biology, cell-shape regulation and the vessels' responses to physical forces. Linking *in vivo* with *in vitro* research has not always been successful and represents a major challenge in the field. In particular, most *in vitro* models lack the three-dimensional complexity, blood flow, cell–cell interactions or proper extracellular (matrix) environment that are typical of living tissues.

Microfluidic devices, consisting of submillimetre-scale channels or tunnels through which liquid flows in a controlled manner, are an attractive alternative for studying blood-vessel development and function. Scientists can build precast three-dimensional micronetworks

using various polymers, and can seed endothelial cells that form tubular microvessels in which blood flow can be mimicked and regulated. However, previous attempts<sup>3</sup> — mostly using simple silicone polymers such as polydimethylsiloxane — have failed to implement, and therefore to address, crucial steps of angiogenesis<sup>4</sup> (formation of new blood vessels). Moreover, research using microfluidic devices has generally concentrated on studying the influence of variations in flow on the function and permeability of endothelial cells, or on the interactions between these cells and blood cells.

Using silicone moulds together with casting gels made out of collagen, Zheng and co-workers created microvessels that replicated some aspects of angiogenesis (Fig. 1). Collagen gels have been used before for this purpose<sup>5</sup>, but the resulting devices never delivered the level of endothelial functionality that the authors' system has now achieved. The researchers report that the microvessels were beautifully lined with continuous endothelium and did not leak. Moreover, the vessels — when activated with appropriate biochemical signals — produced new branches in a process known as sprouting angiogenesis, and recruited pre-seeded mural cells, which normally associate with blood vessels and affect their functions. As such, the device provides the important advance of not only allowing the researchers to shape the network, but also permitting the biological elements (cells and their products) to reshape or remodel the system dynamically.

As an example of the possible uses of their *in vitro* microvessels, the authors used whole blood to analyse platelet aggregation, a process that, when uncontrolled, can lead to the formation of a blood clot that interrupts the

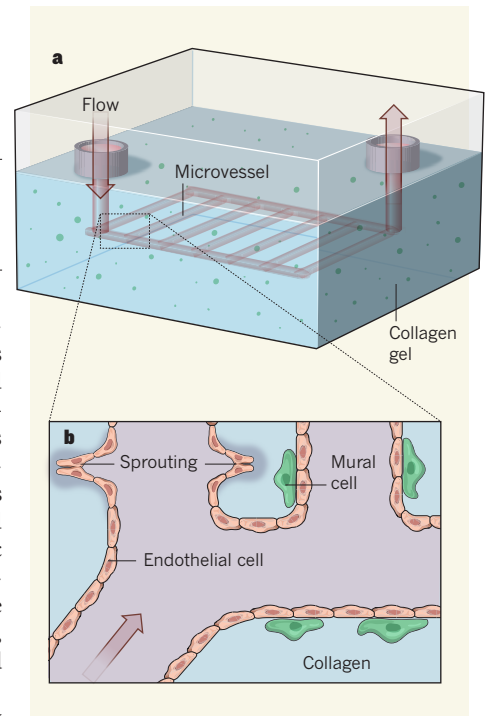


**Figure 1 | *In vitro* microvessels.** **a**, Zheng *et al.*<sup>2</sup> used a temporary silicone scaffold (not shown) and a collagen gel to create a miniaturized tubular network that resembled blood vessels. In this system, some of the cell types that are normally associated with blood vessels (such as mural cells) can be incorporated in the gel, whereas others (endothelial cells) can be added in the culture medium that flows through the channels. **b**, The authors replicated in their device several processes commonly associated with blood vessels, such as the formation of branches (sprouting) and the interaction of endothelial cells with mural cells. (Modified from ref. 2.)

flow in a vessel (thrombosis). In agreement with an earlier study<sup>6</sup>, they found that adding a proinflammatory compound to the *in vitro* vessels induced changes in the endothelium ('activation') that promoted platelet aggregation and formation of blood clots. The mechanism involved two proteins, protein kinase C and von Willebrand factor. Protein kinase C stimulated endothelial cells to secrete von Willebrand factor, which then formed fibres on the cells' surface. The fibres promoted platelet adhesion and accumulation, leading to vessel occlusion.



These simple results, although preliminary, highlight the potential for microfluidic devices to improve our knowledge of fundamental aspects of blood-vessel physiology.

However, the remodelling of the microvascular network demonstrated by Zheng *et al.* is still rudimentary, and does not fulfil all of the requirements for the replacement of *in vivo* models. Sprouting in their system, and the additional remodelling of the vascular structures that occurs afterwards, remain unsatisfactory, and improvements in culture conditions will be required to emulate the dynamic complexity seen *in vivo*. Yet the authors' report demonstrates the possibility of creating an open and flexible assay in which blood, plasma or culture medium flows through vessels that can be stimulated and manipulated, and that allows real-time observation of the dynamics of endothelial-cell behaviour through the different phases of angiogenesis. We envisage that improved versions of Zheng and colleagues' device will permit quick and accurate manipulation of plasma flow and composition, as well as the delivery of experimental molecules to screen their effects on endothelial function.

Today, the full pattern of vascular remodelling is still beyond the reach of existing microfluidic devices. Moreover, achieving an adequate flow in complex vascular networks *in vitro* remains problematic; most current systems rely on gravity-driven flow, which provides insufficient shear forces to mimic *in vivo* conditions. Looking ahead, from an experimentalist's point of view, the ideal microfluidic device should mimic conditions in living organisms and be easy to assemble. It should also enable the tight control and manipulation of all parameters relevant to angiogenesis, be scalable to high-throughput analysis, and facilitate the application of standard methods of molecular analysis and live imaging.

Developments such as the one reported by Zheng and colleagues are closing the technological gaps, and we foresee a strengthening of microfluidic devices as platforms to investigate blood-vessel function and the interaction of blood vessels with tumours. Moreover, the establishment of a functional, hierarchically branched vascular network *in vitro* that could support the formation of new tissues from stem cells would be an extraordinary achievement that would boost the field of tissue engineering. Time will tell whether the vessel remodelling observed in the authors' microfluidic chamber can be driven far enough to develop systems conducive to large-scale tissue engineering for transplantation. ■

**Claudio Franco and Holger Gerhardt**  
are at the Vascular Biology Laboratory,  
London Research Institute, Cancer Research  
UK, Lincoln's Inn Fields Laboratories,  
London WC2A 3LY, UK. H.G. is also at  
the Vascular Patterning Laboratory,

Vesalius Research Center, Leuven, Belgium.  
e-mail: holger.gerhardt@cancer.org.uk

1. Carmeliet, P. *Nature* **438**, 932–936 (2005).
2. Zheng, Y. *et al. Proc. Natl Acad. Sci. USA* **109**, 9342–9347 (2012).
3. van der Meer, A. D., Poot, A. A., Duits, M. H., Feijen, J. & Vermes, I. *J. Biomed. Biotechnol.* **2009**, 8231–8248 (2009).
4. Potente, M., Gerhardt, H. & Carmeliet, P. *Cell* **146**, 873–887 (2011).
5. Price, G. M. *et al. Biomaterials* **31**, 6182–6189 (2010).
6. Tsai, M. *et al. J. Clin. Invest.* **122**, 408–418 (2012).

## PLANT NUTRITION

# Rooting for more phosphorus

The identification of an enzyme in rice that confers improved plant yields on phosphorus-deficient soils could open up new avenues for generating nutrient-efficient crops that can thrive on marginally fertile soils. [SEE LETTER P.535](#)

LEON V. KOCHIAN

Phosphorus is probably the most limiting mineral nutrient for plants. Many of our planet's soils are low in the mineral, and this includes approximately half of the world's agricultural lands<sup>1</sup>. Hence, there is considerable interest in developing plant varieties that are more phosphorus efficient — that is, crops that can produce higher yields while using less soil phosphorus. On page 535 of this issue, Gamuyao *et al.*<sup>2</sup> report the identification of the first phosphorus-efficiency gene in plants. The gene encodes a protein kinase enzyme that significantly enhances grain yield from rice plants grown on phosphorus-deficient soils.

Multiple factors contribute to the phosphorus problem. A large fraction of soil phosphorus is held very tightly to the surface of soil

particles or is tied up (fixed) as organic phosphorus compounds, and is therefore relatively unavailable for plant uptake (Fig. 1). Furthermore, many low-phosphorus regions are in developing countries, where soils are often degraded and where many farmers lack the financial resources to purchase phosphorus fertilizers. Thus, plant access to the mineral plays a part in the precarious food-security situation in some of these regions. To further exacerbate the problem, the phosphorus used in fertilizers is obtained from rock phosphate, which is a non-renewable resource that could be depleted in 50–100 years<sup>3</sup>. Even for the high-input agriculture common in developed countries, much of the fertilizer-derived phosphorus either becomes fixed (and therefore unavailable to plants) or is lost through leaching into ground and surface waters, which is damaging

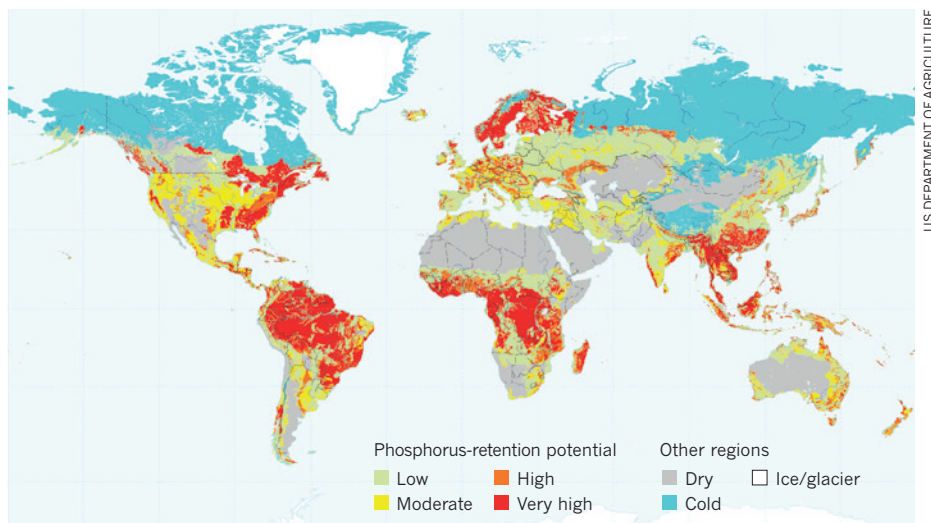


**Figure 1 | The problem of phosphorus.** Many of the world's agricultural soils are in regions of high or very high phosphorus-retention potential, which means that the phosphorus is tightly bound to soil particles or fixed in phosphorus-containing organic compounds. High phosphorus retention leads to low availability of phosphorus for plants in these regions. Gamuyao *et al.*<sup>2</sup> have identified a rice enzyme that enhances grain yield from plants grown on phosphorus-deficient soils.

to the surrounding environment.

A possible way to circumvent these problems is to generate plant varieties that simply need less of the nutrient. This particular episode in that quest began around 15 years ago, when researchers from the group presenting the current paper began to study a subpopulation of rice plants called the *aus* varieties, which originated from nutrient-poor soils in India. There was a growing awareness that these traditional rice varieties were likely to be a rich source of genes encoding tolerance to abiotic stresses, such as prolonged flooding<sup>4</sup>. A genetic screen of multiple rice varieties led to the identification<sup>5</sup> of Kasalath, an *aus* line that is significantly more phosphorus efficient than the varieties currently used for rice production. A subsequent genetic analysis of plants generated from a cross between Kasalath and a modern, phosphorus-inefficient rice variety determined that several regions of the rice genome are associated with improved phosphorus efficiency<sup>5,6</sup>. The phosphorus uptake (PUP) genomic region that has the largest effect is located on rice chromosome 12 and has been named *Pup1* (ref. 7).

However, subsequent efforts to identify the specific gene, or genes, responsible for phosphorus efficiency in the Kasalath strain were complicated by the fact that greater phosphorus efficiency can arise from several aspects of plant physiology. For example, more-active root growth that positions roots closer to where the soil phosphorus is located, or greater root-mediated biological and chemical activity to solubilize and absorb fixed phosphorus can both lead to more efficient acquisition. In addition, more-efficient cellular use of the mineral can contribute to enhanced phosphorus efficiency.

To try to tease apart which of these processes are influenced by *Pup1*, the researchers used breeding techniques to introduce the *Pup1*-containing region into modern rice lines that are phosphorus inefficient. The offspring lines had significantly higher grain and biomass yields than the parent lines when grown on phosphorus-deficient soils, and physiological analysis showed that this resulted from significantly greater phosphorus uptake and accumulation<sup>8</sup>.

The research group subsequently compared<sup>9</sup> the DNA sequence containing the *Pup1* region in the Kasalath variety with the reference genome sequence for rice, which was generated from the modern variety, Nipponbare. The sequences differed considerably, with the Kasalath sequence containing several putative genes not present in Nipponbare. Gene-expression analysis allowed the authors to single out one of these inserted genes, which encodes a protein kinase. This gene is expressed at high levels in the roots of plants harbouring the Kasalath *Pup1* region, and expression of the gene is further enhanced in phosphorus-deficient conditions.

In the current paper<sup>2</sup>, Gamuyao and colleagues further characterize this gene, which they have named *PSTOL1*, for phosphorus-starvation tolerance 1. The authors demonstrate that modern rice lines that are genetically engineered to overexpress *PSTOL1* show significant increases in grain and biomass production compared with wild-type plants when the plants are grown on phosphorus-deficient soils. They also show that the *PSTOL1* protein belongs to the receptor-like cytoplasmic kinase sub-group of protein kinases. This is interesting, because receptor-like kinases have been implicated in plant responses to several types of abiotic stress, including drought<sup>10</sup>.

By comparing the root architecture of rice plants overexpressing *PSTOL1* with that of the corresponding lines lacking the kinase, the authors found that *PSTOL1* expression resulted in increased early root growth and root proliferation, suggesting that the kinase enhances the plants' ability to 'mine' soil phosphorus. The proposal that *PSTOL1* functions in root development and growth was supported by studies showing that *PSTOL1* expression is confined to specific tissue regions where crown roots, which make up a substantial portion of the mature rice root system, begin to emerge.

These findings have opened up new avenues for improving crop plant phosphorus efficiency — and possibly the efficiency of the uptake of other nutrients as well. Considerable work remains to be done to elucidate the molecular mechanisms and downstream targets of *PSTOL1*. But the researchers are already attempting to translate their discoveries into

improved phosphorus efficiency in rice crops by use of targeted inter-variety breeding. It will be interesting to see how stable this trait is in plant varieties from different genetic backgrounds and in different growth environments. In addition, the authors' earlier genetic screens identified other genomic regions associated with enhanced phosphorus efficiency, and it will be exciting to watch for the identification of specific genes within these regions, and for the discovery of potential synergistic effects on plant-nutrient efficiency when these genes or regions are combined. Finally, Gamuyao and colleagues' research has highlighted the value that lies in investigating traditional plant varieties for beneficial traits that might have been lost during domestication. ■

**Leon V. Kochian** is at the US Department of Agriculture's Robert W. Holley Center for Agriculture and Health, and the Department of Plant Biology, Cornell University, Ithaca, New York 14853, USA.  
e-mail: [leon.kochian@ars.usda.gov](mailto:leon.kochian@ars.usda.gov)

1. Lynch, J. P. *Plant Physiol.* **156**, 1041–1049 (2011).
2. Gamuyao, R. et al. *Nature* **488**, 535–539 (2012).
3. Cordell, D., Drangert, J.-O. & White, S. *Glob. Environ. Change* **19**, 292–305 (2009).
4. Xu, K. et al. *Nature* **442**, 705–708 (2006).
5. Wissuwa, M. & Ae, N. *Plant Breed.* **120**, 43–48 (2001).
6. Wissuwa, M., Yano, M. & Ae, N. *Theor. Appl. Genet.* **97**, 777–783 (1998).
7. Wissuwa, M., Wegner, J., Ae, N. & Yano, M. *Theor. Appl. Genet.* **105**, 890–897 (2002).
8. Wissuwa, M. *Plant Soil* **269**, 57–68 (2005).
9. Heuer, S. et al. *Plant Biotechnol. J.* **7**, 456–471 (2009).
10. Marshall, A. et al. *Plant Cell* **24**, 2262–2278 (2012).

## GENETICS

# The rate of human mutation

**A comprehensive analysis of human spontaneous mutation has revealed a strong influence of paternal age, suggesting a link between an increasing number of older fathers and the rise in disorders such as autism. [SEE ARTICLE P.471](#)**

ALEXEY KONDRASHOV

Mutations are common on the scale of whole genomes, but rare on the scale of individual nucleotides. So until large-scale DNA sequencing became practical, measuring the rate at which novel mutations accumulate in a genome was a daunting task. Now, however, *de novo* mutations can be detected by a straightforward comparison of parent and offspring genotypes, making obsolete several ingenious methods that were previously used for this purpose. Such comparisons will rapidly produce reliable estimates of the

parameters of spontaneous mutation in many species. On page 471 of this issue, Kong et al.<sup>1</sup> report these figures for humans. They show that a newborn's genome sequence contains, on average, 60 new small-scale mutations, and that this number depends strongly on the age of the father at the time of conception.

Kong and colleagues' study is by far the largest of its kind yet conducted, involving 78 Icelandic parent–offspring trios. Their estimate of 60 new mutations per generation is in agreement with previous calculations<sup>2</sup>, but their data also reveal that, although a 20-year-old father transmits, on average, approximately



25 mutations to his child, a 40-year-old father transmits around 65. This means that every additional year of paternal age results in an average of two extra mutations in human offspring. By contrast, the authors found that the number of *de novo* mutations transmitted by the mother is always roughly 15, regardless of her age.

That the male parent makes a disproportionate contribution to mammalian mutation has been described previously<sup>3</sup>, as has an effect of paternal age on the number of mutations in an offspring<sup>4</sup>. These findings are easily explained by the fact that, in mammals, male germ cells (sperm) are continually produced, so they go through many more cell divisions over the course of a generation than do female germ cells (eggs), which are not actively dividing in individuals of reproductive age. However, Kong and colleagues' estimates of the effect of these differences on mutation rates are the most precise and definite that we have so far.

In humans, as many as 10% of point mutations are deleterious<sup>5</sup>, so Kong and colleagues' findings suggest that an average newborn carries six new deleterious mutations. Although most of these mutations will, on their own, have only mild effects, collectively they could have a substantial impact on health. Perhaps most immediately pertinent to the authors' findings are data showing that the prevalence of several single-gene and multifactorial diseases increases with paternal age<sup>4</sup>. Although in some cases this increase is due to selection pressures exerted on germ-line cells<sup>6</sup>, there is little doubt that its main cause is the effect of paternal age on the number of new mutations in the offspring's genome. For example, a causal role of *de novo* mutations has recently been demonstrated in autism<sup>7</sup>. It seems that multifactorial disorders that result from impaired brain function, such as autism, schizophrenia, dyslexia and reduced intelligence, are particularly susceptible to the paternal-age effect<sup>8</sup>. This is consistent with the fact that more genes are expressed in the brain than in any other organ, meaning that the fraction of new mutations that will affect its functions is the highest.

Kong and colleagues' findings suggest that the difference in health between children of fathers younger than 20 years and those of fathers older than 40 years (with all other factors being equal) is equivalent to about half the average decline in human health that results from the free accumulation of spontaneous mutations with each generation. Modern human populations are subject to many fewer selection pressures than has been the case throughout human evolutionary history. Because deleterious mutations are much more common than beneficial ones, evolution under this relaxed selection will inevitably lead to a decline in the mean fitness of the population. Indeed, data obtained from *Drosophila* fruitflies in experimental situations of relaxed selection suggest that this decline can be quite

rapid<sup>9</sup>. It is therefore reasonable to assume that the ongoing increase in the incidence and prevalence of autism in many human populations<sup>10</sup> could be due, at least in part, to the accumulation of mutations resulting from relaxed selection and a higher average paternal age — and not only to better recognition of cases.

A valuable opportunity to further study the impact of *de novo* mutations on human health may be provided by mutator alleles — defective versions of genes involved in DNA replication or repair that cause an increase in the mutation rate. For example, a type of colorectal cancer is caused by a mutation that results in the loss of function of one copy of a gene encoding a protein involved in DNA mismatch repair (a process whereby erroneous DNA sequences are fixed during replication). In rats, the presence of such a mutation in both gene copies increases the spontaneous mutation rate by a factor of 30 (ref. 11) and reduces lifespan. In humans, a complete lack of DNA mismatch repair function leads to multiple childhood cancers, and patients do not live to reproductive age<sup>12</sup>. Even single-copy mutations in DNA repair genes can substantially increase the mutation rate. A detailed evaluation of children of individuals who carry such mutator alleles might allow us to assess the impact of several generations of unchecked accumulation of *de novo* mutations.

If the paternal-age effect on the *de novo* mutation rate does lead to substantially impaired health in the children of older fathers, then collecting the sperm of young adult men

and cold-storing it for later use<sup>4</sup> could be a wise individual decision. It might also be valuable for public health, as such action could, according to Kong and colleagues' findings, substantially reduce the rate of deterioration of the gene pool in human populations under relaxed selection. By contrast, any attempt to reduce mutation accumulation in our gene pool by restoring selection pressures would probably be much more controversial and painful. Thus, Kong *et al.* have certainly provided food for thought, on both an individual and a population level. ■

Alexey Kondrashov is in the Department of Ecology and Evolutionary Biology and the Life Sciences Institute, University of Michigan, Ann Arbor, Michigan 48109, USA.  
e-mail: kondrash@umich.edu

1. Kong, A. *et al.* *Nature* **488**, 471–475 (2012).
2. Keightley, P. D. *Genetics* **190**, 295–304 (2012).
3. Shimmin, L. C., Chang, B. H.-J. & Li, W.-H. *Nature* **362**, 745–747 (1993).
4. Crow, J. F. *Proc. Natl Acad. Sci. USA* **94**, 8380–8386 (1997).
5. Shabalina, S. A., Ogurtsov, A. Y., Kondrashov, V. A. & Kondrashov, A. S. *Trends Genet.* **17**, 373–376 (2001).
6. Goriely, A. & Wilkie, A. O. *Am. J. Hum. Genet.* **90**, 175–200 (2012).
7. Sanders, S. J. *et al.* *Nature* **485**, 237–241 (2012).
8. Saha, S. *et al.* *PLoS Med.* **6**, e1000040 (2009).
9. Shabalina, S. A., Yampolsky, L. Y. & Kondrashov, A. S. *Proc. Natl Acad. Sci. USA* **94**, 13034–13039 (1997).
10. Keyes, K. M. *et al.* *Int. J. Epidemiol.* **41**, 495–503 (2012).
11. van Bostel, R. *et al.* *Carcinogenesis* **29**, 1290–1297 (2008).
12. Wimmer, K. & Etzler, J. *Hum. Genet.* **124**, 105–122 (2008).

## CLIMATE SCIENCE

## Himalayan glaciers in the balance

A measurement by satellite altimetry shows the Himalayan glaciers to be losing mass at only moderate rates, but raises broader questions about other methods for estimating mass balance. [SEE LETTER P.495](#)

J. GRAHAM COGLEY

The Himalayas continue to be interesting to glaciologists, which is not surprising when one considers the formidable water-resource problems in the glaciers' regional context and the controversy<sup>1</sup> over the rate at which the ice is disappearing. The claim that the glaciers are vanishing rapidly is not difficult to discredit. In the Karakoram, at the western end of the Himalayan arc, glacier mass balance — the change of glacier mass over a given time span — has, in fact, been slightly positive over the past decade<sup>2</sup>. Kääb *et al.*<sup>3</sup> (page 495 of this issue) clarify this

matter further by providing an independent measurement of glacier mass balance based on elevation changes detected by the ICESat satellite's GLAS altimeter. Although these data were collected over only five years (2003–08), they cover the entirety of the Himalayas.

At  $-210 \pm 50$  kilograms per square metre per year, the new estimate of glacier mass balance in the Himalayas is more negative than a recent gravimetric estimate<sup>4</sup>, which is based on satellite measurements of Earth's changing gravitational field. But it is less negative than the current estimate<sup>5,6</sup> obtained by the more established method of interpolation from sparse field measurements. The new estimate

may help to allay panic about regional water resources, but as far as glaciological methodology is concerned it will set the cat among the pigeons.

Glaciers are often likened to water towers. A sustained negative mass balance means that there is progressively less water in the 'tower', but more in transit to the ocean as meltwater. Because the latter is available for exploitation downstream, this equates to short-term gain in a region with water deficits, but big problems later when the water tower runs dry. If, as now, someone presents a less-negative estimate, our assessment changes. The tower is delivering less water for current use, but will hold water for longer. It is not clear whether such a change is bad news or good. Certainly, if the change were in the other direction, to a more-negative balance, questions would arise about equity between successive generations of water users and about possible ways of keeping the water in the tower<sup>1</sup>.

Kääb and colleagues' methods raise the bar for future altimetric studies. The Supplementary Information to their paper<sup>3</sup> comprises 10,000 well-chosen words about the processing and correction of the raw data. This provides a striking illustration of the time it can take to learn to put new instruments to work effectively. ICESat was launched in 2003, and better information is still being squeezed out of it nearly three years after the last of its three lasers failed in October 2009.

This information includes better-quantified errors than those that accompany the recent gravimetric estimate<sup>4</sup> from the GRACE satellite mission. In glaciological interpretation of GRACE data, it is customary to correct for non-glacial mass transfers — mainly, of surface water and groundwater, and of rock in Earth's deep interior — by hydrological and geophysical modelling. The outputs of the models are the largest sources of gravimetric uncertainty. One of Kääb and colleagues' more provocative points is that it could be advantageous to reverse this procedure. If a really good measurement of the glacier mass change is available, as is now true of the Himalayas, why not use it to correct the gravimetric data, which would then contain only the hydrological and deep-interior signals?

The most spirited reactions to this study will probably come not from GRACE specialists but from practitioners of more traditional methods. In the Himalayas, it typically takes five days to walk from the road head to the glacier terminus, and the glacier itself, if it is accessible at all, is extremely difficult to work on (Fig. 1). The fieldwork has nevertheless yielded a small but precious body of facts about Himalayan mass balance. However, the arithmetic average<sup>5</sup> of the field measurements obtained over the same time span as Kääb and colleagues' estimate is, at  $-746 \text{ kg m}^{-2} \text{ yr}^{-1}$ , more than three times as negative.

Why are the field measurements seemingly

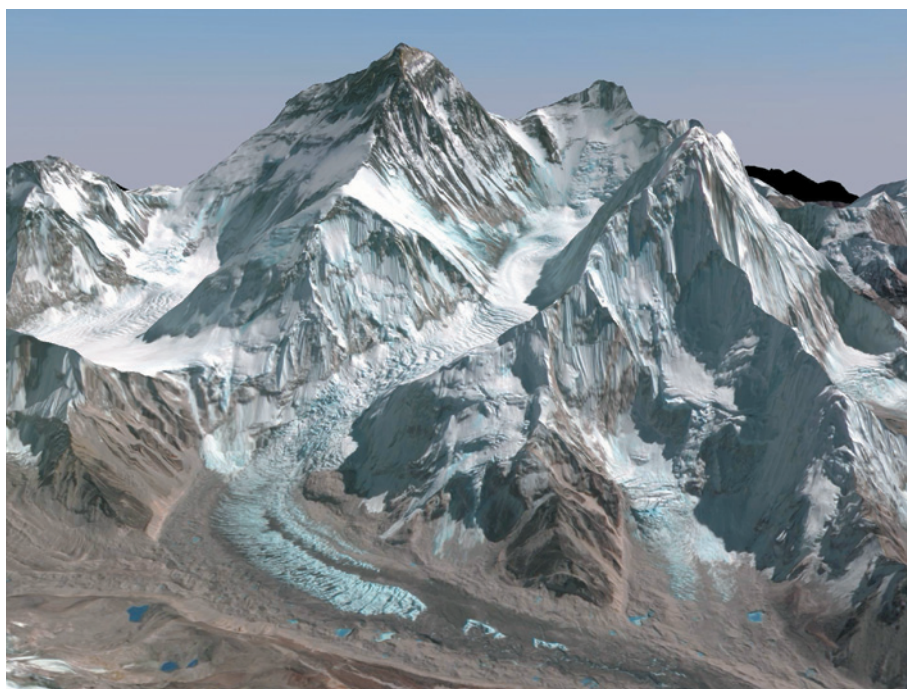


**Figure 1 | A difficult work environment.** Khumbu Glacier on the flank of Mount Everest, in a 2009 SPOT5 satellite image draped over a digital elevation model from the same sensor. On this and many other Himalayan glaciers, avalanches deliver both debris and snow to the often crevassed surface. *In situ* measurements of mass balance therefore become almost impossible, and hard to interpret when obtained. Kääb *et al.*<sup>3</sup> avoid these difficulties by measuring the mass balance of all Himalayan glaciers from space.

so unrepresentative? The usual answers appeal to several factors: to the smallness of the glaciers chosen for fieldwork, although nobody has explained why smaller glaciers should lose mass faster than larger ones; to the accessibility of the chosen glaciers, which probably implies lower altitude and therefore more intense melting, although this implication has yet to be investigated systematically; and to unquantified uncertainties in the field measurements themselves. The last objection carries less force now, because recent work tends to address the errors more explicitly, but local factors could play a part. For example, mass gain by snow avalanching (Fig. 1) is practically unmeasurable in the field.

Some other regional-scale studies<sup>8,9</sup> have reported less-negative mass balances than those obtained either by fieldwork or by interpolation from fieldwork. Kääb and colleagues' results therefore add to accumulating evidence that increases the number of questions, rather than the number of answers, about the measurement of glacier mass balance. These questions could be of worldwide import.

The new measurement<sup>3</sup> agrees with a recent review of the state of Tibetan glaciers<sup>10</sup>, which noted a trend towards smaller rates of mass loss farther north and presented the first field report of mass gain, measured on a glacier in the Pamir mountains. Kääb and colleagues also find positive mass balance, just to the south of the Pamir. Thus, three independent sources<sup>2,3,10</sup> now confirm this 'Karakoram anomaly', with Kääb *et al.* offering the most

geographically extensive picture.

Kääb and colleagues have shown that the state<sup>5</sup> of Himalayan glaciers is not as dire as was widely and wrongly assumed until recently, but their short-term observations tell us nothing about the fate<sup>5</sup> of Himalayan glaciers. The observations were made by a now-defunct satellite, the successor of which will not be launched until 2016, and they pose searching questions about GRACE results and about longer-established methods. Monitoring the Himalayan glaciers is clearly going to be a continuing practical and interpretative challenge. ■

**J. Graham Cogley** is in the Department of Geography, Trent University, Peterborough, Ontario K9J 7B8, Canada.  
e-mail: gcogley@trentu.ca

1. Cogley, J. G., Kargel, J. S., Kaser, G. & van der Veen, C. J. *Science* **327**, 522 (2010).
2. Gardelle, J., Berthier, E. & Arnaud, Y. *Nature Geosci.* **5**, 322–325 (2012).
3. Kääb, A., Berthier, E., Nuth, C., Gardelle, J. & Arnaud, Y. *Nature* **488**, 495–498 (2012).
4. Jacob, T., Wahr, J., Pfeffer, W. T. & Swenson, S. *Nature* **482**, 514–518 (2012).
5. Bolch, T. *et al. Science* **336**, 310–314 (2012).
6. Cogley, J. G. *Ann. Glaciol.* **50**(50), 96–100 (2009).
7. Pachauri, R. K. *et al.* (eds) *Climate Change 2007: Synthesis Report* (IPCC, 2007).
8. Berthier, E., Schiefer, E., Clarke, G. K. C., Menounos, B. & Rémy, F. *Nature Geosci.* **3**, 92–95 (2010).
9. Moholdt, G., Wouters, B. & Gardner, A. S. *Geophys. Res. Lett.* **39**, L10502 (2012).
10. Yao, T. *et al. Nature Clim. Change* <http://dx.doi.org/10.1038/nclimate1580> (2012).



# Rate of *de novo* mutations and the importance of father's age to disease risk

Augustine Kong<sup>1</sup>, Michael L. Frigge<sup>1</sup>, Gisli Masson<sup>1</sup>, Soren Besenbacher<sup>1,2</sup>, Patrick Sulem<sup>1</sup>, Gisli Magnusson<sup>1</sup>, Sigurjon A. Gudjonsson<sup>1</sup>, Asgeir Sigurdsson<sup>1</sup>, Aslaug Jonasdottir<sup>1</sup>, Adalbjorg Jonasdottir<sup>1</sup>, Wendy S. W. Wong<sup>3</sup>, Gunnar Sigurdsson<sup>1</sup>, G. Bragi Walters<sup>1</sup>, Stacy Steinberg<sup>1</sup>, Hannes Helgason<sup>1</sup>, Gudmar Thorleifsson<sup>1</sup>, Daniel F. Gudbjartsson<sup>1</sup>, Agnar Helgason<sup>1,4</sup>, Olafur Th. Magnusson<sup>1</sup>, Unnur Thorsteinsdottir<sup>1,5</sup> & Kari Stefansson<sup>1,5</sup>

Mutations generate sequence diversity and provide a substrate for selection. The rate of *de novo* mutations is therefore of major importance to evolution. Here we conduct a study of genome-wide mutation rates by sequencing the entire genomes of 78 Icelandic parent-offspring trios at high coverage. We show that in our samples, with an average father's age of 29.7, the average *de novo* mutation rate is  $1.20 \times 10^{-8}$  per nucleotide per generation. Most notably, the diversity in mutation rate of single nucleotide polymorphisms is dominated by the age of the father at conception of the child. The effect is an increase of about two mutations per year. An exponential model estimates paternal mutations doubling every 16.5 years. After accounting for random Poisson variation, father's age is estimated to explain nearly all of the remaining variation in the *de novo* mutation counts. These observations shed light on the importance of the father's age on the risk of diseases such as schizophrenia and autism.

The rate of *de novo* mutations and factors that influence it have always been a focus of genetics research<sup>1</sup>. However, investigations of *de novo* mutations through direct examinations of parent-offspring transmissions were previously mostly limited to studying specific genes<sup>2,3</sup> or regions<sup>4-7</sup>. Recent studies that used whole-genome sequencing<sup>8,9</sup> are important but too small to address the question of diversity in mutation rate adequately. To understand the nature of *de novo* mutations better we designed and conducted a study as follows.

## Samples and mutation calls

As part of a large sequencing project in Iceland<sup>10-12</sup> (Methods), we sequenced 78 trios, a total of 219 distinct individuals, to more than 30× average coverage (Fig. 1). Forty-four of the probands (offspring) have autism spectrum disorder (ASD), and 21 are schizophrenic. The other 13 probands were included for various reasons, including the construction of multigeneration families. The probands include five cases in which at least one grandchild was also sequenced. In addition, 1,859 other Icelanders, treated as population samples, were also whole-genome sequenced (all at least 10×, 469 more than 30×). These were used as population samples to help to filter out artefacts. Sequence calling was performed for each individual using the Genome Analysis Toolkit (GATK) (Methods). The focus here is on single nucleotide polymorphism (SNP) mutations. The investigation was restricted to autosomal chromosomes.

Criteria for calling a *de novo* SNP mutation were as follows. (1) All variants that have likelihood ratio:  $\text{lik}(AR)/\text{lik}(RR)$  or  $\text{lik}(AA)/\text{lik}(RR) > 10^4$ , in which  $R$  denotes the reference allele and  $A$  the alternative allele, in any of the 1,859 population samples, were excluded. Some recurrent mutations could have been filtered out, but the number should be small. The *de novo* mutation calls further satisfy the conditions that (2) there are at least 16 quality reads for the proband at the mutated site; (3) the likelihood ratio  $\text{lik}(AR)/\text{lik}(RR)$  is above  $10^{10}$ ; and (4) for both parents, the ratio  $\text{lik}(RR)/\text{lik}(AR)$  is above 100. Applying criteria (1) to (4) gave 6,221 candidate mutations. Further

examination led us to apply extra filtering (5) by including only SNPs in which the number of  $A$  allele calls is above 30% among the quality sequence reads of the proband. This was considered necessary because there was an abnormally high number of putative mutation calls in which, despite extremely high  $\text{lik}(AR)/\text{lik}(RR)$  ratios for the proband, the fraction of  $A$  calls was low (Supplementary Fig. 1). Applying (5) eliminated 1,285 candidate mutations (Supplementary Information). With high coverage, the false negatives resulting from (5) is estimated to be a modest 2% (Supplementary Information). After three more candidates were identified as false

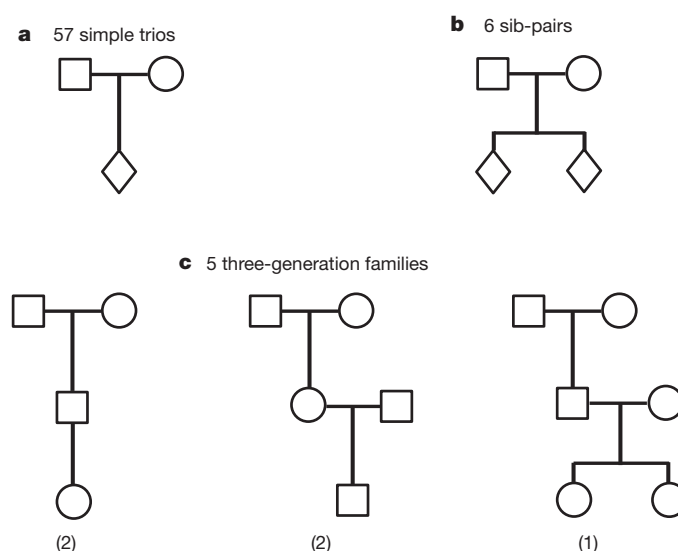


**Figure 1** | A summary of the family types. **a**, Fifty-seven simple trios. **b**, Six sib-pairs accounting for 12 trios. **c**, Five three-generation families accounting for nine trios.

<sup>1</sup>deCODE Genetics, Sturlugata 8, 101 Reykjavik, Iceland. <sup>2</sup>Bioinformatics Research Centre, Aarhus University, 8000 Aarhus, Denmark. <sup>3</sup>Illumina Cambridge Ltd, Chesterford Research Park, Little Chesterford, Essex CB10 1XL, UK. <sup>4</sup>University of Iceland, 101 Reykjavik, Iceland. <sup>5</sup>Faculty of Medicine, University of Iceland, 101 Reykjavik, Iceland.

positives by Sanger sequencing (see section on validation), a total of 4,933 *de novo* mutations, or an average of 63.2 per trio, were called. (The *de novo* mutations are listed individually in Supplementary Table 1.)

### Parent of origin and father's age

For the five trios in which a child of the proband was also sequenced, the parent of origin of each *de novo* mutation called was determined as follows. If the paternal haplotype of the proband was transmitted to his/her child, and the child also carries the mutation, then the mutation was considered to be paternal in origin. If the child carrying the paternal haplotype of the parent does not have the mutation, then it is inferred that the mutation is on the maternal chromosome of the proband. Similar logic was applied when the child inherited the maternal haplotype of the proband. In the five trios, the average number of paternal and maternal mutations is 55.4 and 14.2, respectively (Table 1). If mutations were purely random with no systematic difference between trios, their number should be Poisson distributed with the variance equal to the mean. The data, however, show over-dispersion (Table 1). This is much more notable for the paternal mutations (variance = 428.8,  $P = 1.2 \times 10^{-5}$ ) than the maternal mutations (variance = 48.7,  $P = 0.016$ ). Moreover, the number of paternal mutations has a monotonic relationship with the father's age at conception of the child. Here, the mean number of paternal mutations is substantially higher than the mean number of maternal mutations (ratio = 3.9), but the difference is even greater for the variance (ratio = 8.8). Hence, variation of *de novo* mutation counts in these individuals is mostly driven by the paternal mutations.

Relationships between parents' age and the number of mutations (paternal and maternal combined, as they could not be reliably separated without data from a grandchild) were examined using all 78 trios (Fig. 2). The number of mutations increases with father's age ( $P = 3.6 \times 10^{-19}$ ) with an estimated effect of 2.01 mutations per year (standard error = 0.17). Mother's age is substantially correlated with father's age ( $r = 0.83$ ) and, not surprisingly, is also associated with the number of *de novo* mutations ( $P = 1.9 \times 10^{-12}$ ). However, when father's age and mother's age were entered jointly in a multiple regression, father's age remained highly significant ( $P = 3.3 \times 10^{-8}$ ), whereas mother's age did not ( $P = 0.49$ ). On the basis of existing knowledge about the mutational mechanisms in sperm and eggs<sup>2</sup>, the results support the notion that the increase in mutations with parental age manifests itself mostly, maybe entirely, on the paternally inherited chromosome.

Given a particular mutation rate, due to random variation, the number of actual mutations is expected to have a Poisson distribution. After taking Poisson variation into account, with a linear fit (effect = 2.01 mutations per year), father's age explains 94.0% (90% confidence interval: 80.1%, 100%) (Supplementary Information) of the remaining variation in the observed mutation counts. When an exponential model is fitted (red curve in Fig. 2), the number of paternal and maternal mutations combined is estimated to increase by 3.23% per year. This model explains 96.6% (90% confidence interval: 83.2%, 100%) of the remaining variation. A third model fitted

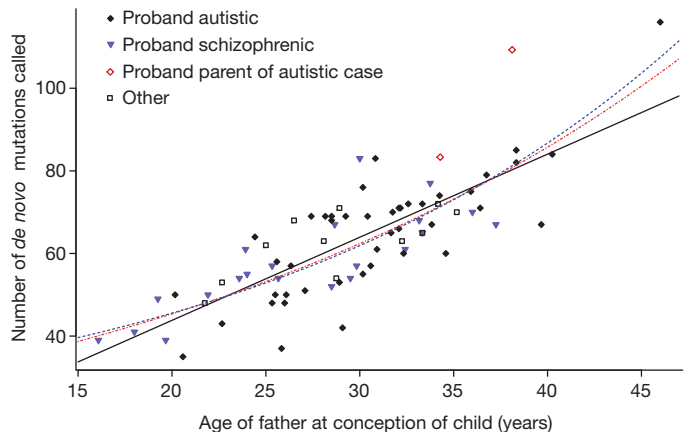


**Figure 2 | Father's age and number of *de novo* mutations.** The number of *de novo* mutations called is plotted against father's age at conception of child for the 78 trios. The solid black line denotes the linear fit. The dashed red curve is based on an exponential model fitted to the combined mutation counts. The dashed blue curve corresponds to a model in which maternal mutations are assumed to have a constant rate of 14.2 and paternal mutations are assumed to increase exponentially with father's age.

(blue curve in Fig. 2) assumes that the maternal mutation rate is constant at 14.2 and paternal mutations increase exponentially. This explains 97.1% (90% confidence interval: 84.3%, 100%) of the remaining variation and the rate of paternal mutations is estimated to increase by 4.28% per year, which corresponds to doubling every 16.5 years and increasing by 8-fold in 50 years. Seventy-six of the 78 trios have father's ages between 18 and 40.5, a range in which the differences between the three models are modest. Hence, although it seems that the number of paternal *de novo* mutations increases at a rate that accelerates with father's age, more data at the upper age range are needed to evaluate the nature of the acceleration better.

### Validation and the nature of errors

Among the *de novo* mutations originally called, two were observed twice, both in siblings, one on chromosome 6 and one on chromosome 10. These cases were examined by Sanger sequencing. The mutation on chromosome 6 is not actually *de novo* as it was seen in the mother also. The one on chromosome 10 was confirmed, that is, it was observed in both siblings, who share the paternal haplotype in this region, but not the parents. This supports the theory that *de novo* mutations in different sperms of a man are not entirely independent<sup>2</sup>. Our trios include seven sib-pairs with 921 *de novo* mutations called. A false *de novo* mutation call for one sib resulting from a missed call in the parent would also show up in the other sib about 50% of the time. Only one such false positive was detected, indicating that this type of error accounts for a small percentage ( $2/(920/2) = 0.43\%$ ) of the called mutations. To evaluate the overall number of false positives, 111 called *de novo* mutations were randomly selected for Sanger sequencing. Eleven failed primer design. Six did not produce results of good quality in at least one member of the corresponding trio (Supplementary Information). For the remaining 94 cases, 93 were confirmed as *de novo* mutations—that is, the mutated allele was observed in the proband but not in the parents. One false positive, in which the putative mutation was not observed in the proband, was identified. The 17 cases that could not be verified are more likely to be located in genomic regions that are more difficult to analyse and hence probably have higher false-positive rates than average. Even so, the overall false-positive rate for the *de novo* mutation calls cannot be high.

The variance of the number of false positives is as important as the mean. False positives that are Poisson distributed, although adding noise, would not create bias for the effect estimates in either the linear

**Table 1 | *De novo* mutations observed with parental origin assigned**

	Father's age (yr)	Mother's age (yr)	Number of <i>de novo</i> mutations in proband		
			Paternal chromosome	Maternal chromosome	Combined
Trio 1	21.8	19.3	39	9	48
Trio 2	22.7	19.8	43	10	53
Trio 3	25.0	22.1	51	11	62
Trio 4	36.2	32.2	53	26	79
Trio 5	40.0	39.1	91	15	106
Mean	29.1	26.5	55.4	14.2	69.6
s.d.	8.4	8.8	20.7	7.0	23.5
Variance	70.2	77.0	428.8	48.7	555.3

or the exponential models for father's age, nor would they bias the estimate of the fraction of variance explained after accounting for Poisson variation. In general, they do not create substantial bias for analyses of differences and ratios. However, if the variance of the false positives is higher than the mean, resulting from systematic effects that affect trios differently, such as DNA quality and library construction, it would increase the unexplained variance and reduce the fraction of variance explained by father's age. The candidates filtered out by criterion (5), if kept, would have introduced false positives of this kind (Supplementary Information). Because father's age explains such a high fraction of the systematic variance of the currently called *de novo* mutations, false positives with this property cannot be common. A similar discussion about false negatives<sup>13</sup> is in Supplementary Information.

### Father's age and diseases

Consistent with other epidemiological studies<sup>14,15</sup>, in Iceland, the risk of schizophrenia increases significantly with father's age at conception ( $n = 569$ ,  $P = 2 \times 10^{-5}$ ). Father's age is also associated with the risk of ASD. The observed effect is limited to non-familial cases ( $n = 631$ ,  $P = 5.4 \times 10^{-4}$ ), defined as those in which the closest ASD relative is farther than cousins. The epidemiological results, the effect of father's age on *de novo* mutation rate shown here, together with other studies that have linked *de novo* mutations to autism and schizophrenia, including three recent studies of autism through exome sequencing<sup>4–6</sup>, all point to the possibility that, as a man ages, the number of *de novo* mutations in his sperm increases, and the chance that a child would carry a deleterious mutation (not necessarily limited to SNP mutations) that could lead to autism or schizophrenia increases proportionally. However, this model does not indicate that the relationship observed here between mutation rate and father's age would have been much different if the probands studied were chosen to be all non-ASD/schizophrenic cases instead. For example, assume that autism/schizophrenia is in each case caused by only one *de novo* mutation. Then autism/schizophrenia cases would on average have more *de novo* mutations than population samples. The magnitude could be substantial if the distribution of father's age has a large spread in the population, but then most of the difference would be caused by the cases having older fathers. If we control for the age of the father at the conception of the individual, then this difference in the average number of *de novo* mutations between control individuals and those with autism/schizophrenia would be reduced to approximately one (Supplementary Information).

### Mutations by type and by chromosome

Examination of the 4,933 *de novo* mutations showed that 73 are exonic, including two stop-gain SNPs and 60 non-synonymous SNPs (Supplementary Table 2). One non-familial schizophrenic proband carries a *de novo* stop-gain mutation (p.Arg113X) in the neurexin 1 (*NRXN1*) gene, previously associated with schizophrenia<sup>16–20</sup>. One non-familial autistic proband has a stop-gain *de novo* mutation (p.R546X) in the cullin 3 (*CUL3*) gene. *De novo* loss of function mutations in *CUL3* have been reported to cause hypertension and electrolyte abnormalities<sup>21</sup>. Recently, a separate stop-gain *de novo* mutation (p.E246X) in *CUL3* was reported in an autistic case<sup>5</sup>. Another one of our mutations is a non-synonymous variant (p.G900S) two bases from a splice site in the EPH receptor B2 (*EPHB2*), a gene implicated in the development of the nervous system. A *de novo* stop-gain mutation (p.Q858X) in this gene has recently been described in another autistic case<sup>6</sup>. Given the small number of loss of function *de novo* mutations we and others have reported (approximately 70 genes in the three autism exome scans<sup>4–6</sup>), the overlap is unlikely to be a coincidence. Hence, *CUL3* and *EPHB2* can be added to the list of genes that are relevant for ASD. Effective genome coverage, computed by discounting regions that have either very low (less than half genome average) or very high (more than three times genome average) local coverage, the latter often

**Table 2 | Germline mutation rates at CpG and non-CpG sites**

Type of mutation	<i>n</i>	Rate per base per generation
Transition at non-CpG	2,489	$6.18 \times 10^{-9}$
Transition at CpG	855	$1.12 \times 10^{-7}$
Transversion at non-CpG	1,516	$3.76 \times 10^{-9}$
Transversion at CpG	73	$9.59 \times 10^{-9}$
All	4,933	$1.20 \times 10^{-8}$

Mutation rates are per generation per base. For non-CpG sites, the effective number of bases examined is taken as 2.583 billion, whereas for CpG sites the number is 48.8 million. These numbers take into account the variation of local coverage in sequencing (Supplementary Information).

a symptom of misaligning reads, was estimated to be 2.63 billion base pairs (Supplementary Information). From that, 4,933 mutations correspond to a germline mutation rate of  $1.20 \times 10^{-8}$  per nucleotide per generation, falling within the range between  $1.1 \times 10^{-8}$  and  $3.8 \times 10^{-8}$  previously reported<sup>3,7,8,22,23</sup>. Tables 2 and 3 summarize the nature of the *de novo* mutations with respect to sequence context. Approximately two-thirds ( $3,344/4,933 = 67.8\%$ ) are transitions. Moreover, there is a clear difference between mutation rates at CpG and non-CpG sites. CpG dinucleotides are known to be mutational hotspots in mammals, ostensibly because spontaneous oxidative deamination of methylated cytosines leads to an increase in transition mutations<sup>24</sup>. The observed rate of transitions here is 18.2 times that at non-CpG sites, higher than but not inconsistent with previous estimates of 13.3 (ref. 23) and 15.4 (ref. 3). The transversion rate is also higher at CpG sites, 2.55-fold that at non-CpG sites. Most of this increased transversion rate at CpG sites is presumably due to general mutation bias favouring mutations that decrease G+C content. The rate of mutations that change a strong (G:C) base pair to a weak (A:T) one is 2.15-times higher than mutations in the opposite direction. This mutational pressure in the direction of A+T is observed for both transitions (ratio = 2.24) and transversions (ratio = 1.82), and cannot be solely explained by CpG mutations. The father's age does not seem to affect the ratios between the rates of these different classes of mutations, that is, as a man ages rates of all mutation types increase by a similar factor.

The average number of mutations for each chromosome separately and the effect of father's age are displayed in Fig. 3. The effect of father's age is significant ( $P < 0.05$ ) for 14 of the 22 chromosomes when evaluated individually. The solid line in the figure corresponds to a model in which the linear effect of father's age is proportional to the mean number of mutations on the chromosome, or that father's age has a uniform multiplicative effect across the chromosomes. All 22 95% confidence intervals overlap the line, indicating that the results are consistent with the model.

### Discussion

The recombination rate is higher for women than men, and children of older mothers have more maternal recombinations than those of young mothers<sup>25</sup>. However, men transmit a much higher number of mutations to their children than women. Furthermore, even though our data also show some overdispersion in the number of maternal *de novo* mutations, it is the age of the father that is the dominant factor in determining the number of *de novo* mutations in the child. Seeing an association between father's age and mutation rate is not surprising<sup>2</sup>, but the large linear effect of more than two extra mutations per year, or the estimated exponential effect of paternal mutations doubling every 16.5 years, is striking. Even more so is the fraction of the

**Table 3 | Strong-to-weak and weak-to-strong mutation rates**

Mutation type	S→W ( <i>n</i> ) rate	W→S ( <i>n</i> ) rate	S→W rate/W→S rate
Transition	(2,025) $1.21 \times 10^{-8}$	(1,319) $5.42 \times 10^{-9}$	2.24
Transversion	(446) $2.67 \times 10^{-9}$	(358) $1.47 \times 10^{-9}$	1.82
All	(2,471) $1.48 \times 10^{-8}$	(1,677) $6.89 \times 10^{-9}$	2.15

*n* denotes observed mutation counts, and mutation rates are calculated per generation per base. For strong (S; G:C) to weak (W; A:T), the effective number of sites examined is taken as 1.071 billion, and for weak to strong the number is 1.56 billion.



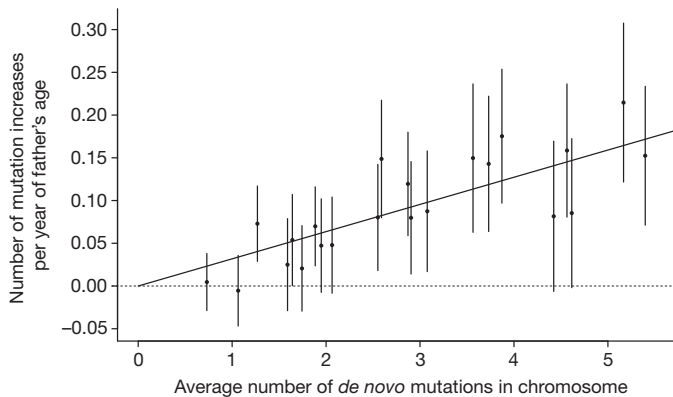


**Figure 3 | Effect of father's age by chromosome.** By chromosome, the estimated increase in the number of *de novo* mutations per year of father's age is plotted against the average number of mutations observed. The 95% confidence intervals are given. The solid straight line corresponds to the model in which the additive effect of father's age on the number of *de novo* mutations is assumed to be proportional to the mean number of mutations on the chromosome. From left to right, the points correspond to chromosome 21, 22, 19, 20, 15, 17, 18, 14, 16, 13, 12, 9, 10, 11, 8, 7, 6, 3, 5, 4, 2 and 1.

variation it explains, which limits the possible contribution by other factors, such as the environment and the genetic and non-genetic differences between individuals, to mutation rate on a population level. Given the results, it may no longer be meaningful to discuss the average mutation rate in a population without consideration of father's age. Also, even though factors other than father's age do not seem to contribute substantially to the mutation rate diversity in our data, it does not mean that hazardous environmental conditions could not cause a meaningful increase in mutation rate. Rather, the results indicate that, to estimate such an effect for a specific incident, it is crucial to take the father's age into account.

It is well known that demographic characteristics shape the evolution of the gene pool through the forces of genetic drift, gene flow and



**Figure 4 | Demographics of Iceland and *de novo* mutations.** The deCODE Genetics genealogy database was used to assess fathers' age at conception for all available 752,343 father-child pairs, in which the child's birth year was  $\geq 1650$ . The mean age of fathers at conception (left vertical axis) is plotted by birth year of child, grouped into ten-year intervals. On the basis of the linear model fitted for the relationship between father's age and the number of *de novo* mutations, the same plot, using the right vertical axis, shows the mean number of expected mutations for each ten-year interval.

natural selection. With the results here, it is now clear that demographic transitions that affect the age at which males reproduce can also have a considerable effect on the rate of genomic change through mutation. There has been a recent transition of Icelanders from a rural agricultural to an urban industrial way of life, which engendered a rapid and sequential drop in the average age of fathers at conception from 34.9 years in 1900 to 27.9 years in 1980, followed by an equally swift climb back to 33.0 years in 2011, primarily owing to the effect of higher education and the increased use of contraception (Fig. 4). On the basis of the fitted linear model, whereas individuals born in 1900 carried on average 73.7 *de novo* mutations, those born in 1980 carried on average only 59.7 such mutations (a decrease of 19.1%), and the mutational load of individuals born in 2011 has increased by 17.2% to 69.9. Demographic change of this kind and magnitude is not unique to Iceland, and it raises the question of whether the reported increase in ASD diagnosis lately is at least partially due to an increase in the average age of fathers at conception. Also, the observations here are likely to have important implications for the use of genetic variation to estimate divergence times between species or populations, because the mutation rate cannot be treated as a constant scaling factor, but rather must be considered along with the paternal generation interval as a time-dependent variable.

## METHODS SUMMARY

Whole-genome sequence data for this study were generated using the Illumina GALLx and HiSeq2000 instruments. The sequencing reads were aligned to the hg18 reference genome with Burrows-Wheeler aligner (BWA)<sup>26</sup> and duplicates were marked with Picard (<http://picard.sourceforge.net/>). Quality score recalibration, indel realignment and SNP/indel discovery were then performed on each sample separately, using GATK 1.2 (ref. 27). Likelihoods presented are based on the normalized Phred-scaled likelihoods that are calculated by the GATK variant calling. Statistical analysis was performed in part using the R statistical package. Estimates and confidence intervals for the fraction of variance explained after accounting for Poisson variation were calculated using Monte Carlo simulations (Supplementary Information). Variants were annotated using SNP effect predictor (snpeff2.0.5, database hg36.5) and GATK 1.4-9-g1f1233b with only the highest-impact effect (P. Cingolani, 'snpeff:Variant effect prediction', <http://snpeff.sourceforge.net>, 2012). More details are in Supplementary Information.

Received 28 February; accepted 4 July 2012.

1. Keightley, P. D. Rates and fitness consequences of new mutations in humans. *Genetics* **190**, 295–304 (2012).
2. Crow, J. F. The origins, patterns and implications of human spontaneous mutation. *Nature Rev. Genet.* **1**, 40–47 (2000).
3. Kondrashov, A. S. Direct estimates of human per nucleotide mutation rates at 20 loci causing Mendelian diseases. *Hum. Mutat.* **21**, 12–27 (2003).
4. Neale, B. M. *et al.* Patterns and rates of exonic *de novo* mutations in autism spectrum disorders. *Nature* **485**, 242–245 (2012).
5. O'Roak, B. J. *et al.* Sporadic autism exomes reveal a highly interconnected protein network of *de novo* mutations. *Nature* **485**, 246–250 (2012).
6. Sanders, S. J. *et al.* *De novo* mutations revealed by whole-exome sequencing are strongly associated with autism. *Nature* **485**, 237–241 (2012).
7. Xue, Y. *et al.* Human Y chromosome base-substitution mutation rate measured by direct sequencing in a deep-rooting pedigree. *Curr. Biol.* **19**, 1453–1457 (2009).
8. Conrad, D. F. *et al.* Variation in genome-wide mutation rates within and between human families. *Nature Genet.* **43**, 712–714 (2011).
9. Roach, J. C. *et al.* Analysis of genetic inheritance in a family quartet by whole-genome sequencing. *Science* **328**, 636–639 (2010).
10. Holm, H. *et al.* A rare variant in *MYH6* is associated with high risk of sick sinus syndrome. *Nature Genet.* **43**, 316–320 (2011).
11. Rafnar, T. *et al.* Mutations in *BRIP1* confer high risk of ovarian cancer. *Nature Genet.* **43**, 1104–1107 (2011).
12. Sulem, P. *et al.* Identification of low-frequency variants associated with gout and serum uric acid levels. *Nature Genet.* **43**, 1127–1130 (2011).
13. Keightley, P. D. *et al.* Analysis of the genome sequences of three *Drosophila melanogaster* spontaneous mutation accumulation lines. *Genome Res.* **19**, 1195–1201 (2009).
14. Malaspina, D. Paternal factors and schizophrenia risk: *de novo* mutations and imprinting. *Schizophr. Bull.* **27**, 379–393 (2001).
15. Croen, L. A., Najjar, D. V., Fireman, B. & Grether, J. K. Maternal and paternal age and risk of autism spectrum disorders. *Arch. Pediatr. Adolesc. Med.* **161**, 334–340 (2007).

16. Duong, L. *et al.* Mutations in *NRXN1* in a family multiply affected with brain disorders: *NRXN1* mutations and brain disorders. *Am. J. Med. Genet.* **159B**, 354–358 (2012).
17. Gauthier, J. *et al.* Truncating mutations in *NRXN2* and *NRXN1* in autism spectrum disorders and schizophrenia. *Hum. Genet.* **130**, 563–573 (2011).
18. Kirov, G. *et al.* Comparative genome hybridization suggests a role for *NRXN1* and *APBA2* in schizophrenia. *Hum. Mol. Genet.* **17**, 458–465 (2008).
19. Levinson, D. F. *et al.* Copy number variants in schizophrenia: confirmation of five previous findings and new evidence for 3q29 microdeletions and *VIPR2* duplications. *Am. J. Psychiatry* **168**, 302–316 (2011).
20. Rujescu, D. *et al.* Disruption of the neurexin 1 gene is associated with schizophrenia. *Hum. Mol. Genet.* **18**, 988–996 (2009).
21. Boyden, L. M. *et al.* Mutations in kelch-like 3 and cullin 3 cause hypertension and electrolyte abnormalities. *Nature* **482**, 98–102 (2012).
22. Lynch, M. Rate, molecular spectrum, and consequences of human mutation. *Proc. Natl Acad. Sci. USA* **107**, 961–968 (2010).
23. Nachman, M. W. & Crowell, S. L. Estimate of the mutation rate per nucleotide in humans. *Genetics* **156**, 297–304 (2000).
24. Coulondre, C., Miller, J. H., Farabaugh, P. J. & Gilbert, W. Molecular basis of base substitution hotspots in *Escherichia coli*. *Nature* **274**, 775–780 (1978).
25. Kong, A. *et al.* Recombination rate and reproductive success in humans. *Nature Genet.* **36**, 1203–1206 (2004).
26. Li, H. & Durbin, R. Fast and accurate short read alignment with Burrows-Wheeler transform. *Bioinformatics* **25**, 1754–1760 (2009).
27. McKenna, A. *et al.* The Genome Analysis Toolkit: a MapReduce framework for analyzing next-generation DNA sequencing data. *Genome Res.* **20**, 1297–1303 (2010).

**Supplementary Information** is available in the online version of the paper.

**Acknowledgements** This research was partly funded by The National Institutes of Health grant MH071425 (K.S.); the European Community's Seventh Framework Programme, PsychCNVs project, grant agreement HEALTH-F2-2009-223423, and NextGene project, grant agreement IAPP-MC-251592; The European Community IMI grant EU-AIMS, grant agreement 115300.

**Author Contributions** A.K. and K.S. planned and directed the research. A.K. wrote the first draft and together with K.S., S.B., P.S., A.H. and U.T. wrote the final version. O.T.M. and U.T. oversaw the sequencing and laboratory work. G. Masson, G. Magnusson and G.S. processed the raw sequencing data. A.K. and M.L.F. analysed the data, with W.S.W.W., H.H., G.B.W., S.S., G.T. and D.F.G. providing assistance. P.S. and S.A.G. performed functional annotations. S.B. analysed the mutations with respect to sequence content. A.S., Aslaug J. and Adalbjorg J. did the Sanger sequencing. A.H. investigated the contribution of demographics.

**Author Information** Reprints and permissions information is available at [www.nature.com/reprints](http://www.nature.com/reprints). The authors declare competing financial interests: details are available in the online version of the paper. Readers are welcome to comment on the online version of the paper. Correspondence and requests for materials should be addressed to A.K. (kong@decode.is) or K.S. (kari.stefansson@decode.is).

# Non-classical light generated by quantum-noise-driven cavity optomechanics

Daniel W. C. Brooks<sup>1</sup>, Thierry Botter<sup>1</sup>, Sydney Schreppler<sup>1</sup>, Thomas P. Purdy<sup>1†</sup>, Nathan Brahms<sup>1</sup> & Dan M. Stamper-Kurn<sup>1,2</sup>

**Optomechanical systems<sup>1</sup>, in which light drives and is affected by the motion of a massive object, will comprise a new framework for nonlinear quantum optics, with applications ranging from the storage<sup>2–4</sup> and transduction<sup>5,6</sup> of quantum information to enhanced detection sensitivity in gravitational wave detectors<sup>7,8</sup>. However, quantum optical effects in optomechanical systems have remained obscure, because their detection requires the object's motion to be dominated by vacuum fluctuations in the optical radiation pressure; so far, direct observations have been stymied by technical and thermal noise. Here we report an implementation of cavity optomechanics<sup>9,10</sup> using ultracold atoms in which the collective atomic motion is dominantly driven by quantum fluctuations in radiation pressure. The back-action of this motion onto the cavity light field produces ponderomotive squeezing<sup>11,12</sup>. We detect this quantum phenomenon by measuring sub-shot-noise optical squeezing. Furthermore, the system acts as a low-power, high-gain, nonlinear parametric amplifier for optical fluctuations, demonstrating a gain of 20 dB with a pump corresponding to an average of only seven intracavity photons. These findings may pave the way for low-power quantum optical devices, surpassing quantum limits on position and force sensing<sup>13,14</sup>, and the control and measurement of motion in quantum gases.**

Cavity optomechanics has led to powerful applications, including the cooling of massive objects to their motional ground state<sup>15,16</sup> and highly sensitive detection of force and motion. In such systems, displacements as minute as attometers<sup>17</sup> are converted into detectable optical signals, while concurrently the radiation pressure exerted by the light<sup>18,19</sup> strongly modifies the object's oscillations. This disturbance feeds back onto the light field, resulting in high-gain, nonlinear optical parametric amplification. However, observing distinctly quantum optical effects using optomechanical systems has proven elusive. Two such effects have been long-sought goals of optomechanics: the observation of light squeezed by its interaction with a moving mass and the observation of motion driven by light's quantum fluctuations.

In this work, we demonstrate these two phenomena. We establish a novel source of squeezing, generating non-classical light from an optically induced mechanical displacement, and we characterize an optomechanical amplifier driven by quantum fluctuations. Standard methods of generating squeezed light rely on the saturation of a nonlinear medium's electronic energy levels. In contrast, ponderomotive squeezing is predicted to arise when a massive object responds mechanically to quantum optical fluctuations, causing frequency-dependent gain and attenuation of the optical noise spectrum<sup>11,12</sup>. So far, thermal effects of the mechanical bath and optical technical noise have prevented optical observations of a cavity-optomechanical system driven by quantum fluctuations in radiation pressure. Therefore, experiments have focused on simulating ponderomotive squeezing by applying classical optical drives<sup>20,21</sup>. Here we measure a  $1.4\% \pm 0.1\% \pm 0.1\%$  reduction in the light's noise power below shot noise. (Throughout this Letter, the first uncertainty is statistical and the second, if present, is systematic.) A thorough examination of

statistical and systematic effects (Supplementary Information, section 5) confirms that this noise reduction, although slight, is due to non-classical light and demonstrates ponderomotive squeezing. In comparison with the prediction of the standard linearized theory<sup>22</sup>, the actual response of our strongly coupled optomechanical system shows significant differences, suggesting that a nonlinear optomechanical theory<sup>23,24</sup> is required to account for our observations.

We use a cavity-optomechanics system whose mechanical element consists of a cloud of ultracold atoms<sup>9,10</sup>. The atoms are trapped within a few adjacent sites of an optical lattice resonating within a Fabry–Pérot cavity. The atoms are prepared such that the energy of their axial motion is near that of the ground state. The gas couples dispersively to probe light that is nearly resonant with a second cavity mode, detuned by  $-31$  GHz from the atomic D2 resonance. At this detuning, the atoms act as a position-dependent refractive medium, which shifts the cavity resonance frequency. By placing the atoms at lattice sites centred at locations of maximum probe-intensity gradient, we ensure that the probe's cavity resonance frequency varies linearly with the centre-of-mass position of the atoms. When the atoms are centred at these sites, intensity fluctuations in the probe light produce radiation-pressure forces that drive collective atomic motion<sup>25</sup>. By first applying classical modulation to the optical field we demonstrate that the system behaves as a high-gain parametric optomechanical amplifier, using an input pump that feeds just 36 pW of power into the cavity. We then extinguish the classical drive to study the system's response to quantum radiation-pressure fluctuations, mapping the inhomogeneous spectrum of ponderomotive squeezing versus frequency, in both the amplitude- and phase-modulation quadratures of the optical field.

A linearized theory illuminates how ponderomotive squeezing is produced by cavity optomechanics. The optomechanical interaction is encapsulated by the interaction Hamiltonian  $\hbar g \hat{a}^\dagger \hat{a} (\hat{b} + \hat{b}^\dagger)$ , where  $\hat{a}$  and  $\hat{b}$  are the annihilation operators for the optical and mechanical fields, respectively (the dagger indicates Hermitian conjugate),  $g$  is the optomechanical coupling rate and  $\hbar$  is Planck's constant divided by  $2\pi$ . For small fluctuations, the probe intensity can be linearized about the mean optical field. In this approximation, the cavity-optomechanical system acts as a quadrature-sensitive linear amplifier for optical fluctuations<sup>22</sup>. The steady-state dynamical response of this amplifier at frequency  $\omega$ , neglecting additional external forces on the mechanical oscillator, is given by the relation between fluctuations in the Fourier-transformed intracavity field  $\tilde{a}$  and those of the cavity-filtered input field  $\tilde{\zeta}$  (Supplementary Information, section 2). Amplitude fluctuations in the cavity-filtered input field, proportional to  $\tilde{\zeta}(\omega) + \tilde{\zeta}^\dagger(-\omega)$ , induce motion of the mechanical oscillator, which is then transduced back onto the cavity field with a gain  $G(\omega)$ :

$$\tilde{a}(\omega) = \tilde{\zeta}(\omega) + \frac{1}{2} G(\omega) [\tilde{\zeta}(\omega) + \tilde{\zeta}^\dagger(-\omega)] \quad (1)$$

$$G(\omega) \approx \frac{(ik - \Delta)s_{\text{opt}}}{\omega_s^2 - \omega^2 - i\omega\Gamma_{\text{tot}}} \quad (2)$$

<sup>1</sup>Department of Physics, University of California, Berkeley, California 94720, USA. <sup>2</sup>Materials Sciences Division, Lawrence Berkeley National Laboratory, Berkeley, California 94720, USA. <sup>†</sup>Present address: JILA, University of Colorado, Boulder, Colorado 80309, USA.



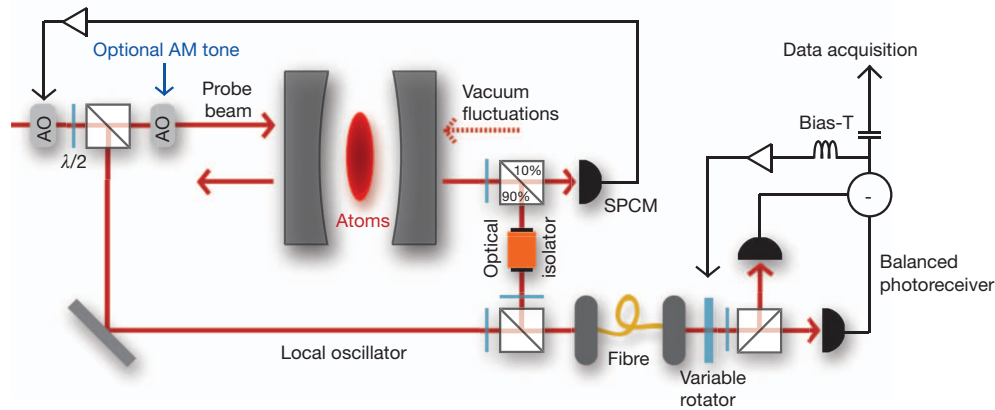


**Figure 1 | Schematic of cavity and heterodyne detection set-up.** Ten per cent of the cavity output light is diverted to a single-photon counting module (SPCM), and the remainder goes to a heterodyne detector. All beam splitters are polarizing beam-splitter cubes preceded by half-wave plates ( $\lambda/2$ ). The SPCM signal is fed back to control the frequency of an acousto-optic modulator (AO),

Here  $\kappa$  is the cavity half-linewidth,  $\Delta$  is the probe detuning from cavity resonance and  $\Gamma_{\text{tot}} = \Gamma_m + \Gamma_{\text{opt}}$  is the combination of mechanical and optomechanical damping. The optomechanical stiffening parameter  $s_{\text{opt}} \propto \langle \hat{a}^\dagger \hat{a} \rangle g^2$  shifts the mechanical resonance frequency from its unperturbed value,  $\omega_m$ , to  $\omega_s = \sqrt{\omega_m^2 + \Delta s_{\text{opt}}}$ . When  $\Delta = 0$ , the transduced optomechanical response appears in the phase of the optical field, and does not interfere with the input radiation-pressure fluctuations. When  $\Delta \neq 0$ , the gain becomes closed-loop and the optomechanically induced response can interfere destructively with the input fluctuations. When technical and thermal fluctuations are sufficiently small, the ponderomotive suppression of quantum optical fluctuations is resolved as sub-shot-noise squeezing at frequencies near  $\omega_m$ .

For the studies of ponderomotive amplification and squeezing described below, we repeatedly prepare and measure new samples of  $\sim 3,500$   $^{87}\text{Rb}$  atoms. For each measurement cycle, a microfabricated atom chip delivers the atomic ensemble to two to four adjacent sites of the intracavity optical lattice. Evaporative cooling brings each axial vibrational mode of the gas to near its quantum ground state<sup>26</sup>. The optically bound centre of mass serves as the mechanical element. By controlling the intensity of the optical lattice,  $\omega_m/2\pi$  can be changed from a few to several hundred kilohertz. For these experiments,  $\omega_m = 2\pi \times 155.5$  kHz is set significantly lower than the cavity half-linewidth,  $\kappa = 2\pi \times 1.8$  MHz. The optomechanical coupling rate is then  $g = (d\omega_0/dz)z_{\text{zp}} = 2\pi \times 54$  kHz, where  $z_{\text{zp}} = \sqrt{\hbar/2m\omega_m}$  is the mechanical harmonic oscillator length,  $\omega_0$  is the resonance frequency of the cavity and  $m = 0.5$  ag is the total mass of the atomic ensemble.

Because ponderomotive squeezing is observable only when the probe light is detuned from the cavity resonance, we stabilize the probe frequency to  $\Delta = -2\pi \times 1.1$  MHz. The use of a balanced heterodyne configuration to detect the light transmitted through the cavity reduces the contamination of our measurements by optical technical noise (Supplementary Information, section 5.1). To achieve an overall quantum efficiency of 10.1% for detecting intracavity photons (Fig. 1), we made the cavity mirror on the detector side a factor of eight more transmissive than the input mirror. We restrict the heterodyne signal record to the first 5 ms of probing, after which the atomic sample is significantly heated by radiation pressure fluctuations (Supplementary Information, section 3). In each experimental cycle, we also acquire two additional data streams from the heterodyne receiver: one after the optical cavity is emptied of atoms and one with the probe light extinguished. These record the spectra of technical and shot noise, respectively. The back-to-back recording of squeezed and shot-noise signals every cycle helps eliminate effects of long-term drifts.

We study the optomechanical response to both classical and quantum optical drives. In the first experiment, following recent

maintaining a constant probe detuning from the shifted cavity resonance.

Additional AOs shift the probe beam 10 MHz relative to the local oscillator and can be used to add amplitude modulation (AM). The probe and local oscillators are mode-matched through a fibre and sent into the detector, which is balanced by controlling the beam polarization with a liquid-crystal rotator.

work<sup>20,21</sup>, we measure the classical linear response of the optomechanical amplifier by applying single-frequency amplitude modulation to the input optical field. The complex gain  $G(\omega)$  transduces the input modulation onto the amplitude-modulation and phase-modulation quadratures of the optical output field. For each experimental cycle, a single amplitude-modulation tone is applied (Fig. 1). To avoid saturating the response as the drive frequency approaches  $\omega_m$ , the sideband power is reduced from  $-17$  dB to  $-33$  dB with respect to the carrier. Using a superheterodyne technique, we determine the complex response in both quadratures as a function of frequency. The response is characterized (Fig. 2) by a power gain and phase shift relative to the input drive tone, which is independently measured by the empty-cavity data record.

The measured power gain shows regions of strong enhancement of fluctuations (up to 20 dB in power) at frequencies less than  $\omega_m$ . Remarkably, the large gain is achieved with only 36 pW of optical pump power coupled into the cavity, maintaining an average intracavity photon number of seven. This observation suggests that an optomechanical system configured for high input-coupling efficiency could be applied in ultralow-power photonics as an amplifier, filter or switch. At higher frequencies, we observe strong suppression of amplitude fluctuations, with maximal suppression by 26 dB at  $\omega_m$ . The phase shift shows a transition from a delayed to an advanced response, indicated by the response crossing  $0^\circ$  in the amplitude modulation quadrature and  $-180^\circ$  in the phase modulation quadrature. The amplifier's stability is maintained because the gain is less than one at the frequencies where there is an advanced response.

Having characterized the ponderomotive optical amplification of our system, we extinguish the deliberate amplitude modulation and drive our system with quantum radiation-pressure fluctuations. Ponderomotive squeezing should result in a strongly squeezed optical field within the cavity with maximal attenuation of  $\sim 20$  dB at  $\omega_m$  in the amplitude modulation quadrature. Outside the cavity, interference with reflected shot noise shifts the optimally squeezed frequency and quadrature in a  $\Delta$ -dependent manner<sup>11,12,22</sup>. At our detector, we expect sub-shot-noise squeezing of only a few per cent owing to this interference, optical losses and the heterodyne detector's quantum efficiency. For each run of the experiment, we extract the noise power spectral density (PSD) of the demodulated heterodyne signal. Each cycle of the experiment lasts 40 s, providing a 5-ms-long recording of quantum-noise-driven optomechanical response, as well as empty-cavity and shot-noise records. To obtain sufficient sensitivity to observe low levels of squeezing, we average data from nearly 2,000 cycles of the experiment, yielding a total of 10 s of integration time.

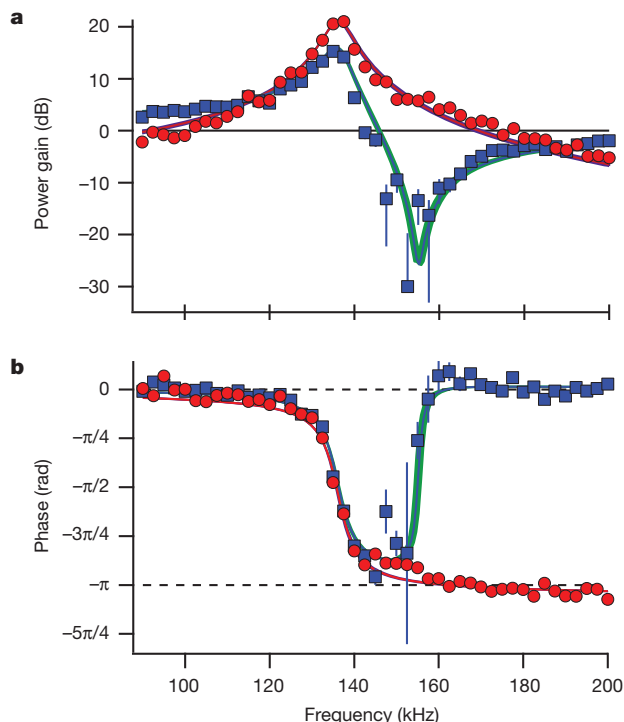


**Figure 2 | Optomechanical transduction of classical amplitude modulation.** Transduction indicated by the square magnitude of the gain (a) and by the phase offset relative to the drive tone (b). In the amplitude-modulation quadrature (blue squares in a and b), the drive is maximally attenuated at  $\omega_m$  to 26 dB below the response without amplification (horizontal black line in a). The drive is also transduced into the phase-modulation quadrature (red circles in a and b), yielding a strong power response centred at  $\omega_s$ . At low frequencies, the optomechanical response adds a phase delay. At frequencies greater than  $\omega_m$ , the optomechanical damping,  $\Gamma_{\text{opt}}$ , changes sign, causing the phase offsets of the amplitude- and phase-modulation quadratures to cross  $0^\circ$  and  $180^\circ$ , respectively (dashed lines in b). Error bars indicate the measured  $1\sigma$  statistical uncertainty. The data are in good agreement with the predicted amplitude-modulation response (blue lines) and phase-modulation response (red lines). The effects of systematic uncertainties on the theory are shown in the green and purple shaded regions. By fitting predicted responses to the data, we extract the optomechanically shifted mechanical oscillation frequency ( $\omega_s = 2\pi \times 136$  kHz) and the mechanical damping rate ( $\Gamma_m = 2\pi \times 1.9$  kHz).

In the PSD, we observe ponderomotive squeezing in the amplitude-modulation quadrature of  $1.2\% \pm 0.1\%$  below the measured noise power of uncorrelated vacuum (Fig. 3), without accounting for systematic effects. Correcting for systematic effects (clipping and nonlinear gain in the detection chain, optical power variations, optical path length variations, the detector noise floor and technical noise on the local-oscillator path) the observed squeezing is  $1.4\% \pm 0.1\% \pm 0.1\%$  below shot noise, with statistical and systematic errors reported at the 68% confidence level. The measurement is not adjusted for technical noise in the probe path, which also reduces the amount of squeezing observed. The statistical uncertainty arises from an average over the frequency range indicated in Fig. 3. This frequency range is limited by technical optical noise (Brownian noise at low frequencies and additional narrow-band spikes) and by optomechanical response which deviates from the linear theory. To define the limits of the selected frequency range without introducing bias in our analysis of the amplitude-modulation quadrature, we have used independent measurements from the orthogonal phase-modulation quadrature. At frequencies less than  $\omega_s$ , at a quadrature angle around  $-40^\circ$  from amplitude modulation and at frequencies with sufficiently low technical input noise, we observe an additional region of squeezing with the detected noise reduced by  $0.8\% \pm 0.2\% \pm 0.1\%$  of shot noise. The overall variation in the PSD with frequency and detection quadrature

matches closely with the prediction of the extracavity linear theory of ponderomotive amplification and squeezing (Fig. 3c).

Focusing on frequencies greater than  $\omega_s$ , we find three features in the PSD that differ significantly from the predictions of linear optomechanical theory. Two of these features are the additional noise peaks at  $\omega_m$  and  $2\omega_s$ , which are most significant in the phase-modulation quadrature. The third feature is the level of amplitude-modulation squeezing, which does not reach the 3.7% maximal or 2.4% average (over the indicated range) reduction below shot noise that is expected from linear theory (Fig. 3b) given our system parameters, even after accounting for systematic detection effects. We ascribe these deviations to two causes. The first is the nonlinear wave mixing inherent in the optomechanical interaction, which is predicted to be significant<sup>23,24</sup> in the single-photon strong coupling regime,  $g/\omega_m > 1$ . Given that in our system  $g/\omega_m = 0.35$ , we believe that the emergence of the peak near  $2\omega_s$  is due to the onset of this nonlinearity. Wave mixing between the Brownian technical noise at low frequencies and the amplified response near  $\omega_s$  could also contribute to the limited squeezing observed. Nonlinear effects due to single-photon strong coupling will be the subject of future investigation. A second effect is the disturbance of the centre-of-mass mode by the remaining axial mechanical modes of the atomic ensemble, all of which resonate at frequencies near  $\omega_m$ . These additional modes, which are not sensed directly by the cavity field, serve as the mechanical thermal bath, whose energy exchange with the centre-of-mass mode contributes to  $\Gamma_m$  and may contribute to the noise peak at  $\omega_m$ .

The ponderomotive squeezing observed in the cavity output spectrum results from coherence between the optical vacuum noise reflected off the cavity mirrors and the radiation-pressure fluctuations driving the intracavity mechanical element. Such squeezing implies that our optomechanical system is dominantly driven by quantum fluctuations in radiation pressure, also known as radiation-pressure shot noise (RPSN). We confirm from the empty-cavity heterodyne record (Supplementary Fig. 3) that, whereas Brownian technical noise contributes significantly to the intracavity fluctuations for  $\omega < 2\pi \times 75$  kHz, the noise that drives atomic motion is dominated by shot noise at higher frequencies. This conclusion relies crucially on the fact that only intracavity amplitude-modulation noise contributes to radiation-pressure fluctuations. Accordingly, phase noise inside the cavity does not perturb atomic motion, despite being larger than shot noise by a factor of about ten across the relevant frequency range. (The phase noise is largely common mode to the probe and local oscillator; the residual noise registered by the heterodyne detector is a small fraction of shot noise; see Supplementary Fig. 3.) Whereas previous experiments quantified RPSN bolometrically<sup>25,27</sup>, here the dominant role of RPSN can be directly quantified by comparing the observed PSD of the cavity output (Fig. 3) with the values predicted for optomechanical amplification of a pure quantum noise optical input. For instance, at  $\omega_s = 2\pi \times 140$  kHz, 97% of the observed phase modulation PSD is expected from RPSN alone, with the remaining 3% resulting from the residual technical, thermal and motional zero-point noise. The close quantitative agreement in frequency regions with large amplification, along with the characterization of squeezing, indicates our observation of both the amplification and suppression of the optical vacuum field due to its interaction with the motion of a mechanical element.

Two key features enable our observations of ponderomotive squeezing and RPSN. First, optical trapping decouples the mechanical element from the surrounding environment. Second, our system operates in a regime where the optical output spectrum is far more sensitive to optical inputs than to mechanical inputs<sup>22</sup>. As a result, nonlinear optical effects such as parametric amplification are observed with extremely weak pump power. Although the observed level of squeezing is small, it nevertheless confirms that optomechanical interactions do indeed generate non-classical light and must be accounted for when using squeezed light to reduce noise in optomechanical force detectors<sup>8</sup>. Established methods for increasing the magnitude of optical

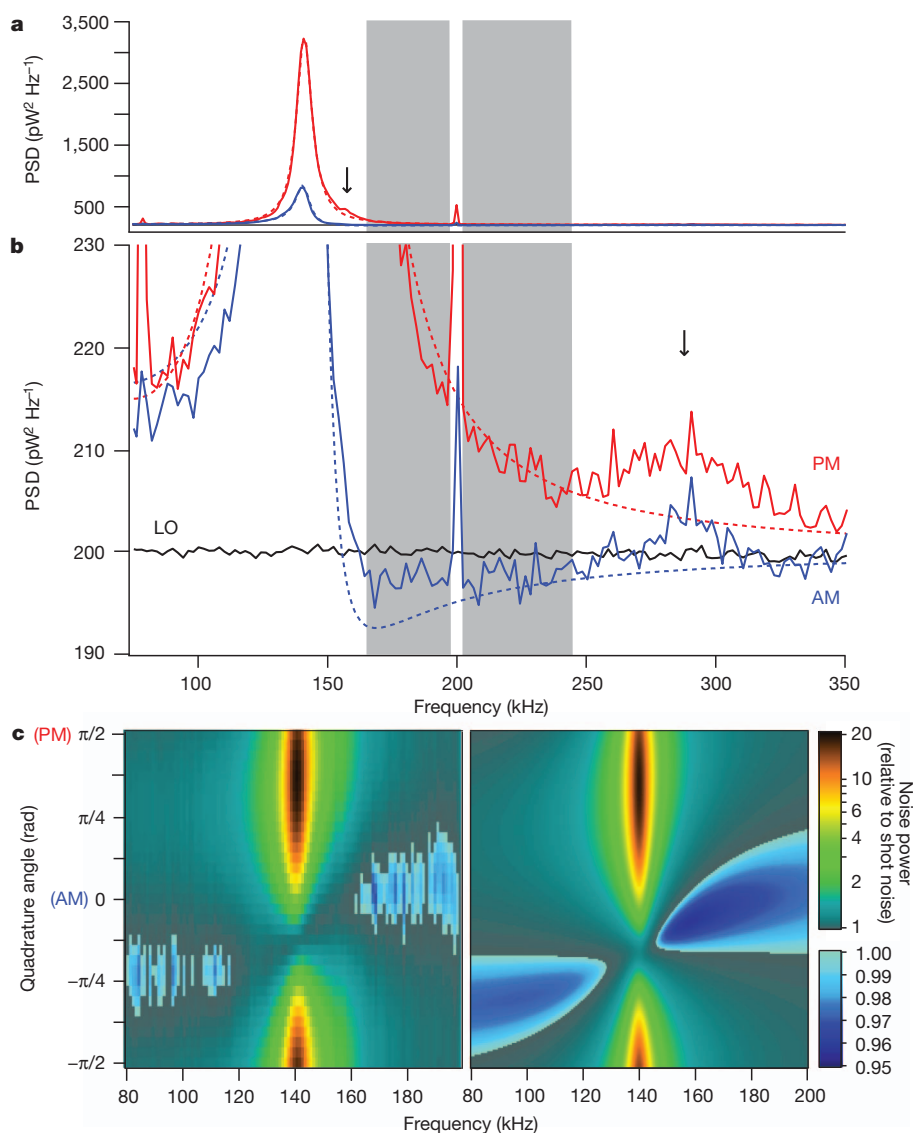


**Figure 3 | Ponderomotive squeezing and the optomechanical response to quantum radiation pressure fluctuations.** **a, b,** Power spectral densities (PSDs) of the optomechanical response are shown with a common abscissa at full scale (**a**) and magnified about the region of shot noise (**b**), in the phase-modulation (PM; red) and amplitude-modulation (AM; blue) quadratures (solid, data; dashed, theory). Theoretical parameters, determined by fitting both the phase-modulation PSD and the technical noise measured in empty-cavity spectra (Supplementary Fig. 3), give the zero-free-parameter amplitude modulation theory line. The local-oscillator PSD (LO; black) determines the

shot-noise level. The amplitude-modulation PSD is found to be less than shot noise for frequencies greater than  $\omega_m$  (grey shaded region). Bounds on the region are identified by a technical noise spike at 200 kHz, and by peaks (black arrows) in the phase-modulation optomechanical response that were not predicted by linear theory. **c,** PSD versus quadrature, shown relative to shot noise. The colour scale changes for squeezed regions. The measured PSD (left) indicates the frequency dependence of the maximally squeezed quadrature and shows overall agreement, especially for regions of amplification, with the linear theory (right), which is shown without technical noise.

squeezing, including implementing homodyne detection, improving detection efficiency and eliminating more low-frequency technical noise, are readily available for future experiments. For a full understanding of ponderomotive amplification, however, our results show that theoretical treatments that go beyond the linear model will be necessary.

Received 5 April; accepted 14 June 2012.

Published online 15 August 2012.

- Kippenberg, T. J. & Vahala, K. J. Cavity optomechanics: back-action at the mesoscale. *Science* **321**, 1172–1176 (2008).
- Teufel, J. D. *et al.* Circuit cavity electromechanics in the strong-coupling regime. *Nature* **471**, 204–208 (2011).
- Weis, S. *et al.* Optomechanically induced transparency. *Science* **330**, 1520–1523 (2010).
- Safavi-Naeini, A. H. *et al.* Electromagnetically induced transparency and slow light with optomechanics. *Nature* **472**, 69–73 (2011).

- Safavi-Naeini, A. H. & Painter, O. Proposal for an optomechanical traveling wave phonon–photon translator. *N. J. Phys.* **13**, 013017 (2011).
- Regal, C. A. & Lehnert, K. W. From cavity electromechanics to cavity optomechanics. *J. Phys. Conf. Ser.* **264**, 012025 (2011).
- Kimble, H. J., Levin, Y., Matsko, A. B., Thorne, K. S. & Vyatchanin, S. P. Conversion of conventional gravitational-wave interferometers into quantum non-demolition interferometers by modifying their input and/or output optics. *Phys. Rev. D* **65**, 022002 (2001).
- Corbitt, T. *et al.* Squeezed-state source using radiation-pressure-induced rigidity. *Phys. Rev. A* **73**, 023801 (2006).
- Gupta, S., Moore, K. L., Murch, K. W. & Stamper-Kurn, D. M. Cavity non-linear optics at low photon numbers from collective atomic motion. *Phys. Rev. Lett.* **99**, 213601 (2007).
- Brennecke, F., Ritter, S., Donner, T. & Esslinger, T. Cavity optomechanics with a Bose-Einstein condensate. *Science* **322**, 235–238 (2008).
- Fabre, C. *et al.* Quantum-noise reduction using a cavity with a movable mirror. *Phys. Rev. A* **49**, 1337–1343 (1994).
- Mancini, S. & Tombesi, P. Quantum noise reduction by radiation pressure. *Phys. Rev. A* **49**, 4055–4065 (1994).
- Caves, C. M. Quantum-mechanical noise in an interferometer. *Phys. Rev. D* **23**, 1693–1708 (1981).



14. Clerk, A. A., Devoret, M. H., Girvin, S. M., Marquardt, F. & Schoelkopf, R. J. Introduction to quantum noise, measurement, and amplification. *Rev. Mod. Phys.* **82**, 1155–1208 (2010).
15. Teufel, J. D. *et al.* Sideband cooling of micromechanical motion to the quantum ground state. *Nature* **475**, 359–363 (2011).
16. Chan, J. *et al.* Laser cooling of a nanomechanical oscillator into its quantum ground state. *Nature* **478**, 89–92 (2011).
17. Abbott, B. P. *et al.* An upper limit on the stochastic gravitational-wave background of cosmological origin. *Nature* **460**, 990–994 (2009).
18. Braginskii, V. B. & Manukin, A. B. Ponderomotive effects of electromagnetic radiation. *Sov. Phys. JETP* **24**, 653–655 (1967).
19. Caves, C. M. Quantum-mechanical radiation-pressure fluctuations in an interferometer. *Phys. Rev. Lett.* **45**, 75–79 (1980).
20. Marino, F., Cataliotti, F. S., Farsi, A., de Cumis, M. S. & Marin, F. Classical signature of ponderomotive squeezing in a suspended mirror resonator. *Phys. Rev. Lett.* **104**, 073601 (2010).
21. Verlot, P., Tavernarakis, A., Briant, T., Cohadon, P.-F. & Heidmann, A. Backaction amplification and quantum limits in optomechanical measurements. *Phys. Rev. Lett.* **104**, 133602 (2010).
22. Botter, T., Brooks, D. W. C., Brahms, N., Schreppler, S. & Stamper-Kurn, D. M. Linear amplifier model for optomechanical systems. *Phys. Rev. A* **85**, 013812 (2012).
23. Nunnenkamp, A., Børkje, K. & Girvin, S. M. Single-photon optomechanics. *Phys. Rev. Lett.* **107**, 063602 (2011).
24. Rabl, P. Photon blockade effect in optomechanical systems. *Phys. Rev. Lett.* **107**, 063601 (2011).
25. Murch, K. W., Moore, K. L., Gupta, S. & Stamper-Kurn, D. M. Observation of quantum-measurement backaction with an ultracold atomic gas. *Nature Phys.* **4**, 561–564 (2008).
26. Purdy, T. P. *et al.* Tunable cavity optomechanics with ultracold atoms. *Phys. Rev. Lett.* **105**, 133602 (2010).
27. Brahms, N., Botter, T., Schreppler, S., Brooks, D. W. C. & Stamper-Kurn, D. M. Optical detection of the quantization of collective atomic motion. *Phys. Rev. Lett.* **108**, 133601 (2012).

**Supplementary Information** is available in the online version of the paper.

**Acknowledgements** We acknowledge C. McLeod for assistance with the manuscript. This work was supported by the AFSOR and NSF. T.B. acknowledges support from the FQRNT.

**Author Contributions** T.P.P. contributed to the design of the experiment and the development of the theory. All other authors contributed to the design of the experiment, the development of the theory, data acquisition and analysis.

**Author Information** Reprints and permissions information is available at [www.nature.com/reprints](http://www.nature.com/reprints). The authors declare no competing financial interests. Readers are welcome to comment on the online version of the paper. Correspondence and requests for materials should be addressed to D.B. ([dwb@berkeley.edu](mailto:dwb@berkeley.edu)).

# Exciton condensation and perfect Coulomb drag

D. Nandi<sup>1</sup>, A. D. K. Finck<sup>1</sup>, J. P. Eisenstein<sup>1</sup>, L. N. Pfeiffer<sup>2</sup> & K. W. West<sup>2</sup>

**Coulomb drag is a process whereby the repulsive interactions between electrons in spatially separated conductors enable a current flowing in one of the conductors to induce a voltage drop in the other<sup>1–3</sup>. If the second conductor is part of a closed circuit, a net current will flow in that circuit. The drag current is typically much smaller than the drive current owing to the heavy screening of the Coulomb interaction. There are, however, rare situations in which strong electronic correlations exist between the two conductors. For example, double quantum well systems can support exciton condensates, which consist of electrons in one well tightly bound to holes in the other<sup>4–6</sup>. ‘Perfect’ drag is therefore expected; a steady transport current of electrons driven through one quantum well should be accompanied by an equal current of holes in the other<sup>7</sup>. Here we demonstrate this effect, taking care to ensure that the electron–hole pairs dominate the transport and that tunnelling of charge between the quantum wells, which can readily compromise drag measurements, is negligible. We note that, from an electrical engineering perspective, perfect Coulomb drag is analogous to an electrical transformer that functions at zero frequency.**

The exciton condensate of interest here develops at high perpendicular magnetic field  $B_{\perp}$  when the separation  $d$  between two parallel two-dimensional electron systems (2DESs) is comparable to the magnetic length  $l = (\hbar/eB_{\perp})^{1/2}$  and the total density  $n_T = n_1 + n_2$  of electrons in the bilayer matches the degeneracy  $eB_{\perp}/h$  of a single spin-resolved Landau level (ref. 6 and references therein, refs 8, 9). (We consider here only the balanced case, with  $n_1 = n_2$ ;  $\hbar$  is Planck’s constant  $h$  divided by  $2\pi$ , and  $e$  is the electronic charge.) Hence, the total Landau level filling factor is  $\nu_T = 1$ . When  $d/l \lesssim 1.8$ , an energy gap to charged excitations opens and the bilayer electron system displays a quantized Hall plateau  $\rho_{xy} = h/e^2$ . The interlayer tunnelling conductance becomes strongly enhanced near zero bias and, when equal electrical currents are driven in opposite directions through the two layers, the Hall effect vanishes at low temperature<sup>10–13</sup>.

Even in the limit of zero tunnelling through the barrier separating the layers, interlayer Coulomb interactions at  $\nu_T = 1$  are believed to be sufficient to both open a charge gap and to spontaneously generate quantum phase coherence between electrons in opposite layers<sup>6,8,9</sup>. Spontaneous interlayer phase coherence allows the system ground state to be described as a Bose condensate of interlayer excitons. At low temperatures, the charged excitations of the  $\nu_T = 1$  system are frozen out and unable to transport current across the bulk of the two-dimensional system. In contrast, the neutral electron–hole pairs in the condensate remain abundant and free to move about the bulk. Transport of these excitons is equivalent to counter-flowing electrical currents in the two layers. Interestingly, the  $\nu_T = 1$  quantum Hall system is closely related to exciton and exciton–polariton condensates at zero magnetic field, for which evidence of spontaneous phase coherence has recently been reported<sup>14–16</sup>.

Evidence for exciton transport at  $\nu_T = 1$  was obtained from Hall effect measurements in which counter-flowing electrical currents were driven through the two layers<sup>11–13</sup>. The observed vanishing of the Hall voltage at  $\nu_T = 1$  is consistent with the counter-flowing currents being carried by excitons. However, interpretation of these experiments is complicated by the conducting edge states which exist at the boundary

of all quantum Hall systems. Furthermore, because the experiments were performed using simply-connected Hall bar geometries, they were incapable of proving that excitons were moving through the bulk of the 2DES. Subsequent experiments by Tiemann *et al.*<sup>17,18</sup> and Finck *et al.*<sup>19</sup> employed the multiply connected Corbino geometry (essentially an annulus with separated edge states on the two rims) in order to search for exciton transport across the insulating bulk. By connecting the two layers together at one rim while applying a voltage between the layers at the other rim, Finck *et al.* observed that relatively large, oppositely directed currents would flow across the bulk of the  $\nu_T = 1$  quantum Hall state<sup>19</sup>. This observation contrasts sharply with the observed inability of the bulk to support co-directed currents in the two layers. Finck *et al.* concluded that bulk exciton transport was responsible for their results<sup>19</sup>.

We show here that the excitonic correlations built into the  $\nu_T = 1$  quantum Hall state can force oppositely directed currents to flow in the two layers even when there is no electrical connection between them. For small driving currents the observed drag current is closely equal in magnitude to the drive current; that is, the drag is ‘perfect’. The role of interlayer tunnelling is investigated and shown to be irrelevant in the proper circumstances.

Our sample consists of two parallel 2DESs confined in a GaAs/AlGaAs double quantum well structure, the details of which are given below. The bilayer 2DES is patterned into an annulus (1 mm inner diameter, 1.4 mm outer diameter) with arms extending from each rim to ohmic contacts; a schematic plan-view of the device is shown in Fig. 1a. Each ohmic contact may be connected either to both two-dimensional layers simultaneously or to either layer separately<sup>20</sup>. Electrostatic gating of the 2DESs in the annulus (but not the contact arms) allows the key parameter  $d/l$  to be tuned from 2.35 down to about 1.49 at  $\nu_T = 1$ . In addition to the perpendicular magnetic field

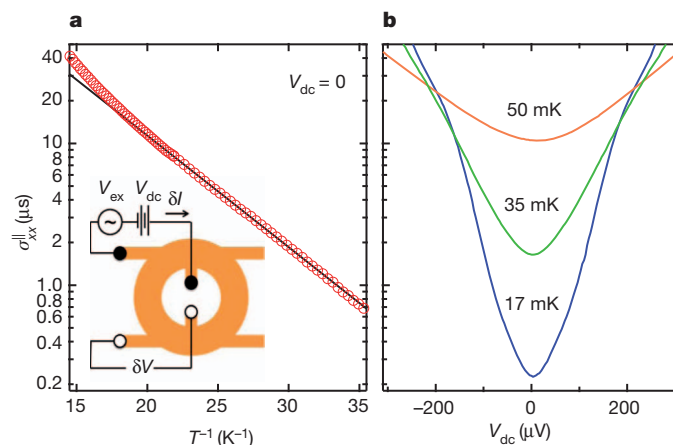


**Figure 1 | Corbino conductance  $\sigma_{xx}^{\parallel}$  at  $\nu_T = 1$ .** **a**,  $\partial I/\partial V (= \sigma_{xx}^{\parallel})$  at zero d.c. voltage versus  $T^{-1}$  at  $\nu_T = 1$  with  $d/l = 1.5$  and  $\theta = 26^\circ$ . Solid line implies an energy gap of  $\Delta \approx 360$  mK. Inset, schematic plan-view of device; see text for details. Filled dots indicate contacts to both layers; open dots show contacts to lower layer only. **b**,  $\sigma_{xx}^{\parallel}$  versus applied d.c. voltage  $V_{dc}$  under same conditions as in **a** for various temperatures.

<sup>1</sup>Condensed Matter Physics, California Institute of Technology, Pasadena, California 91125, USA. <sup>2</sup>Department of Electrical Engineering, Princeton University, Princeton, New Jersey 08544, USA.



$B_{\perp}$  needed to establish  $\nu_T = 1$ , an in-plane field  $B_{\parallel}$  may also be applied by tilting the sample relative to the total magnetic field. This allows us to suppress<sup>21</sup> the interlayer tunnelling which can otherwise pollute Coulomb drag measurements. The sample displays a robust quantum Hall effect at  $\nu_T = 1$  for  $d/l \lesssim 1.8$  for all tilt angles up to at least  $\theta = 66^\circ$ . Figure 1a illustrates the insulating character of the bulk of the two-dimensional system at  $\nu_T = 1$  (with  $d/l = 1.5$  and  $\theta = 26^\circ$ ) in an Arrhenius plot of the Corbino conductance  $\sigma_{xx}^{\parallel}$  for parallel transport in the two layers. A small a.c. excitation voltage ( $V_{ex} \approx 18 \mu\text{V}$  at 13 Hz) is applied between contacts (to both layers) on the inner and outer rim of the annulus. The resulting current flow  $\delta I$ , plus the rim-to-rim voltage difference  $\delta V$  between two additional contacts, are recorded and used to compute  $\sigma_{xx}^{\parallel} = \partial I / \partial V$ . As expected, the conductance is thermally activated,  $\sigma_{xx}^{\parallel} \propto e^{-\Delta/2T}$ , and gives an energy gap  $\Delta \approx 360 \text{ mK}$ . When a d.c. voltage  $V_{dc}$  is added to the a.c. excitation voltage  $V_{ex}$ , the conductance  $\sigma_{xx}^{\parallel}$  increases. This smooth ‘breakdown’ of the  $\nu_T = 1$  quantum Hall effect, shown in Fig. 1b, has important consequences for the Coulomb drag results to which we now turn.

In a Corbino Coulomb drag measurement, a voltage  $V$  is again applied between the inner and outer rims of the annulus, but only via contacts to one of the two two-dimensional layers. The other layer is either left open or is closed upon itself by connecting an external resistor between the two rims. The open-circuit case is similar to the  $\sigma_{xx}^{\parallel}$  measurement discussed above; current will flow in the drive layer, but only in proportion to  $\sigma_{xx}^{\parallel}$ . The closed-circuit case is potentially different; if strong interlayer correlations are present, relatively large oppositely directed currents, mediated by exciton transport, might flow in the two layers.

Figure 2 shows the results of such closed-circuit drag measurements. External resistors in both the drive and drag loops allow us to monitor the currents  $I_1$  and  $I_2$  flowing in each. This arrangement is illustrated in Fig. 2a inset;  $I_1$  and  $I_2$  are defined as positive if they flow in the direction of the arrows. Whereas the drive circuit is grounded at one point, the

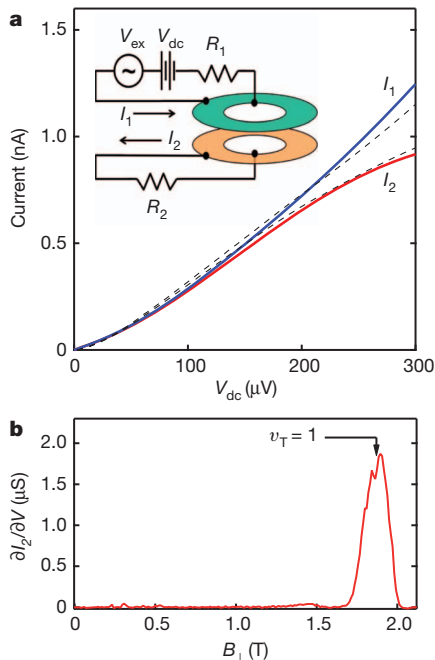


**Figure 2 | Corbino Coulomb drag.** **a**, Solid lines, drive and drag currents,  $I_1$  and  $I_2$ , respectively, versus d.c. voltage  $V_{dc}$  at  $\nu_T = 1$ , with  $d/l = 1.5$  and  $T = 17 \text{ mK}$ . Dashed lines are simulations incorporating estimated series resistances and measured Corbino conductivity  $\sigma_{xx}^{\parallel}$ . Inset, measurement circuit, with the two two-dimensional layers shaded green and orange. The resistors  $R_1$  and  $R_2$  comprise both external circuit resistors and resistances intrinsic to the device. **b**, Drag transconductance,  $\partial I_2 / \partial V$  at  $V_{dc} = 0$  versus perpendicular magnetic field at  $T \approx 25 \text{ mK}$ . All data taken at  $\theta = 26^\circ$ .

drag circuit is left to float. Figure 2a shows the d.c. currents  $I_1$  and  $I_2$  flowing, at  $T \approx 17 \text{ mK}$ , in response to a d.c. drive voltage  $V_{dc}$  at  $\nu_T = 1$ , with  $d/l = 1.49$  and  $\theta = 26^\circ$ . For small  $V_{dc}$ ,  $I_1$  and  $I_2$  are very nearly equal and grow steadily, if somewhat super-linearly, with voltage. In the  $V_{dc} \rightarrow 0$  limit, the conductances  $\partial I_1 / \partial V \approx \partial I_2 / \partial V$  exceed the parallel flow Corbino conductance  $\sigma_{xx}^{\parallel}$  at  $\nu_T = 1$  by a factor of 5. At large  $V_{dc}$ , the currents separate, with  $I_1$  continuing to grow steadily while  $I_2$  begins to saturate. Figure 2b shows the magnetic field dependence (at  $\theta = 26^\circ$ ) of the drag transconductance  $\partial I_2 / \partial V$  at  $V_{dc} = 0$  (obtained by applying a weak purely a.c. excitation voltage  $V_{ex}$  across the drive circuit) at  $T \approx 25 \text{ mK}$ . As expected, significant drag is found only in the vicinity of  $\nu_T = 1$  at  $B_{\perp} = 1.87 \text{ T}$ .

Because the currents  $I_1$  and  $I_2$  are detected outside the bilayer 2DES, it is not obvious that the drive current is truly passing through the top two-dimensional layer and the drag current through the bottom two-dimensional layer. Instead, interlayer tunnelling could allow the current to shunt from the top to the bottom layer near the outer rim of the device, pass through the external drag layer loop, and then tunnel back from the bottom to the top layer near the inner rim. If this is the case, the current  $I_2$  need not be due to Coulomb drag, as recognized in the prior Corbino transport measurements<sup>17,18</sup> of Tiemann *et al.* To eliminate this possibility, we intentionally suppress interlayer tunnelling by tilting our sample relative to the applied magnetic field.

Figure 3 shows d.c. tunnelling current–voltage characteristics at  $\nu_T = 1$  and  $d/l = 1.49$ , for  $\theta = 0$  and  $26^\circ$ . These data were obtained at  $T \approx 20 \text{ mK}$  by applying an external d.c. voltage  $V_{dc}$  between contacts to the ‘upper’ and ‘lower’ 2DES layer on the outside rim of the annulus and recording both the resultant tunnelling current  $I$  and the interlayer voltage  $V_{int}$  between the two remaining outside rim contacts. Figure 3a shows the tunnelling currents plotted versus  $V_{int}$  while Fig. 3b plots the currents versus  $V_{dc}$ ; the two figures therefore contrast the ‘four-terminal’ and ‘two-terminal’ tunnelling current–voltage characteristics of the bilayer system. The four-terminal  $I$ – $V_{int}$  characteristic at  $\theta = 0$  clearly shows the Josephson-like near-discontinuity at  $V_{int} = 0$  reported previously<sup>10,18,21,22</sup>. In contrast, the two-terminal  $I$ – $V_{dc}$  characteristic shows the tunnelling current initially rising smoothly with  $V_{dc}$ . This difference is due almost entirely to the extrinsic series resistances presented by the arms leading into the annulus. Indeed, comparison of the two- and four-terminal tunnelling data allows us to accurately estimate the series resistances and their nonlinearity with voltage; these estimates are important in the analysis of the Coulomb

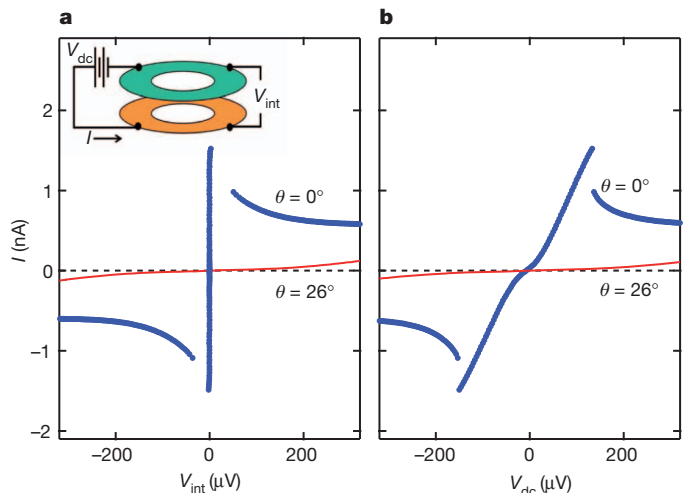


**Figure 3 | Four-terminal versus two-terminal tunnelling characteristics at  $\nu_T = 1$ .** **a**, Tunnel current versus measured interlayer voltage  $V_{int}$ . Blue traces,  $\theta = 0^\circ$ ; red traces,  $\theta = 26^\circ$ . Inset, measurement circuit. **b**, Same as **a** except tunnel current is plotted versus applied interlayer voltage  $V_{dc}$ . All data taken at  $d/l = 1.49$  and  $T \approx 20 \text{ mK}$ . Dashed line indicates zero tunnel current.

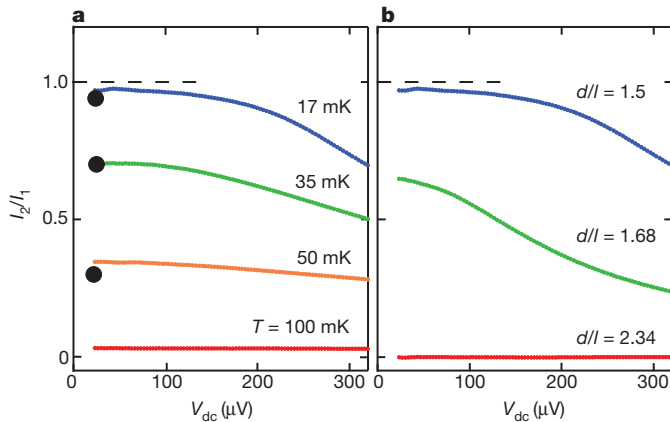


**Figure 4 | Coulomb drag current ratio,  $I_2/I_1$  at  $\nu_T = 1$ .** **a**,  $I_2/I_1$  versus d.c. voltage  $V_{dc}$  at  $\nu_T = 1$  for  $d/l = 1.5$  at various temperatures. Filled circles are estimates based on measurements of  $\sigma_{xx}^{\parallel}$  at  $V_{dc} = 0$ , as described in text. **b**,  $I_2/I_1$  versus  $V_{dc}$  at  $\nu_T = 1$  and  $T = 17$  mK for various  $d/l$ . All data taken at  $\theta = 26^\circ$ . Dashed lines indicate perfect drag limit.

drag data. Note that for  $\theta = 0^\circ$  the maximum tunnelling currents are comparable to the currents  $I_1$  and  $I_2$  observed in the drag measurement and shown in Fig. 2a.

Most importantly, Fig. 3a and b reveal the expected<sup>21</sup> suppression of the tunnelling current resulting from tilting the sample. At  $\theta = 26^\circ$  the zero bias anomaly so prominent at  $\theta = 0$  in the four-terminal  $I-V_{int}$  characteristic is essentially obliterated. Even at the relatively high applied voltage of  $|V_{dc}| = 300 \mu\text{V}$  the tunnel current is only  $\sim 0.1$  nA. The two- and four-terminal characteristics at  $\theta = 26^\circ$  are very similar, because the tunnelling resistance at this tilt angle is much larger than the extrinsic series resistances.

Comparing the tunnelling data in Fig. 3 with the Coulomb drag data in Fig. 2a demonstrates that tunnelling is not an important contributor to the drag current  $I_2$  at  $\theta = 26^\circ$ . Ignoring, for the moment, the different excitation means in the two cases (interlayer versus intralayer biasing), it is clear that the tunnelling conductance near  $V_{dc} = 0$  is at least 10 times smaller than the drag transconductance  $\partial I_2/\partial V$ . Similarly, the drag current at  $V_{dc} = 200 \mu\text{V}$  is  $I_2 \approx 650$  pA, while the tunnelling current at the same bias is only 44 pA. This comparison, however, greatly exaggerates the importance of tunnelling precisely because of the different means of excitation in the two experiments. In a drag measurement, the bias voltage  $V_{dc}$  is applied across the drive layer; the drag layer is allowed to float. Direct measurements of the interlayer voltage under these conditions shows it to be quite small ( $< 15 \mu\text{V}$ ), even when the intralayer drive voltage reaches  $|V_{dc}| \approx 300 \mu\text{V}$ . At such small interlayer voltages the tunnelling current (at  $\theta = 26^\circ$ ) is extremely small ( $\lesssim 4$  pA). Note that this argument fails at  $\theta = 0$  where, as Fig. 3a shows, a large ( $> 1$  nA) and virtually discontinuous jump in the tunnelling current occurs at zero interlayer voltage.

The above discussion enables us to conclude that the drive and drag currents shown in Fig. 2b do indeed flow across the bulk of the top and bottom two-dimensional layers in the annulus, and in opposite directions. For small drive voltages,  $I_1 \approx I_2$  and thus the drag is essentially perfect. In this nearly pure counter-flow regime, the drag process is dominated by neutral exciton transport.

Figure 4a and b shows how the drag ratio  $I_2/I_1$  depends on temperature  $T$  and effective layer separation  $d/l$ , respectively. For small drive voltages  $V_{dc}$ , the drag ratio is close to unity ( $I_2/I_1 \approx 0.97$ ) only at the lowest  $T$  and  $d/l$ , where the  $\nu_T = 1$  quantum Hall state is strongest. Increasing either parameter reduces the drag ratio at small  $V_{dc}$ . In all cases, the drag ratio also falls with increasing drive voltage. We believe that these deviations from perfect drag are due primarily to the finite

Corbino conductance  $\sigma_{xx}^{\parallel}$ , which allows parallel charge transport across the bulk to occur alongside the neutral exciton transport.

Assuming  $\sigma_{xx}^{\parallel} = 0$  and dissipationless exciton transport, it is predicted<sup>7</sup> that  $I_1 = I_2 = V/(R_1 + R_2)$ , where  $R_1$  and  $R_2$  are the net resistances in series with the Corbino annulus in the drive and drag circuits, respectively. These include the external circuit resistors  $R_{ext}$ , the resistances  $R_{arm}$  of the 2DES arms leading into the annulus, and quantum Hall ‘contact’ resistances  $R_c$  of order  $h/e^2$ . Generalizing this model to include non-zero  $\sigma_{xx}^{\parallel}$ , we find, assuming linear response, the drag current reduces to  $I_2 = V/(R_1 + R_2 + R_1 R_2 \sigma_{xx}^{\parallel})$  and the drag ratio to  $I_2/I_1 = 1/(1 + R_2 \sigma_{xx}^{\parallel})$ . Using the tunnelling data in Fig. 3a to estimate  $R_1$  and  $R_2$  and the measured  $\sigma_{xx}^{\parallel}$  data in Fig. 1a, we can estimate the expected drag ratio  $I_2/I_1$  near zero bias. These estimates, shown in Fig. 4a, compare quite favourably with the observed drag ratios at  $T = 17, 35$  and  $50$  mK. At higher  $V_{dc}$  the nonlinearity of  $\sigma_{xx}^{\parallel}$  (shown in Fig. 1b) and the series resistances  $R_1$  and  $R_2$  must also be taken into account. The dashed lines in Fig. 2b display the results of one such calculation of the drag and drive currents. The qualitative agreement with the experimental results is strong evidence that the enhanced Corbino conductance  $\sigma_{xx}^{\parallel}$  at elevated temperatures and drive voltages is the dominant source of deviations from perfect Coulomb drag at  $\nu_T = 1$ .

The assumption that exciton transport across the bulk of the 2DES is dissipationless can be questioned in real, disordered samples such as ours<sup>23–26</sup>. A phenomenological excitonic ‘resistance’  $R_s$  can be introduced whereby  $R_s(I_1 + I_2)$  equals the difference  $\Delta V_{int}$  between the interlayer voltages on the two rims of the annulus (a spatially uniform interlayer voltage would produce no dissipation). In the  $\sigma_{xx}^{\parallel} = 0$  limit, this new resistance leaves the drag perfect, but reduces the currents to  $I_1 = I_2 = V/(R_1 + R_2 + R_s)$ . The relatively large magnitude of  $R_1 + R_2$  (never less than  $2h/e^2$ )<sup>7,27</sup> limits the ability of the present Coulomb drag experiments to detect small values of  $R_s$ . Future multi-terminal measurements should be able to set stringent limits on any dissipation occurring in the exciton channel.

## METHODS SUMMARY

The present sample consists of two 18-nm GaAs quantum wells separated by a 10-nm  $\text{Ga}_{0.1}\text{Al}_{0.9}\text{As}$  barrier. The centre-to-centre layer separation is therefore  $d = 28$  nm. This double well structure is flanked by thick  $\text{Ga}_{0.7}\text{Al}_{0.3}\text{As}$  cladding layers. Si doping sheets within the cladding layers populate the lowest subband of each quantum well with a 2DES of nominal density  $5.5 \times 10^{10} \text{ cm}^{-2}$  and low temperature mobility of  $1 \times 10^6 \text{ cm}^2 \text{ V}^{-1} \text{ s}^{-1}$ . Standard photo-lithographic techniques are used to pattern the bilayer 2DES into the geometry depicted in Fig. 1. Diffused AuNiGe ohmic contacts are positioned at the ends of arms extending away from both rims of the annulus. Electrostatic gates cross these arms (both on the top and on the thinned back side of the sample) in order to use a selective depletion scheme which allows the contacts to communicate with the 2DES in the annulus either via both layers in parallel or either layer separately<sup>20</sup>. Additional gates control the two-dimensional layer densities in the annulus itself. The sample is mounted on a Ag platform in good thermal contact with the mixing chamber of a  $^3\text{He}$ - $^4\text{He}$  dilution refrigerator. The electrical transport measurements reported here employ standard d.c. and/or low frequency a.c. techniques. The d.c. drive and drag currents  $I_1$  and  $I_2$  can be determined either by exciting the drive circuit with a purely d.c. voltage, or by numerical integration of the ac currents  $\delta I_1$  and  $\delta I_2$  flowing in response to a weak a.c. voltage ( $V_{ex} \approx 18 \mu\text{V}$  at 13 Hz) added to the d.c. component of  $V$ . Although the two methods are in excellent agreement, the a.c. technique is less noisy.

Received 6 March; accepted 11 June 2012.

1. Pogrebinsky, M. B. Mutual drag of carriers in a semiconductor-insulator-semiconductor system. *Fiz. Tekh. Poluprovodn.* **11**, 637–644 (1977); *Sov. Phys. Semicond.* **11**, 372–376 (1977).
2. Price, P. M. Hot electron effects in heterolayers. *Physica B* **117**, 750–752 (1983).
3. Rojo, A. G. Electron-drag effects in coupled electron systems. *J. Phys. Condens. Matter* **11**, R31–R52 (1999).
4. Snoke, D. Spontaneous Bose coherence of excitons and polaritons. *Science* **298**, 1368–1372 (2002).
5. Butov, L. V. Exciton condensation in coupled quantum wells. *Solid State Commun.* **127**, 89–98 (2003).

6. Eisenstein, J. P. & MacDonald, A. H. Bose-Einstein condensation of excitons in bilayer electron systems. *Nature* **432**, 691–694 (2004).
7. Su, J.-J. & MacDonald, A. H. How to make a bilayer exciton condensate flow. *Nature Phys.* **4**, 799–802 (2008).
8. Fertig, H. A. Energy spectrum of a layered system in a strong magnetic field. *Phys. Rev. B* **40**, 1087–1095 (1989).
9. MacDonald, A. H. & Girvin, S. M. in *Perspectives in Quantum Hall Effects* (eds Das Sarma, S. & Pinczuk, A.) 161–224 (Wiley, 1997).
10. Spielman, I. B., Eisenstein, J. P., Pfeiffer, L. N. & West, K. W. Resonantly enhanced tunneling in a double layer quantum Hall ferromagnet. *Phys. Rev. Lett.* **84**, 5808–5811 (2000).
11. Kellogg, M., Eisenstein, J. P., Pfeiffer, L. N. & West, K. W. Vanishing Hall resistance at high magnetic field in a double-layer two-dimensional electron system. *Phys. Rev. Lett.* **93**, 036801 (2004).
12. Tutuc, E., Shayegani, M. & Huse, D. A. Counterflow measurements in strongly correlated GaAs hole bilayers: evidence for electron-hole pairing. *Phys. Rev. Lett.* **93**, 036802 (2004).
13. Wiersma, R. *et al.* Activated transport in the separate layers that form the  $\nu_T = 1$  exciton condensate. *Phys. Rev. Lett.* **93**, 266805 (2004).
14. Yang, S., Hammack, A. T., Fogler, M. M., Butov, L. V. & Gossard, A. C. Coherence length of cold exciton gases in coupled quantum wells. *Phys. Rev. Lett.* **97**, 187402 (2006).
15. High, A. A. *et al.* Spontaneous coherence in a cold exciton gas. *Nature* **483**, 584–588 (2012).
16. Kasprzak, J. *et al.* Bose-Einstein condensation of exciton polaritons. *Nature* **443**, 409–414 (2006).
17. Tiemann, L. *et al.* Exciton condensate at a total filling factor of one in Corbino two-dimensional electron bilayers. *Phys. Rev. B* **77**, 033306 (2008).
18. Tiemann, L., Dietsche, W., Hauser, M. & von Klitzing, K. Critical tunneling currents in the regime of bilayer excitons. *N. J. Phys.* **10**, 045018 (2008).
19. Finck, A. D. K., Eisenstein, J. P., Pfeiffer, L. N. & West, K. W. Exciton transport and Andreev reflection in a bilayer quantum Hall system. *Phys. Rev. Lett.* **106**, 236807 (2011).
20. Eisenstein, J. P., Pfeiffer, L. N. & West, K. W. Independently contacted two-dimensional electron systems in double quantum wells. *Appl. Phys. Lett.* **57**, 2324–2326 (1990).
21. Spielman, I. B., Eisenstein, J. P., Pfeiffer, L. N. & West, K. W. Observation of a linearly dispersing Goldstone mode in a quantum Hall ferromagnet. *Phys. Rev. Lett.* **87**, 036803 (2001).
22. Tiemann, L. & Yoon, Y., Dietsche, W., von Klitzing, K. & Wegscheider, W. Dominant parameters for the critical tunneling current in bilayer exciton condensates. *Phys. Rev. B* **80**, 165120 (2009).
23. Huse, D. A. Resistance due to vortex motion in the  $\nu = 1$  bilayer quantum Hall superfluid. *Phys. Rev. B* **72**, 064514 (2005).
24. Fertig, H. A., & Murthy, G. Coherence network in the quantum Hall bilayer. *Phys. Rev. Lett.* **95**, 156802 (2005).
25. Fil, D. V. & Shevchenko, S. I. Interlayer tunneling and the problem of superfluidity in bilayer quantum Hall systems. *Low Temp. Phys.* **33**, 780–782 (2007).
26. Lee, D. K. K., Eastham, P. R. & Cooper, N. R. Breakdown of counterflow superfluidity in a disordered quantum Hall bilayer. *Adv. Condens. Matter Phys.* **2011**, 792125 (2011).
27. Pesin, D. A. & MacDonald, A. H. Scattering theory of transport in coherent quantum Hall bilayers. *Phys. Rev. B* **84**, 075308 (2011).

**Acknowledgements** We thank A.H. MacDonald and D. Pesin for discussions. This work was supported by NSF grant DMR-1003080.

**Author Contributions** D.N., A.D.K.F. and J.P.E. conceived the project. L.N.P. and K.W.W. grew the samples. D.N. and A.D.K.F. performed the experiment and, along with J.P.E., analysed the data and wrote the manuscript.

**Author Information** Reprints and permissions information is available at [www.nature.com/reprints](http://www.nature.com/reprints). The authors declare no competing financial interests. Readers are welcome to comment on the online version of this article at [www.nature.com/nature](http://www.nature.com/nature). Correspondence and requests for materials should be addressed to J.P.E. ([jpe@caltech.edu](mailto:jpe@caltech.edu)).



# Room-temperature ferroelectricity in supramolecular networks of charge-transfer complexes

Alok S. Tayl<sup>1\*</sup>, Alexander K. Shveyd<sup>2\*</sup>, Andrew C.-H. Sue<sup>2,3</sup>, Jodi M. Szarko<sup>2,4,5</sup>, Brian S. Rolczynski<sup>2,4,5</sup>, Dennis Cao<sup>2,6</sup>, T. Jackson Kennedy<sup>7</sup>, Amy A. Sarjeant<sup>2</sup>, Charlotte L. Stern<sup>2</sup>, Walter F. Paxton<sup>2</sup>, Wei Wu<sup>8</sup>, Sanjeev K. Dey<sup>2</sup>, Albert C. Fahrenbach<sup>2,6</sup>, Jeffrey R. Guest<sup>9</sup>, Hooman Mohseni<sup>8</sup>, Lin X. Chen<sup>2,4,5</sup>, Kang L. Wang<sup>3</sup>, J. Fraser Stoddart<sup>2,6</sup> & Samuel I. Stupp<sup>1,2,10,11</sup>

Materials exhibiting a spontaneous electrical polarization<sup>1,2</sup> that can be switched easily between antiparallel orientations are of potential value for sensors, photonics and energy-efficient memories. In this context, organic ferroelectrics<sup>3,4</sup> are of particular interest because they promise to be lightweight, inexpensive and easily processed into devices. A recently identified family of organic ferroelectric structures is based on intermolecular charge transfer, where donor and acceptor molecules co-crystallize in an alternating fashion known as a mixed stack<sup>5–8</sup>: in the crystalline lattice, a collective transfer of electrons from donor to acceptor molecules results in the formation of dipoles that can be realigned by an external field as molecules switch partners in the mixed stack. Although mixed stacks have been investigated extensively, only three systems are known<sup>9,10</sup> to show ferroelectric switching, all below 71 kelvin. Here we describe supramolecular charge-transfer networks that undergo ferroelectric polarization switching with a ferroelectric Curie temperature above room temperature. These polar and switchable systems utilize a structural synergy between a hydrogen-bonded network and charge-transfer complexation of donor and acceptor molecules in a mixed stack. This supramolecular motif could help guide the development of other functional organic systems that can switch polarization under the influence of electric fields at ambient temperatures.

Ordered networks of electron donors and acceptors are good candidates for organic ferroelectrics because of the possible long-range orientation of their charge-transfer dipoles. The canonical electron donor-acceptor systems—the mixed-stack tetrathiafulvalene (TTF) with halogenated quinones (Q)<sup>2,3,7,11–13</sup>, like TTF·chloranil (TTF·QCl<sub>4</sub>) and TTF·bromanil (TTF·QBr<sub>4</sub>)—have been investigated by X-ray crystallography<sup>7,11</sup>, vibrational spectroscopy<sup>5,7,11,12</sup> and electrical measurements<sup>2,3,9,10,14</sup>. The TTF·QCl<sub>4</sub> complex undergoes a ferroelectric phase transition at the Curie temperature ( $T_C = 81$  K), evidenced by a discontinuous jump in ionicity ( $\rho$ ) and dimerization into donor (D)–acceptor (A) pairs ( $D^0 A^0 D^0 A^0 \rightarrow D^{\delta+} A^{\delta-} D^{\delta+} A^{\delta-}$ ); this dimerization breaks the centre of symmetry of the lattice. Categorizing this phase transition as a ferroelectric transition was first suggested<sup>13</sup> in 1991, when an anomalous spike in the dielectric constant was observed at  $T_C$  for TTF·QCl<sub>4</sub>. In TTF·QBr<sub>4</sub>, which is already ionic ( $\rho > 0.5$ ) at room temperature, the molecules in the crystal have been shown to dimerize, giving donor–acceptor pairs at 53 K as result of a spin-Peierls instability<sup>10,14,15</sup>. In the ferroelectric ground state of these mixed-stack systems, measurable reversible polarization under an electric field has only been shown<sup>9,10</sup> for TTF·QCl<sub>4</sub>, TTF·QBrCl<sub>3</sub> and TTF·QBr<sub>4</sub>.

We describe here charge-transfer pairs that are capable of assembling into ordered three-dimensional supramolecular networks. This

series of charge-transfer crystals is based on complexes between a pyromellitic diimide-based acceptor (**1** in Fig. 1a) and donors (**2**, **3** and **4** and Fig. 1a) that are derivatives of naphthalene, pyrene and TTF, respectively. These charge-transfer pairs co-crystallize (see below) under ambient conditions and the resulting solid-state superstructures were characterized (Supplementary Table 1) by X-ray crystallography (Fig. 1b–d). In these networks, the assembly of the acceptor (**1**) and donor (**2**, **3**, **4**) components in the lattice are stabilized by four primary non-covalent bonding interactions: charge-transfer, hydrogen-bonding,  $\pi$ – $\pi$  stacking and van der Waals forces. Diimide **1** was functionalized with diethylene glycol ‘arms’ that are capable of acting as both donors and acceptors in the formation of hydrogen bonds. Electron-rich compounds **2**, **3** and **4** can also interact through hydrogen-bonding because their shorter ‘arms’ are terminated by hydroxyl or amino groups. An extensive hydrogen-bonded network, composed of interstack and intrastack hydrogen bonds (Fig. 1b–d), is formed during the self-assembly process. We refer to this modular design as lock arm supramolecular ordering (LASO), an approach which enables complementary molecules to crystallize rapidly into functional networks from solution under ambient conditions (Fig. 2a–c). The overall motif for LASO structures requires a hierarchical organization based on non-covalent bonding interactions that bridge distances from ångströms to nanometres and are considerably stronger than van der Waals forces. Locally, the charge-transfer and  $\pi$ – $\pi$  stacking interactions are directed along a single direction parallel to the mixed-stack axis, while the hydrogen bonds extend into three dimensions. This panoply of supramolecular interactions leads to a tightly packed network of mixed stacks locked over larger length scales by hydrogen bonds,  $\pi$ – $\pi$  stacking and charge transfer.

To illustrate the connectivity of the hydrogen-bonded network in the interstitial regions between the stacks, Hirshfeld surface analysis<sup>16,17</sup> was used to measure the distribution of close contact interactions (Fig. 2). The Hirshfeld surface is a graphical tool that compares the atomically averaged electron density of a molecule to the electron density of the entire crystal, and partitions the lattice into molecular surfaces that map the spatial contacts. White regions represent molecular contacts at the van der Waals distance, while red and blue portions represent lengths shorter and longer than the van der Waals distance, respectively (Fig. 2). This type of analysis helps identify which interactions are the most dominant among neighbouring stacks. In Fig. 2, the bar graphs on the left show that [O···H] interactions responsible for hydrogen-bonding make up 37–41% of all interstack contacts while [H···H] interactions are 42–50% of such contacts, revealing the close-packed nature of the superstructure. The lengths shorter than the van der Waals distance are significant because they

<sup>1</sup>Department of Materials Science and Engineering, Northwestern University, Evanston, Illinois 60208, USA. <sup>2</sup>Department of Chemistry, Northwestern University, Evanston, Illinois 60208, USA. <sup>3</sup>Department of Electrical Engineering, University of California, Los Angeles, Los Angeles, California 90095, USA. <sup>4</sup>ANSER Center, Northwestern University, Evanston, Illinois 60208, USA. <sup>5</sup>Chemical Sciences and Engineering Division, Argonne National Laboratory, Argonne, Illinois 60439, USA. <sup>6</sup>Graduate School of EEWS, Korea Advanced Institute of Science and Technology, Daejeon, 305-701, South Korea. <sup>7</sup>Department of Physics, Northwestern University, Evanston, Illinois 60208 USA. <sup>8</sup>Department of Electrical Engineering, Northwestern University, Evanston, Illinois 60208, USA. <sup>9</sup>Center for Nanoscale Materials, Argonne National Laboratory, Argonne, Illinois 60439, USA. <sup>10</sup>Department of Medicine, Northwestern University, Chicago, Illinois 60611, USA. <sup>11</sup>Institute for BioNanotechnology in Medicine, Northwestern University, Chicago, Illinois 60611, USA.

\*These authors contributed equally to this work.

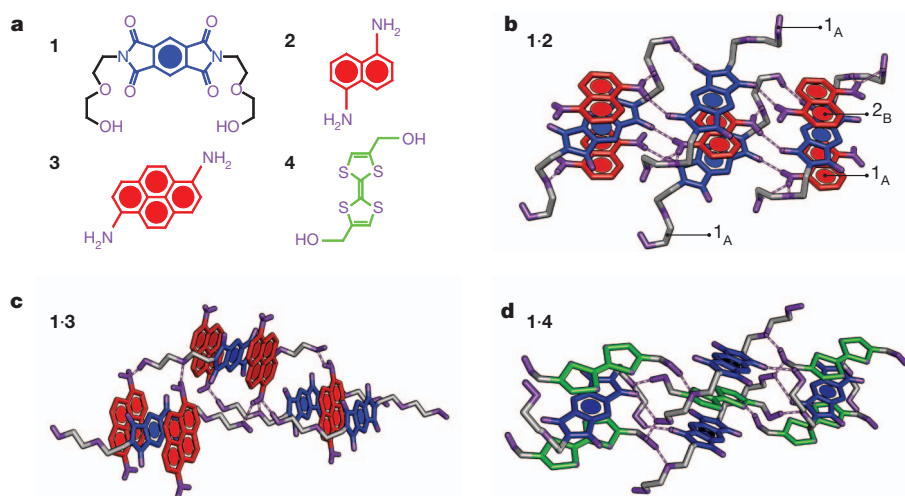


**Figure 1 | Crystal structures of LASO complexes.** **a**, Structural formulae of electron donor and acceptor molecules used in this research. Compound **1** is a pyromellitic diimide-based electron acceptor (blue). Compounds **2** and **3** are aromatic electron donors (red). Compound **4** is an electron-rich TTF derivative (green). The sites that participate in non-covalent bonding interactions are depicted in purple, and hydrogen bonds are depicted as purple dashed lines.

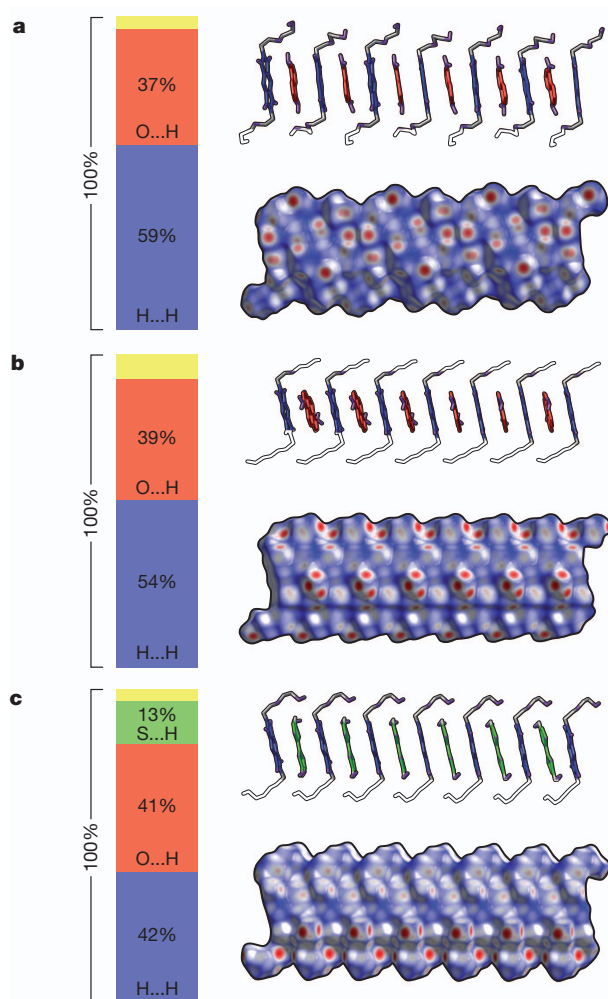


**Figure 2 | Hirshfeld surface analysis.** The Hirshfeld surface is a spatial map that uses colour coding to represent the proximity of close contacts around (a) molecule(s) within a network (white, distance ( $d$ ) equals the van der Waals distance; blue,  $d$  exceeds the van der Waals distance; red,  $d$  is less than the van der Waals distance). Right, the Hirshfeld surface shown was calculated for  $n = 13$  molecules within a stack for **1:2** (a), **1:3** (b) and **1:4** (c). In each panel a–c, the upper rectangle shows a portion of a donor–acceptor stack, while the lower region displays the corresponding Hirshfeld surface. Left, the percentage contribution of atomic contacts to the Hirshfeld surface is shown in the bar graph.

arise from short  $[O\cdots H]$  and  $[H\cdots H]$  distances when interstack hydrogen bonds are formed. These interstack interactions are between neighbouring arms and allow the stacks to pack tightly into a supra-molecular network.

Because the electron transfer occurs along the stacking axis, we characterized ionicity<sup>12,14</sup>,  $\rho$ , which is a measure of the extent of charge transfer, to investigate how its magnitude affects ferroelectric behaviour. Polarized vibrational spectroscopy<sup>12,15</sup> (Fourier transform infrared) was used to determine  $\rho$  for each complex (Supplementary Information). The *ungerade* modes were used to calculate<sup>12</sup>  $\rho$  because they are not influenced by electron–molecular vibrational interactions. At room temperature,  $\rho$  values for LASO complexes **1:2**, **1:3** and **1:4** (crystals shown in Fig. 3a–c) were determined by following the linear shift of the C=O stretch ( $1,728$ – $1,716\text{ cm}^{-1}$ ) polarized parallel to the donor–acceptor stack. Complexes **1:2** and **1:3** were found to be ionic with  $\rho = 0.68$  and  $0.89$ , respectively, while **1:4** lies close to the neutral–ionic border<sup>12,13</sup> ( $\rho = 0.5$ ) with  $\rho = 0.43$ . The polar nature of the crystals enables, therefore, the LASO network to be ferroelectric. Along with significant electron transfer, a violation of the mutual exclusion rule

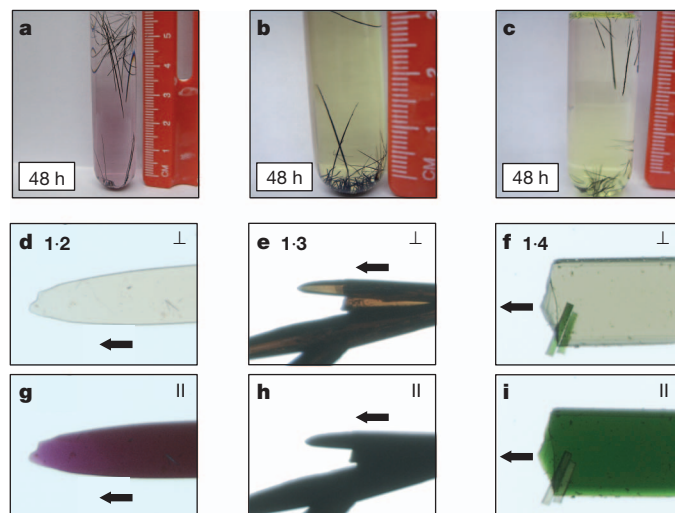


**Figure 3 | Growth and charge-transfer anisotropy of LASO complexes.** **a–c**, Images showing the growth of LASO networks **1:2** (a), **1:3** (b) and **1:4** (c) after 48 h. The long axis corresponds to the charge-transfer axis and the systems are single crystalline. **d–i**, Optical microscopy of very thin ( $<10\text{ }\mu\text{m}$ ) co-crystals with linearly polarized white light. In **d–f**, light is polarized perpendicular to the long axis of the crystals for **1:2**, **1:3** and **1:4**, respectively. In **g–i**, the same structures are shown with the light polarized parallel to the charge-transfer axis, demonstrating the strong absorbance along a single axis on account of the photoexcitation of the donor–acceptor dimer.

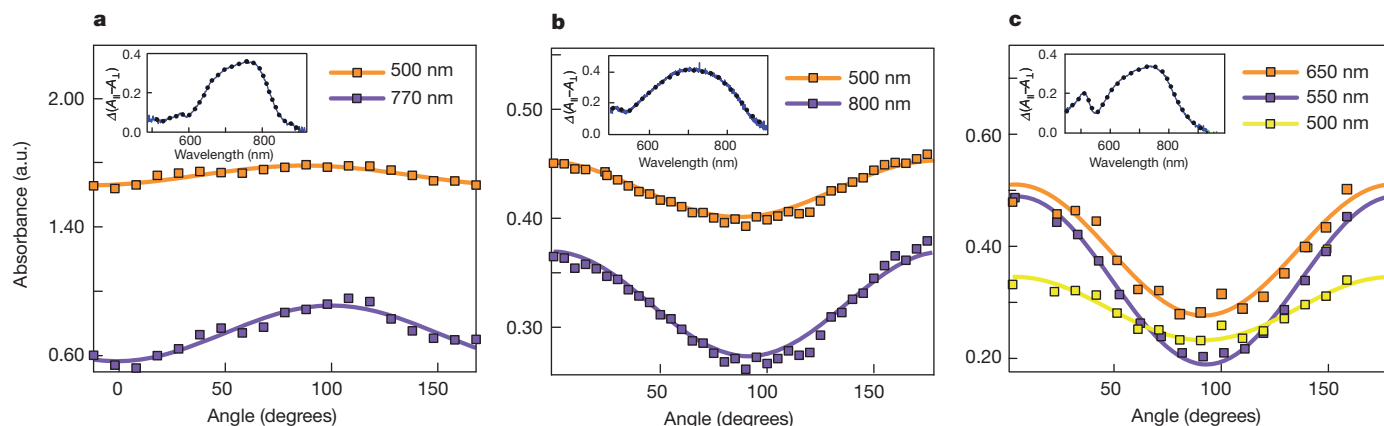


**Figure 4 | Linear dichroism of LASO networks.** a, 1·2; b, 1·3; c, 1·4. When the electric field of linearly polarized light is oriented parallel to the charge-transfer axis, a strong absorbance is produced by the excitation of a donor-acceptor dimer ( $D^{\delta+}A^{\delta-} \rightarrow [D^{\delta+}A^{\delta-}]^*$ ). The difference between the local minima (perpendicular polarizer orientation) and the local maxima (parallel

polarizer orientation) of the absorbance will be largest at the onset of the charge-transfer band. The inset shows, as a function of wavelength, the difference in absorbance,  $\Delta(A_{||} - A_{\perp})$ , as a function of wavelength at parallel and perpendicular polarizations in transmission mode.

between the infrared and Raman modes<sup>5,12,15</sup> exists (Supplementary Information) in all three systems at 300 K, indicating a non-centrosymmetric lattice. This behaviour in mixed-stack crystals, composed of symmetric molecules, demonstrates that LASO networks fulfil the requirements for a ferroelectric system—namely donor-acceptor dimerization and a polar lattice.

Polarized optical microscopy (Fig. 3d–f) and polarized ultraviolet-visible transmission spectroscopy<sup>18</sup> (Fig. 4) were employed to elucidate the anisotropy of the charge-transfer in LASO networks with regard to the crystal axis. When the linear polarization of white light was oriented parallel to the polar mixed stack (long axis), the system absorbed intensely (Fig. 3g–i). Conversely, when the polarization was oriented perpendicular to the stack axis there was a clear lack of colour. The absorbance bands (Fig. 4a–c) associated with this colour change showed a maximum when the polarization was aligned with the direction of the stacks for 1·2, 1·3 and 1·4 (Fig. 4a–c). These transitions (Fig. 4a–c, inset), located in the range 1.38–1.77 eV (700–900 nm), were attributed to the lowest intra-dimer charge-transfer exciton state<sup>19</sup> ( $D^{\delta+}A^{\delta-} \rightarrow [D^{\delta+}A^{\delta-}]^*$ ). On the basis of this pronounced dichroism, it is possible to establish unequivocally that the polar axis of the material is aligned with the long axis of the crystal.

In order to determine the ferroelectric Curie temperature of each structure, the dielectric constant ( $\epsilon_r$ ) along the ferroelectric axis was measured<sup>10</sup> as a function of temperature. For crystals of 1·2, 1·3 and 1·4, no characteristic discontinuity was observed (Fig. 5a–c) between 5 K and 400 K. These results suggest that the ferroelectric phase exists at room temperature, an observation which is consistent

with spectroscopic and crystallographic evidence. Further evidence for room-temperature ferroelectricity was obtained by measuring hysteresis curves of electric displacement versus electric field ( $D$ – $E$ ) along the ferroelectric axis (Fig. 6a, c and f). Polarization hysteresis was observed in complexes 1·2, 1·3 and 1·4 at 300 K with remnant polarizations ( $P_r$ ) exceeding  $1 \mu\text{C cm}^{-2}$ . Attempts to observe saturation by applying higher electric fields resulted in dielectric breakdown and crystal melting. Larger polarization hysteresis loops were obtained at lower temperatures down to 7 K where leakage currents were minimized (Fig. 6b, d, e and g). At low temperature,  $D$ – $E$  curves for complex 1·4 were unexpectedly large. Surprisingly, the  $P_r$  for this network was found to be approximately  $55 \mu\text{C cm}^{-2}$ , that is, much larger than for complexes 1·2 and 1·3. This large polarization could result from the combination of the charge-transfer process and proton dynamics<sup>3,4</sup> within the crystal. The  $P_r$  of 1·4 at 7 K is amongst the highest reported<sup>4,10,20,21</sup> for organic ferroelectrics, and merits further study to elucidate the mechanism causing the polarization. However, the resistivity of all LASO systems investigated was found to be very high ( $>10^9 \Omega \text{ cm}^{-1}$ ) at room temperature (Supplementary Information).

The ferroelectric curves obtained at room temperature were biased at a lower electric field than those obtained at cryogenic temperatures. At high electric fields at room temperature, dielectric leakage and Joule heating prevented the saturation of polarization hysteretic loops. Curves measured at 300 K were obtained by applying a smaller electric field than that required for saturation. As a result, these systems are inherently under-polarized and have smaller remnant polarizations than saturated loops. Even at these lower voltages, leakage

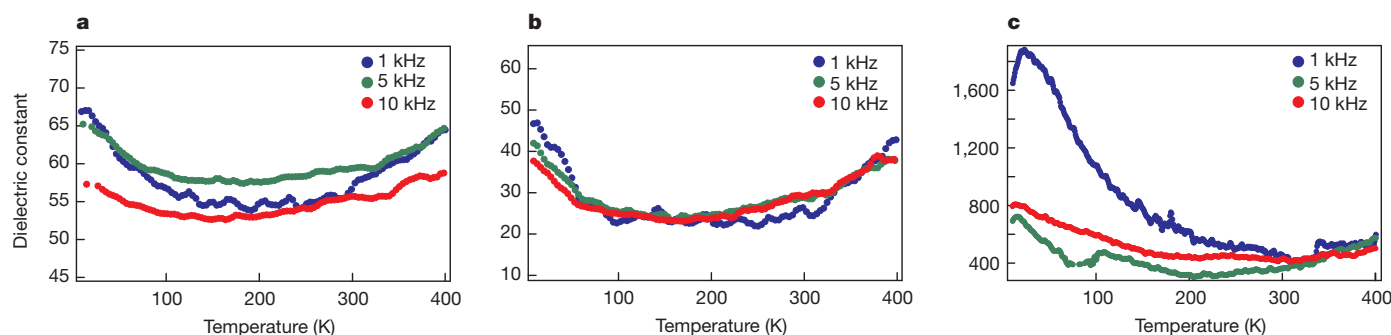


**Figure 5 | Temperature-dependent dielectric constant measurements of LASO networks.** The temperature-dependent dielectric constants were measured for complexes 1·2 (a), 1·3 (b) and 1·4 (c). Between 5 and 400 K, no reproducible characteristic discontinuity was observed in any of the networks.

This observation indicates that the ferroelectric Curie temperatures,  $T_C$ , are likely to be outside the measurement range of the system. The dielectric constants for LASO networks were measured at 10 V with  $f = 1, 5$  or 10 kHz.



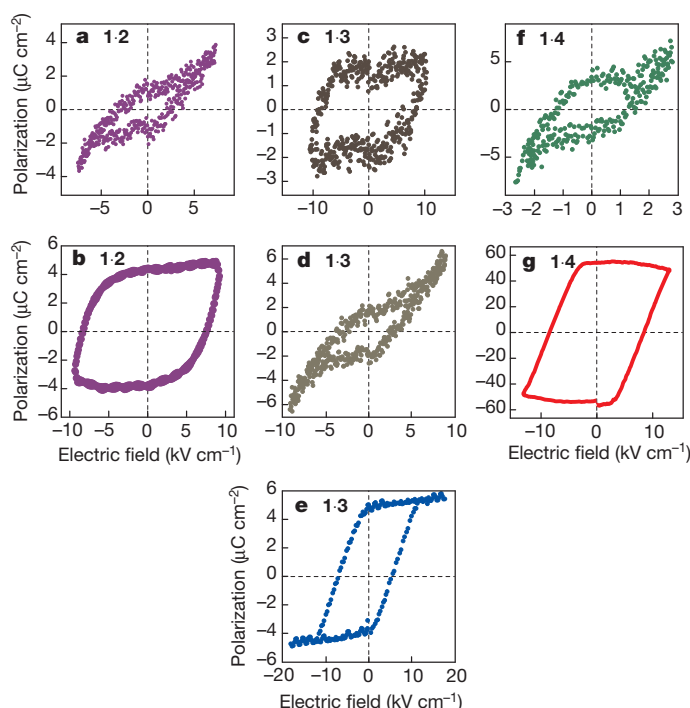


**Figure 6 | Polarization hysteresis in supramolecular networks.** Polarization versus electric field curves for LASO complexes **1·2** (a, b), **1·3** (c–e) and **1·4** (f, g). Polarization hysteresis curves for complex **1·2** were measured at 300 K (a) and 74 K (b), for complex **1·3** at 300 K (c, d) and 7 K (e), and for complex **1·4** at 300 K (f) and 7 K (g). Room-temperature hysteresis curves for LASO complexes are underpolarized because of leakage currents at high voltage. The ferroelectric network **1·3** showed hysteresis similar to that of **1·2** and **1·4** at small electric fields (d), and at higher electric fields revealed larger hysteresis loops (c). Hysteresis curve measurements were performed at  $f = 0.1$  Hz (a–e, g) or  $f = 1$  Hz (f).

current and degradation are possible, thus limiting the performance of devices.

Larger hysteresis loops were obtained (Fig. 6) in complex **1·3** at 300 K because this network is able to withstand higher voltages. It is interesting to note that this hydrogen-bonded network has the highest ionicity ( $\rho \approx 0.89$ ) of all three materials presented here. The only charge-transfer ferroelectrics that demonstrate polarization bistability<sup>9,10</sup> are TTF·QCl<sub>4</sub>, TTF·QBrCl<sub>3</sub> and TTF·QBr<sub>4</sub>; for all three crystals,  $T_C$  occurs at cryogenic temperatures. As pointed out in ref. 22, high ionicities inhibit current flow in charge-transfer crystals because of Coulombic interactions. Negative and positive ions in a lattice can behave as ionic impurities that actively scatter moving electrons. Complexes that have large ionicities may therefore mitigate leakage current to some degree, for example, **1·3** and TTF·QBr<sub>4</sub>. In this context, developing networks of charge-transfer complexes with large ionicities may be a useful design rule to achieve ferroelectricity at room temperature and above.

Ferroelectric complexes **1·2** and **1·4**, when characterized by SQUID magnetometry, revealed magnetic hysteresis loops (Supplementary Information). Extensive elemental analysis described in Supplementary Information showed that any magnetic impurities present are below the present detection limits of inductively coupled plasma atomic emission spectroscopy. Other measurements described in Supplementary Information (magnetic force microscopy) were carried out in an attempt to verify the ferromagnetic behaviour. The small magnitude of the magnetization (Supplementary Fig. 14) in the hysteresis loop precludes us, however, from labelling these systems as ferromagnetic. Nonetheless, the unprecedented room-temperature ferroelectricity in these supramolecular networks and the observation of magnetization make the LASO design relevant to future explorations of multiferroic behaviour in metal-free systems at ambient temperatures.

In summary, we have developed a molecular design that allows donor and acceptor molecules to self-assemble into charge-transfer ferroelectric networks at ambient temperatures. The new structures challenge the long-standing notion that donor–acceptor mixed-stack materials cannot exhibit a ferroelectric  $T_C$  above room temperature. The demonstration of ferroelectric properties in an organic network affords us opportunities to produce these systems in new forms—such as electrically addressable hydrogels, ferroelectric catalysts and charge-transfer-based sensitizers for photovoltaics. The combination of donor–acceptor interactions with hydrogen-bonded networks offers a promising supramolecular platform to design novel organic electronic structures.

## METHODS SUMMARY

**Synthesis.** Compound **1** was obtained (Supplementary Information) in one step by imidization<sup>23</sup> of the anhydride. The compound was purified by recrystallization from tetrahydrofuran and hexanes. Compounds **2** and **3** are commercially available, but were recrystallized from tetrahydrofuran and hexanes before use. The TTF-based donor **4** was synthesized using published procedures<sup>24</sup>. Standard purification was adequate to produce functional and robust ferroelectrics.

**Network crystallization.** The crystals were grown under darkness from a layered solvent system of 1-chlorobutane over 1,2-dichloroethane/diethyl ether (2/1 v/v %) at ambient temperatures. A dry 1:1 donor–acceptor mixture, with an acceptor (**1**) concentration of 2 mg ml<sup>−1</sup> for **1·2**, 1 mg ml<sup>−1</sup> for **1·3** and 0.5 mg ml<sup>−1</sup> for **1·4**, produced crystals that grew to several centimetres in size in ~72 h after the first crystals had become visible (within 10 min). Anhydrous conditions are crucial for the growth of high-quality single crystalline networks. If traces of water are present in the solvent or the starting materials, growth is heavily branched (Supplementary Information) or sometimes even non-existent. Compound purity and concentration are also very important growth parameters. Impurities were found to induce epitaxial branching or even inhibit crystal growth, while concentration affects growth times and structure lengths.

**Electronic measurements.** The ferroelectric structures are mechanically robust and can be handled with vacuum tweezers. Gold wire electrodes (12.5 μm) were attached on either end using gold paint (Ted Pella Gold Paste). The resulting devices were tested for ferroelectricity in a physical properties measurement system (Quantum Design PPMS 6000) under an inert atmosphere. The temperature-dependent dielectric constants of LASO complexes were measured at 10 V with a 1, 5 or 10 kHz frequency. These measurements were performed using an Agilent E4980A LCR meter. Polarization hystereses were measured using a ferroelectric tester at 0.1 or 1 Hz frequency (Radiant Technologies Precision LC with Trek amplifier).

Received 4 June; accepted 11 July 2012.

- Stupp, S. I. *et al.* Supramolecular materials: self-organized nanostructures. *Science* **276**, 384–389 (1997).
- Horiuchi, S., Okimoto, Y., Kumai, R. & Tokura, Y. Quantum phase transition in organic charge-transfer complexes. *Science* **299**, 229–232 (2003).
- Horiuchi, S. & Tokura, Y. Organic ferroelectrics. *Nature Mater.* **7**, 357–366 (2008).
- Horiuchi, S. *et al.* Above-room-temperature ferroelectricity in a single-component molecular crystal. *Nature* **463**, 789–792 (2010).
- Torrance, J. B., Vazquez, J. E., Mayerle, J. J. & Lee, V. Y. Discovery of a neutral-to-ionic phase-transition in organic materials. *Phys. Rev. Lett.* **46**, 253–257 (1981).
- Tokura, Y. *et al.* Domain-wall dynamics in organic charge-transfer compounds with one-dimensional ferroelectricity. *Phys. Rev. Lett.* **63**, 2405–2408 (1989).
- Collet, E. *et al.* Laser-induced ferroelectric structural order in an organic charge-transfer crystal. *Science* **300**, 612–615 (2003).
- Hamilton, D. G., Lynch, D. E., Byriel, K. A. & Kennard, C. H. L. A neutral donor–acceptor  $\pi$ -stack: solid-state structures of 1:1 pyromellitic diimide-dialkoxynaphthalene cocrystals. *Aust. J. Chem.* **50**, 439–445 (1997).
- Kobayashi, K. *et al.* Electronic ferroelectricity in a molecular crystal with large polarization directing antiparallel to ionic displacement. *Phys. Rev. Lett.* **108**, 237601 (2012).
- Kagawa, F. *et al.* Electric-field control of solitons in a ferroelectric organic charge-transfer salt. *Phys. Rev. Lett.* **104**, 227602 (2010).
- Torrance, J. B. *et al.* Anomalous nature of neutral-to-ionic phase-transition in tetrathiafulvalene-chloranil. *Phys. Rev. Lett.* **47**, 1747–1750 (1981).
- Girlando, A., Marzola, F., Pecile, C. & Torrance, J. B. Vibrational spectroscopy of mixed stack organic semiconductors — neutral and ionic phases of tetrathiafulvalene chloranil (TTF-CA) charge-transfer complex. *J. Chem. Phys.* **79**, 1075–1085 (1983).
- Okamoto, H. *et al.* Anomalous dielectric response in tetrathiafulvalene-*para*-chloranil as observed in temperature-induced and pressure-induced neutral-to-ionic phase-transition. *Phys. Rev. B* **43**, 8224–8232 (1991).
- Soos, Z. G. Identification of dimerization phase transitions driven by Peierls and other mechanisms. *Chem. Phys. Lett.* **440**, 87–91 (2007).

15. Girlando, A., Pecile, C. & Torrance, J. B. A key to understanding ionic mixed stacked organic-solids — tetrathiafulvalene-bromanil (TTF-BA). *Solid State Commun.* **54**, 753–759 (1985).
16. McKinnon, J. J., Spackman, M. A. & Mitchell, A. S. Novel tools for visualizing and exploring intermolecular interactions in molecular crystals. *Acta Crystallogr. B* **60**, 627–668 (2004).
17. Crystal Explorer v.2.1 (Univ. Western Australia, Perth, 2007); available at <http://hirshfeldsurface.net/>.
18. Kuwata-Gonokami, M. *et al.* Exciton strings in an organic charge-transfer crystal. *Nature* **367**, 47–48 (1994).
19. Meneghetti, M. & Pecile, C. TTF-TCNE a charge transfer  $\pi$ -molecular crystal with partial ionic ground state: optical properties and electron-molecular vibrations interaction. *J. Chem. Phys.* **105**, 397–407 (1996).
20. Miyajima, D. *et al.* Ferroelectric columnar liquid crystal featuring confined polar groups within core-shell architecture. *Science* **336**, 209–213 (2012).
21. Zhang, Q. M., Bharti, V. & Zhao, X. Giant electrostriction and relaxor ferroelectric behavior in electron-irradiated poly(vinylidene fluoride-trifluoroethylene) copolymer. *Science* **280**, 2101–2104 (1998).
22. Torrance, J. B. The difference between metallic and insulating salts of tetracyanoquinodimethone (TCNQ): how to design an organic metal. *Acc. Chem. Res.* **12**, 79–86 (1979).
23. Brøndsted Nielsen, M., Hansen, J. G. & Becher, J. Self-complexing tetrathiafulvalene-based donor-acceptor macrocycles. *Eur. J. Org. Chem.* **1999**, 2807–2815 (1999).
24. Saha, S. *et al.* A photoactive molecular triad as a nanoscale power supply for a supramolecular machine. *Chem. Eur. J.* **11**, 6846–6858 (2005).

**Supplementary Information** is available in the online version of the paper.

**Acknowledgements** This work was supported by the Non-equilibrium Energy Research Center (NERC) at Northwestern University, funded by the US Department of Energy (DOE), Office of Basic Energy Sciences under award number DE-SC0000989. A.K.S. received support from the Materials Research Science and Engineering Centre (MRSEC) at Northwestern University, funded by the National Science Foundation

(NSF). D.C., A.C.F. and J.F.S. were supported by the WCU program (R-31-2008-000-10055-0) at KAIST in Korea. Use of the Center for Nanoscale Materials was supported by the US Department of Energy, Office of Science, Office of Basic Energy Sciences, under contract no. DE-AC02-06CH11357. D.C. and A.C.F. were supported by NSF Graduate Research Fellowships. A.K.S. and A.C.-H.S. were supported by a fellowship from the NERC. A.S.T. was supported by a fellowship from the Initiative for Sustainability and Energy at Northwestern (ISEN) and NERC. We thank J. B. Ketterson and O. Chernyashevsky (Northwestern University) for discussions and advice, Y. D. Shah (Northwestern University) for assistance with ferroelectricity measurements, A. M. Z. Slawin (University of St Andrews) for initial help with crystallographic data collection and refinement, M. Mara (Northwestern University) for assistance with spectroscopy, Y. Liu (The Molecular Foundry, Lawrence Berkeley National Laboratory) for discussions, and the Integrated Molecular Structure Education and Research Centre (IMSERC) and the Magnet and Low Temperature Facility at Northwestern University for providing access to equipment for the relevant experiments. Molecular crystal images were produced using the UCSF Chimera package from the Resource for Biocomputing, Visualisation and Informatics at the University of California, San Francisco.

**Author Contributions** A.S.T., A.K.S. and A.C.-H.S. conceived and designed the LASO networks. A.K.S., A.C.-H.S., D.C. and S.K.D. synthesized the compounds studied in this work; A.S.T., T.J.K. and W.W. performed device fabrication and testing; A.K.S., J.M.S. and B.R. performed spectroscopic studies. C.L.S. and A.A.S. collected crystallography data, and A.A.S. and A.K.S. performed crystal structure refinement; A.C.F. performed cyclic voltammetry experiments; J.R.G. helped with magnetic force microscopy experiments; H.M. provided testing equipment; J.F.S., S.I.S., L.X.C. and K.L.W. offered intellectual input; A.S.T., A.K.S., A.C.-H.S., J.F. S. and S.I.S. wrote the manuscript.

**Author Information** Reprints and permissions information is available at [www.nature.com/reprints](http://www.nature.com/reprints). The authors declare no competing financial interests. Readers are welcome to comment on the online version of the paper. Correspondence and requests for materials should be addressed to J.F.S. ([stoddart@northwestern.edu](mailto:stoddart@northwestern.edu)) or S.I.S. ([s-stupp@northwestern.edu](mailto:s-stupp@northwestern.edu)).

# Long-term decline of global atmospheric ethane concentrations and implications for methane

Isobel J. Simpson<sup>1</sup>, Mads P. Sulbaek Andersen<sup>1,2</sup>, Simone Meinardi<sup>1</sup>, Lori Bruhwiler<sup>3</sup>, Nicola J. Blake<sup>1</sup>, Detlev Helmig<sup>4</sup>, F. Sherwood Rowland<sup>1</sup> & Donald R. Blake<sup>1</sup>

After methane, ethane is the most abundant hydrocarbon in the remote atmosphere. It is a precursor to tropospheric ozone and it influences the atmosphere's oxidative capacity through its reaction with the hydroxyl radical, ethane's primary atmospheric sink<sup>1–3</sup>. Here we present the longest continuous record of global atmospheric ethane levels. We show that global ethane emission rates decreased from 14.3 to 11.3 teragrams per year, or by 21 per cent, from 1984 to 2010. We attribute this to decreasing fugitive emissions from ethane's fossil fuel source—most probably decreased venting and flaring of natural gas in oil fields—rather than a decline in its other major sources, biofuel use and biomass burning. Ethane's major emission sources are shared with methane, and recent studies have disagreed on whether reduced fossil fuel or microbial emissions have caused methane's atmospheric growth rate to slow<sup>4,5</sup>. Our findings suggest that reduced fugitive fossil fuel emissions account for at least 10–21 teragrams per year (30–70 per cent) of the decrease in methane's global emissions, significantly contributing to methane's slowing atmospheric growth rate since the mid-1980s.

The estimated emissions budget for ethane ( $C_2H_6$ ) is approximately 13 teragrams ( $1\text{ Tg} = 10^{12}\text{ g}$ ) per year. Its primary sources are fossil fuels (mainly evaporative emissions from their production, transmission and processing;  $8.0\text{--}9.2\text{ Tg yr}^{-1}$ ), biomass burning ( $2.4\text{--}2.8\text{ Tg yr}^{-1}$ ) and biofuel use ( $2.6\text{ Tg yr}^{-1}$ ), with minor oceanic and biogenic sources and a possible geological source<sup>3,6–8</sup>. Ethane has a strong interhemispheric gradient because its major sources are primarily located in the Northern Hemisphere and its atmospheric lifetime (about two months) is shorter than the interhemispheric mixing time (about a year) (refs 1, 2). Ethane emissions in the Northern Hemisphere have been estimated to be about  $12\text{ Tg yr}^{-1}$ , of which  $1.7\text{--}2.0\text{ Tg yr}^{-1}$  are transported to the Southern Hemisphere via interhemispheric transport<sup>1,7</sup>. An additional  $1.0\text{ Tg yr}^{-1}$  is released within the Southern Hemisphere, primarily from biomass burning<sup>7</sup>.

Whereas early measurements of atmospheric ethane in Switzerland (1951–1988) recorded an average increase of  $0.8 \pm 0.3\% \text{ yr}^{-1}$ , subsequent field studies (1977–2000) have reported either steady or declining ethane levels in both hemispheres (Supplementary Table 1). The present work covers latitudes from  $71^\circ\text{ N}$  (Barrow, Alaska) to  $47^\circ\text{ S}$  (Slope Point, New Zealand) and represents the world's longest-running global atmospheric ethane monitoring program. The measurements began in 1984 as part of our established network to monitor global concentrations of trace gases including methane, chlorofluorocarbons and other light hydrocarbons<sup>2,9,10</sup>. Each season between 60–80 air samples were collected at 40–45 remote surface locations in the Pacific Basin (Fig. 1). These samples were analysed at our UCI laboratory using gas chromatography and were used to calculate a globally averaged ethane mixing ratio (see Methods Summary). Based on an intercomparison with ethane data from 2006–2010 from the NOAA/INSTAAR global non-methane hydrocarbon monitoring programme, which is not limited to the Pacific basin, we estimate that

our data realistically approximate the average global tropospheric ethane concentration to within 15–20%, which is within the combined uncertainty margin of both records (Supplementary Figs 1–2).

Consistent with its source distribution, ethane mixing ratios are greatest at latitudes north of  $30^\circ\text{ N}$ , then drop precipitously from  $30^\circ\text{ N}$  to the Intertropical Convergence Zone (Fig. 2a). Ethane is fairly well-mixed south of the Intertropical Convergence Zone, with typical variability of less than 30% among the latitudinal bands shown in

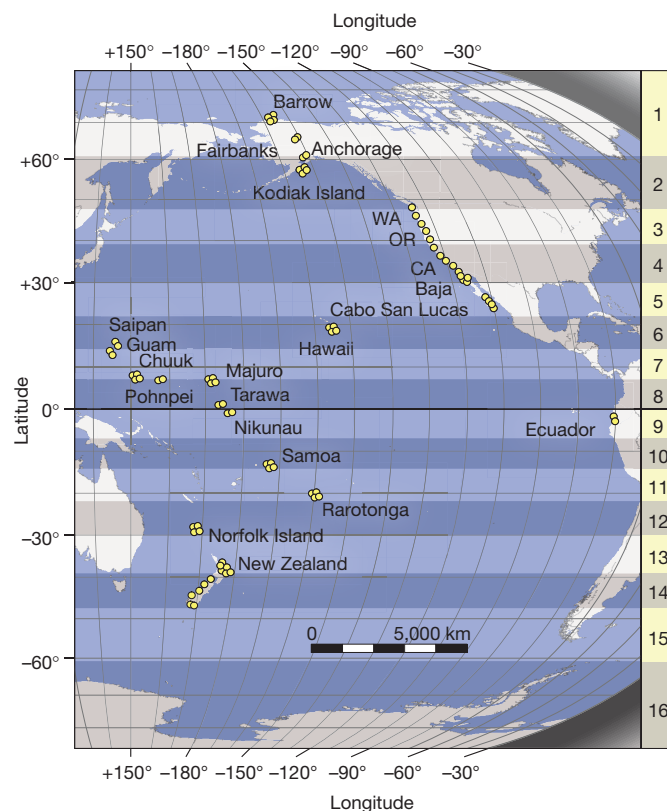


**Figure 1 | Individual air sampling locations for the UCI global trace gas monitoring network.** Each air sample is collected for one minute into a conditioned, evacuated two-litre stainless steel canister, typically at a site (yellow circles) on the coast when the wind is blowing from the ocean. Air samples are usually collected over a 3-week period each season (March, June, September and December), though samples were collected less frequently in 1991 and 1992 (April, August and December) because of political events at the time. We have also collected biweekly air samples on Norfolk Island ( $29^\circ\text{ S}$ ) since June 2001. Boundaries that separate the Earth's surface into 16 latitudinal bands, each with an equal volume of air, are shown on the right (see Supplementary Information). The global representativeness of our Pacific-based measurements, both spatial and temporal, is discussed in the Supplementary Information. WA, Washington; OR, Oregon; CA, California.

<sup>1</sup>Department of Chemistry, University of California—Irvine (UCI), Irvine, California 92697, USA. <sup>2</sup>Jet Propulsion Laboratory, California Institute of Technology, Pasadena, California 91109, USA. <sup>3</sup>NOAA Earth System Research Laboratory (ESRL), 325 Broadway, Boulder, Colorado 80305, USA. <sup>4</sup>Institute of Arctic and Alpine Research (INSTAAR), University of Colorado, Boulder, Colorado 80309, USA.



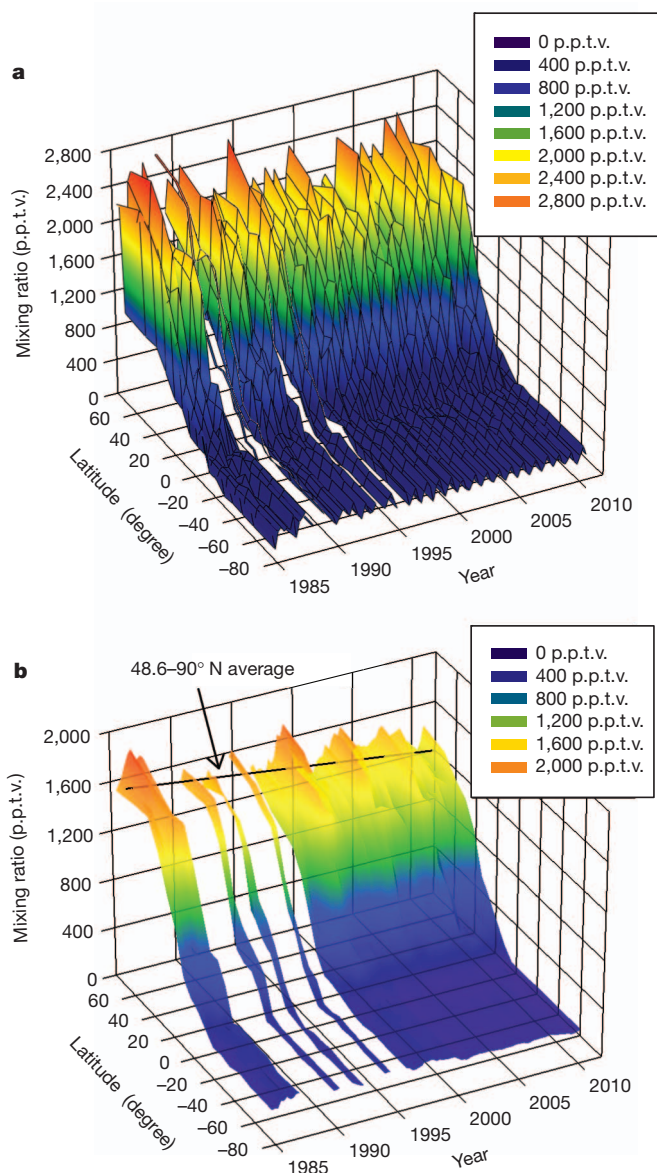


**Figure 2 | Latitudinal distribution of ethane mixing ratios from 1984–2010.** **a**, Seasonal averages for each of the 16 latitudinal bands shown in Fig. 1; and **b**, running annual averages for each latitudinal band. Our 26-year data set, from September 1984 to December 2010, is missing six seasons of ethane data from earlier in our programme (December 1987, June–September 1988, June 1989, September 1993 and June 1995).

Fig. 1. From 1984–2010 the average ethane mixing ratio was  $1,443 \pm 49$  parts per trillion by volume (p.p.t.v.) in the high Northern Hemisphere (defined here as  $30^\circ\text{N}$ – $90^\circ\text{N}$ ), and  $269 \pm 2$  p.p.t.v. for the mid-Southern Hemisphere (defined as  $15^\circ\text{S}$ – $49^\circ\text{S}$ ) (see Supplementary Information for uncertainty calculations). Full hemispheric averages over this period were  $1,049 \pm 99$  p.p.t.v. for the Northern Hemisphere and  $277 \pm 34$  p.p.t.v. for the Southern Hemisphere, with an average ( $\pm 1\sigma$ ) interhemispheric ratio of  $4.1 \pm 0.4$  (see Supplementary Information).

In addition to pronounced latitudinal variations, atmospheric ethane concentrations vary both seasonally and interannually. Ethane shows a late winter maximum and summer minimum in each hemisphere, with a crossover point near the Equator (Fig. 2a). Ethane's fossil fuel source is not believed to have a strong seasonal cycle<sup>3</sup>, so the clear, anticorrelated seasonal signals in each hemisphere are principally attributed to enhanced summertime photochemical sinks. From 1984 to 2010 the average ( $\pm 1\sigma$ ) amplitude of ethane's

seasonal signal was much larger in the high Northern Hemisphere ( $800 \pm 59$  p.p.t.v.) than in the mid-Southern Hemisphere ( $35 \pm 11$  p.p.t.v.), which is again consistent with ethane's source distribution. The northern seasonal signal also shows significant interannual variability, with several large positive short-term anomalies of up to 30% that typically occur every 3–5 years (Fig. 2a) and have been linked to fluctuations in biomass burning emissions<sup>10</sup>.

Atmospheric ethane mixing ratios have declined significantly since 1984, with the strongest decrease at high northern latitudes (Fig. 2b). From a linear fit to running annual averages from 1984 to 2010, we conclude that ethane declined by an average of  $-12.4 \pm 1.3$  p.p.t.v.  $\text{yr}^{-1}$  in the high Northern Hemisphere,  $-8.0 \pm 1.0$  p.p.t.v.  $\text{yr}^{-1}$  in the tropical Northern Hemisphere, defined as  $0^\circ$ – $30^\circ\text{N}$ , and  $-3.0 \pm 0.3$  p.p.t.v.  $\text{yr}^{-1}$  in the mid-Southern Hemisphere (uncertainties are the standard error of the slope). Globally, ethane has decreased by an average of  $-6.8 \pm 0.6$  p.p.t.v.  $\text{yr}^{-1}$ , from  $791 \pm 19$  p.p.t.v. in 1986 to  $625 \pm 12$  p.p.t.v. in 2010, making a total decline of 165 p.p.t.v. (approximately 21%). The global decline was stronger from 1984 to 1999 ( $-7.2 \pm 1.7$  p.p.t.v.  $\text{yr}^{-1}$ ) than from 2000 to 2010 ( $-1.9 \pm 1.3$  p.p.t.v.  $\text{yr}^{-1}$ ). Firm air measurements suggest that the global ethane concentration peaked in the 1960s and 1970s (ref. 4), before global observational networks were established, which is consistent with results from single-site field studies (see Supplementary Information).

The translation of ethane's global mixing ratio (in units of p.p.t.v.) into the annual emission rates needed to sustain it (in units of  $\text{Tg yr}^{-1}$ ) requires knowledge of the spatial distribution and atmospheric removal rates of ethane. For example, using a comprehensive suite of ground-based and aircraft measurements, ref. 1 converted a global ethane burden of 860 p.p.t.v. to an emission rate of  $15.5 \text{ Tg yr}^{-1}$ . These 'top-down' global ethane emission estimates lie in the range  $10.4$ – $17.6 \text{ Tg yr}^{-1}$  (ref. 7 and references therein), and agree with recent 'bottom-up' (inventory-based) estimates of  $12.5$ – $13.0 \text{ Tg yr}^{-1}$  (refs 3,7). Using the top-down method as ref. 1, we calculate that ethane's annual global emission was  $14.3 \pm 0.3 \text{ Tg yr}^{-1}$  in 1986, declining to  $11.3 \pm 0.2 \text{ Tg yr}^{-1}$  in 2010, for an overall decrease of  $3.0 \pm 0.4 \text{ Tg yr}^{-1}$ . The good agreement between our top-down emission rates and the recent bottom-up estimates suggests that the ethane budget is well balanced. Therefore, major additional sources are unlikely, making it improbable that ethane has a large geological source. However, confirmation of this would require detailed analysis of the ethane budget, which is beyond the scope of this work.

To investigate the dominant processes that control the abundance of ethane in each hemisphere, simulations were run using the TM5 atmospheric tracer transport model (see Methods Summary) together with ethane data collected from 2000 to 2010 at selected sites, namely Barrow ( $71^\circ\text{N}$ ), Majuro ( $7^\circ\text{N}$ ) and Norfolk Island ( $29^\circ\text{S}$ ). The model reproduced the observational data well at Barrow and Norfolk Island (Fig. 3). Poorer agreement was found in Majuro, probably because it lies near the transitional zone between the two hemispheres (Supplementary Fig. 3). Anthropogenic sources (that is, fossil fuel sources) were the main driver of the ethane signal in Barrow, with a smaller biomass burning component that peaks during summer (Fig. 3a). The observations and model both showed maximum concentrations in air arriving at Norfolk Island during September and October (Fig. 3b), consistent with a predominant biomass burning signal in the Southern Hemisphere<sup>11</sup>.

The model simulations discussed above inform our investigation of the causes of ethane's decline over the past 25 years. It is unlikely that changes in global levels of the hydroxyl radical (OH) were responsible for ethane's long-term global decline, because global OH levels have shown little interannual variability since the late 1990s and are generally well buffered against changes on interannual timescales<sup>12</sup>. Instead, because anthropogenic emissions dominate the ethane budget in the high Northern Hemisphere, where the strongest ethane decline has occurred, we attribute ethane's decline primarily to reduced emissions from the fossil fuel sector, specifically fugitive emissions of

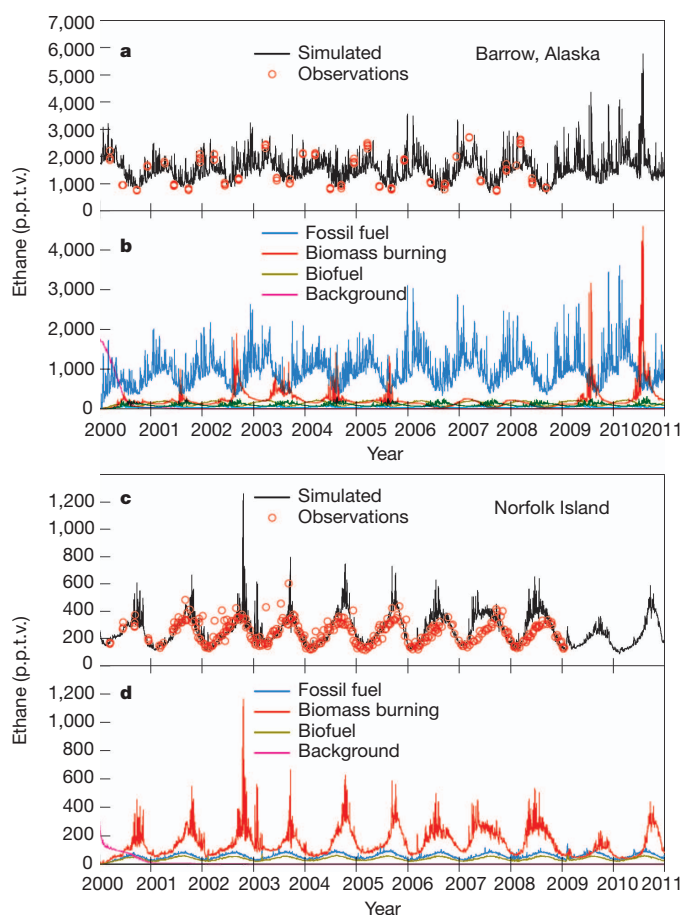


**Figure 3 | Simulated and observed ethane mixing ratios from 2000 to 2010.** **a, b,** Barrow, Alaska ( $71^{\circ}$  N,  $157^{\circ}$  W). **c, d,** Norfolk Island ( $29^{\circ}$  S,  $168^{\circ}$  E). The Barrow observations were made seasonally, and the Norfolk Island observations were made seasonally until June 2001 and bi-weekly thereafter. Even though the TM5 model is capable of much higher spatial resolution (that is,  $1^{\circ} \times 1^{\circ}$ ), for this work the model used nested grids at a lower resolution ( $6^{\circ} \times 4^{\circ}$ ) that is more appropriate to our observational network, which represents well-mixed background air. Ethane simulations (summed sources) are shown as a black line, ethane observations as red circles, fossil fuel simulations as a blue line, biomass burning simulations as a red line, biofuel simulations as a green line, and background simulations as a pink line.

natural gas, which is ethane's main fossil fuel source. Fugitive emissions include venting and flaring, evaporative losses, and equipment leaks and failures, but exclude the combustion of fuels. Natural gas associated with oil fields, also known as associated gas, is commonly vented or flared when it cannot be used directly or transported away<sup>13,14</sup>. Although no reliable global data are available, most natural gas venting occurs at upstream production facilities<sup>14</sup>. Flaring is estimated to have peaked in the 1970s, after which high energy prices encouraged the use of more natural gas as a fuel<sup>15</sup>, and global gas flaring has remained fairly constant since the mid-1990s (ref. 13). Although increased use of catalytic converters on internal combustion engines has effectively reduced the emissions of many hydrocarbons, it does not appear to have similarly affected ethane levels (see Supplementary Information).

Quantifying and understanding ethane's long-term global decline provides valuable constraints on how we understand the long-term slowdown in the global growth rate of atmospheric methane<sup>10,16</sup>, an important greenhouse gas and tropospheric ozone ( $O_3$ ) precursor. Following strong growth of  $1.0\text{--}1.2\text{ yr}^{-1}$  in the early and mid-1980s, the methane growth rate slowed to  $0.40 \pm 0.31\text{ yr}^{-1}$  in the 1990s and to  $0.11 \pm 0.15\text{ yr}^{-1}$  in the 2000s, with strong interannual

variability<sup>10</sup>. Because methane has a relatively long atmospheric lifetime (about nine years), its atmospheric concentrations respond more slowly to changes in emissions than is the case for ethane. Consequently, methane's atmospheric growth rate is a more sensitive indicator of fluctuations in methane's emissions. Although a change in methane emission rate is strongly connected to a change in growth rate, we note that the two are not equivalent.

A graph of atmospheric ethane mixing ratio versus methane growth rate reveals a remarkably strong correlation between the two gases over the past 25 years (Fig. 4) and indicates that there has been a long-term change in a source common to both compounds. The above discussion suggests that this common source is fugitive emissions from the oil and natural gas industries. Because methane and ethane are emitted from fossil fuel sources with characteristic emission ratios<sup>7,17,18</sup>, our long-term ethane record can be used to quantitatively investigate methane's slowing growth rate. We note that this analysis does not exclude the possibility that changes in other sources have also contributed to methane's long-term growth rate decline.

Using ethane measurements in firm air, ref. 4 estimated a  $5\text{--}6\text{ Tg yr}^{-1}$  decline in global fossil fuel ethane emissions from 1980 to 2000. Combining this with mass-based methane-to-ethane emission ratios (MERs) of 3–5, these authors calculated a corresponding  $15\text{--}30\text{ Tg yr}^{-1}$  drop in fossil fuel methane emissions, and concluded that the slowdown in global atmospheric methane growth was probably caused by decreasing fossil fuel emissions<sup>4</sup>, in general agreement with a previous inversion analysis<sup>19</sup>. In contrast, using an independent approach based on methane isotope analysis, ref. 5 attributed the methane slowdown in the late twentieth century to decreases in Northern Hemisphere microbial sources. A new analysis of global methane isotope data from 1988 to 2005 could not confirm the conclusion of ref. 5 that northern microbial sources have declined significantly in recent decades<sup>20</sup>. However, this new study also implies that fossil fuel emissions of methane may have remained mostly constant<sup>20</sup>. These multiple conflicting results are unexpected, and we use the global ethane data presented above to address these unresolved scientific questions.

First, because the measurements of ref. 4 were from polar latitudes only, it was not possible for them to rule out whether a large shift in fossil fuel emissions, towards lower latitudes in the Northern Hemisphere, contributed to their observed long-term ethane decline.

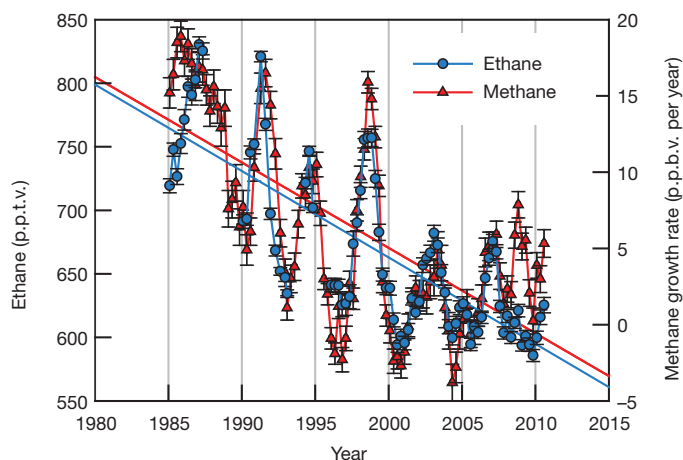


**Figure 4 | Running global averages of ethane mixing ratios and methane growth rate.** The methane measurements, which were co-sampled with ethane, are also from the UCI global monitoring network and are described in ref. 10. Solid lines are linear fits to the ethane (blue circles) and methane (red triangles) data using a least-squares regression. Each global average is based on 55–75 individual mixing ratios. The averaging procedure and uncertainty calculations are described in the Supplementary Information.



Our global data suggests that this was not the case. Although the decline in ethane emissions has been greatest at high northern latitudes ( $1.4 \pm 0.2 \text{ Tg yr}^{-1}$  for the high Northern Hemisphere), a similar trend has occurred at all latitudes within the Northern Hemisphere ( $0.9 \pm 0.1 \text{ Tg yr}^{-1}$  for the tropical Northern Hemisphere) and there is no evidence to suggest that ethane emissions have shifted to lower latitudes in the Northern Hemisphere. This supports the extrapolation by ref. 4 of polar firn air measurements to global trends.

Second, if we attribute our calculated  $3.0 \pm 0.4 \text{ Tg yr}^{-1}$  decline in global ethane emissions from 1984 to 2010 solely to a decline in ethane's fossil fuel source, we can estimate the concurrent decline in methane emissions from fossil fuel. However, this approach assumes that ethane's other two major sources—biomass burning and biofuel use—have remained constant during the past three decades. In fact, global emissions of ethane from biomass burning (wildland fires) are estimated to have increased by  $0.52 \text{ Tg yr}^{-1}$  from the 1980s to the 1990s (ref. 21), and then to have stayed fairly constant from 1997–2010 (refs 22,23) with the exception of anomalously large biomass burning years such as 1997–1998 (refs 10,22). Therefore we estimate that ethane emissions from biomass burning have increased by approximately  $0.26 \text{ Tg yr}^{-1}$  since 1985. Global biofuel use also increased by 14% from 1985 to 2000 (ref. 24), which corresponds to a  $0.36 \text{ Tg yr}^{-1}$  increase in ethane's biofuel source, assuming that biofuel emissions of ethane increase in parallel with global biofuel use. If we extrapolate the upward trend in global biofuel use to include 2000–2010, biofuel emissions of ethane increase another 9% ( $0.23 \text{ Tg yr}^{-1}$ ) for a combined increase of  $0.59 \text{ Tg yr}^{-1}$  from 1985 to 2010.

In total, we estimate that ethane emissions from biomass burning and biofuel have increased by approximately  $0.85 \text{ Tg yr}^{-1}$  since 1985. Although the uncertainty associated with the estimated biomass and biofuel increases is unclear, and the uncertainty in our calculations increases as we transition from our global measurements to emission rate changes, applying this offset to our estimate of  $3.0 \pm 0.4 \text{ Tg yr}^{-1}$  suggests a likely range of  $3.4\text{--}4.2 \text{ Tg yr}^{-1}$  for the decline in the fossil fuel component of ethane emissions since the mid-1980s.

Applying the same range of MER values as ref. 4 (that is, 3–5), we calculate that global fossil fuel emissions of methane declined by  $10\text{--}21 \text{ Tg yr}^{-1}$  from 1984 to 2010. However, the MERs employed by ref. 4 were based on emission ratios measured near oil storage and processing facilities, and they lie at the lower end of MER values representing the fossil fuel industry as a whole<sup>17,18,25</sup>. For example, the MER of natural gas varies considerably depending on the type of deposit, with mass-based values of the order of 3 for gas associated with oil fields, 6 for gas condensate (or 'wet' gas), and 10 or more for 'dry' gas fields, although there is substantial overlap among the categories<sup>17,18</sup>. Further, the MER for coalbed gas can exceed 5,000 in certain basins<sup>25</sup>. Because the MER of associated gas (that is, approximately 3) is on the lower end of the mass-based MER scale, our above estimate of  $10\text{--}21 \text{ Tg yr}^{-1}$  should be a fairly accurate assessment of the component of methane's decline associated with fossil fuel use. However, if more methane-enriched fossil fuel sources also contributed to the decline in methane emissions, then  $10\text{--}21 \text{ Tg yr}^{-1}$  may be an underestimate.

Our estimates of global ethane concentrations and emissions indicate a significant decrease in fugitive fossil fuel methane emissions of at least  $10\text{--}21 \text{ Tg yr}^{-1}$ , or more than 30%–70% of the total decline in global methane emissions from 1984–2010 (approximately  $30 \text{ Tg yr}^{-1}$ ; ref. 5). That is, our results are incompatible with a roughly constant fossil fuel source of methane since the 1980s, as put forward in a recent scenario<sup>20</sup>. Further, we have demonstrated the utility of long-term co-measurement of ethane and methane, and we encourage close scrutiny of ethane levels and corresponding methane growth rates in the future. For example, signals such as a significant upturn in methane growth, without a corresponding increase in global ethane levels, may indicate releases of methane from methane-rich sources such as wetlands or melting permafrost.

## METHODS SUMMARY

**Air sampling and analysis.** Ethane measurements were made using our established technique of whole-air sampling followed by analysis using gas chromatography with flame ionization detection<sup>2,9,10</sup>. The samples were analysed at our UCI laboratory within one month of collection. Rigorous tests have shown that light alkanes are stable in the canisters over this period. The measurements for each trace gas use an internally consistent, internationally recognized calibration scale and detailed quality control procedures. The precision of the ethane measurements is 1%, the accuracy 5%, and the detection limit 3 p.p.t.v. Ethane mixing ratios that appear contaminated by local sources are removed from the data set (typically 2–6 per season), and the remaining data are used to construct a seasonal global ethane average using an equal surface area weighting method (see Supplementary Information). Running annual global averages are in turn calculated from these seasonal means. The measurements are archived at <http://cdiac.ornl.gov/tracegases.html>.

**Atmospheric modelling.** Ethane simulations were run using the TM5 model of atmospheric tracer transport<sup>26</sup>. Assimilated meteorology data from the European Centre for Medium Range Weather Forecasting were used to calculate the atmospheric transport. A repeating seasonal cycle of OH (ref. 27) and the Jet Propulsion Laboratory kinetics data evaluation for the photochemical destruction of ethane (ref. 28) were used to calculate the reaction rate between ethane and OH. Anthropogenic ethane sources were estimated using the Emission Database for Global Atmospheric Research data set for methane, release version 4.0 (<http://edgar.jrc.ec.europa.eu>, 2009) together with the appropriate methane-to-ethane emission ratios<sup>7</sup>. Ethane emissions from biomass burning were estimated from the Global Fire Emissions Database version 2 and published emission ratios<sup>29</sup>. Biofuel emissions were retrieved from ref. 30. The relatively small ethane emissions from biogenic sources and the ocean were not included because of concern about their uncertainty.

Received 2 February; accepted 19 June 2012.

- Rudolph, J. The tropospheric distribution and budget of ethane. *J. Geophys. Res.* **100** (D6), 11369–11381 (1995).
- Gupta, M. L., Cicerone, R. J., Blake, D. R., Rowland, F. S. & Isaksen, I. S. A. Global atmospheric distributions and source strengths of light hydrocarbons and tetrachloroethene. *J. Geophys. Res.* **103** (D28), 28219–28235 (1998).
- Pozzer, A. et al. Observed and simulated global distribution and budget of atmospheric C<sub>2</sub>–C<sub>5</sub> alkanes. *Atmos. Chem. Phys.* **10**, 4403–4422 (2010).
- Aydin, M. et al. Recent decreases in fossil-fuel emissions of ethane and methane derived from firn air. *Nature* **476**, 198–201 (2011).
- Kai, F. M., Tyler, S. C., Randerson, J. T. & Blake, D. R. Reduced methane growth rate explained by decreased Northern Hemisphere microbial sources. *Nature* **476**, 194–197 (2011).
- Stein, O. & Rudolph, J. Modeling and interpretation of stable carbon isotope ratios of ethane in global chemical transport models. *J. Geophys. Res.* **112**, D14308 (2007).
- Xiao, Y. et al. Global budget of ethane and regional constraints on U.S. sources. *J. Geophys. Res.* **113**, D21306 (2008).
- Etioppe, G. & Ciccioli, P. Earth's degassing: a missing ethane and propane source. *Science* **323**, 478 (2009).
- Blake, D. R. & Rowland, F. S. Global atmospheric concentrations and source strengths of ethane. *Nature* **321**, 231–233 (1986).
- Simpson, I. J., Rowland, F. S., Meinardi, S. & Blake, D. R. Influence of biomass burning during recent fluctuations in the slow growth of global tropospheric methane. *Geophys. Res. Lett.* **33**, L22808 (2006).
- Rinsland, C. P. et al. Multiyear infrared solar spectroscopic measurements of HCN, CO, C<sub>2</sub>H<sub>6</sub>, and C<sub>2</sub>H<sub>2</sub> tropospheric columns above Lauder, New Zealand (45°S latitude). *J. Geophys. Res.* **107** (D14), 4185 (2002).
- Montzka, S. A. et al. Small interannual variability of global atmospheric hydroxyl. *Science* **331**, 67–69 (2011).
- Elvidge, C. D. et al. A fifteen year record of global natural gas flaring derived from satellite data. *Energies* **2**, 595–622 (2009).
- Johnson, M. R. & Coderre, A. R. An analysis of flaring and venting activity in the Alberta upstream oil and gas industry. *J. Air Waste Manage. Assoc.* **61**, 190–200 (2011).
- Stern, D. I. & Kaufmann, R. K. Estimates of global anthropogenic methane emissions 1860–1993. *Chemosphere* **33**, 159–176 (1996).
- Blugokenky, E. J. et al. Atmospheric methane levels off: temporary pause or a new steady-state? *Geophys. Res. Lett.* **30**, 1992 (2003).
- Katzenstein, A. S., Doeze, L. A., Simpson, I. J., Blake, D. R. & Rowland, F. S. Extensive regional atmospheric hydrocarbon pollution in the southwestern United States. *Proc. Natl Acad. Sci. USA* **100**, 11975–11979 (2003).
- Jones, V. T., Matthews, M. D. & Richers, D. M. Light hydrocarbons for petroleum and gas prospecting. In *Geochemical Remote Sensing of the Sub-Surface Vol. 7 Handbook of Exploration Geochemistry* (eds Govett, G. J. S. & Hale, M.) 133–211 (Elsevier, 2000).
- Bousquet, P. et al. Contribution of anthropogenic and natural sources to atmospheric methane variability. *Nature* **443**, 439–443 (2006).
- Levin, I. et al. No inter-hemispheric  $\delta^{13}\text{C}_{\text{CH}_4}$  trend observed. *Nature* **486**, E3–E4 (2012).



21. Schultz, M. G. *et al.* Global wildland fire emissions from 1960 to 2000. *Glob. Biogeochem. Cycles* **22**, GB2002 (2008).
22. van der Werf, G. R. *et al.* Global fire emissions and the contribution of deforestation, savanna, forest, agricultural, and peat fires (1997–2009). *Atmos. Chem. Phys.* **10**, 11707–11735 (2010).
23. Wiedinmyer, C. *et al.* The Fire INventory from NCAR (FINN): a high resolution global model to estimate the emissions from open burning. *Geosci. Model Dev.* **4**, 625–641 (2011).
24. Fernandes, S. D., Trautmann, N. M., Streets, D. G., Roden, C. A. & Bond, T. C. Global biofuel use, 1850–2000. *Glob. Biogeochem. Cycles* **21**, GB2019 (2007).
25. Strapoć, D., Mastalerz, M., Eble, C. & Schimmelmann, A. Characterization of the origin of coalbed gases in southeastern Illinois Basin by compound-specific carbon and hydrogen stable isotope ratios. *Org. Geochem.* **38**, 267–287 (2007).
26. Krol, M. C. *et al.* The two-way nested global chemistry-transport zoom model TM5: algorithm and applications. *Atmos. Chem. Phys.* **5**, 417–432 (2005).
27. Spivakovsky, C. M. *et al.* Three dimensional climatological distribution of tropospheric OH: update and evaluation. *J. Geophys. Res.* **105** (D7), 8931–8980 (2000).
28. Sander, S. P. *et al.* Chemical kinetics and photochemical data for use in atmospheric studies. Evaluation No. 17, JPL Publication No. 10–6, <http://jpldataeval.jpl.nasa.gov> (Jet Propulsion Laboratory, 2011).
29. Andreae, M. O. & Merlet, P. Emission of trace gases and aerosols from biomass burning. *Glob. Biogeochem. Cycles* **15**, 955–966 (2001).
30. Yevich, R. & Logan, J. A. An assessment of biofuel use and burning of agricultural waste in the developing world. *Glob. Biogeochem. Cycles* **17**, 1095 (2003).

**Supplementary Information** is linked to the online version of the paper at [www.nature.com/nature](http://www.nature.com/nature).

**Acknowledgements** This research was funded by NASA (grant NAG5-8935), with contributions from the Gary Comer Abrupt Climate Change Fellowship. We acknowledge discussions with many colleagues, especially M. Aydin and C. Wiedinmyer. We thank colleagues at the Norfolk Island Bureau of Meteorology and the NOAA research stations in Samoa and Barrow for sample collection; the UCI team for sample collection and analysis, especially B. Chisholm, R. Day, G. Liu, B. Love and M. McEachern; and K. Masarie for work with the NOAA/INSTAAR data. M.P.S.A. is supported at JPL by an appointment to the NASA Postdoctoral Program, administered by Oak Ridge Associated Universities through a contract with NASA.

**Author Contributions** I.J.S. was responsible for data quality assurance, global averaging and emission calculations and manuscript preparation. M.P.S.A. prepared the figures and improved the manuscript. S.M. was responsible for sample analysis and calibration, and data quality assurance. L.B. did the ethane modelling. N.J.B. improved the manuscript. D.H. made the NOAA/INSTAAR measurements and improved the manuscript. F.S.R. was responsible for study design and data quality assurance. D.R.B. was responsible for study design and data quality assurance, and improved the manuscript.

**Author Information** Reprints and permissions information is available at [www.nature.com/reprints](http://www.nature.com/reprints). The authors declare no competing financial interests. Readers are welcome to comment on the online version of this article at [www.nature.com/nature](http://www.nature.com/nature). Correspondence and requests for materials should be addressed to I.J.S. ([isimpson@uci.edu](mailto:isimpson@uci.edu)).

# Contrasting patterns of early twenty-first-century glacier mass change in the Himalayas

Andreas Kääb<sup>1</sup>, Etienne Berthier<sup>2</sup>, Christopher Nuth<sup>1</sup>, Julie Gardelle<sup>3</sup> & Yves Arnaud<sup>4</sup>

Glaciers are among the best indicators of terrestrial climate variability, contribute importantly to water resources in many mountainous regions<sup>1,2</sup> and are a major contributor to global sea level rise<sup>3,4</sup>. In the Hindu Kush–Karakoram–Himalaya region (HKKH), a paucity of appropriate glacier data has prevented a comprehensive assessment of current regional mass balance<sup>5</sup>. There is, however, indirect evidence of a complex pattern of glacial responses<sup>5–8</sup> in reaction to heterogeneous climate change signals<sup>9</sup>. Here we use satellite laser altimetry and a global elevation model to show widespread glacier wastage in the eastern, central and south-western parts of the HKKH during 2003–08. Maximal regional thinning rates were  $0.66 \pm 0.09$  metres per year in the Jammu–Kashmir region. Conversely, in the Karakoram, glaciers thinned only slightly by a few centimetres per year. Contrary to expectations, regionally averaged thinning rates under debris-mantled ice were similar to those of clean ice despite insulation by debris covers. The 2003–08 specific mass balance for our entire HKKH study region was  $-0.21 \pm 0.05 \text{ m yr}^{-1}$  water equivalent, significantly less negative than the estimated global average for glaciers and ice caps<sup>4,10</sup>. This difference is mainly an effect of the balanced glacier mass budget in the Karakoram. The HKKH sea level contribution amounts to one per cent of the present-day sea level rise<sup>11</sup>. Our 2003–08 mass budget of  $-12.8 \pm 3.5$  gigatonnes (Gt) per year is more negative than recent satellite-gravimetry-based estimates of  $-5 \pm 3 \text{ Gt yr}^{-1}$  over 2003–10 (ref. 12). For the mountain catchments of the Indus and Ganges basins<sup>13</sup>, the glacier imbalance contributed about 3.5% and about 2.0%, respectively, to the annual average river discharge<sup>13</sup>, and up to 10% for the Upper Indus basin<sup>14</sup>.

The HKKH is an ensemble of mountain ranges stretching east to west over 2,000 km, containing around 60,000 km<sup>2</sup> of glaciers, glacierets and perennial surface ice in varying climatic regimes. In the east, glaciers receive most accumulation during summer from the Indian monsoon, whereas in the west they accumulate snow mostly in winter through westerly atmospheric circulations<sup>9,13,15</sup>. In addition, a strong northward decrease in precipitation is caused by the extreme topography. Therefore, variability in observed glacier changes within the region is large<sup>5–8,16–19</sup>, and quantifying the current glacier mass change and its impacts on sea-level rise, water resources and natural hazards is hampered by a lack of sufficiently distributed and accurate data. The annual glacier mass balances of a few small and mainly debris-free glaciers<sup>18,20</sup> are unlikely to be representative of the entire region.

In this study, we provide glacier thickness changes and estimated mass changes over the HKKH, specifically the Indus and Ganges river basins and their surroundings (Fig. 1). This is achieved by combining two elevation data sets, the sparse laser measurements from the Ice, Cloud and land Elevation Satellite (ICESat) over 2003–09 and the Digital Elevation Model (DEM) from the Shuttle Radar Topography Mission (SRTM) of February 2000. Standard ICESat analysis<sup>21</sup> is not applicable in the HKKH owing to large cross-track separation and topographic roughness between repeat tracks. Unknown and spatially

variable penetration of the SRTM 5.6-cm radar waves (C-band) into snow and ice<sup>22,23</sup> also complicates the direct extraction of glacier thickness changes from the differences between the SRTM and ICESat elevations.

However, the SRTM DEM ensures that the repeat ICESat analysis samples consistent slopes and similar hypsometry over time so that temporal trends in elevation difference can be estimated through the entire ICESat acquisition series (Figs 1 and 2). The SRTM DEM is subtracted from all ICESat footprint elevations. The digital numbers of multispectral Landsat images of around the year 2000, selected with minimum snow cover, are extracted for each footprint for initial classification into five categories (glacier clean ice, glacier debris cover, glacier firn and snow, open water and off-glacier) and then manually edited. The last ICESat campaign (2F) before sensor failure, and the June campaigns (2C, 3C, 3F) are excluded (Methods, Supplementary Information).

On glaciers, elevation difference trends derived over  $2^\circ \times 2^\circ$ -sized geographic cells depict pronounced regional variations (Fig. 1) and suggest, together with climatological and glaciological patterns, five major sub-regions for further analysis: the Hindu-Kush south of the Wakhan Corridor (HK), the Karakoram (KK), Jammu–Kashmir (JK), Himachal Pradesh, Uttarakhand and West Nepal (HP), and East Nepal and Bhutan (NB). On the basis of the autumn ICESat data only (2003–08), HKKH glaciers thinned on average,  $-0.26 \pm 0.06 \text{ m yr}^{-1}$ , and in all subregions with significant spatial differences (Figs 1 and 2; Table 1). (Error levels correspond to one standard error; Supplementary Information). Thickening is found only in the northern and eastern parts of KK (northeast of the Indus basin:  $+0.14 \pm 0.06 \text{ m yr}^{-1}$ ). Disregarding ice/firn/snow footprints that cannot clearly be assigned to a glacier has no significant effect on the trends in HK, KK and JK but leads to 25% and 50% more-negative trends in HP and NB, respectively (Supplementary Information).

Comparing the autumn glacier trends, which represent annual glacier mass balances, to trends from winter ICESat data (Supplementary Information) suggests an increasing mass turnover in KK and JK. The similarity between autumn and winter trends in HP and NB is consistent with glaciers in the east being of the summer-accumulation type<sup>15</sup>. For off-glacier terrain, secular trends are statistically indistinguishable from zero (Table 1). Off-glacier seasonal cycles are minimal (largest for HK) yet roughly congruent with glacier seasonality (Fig. 2).

C-band SRTM elevations are influenced by the varying penetration of the radar wave into ice, firn and snow<sup>22,23</sup>. Consequently, extrapolation of ICESat-derived glacier elevation trends (Fig. 2) back to the SRTM acquisition date of February 2000 reveals first-order C-band penetration estimates of several metres, largest for firn/snow and smallest for debris-covered ice, and largest for KK and smallest for HP and NB (Supplementary Table 2).

For the entire HKKH, our elevation trends on clean and debris-covered ice show no significant difference (Table 1). To avoid bias related to differences in the geographic and topographic distributions between clean and debris-covered ice, this comparison is based upon

<sup>1</sup>Department of Geosciences, University of Oslo, PO Box 1047, Blindern, 0316 Oslo, Norway. <sup>2</sup>CNRS, Université de Toulouse, LEGOS, 14 avenue Ed. Belin, Toulouse 31400, France. <sup>3</sup>CNRS- Université Grenoble 1, LGGE, 54 rue Molière, BP 96, 38402 Saint Martin d'Hères Cedex, France. <sup>4</sup>IRD- Université Grenoble 1, LTHE/LGGE, 54 rue Molière, BP 96, 38402 Saint Martin d'Hères Cedex, France.

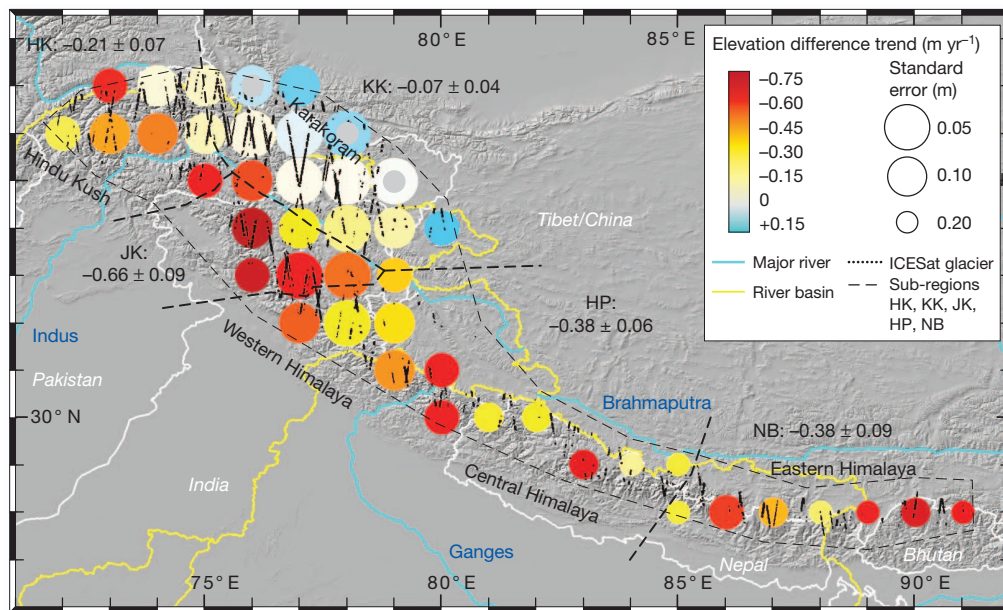


**Figure 1 | Study region and trends of elevation differences between ICESat and SRTM over 2003–08.** Data are shown on a  $1^\circ$  grid with overlapping rectangular geographic averaging cells of  $2^\circ \times 2^\circ$ . Trends are based on autumn ICESat acquisitions. The mean trends for each subregion are given in metres

pairs of footprints sharing similar location, elevation, slope and aspect. For KK, JK, HP and NB, thinning on debris-covered ice is not statistically different from, and for HK exceeds, thinning on clean ice<sup>17,19,24</sup> despite the widely assumed insulating effect of debris<sup>25</sup>. In KK, though, the sparse ICESat tracks might not sample the high variability of elevation changes, in particular of the glacier tongues<sup>19</sup>, in a regionally representative way. Glacier elevation changes at a specific location are the combined effect of surface mass balance and ice flux budget. Given that our pairs of neighbouring footprints (the mean distance between them is approximately 1 km) typically occur on the same glacier, differences in ice flux budget within a pair are expected to be small. Thus,

per year. Only ICESat footprints over glaciers are indicated (the glacier mark is shown in Supplementary Fig. 1). Trends for all cells (coloured data circles) are statistically significant except for three cells in the Karakoram that are indicated with grey centres. Errors are one standard error (1 s.e.).

we assume that the comparison between clean and debris-covered ice elevation trends at least partly reflects differences in ablation rates of the two. The similar thinning rates between both glacier cover types are presumably caused by thermokarst processes on debris-covered tongues that are dynamically inactive<sup>6,17,26,27</sup>. Our findings suggest that the well-proved insulating effect of debris layers with thicknesses exceeding a few centimetres<sup>28</sup> acts on local scales of intact covers, but not in general on the spatial scale of entire glacier tongues. The substantial ice thickness loss over debris-covered ice allows continued, and possibly enhanced, evolution of supraglacial and moraine lakes, and associated outburst hazards<sup>7,29</sup>.

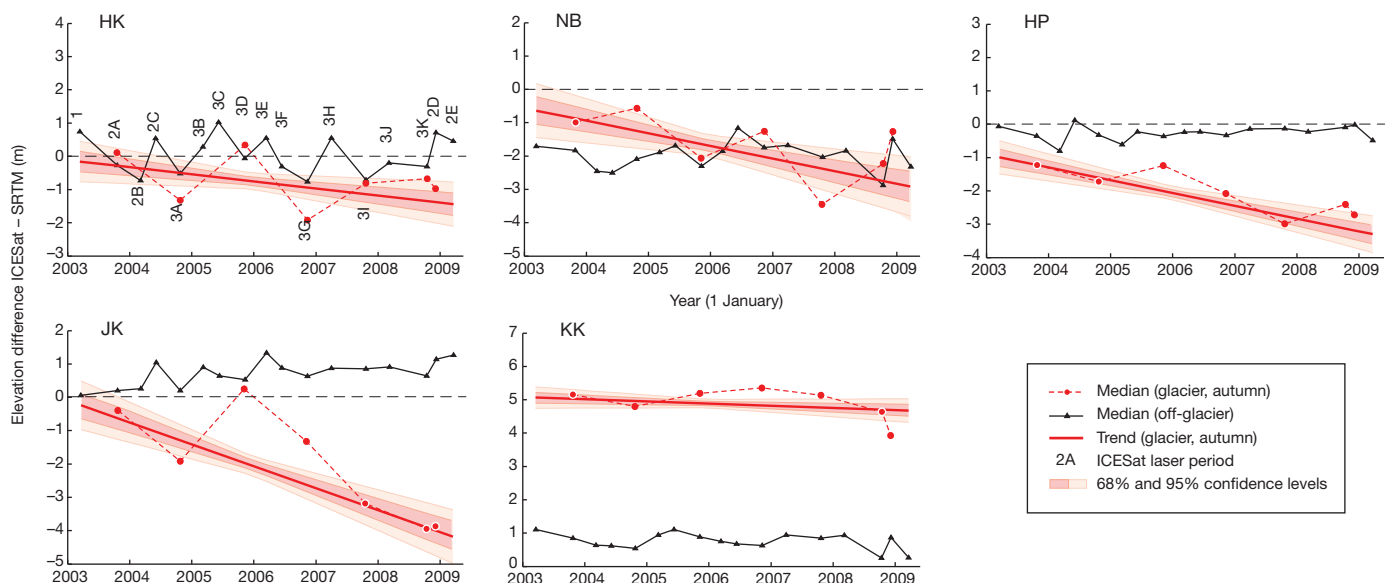


**Figure 2 | Median elevation differences between ICESat and SRTM for ICESat laser periods and glacier elevation difference trends.** Data are given for the five sub-regions defined in Fig. 1. For off-glacier terrain (black triangles and curves) all medians are shown; for glaciers only autumn laser altimetry periods (red dots and dashed curves; compare Supplementary Fig. 2) are shown. Autumn trends (red bold lines) are fitted through all individual

elevation differences using a robust fitting method, not through the laser altimetry period median elevation differences, creating small offsets between the trends shown and a virtual regression through the laser period medians. The 68% and 95% confidence levels (shaded medium red and light red) represent solely the statistical error of the trend fitting.



**Table 1 | Glacier elevation difference trends and mass balances 2003–09**

	Hindu Kush (HK)	Karakoram (KK)	Jammu Kashmir (JK)	Himachal Pradesh, Uttarakhand and West Nepal (HP)	East Nepal and Bhutan (NB)	Sum (first 3 rows) or area-weighted mean (HKKH)
Glacier area (km <sup>2</sup> )	9,350	21,750	4,900	14,550	9,550	60,100
Number of ICESat glacier footprints (Oct–Nov)	6,300	18,050	4,200	9,850	5,650	44,050
Number of ICESat glacier footprints (Feb–Mar)	4,600	12,050	2,750	6,800	5,050	31,250
Clean ice/debris-covered ice/AAR around year 2000 (as percentage of glacier area)	54 / 16 / 30	44 / 9 / 47	57 / 14 / 29	51 / 14 / 35	38 / 15 / 47	47 / 13 / 40
Elevation difference trends (m yr <sup>-1</sup> ± 1 s.e.)						
Off-glacier	+0.01 ± 0.05	-0.02 ± 0.02	+0.02 ± 0.05	+0.01 ± 0.02	-0.02 ± 0.04	0.0 ± 0.03
Glaciers (Oct–Nov 2003–08)	-0.21 ± 0.07	-0.07 ± 0.04	-0.66 ± 0.09	-0.38 ± 0.06	-0.38 ± 0.09	-0.26 ± 0.06
Glaciers (Feb–Mar 2003–09)	-0.48 ± 0.07	+0.41 ± 0.04	-0.26 ± 0.09	-0.38 ± 0.06	-0.38 ± 0.09	-0.10 ± 0.06
Clean ice	-0.21 ± 0.32	-0.54 ± 0.25	-1.28 ± 0.54	-1.20 ± 0.33	-2.30 ± 0.53	-0.78 ± 0.16
Debris-covered ice	-1.54 ± 0.31	-0.04 ± 0.26	-1.05 ± 0.44	-1.02 ± 0.29	-1.53 ± 0.43	-0.76 ± 0.16
Mass balance						
Density scenario a (m yr <sup>-1</sup> WE ± 1 s.e.)	-0.19 ± 0.06	-0.06 ± 0.04	-0.59 ± 0.08	-0.34 ± 0.05	-0.34 ± 0.08	-0.23 ± 0.05
Density scenario a (Gt yr <sup>-1</sup> ± 1 s.e.)	-1.8 ± 0.6	-1.3 ± 0.9	-2.9 ± 0.5	-5.0 ± 0.9	-3.3 ± 0.9	-14.3 ± 3.5
Density scenario b (m yr <sup>-1</sup> WE ± 1 s.e.)	-0.20 ± 0.05	0.0 ± 0.03	-0.51 ± 0.06	-0.30 ± 0.04	-0.26 ± 0.07	-0.19 ± 0.04
Density scenario b (Gt yr <sup>-1</sup> ± 1 s.e.)	-1.8 ± 0.5	0.0 ± 0.8	-2.5 ± 0.4	-4.4 ± 0.8	-2.5 ± 0.7	-11.2 ± 3.1
Density scenario ab (m yr <sup>-1</sup> WE ± 1 s.e.)	-0.20 ± 0.06	-0.03 ± 0.04	-0.55 ± 0.08	-0.32 ± 0.06	-0.30 ± 0.09	-0.21 ± 0.05
Density scenario ab (Gt yr <sup>-1</sup> ± 1 s.e.)	-1.8 ± 0.6	-0.6 ± 0.9	-2.7 ± 0.5	-4.7 ± 1.0	-2.9 ± 0.9	-12.8 ± 3.5
Density scenario ab (mm yr <sup>-1</sup> SLE ± 1 s.e.)	-0.005 ± 0.002	-0.001 ± 0.002	-0.008 ± 0.001	-0.013 ± 0.003	-0.008 ± 0.003	-0.035 ± 0.009

All analyses refer to the perennial surface ice features such as glaciers, glacierets and perennial ice patches. Footprints over SRTM voids and from laser period 2F are discarded. Errors given (one standard error, s.e.) are the root of sum of squares (RSS) of the standard error of fits, the off-glacier trend, and a simulated effect of elevation variations within a season. Elevation difference trends for clean and debris-covered ice were computed for pairs of neighbouring footprints on clean and debris-covered ice. The density assumption scenarios are: a, 900 kg m<sup>-3</sup>; b, 900 kg m<sup>-3</sup> for ice and 600 kg m<sup>-3</sup> for firn and snow footprints; ab is the mean of scenarios a and b. The error of scenario ab is a combined error (RSS) including the trend error and the standard deviation of the mean of scenarios a and b. For the total mass changes (Gt yr<sup>-1</sup>) and sea level equivalent (SLE), the errors also include (RSS) a 10% uncertainty for the glacier areas. AAR, accumulation area ratio (here the ratio between snow and firn areas to total glacier area); WE, water equivalent.

Scaling up of ICESat footprint classes indicates a total perennial surface ice area of around 60,000 km<sup>2</sup> (Table 1, Supplementary Information). Using a glacier mask based on a ratio between visible and short-wave infrared Landsat bands and glacier inventories available for the HKKH, the SRTM glacier hypsometry verifies the spatial and hypsometric representativeness of the ICESat footprint classification and distribution for all HKKH glaciers (Supplementary Fig. 3), so elevation difference trends can be applied to the total ice-covered area. A first density scenario (a) assumes all glacier thickness changes are loss and gain of ice (900 kg m<sup>-3</sup>), a second density scenario (b) assumes 900 kg m<sup>-3</sup> for thickness changes over ice and 600 kg m<sup>-3</sup> for changes over firn and snow (Table 1, Supplementary Information). Our final mass budget estimate is the average of the two scenarios (ab), resulting in a mass change of  $-12.8 \pm 3.5$  gigatonnes per year (Gt yr<sup>-1</sup>) and a sea level rise contribution of  $0.035 \pm 0.009$  mm yr<sup>-1</sup> for HKKH glaciers, which is 3% to 4% of the total contribution from global glaciers and ice caps<sup>3,4</sup>.

The specific mass balances measured on HKKH glaciers over 2003–08 are less negative than various estimates of the global average for glaciers and ice caps outside Greenland and Antarctica of around  $-0.75$  m yr<sup>-1</sup> water equivalent (WE)<sup>4,10</sup> based on in-situ mass-balance measurements. Our 2003–08 HKKH mass budget of  $-12.8 \pm 3.5$  Gt yr<sup>-1</sup> is, however, considerably more negative than a recent estimate of  $-5 \pm 3$  Gt yr<sup>-1</sup> based on satellite gravimetry (GRACE) over 2003–10 (ref. 12; their original uncertainty at 2- $\sigma$  level was converted to 1- $\sigma$  level; see Supplementary Information for full multi-study comparisons).

The annual average 2003–08 glacier imbalances for the Indus (about 1,150,000 km<sup>2</sup>) and Ganges ( $\sim 1,030,000$  km<sup>2</sup>) basins amount to approximately  $300 \pm 53$  m<sup>3</sup> s<sup>-1</sup> discharge equivalent (mass imbalance units of Gt yr<sup>-1</sup> converted to m<sup>3</sup> s<sup>-1</sup>) for the Indus basin and approximately  $185 \pm 45$  m<sup>3</sup> s<sup>-1</sup> for the Ganges basin, respectively, neglecting any processes other than direct river runoff. The actual contribution of glacier imbalance to total discharge depends on the distance from glaciers and the seasonality of the glacier imbalance<sup>1</sup>, which is, however, not directly accessible from our ICESat measurements. As an annual average for the combined outlets of the mountain catchments within the Indus and Ganges river basins defined by ref. 13 (the Indus about 320,000 km<sup>2</sup>, and the Ganges about 182,000 km<sup>2</sup>; Supplementary Fig. 1) and neglecting any water loss due to evaporation or groundwater storage, our glacier imbalances amount to about

3.5% and about 2.0% of the total modelled discharges<sup>13</sup> for the Indus and Ganges mountain catchments, respectively. For the outlet of the Upper Indus basin ( $\sim 200,000$  km<sup>2</sup>, Supplementary Fig. 1) at the Tarbela dam<sup>14</sup> the annual average glacier imbalance, about  $231 \pm 46$  m<sup>3</sup> s<sup>-1</sup>, amounts to about 10% of the modelled and measured annual river discharge<sup>14</sup>, and explains most of the approximately  $300$  m<sup>3</sup> s<sup>-1</sup> discrepancy between total annual precipitation ( $311$  mm yr<sup>-1</sup> or around  $1,980$  m<sup>3</sup> s<sup>-1</sup>) and observed annual stream flow (around  $2,290$  m<sup>3</sup> s<sup>-1</sup>) (ref. 14). The increase of precipitation with altitude (unaccounted for in the mean basin precipitation estimate<sup>14</sup>) may also have contributed to this discrepancy<sup>30</sup>.

The glacier thickness changes presented here underpin the first spatially resolved mass budget over the entire HKKH, and in turn the first quantitative observational assessment of the contribution of glacier imbalance to river runoff, to our knowledge. That debris-covered ice thins at a rate similar to that of exposed ice shows that the role of debris mantles in glacier mass balance must be reassessed. In particular, in regions of highly discontinuous glacier coverage, we suggest that satellite gravimetry will be very useful to better detect large-scale sub-surface mass changes such as from hydrology or tectonics, or to better quantify errors in the corrections of these, respectively, by relying on glacier mass changes from studies such as ours. Our results will thus enable improved estimates of groundwater depletion in northern India<sup>31</sup>, which has thus far been difficult to discriminate from glacier loss in satellite gravity observations<sup>12</sup>.

## METHODS SUMMARY

Cloud-free 30-m resolution Landsat Thematic Mapper (TM) and Enhanced Thematic Mapper (ETM) scenes from around the year 2000 with minimal snow cover were obtained from the United States Geological Survey as a topographically corrected version (L1T; <http://glovis.usgs.gov>; Supplementary Table 1). A band ratio denotes snow/firn/clean ice areas (Supplementary Data). All ICESat footprint elevations during 2003–09 (about 70 m footprint diameter and 170 m along-track spacing), obtained from the National Snow and Ice Data Center (<http://nsidc.org/data/icesat/index.html>; release 531), within a 10-km buffer around the snow/firn/clean-ice mask are compared to the  $\sim 90$ -m gridded SRTM DEM for February 2000 (void-filled version 4 from the Consultative Group on International Agricultural Research; <http://srtm.csi.cgiar.org/>) through bilinear interpolation of the estimated footprint centre. ICESat points within the SRTM void mask are disregarded. SRTM geoid elevations are converted from the Earth Gravity Model (EGM) 1996 to EGM2008, which is used for ICESat release 531. The

SRTM DEM is co-registered with the 17 ICESat campaigns. Landsat band ratios for snow/firn/clean ice and snow/firn were computed at ICESat footprint locations. Footprints over debris-covered glacier sections are initially labelled using glacier outlines, where available (<http://glims.colorado.edu/glacierdata/>, <http://glims.org/RGI/randolph.html>). The footprint classifications were superimposed over the Landsat mosaic and edited manually to clean ice, snow/firn, debris-covered ice and off-glacier classes, and to introduce an additional water class (Supplementary Data). Elevation trends were derived using a robust linear regression through all ICESat-SRTM elevation differences. Various tests (Supplementary Information) showed that these trends are not very sensitive to the type of ICESat waveform fitting, the spatial elevation sampling and the timing of ICESat acquisitions. Interestingly, an even lower spatial sampling than the ICESat acquisition programme would produce significant results. Histogram adjustments were required to compare off- and on-glacier trends due to significant biases from saturation of ICESat waveforms on steep slopes, mainly off-glacier. Glacier thickness changes were converted to mass changes using two density scenarios. More details about the data and methods can be found in the Supplementary Information.

Received 13 April; accepted 12 June 2012.

- Kaser, G., Grosshauser, M. & Marzeion, B. Contribution potential of glaciers to water availability in different climate regimes. *Proc. Natl Acad. Sci. USA* **107**, 20223–20227 (2010).
- Immerzeel, W. W., van Beek, L. P. H. & Bierkens, M. F. P. Climate change will affect the Asian water towers. *Science* **328**, 1382–1385 (2010).
- Church, J. A. *et al.* Revisiting the Earth's sea-level and energy budgets from 1961 to 2008. *Geophys. Res. Lett.* **38**, L18601 (2011).
- Cogley, J. G. Geodetic and direct mass-balance measurements: comparison and joint analysis. *Ann. Glaciol.* **50**, 96–100 (2009).
- Bolch, T. *et al.* The state and fate of Himalayan glaciers. *Science* **336**, 310–314 (2012).
- Scherler, D., Bookhagen, B. & Strecker, M. R. Spatially variable response of Himalayan glaciers to climate change affected by debris cover. *Nature Geosci.* **4**, 156–159 (2011).
- Gardelle, J., Arnaud, Y. & Berthier, E. Contrasted evolution of glacial lakes along the Hindu Kush Himalaya mountain range between 1990 and 2009. *Global Planet. Change* **75**, 47–55 (2011).
- Hewitt, K. Glacier change, concentration, and elevation effects in the Karakoram Himalaya, Upper Indus Basin. *Mount. Res. Dev.* **31**, 188–200 (2011).
- Fowler, H. J. & Archer, D. R. Conflicting signals of climatic change in the Upper Indus basin. *J. Clim.* **19**, 4276–4293 (2006).
- World Glacier Monitoring Service. <http://www.wgms.ch> (2012).
- Cazenave, A. *et al.* Sea level budget over 2003–2008: a reevaluation from GRACE space gravimetry, satellite altimetry and Argo. *Global Planet. Change* **65**, 83–88 (2009).
- Jacob, T., Wahr, J., Pfeffer, W. T. & Swenson, S. Recent contributions of glaciers and ice caps to sea level rise. *Nature* **482**, 514–518 (2012).
- Bookhagen, B. & Burbank, D. W. Toward a complete Himalayan hydrological budget: spatiotemporal distribution of snowmelt and rainfall and their impact on river discharge. *J. Geophys. Res.* **115**, F03019 (2010).
- Immerzeel, W. W., Droogers, P., de Jong, S. M. & Bierkens, M. F. P. Large-scale monitoring of snow cover and runoff simulation in Himalayan river basins using remote sensing. *Remote Sens. Environ.* **113**, 40–49 (2009).
- Fujita, K. Effect of precipitation seasonality on climatic sensitivity of glacier mass balance. *Earth Planet. Sci. Lett.* **276**, 14–19 (2008).
- Berthier, E. *et al.* Remote sensing estimates of glacier mass balances in the Himachal Pradesh (Western Himalaya, India). *Remote Sens. Environ.* **108**, 327–338 (2007).
- Bolch, T., Pieczonka, T. & Benn, D. Multi-decadal mass loss of glaciers in the Everest area (Nepal Himalaya) derived from stereo imagery. *Cryosphere* **5**, 349–358 (2011).
- Fujita, K. & Nuimura, T. Spatially heterogeneous wastage of Himalayan glaciers. *Proc. Natl Acad. Sci. USA* **108**, 14011–14014 (2011).
- Gardelle, J., Berthier, E. & Arnaud, Y. Slight mass gain of Karakoram glaciers in the early 21st century. *Nature Geosci.* **5**, 322–325 (2012).
- Azam, M. F. *et al.* From balance to imbalance: a shift in the dynamic behaviour of Chhota Shigri Glacier (Western Himalaya, India). *J. Glaciol.* **58**, 315–324 (2012).
- Moholdt, G., Nuth, C., Hagen, J. O. & Kohler, J. Recent elevation changes of Svalbard glaciers derived from ICESat laser altimetry. *Remote Sens. Environ.* **114**, 2756–2767 (2010).
- Rignot, E., Echelmeyer, K. & Krabill, W. Penetration depth of interferometric synthetic-aperture radar signals in snow and ice. *Geophys. Res. Lett.* **28**, 3501–3504 (2001).
- Gardelle, J., Berthier, E. & Arnaud, Y. Impact of resolution and radar penetration on glacier elevation changes computed from multi-temporal DEMs. *J. Glaciol.* **58**, 419–422 (2012).
- Nuimura, T., Fujita, K., Yamaguchi, S. & Sharma, R. Elevation changes of glaciers revealed by multitemporal digital elevation models calibrated by GPS survey in the Khumbu region, Nepal Himalaya, 1992–2008. *J. Glaciol.* **58**, 648–656 (2012).
- Reid, T. D. & Brock, B. W. An energy-balance model for debris-covered glaciers including heat conduction through the debris layer. *J. Glaciol.* **56**, 903–916 (2010).
- Kääb, A. Combination of SRTM3 and repeat ASTER data for deriving alpine glacier flow velocities in the Bhutan Himalaya. *Remote Sens. Environ.* **94**, 463–474 (2005).
- Sakai, A., Takeuchi, N., Fujita, K. & Nakawo, M. in *Debris-covered Glaciers* (eds Nakawo, M., Raymond, C. F. & Fountain, A.) Vol. 264 119–130 (IAHS, 2000).
- Mattson, L., Gardner, J. & Young, G. in *Snow and Glacier Hydrology* (ed. Young, G. H.) Vol. 218 289–296 (IAHS, 1993).
- Quincey, D. J. *et al.* Early recognition of glacial lake hazards in the Himalaya using remote sensing datasets. *Global Planet. Change* **56**, 137–152 (2007).
- Immerzeel, W. W., Pellicciotti, F. & Shrestha, A. B. Glaciers as a proxy to quantify the spatial distribution of precipitation in the Hunza basin. *Mount. Res. Dev.* **32**, 30–38 (2012).
- Rodell, M., Velicogna, I. & Famiglietti, J. S. Satellite-based estimates of groundwater depletion in India. *Nature* **460**, 999–1002 (2009).

**Supplementary Information** is linked to the online version of the paper at [www.nature.com/nature](http://www.nature.com/nature).

**Acknowledgements:** We thank G. Cogley and A. Gardner for their exceptionally thorough and constructive comments. This study was supported by the European Space Agency (ESA) through the projects GlobGlacier (21088/07/I-EC) and Glaciers\_cci (4000101778/10/I-AM). The study is further a contribution to the Global Land Ice Measurements from Space (GLIMS) initiative and the International Centre for Geohazards (ICG). NASA's ICESat GLAS data were obtained from NSIDC, Landsat data are courtesy of NASA and USGS, and the SRTM elevation model version is courtesy of NASA JPL and was further processed by CGIAR. A number of glacier outlines were provided by GLIMS. E.B. and Y.A. acknowledge support from the Centre National d'Etudes Spatiales (CNES) through the TOSCA and ISIS programmes, from the French National Research Agency through ANR-09-CEP-005-01/PAPRIKA, and from the PNTS. J.G. was funded through CNES/CNRS.

**Author Contributions:** A.K. designed the study, processed and analysed the data, created the figures, and wrote the paper. All other co-authors wrote and edited the paper and assisted in interpretations. J.G., E.B. and Y.A. provided additional data, and C.N. assisted in data processing.

**Author Information** Reprints and permissions information is available at [www.nature.com/reprints](http://www.nature.com/reprints). The authors declare no competing financial interests. Readers are welcome to comment on the online version of this article at [www.nature.com/nature](http://www.nature.com/nature). Correspondence and requests for materials should be addressed to A.K. ([kaeab@geo.uio.no](mailto:kaeab@geo.uio.no)).

# Mutations in the profilin 1 gene cause familial amyotrophic lateral sclerosis

Chi-Hong Wu<sup>1</sup>, Claudia Fallini<sup>2</sup>, Nicola Ticozzi<sup>3</sup>, Pamela J. Keagle<sup>1</sup>, Peter C. Sapp<sup>1,4</sup>, Katarzyna Piotrowska<sup>1</sup>, Patrick Lowe<sup>1</sup>, Max Koppers<sup>5</sup>, Diane McKenna-Yasek<sup>1</sup>, Desiree M. Baron<sup>1</sup>, Jason E. Kost<sup>1</sup>, Paloma Gonzalez-Perez<sup>1</sup>, Andrew D. Fox<sup>1</sup>, Jenni Adams<sup>1</sup>, Franco Taroni<sup>6</sup>, Cinzia Tiloca<sup>3,7</sup>, Ashley Lyn Leclerc<sup>1</sup>, Shawn C. Chafe<sup>8</sup>, Dev Mangroo<sup>8</sup>, Melissa J. Moore<sup>9</sup>, Jill A. Zitzewitz<sup>10</sup>, Zuo-Shang Xu<sup>10</sup>, Leonard H. van den Berg<sup>5</sup>, Jonathan D. Glass<sup>11</sup>, Gabriele Siciliano<sup>12</sup>, Elizabeth T. Cirulli<sup>13</sup>, David B. Goldstein<sup>13</sup>, Francois Salachas<sup>14</sup>, Vincent Meininger<sup>14</sup>, Wilfried Rossoll<sup>2</sup>, Antonia Ratti<sup>3,15</sup>, Cinzia Gellera<sup>6</sup>, Daryl A. Bosco<sup>1</sup>, Gary J. Bassell<sup>2,11</sup>, Vincenzo Silani<sup>3,15</sup>, Vivian E. Drory<sup>16</sup>, Robert H. Brown Jr<sup>1</sup> & John E. Landers<sup>1</sup>

**Amyotrophic lateral sclerosis (ALS) is a late-onset neurodegenerative disorder resulting from motor neuron death. Approximately 10% of cases are familial (FALS), typically with a dominant inheritance mode. Despite numerous advances in recent years<sup>1–9</sup>, nearly 50% of FALS cases have unknown genetic aetiology. Here we show that mutations within the profilin 1 (*PFN1*) gene can cause FALS. *PFN1* is crucial for the conversion of monomeric (G)-actin to filamentous (F)-actin. Exome sequencing of two large ALS families showed different mutations within the *PFN1* gene. Further sequence analysis identified 4 mutations in 7 out of 274 FALS cases. Cells expressing *PFN1* mutants contain ubiquitinated, insoluble aggregates that in many cases contain the ALS-associated protein TDP-43. *PFN1* mutants also display decreased bound actin levels and can inhibit axon outgrowth. Furthermore, primary motor neurons expressing mutant *PFN1* display smaller growth cones with a reduced F/G-actin ratio. These observations further document that cytoskeletal pathway alterations contribute to ALS pathogenesis.**

To identify causative genes for familial ALS, we performed exome capture followed by deep sequencing on two large ALS families (Fig. 1a, b) of Caucasian (family 1) and Sephardic Jewish (family 2) origin. Both display a dominant inheritance mode and are negative for known ALS-causing mutations, including the newly identified hexanucleotide repeat expansion in *C9orf72* (refs 6, 8, 9; Supplementary Fig. 1). For each family, two affected members with maximum genetic distance were selected for exome sequencing. A high level of coverage ( $>150\times$ ) was achieved with an average of  $1.1 \times 10^{10}$  and  $2.3 \times 10^{10}$  base pairs sequenced for members of families 1 and 2, respectively (Supplementary Tables 1 and 2). To identify candidate causative mutations, variants were identified and filtered, as in previous exome sequencing reports<sup>5</sup>, using several criteria: the variant is observed in both family members, alters the amino acid sequence, is not excluded by linkage analysis (Supplementary Fig. 2), and is absent from dbSNP132, the 1000 Genomes Project (May 2011 release) or the National Heart, Lung, and Blood Institute (NHLBI) Exome Sequencing Project (ESP) Exome Variant Server (5,379 sequenced exomes; <http://evs.gs.washington.edu/EVS/>). Remaining variants were confirmed by Sanger sequencing and tested for Mendelian segregation in all affected family members. The resulting number of candidate

causative mutations identified was two within family 1 and three within family 2 (Supplementary Tables 3 and 4). Interestingly, the two families contain different mutations (C71G and M114T) within a single common gene: *PFN1*, located on chromosome 17p13.2. *PFN1* is an 140-amino-acid protein and major growth regulator of filamentous (F)-actin through its binding of monomeric (G)-actin<sup>10</sup>.

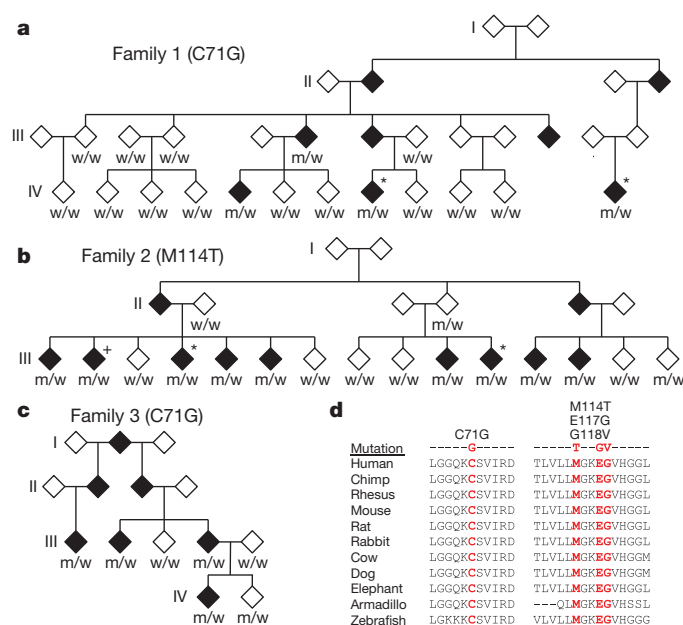


**Figure 1 | Exome sequencing identifies *PFN1* gene mutations in familial ALS.** a–c, Familial ALS pedigrees containing *PFN1* mutations are shown. Asterisks indicate samples subjected to exome sequencing. To prevent identification of individual family members, the gender of each subject and information on the lower generation are withheld. Genotypes of available DNA samples for the indicated *PFN1* mutation are shown ('w' denotes wild type, 'm' denotes mutant). The genotype of sample III:2 in family 2 (+) was inferred from the genotypes of spouse and progeny (not shown). d, The evolutionary conservation of *PFN1* mutations is shown. For each, the mutated amino acid is coloured red.

<sup>1</sup>Department of Neurology, University of Massachusetts Medical School, Worcester, Massachusetts 01605, USA. <sup>2</sup>Department of Cell Biology, Emory University School of Medicine, Atlanta, Georgia 30322, USA. <sup>3</sup>Department of Neurology and Laboratory of Neuroscience, IRCCS Istituto Auxologico Italiano, Milan 20149, Italy. <sup>4</sup>Howard Hughes Medical Institute (HHMI), Department of Biology, Massachusetts Institute of Technology, 77 Massachusetts Avenue, Cambridge, Massachusetts 02139, USA. <sup>5</sup>Department of Neurology, Rudolf Magnus Institute of Neuroscience, University Medical Centre Utrecht, 3584 CX Utrecht, The Netherlands. <sup>6</sup>Unit of Genetics of Neurodegenerative and Metabolic Diseases, Fondazione IRCCS Istituto Neurologico 'Carlo Besta', Milan 20133, Italy. <sup>7</sup>Doctoral School in Molecular Medicine, Department of Sciences and Biomedical Technologies, Università degli Studi di Milano, Milan 20122, Italy. <sup>8</sup>Department of Molecular and Cellular Biology, University of Guelph, Guelph, Ontario N1G2W1, Canada. <sup>9</sup>Department of Biochemistry and Molecular Pharmacology, Howard Hughes Medical Institute, University of Massachusetts Medical School, Worcester, Massachusetts 01605, USA. <sup>10</sup>Department of Biochemistry and Molecular Pharmacology, University of Massachusetts Medical School, Worcester, Massachusetts 01605, USA. <sup>11</sup>Department of Neurology, Center for Neurodegenerative Disease, Emory University School of Medicine, Atlanta, Georgia 30322, USA. <sup>12</sup>Department of Neuroscience, University of Pisa, 56126 Pisa, Italy. <sup>13</sup>Center for Human Genome Variation, Duke University School of Medicine, Durham, North Carolina 27708, USA. <sup>14</sup>Centre Référent Maladies Rares, APHP, UPMC, Hôpital de la Salpêtrière, Paris 75013, France. <sup>15</sup>Dipartimento di Fisiopatologia Medico-Chirurgica e dei Trapianti, 'Dino Ferrari' Center, Università degli Studi di Milano, Milan 20122, Italy. <sup>16</sup>Department of Neurology, Tel-Aviv Sourasky Medical Center, 6 Weizmann Street, 64239 Tel-Aviv, Israel.



On the basis of these data, we tested the hypothesis that *PFN1* gene mutations cause familial ALS.

Figure 1 shows sequence analysis of all available members of families 1 and 2. All four affected members of family 1 for which DNA was available possess the *PFN1*(C71G) variant. A single obligate carrier of the C71G variant (III:13) did not develop disease; however, death occurred before the average age of onset of this family (Supplementary Table 5). All unaffected family 1 members displayed the wild-type genotype (Fig. 1a). Within family 2, all eight affected members for which DNA was available contained the M114T variant. On the basis of the genotypes of spouse and progeny (not shown), we confirmed that a ninth affected family member (III:2) also carries the mutation. Of 7 unaffected members, 5 do not contain the M114T variant. One unaffected mutation carrier is now in their mid-40s (III:15) and a second obligate carrier (II:4) was asymptomatic into their 70s (Fig. 1b). Our results suggest that these mutations have a high degree of penetrance. Affected-only linkage analysis of the *PFN1* variants in family 1 and 2 yielded a logarithm of the odds (lod) scores of 1.80 and 2.71, respectively.

To determine whether *PFN1* mutations cause familial ALS, the coding region was sequenced in a panel of 272 further FALS cases prescreened for common causative mutations. Five other familial ALS cases containing alterations in the *PFN1* gene (Supplementary Figs 3 and 4) were identified. Interestingly, the C71G alteration originally identified in family 1 was discovered in two other families. For one of these families (family 3), DNA was available for three other affected family members. Sequencing of these samples showed that the mutation co-segregates with ALS (Fig. 1c). A single unaffected member of the family (IV:2) also contains the mutation; the current age of this family member is mid-40s. Affected-only linkage analysis of family 3 yielded a lod score of 1.50 and a combined lod score of 6.01 for families 1–3. A second M114T mutation was identified in an ALS family of Italian origin (family 4, Supplementary Fig. 3). DNA available for one sibling was shown by sequencing to contain this mutation. *PFN1* variants were observed in two other FALS cases: a consecutive base-pair change (AA to GT) resulting in an E117G mutation, and a G-to-T transversion resulting in a G118V mutation (Supplementary Figs 3 and 4). DNA was not available from other family members for these cases. Sequencing of the *PFN1* coding region in 816 sporadic ALS (SALS) samples identified two samples containing the E117G mutation. No further non-synonymous changes were identified in the FALS and SALS samples (Supplementary Table 6). Haplotype analysis using surrounding single nucleotide polymorphisms (SNPs) suggests that the C71G mutation derives from a single ancestral mutation (Supplementary Table 7).

To confirm further that the newly identified variants (E117G and G118V) represent causal mutations, not benign polymorphisms, each was interrogated in the 1000 Genomes Project database and the NHLBI ESP Exome Variant Server. The G118V mutation was not identified in either database. However, the E117G variant was observed in 2 samples out of 5,379 at the NHLBI ESP Exome Variant Server. We extended this analysis by genotyping all mutations in an independent set of 1,089 control samples. Three of the mutations (C71G, M114T and G118V) were not observed in the 1,089 control samples; however, the E117G variant was observed in a single control (Supplementary Table 8). By combining data from the 1000 Genome Project, the NHLBI ESP Exome Variant Server and independent genotyping, three of the ALS-linked variants were not present in 7,560 control samples (15,120 alleles), whereas the fourth (E117G) was found in 3 out of 1,090 ALS cases and in 3 out of 7,560 control samples ( $2.75 \times 10^{-3}$  versus  $3.97 \times 10^{-4}$ ;  $P = 0.030$ , two-tailed Fisher's exact test). Thus, it could be argued that the E117G variant is either non-pathogenic or, more likely, represents a less pathogenic mutation.

In total, we identified 4 mutations in 7 out of 274 FALS cases. In each case, the altered amino acid was evolutionarily conserved down to the level of zebrafish (Fig. 1d), supporting the possibility that these

mutations are pathogenic. The age of onset for FALS cases with *PFN1* mutations is  $44.8 \pm 7.4$  (Supplementary Table 5). All *PFN1* mutant cases displayed limb onset; no bulbar onset was observed ( $n = 22$ , Supplementary Table 5). Given that bulbar onset represents ~25% of ALS cases<sup>11</sup>, this result suggests a common clinical phenotype among patients with *PFN1* mutations.

Ubiquitinated, insoluble aggregates are pathological hallmarks of several neurodegenerative diseases including ALS, Parkinson's disease and Alzheimer's disease. To investigate whether the observed *PFN1* mutants form insoluble aggregates, western blot analysis of NP-40-soluble and insoluble fractions was performed on Neuro-2A (N2A) cells transfected with wild-type or one of the four *PFN1* mutants. *PFN1* protein was present predominantly in the soluble fraction of cells transfected with the wild-type construct as compared with the insoluble fraction (Fig. 2a). Conversely, a considerable proportion of the C71G, M114T and G118V mutant proteins were detected in the insoluble fraction. Furthermore, several higher molecular mass species were

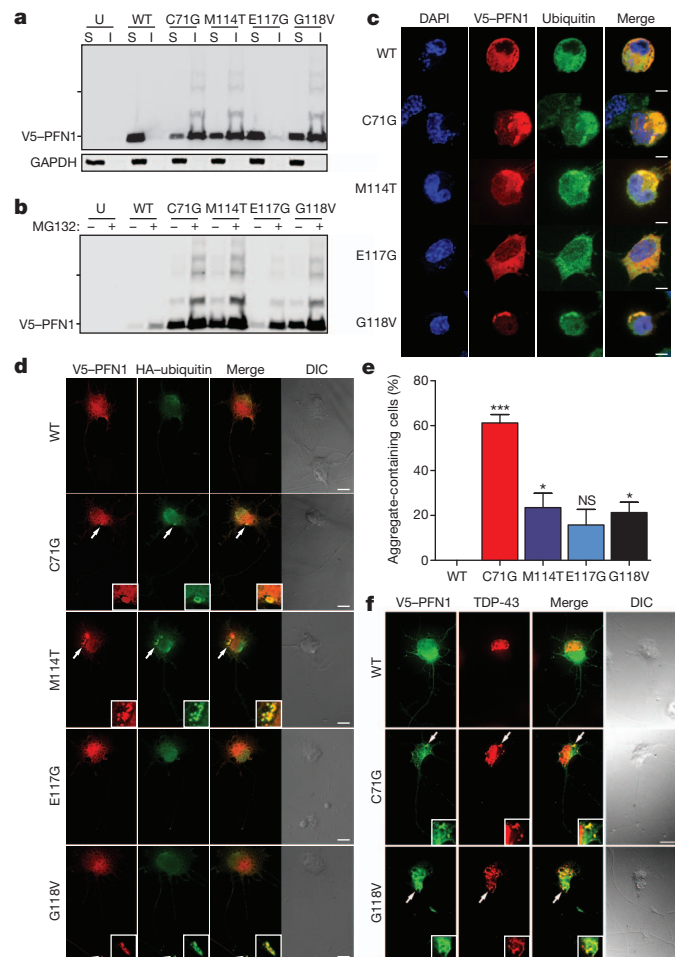


**Figure 2 | Mutant *PFN1* produces ubiquitinated insoluble aggregates.** **a**, Western blot analysis of transfected N2A cells subject to NP-40-soluble (S) and insoluble (I) fractionation. U, untransfected; WT, wild-type. **b**, Transfected cells were treated with MG132 and processed as in **a**. Tick marks indicate 20-kDa and 37-kDa markers. **c**, **d**, Transfected N2A cells (**c**) and transfected PMNs (**d**) were stained with V5, haemagglutinin (HA) (PMNs) and ubiquitin (N2A) antibodies. Example aggregates are enlarged in the insets in **d**. DAPI, 4',6-diamidino-2-phenylindole; DIC, differential interference contrast. **e**, Transfected N2A cells displaying insoluble aggregates were counted and analysed using one-way analysis of variance (ANOVA) testing with Dunnett's multiple test comparison ( $n = 127$ –135 transfected cells from three independent experiments). \* $P < 0.05$ ; \*\*\* $P < 0.001$ ; NS, not significant ( $P > 0.05$ ). Error bars indicate s.e.m. **f**, Transfected PMNs stained with V5 and TDP-43 antibodies. Scale bars, 5  $\mu$ m (**c**) and 10  $\mu$ m (**d**, **f**).

observed, indicative of SDS-resistant PFN1 oligomers. However, the E117G mutant displayed a pattern more similar to wild-type PFN1 with most of the expressed protein in the soluble fraction. Differential expression of PFN1 constructs was ruled out by western blot analysis of whole cell lysates (Supplementary Fig. 5). Analysis of lymphoblast cell lines derived from affected and unaffected members of family 1 did not display any differences in PFN1 protein solubility (Supplementary Fig. 6). Autopsy material was not available for any affected individual.

We extended these observations by staining the PFN1 protein in transfected cells. Wild-type PFN1 exhibited a diffuse cytoplasmic expression pattern in transfected N2A cells (Fig. 2c), as previously reported<sup>12</sup>. By contrast, ALS-linked PFN1 mutants often assembled into cytoplasmic aggregates. Image analysis determined that 15–61% of mutant-expressing cells contain cytoplasmic aggregates, including the E117G mutant, which showed minimal insoluble PFN1 protein by western blot analysis. No aggregates were observed for cells expressing wild-type PFN1 (Fig. 2e). Co-staining revealed that these aggregates were also ubiquitinated. Primary motor neurons (PMNs) expressing the C71G, M114T and G118V mutants similarly demonstrated ubiquitinated aggregates, albeit at a lower percentage (Fig. 2d); aggregates were not observed in cells expressing the E117G mutant or wild-type PFN1. Immunoprecipitation of the PFN1 protein followed by western blot analysis confirmed that the insoluble mutant PFN1 protein is polyubiquitinated (Supplementary Fig. 7).

To determine whether ubiquitin–proteasome system impairment causes accumulation of mutant PFN1 aggregates, transfected N2A cells were exposed to the proteasome inhibitor MG132. ALS-linked PFN1 mutants, including E117G, showed increased insoluble protein levels and increased levels of higher molecular mass species by western blot analysis. Minimal insoluble protein was observed for the wild-type PFN1 protein (Fig. 2b). PFN1 staining in N2A cells and PMNs confirmed these results. Cells expressing C71G, M114T and G118V mutant PFN1 had numerous, large aggregates after MG132 treatment. E117G mutants showed a moderate aggregate level, and the wild-type protein displayed minimal levels (Supplementary Figs 8 and 9).

Given the propensity of mutant PFN1 to form aggregates, we investigated whether other ALS-related proteins may be present within these aggregates. Thus, we transfected PMNs with mutant PFN1 and tested for alterations in the cellular localization of the ALS-related proteins FUS and TDP-43. Furthermore, we also tested for alterations in the spinal muscular atrophy-related protein SMN owing to its ability to bind PFN1 (ref. 13). No co-aggregation of either FUS or SMN with mutant PFN1 was observed (Supplementary Figs 10 and 11). However, ~30–40% of cells contained cytoplasmic PFN1 aggregates co-stained with TDP-43 (Fig. 2f). These results suggest that mutant PFN1 may contribute to ALS pathogenesis by inducing aggregation of TDP-43. On the basis of these observations, we investigated whether aggregates of TDP-43 contain PFN1 by staining spinal cord tissues from 18 SALS cases displaying TDP-43 pathology and 6 non-ALS controls without TDP-43 pathology (Supplementary Fig. 12). Abnormal PFN1 pathology was not discovered in SALS cases, suggesting that TDP-43 aggregation does not induce PFN1 aggregation. Expression of the carboxy-terminal fragment of TDP-43, which produces insoluble aggregates, in PMNs also failed to co-aggregate wild-type PFN1, thus supporting this observation (Supplementary Fig. 13).

Evaluation of the PFN1–actin complex crystal structure showed that all ALS-linked mutations lie in close proximity to actin-binding residues of PFN1 (ref. 14; Fig. 3a). Therefore, we investigated whether the ALS-linked mutations display a decreased level of bound actin. Towards this end, we performed immunoprecipitation and western blot analysis of cells transfected with wild-type and mutant PFN1. As a control, we also transfected cells with a construct expressing a synthetic PFN1(H120E) mutant protein. This alteration is located at a crucial residue previously shown to abolish PFN1 binding to actin<sup>12</sup>. We observed that C71G, M114T, G118V and H120E mutants had reduced levels of bound actin relative to wild-type PFN1 (Fig. 3b).

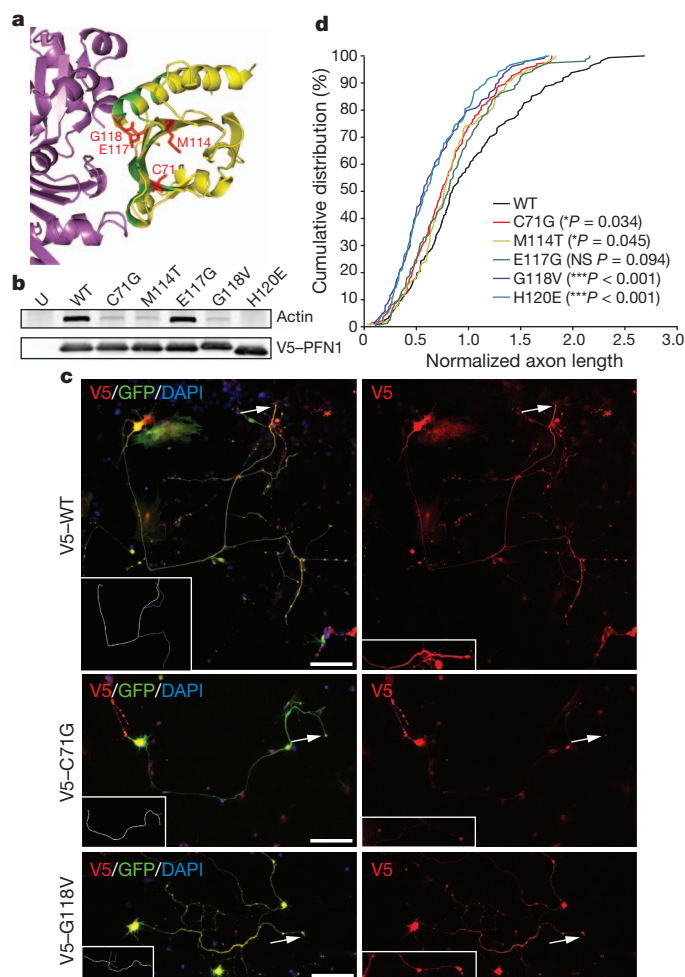


**Figure 3 | Mutant PFN1 inhibits axon outgrowth.** **a**, PFN1–actin interaction region (Protein Data Bank accession 2BTF) using the PyMOL Molecular Graphics System (v.1.4). Magenta: actin; yellow: PFN1; green: actin-binding PFN1 residues; red: ALS-linked mutated PFN1 residues. **b**, Transfected HEK293 cells were immunoprecipitated with a V5 antibody and then immunoblotted with antibodies for either V5–PFN1 or actin. **c**, PMNs transfected with wild-type or mutant V5–PFN1 and a green fluorescent protein (GFP)-expressing construct were stained to detect V5–PFN1. The axon tip, indicated by arrows, is enlarged in the inset, right panel. Scale bars, 100  $\mu$ m. **d**, Cumulative distribution of axon lengths relative to the mean of wild-type PFN1-transfected cells was plotted.  $P$  values are given in the legend ( $n = 104$ –161 cells from four independent experiments).

The E117G mutant did not show a reduction of bound actin relative to wild-type PFN1.

Previous reports have shown that PFN1 protein alterations inhibit neurite outgrowth<sup>12,15</sup>. We investigated whether ALS-linked PFN1 mutants inhibit neurite outgrowth by measuring axonal length in PMNs transfected with wild-type or mutant PFN1. As a positive control, we also transfected PMNs with the H120E-expressing construct. In addition to lacking actin-binding ability, the H120E protein inhibits neurite outgrowth<sup>12</sup>. As expected, the H120E-expressing cells displayed a pronounced decrease in axon length relative to the wild-type construct (Fig. 3d). Three ALS-linked PFN1 mutations (C71G, M114T and G118V) also showed a significant decrease in axon outgrowth (Fig. 3c, d). In particular, the G118V-associated reduction is similar to that observed with the H120E construct. Axon outgrowth inhibition was observed with the E117G mutant but did not reach statistical significance. These results suggest that mutations in PFN1 may contribute to ALS pathogenicity in part by inhibiting axon dynamics.

The regulation of actin dynamics in the growth cone is necessary for axon outgrowth. Defects in PFN1 are associated with growth cone



arrest and reduced axon outgrowth in embryonic motor neurons of *Drosophila*<sup>15</sup>. To determine whether ALS-linked PFN1 mutants have a similar phenotype, PMNs transfected with wild-type and two mutant *PFN1* constructs (C71G and G118V) were stained to detect F- and G-actin localization patterns in the highly dynamic and actin-rich growth cone. These mutants were selected owing to their greater influence on axon outgrowth. PFN1 mutant expression in PMNs led to a significantly reduced growth cone size ( $\sim 43$ – $52\%$ ) relative to wild-type PFN1 (Fig. 4b). Also, mutant PFN1 expression significantly altered growth cone morphology. In wild-type PFN1-expressing cells, growth cones had elaborate structures with several F-actin rich filopodia (Fig. 4a), whereas virtually no filopodia were visible in the mutant PFN1 growth cones. Similar results were observed for the synthetic H120E mutant defective in actin binding. The growth cones in mutant-expressing PMNs also had a lower ratio of F/G-actin relative to wild-type-expressing PMNs (Fig. 4c). In particular, the C71G mutant-expressing PMNs displayed an F/G-actin ratio 24.4% of the wild-type expressing PMNs. These results suggest that mutant PFN1 can inhibit the conversion of G-actin to F-actin within the growth cone region, thus affecting its morphology.

*PFN1* expression is ubiquitous in non-muscle cells, whereas *PFN2* is expressed in brain and neuronal tissues<sup>16</sup>, and *PFN3* in the testis<sup>17</sup>. To determine whether mutations in *PFN2* or *PFN3* may also contribute to FALS, we sequenced the entire coding sequence of both genes in 274 FALS cases. In contrast to *PFN1*, no non-synonymous alterations were observed in these FALS cases (Supplementary Table 6), which suggests that *PFN2* and *PFN3* mutations are not an important cause of FALS.

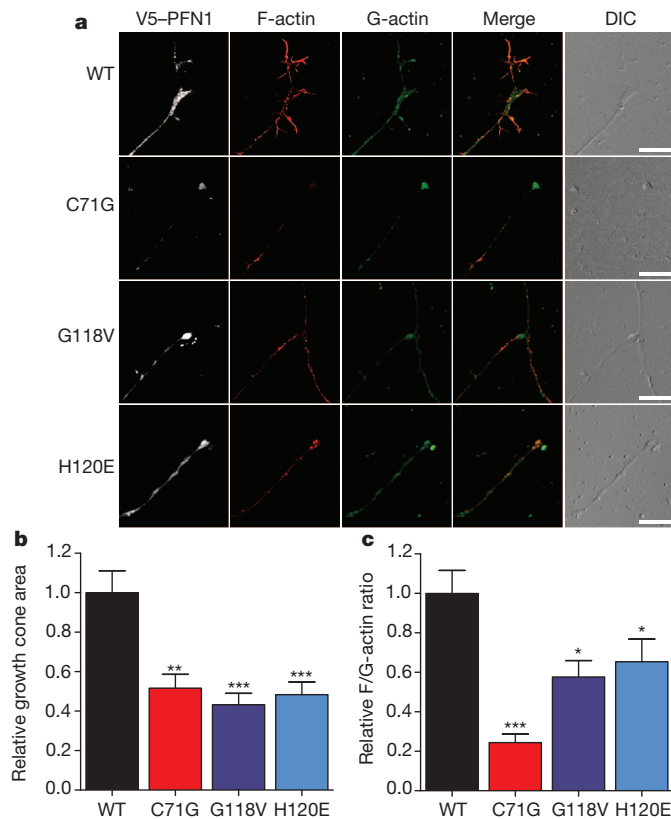


**Figure 4 | Mutant PFN1 reduces growth cone size and F/G-actin expression.** **a**, PMNs were transfected with either wild-type or mutant V5-PFN1. At 3 days after transfection, cells were fixed and stained to detect V5-PFN1, F-actin (phalloidin, red) and G-actin (DNase I, green). The growth cone region of representative cells is shown. Scale bars, 10  $\mu$ m. **b**, **c**, The growth cone area (**b**) and F/G-actin expression (**c**) of transfected cells were determined and plotted. Comparisons to the wild-type V5-PFN1-transfected cells were made using one-way ANOVA testing. \* $P < 0.05$ ; \*\* $P < 0.01$ ; \*\*\* $P < 0.001$  ( $n = 27$ – $35$  cells from three independent experiments). Error bars indicate s.e.m.

Here, we have applied exome sequencing to two large families displaying ALS. Through this approach, we were able to restrict the number of causal candidates in each family to two and three genes. Fortunately, both families had mutations in the same gene, *PFN1*. Although we cannot rule out the possibility that mutations in other candidate genes may be causative, several lines of evidence demonstrate *PFN1* as the causative gene. First, we identified a further five families with mutations in the *PFN1* gene, including a third large family in which we confirmed segregation of the mutations. Second, mutant PFN1 displayed aggregation propensities analogous to those of other proteins implicated in neurodegenerative diseases such as ALS. Third, the mutants displayed several functional differences compared with the wild-type protein, including a lower bound actin level, an axonal outgrowth inhibition, and growth cone size reduction. Taken together, these results strongly support the view that mutations in the *PFN1* gene cause familial ALS.

*PFN1* is an intensely studied protein owing in part to its regulation of actin polymerization. *PFN1* promotes nucleotide exchange on actin, converting monomeric ADP-actin to ATP-actin<sup>10</sup>. *PFN1*–ATP-actin complexes can bind to the fast-growing end of actin filaments. Dissociation of the complex allows the ATP-actin monomer to be added to the growing actin filament<sup>18</sup>. Here we show that mutant *PFN1* may contribute to ALS pathogenesis by altering actin dynamics and inhibiting axon outgrowth. Similarly, expression of either mutant SOD1 (ref. 19) or mutant TDP-43 (ref. 20) inhibits neurite outgrowth, and primary neurons from *FUS*-deficient mice have reduced spine numbers and abnormal morphology<sup>21</sup>. These observations suggest a common pathogenic feature among diverse ALS genes. However, there is also the possibility that alterations to other *PFN1* functions may contribute to the pathogenesis. *PFN1* is also a complex regulator of cellular processes through its interactions with several proteins. Indeed, it has been shown to interact directly with more than 50 proteins (reviewed in ref. 22). Of interest, *PFN1* directly interacts with three proteins that, when mutated, cause neurodegenerative disease—VCP (ALS-frontotemporal dementia, inclusion body myositis and Paget's disease)<sup>16</sup>; SMN (spinal muscular atrophy)<sup>13</sup>; and HTT (Huntington's disease)<sup>23</sup>.

There is increasing evidence that cytoskeletal defects have a major role in motor neuron diseases. Rarely, mutations in genes encoding neurofilament heavy polypeptide (NEFH)<sup>24</sup>, peripherin (PRPH)<sup>25</sup> and dynactin (DCTN1)<sup>26</sup> are associated with ALS. Spastin<sup>27</sup> and KIF5A (ref. 28) are mutated in hereditary spastic paraplegia, whereas Charcot-Marie-Tooth neuropathy type 2E (ref. 29) is caused by mutations in the neurofilament light polypeptide (NEFL) gene. Furthermore, several mouse models clearly document that defects in cytoskeletal proteins can cause motor neuron disease (see ref. 30 for a review). Here we report that mutations in the *PFN1* gene account for 1–2% of FALS. Our observations emphasize that disruption of cytoskeletal pathways contribute importantly to ALS pathogenesis.

## METHODS SUMMARY

Exome sequencing was accomplished using an exome array (SeqCap EZ Exome Library, Nimblegen) adapted for sequencing on the Illumina DNA sequencing platform. Alignment of sequence to the human genome and variant detection was accomplished using the applications SOAPaligner and SOAPsnp. Expression constructs for wild-type and mutant *PFN1* were transfected into N2A cells using Lipofectamine 2000 (Invitrogen). Inhibition of proteasome activity in N2A cells was performed by incubation with 10  $\mu$ M MG132 (Sigma-Aldrich) after transfection for 16h before collection. Insolubility of *PFN1* mutants was assessed by sequential NP-40/urea protein extraction followed by western blot analysis. Transfected HEK293 cells were lysed at 24 h with RIPA buffer and immunoprecipitated with an anti-V5 antibody to investigate the interactions of *PFN1* and actin. Primary motor neurons were isolated and cultured from embryonic day (E)13.5 mouse embryos and transfected by magnetofection. Axon length measurements were determined from low magnification images ( $\times 10$ ). The length of the longest axon branch was measured using ImageJ plug-in NeuronJ. F-actin and G-actin were labelled with fluorescent-conjugated Phalloidin (Invitrogen) and DNase I



(Invitrogen), respectively. Deconvolution of images was performed using Autoquant (MediaCybernetics). The growth cone area and the fluorescence intensity for F-actin and G-actin staining were measured using ImageJ software.

**Full Methods** and any associated references are available in the online version of the paper.

**Received 12 January; accepted 31 May 2012.**

**Published online 15 July 2012.**

- Kabashi, E. *et al.* *TARDBP* mutations in individuals with sporadic and familial amyotrophic lateral sclerosis. *Nature Genet.* **40**, 572–574 (2008).
- Sreedharan, J. *et al.* TDP-43 mutations in familial and sporadic amyotrophic lateral sclerosis. *Science* **319**, 1668–1672 (2008).
- Kwiatkowski, T. J. Jr *et al.* Mutations in the *FUS/TLS* gene on chromosome 16 cause familial amyotrophic lateral sclerosis. *Science* **323**, 1205–1208 (2009).
- Vance, C. *et al.* Mutations in *FUS*, an RNA processing protein, cause familial amyotrophic lateral sclerosis type 6. *Science* **323**, 1208–1211 (2009).
- Johnson, J. O. *et al.* Exome sequencing reveals VCP mutations as a cause of familial ALS. *Neuron* **68**, 857–864 (2010).
- DeJesus-Hernandez, M. *et al.* Expanded GGGGCC exanucleotide repeat in noncoding region of *C9ORF72* causes chromosome 9p-linked FTD and ALS. *Neuron* **72**, 245–256 (2011).
- Deng, H. X. *et al.* Mutations in *UBQLN2* cause dominant X-linked juvenile and adult-onset ALS and ALS/dementia. *Nature* **477**, 211–215 (2011).
- Renton, A. E. *et al.* A hexanucleotide repeat expansion in *C9ORF72* is the cause of chromosome 9p21-linked ALS-FTD. *Neuron* **72**, 257–268 (2011).
- Gijssels, I. *et al.* A *C9orf72* promoter repeat expansion in a Flanders-Belgian cohort with disorders of the frontotemporal lobar degeneration-amyotrophic lateral sclerosis spectrum: a gene identification study. *Lancet Neurol.* **11**, 54–65 (2012).
- Mockrin, S. C. & Korn, E. D. Acanthamoeba profilin interacts with G-actin to increase the rate of exchange of actin-bound adenosine 5'-triphosphate. *Biochemistry* **19**, 5359–5362 (1980).
- Landers, J. E. *et al.* Reduced expression of the *Kinesin-Associated Protein 3* (*KIFAP3*) gene increases survival in sporadic amyotrophic lateral sclerosis. *Proc. Natl Acad. Sci. USA* **106**, 9004–9009 (2009).
- Suetsugu, S. *et al.* The essential role of profilin in the assembly of actin for microspike formation. *EMBO J.* **17**, 6516–6526 (1998).
- Giesemann, T. *et al.* A role for polyproline motifs in the spinal muscular atrophy protein SMN. *J. Biol. Chem.* **274**, 37908–37914 (1999).
- Schutt, C. E. *et al.* The structure of crystalline profilin- $\beta$ -actin. *Nature* **365**, 810–816 (1993).
- Wills, Z. *et al.* Profilin and the Abl tyrosine kinase are required for motor axon outgrowth in the *Drosophila* embryo. *Neuron* **22**, 291–299 (1999).
- Witke, W. *et al.* In mouse brain profilin I and profilin II associate with regulators of the endocytic pathway and actin assembly. *EMBO J.* **17**, 967–976 (1998).
- Braun, A. *et al.* Genomic organization of profilin-III and evidence for a transcript expressed exclusively in testis. *Gene* **283**, 219–225 (2002).
- Tilney, L. G. *et al.* Actin from *Thyone* sperm assembles on only one end of an actin filament: a behavior regulated by profilin. *J. Cell Biol.* **97**, 112–124 (1983).
- Takeuchi, H. *et al.* Hsp70 and Hsp40 improve neurite outgrowth and suppress intracytoplasmic aggregate formation in cultured neuronal cells expressing mutant SOD1. *Brain Res.* **949**, 11–22 (2002).
- Duan, W. *et al.* MG132 enhances neurite outgrowth in neurons overexpressing mutant TAR DNA-binding protein-43 via increase of HO-1. *Brain Res.* **1397**, 1–9 (2011).
- Fujii, R. *et al.* The RNA binding protein TLS is translocated to dendritic spines by mGluR5 activation and regulates spine morphology. *Curr. Biol.* **15**, 587–593 (2005).
- Witke, W. The role of profilin complexes in cell motility and other cellular processes. *Trends Cell Biol.* **14**, 461–469 (2004).
- Shao, J. *et al.* Phosphorylation of profilin by ROCK1 regulates polyglutamine aggregation. *Mol. Cell Biol.* **28**, 5196–5208 (2008).
- Al-Chalabi, A. *et al.* Deletions of the heavy neurofilament subunit tail in amyotrophic lateral sclerosis. *Hum. Mol. Genet.* **8**, 157–164 (1999).
- Gros-Louis, F. *et al.* A frameshift deletion in peripherin gene associated with amyotrophic lateral sclerosis. *J. Biol. Chem.* **279**, 45951–45956 (2004).
- Puls, I. *et al.* Mutant dynactin in motor neuron disease. *Nature Genet.* **33**, 455–456 (2003).
- Hazan, J. *et al.* Spastin, a new AAA protein, is altered in the most frequent form of autosomal dominant spastic paraplegia. *Nature Genet.* **23**, 296–303 (1999).
- Reid, E. *et al.* A kinesin heavy chain (*KIF5A*) mutation in hereditary spastic paraplegia (SPG10). *Am. J. Hum. Genet.* **71**, 1189–1194 (2002).
- Mersiyanova, I. V. *et al.* A new variant of Charcot-Marie-Tooth disease type 2 is probably the result of a mutation in the neurofilament-light gene. *Am. J. Hum. Genet.* **67**, 37–46 (2000).
- Perrot, R. & Eyer, J. Neuronal intermediate filaments and neurodegenerative disorders. *Brain Res. Bull.* **80**, 282–295 (2009).

**Supplementary Information** is linked to the online version of the paper at [www.nature.com/nature](http://www.nature.com/nature).

**Acknowledgements** Support was provided by the ALS Therapy Alliance, Project ALS, P2ALS, the Angel Fund, the Pierre L. de Bourgneault ALS Research Foundation, the Al-Athel ALS Research Foundation, the ALS Family Charitable Foundation and a Francesco Caleffi donation (N.T. and V.S.). Grant support was provided by the National Institutes of Health (NIH)/National Institute of Neurological Disorders and Stroke (NINDS) (1R01NS065847 (J.E.L.), 1R01NS050557 (R.H.B.), and RC2-NS070-342 (R.H.B.)), Muscular Dystrophy Association (MDA173851 (W.R.)) and AriSLA co-financed with support of '5x1000'—Healthcare research of the Ministry of Health (EXOMEFALS (N.T., C.G., V.S. and J.E.L.)). Support was provided by an SMA Europe fellowship to C.F. P.C.S. was supported through the auspices of H. R. Horvitz (Massachusetts Institute of Technology), an investigator of the Howard Hughes Medical Institute. We thank the laboratory of S. Duxey, the UMass Medical School Digital Light Microscopy Core, the UMass Medical School Deep Sequencing Core, the Emory University Neuropathology Core, and M. Gearing and D. Cooper for their assistance.

**Author Contributions** Sample collection, preparation and clinical evaluation: N.T., P.C.S., D.M.-Y., F.T., C.T., J.D.G., G.S., F.S., V.M., A.R., C.G., V.S., V.E.D., R.H.B. Performed experiments and data analysis: C.-H.W., C.F., N.T., P.J.K., P.C.S., K.P., P.L., D.M.B., J.E.K., P.G.-P., A.D.F., M.K., J.A., F.T., C.T., A.L.L., S.C.C., E.T.C., D.A.B., J.E.L. Scientific planning and direction: C.-H.W., C.F., N.T., D.M., M.J.M., J.A.Z., Z.-S.X., L.H.V., J.D.G., D.B.G., V.M., W.R., A.R., C.G., D.A.B., G.J.B., V.S., V.E.D., R.H.B., J.E.L. Initial manuscript preparation: C.-H.W., C.F., N.T., W.R., D.A.B., G.J.B., V.S., R.H.B., J.E.L.

**Author Information** Reprints and permissions information is available at [www.nature.com/reprints](http://www.nature.com/reprints). The authors declare no competing financial interests. Readers are welcome to comment on the online version of this article at [www.nature.com/nature](http://www.nature.com/nature). Correspondence and requests for materials should be addressed to J.E.L. ([john.landiers@umassmed.edu](mailto:john.landiers@umassmed.edu)).

## METHODS

**Human subjects.** DNA samples were collected from familial and sporadic ALS cases and control individuals after informed consent was obtained. All protocols were approved by the Institutional Review Boards at the institutions involved. All familial ALS samples were prescreened for common mutations/expansions in *SOD1*, *FUS*, *TARDBP*, *C9orf72*, *VCP*, *VAPB* and *ANG*. A subset of the samples was obtained from the NINDS Repository at Coriell Cell Repositories.

**Plasmids and cloning.** PFN1 expression vectors with V5 epitope tags were constructed using the backbone pcDNA3.1/nV5-DEST (Invitrogen) by way of Gateway Technology according to manufacturer's protocol. In brief, attB-flanked primers were used to amplify PFN1 from human complementary DNA samples (Supplementary Table 9). The PCR product was recombined into pDONR221 to create the entry clone. pDONR221-PFN1 was then recombined with pcDNA3.1/nV5-DEST to create the wild-type PFN1 expression vector. For establishment of mutant PFN1 plasmids, site-directed mutagenesis was performed according to manufacturer's protocol (Quickchange Multi Site-Directed Mutagenesis Kit, Agilent). All constructs were verified by DNA sequencing. A plasmid map is shown in Supplementary Fig. 14.

**Linkage analysis and exome sequencing.** Linkage peaks were identified by subjecting DNA to genome-wide genotyping using the Affymetrix 10K SNP arrays and analysed using the software application Allegro v2.0 (ref. 31) to generate multi-point lod scores. Only affected members (and married-in samples) were used for the analysis. Targeted exome capture and deep sequencing was accomplished using a exome array (SeqCap EZ Exome Library, Nimblegen) adapted for sequencing on the Illumina DNA sequencing platform<sup>32</sup>. Paired-end sequencing was performed on either an Illumina Genome Analyzer II or HiSeq2000. Alignment to the human genome (hg19) was accomplished using SOAPaligner<sup>33</sup> and quality control assessments were performed using SOAPcoverage. Variants were detected in each sample with the application SOAPsnp<sup>34</sup> using the default settings. A minimum quality score of 10 was required to define a variant. The conversion of variants to amino acid position was accomplished using the software application SIFT<sup>35</sup> based on Ensembl annotation release 55. Filtering of variants was accomplished with a custom designed database using data from the 1000 Genomes Project (May 2011 release)<sup>36</sup> and the NHLBI ESP Exome Variant Server (5,379 sequenced exomes; <http://evs.gs.washington.edu/EVS/>).

**Mutation screening.** Repeat expansion PCR for the hexanucleotide repeat expansion in the *C9orf72* gene was performed as previously described<sup>6</sup>. Sequencing of PFN1, PFN2, PFN3 and intron 2 of PFN1 was performed by touchdown PCR (30 cycles with annealing temperature starting at 65 °C and decreasing 0.5 °C per cycle, followed by 15 cycles with an annealing temperature of 65 °C), using primers with M13 tails (Supplementary Table 9). Amplification was performed using either AmpliTaq Gold (Applied Biosystems) or AccuPrime GC rich Polymerase (Invitrogen). DNA samples were extracted from either lymphoblastoid cell lines or whole blood; a subset of the samples was whole genome amplified using the GenomiPhi DNA amplification kit (GE Healthcare Lifesciences). PCR products were subsequently purified by incubation with exonuclease I and shrimp alkaline phosphatase, and sequenced at the Massachusetts General Hospital DNA Core Facility). Sequence analysis was performed using the PHRED/PHRAP/Consed software suite (<http://www.phrap.org/>) and variations in the sequences were identified with the Polyphred v6.15 software (<http://droog.gs.washington.edu/polyphred/>). The sequencing primers are listed in Supplementary Table 9.

**Cell culture and transfections of N2A cells.** N2A cells were maintained in MEM with 10% fetal bovine serum, 2 mM L-glutamine and 100 U penicillin per 100 µg streptomycin at 5% CO<sub>2</sub>. For cell lysis and western blot analyses, transfections were performed in 6-well plates with 4 µg of plasmid DNA using Lipofectamine 2000 (Invitrogen) according to the manufacturer's protocol. For immunofluorescence, cells were plated onto 12-mm round coverslips in 24-well plates and transfected with 0.8 µg of DNA.

**Immunofluorescence of N2A cells.** Immunofluorescence was performed as previously described<sup>37</sup>. In brief, at 48 h after transfection, cells were fixed with 4% paraformaldehyde at room temperature for 15 min, permeabilized with 1% Triton X-100 at room temperature for 10 min, and then blocked with blocking buffer (50 mM NH<sub>4</sub>Cl, 10 mg ml<sup>-1</sup> BSA, 2% natural goat serum, 0.1% Triton X-100 in Dulbecco's PBS) at 37 °C for 1 h. Appropriate fluorophore-conjugated antibody was diluted in dilution buffer (0.1% Triton X-100, 0.15% goat serum in Dulbecco's PBS) and added at 4 °C overnight. After three washes with PBST (0.1% Tween-20), cells were mounted with Vectashield Hard Set Mounting Medium containing DAPI (Vector Laboratories). Confocal images were obtained with a ×100 Plan Apo oil objective lens on a Nikon TE-2000E2 inverted microscope (Nikon Instruments) with a Yokogawa CSU10 Spinning Disk Confocal Scan Head (Solanere Technology Group) and processed with ImageJ software. For confocal imaging, mouse Dylight 549-V5 antibody (1:100, AbDserotec) and rabbit Dylight 488-ubiquitin antibody (1:100, Enzo Life Sciences) were used. For aggregate

counting, mouse Alexa Fluor 488-V5 antibody (1:100, AbDserotec) was used. To count the number of cells containing insoluble aggregates, images were obtained with a Zeiss Axioskop 2 microscope with a ×100 objective. The images were processed with MetaMorph (v.7.5, Molecular Devices) image analysis software.

**Fractionation of insoluble/soluble PFN1 and western blotting.** Transfected cells were washed with cold PBS and then scraped directly in NP-40 lysis buffer (1% NP-40, 20 mM Tris-HCl, pH 7.4, 150 mM NaCl, 5 mM EDTA, 10% glycerol, 1 mM dithiothreitol (DTT), 10 mM sodium fluoride, 1 mM sodium orthovanadate and 5 mM sodium pyrophosphate) with EDTA-free protease inhibitors (Roche). The lysates were rotated for 30 min at 4 °C followed by centrifugation at 15,800g for 20 min. The supernatant was removed and used as the soluble fraction. To remove carryovers, the pellet was washed with lysis buffer, and then resuspended in urea-SDS buffer (NP-40 lysis buffer with 8 M urea, 3% SDS) followed by sonication. The lysate was then spun again for 20 min at 4 °C and the supernatant was removed (insoluble fraction). Protein concentrations were determined by the BCA assay. Western blot detection was performed on Odyssey Infrared Imager (Li-Cor Biosciences). Antibodies for western blotting are as follows: mouse monoclonal anti-GAPDH (1:1,000, Sigma-Aldrich); mouse monoclonal anti-V5 (1:2,000, Invitrogen); polyclonal IRDye 800CW goat anti-mouse IgG (1:8,000, LI-COR); polyclonal IRDye 680 goat anti-rabbit IgG (1:8,000, LI-COR); and polyclonal IRDye 800CW goat anti-rabbit IgG (1:8,000, LI-COR). To inhibit proteasome activity in N2A cells, cells were incubated with 10 µM MG132 (Sigma-Aldrich) after transfection for 16 h before collection.

**Immunoprecipitations.** V5-PFN1-transfected HEK293 cells were lysed at 24 h with RIPA buffer (150 mM NaCl, 50 mM Tris-HCl, pH 7.5, 1% NP40, 0.1% SDS, 0.5% sodium deoxycholate, 5 mM EDTA, 10 mM sodium fluoride, 1 mM sodium orthovanadate and 1× protease inhibitor cocktail). The lysates were precleared with Dynabeads Protein G (Invitrogen) followed by immunoprecipitation with 1 µg anti-V5 antibody at 4 °C overnight followed by incubation with Dynabeads Protein G for 1 h. The protein-bead complexes were washed four times with RIPA buffer, eluted by boiling at 95 °C for 5 min and then subjected to western blot analysis to detect V5-PFN1 and actin. Antibodies: mouse anti-V5 (1:5,000, Invitrogen); mouse anti-β-actin (1:1,000, Sigma); and goat anti-mouse 800CW (1:10,000, LICOR). To demonstrate conjugation of mutant PFN1 by ubiquitin, HA-ubiquitin was co-transfected into N2A with either V5-PFN1(C71G) or V5 vector at a ratio of 1:1. At 48 h after transfection, cells were lysed and soluble fractions were prepared as described above. NP-40-resistant pellets were further dissolved in RIPA buffer and immunoprecipitated with 1 µg anti-V5 antibody and washed with lysis buffer three times. Western blot analysis was performed with an anti-HA-biotin antibody (1:2,000, sigma) and IRDye 800CW streptavidin (1:2,000, LI-COR). After stripping the membrane, it was reprobed with mouse anti-V5 antibody (1:5,000, Invitrogen).

**Primary motor neuron culture, transfection and immunofluorescence.** Primary motor neurons from embryonic day (E)13.5 mouse embryos were isolated, cultured and transfected as previously described<sup>38</sup>. Ubiquitin protein fused to an HA tag was cloned into the pcDNA plasmid by PCR amplification. To inhibit proteasome activity, cells were treated with 10 µM MG132 for 12 h. Motor neurons were fixed for 15 min with 4% paraformaldehyde in PBS two or three days after transfection, as indicated. Anti-V5 (1:1,000; Invitrogen), HA (1:1,000; Cell Signaling Technology), TDP-43 (1:500, ProteinTech Group), FUS (1:500, Bethyl labs), SMN (1:500, Santa Cruz) and PFN1 (1:500, Sigma) antibodies were incubated overnight at 4 °C. Dylight488-, Cy3-, Cy2- or Cy5-conjugated secondary antibodies (Jackson ImmunoResearch) were incubated for 1 h at room temperature. Cell staining with anti-PFN1 and anti-V5 yielded overlapping staining patterns (Supplementary Fig. 15). F-actin and G-actin were labelled with rhodamine-conjugated phalloidin (1:1,000, Invitrogen) and Alexa488-DNase I (1:250, Invitrogen), respectively. Z-series (5–10 sections, 0.2 µm thickness) were acquired with an epifluorescence microscope (Ti, Nikon) equipped with a cooled CCD camera (HQ2, Photometrics). Images were deconvolved (Autoquant, MediaCybernetics) and analysed. The growth cone area and the fluorescence intensity for F-actin and G-actin staining was measured using ImageJ software. The ratio between the two values was averaged and compared between different conditions. Statistical significance was assessed using Kruskal-Wallis one-way ANOVA test and Dunn's post-hoc test. For the analysis of axon length, cells were fixed and stained to detect V5-PFN1 at 3 days after transfection. Low magnification images (×10) were acquired and, if necessary, reassembled in Adobe Photoshop. The axon was identified morphologically as the longest neurite. The length of the longest axon branch was measured using ImageJ plug-in NeuronJ<sup>39</sup>. Statistical significance was assessed with the Kolmogorov-Smirnov test.

**Immunohistochemistry.** Paraffin-embedded sections from post-mortem human spinal cord (8 µm thick) were deparaffinized and endogenous peroxidase activity was blocked with 3% hydrogen peroxide at 40 °C. Sections were then incubated

with normal horse serum for 15 min at 40 °C, followed by anti-PFN1 primary antibody (1:2,000, Sigma rabbit polyclonal) or anti-pTDP-43 (1:8,000, Cosmo Bio) diluted in 1% BSA overnight at 4 °C. The next day, sections were incubated with biotinylated secondary antibody for 30 min at 37 °C followed by avidin–biotin peroxidase complex (Vector Laboratories) for 60 min at 37 °C. DAB (3,3'-diaminobenzidine) was used as the chromogen (for colour development); tissues were then counterstained with haematoxylin.

31. Gudbjartsson, D. F. *et al.* Allegro, a new computer program for multipoint linkage analysis. *Nature Genet.* **25**, 12–13 (2000).
32. Choi, M. *et al.* Genetic diagnosis by whole exome capture and massively parallel DNA sequencing. *Proc. Natl Acad. Sci. USA* **106**, 19096–19101 (2009).
33. Li, R. *et al.* SOAP2: an improved ultrafast tool for short read alignment. *Bioinformatics* **25**, 1966–1967 (2009).
34. Li, R. *et al.* SNP detection for massively parallel whole-genome resequencing. *Genome Res.* **19**, 1124–1132 (2009).
35. Kumar, P. *et al.* Predicting the effects of coding non-synonymous variants on protein function using the SIFT algorithm. *Nature Protocols* **4**, 1073–1081 (2009).
36. The 1000 Genomes Project Consortium. A map of human genome variation from population-scale sequencing. *Nature* **467**, 1061–1073 (2010).
37. Bosco, D. A. *et al.* Wild-type and mutant SOD1 share an aberrant conformation and a common pathogenic pathway in ALS. *Nature Neurosci.* **13**, 1396–1403 (2010).
38. Fallini, C. *et al.* High-efficiency transfection of cultured primary motor neurons to study protein localization, trafficking, and function. *Mol. Neurodegener.* **5**, 17 (2010).
39. Meijering, E. *et al.* Design and validation of a tool for neurite tracing and analysis in fluorescence microscopy images. *Cytometry A* **58A**, 167–176 (2004).



# Chromatin organization is a major influence on regional mutation rates in human cancer cells

Benjamin Schuster-Böckler<sup>1,2</sup> & Ben Lehner<sup>1,3</sup>

**Cancer genome sequencing provides the first direct information on how mutation rates vary across the human genome in somatic cells<sup>1–7</sup>. Testing diverse genetic and epigenetic features, here we show that mutation rates in cancer genomes are strikingly related to chromatin organization. Indeed, at the megabase scale, a single feature—levels of the heterochromatin-associated histone modification H3K9me3—can account for more than 40% of mutation-rate variation, and a combination of features can account for more than 55%. The strong association between mutation rates and chromatin organization is upheld in samples from different tissues and for different mutation types. This suggests that the arrangement of the genome into heterochromatin- and euchromatin-like domains is a dominant influence on regional mutation-rate variation in human somatic cells.**

Comparative genomics and population studies suggest that human germline mutation rates are not constant across the genome<sup>8,9</sup>. Many genetic and epigenetic properties have been proposed to influence the rate of single nucleotide changes, including local base composition<sup>8,10</sup>, DNA replication timing<sup>8,11</sup>, chromatin structure<sup>12</sup> and the formation of double-strand breaks<sup>13</sup>. The sequencing of cancer genomes provides a unique opportunity to assess directly how mutation rates vary across the human genome<sup>1–7</sup>; by subtracting base changes observed in normal tissue from the same individual, a set of somatic single nucleotide variants (SNVs) can be derived. Moreover, the large number of genome-scale data sets available for human somatic cells enables the investigation of potential causes of mutation rate variation. It has been noted that tumours from different tissues show biases in mutation type<sup>2,3</sup> and evidence of transcription-coupled repair<sup>3,6</sup>. In addition, another study<sup>7</sup> showed that, at the 1-megabase (Mb) scale, there is substantial variation in the density of somatic mutations along the human genome and, moreover, that this regional variation in mutation density was correlated in three different tumour genomes. They also showed that somatic mutation rates measured in cancer genomes moderately correlate with those inferred in the germline from human–chimp sequence divergence<sup>7</sup> (Supplementary Fig. 1). However, so far, the individual features associated with mutation-rate variation explain very little of the regional variance across the genome<sup>7</sup>.

We gathered a total of 84,879 unique SNV positions from individual leukaemia<sup>5</sup>, melanoma<sup>3</sup>, small cell lung cancer<sup>2</sup> and prostate cancer<sup>4</sup> genomes. To identify potential causes of mutation-rate variation across the genome, we compiled a set of diverse genetic and epigenetic features that have been mapped genome-wide in human cells. In total we examined 46 features, including base composition, CpG content, gene density, DNA replication timing<sup>14</sup>, nucleosome occupancy<sup>15</sup>, long-range chromatin interactions (Hi-C)<sup>16</sup>, recombination rate<sup>17</sup>, the density of unique sequences (mappability of 24-base polymers<sup>18</sup>), levels of 18 histone acetylations<sup>19</sup>, levels of 17 histone methylations<sup>20</sup>, and occupancy of RNA polymerase II, the CTCF insulator protein and the histone variant H2AZ<sup>20</sup>. We then calculated the correlation coefficient for all pairwise combinations of features, including cancer SNV density, human–chimp divergence and germline single

nucleotide polymorphism (SNP) density, and clustered the features using these correlation coefficients as a distance metric.

Surprisingly, we found that at the megabase scale, cancer SNV density is strikingly correlated with many features of somatic cell chromatin organization (Fig. 1). The feature most strongly correlated with cancer SNV density is the repressive histone modification H3K9me3 ( $r = 0.64$ ,  $P < 2.2 \times 10^{-16}$ ). Positive correlations are also observed with other repressive marks including H3K9me2 ( $r = 0.53$ ,  $P < 2.2 \times 10^{-16}$ ) and H4K20me3 ( $r = 0.39$ ,  $P < 2.2 \times 10^{-16}$ ). In contrast, cancer SNV density anti-correlates with levels of many histone modifications associated with open chromatin, such as H3K4me3 ( $r = -0.59$ ,  $P < 2.2 \times 10^{-16}$ ) and H3K9ac ( $r = -0.59$ ,  $P < 2.2 \times 10^{-16}$ ). More moderate anti-correlation is observed with GC content ( $r = -0.47$ ,  $P < 2.2 \times 10^{-16}$ ), gene density ( $r = -0.42$ ,  $P < 2.2 \times 10^{-16}$ ), early replication timing ( $r = -0.30$ ,  $P < 2.2 \times 10^{-16}$ ) and the density of highly positioned nucleosomes ( $r = -0.43$ ,  $P < 2.2 \times 10^{-16}$ ). These conclusions are upheld when using alternative genomic window sizes (Fig. 1a): for example, the correlation with H3K9me3 is 0.37 at 100-kilobase resolution and 0.69 at 10-Mb resolution. We note that the weaker correlations when considering smaller window sizes may be due to the low median number of SNVs per window (Supplementary Fig. 10). Taken together this shows that, at least at the megabase scale, regional mutation-rate variation is strongly associated with regional variation in chromatin organization.

We used principal component analysis to investigate further the inter-dependencies among the different chromosome features. This revealed that at 1-Mb resolution, nearly 60% of the variance in these diverse features could be accounted for by a first principal component (Supplementary Fig. 3b). That is, the regional variation in many different genetic and epigenetic features can be captured by variation in a single underlying component along the genome. Features with a strong loading on this first principal component include many histone modifications and other features classically associated with either highly accessible euchromatin or inaccessible heterochromatin (Supplementary Fig. 3a). For example, the histone modifications H3K9me3 and H4K20me3 have strong negative loadings on this component, and GC content, gene density, early DNA replication and many activation marks show strong positive loadings (Supplementary Fig. 3a). Cancer SNV density also has a strong negative loading on this first component, consistent with the idea that somatic mutation rates in cancer cells are highest in inaccessible, heterochromatin-like regions and lowest in accessible euchromatin-like domains. In contrast, germline SNP density and human–chimp divergence have stronger loadings on the second orthogonal principal component (Supplementary Fig. 3). Indeed, consistent with previous findings<sup>13</sup> and an important role for background selection and/or genetic hitchhiking in determining human diversity levels<sup>21</sup>, germline SNP density is most positively correlated with the rate of recombination during meiosis ( $r = 0.45$ ,  $P < 2.2 \times 10^{-16}$ ).

To confirm that our conclusions were not tumour-type-specific, we also analysed the mutations from each cancer sample in isolation. The

<sup>1</sup>EMBL-CRG Systems Biology Unit, CRG and UPF, Barcelona 08003, Spain. <sup>2</sup>Pear Computer LLP, London W5 1SH, UK. <sup>3</sup>Institució Catalana de Recerca i Estudis Avançats (ICREA), Passeig Lluís Companys, 23, Barcelona 08010, Spain.

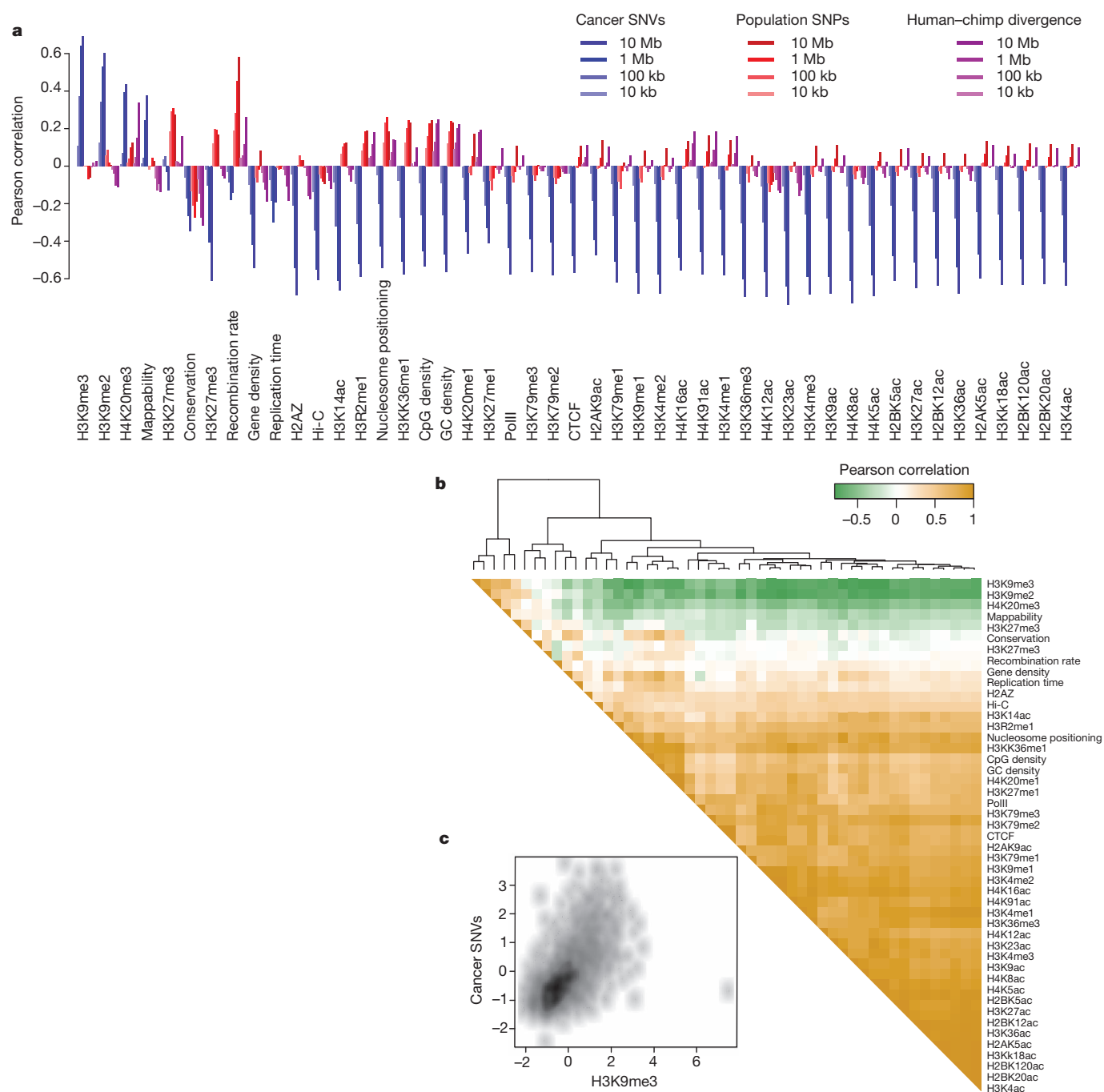


**Figure 1 | The density of somatic mutations in cancer genomes correlates with H3K9me3 modification levels and anti-correlates with genomic features associated with open chromatin.** **a**, Pearson correlation coefficients of cancer SNVs (blue), dbSNP density (red) and human-chimp divergence (purple) with genomic features in non-overlapping, non-repetitive windows of different sizes along the genome. **b**, The correlation matrix. Dark green denotes

negative and yellow positive correlation at 1-Mb resolution. **c**, Smoothed scatter-plot of cancer SNV density against H3K9me3 modification levels, both normalized to standard scores. Correlation plots for all other features are available in Supplementary Figs 5–8. The measure of replication timing used here is high for early replicating regions.

individual samples derived from distinct tissues and showed signatures of exposure to different environmental mutagens such as ultraviolet radiation in the melanoma<sup>3</sup> and carcinogens from tobacco smoke in the lung cancer sample<sup>2</sup>. However, SNV density is positively correlated with levels of H3K9me3 and negatively correlated with many features associated with open chromatin in each of the individual tumour samples, supporting the generality of our findings (Fig. 2).

Considering transition mutations separately from transversions, or CpG mutations separately from non-CpG mutations, also does not change our conclusions: elevated mutation rates are strongly associated with H3K9me3 (Fig. 3a) and other indicators of heterochromatin

(Supplementary Fig. 11), irrespective of the mutation type. Likewise, the association remains strong when considering only non-genic or only genic regions of the genome (Fig. 3b), so cannot be accounted for by transcription- or expression-coupled repair. The correlation is also strong when only considering SNVs surrounded by unique sequence (Fig. 3c and Supplementary Fig. 9), after filtering out regions of the genome with extreme GC content (Fig. 3c), and when excluding evolutionarily conserved bases (Fig. 3c). The association between chromatin organization and mutation-rate variation is therefore upheld for diverse tissue types, diverse mutation types and diverse genomic regions.

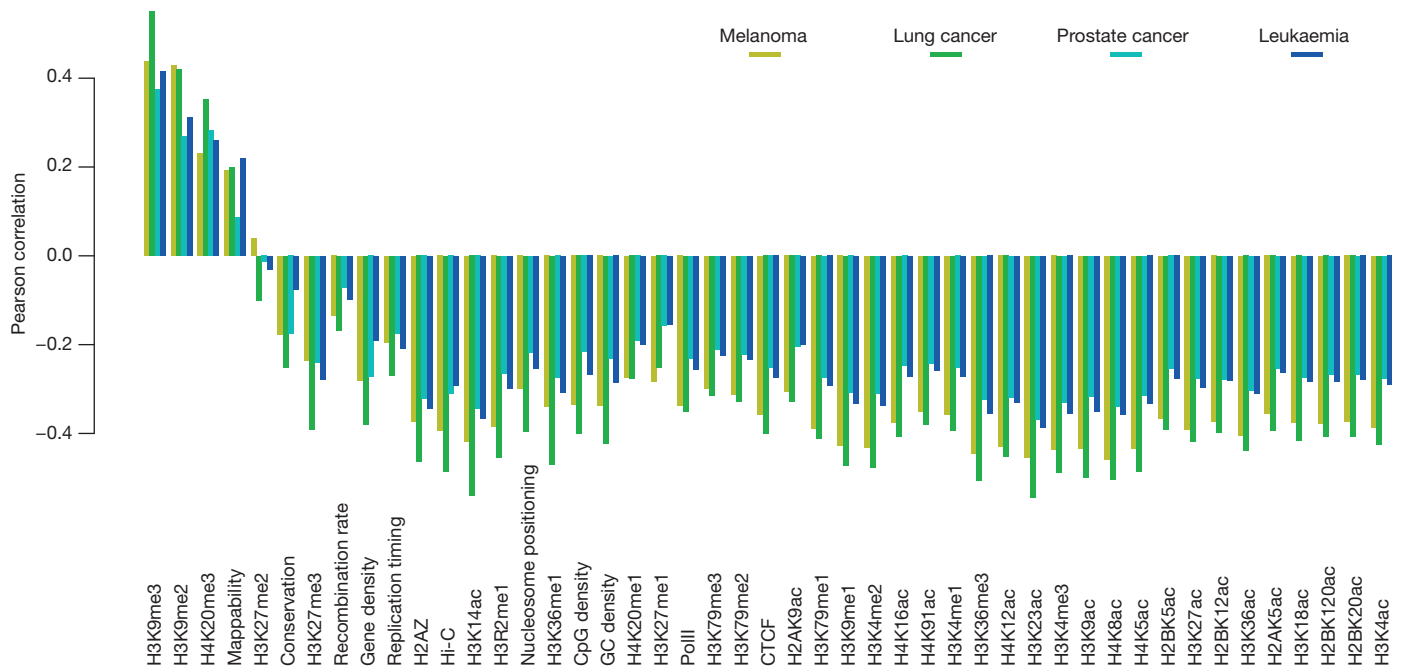


**Figure 2 | Correlation coefficients of SNV density from individual cancer genomes at 1-Mb resolution with diverse genetic and epigenetic features.**

Last, we examined the extent to which predictions of mutation-rate variation could be improved by combining the information from multiple genomic features. We used an iterative procedure to identify the combination of features that provide the best predictions in multiple linear regression models using increasing numbers of features (see Methods) and found that more than 55% of the variance in cancer SNV density along the genome could be explained by combining features (Fig. 4). In contrast, predictions of germline SNP density or human–chimp divergence never accounted for more than 35% of the variance, with recombination rate alone accounting for 20.5% of the observed variance in germline SNP density (Supplementary Fig. 4). In the cancer cells, H3K9me3 alone can account for more than 40% of the observed variance in SNV density. The remaining predictive features included in the models mark regions with open chromatin, or in the case of Hi-C, further distinguish the compartmental organization of the genome. The Hi-C metric used here is a measure devised previously<sup>16</sup> and uses genome-wide data on physical contacts between

regions through three-dimensional folding of the chromosome. It distinguishes between densely packed chromatin with strong short-range interactions and accessible euchromatin with a more diverse interaction pattern. The Hi-C metric anti-correlates with somatic SNV density ( $r = -0.55$ ,  $P < 2.2 \times 10^{-16}$ ), further supporting a model in which chromatin organization is a major determinant of variation in regional mutation rate.

The epigenetic modifications analysed here were not profiled in the same cell types as the somatic mutations, which suggests that the actual influence of chromatin organization on regional mutation rates may have been underestimated in our analyses. Furthermore, chromatin could also have an important influence on germline mutation rates, particularly if chromatin organization in the germline is substantially different to that in somatic cells<sup>22</sup>. An improved understanding of chromosome organization in the germline will be required to test this possibility.

However, at least in cancer cells, our analyses indicate that the dominant determinant of regional mutation rate variation is chromatin

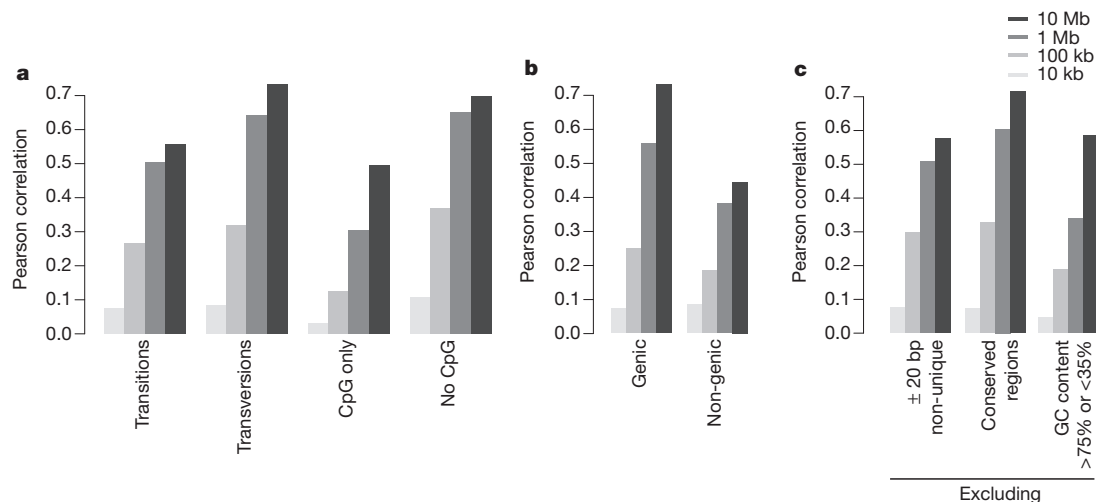


**Figure 3 | Chromatin organization predicts cancer genome mutation density for diverse mutation types and sequence contexts.** a–c, Correlations by mutation type (a), in genic or non-genic regions only (b), and only

considering SNVs surrounded by 20 base pairs of unique sequence, after filtering out regions of the genome with average GC density of less than 35% or more than 75%, or when excluding evolutionarily conserved bases (c) (see Methods).



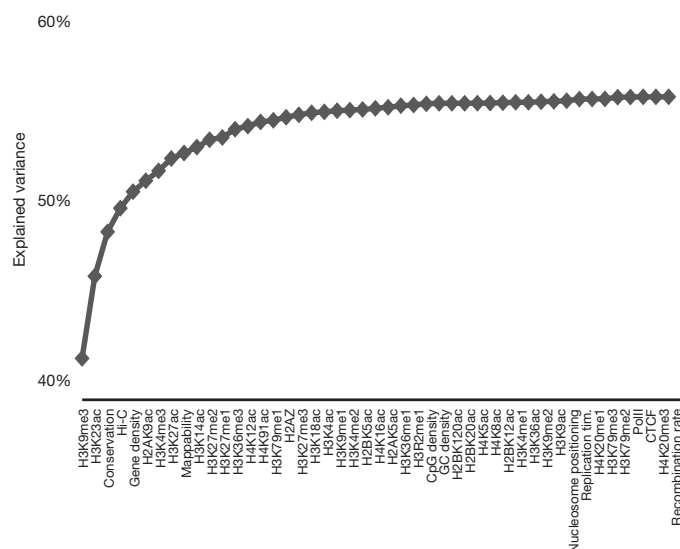


**Figure 4 | Prediction of cancer SNV density variation using integrated models.** Cumulative  $R^2$  of linear models, adding the feature on the x axis as a predictor at each step.

organization, with mutation rates elevated in more heterochromatin-like domains and repressed in more open chromatin. This could reflect differing accessibility to DNA repair complexes<sup>23</sup>, variation in the ability to signal repair<sup>24</sup> or perhaps increased exposure to mutagens at the nuclear periphery<sup>25</sup>. The somatic mutations considered here all arose in lineages that ultimately gave rise to tumours; although the mutation process may be different in tumour lineages, the tumours analysed here derive from diverse tissue types, which suggests the intriguing possibility that chromatin organization will be a major influence on regional mutation rates in all human somatic cells.

## METHODS SUMMARY

SNVs of human cancer cells were obtained from recent publications<sup>1–5</sup>. Germline polymorphisms were taken from dbSNP<sup>26</sup> and the 1000 genomes project<sup>27</sup>. Ensembl Compara provided the human–chimpanzee divergence data<sup>28</sup>. Histone methylation<sup>20</sup> and acetylation<sup>19</sup> states were mapped to the genome, as well as an array of additional genomic feature sets from various sources: recombination rate<sup>17</sup>, nucleosome positioning<sup>15,29</sup>, spatial proximity<sup>16</sup>, replication timing<sup>14</sup>, gene density and evolutionary conservation<sup>30</sup>. Genomes were then split into evenly sized windows, and windows with a high repeat content<sup>18</sup> were excluded to calculate Pearson correlations between features.

**Full Methods** and any associated references are available in the online version of the paper.

**Received 29 September 2011; accepted 31 May 2012.**

**Published online 22 July 2012.**

1. Ley, T. J. *et al.* DNA sequencing of a cytogenetically normal acute myeloid leukaemia genome. *Nature* **456**, 66–72 (2008).
2. Pleasance, E. D. *et al.* A small-cell lung cancer genome with complex signatures of tobacco exposure. *Nature* **463**, 184–190 (2010).
3. Pleasance, E. D. *et al.* A comprehensive catalogue of somatic mutations from a human cancer genome. *Nature* **463**, 191–196 (2010).
4. Berger, M. F. *et al.* The genomic complexity of primary human prostate cancer. *Nature* **470**, 214–220 (2011).

5. Puente, X. S. *et al.* Whole-genome sequencing identifies recurrent mutations in chronic lymphocytic leukaemia. *Nature* **475**, 101–105 (2011).
6. Lee, W. *et al.* The mutation spectrum revealed by paired genome sequences from a lung cancer patient. *Nature* **465**, 473–477 (2010).
7. Hodgkinson, A., Chen, Y. & Eyre-Walker, A. The large-scale distribution of somatic mutations in cancer genomes. *Hum. Mutat.* **33**, 136–143 (2012).
8. Wolfe, K. H., Sharp, P. M. & Li, W. H. Mutation rates differ among regions of the mammalian genome. *Nature* **337**, 283–285 (1989).
9. Ellegren, H., Smith, N. G. C. & Webster, M. T. Mutation rate variation in the mammalian genome. *Curr. Opin. Genet. Dev.* **13**, 562–568 (2003).
10. Cooper, D. N. & Krawczak, M. Cytosine methylation and the fate of CpG dinucleotides in vertebrate genomes. *Hum. Genet.* **83**, 181–188 (1989).
11. Stamatoiyannopoulos, J. *et al.* Human mutation rate associated with DNA replication timing. *Nature Genet.* **41**, 393–395 (2009).
12. Prendergast, J. G. D. *et al.* Chromatin structure and evolution in the human genome. *BMC Evol. Biol.* **7**, 72 (2007).
13. Lercher, M. J. & Hurst, L. D. Human SNP variability and mutation rate are higher in regions of high recombination. *Trends Genet.* **18**, 337–340 (2002).
14. Hansen, R. S. *et al.* Sequencing newly replicated DNA reveals widespread plasticity in human replication timing. *Proc. Natl Acad. Sci. USA* **107**, 139–144 (2010).
15. Schones, D. E. *et al.* Dynamic regulation of nucleosome positioning in the human genome. *Cell* **132**, 887–898 (2008).
16. Lieberman-Aiden, E. *et al.* Comprehensive mapping of long-range interactions reveals folding principles of the human genome. *Science* **326**, 289–293 (2009).
17. Kong, A. *et al.* A high-resolution recombination map of the human genome. *Nature Genet.* **31**, 241–247 (2002).
18. Dreszer, T. R. *et al.* The UCSC Genome Browser database: extensions and updates 2011. *Nucleic Acids Res.* **40**, D918–D923 (2012).
19. Wang, Z. *et al.* Combinatorial patterns of histone acetylations and methylations in the human genome. *Nature Genet.* **40**, 897–903 (2008).
20. Barski, A. *et al.* High-resolution profiling of histone methylations in the human genome. *Cell* **129**, 823–837 (2007).
21. Gossman, T. I., Woolfit, M. & Eyre-Walker, A. Quantifying the variation in the effective population size within a genome. *Genetics* **189**, 1389–1402 (2011).
22. Vavouri, T. & Lehner, B. Chromatin organization in sperm may be the major functional consequence of base composition variation in the human genome. *PLoS Genet.* **7**, e1002036 (2011).
23. Peterson, C. L. & Côté, J. Cellular machineries for chromosomal DNA repair. *Genes Dev.* **18**, 602–616 (2004).
24. Goodarzi, A. A. *et al.* ATM signaling facilitates repair of DNA double-strand breaks associated with heterochromatin. *Mol. Cell* **31**, 167–177 (2008).
25. Misteli, T. Beyond the sequence: cellular organization of genome function. *Cell* **128**, 787–800 (2007).
26. Wheeler, D. L. *et al.* Database resources of the National Center for Biotechnology Information. *Nucleic Acids Res.* **35**, D5–D12 (2007).
27. A map of human genome variation from population-scale sequencing. *Nature* **467**, 1061–1073 (2010).
28. Paten, B., Herrero, J., Beal, K., Fitzgerald, S. & Birney, E. Enredo and Pecan: genome-wide mammalian consistency-based multiple alignment with paralogs. *Genome Res.* **18**, 1814–1828 (2008).
29. Zhang, Y., Shin, H., Song, J. S., Lei, Y. & Liu, X. S. Identifying positioned nucleosomes with epigenetic marks in human from ChIP-Seq. *BMC Genomics* **9**, 537 (2008).
30. Broad Institute Sequencing Platform and Whole Genome Assembly Team *et al.* A high-resolution map of human evolutionary constraint using 29 mammals. *Nature* **478**, 476–481 (2011).

**Supplementary Information** is linked to the online version of the paper at [www.nature.com/nature](http://www.nature.com/nature).

**Acknowledgements** This work was funded by an European Research Council (ERC) Starting Grant, European Union Framework 7 project 277899 4DCellFate, ERASysBioPLUS, Ministerio de Ciencia e Innovación (MICINN) grants BFU2008-00365 and BFU2011-26206, Agència de Gestió d'Ajuts Universitaris i de Recerca (AGAUR), the European Molecular Biology Organization (EMBO) Young Investigator Program, the EMBL-CRG Systems Biology Program and a Juan de la Cierva postdoctoral fellowship to B.S.-B. We thank T. Vavouri and T. Warnecke for comments on the manuscript, and R.S. Hansen for assistance with analysing replication timing data.

**Author Contributions** B.S.-B. performed all analyses. B.S.-B. and B.L. designed analyses and wrote the manuscript. B.L. conceived the study.

**Author Information** Reprints and permissions information is available at [www.nature.com/reprints](http://www.nature.com/reprints). The authors declare no competing financial interests. Readers are welcome to comment on the online version of this article at [www.nature.com/nature](http://www.nature.com/nature). Correspondence and requests for materials should be addressed to B.L. ([ben.lehner@crg.es](mailto:ben.lehner@crg.es)).

## METHODS

**Cancer single nucleotide variation data.** Autosomal SNVs of human cancer cells were obtained from the supplementary data files of the respective publications: 32,075 SNVs for melanoma<sup>3</sup>, 27,246 for prostate cancer<sup>4</sup>, 21,707 for lung cancer<sup>2</sup> and 3,861 SNVs for leukaemia<sup>5</sup>. For the leukaemia data, only the locations of mutations were available, so they are not included in the calculation of transition/transversion correlations.

**Germline polymorphism data.** dbSNP build 130 comprising 4,118,806 SNPs was downloaded from the NCBI FTP server<sup>26</sup>. SNP data from 1000 genomes pilot 2 for two family trios of Central European and West African descent were downloaded from the 1000 genomes FTP server, yielding 5,739,704 unique SNPs<sup>27</sup>. Where necessary, coordinates were mapped to the NCBI36/hg18 assembly of the human genome using the liftOver tool with standard parameters<sup>18</sup>.

**Human–chimp sequence divergence.** Divergence data between *Homo sapiens* and *Pan troglodytes* were extracted from EPO (Enredo–Pecan–Ortheus) whole-genome alignments<sup>28</sup> available from Ensembl release 54. The species tree used to construct the alignment contained genomic sequences of human, chimp, orangutan, macaque, mouse, rat, dog, horse and cow. This enabled the inference of ancestral alleles for each change. The human–chimp alignment covers more than 88% of the human genome, yielding approximately  $10^8$  substitutions across all autosomes.

**Genome-wide feature sets.** Recombination rates were reported using data from the deCODE genetic map<sup>17</sup> at 1-Mb resolution. The genome-wide uniqueness of 24-base polymers was calculated by the ENCODE project and downloaded from the University of California, Santa Cruz (UCSC) genome browser<sup>18</sup>. Highly positioned nucleosomes were predicted with the NPS algorithm<sup>29</sup> using short read densities from micrococcal nuclease digested chromatin extracted from resting CD4 T cells as reported by Schones *et al.*<sup>15</sup>. Short sequence tags for histone methylations, H2AZ, CTCF, PolII binding<sup>20</sup> and histone acetylations<sup>19</sup> were converted to read densities by sliding a 160-base-pair window across each chromosome, summing up reads 80 base pairs upstream on the forward and 80 base pairs downstream on the reverse strand<sup>15</sup>. Hi-C eigenvectors at 100-kilobase resolution for the lymphoblastoid cell line GM06990 were downloaded from the Gene Expression Omnibus (GEO) entry with accession number GSE18199. In accordance with the original paper, eigenvector 1 was used for all chromosomes except chromosomes 4 and 5 for which eigenvector 2 was chosen. Replication timing was calculated using data from Hansen *et al.*<sup>14</sup>. Raw reads were downloaded for four cell-cycle fractions (G1B,

S1, S4 and G2), mapped to the NCBI36/hg18 assembly of the human genome using the GEM library ([http://big.crg.cat/services/gem\\_genome\\_multi\\_tool\\_library](http://big.crg.cat/services/gem_genome_multi_tool_library)), averaged to 4 million reads each, and normalized to percentage replication per nucleotide position. Finally, an early-to-late ratio was calculated as  $(G1B + S1)/(S4 + G2)$ . CpG density is the fraction of residues in CpG dinucleotides. GC density refers to the fraction of all G or C residues per window. Gene density refers to the fraction of nucleotides covered by a gene (including introns) per window. Locations of known coding genes were downloaded from Ensembl BioMart (release 56) and mapped to the NCBI36/hg18 assembly of the human genome using the liftOver tool<sup>18</sup>. Evolutionarily conserved bases were identified using the recently published analysis of 29 mammalian genomes<sup>30</sup>.

**Filtering of data.** The mappability feature described above assigns values of 1 to unique 24-base polymers in the genome, 0.5 to those that occur twice, 0.33 to those that occur three times, and 0 otherwise. We empirically established a conservative cut-off value of 0.8 for the average mappability per window, excluding windows with highly repetitive DNA elements. We used the log-odds Siphy- $\pi$  scores with a cut-off threshold of 3 to identify conserved residues. To mask certain genomic regions while calculating the window averages of each property, we only counted those nucleotides in each genomic window that were not masked by the applied filter. Individual windows were excluded from the analysis if more than 90% of the nucleotides were masked.

**Principal component analysis.** Principal component analysis was performed on the mappability-filtered matrix of 2015 rows representing 1-Mb windows and columns corresponding to 47 genomic features as well as cancer SNV, germline SNP and human–chimp divergence densities. Calculations were performed in R using the princomp function. All feature vectors were scaled to mean 0 and standard deviation 1.

**Iterative model refinement.** To identify the minimal informative set of predictive features for somatic SNV, germline SNP and human–chimp divergence densities, linear models were fitted by generalized least-squares estimation between each individual feature and somatic/germline SNP density. We compared the models by their Akaike information criterion (AIC) and chose the feature with minimal AIC. This procedure was repeated 46 times, adding one feature to the model at each iteration. The set of features with minimal AIC was chosen as the minimal informative set of predictive features. Percentage explained variance was calculated as the  $R^2$  of a linear regression model using these sets of predictive features. Calculations were performed in R using the AIC, gls and lm functions.

# A subset of dopamine neurons signals reward for odour memory in *Drosophila*

Chang Liu<sup>1,2,3</sup>, Pierre-Yves Plaçais<sup>4</sup>, Nobuhiro Yamagata<sup>1</sup>, Barret D. Pfeiffer<sup>5</sup>, Yoshinori Aso<sup>1,5</sup>, Anja B. Friedrich<sup>1</sup>, Igor Siwanowicz<sup>1</sup>, Gerald M. Rubin<sup>5</sup>, Thomas Preat<sup>4</sup> & Hiromu Tanimoto<sup>1</sup>

Animals approach stimuli that predict a pleasant outcome<sup>1</sup>. After the paired presentation of an odour and a reward, *Drosophila melanogaster* can develop a conditioned approach towards that odour<sup>2,3</sup>. Despite recent advances in understanding the neural circuits for associative memory and appetitive motivation<sup>4</sup>, the cellular mechanisms for reward processing in the fly brain are unknown. Here we show that a group of dopamine neurons in the protocerebral anterior medial (PAM) cluster signals sugar reward by transient activation and inactivation of target neurons in intact behaving flies. These dopamine neurons are selectively required for the reinforcing property of, but not a reflexive response to, the sugar stimulus. *In vivo* calcium imaging revealed that these neurons are activated by sugar ingestion and the activation is increased on starvation. The output sites of the PAM neurons are mainly localized to the medial lobes of the mushroom bodies (MBs), where appetitive olfactory associative memory is formed<sup>5,6</sup>. We therefore propose that the PAM cluster neurons endow a positive predictive value to the odour in the MBs. Dopamine in insects is known to mediate aversive reinforcement signals<sup>5,7–11</sup>. Our results highlight the cellular specificity underlying the various roles of dopamine and the importance of spatially segregated local circuits within the MBs.

Reward is positive reinforcement and drives the formation of appetitive associative memory. In insects, octopamine was shown to be involved in reward<sup>5,11–13</sup> (see also ref. 14), whereas specific sets of dopamine neurons were identified to mediate aversive reinforcement<sup>8,10</sup>. Recent studies in *Drosophila* suggest that dopamine in the MBs is involved in appetitive odour memory<sup>15–17</sup>, but the specific role of dopamine and the underlying circuit are unclear.

To examine whether the activation of dopamine neurons can substitute for a rewarding stimulus in the formation of an appetitive odour memory, we targeted the expression of a thermosensitive cation channel dTRPA1 (ref. 18) to different, but overlapping sets of, dopamine neurons by using two GAL4 drivers (Fig. 1a, b), *TH-GAL4* and *DDC-GAL4*. Activation of dTRPA1 in *DDC-GAL4* flies during the presentation of an odour (Fig. 1c)<sup>10</sup> resulted in a weak appetitive memory, but robust aversive memory in *TH-GAL4* flies (Fig. 1d)<sup>8,10,13</sup>. The same activation on starvation induced a much greater appetitive memory in *DDC-GAL4/UAS-dTrpA1* flies (Fig. 1d). Activation of dTRPA1 that was not paired with an odour did not induce appetitive memory (Supplementary Fig. 1a, b). Thermo-activation with the driver *HL9-GAL4*, a variant of *DDC-GAL4* (ref. 8), induced similar appetitive memory (Supplementary Fig. 1e, f). Furthermore, *TH-GAL80* (ref. 19) did not significantly suppress induced memory in *DDC-GAL4/UAS-dTrpA1* flies (Supplementary Fig. 1g, h), suggesting that the neurons labelled in *DDC-GAL4* but not in *TH-GAL4* flies are responsible for signalling reward. As in appetitive memory with sugar, a single thermo-activation using *DDC-GAL4* induced persistent appetitive memory, which lasted for up to 24 h (Fig. 1e). We therefore conclude that *DDC-GAL4* labels neurons signalling reward.

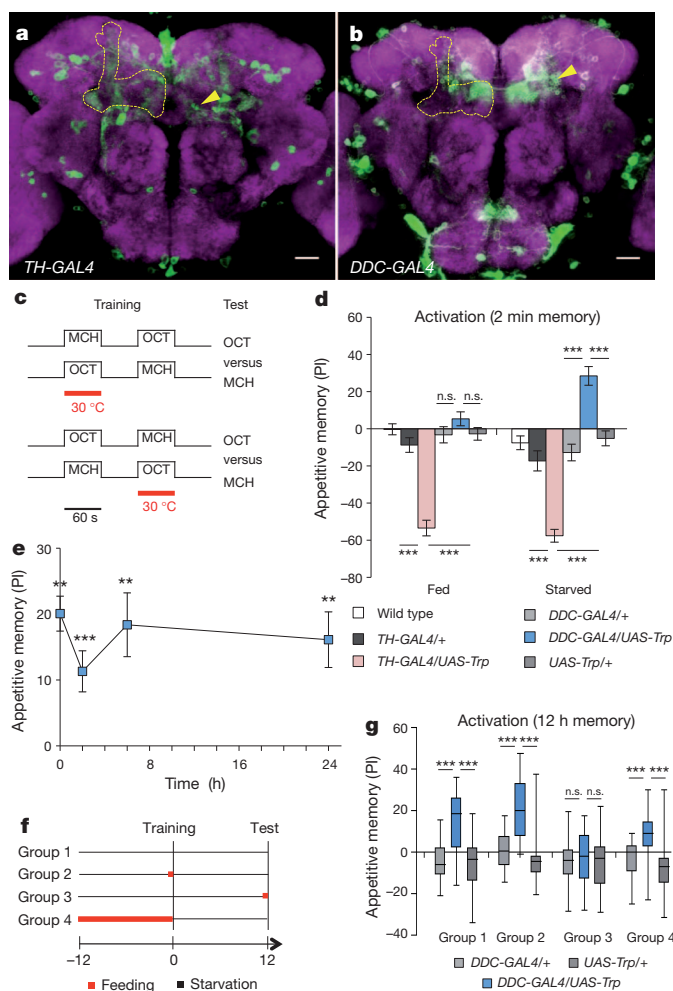


**Figure 1 | Thermo-activation with *DDC-GAL4* induces appetitive memory.** **a, b,** Expression patterns of *TH-GAL4* (**a**) and *DDC-GAL4* (**b**) in the brain with a neuropile counterstaining (magenta). Outline, MB; arrowheads, PAM neurons. Scale bars, 20  $\mu$ m. **c,** Protocol for dTRPA1 (Trp)-mediated reinforcement substitution. MCH, 4-methylcyclohexanol; OCT, octan-3-ol. **d,** Thermo-activation with *DDC-GAL4* and *TH-GAL4* with or without starvation. PI, performance index.  $n = 16$ . **e,** Retention of induced memory.  $n = 10–27$ . **f,** Protocol for feeding before the training or the test of 12-h memory. Flies were satiated with a short feed (30 min) or continuous feeding. **g,** Test of 12-h memory by thermo-activation with *DDC-GAL4*.  $n = 16$ . Midline, box boundaries and whiskers are median, quartiles and 10th and 90th centiles, respectively. Results in **d** and **e** are means  $\pm$  s.e.m. Two asterisks,  $P < 0.01$ ; three asterisks,  $P < 0.001$ ; n.s., not significant.

<sup>1</sup>Max-Planck-Institut für Neurobiologie, Martinsried 82152, Germany. <sup>2</sup>Laboratory of Primate Cognitive Neuroscience, Kunming Institute of Zoology, The Chinese Academy of Sciences, Kunming, Yunnan 650223, China. <sup>3</sup>Graduate University of the Chinese Academy of Sciences, Beijing 100049, China. <sup>4</sup>Genes and Dynamics of Memory Systems, Neurobiology Unit, Centre National de la Recherche Scientifique, École Supérieure de Physique et de Chimie Industrielles, 75005 Paris, France. <sup>5</sup>Janelia Farm Research Campus, Howard Hughes Medical Institute, Ashburn, Virginia 20147, USA.



To address when starvation is required for the dTRPA1-induced memory performance, we examined the effect of changing motivational states before either training or test by a brief feeding (Fig. 1f). Appetitive memory was induced on thermo-activation despite feeding before training (groups 2 and 4 in Fig. 1f, g). If applied before the test, feeding fully suppressed the behavioural expression of 12-h memories (group 3 in Fig. 1f, g). These results suggest that starvation is required for the retrieval, but not the acquisition, of appetitive memory induced by thermo-activation.

To explore the role of *DDC-GAL4*-labelled neurons in mediating the sugar reward, we blocked the output of these neurons using *Shi<sup>ts1</sup>*, which inhibits neuronal output at high temperature<sup>20</sup>. Unlike another known type of dopamine neurons that restricts appetitive memory retrieval<sup>15</sup>, blocking the *DDC-GAL4*-labelled neurons did not release memory expression in fed flies (Supplementary Fig. 2). Instead, the blockade impaired the acquisition, but not the expression, of the sugar-induced memory (Supplementary Fig. 3a, b). Neither memory

performance at the permissive temperature nor sugar preference at the restrictive temperature was impaired (Supplementary Fig. 3c, d).

Next we sought to identify the cells responsible for reward processing. *DDC-GAL4* heavily labels the PAM cluster neurons, whereas this cluster is sparsely labelled by *TH-GAL4* (Fig. 1a, b)<sup>8</sup>. For selective manipulation of the PAM cluster neurons, we screened a collection of *GAL4* driver lines<sup>21</sup> and identified *R58E02-GAL4*. This driver strongly labels the PAM cluster neurons and glial cells in the optic lobes with little expression elsewhere (Fig. 2a, Supplementary Fig. 4a and Supplementary Movie 1). Arbores of the PAM neurons in the MBs are largely localized to the medial lobes (Fig. 2a and Supplementary Fig. 3b). The enhancer of *R58E02-GAL4* is derived from the first intron of the *Drosophila* dopamine transporter gene. Consistently, the PAM neurons labelled in *R58E02-GAL4* as well as in *DDC-GAL4* flies are dopamine immunoreactive (Fig. 2b–e) with no detectable serotonin labelling (Supplementary Fig. 5). Thermo-activation of the PAM neurons with the use of *R58E02-GAL4* induced robust appetitive odour memory in starved flies

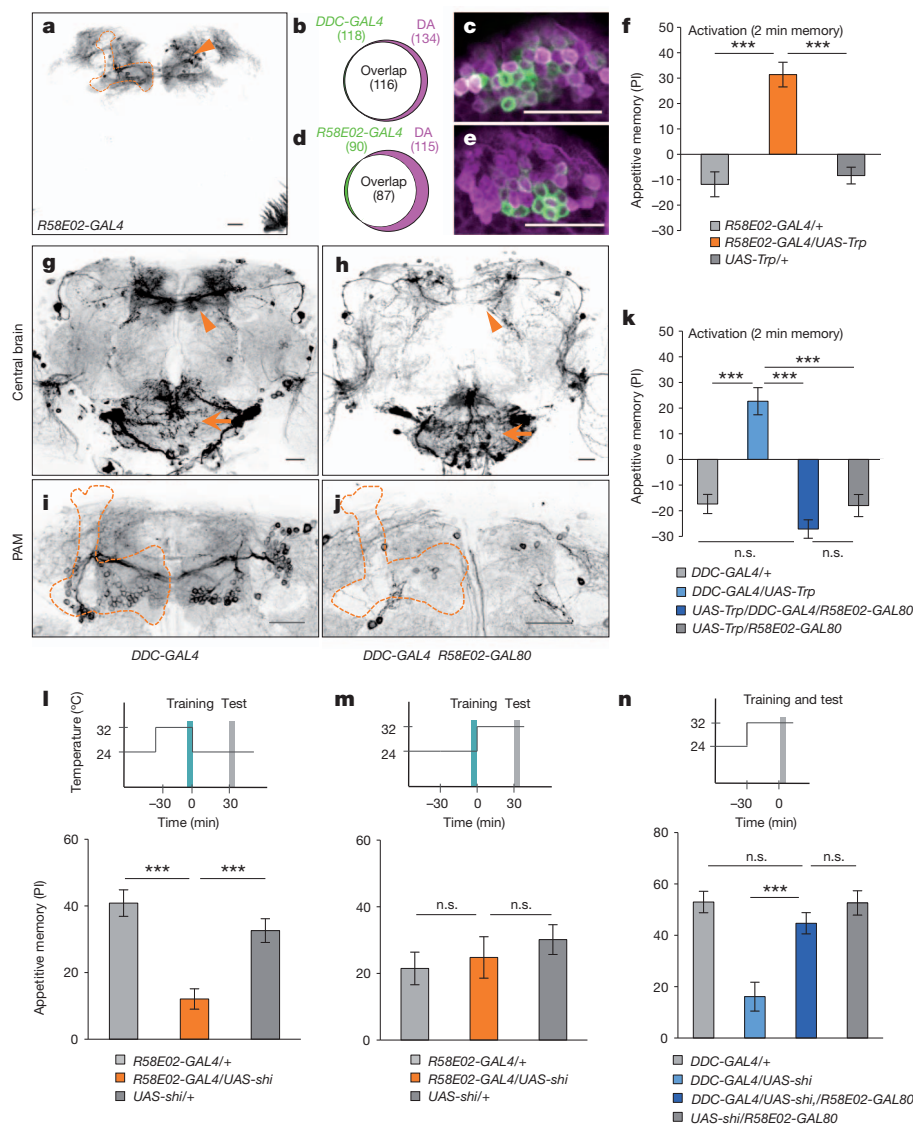


**Figure 2 | The PAM cluster neurons signal reward for olfactory memory.** **a**, Expression pattern of *R58E02-GAL4* in the central brain revealed with *UAS-mCD8::GFP*. **b–e**, Co-localization of dopamine (magenta) and *GAL4*-expressing cells (green) in the PAM cluster of *DDC-GAL4* (**b**, **c**,  $n = 6$ ) and *R58E02-GAL4* (**d**, **e**,  $n = 4$ ). **f**, Thermo-activation with *R58E02-GAL4/UAS-dTrpA1* induces significant appetitive memory.  $n = 16$ . **g–j**, *R58E02-GAL80* silences transgene expression in most PAM neurons of *DDC-GAL4* (arrowheads in **g** and **h**) without greatly affecting other neurons (such as the

subesophageal ganglion (arrows)). **k**, *R58E02-GAL80* suppresses the induction of appetitive memory by *DDC-GAL4/UAS-dTrpA1*.  $n = 10$ . **l, m**, Blockade of the PAM neurons in *R58E02-GAL4/UAS-shi<sup>ts1</sup>* during memory acquisition (**l**) or applied after training (**m**). **n**, *R58E02-GAL80* rescues the memory impairment in *DDC-GAL4/UAS-shi<sup>ts1</sup>*,  $n = 14–20$ . Upper panels in **l–n**, protocols; lower panels, sugar conditioning. Results with error bars are means  $\pm$  s.e.m. Three asterisks,  $P < 0.001$ ; n.s., not significant. Scale bars, 20  $\mu$ m.

(Fig. 2f), whereas the activation itself did not cause any obvious reflexive appetitive behaviour (such as proboscis extension; data not shown).

*DDC-GAL4* labels many neurons outside the PAM cluster, including those projecting to the subesophageal ganglion, where sweet taste neurons terminate (Fig. 1b). To address the contribution of the non-PAM cells in *DDC-GAL4* flies, we generated *R58E02-GAL80*, a *GAL80* line using the same enhancer integrated at the same genomic location as in *R58E02-GAL4*. Combination of *R58E02-GAL80* with *DDC-GAL4* suppressed transgene expression in most PAM neurons in *DDC-GAL4* flies (Fig. 2g–j and Supplementary Movies 2 and 3; see also Supplementary Fig. 6e). Thermo-activation with *DDC-GAL4/R58E02-GAL80* did not induce appetitive memory (Fig. 3k), demonstrating the importance of PAM neurons in reward signalling.

A transient *Shi<sup>ts1</sup>* block of the PAM neurons by *R58E02-GAL4* impaired the acquisition, but not the expression, of sugar-induced memory (Fig. 2l, m). Furthermore, blocking the PAM neurons did not impair the reflexive choice of sugar (Supplementary Fig. 4c). Consistently, *R58E02-GAL80* rescued the memory impairment of *DDC-GAL4/UAS-shi<sup>ts1</sup>* flies (Fig. 2n). Thus, the PAM neurons are necessary and sufficient for signalling the sugar reward.

Expression of a presynaptic marker using *R58E02-GAL4* demonstrated that input and output sites of the PAM neurons are highly segregated, with presynaptic terminals localized predominantly in the MBs (Fig. 3a–c). To address whether the signal from the PAM neurons is mediated by dopamine receptors, we activated these neurons in the background of *dumb<sup>2</sup>*, a mutant for the *dDA1* gene (also known as *DopR*), which encodes a D1-type dopamine receptor. We first confirmed the previously reported role of *dDA1* in the Kenyon cells of the MBs for sugar-induced appetitive memory (Fig. 3d)<sup>16</sup>. Because we wished to use a *GAL4* driver to express *dDA1* in Kenyon cells simultaneously with *dTRPA1* in the PAM neurons, we generated a *LexA* driver *R58E02-LexA::p65*. It recapitulated the expression pattern in *R58E02-GAL4* and was able to induce appetitive memory using *LexAop2-dTrpA1* (Fig. 3e and Supplementary Fig. 6c, d). Activation of the PAM neurons failed to induce marked appetitive memory in flies lacking *dDA1* (Fig. 3f). Driving wild-type *dDA1* expression in  $\alpha/\beta$  and  $\gamma$  Kenyon cells by using the driver *MB247-GAL4* restored appetitive memory in *R58E02-LexA/LexAop2-dTrpA1* flies (Fig. 3f). These results indicate the importance of dopamine signalling in the MBs for reward processing, but do not exclude a role for other possible co-transmitters released by the PAM neurons.

We previously identified that MB-M3 neurons in the PAM cluster are important for aversive memory formation<sup>10</sup>. We labelled both MB-M3 and the reward-signalling PAM neurons in the same brain and found no overlap (Fig. 3g–i, Supplementary Fig. 7 and Supplementary Movie 4). This highlights the functional heterogeneity of individual cell types in the PAM cluster.

Similarly, we made different populations of dopamine neurons that signal appetitive and aversive reinforcement visible by using *R58E02-LexA* and *TH-GAL4*, respectively, and examined the distribution of their projections in the MBs. The terminals of the PAM and protocerebral posterior lateral (PPL)1 clusters are largely non-overlapping in the MBs and together cover the entire lobes (Fig. 3j–l and Supplementary Movie 5) despite the simultaneous expression of *R58E02-LexA* and *TH-GAL4* in a few PAM cluster neurons (Supplementary Fig. 8a–d). Thus, axonal compartments of Kenyon cells are targeted by functionally different dopamine neurons.

Given the importance of octopamine signalling in reward processing<sup>5,11–13</sup>, we activated the PAM cluster neurons in *T $\beta$ H* mutants, which lack octopamine<sup>22</sup>. We found no marked effect of *T $\beta$ H* on appetitive memory induced by activation of the PAM neurons (Fig. 4a), indicating that the PAM neurons act in parallel with or downstream of, but not upstream of, octopamine signalling. Consistently, double labelling of the octopamine and PAM cluster dopamine neurons revealed potential direct contacts of these arbourers in the spur of the  $\gamma$  lobe and protocerebral regions (Fig. 4b–d), where

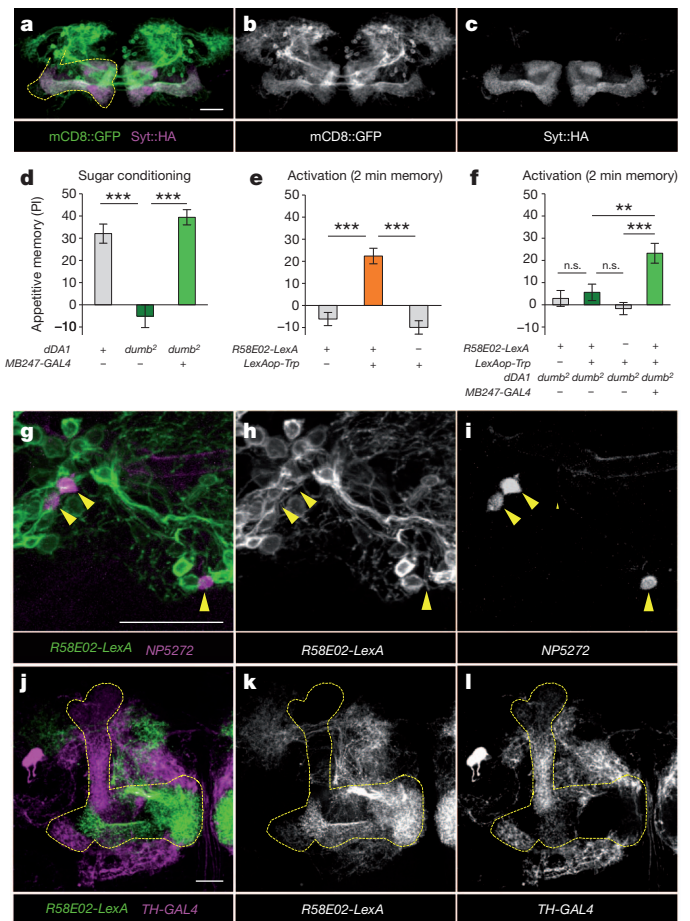


**Figure 3 | The PAM neurons convey the reward signal to the MB.**

**a–c**, Presynaptic terminals (magenta) of the PAM neurons (green) in *R58E02-GAL4* are localized to the MB (outline). **d**, The defect in sugar-induced memory in *dumb<sup>2</sup>*, a piggyBac insertion allowing *GAL4*-mediated *dDA1* expression<sup>16</sup>, is rescued by *MB247-GAL4*.  $n = 16$ . **e**, Appetitive memory induced by thermo-activation in *R58E02-LexA/LexAop2-dTrpA1*.  $n = 16$ . **f**, Thermo-activation of the PAM neurons in *dumb<sup>2</sup>* induces memory by rescuing *dDA1* in the MB.  $n = 14–22$ . **g–i**, No detectable overlap of *R58E02-LexA*-labelled neurons expressing *mCD8::GFP* (green) and MB-M3 neurons (magenta; arrowheads) visualized with *mCD8::RFP*. See also Supplementary Fig. 7. **j–l**, Differential labelling of *R58E02-LexA* (green) and *TH-GAL4* (magenta) in the MB lobe region. Results with error bars are means  $\pm$  s.e.m. Two asterisks,  $P < 0.01$ ; three asterisks,  $P < 0.001$ ; n.s., not significant. Scale bars, 20  $\mu$ m.

the putative input and output sites of the PAM and octopamine neurons, respectively, are located (Fig. 3a–c)<sup>23</sup>. This suggests that octopamine may regulate reward processing by directly modulating the activity of the PAM cluster neurons.

To test whether the PAM neurons respond to the sugar reward, we performed *in vivo* calcium imaging in starved flies expressing the fluorescent calcium reporter *GCaMP3*. We devised a gustatory stimulation protocol with the unrestrained proboscis that enabled confocal imaging of the PAM terminals in the MBs (Supplementary Fig. 9). Sugar ingestion caused stronger calcium responses than water or a bitter caffeine solution (Fig. 4e–g). We found that the calcium response of the PAM neurons on stimulation with sugar was greatly reduced when flies were fed (Fig. 4h). Flies can sense sweet taste with their tarsi, but stimulating tarsi with sugar barely activated the PAM neurons, suggesting that sweet substances need to be ingested to trigger the reward signal (Fig. 4h).

Our data suggest the existence of a reward circuit in which the PAM neurons integrate gustatory reward and other relevant regulatory inputs, and then convey the summed positive value signal to specific subdomains of the MBs (Fig. 4i). The MB lobes can be anatomically



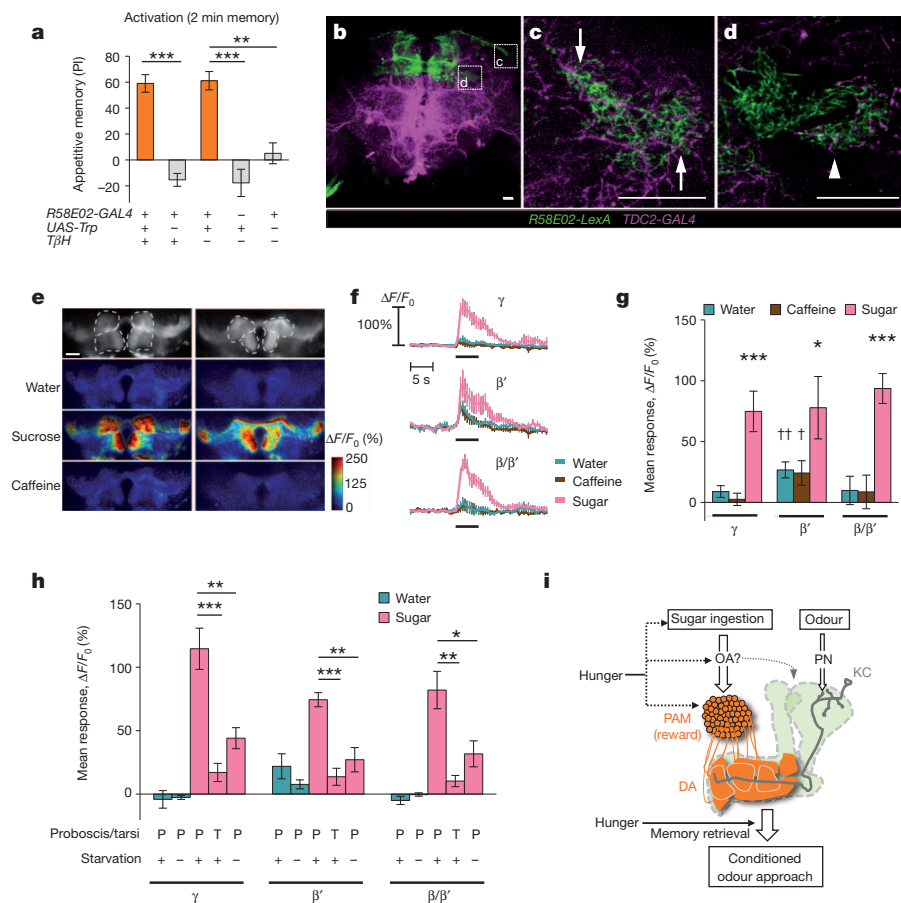


**Figure 4 | The PAM neurons integrate reward and relevant signals.** **a**, Thermo-activation of the PAM neurons induces appetitive memory without octopamine.  $n = 16$ –22. **b–d**, Octopamine and PAM neurons contact each other (arrows) in a protocerebral region (**c**) and the spur of the  $\gamma$  lobe (**d**). **e–g**, The PAM neurons respond selectively to the sugar reward. **e**, Representative images (anterior down) and calcium responses of the PAM neurons at different levels of the MB. **f**, Time course of responses.  $n = 10$ . Black bar: stimulus application. **g**, Average response to different gustatory substances. Terminals in the  $\beta'$  lobe responded significantly to water and caffeine (dagger,  $P < 0.05$ ; two daggers,  $P < 0.01$  in one-sample  $t$ -test from zero). **h**, Response of the PAM neurons without starvation or with tarsal stimulation only.  $n > 7$ . **i**, Model of a reward circuit in the fly brain. Dashed arrows indicate hypothetical pathways. The reward value integrated by the PAM neurons is signalled by dopamine (DA) to the MB (green shading), thus they may drive associative plasticity in odour-representing Kenyon cells (KC, grey). OA, octopamine; PN, projection neurons. Results with error bars are means  $\pm$  s.e.m. Asterisk,  $P < 0.05$ ; two asterisks,  $P < 0.01$ ; three asterisks,  $P < 0.001$ . Scale bars, 20  $\mu$ m.

divided into 35 subdomains that are defined by specific combinations of intrinsic and extrinsic neurons<sup>24</sup>. Distinct sets of dopamine neurons may provide functionally independent local circuits within the MBs, potentially allowing appetitive and aversive modulation of the same odour. The PAM neurons may drive positive associative modulation of concomitant olfactory signals of the Kenyon cells (Fig. 4i). The dual processing of appetitive and aversive stimuli may be a conserved function of dopamine, highlighting the physiological pleiotropy of a neurotransmitter<sup>4,25,26</sup>.

## METHODS SUMMARY

The genomic fragment *R58E02* was cloned into previously described vectors<sup>21,27</sup>. Sugar conditioning and thermo-activation with two odours (4-methylcyclohexanol and octan-3-ol) and fluorescent immunohistochemistry were performed as described previously<sup>10</sup>. Sugar preference was measured with a previously described setup<sup>28</sup>, with slight modification. Most of the groups tested did not violate the assumption of the normal distribution and the homogeneity of variance. Performance indices were therefore subjected to parametric statistics. For data that significantly differed from the normal distribution (Fig. 1g), non-parametric statistics were applied. For *in vivo* calcium imaging, female flies expressing GCaMP3 (ref. 29) with *R58E02-GAL4* were singly prepared as described<sup>30</sup>, with slight modifications. A droplet of 8  $\mu$ l of mineral water, 1 M sucrose or 0.1 M caffeine solution in mineral water was delivered on a plastic plate controlled by a micromanipulator (Supplementary Fig. 9).

**Full Methods** and any associated references are available in the online version of the paper.

Received 10 April; accepted 8 June 2012.

Published online 18 July 2012.

- Schultz, W. Behavioral theories and the neurophysiology of reward. *Annu. Rev. Psychol.* **57**, 87–115 (2006).
- Tempel, B. L., Bonini, N., Dawson, D. R. & Quinn, W. G. Reward learning in normal and mutant *Drosophila*. *Proc. Natl Acad. Sci. USA* **80**, 1482–1486 (1983).

- Kaun, K. R., Azanchi, R., Maung, Z., Hirsh, J. & Heberlein, U. A *Drosophila* model for alcohol reward. *Nature Neurosci.* **14**, 612–619 (2011).
- Waddell, S. Dopamine reveals neural circuit mechanisms of fly memory. *Trends Neurosci.* **33**, 457–464 (2010).
- Schwaerzel, M. et al. Dopamine and octopamine differentiate between aversive and appetitive olfactory memories in *Drosophila*. *J. Neurosci.* **23**, 10495–10502 (2003).
- Tranoy, S., Redt-Clouet, C., Dura, J. M. & Preat, T. Parallel processing of appetitive short- and long-term memories in *Drosophila*. *Curr. Biol.* **21**, 1647–1653 (2011).
- Riemensperger, T., Völler, T., Stock, P., Buchner, E. & Fiala, A. Punishment prediction by dopaminergic neurons in *Drosophila*. *Curr. Biol.* **15**, 1953–1960 (2005).
- Claridge-Chang, A. et al. Writing memories with light-addressable reinforcement circuitry. *Cell* **139**, 405–415 (2009).
- Mao, Z. & Davis, R. L. Eight different types of dopaminergic neurons innervate the *Drosophila* mushroom body neuropil: anatomical and physiological heterogeneity. *Front. Neural Circuits* **3**, 5 (2009).
- Aso, Y. et al. Specific dopaminergic neurons for the formation of labile aversive memory. *Curr. Biol.* **20**, 1445–1451 (2010).
- Mizunami, M. & Matsumoto, Y. Roles of aminergic neurons in formation and recall of associative memory in crickets. *Front. Neurosci.* **4**, 172 (2010).
- Hammer, M. An identified neuron mediates the unconditioned stimulus in associative olfactory learning in honeybees. *Nature* **366**, 59–63 (1993).
- Schroll, C. et al. Light-induced activation of distinct modulatory neurons triggers appetitive or aversive learning in *Drosophila* larvae. *Curr. Biol.* **16**, 1741–1747 (2006).
- Yarali, A. & Gerber, B. A neurogenetic dissociation between punishment-, reward-, and relief-learning in *Drosophila*. *Front. Behav. Neurosci.* **4**, 189 (2010).
- Krashes, M. J. et al. A neural circuit mechanism integrating motivational state with memory expression in *Drosophila*. *Cell* **139**, 416–427 (2009).
- Kim, Y. C., Lee, H. G. & Han, K. A. D1 dopamine receptor dDA1 is required in the mushroom body neurons for aversive and appetitive learning in *Drosophila*. *J. Neurosci.* **27**, 7640–7647 (2007).
- Selcho, M., Pauls, D., Han, K. A., Stocker, R. F. & Thum, A. S. The role of dopamine in *Drosophila* larval classical olfactory conditioning. *PLoS ONE* **4**, e5897 (2009).
- Hamada, F. N. et al. An internal thermal sensor controlling temperature preference in *Drosophila*. *Nature* **454**, 217–220 (2008).
- Sitaraman, D. et al. Serotonin is necessary for place memory in *Drosophila*. *Proc. Natl Acad. Sci. USA* **105**, 5579–5584 (2008).
- Kitamoto, T. Conditional modification of behavior in *Drosophila* by targeted expression of a temperature-sensitive *shibire* allele in defined neurons. *J. Neurobiol.* **47**, 81–92 (2001).



21. Pfeiffer, B. D. *et al.* Tools for neuroanatomy and neurogenetics in *Drosophila*. *Proc. Natl Acad. Sci. USA* **105**, 9715–9720 (2008).
22. Monastirioti, M., Linn, C. E. Jr & White, K. Characterization of *Drosophila* tyramine  $\beta$ -hydroxylase gene and isolation of mutant flies lacking octopamine. *J. Neurosci.* **16**, 3900–3911 (1996).
23. Busch, S., Selcho, M., Ito, K. & Tanimoto, H. A map of octopaminergic neurons in the *Drosophila* brain. *J. Comp. Neurol.* **513**, 643–667 (2009).
24. Tanaka, N. K., Tanimoto, H. & Ito, K. Neuronal assemblies of the *Drosophila* mushroom body. *J. Comp. Neurol.* **508**, 711–755 (2008).
25. van Swinderen, B. & Andretic, R. Dopamine in *Drosophila*: setting arousal thresholds in a miniature brain. *Proc. R. Soc. B* **278**, 906–913 (2011).
26. Bromberg-Martin, E. S., Matsumoto, M. & Hikosaka, O. Dopamine in motivational control: rewarding, aversive, and alerting. *Neuron* **68**, 815–834 (2010).
27. Pfeiffer, B. D. *et al.* Refinement of tools for targeted gene expression in *Drosophila*. *Genetics* **186**, 735–755 (2010).
28. Schnaitmann, C., Vogt, K., Triphan, T. & Tanimoto, H. Appetitive and aversive visual learning in freely moving *Drosophila*. *Front. Behav. Neurosci.* **4**, 10 (2010).
29. Tian, L. *et al.* Imaging neural activity in worms, flies and mice with improved GCaMP calcium indicators. *Nature Methods* **6**, 875–881 (2009).
30. Séjourné, J. *et al.* Mushroom body efferent neurons responsible for aversive olfactory memory retrieval in *Drosophila*. *Nature Neurosci.* **14**, 903–910 (2011).

**Supplementary Information** is linked to the online version of the paper at [www.nature.com/nature](http://www.nature.com/nature).

**Acknowledgements** We thank L. Bräcker, M. Feind, C. Murphy, C. Schnaitmann and T. Templier for technical assistance and experiments that inspired this study; P. Garrity,

the Kyoto *Drosophila* Genetic Resource Center and the Bloomington Stock Center for fly stocks; and Y.Y. Ma, Z. Q. Meng, R. Menzel, A. Thum, S. Waddell and the members of the Tanimoto laboratory for discussion and/or critical reading of the manuscript. C.L., Y.A., N.Y. and P.-Y.P. were sponsored by a Chinese–European doctoral training program from Max-Planck-Gesellschaft and the Chinese Academy of Sciences, the Deutscher Akademischer Austausch Dienst, the Alexander von Humboldt Foundation, and the Région Île-de-France, respectively. This work was supported by the Agence Nationale pour la Recherche (T.P.), the Howard Hughes Medical Institute (G.M.R.), Bernstein Focus Learning from the Bundesministerium für Bildung und Forschung and the Max-Planck-Gesellschaft (H.T.).

**Author Contributions** C.L., N.Y., Y.A. and H.T. designed and C.L. and N.Y. performed all the behavioural experiments in this study. P.Y.P., T.P. and H.T. designed *in vivo* imaging experiments, and P.Y.P. and T.P. devised a new gustatory stimulation method. P.Y.P. performed imaging experiments and analysed the data. B.D.P. and G.M.R. designed and generated the new transgenic flies (GAL4, GAL80, LexA and *LexAop2-dTrpA1* lines). Y.A. and H.T. identified *R58E02* by using a database of GAL4 expression patterns created by G.M.R. and the Janelia Farm Fly Light Project Team. A.B.F. and I.S. performed immunohistochemistry, and C.L., A.B.F. and H.T. analysed the microscopic data. C.L. and H.T. made the figures and wrote the paper with the help of all the other authors.

**Author Information** Reprints and permissions information is available at [www.nature.com/reprints](http://www.nature.com/reprints). The authors declare no competing financial interests. Readers are welcome to comment on the online version of this article at [www.nature.com/nature](http://www.nature.com/nature). Correspondence and requests for materials should be addressed to H.T. ([hiromut@neuro.mpg.de](mailto:hiromut@neuro.mpg.de)).

## METHODS

**Flies.** The 1.2 kb DNA enhancer fragment in *R58E02* was amplified by PCR (primer sequences 5'-cgaaggcgcaacagctccgattttg-3' and 5'-ccttgacccaaatgtggag atccc-3') and originates from the *dopamine transporter* locus<sup>31</sup>. The fragment was cloned into the transformation vectors pBPGUw (ref. 21), pBPGAL80Uw-6 (ref. 27) and pBPLexA::p65Uw (ref. 27). *R58E02-GAL4* and *R58E02-GAL80* were integrated into *attP2* (3L), and *R58E02-LexA::p65* was integrated into *attP40* (2L) using PhiC31 integrase. *pJFRC26-13XLexAop2-IVS-dTrpA1-WPRE* and *pJFRC15-13XLexAop2-mCD8::GFP* were cloned using the modified LexA vector and integrated into *VK00005* (3L) and *su(Hw)attP8* (X), respectively, using PhiC31-mediated site-specific recombination.

Behavioural experiments (except Fig. 4d) used F<sub>1</sub> progenies of crosses between females of *w;UAS-dTrpA1* (ref. 18), *w;UAS-shi<sup>ts1</sup>* (one copy of *UAS-shi* from the Preat laboratory)<sup>20</sup>, *w;LexAop2-dTrpA1*, *w;UAS-dTrpA1;R58E02-GAL80*, *w;UAS-shi<sup>ts1</sup> R58E02-GAL80*, *w;UAS-dTrpA1;dumb<sup>2</sup>*, *TβH<sup>M18</sup>/FM7* (ref. 22), *TβH<sup>M18</sup>/FM7;UAS-dTrpA1*, *w;R58E02-LexA;dumb<sup>2</sup>*, *w;R58E02-LexA;dumb<sup>2</sup> MB247-GAL4*, *w;dumb<sup>2</sup>* or *w* females and males of *w;TH-GAL4* (ref. 32), *w;DDC-GAL4* (ref. 33), *w;HL9-GAL4* (ref. 8), *w;R58E02-GAL4*, *w;R58E02-LexA::p65*, *w;dumb<sup>2</sup>*, *w;LexAop-dTrpA1 dumb<sup>2</sup>* or *w* males, raised 60% relative humidity with a 14h/10h light/dark cycle. Crosses with *UAS-dTrpA1 (LexAop-dTrpA1)* and *UAS-shi<sup>ts1</sup>* flies were raised at 23 and 17 °C, respectively. At experimentation, flies were aged 3–14 days after eclosion and starved according to mortality rate. For the experiments with *TβH*, the performance of the male progeny was used for calculating PI. For immunohistochemistry, female reporter strains *yw UAS-mCD8::GFP<sup>34</sup>*, *w mCD8::GFP;TH-GAL80;mCD8::GFP*, *w UAS-Syt::HA;UAS-mCD8::GFP<sup>35</sup>*, *w;UAS-mCD8::GFP;R58E02-GAL80* or *w pJFRC21-10XUAS-IVS-mCD8::RFP (attP18) pJFRC15-13XLexAop2-mCD8::GFP (su(Hw)attP8)* were crossed to male *GAL4* drivers, *w;TH-GAL4*, *w;DDC-GAL4*, *w;HL9-GAL4*, *w;R58E02-GAL4*, *w;R58E02-LexA::p65*, *w;NP5272* or *w;TDC2-GAL4* (ref. 36). Flies used for whole-mount immunohistochemistry were aged to 5–10 days after eclosion.

**Behavioural assays.** The conditioning protocol was as described previously<sup>10</sup>. Except where noted, behavioural experiments were performed in dim red light for training phases and in complete darkness for tests. A group of about 50 flies in a training tube alternately received octan-3-ol (OCT; Merck) and 4-methylcyclohexanol (MCH; Sigma-Aldrich) for 1 min in a constant air stream (Fig. 1c and Supplementary Fig. 1c). OCT and MCH were diluted 1:10 in paraffin oil (Sigma-Aldrich) and presented in a cup with a diameter of 3 and 5 mm, respectively. For sugar-induced memory, filter paper was soaked in 2 M sucrose solution, dried, and presented together with one of the odours (Supplementary Fig. 1c). Alternately, the control odour was paired with dried filter paper (Supplementary Fig. 1c). For thermo-activation with dTRPA1, flies were trained by being transferred from a background temperature of 24 °C to a pre-warmed tube in a climate box (30 °C) and presented with the trained odorant (Fig. 1c)<sup>10</sup>. Temperature was measured with a VC-960 digital multimeter (Votcraft). For unpaired thermo-activation with dTRPA1, flies were exposed to the pre-warmed tube either between or after the two odorants (Supplementary Fig. 1a). The restrictive temperature for the experiments with *UAS-shi<sup>ts1</sup>* was 32 °C. For memory retention, trained flies were kept in a vial with moistened filter paper. After a given retention time, the trained flies were allowed to choose between MCH and OCT for 2 min in a T-maze. A learning index was then calculated by taking the mean preference of the two reciprocally trained groups<sup>2</sup>. Half of the trained groups received reinforcement together with the first presented odour and the other half with the second odour to cancel the effect of the order of reinforcement. To control feeding motivation, flies were kept in a food vial for 30 min before training or test. For 24-h memory, flies were fed for 1 h after training.

For testing sugar preference, flies were placed in a cylindrical, infrared-illuminated arena, and given a choice between two halves of dried filter paper, one of which was soaked in 2 M sucrose<sup>28</sup>. The arena was video-recorded from above with a CMOS video camera (Firefly MV; Point Grey) at one frame per second, and the first 120 s were analysed. The performance index represents the difference in the number of flies in the two halves, divided by the total number of flies.

**Statistics.** Statistical analyses were performed with Prism5 software (GraphPad). Most tested groups did not violate the assumption of normal distribution and homogeneity of variance. All the data except the experiment in Fig. 1g were therefore analysed with parametric statistics: one-sample *t*-test or one-way analysis of variance followed by the planned pairwise multiple comparisons (Bonferroni). Because the data in Fig. 1g were significantly different from the normal distribution, non-parametric statistics (that is, Kruskal–Wallis test followed by Dunn's multiple pairwise comparison test) were applied. The significance level of statistical tests was set to 0.05.

**Histochemistry.** Immunolabelling was performed with a standard protocol<sup>10</sup>, with the exception of a fixation (0.6% glutaraldehyde in PBS for 30 min) and the following glutaraldehyde protocol for dopamine<sup>23</sup>. Fluorescence of mCD8::GFP and mCD8::RFP was detected without immunohistochemistry. Frontal optical sections of whole-mount brains were sampled with a confocal microscope (Olympus FV1000). To evaluate the effect of *R58E02-GAL80*, brains to be compared were scanned with comparable intensity and offset. Confocal stacks were analysed with Image-J (National Institutes of Health).

**In vivo calcium imaging.** Female flies of the genotype *w<sup>1118</sup>;UAS-GCaMP3/+;R58E02-GAL4/+* aged 1–2 days after eclosion were prepared essentially as described<sup>30</sup>, with the following modifications: the fly was briefly anaesthetized with CO<sub>2</sub>; the proboscis was left free, to enable ingestion (except in tarsal stimulation experiments, in which the proboscis was occluded with the glue); sucrose was replaced with ribose in the solution for bathing the head capsule during surgery<sup>37</sup>. At the end of the surgery, the brain was covered with a drop of the same solution supplemented with 1% agarose, so that the brain was embedded in a gel to limit motion artefacts. Time courses of fluorescence changes were recorded in a transverse section of the brain showing the projections of PAM neurons in the different levels of both MB medial lobes at a rate of two images per second. The terminals on the γ and β' lobes were clearly discernible, whereas the slice of the β terminals might contain some β' terminals. We therefore here use the label 'β/β' terminals' collectively. Three types of stimulation were performed: a droplet of 8 μl of mineral water, 1 M sucrose or 0.1 M caffeine solution in mineral water deposited on a plastic plate was brought within reachable distance of the fly for 5 s with the use of a micromanipulator. These concentrations were chosen because they elicit saturating responses in taste neurons in the subesophageal ganglion (SOG)<sup>37</sup>. The solutions were delivered in random order, and when sucrose was not the last solution tested, an additional sucrose response was measured at the end of the experiment as a positive control, which was not included in analyses.

Image analysis was performed essentially as described<sup>30</sup>. For each region of interest, the baseline (*F*<sub>0</sub>) was estimated as the mean fluorescence over the 10 s preceding the stimulus, and the mean response was calculated as the average of Δ*F*/*F*<sub>0</sub> during the period when the drop of solution was available. Responses from both hemispheres were averaged to yield the mean response of each fly, but for time courses (Fig. 4f) only one hemisphere was considered for each animal (six right, four left).

- Kume, K. *et al.* Dopamine is a regulator of arousal in the fruit fly. *J. Neurosci.* **25**, 7377–7384 (2005).
- Friggi-Grelin, F. *et al.* Targeted gene expression in *Drosophila* dopaminergic cells using regulatory sequences from tyrosine hydroxylase. *J. Neurobiol.* **54**, 618–627 (2003).
- Li, H., Chaney, S., Roberts, I. J., Forte, M. & Hirsh, J. Ectopic G-protein expression in dopamine and serotonin neurons blocks cocaine sensitization in *Drosophila melanogaster*. *Curr. Biol.* **10**, 211–214 (2000).
- Lee, T. & Luo, L. Mosaic analysis with a repressible cell marker for studies of gene function in neuronal morphogenesis. *Neuron* **22**, 451–461 (1999).
- Robinson, I. M., Ranjan, R. & Schwarz, T. L. Synaptotagmins I and IV promote transmitter release independently of Ca<sup>2+</sup> binding in the C<sub>2</sub>A domain. *Nature* **418**, 336–340 (2002).
- Cole, S. H. *et al.* Two functional but non-complementing *Drosophila* tyrosine decarboxylase genes: distinct roles for neural tyramine and octopamine in female fertility. *J. Biol. Chem.* **280**, 14948–14955 (2005).
- Marella, S. *et al.* Imaging taste responses in the fly brain reveals a functional map of taste category and behavior. *Neuron* **49**, 285–295 (2006).

# A subset of dopamine neurons signals reward for odour memory in *Drosophila*

Chang Liu<sup>1,2,3</sup>, Pierre-Yves Plaçais<sup>4</sup>, Nobuhiro Yamagata<sup>1</sup>, Barret D. Pfeiffer<sup>5</sup>, Yoshinori Aso<sup>1,5</sup>, Anja B. Friedrich<sup>1</sup>, Igor Siwanowicz<sup>1</sup>, Gerald M. Rubin<sup>5</sup>, Thomas Preat<sup>4</sup> & Hiromu Tanimoto<sup>1</sup>

Animals approach stimuli that predict a pleasant outcome<sup>1</sup>. After the paired presentation of an odour and a reward, *Drosophila melanogaster* can develop a conditioned approach towards that odour<sup>2,3</sup>. Despite recent advances in understanding the neural circuits for associative memory and appetitive motivation<sup>4</sup>, the cellular mechanisms for reward processing in the fly brain are unknown. Here we show that a group of dopamine neurons in the protocerebral anterior medial (PAM) cluster signals sugar reward by transient activation and inactivation of target neurons in intact behaving flies. These dopamine neurons are selectively required for the reinforcing property of, but not a reflexive response to, the sugar stimulus. *In vivo* calcium imaging revealed that these neurons are activated by sugar ingestion and the activation is increased on starvation. The output sites of the PAM neurons are mainly localized to the medial lobes of the mushroom bodies (MBs), where appetitive olfactory associative memory is formed<sup>5,6</sup>. We therefore propose that the PAM cluster neurons endow a positive predictive value to the odour in the MBs. Dopamine in insects is known to mediate aversive reinforcement signals<sup>5,7–11</sup>. Our results highlight the cellular specificity underlying the various roles of dopamine and the importance of spatially segregated local circuits within the MBs.

Reward is positive reinforcement and drives the formation of appetitive associative memory. In insects, octopamine was shown to be involved in reward<sup>5,11–13</sup> (see also ref. 14), whereas specific sets of dopamine neurons were identified to mediate aversive reinforcement<sup>8,10</sup>. Recent studies in *Drosophila* suggest that dopamine in the MBs is involved in appetitive odour memory<sup>15–17</sup>, but the specific role of dopamine and the underlying circuit are unclear.

To examine whether the activation of dopamine neurons can substitute for a rewarding stimulus in the formation of an appetitive odour memory, we targeted the expression of a thermosensitive cation channel dTRPA1 (ref. 18) to different, but overlapping sets of, dopamine neurons by using two GAL4 drivers (Fig. 1a, b), *TH-GAL4* and *DDC-GAL4*. Activation of dTRPA1 in *DDC-GAL4* flies during the presentation of an odour (Fig. 1c)<sup>10</sup> resulted in a weak appetitive memory, but robust aversive memory in *TH-GAL4* flies (Fig. 1d)<sup>8,10,13</sup>. The same activation on starvation induced a much greater appetitive memory in *DDC-GAL4/UAS-dTrpA1* flies (Fig. 1d). Activation of dTRPA1 that was not paired with an odour did not induce appetitive memory (Supplementary Fig. 1a, b). Thermo-activation with the driver *HL9-GAL4*, a variant of *DDC-GAL4* (ref. 8), induced similar appetitive memory (Supplementary Fig. 1e, f). Furthermore, *TH-GAL80* (ref. 19) did not significantly suppress induced memory in *DDC-GAL4/UAS-dTrpA1* flies (Supplementary Fig. 1g, h), suggesting that the neurons labelled in *DDC-GAL4* but not in *TH-GAL4* flies are responsible for signalling reward. As in appetitive memory with sugar, a single thermo-activation using *DDC-GAL4* induced persistent appetitive memory, which lasted for up to 24 h (Fig. 1e). We therefore conclude that *DDC-GAL4* labels neurons signalling reward.

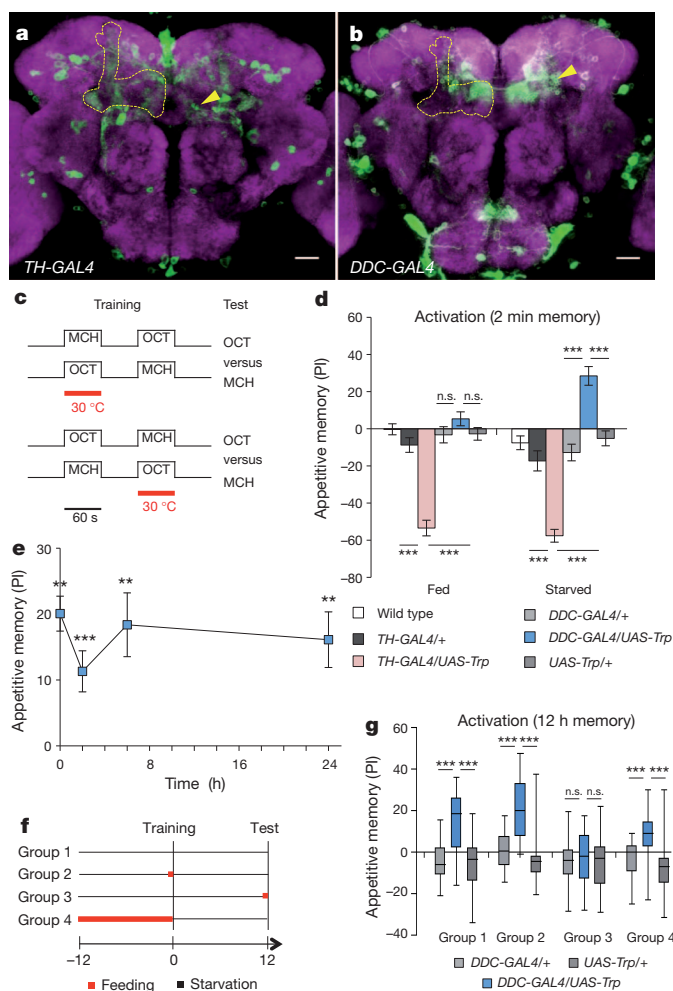


**Figure 1 | Thermo-activation with *DDC-GAL4* induces appetitive memory.** **a, b**, Expression patterns of *TH-GAL4* (**a**) and *DDC-GAL4* (**b**) in the brain with a neuropile counterstaining (magenta). Outline, MB; arrowheads, PAM neurons. Scale bars, 20  $\mu$ m. **c**, Protocol for dTRPA1 (Trp)-mediated reinforcement substitution. MCH, 4-methylcyclohexanol; OCT, octan-3-ol. **d**, Thermo-activation with *DDC-GAL4* and *TH-GAL4* with or without starvation. PI, performance index.  $n = 16$ . **e**, Retention of induced memory.  $n = 10–27$ . **f**, Protocol for feeding before the training or the test of 12-h memory. Flies were satiated with a short feed (30 min) or continuous feeding. **g**, Test of 12-h memory by thermo-activation with *DDC-GAL4*.  $n = 16$ . Midline, box boundaries and whiskers are median, quartiles and 10th and 90th centiles, respectively. Results in **d** and **e** are means  $\pm$  s.e.m. Two asterisks,  $P < 0.01$ ; three asterisks,  $P < 0.001$ ; n.s., not significant.

<sup>1</sup>Max-Planck-Institut für Neurobiologie, Martinsried 82152, Germany. <sup>2</sup>Laboratory of Primate Cognitive Neuroscience, Kunming Institute of Zoology, The Chinese Academy of Sciences, Kunming, Yunnan 650223, China. <sup>3</sup>Graduate University of the Chinese Academy of Sciences, Beijing 100049, China. <sup>4</sup>Genes and Dynamics of Memory Systems, Neurobiology Unit, Centre National de la Recherche Scientifique, École Supérieure de Physique et de Chimie Industrielles, 75005 Paris, France. <sup>5</sup>Janelia Farm Research Campus, Howard Hughes Medical Institute, Ashburn, Virginia 20147, USA.



To address when starvation is required for the dTRPA1-induced memory performance, we examined the effect of changing motivational states before either training or test by a brief feeding (Fig. 1f). Appetitive memory was induced on thermo-activation despite feeding before training (groups 2 and 4 in Fig. 1f, g). If applied before the test, feeding fully suppressed the behavioural expression of 12-h memories (group 3 in Fig. 1f, g). These results suggest that starvation is required for the retrieval, but not the acquisition, of appetitive memory induced by thermo-activation.

To explore the role of *DDC-GAL4*-labelled neurons in mediating the sugar reward, we blocked the output of these neurons using *Shi<sup>ts1</sup>*, which inhibits neuronal output at high temperature<sup>20</sup>. Unlike another known type of dopamine neurons that restricts appetitive memory retrieval<sup>15</sup>, blocking the *DDC-GAL4*-labelled neurons did not release memory expression in fed flies (Supplementary Fig. 2). Instead, the blockade impaired the acquisition, but not the expression, of the sugar-induced memory (Supplementary Fig. 3a, b). Neither memory

performance at the permissive temperature nor sugar preference at the restrictive temperature was impaired (Supplementary Fig. 3c, d).

Next we sought to identify the cells responsible for reward processing. *DDC-GAL4* heavily labels the PAM cluster neurons, whereas this cluster is sparsely labelled by *TH-GAL4* (Fig. 1a, b)<sup>8</sup>. For selective manipulation of the PAM cluster neurons, we screened a collection of *GAL4* driver lines<sup>21</sup> and identified *R58E02-GAL4*. This driver strongly labels the PAM cluster neurons and glial cells in the optic lobes with little expression elsewhere (Fig. 2a, Supplementary Fig. 4a and Supplementary Movie 1). Arbores of the PAM neurons in the MBs are largely localized to the medial lobes (Fig. 2a and Supplementary Fig. 3b). The enhancer of *R58E02-GAL4* is derived from the first intron of the *Drosophila* dopamine transporter gene. Consistently, the PAM neurons labelled in *R58E02-GAL4* as well as in *DDC-GAL4* flies are dopamine immunoreactive (Fig. 2b–e) with no detectable serotonin labelling (Supplementary Fig. 5). Thermo-activation of the PAM neurons with the use of *R58E02-GAL4* induced robust appetitive odour memory in starved flies

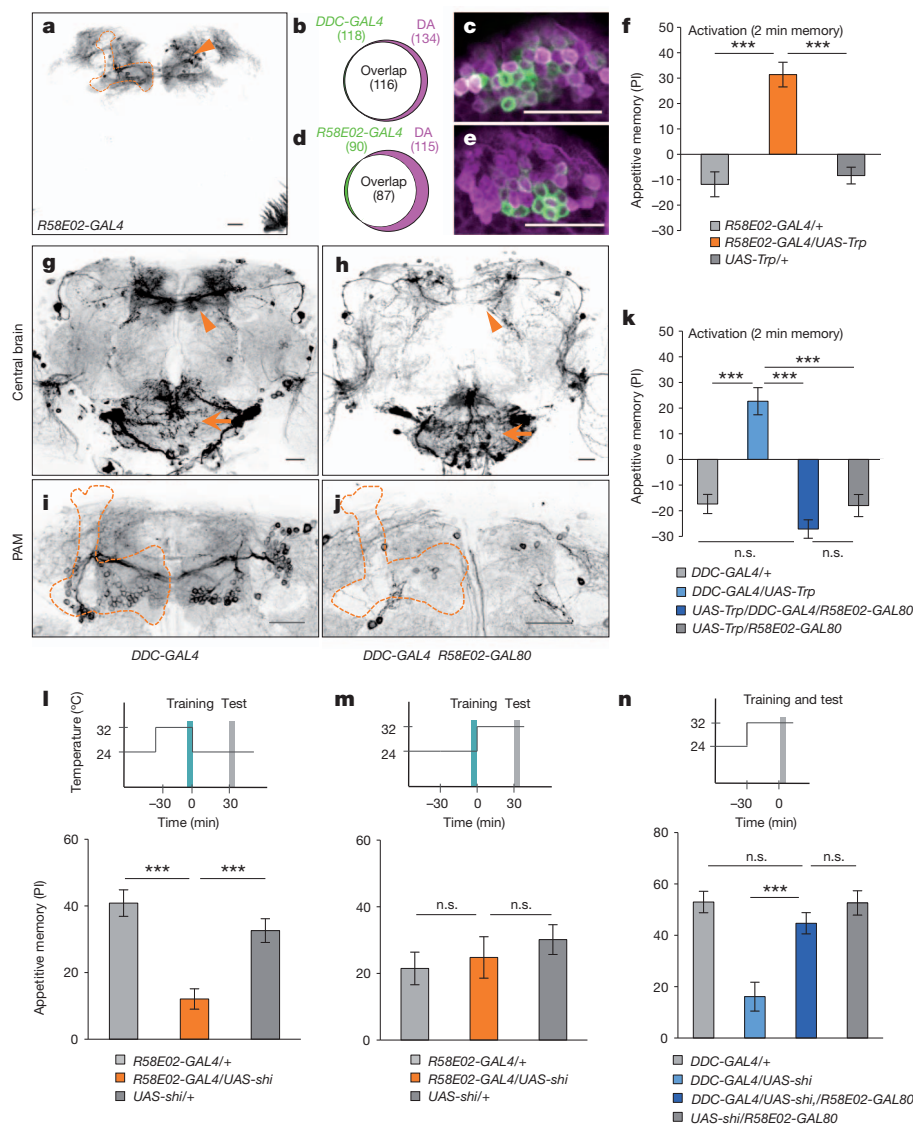


**Figure 2 | The PAM cluster neurons signal reward for olfactory memory.** **a**, Expression pattern of *R58E02-GAL4* in the central brain revealed with *UAS-mCD8::GFP*. **b–e**, Co-localization of dopamine (magenta) and *GAL4*-expressing cells (green) in the PAM cluster of *DDC-GAL4* (**b**, **c**,  $n = 6$ ) and *R58E02-GAL4* (**d**, **e**,  $n = 4$ ). **f**, Thermo-activation with *R58E02-GAL4/UAS-dTrpA1* induces significant appetitive memory.  $n = 16$ . **g–j**, *R58E02-GAL80* silences transgene expression in most PAM neurons of *DDC-GAL4* (arrowheads in **g** and **h**) without greatly affecting other neurons (such as the

subesophageal ganglion (arrows)). **k**, *R58E02-GAL80* suppresses the induction of appetitive memory by *DDC-GAL4/UAS-dTrpA1*.  $n = 10$ . **l**, **m**, Blockade of the PAM neurons in *R58E02-GAL4/UAS-shi<sup>ts1</sup>* during memory acquisition (**l**) or applied after training (**m**). **n**, *R58E02-GAL80* rescues the memory impairment in *DDC-GAL4/UAS-shi<sup>ts1</sup>*,  $n = 14–20$ . Upper panels in **l–n**, protocols; lower panels, sugar conditioning. Results with error bars are means  $\pm$  s.e.m. Three asterisks,  $P < 0.001$ ; n.s., not significant. Scale bars, 20  $\mu$ m.

(Fig. 2f), whereas the activation itself did not cause any obvious reflexive appetitive behaviour (such as proboscis extension; data not shown).

*DDC-GAL4* labels many neurons outside the PAM cluster, including those projecting to the subesophageal ganglion, where sweet taste neurons terminate (Fig. 1b). To address the contribution of the non-PAM cells in *DDC-GAL4* flies, we generated *R58E02-GAL80*, a *GAL80* line using the same enhancer integrated at the same genomic location as in *R58E02-GAL4*. Combination of *R58E02-GAL80* with *DDC-GAL4* suppressed transgene expression in most PAM neurons in *DDC-GAL4* flies (Fig. 2g–j and Supplementary Movies 2 and 3; see also Supplementary Fig. 6e). Thermo-activation with *DDC-GAL4/R58E02-GAL80* did not induce appetitive memory (Fig. 3k), demonstrating the importance of PAM neurons in reward signalling.

A transient *Shi<sup>ts1</sup>* block of the PAM neurons by *R58E02-GAL4* impaired the acquisition, but not the expression, of sugar-induced memory (Fig. 2l, m). Furthermore, blocking the PAM neurons did not impair the reflexive choice of sugar (Supplementary Fig. 4c). Consistently, *R58E02-GAL80* rescued the memory impairment of *DDC-GAL4/UAS-shi<sup>ts1</sup>* flies (Fig. 2n). Thus, the PAM neurons are necessary and sufficient for signalling the sugar reward.

Expression of a presynaptic marker using *R58E02-GAL4* demonstrated that input and output sites of the PAM neurons are highly segregated, with presynaptic terminals localized predominantly in the MBs (Fig. 3a–c). To address whether the signal from the PAM neurons is mediated by dopamine receptors, we activated these neurons in the background of *dumb<sup>2</sup>*, a mutant for the *dDA1* gene (also known as *DopR*), which encodes a D1-type dopamine receptor. We first confirmed the previously reported role of *dDA1* in the Kenyon cells of the MBs for sugar-induced appetitive memory (Fig. 3d)<sup>16</sup>. Because we wished to use a *GAL4* driver to express *dDA1* in Kenyon cells simultaneously with *dTRPA1* in the PAM neurons, we generated a *LexA* driver *R58E02-LexA::p65*. It recapitulated the expression pattern in *R58E02-GAL4* and was able to induce appetitive memory using *LexAop2-dTrpA1* (Fig. 3e and Supplementary Fig. 6c, d). Activation of the PAM neurons failed to induce marked appetitive memory in flies lacking *dDA1* (Fig. 3f). Driving wild-type *dDA1* expression in  $\alpha/\beta$  and  $\gamma$  Kenyon cells by using the driver *MB247-GAL4* restored appetitive memory in *R58E02-LexA/LexAop2-dTrpA1* flies (Fig. 3f). These results indicate the importance of dopamine signalling in the MBs for reward processing, but do not exclude a role for other possible co-transmitters released by the PAM neurons.

We previously identified that MB-M3 neurons in the PAM cluster are important for aversive memory formation<sup>10</sup>. We labelled both MB-M3 and the reward-signalling PAM neurons in the same brain and found no overlap (Fig. 3g–i, Supplementary Fig. 7 and Supplementary Movie 4). This highlights the functional heterogeneity of individual cell types in the PAM cluster.

Similarly, we made different populations of dopamine neurons that signal appetitive and aversive reinforcement visible by using *R58E02-LexA* and *TH-GAL4*, respectively, and examined the distribution of their projections in the MBs. The terminals of the PAM and protocerebral posterior lateral (PPL)1 clusters are largely non-overlapping in the MBs and together cover the entire lobes (Fig. 3j–l and Supplementary Movie 5) despite the simultaneous expression of *R58E02-LexA* and *TH-GAL4* in a few PAM cluster neurons (Supplementary Fig. 8a–d). Thus, axonal compartments of Kenyon cells are targeted by functionally different dopamine neurons.

Given the importance of octopamine signalling in reward processing<sup>5,11–13</sup>, we activated the PAM cluster neurons in *T $\beta$ H* mutants, which lack octopamine<sup>22</sup>. We found no marked effect of *T $\beta$ H* on appetitive memory induced by activation of the PAM neurons (Fig. 4a), indicating that the PAM neurons act in parallel with or downstream of, but not upstream of, octopamine signalling. Consistently, double labelling of the octopamine and PAM cluster dopamine neurons revealed potential direct contacts of these arbourers in the spur of the  $\gamma$  lobe and protocerebral regions (Fig. 4b–d), where

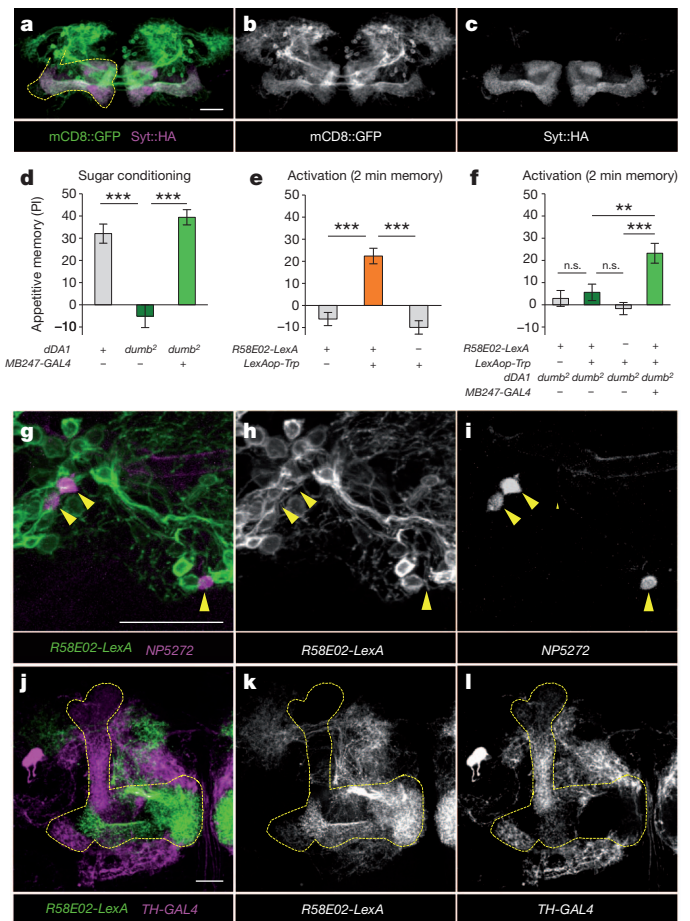


**Figure 3 | The PAM neurons convey the reward signal to the MB.**

**a–c**, Presynaptic terminals (magenta) of the PAM neurons (green) in *R58E02-GAL4* are localized to the MB (outline). **d**, The defect in sugar-induced memory in *dumb<sup>2</sup>*, a piggyBac insertion allowing *GAL4*-mediated *dDA1* expression<sup>16</sup>, is rescued by *MB247-GAL4*.  $n = 16$ . **e**, Appetitive memory induced by thermo-activation in *R58E02-LexA/LexAop2-dTrpA1*.  $n = 16$ . **f**, Thermo-activation of the PAM neurons in *dumb<sup>2</sup>* induces memory by rescuing *dDA1* in the MB.  $n = 14–22$ . **g–i**, No detectable overlap of *R58E02-LexA*-labelled neurons expressing *mCD8::GFP* (green) and MB-M3 neurons (magenta; arrowheads) visualized with *mCD8::RFP*. See also Supplementary Fig. 7. **j–l**, Differential labelling of *R58E02-LexA* (green) and *TH-GAL4* (magenta) in the MB lobe region. Results with error bars are means  $\pm$  s.e.m. Two asterisks,  $P < 0.01$ ; three asterisks,  $P < 0.001$ ; n.s., not significant. Scale bars, 20  $\mu$ m.

the putative input and output sites of the PAM and octopamine neurons, respectively, are located (Fig. 3a–c)<sup>23</sup>. This suggests that octopamine may regulate reward processing by directly modulating the activity of the PAM cluster neurons.

To test whether the PAM neurons respond to the sugar reward, we performed *in vivo* calcium imaging in starved flies expressing the fluorescent calcium reporter *GCaMP3*. We devised a gustatory stimulation protocol with the unrestrained proboscis that enabled confocal imaging of the PAM terminals in the MBs (Supplementary Fig. 9). Sugar ingestion caused stronger calcium responses than water or a bitter caffeine solution (Fig. 4e–g). We found that the calcium response of the PAM neurons on stimulation with sugar was greatly reduced when flies were fed (Fig. 4h). Flies can sense sweet taste with their tarsi, but stimulating tarsi with sugar barely activated the PAM neurons, suggesting that sweet substances need to be ingested to trigger the reward signal (Fig. 4h).

Our data suggest the existence of a reward circuit in which the PAM neurons integrate gustatory reward and other relevant regulatory inputs, and then convey the summed positive value signal to specific subdomains of the MBs (Fig. 4i). The MB lobes can be anatomically



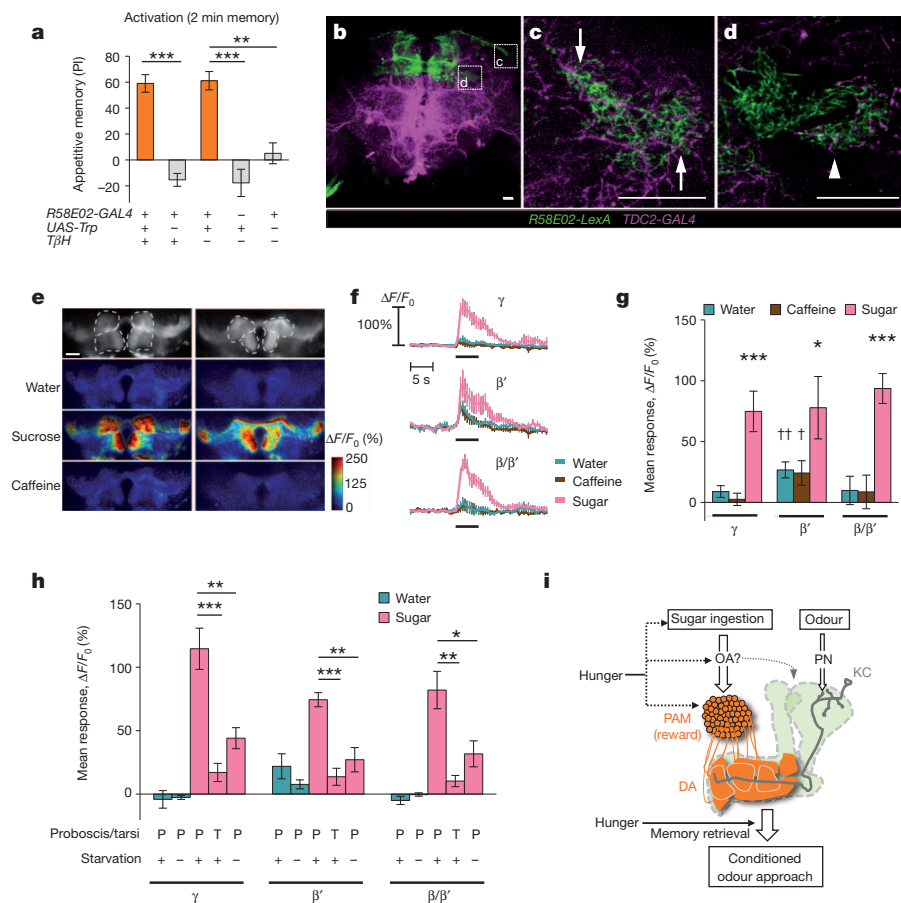


**Figure 4 | The PAM neurons integrate reward and relevant signals.** **a**, Thermo-activation of the PAM neurons induces appetitive memory without octopamine.  $n = 16$ –22. **b–d**, Octopamine and PAM neurons contact each other (arrows) in a protocerebral region (**c**) and the spur of the  $\gamma$  lobe (**d**). **e–g**, The PAM neurons respond selectively to the sugar reward. **e**, Representative images (anterior down) and calcium responses of the PAM neurons at different levels of the MB. **f**, Time course of responses.  $n = 10$ . Black bar: stimulus application. **g**, Average response to different gustatory substances. Terminals in the  $\beta'$  lobe responded significantly to water and caffeine (dagger,  $P < 0.05$ ; two daggers,  $P < 0.01$  in one-sample  $t$ -test from zero). **h**, Response of the PAM neurons without starvation or with tarsal stimulation only.  $n > 7$ . **i**, Model of a reward circuit in the fly brain. Dashed arrows indicate hypothetical pathways. The reward value integrated by the PAM neurons is signalled by dopamine (DA) to the MB (green shading), thus they may drive associative plasticity in odour-representing Kenyon cells (KC, grey). OA, octopamine; PN, projection neurons. Results with error bars are means  $\pm$  s.e.m. Asterisk,  $P < 0.05$ ; two asterisks,  $P < 0.01$ ; three asterisks,  $P < 0.001$ . Scale bars, 20  $\mu$ m.

divided into 35 subdomains that are defined by specific combinations of intrinsic and extrinsic neurons<sup>24</sup>. Distinct sets of dopamine neurons may provide functionally independent local circuits within the MBs, potentially allowing appetitive and aversive modulation of the same odour. The PAM neurons may drive positive associative modulation of concomitant olfactory signals of the Kenyon cells (Fig. 4i). The dual processing of appetitive and aversive stimuli may be a conserved function of dopamine, highlighting the physiological pleiotropy of a neurotransmitter<sup>4,25,26</sup>.

## METHODS SUMMARY

The genomic fragment *R58E02* was cloned into previously described vectors<sup>21,27</sup>. Sugar conditioning and thermo-activation with two odours (4-methylcyclohexanol and octan-3-ol) and fluorescent immunohistochemistry were performed as described previously<sup>10</sup>. Sugar preference was measured with a previously described setup<sup>28</sup>, with slight modification. Most of the groups tested did not violate the assumption of the normal distribution and the homogeneity of variance. Performance indices were therefore subjected to parametric statistics. For data that significantly differed from the normal distribution (Fig. 1g), non-parametric statistics were applied. For *in vivo* calcium imaging, female flies expressing GCaMP3 (ref. 29) with *R58E02-GAL4* were singly prepared as described<sup>30</sup>, with slight modifications. A droplet of 8  $\mu$ l of mineral water, 1 M sucrose or 0.1 M caffeine solution in mineral water was delivered on a plastic plate controlled by a micromanipulator (Supplementary Fig. 9).

**Full Methods** and any associated references are available in the online version of the paper.

Received 10 April; accepted 8 June 2012.

Published online 18 July 2012.

- Schultz, W. Behavioral theories and the neurophysiology of reward. *Annu. Rev. Psychol.* **57**, 87–115 (2006).
- Tempel, B. L., Bonini, N., Dawson, D. R. & Quinn, W. G. Reward learning in normal and mutant *Drosophila*. *Proc. Natl Acad. Sci. USA* **80**, 1482–1486 (1983).

- Kaun, K. R., Azanchi, R., Maung, Z., Hirsh, J. & Heberlein, U. A *Drosophila* model for alcohol reward. *Nature Neurosci.* **14**, 612–619 (2011).
- Waddell, S. Dopamine reveals neural circuit mechanisms of fly memory. *Trends Neurosci.* **33**, 457–464 (2010).
- Schwaerzel, M. et al. Dopamine and octopamine differentiate between aversive and appetitive olfactory memories in *Drosophila*. *J. Neurosci.* **23**, 10495–10502 (2003).
- Tranoy, S., Redt-Clouet, C., Dura, J. M. & Preat, T. Parallel processing of appetitive short- and long-term memories in *Drosophila*. *Curr. Biol.* **21**, 1647–1653 (2011).
- Riemensperger, T., Völler, T., Stock, P., Buchner, E. & Fiala, A. Punishment prediction by dopaminergic neurons in *Drosophila*. *Curr. Biol.* **15**, 1953–1960 (2005).
- Claridge-Chang, A. et al. Writing memories with light-addressable reinforcement circuitry. *Cell* **139**, 405–415 (2009).
- Mao, Z. & Davis, R. L. Eight different types of dopaminergic neurons innervate the *Drosophila* mushroom body neuropil: anatomical and physiological heterogeneity. *Front. Neural Circuits* **3**, 5 (2009).
- Aso, Y. et al. Specific dopaminergic neurons for the formation of labile aversive memory. *Curr. Biol.* **20**, 1445–1451 (2010).
- Mizunami, M. & Matsumoto, Y. Roles of aminergic neurons in formation and recall of associative memory in crickets. *Front. Neurosci.* **4**, 172 (2010).
- Hammer, M. An identified neuron mediates the unconditioned stimulus in associative olfactory learning in honeybees. *Nature* **366**, 59–63 (1993).
- Schroll, C. et al. Light-induced activation of distinct modulatory neurons triggers appetitive or aversive learning in *Drosophila* larvae. *Curr. Biol.* **16**, 1741–1747 (2006).
- Yarali, A. & Gerber, B. A neurogenetic dissociation between punishment-, reward-, and relief-learning in *Drosophila*. *Front. Behav. Neurosci.* **4**, 189 (2010).
- Krashes, M. J. et al. A neural circuit mechanism integrating motivational state with memory expression in *Drosophila*. *Cell* **139**, 416–427 (2009).
- Kim, Y. C., Lee, H. G. & Han, K. A. D1 dopamine receptor dDA1 is required in the mushroom body neurons for aversive and appetitive learning in *Drosophila*. *J. Neurosci.* **27**, 7640–7647 (2007).
- Selcho, M., Pauls, D., Han, K. A., Stocker, R. F. & Thum, A. S. The role of dopamine in *Drosophila* larval classical olfactory conditioning. *PLoS ONE* **4**, e5897 (2009).
- Hamada, F. N. et al. An internal thermal sensor controlling temperature preference in *Drosophila*. *Nature* **454**, 217–220 (2008).
- Sitaraman, D. et al. Serotonin is necessary for place memory in *Drosophila*. *Proc. Natl Acad. Sci. USA* **105**, 5579–5584 (2008).
- Kitamoto, T. Conditional modification of behavior in *Drosophila* by targeted expression of a temperature-sensitive *shibire* allele in defined neurons. *J. Neurobiol.* **47**, 81–92 (2001).



21. Pfeiffer, B. D. *et al.* Tools for neuroanatomy and neurogenetics in *Drosophila*. *Proc. Natl Acad. Sci. USA* **105**, 9715–9720 (2008).
22. Monastirioti, M., Linn, C. E. Jr & White, K. Characterization of *Drosophila* tyramine  $\beta$ -hydroxylase gene and isolation of mutant flies lacking octopamine. *J. Neurosci.* **16**, 3900–3911 (1996).
23. Busch, S., Selcho, M., Ito, K. & Tanimoto, H. A map of octopaminergic neurons in the *Drosophila* brain. *J. Comp. Neurol.* **513**, 643–667 (2009).
24. Tanaka, N. K., Tanimoto, H. & Ito, K. Neuronal assemblies of the *Drosophila* mushroom body. *J. Comp. Neurol.* **508**, 711–755 (2008).
25. van Swinderen, B. & Andretic, R. Dopamine in *Drosophila*: setting arousal thresholds in a miniature brain. *Proc. R. Soc. B* **278**, 906–913 (2011).
26. Bromberg-Martin, E. S., Matsumoto, M. & Hikosaka, O. Dopamine in motivational control: rewarding, aversive, and alerting. *Neuron* **68**, 815–834 (2010).
27. Pfeiffer, B. D. *et al.* Refinement of tools for targeted gene expression in *Drosophila*. *Genetics* **186**, 735–755 (2010).
28. Schnaitmann, C., Vogt, K., Triphan, T. & Tanimoto, H. Appetitive and aversive visual learning in freely moving *Drosophila*. *Front. Behav. Neurosci.* **4**, 10 (2010).
29. Tian, L. *et al.* Imaging neural activity in worms, flies and mice with improved GCaMP calcium indicators. *Nature Methods* **6**, 875–881 (2009).
30. Séjourné, J. *et al.* Mushroom body efferent neurons responsible for aversive olfactory memory retrieval in *Drosophila*. *Nature Neurosci.* **14**, 903–910 (2011).

**Supplementary Information** is linked to the online version of the paper at [www.nature.com/nature](http://www.nature.com/nature).

**Acknowledgements** We thank L. Bräcker, M. Feind, C. Murphy, C. Schnaitmann and T. Templier for technical assistance and experiments that inspired this study; P. Garrity,

the Kyoto *Drosophila* Genetic Resource Center and the Bloomington Stock Center for fly stocks; and Y.Y. Ma, Z. Q. Meng, R. Menzel, A. Thum, S. Waddell and the members of the Tanimoto laboratory for discussion and/or critical reading of the manuscript. C.L., Y.A., N.Y. and P.-Y.P. were sponsored by a Chinese–European doctoral training program from Max-Planck-Gesellschaft and the Chinese Academy of Sciences, the Deutscher Akademischer Austausch Dienst, the Alexander von Humboldt Foundation, and the Région Île-de-France, respectively. This work was supported by the Agence Nationale pour la Recherche (T.P.), the Howard Hughes Medical Institute (G.M.R.), Bernstein Focus Learning from the Bundesministerium für Bildung und Forschung and the Max-Planck-Gesellschaft (H.T.).

**Author Contributions** C.L., N.Y., Y.A. and H.T. designed and C.L. and N.Y. performed all the behavioural experiments in this study. P.Y.P., T.P. and H.T. designed *in vivo* imaging experiments, and P.Y.P. and T.P. devised a new gustatory stimulation method. P.Y.P. performed imaging experiments and analysed the data. B.D.P. and G.M.R. designed and generated the new transgenic flies (GAL4, GAL80, LexA and *LexAop2-dTrpA1* lines). Y.A. and H.T. identified *R58E02* by using a database of GAL4 expression patterns created by G.M.R. and the Janelia Farm Fly Light Project Team. A.B.F. and I.S. performed immunohistochemistry, and C.L., A.B.F. and H.T. analysed the microscopic data. C.L. and H.T. made the figures and wrote the paper with the help of all the other authors.

**Author Information** Reprints and permissions information is available at [www.nature.com/reprints](http://www.nature.com/reprints). The authors declare no competing financial interests. Readers are welcome to comment on the online version of this article at [www.nature.com/nature](http://www.nature.com/nature). Correspondence and requests for materials should be addressed to H.T. ([hiromut@neuro.mpg.de](mailto:hiromut@neuro.mpg.de)).

## METHODS

**Flies.** The 1.2 kb DNA enhancer fragment in *R58E02* was amplified by PCR (primer sequences 5'-cgaaggcgcaacagctccgattttg-3' and 5'-ccttgacccaaatgtggag atccc-3') and originates from the *dopamine transporter* locus<sup>31</sup>. The fragment was cloned into the transformation vectors pBPGUw (ref. 21), pBPGAL80Uw-6 (ref. 27) and pBPLexA::p65Uw (ref. 27). *R58E02-GAL4* and *R58E02-GAL80* were integrated into *attP2* (3L), and *R58E02-LexA::p65* was integrated into *attP40* (2L) using PhiC31 integrase. *pJFRC26-13XLexAop2-IVS-dTrpA1-WPRE* and *pJFRC15-13XLexAop2-mCD8::GFP* were cloned using the modified LexA vector and integrated into *VK00005* (3L) and *su(Hw)attP8* (X), respectively, using PhiC31-mediated site-specific recombination.

Behavioural experiments (except Fig. 4d) used F<sub>1</sub> progenies of crosses between females of *w;UAS-dTrpA1* (ref. 18), *w;UAS-shi<sup>ts1</sup>* (one copy of *UAS-shi* from the Preat laboratory)<sup>20</sup>, *w;LexAop2-dTrpA1*, *w;UAS-dTrpA1;R58E02-GAL80*, *w;UAS-shi<sup>ts1</sup> R58E02-GAL80*, *w;UAS-dTrpA1;dumb<sup>2</sup>*, *TβH<sup>M18</sup>/FM7* (ref. 22), *TβH<sup>M18</sup>/FM7;UAS-dTrpA1*, *w;R58E02-LexA;dumb<sup>2</sup>*, *w;R58E02-LexA;dumb<sup>2</sup> MB247-GAL4*, *w;dumb<sup>2</sup>* or *w* females and males of *w;TH-GAL4* (ref. 32), *w;DDC-GAL4* (ref. 33), *w;HL9-GAL4* (ref. 8), *w;R58E02-GAL4*, *w;R58E02-LexA::p65*, *w;dumb<sup>2</sup>*, *w;LexAop-dTrpA1 dumb<sup>2</sup>* or *w* males, raised 60% relative humidity with a 14h/10h light/dark cycle. Crosses with *UAS-dTrpA1 (LexAop-dTrpA1)* and *UAS-shi<sup>ts1</sup>* flies were raised at 23 and 17 °C, respectively. At experimentation, flies were aged 3–14 days after eclosion and starved according to mortality rate. For the experiments with *TβH*, the performance of the male progeny was used for calculating PI. For immunohistochemistry, female reporter strains *yw UAS-mCD8::GFP<sup>34</sup>*, *w mCD8::GFP;TH-GAL80;mCD8::GFP*, *w UAS-Syt::HA;UAS-mCD8::GFP<sup>35</sup>*, *w;UAS-mCD8::GFP;R58E02-GAL80* or *w pJFRC21-10XUAS-IVS-mCD8::RFP (attP18) pJFRC15-13XLexAop2-mCD8::GFP (su(Hw)attP8)* were crossed to male *GAL4* drivers, *w;TH-GAL4*, *w;DDC-GAL4*, *w;HL9-GAL4*, *w;R58E02-GAL4*, *w;R58E02-LexA::p65*, *w;NP5272* or *w;TDC2-GAL4* (ref. 36). Flies used for whole-mount immunohistochemistry were aged to 5–10 days after eclosion.

**Behavioural assays.** The conditioning protocol was as described previously<sup>10</sup>. Except where noted, behavioural experiments were performed in dim red light for training phases and in complete darkness for tests. A group of about 50 flies in a training tube alternately received octan-3-ol (OCT; Merck) and 4-methylcyclohexanol (MCH; Sigma-Aldrich) for 1 min in a constant air stream (Fig. 1c and Supplementary Fig. 1c). OCT and MCH were diluted 1:10 in paraffin oil (Sigma-Aldrich) and presented in a cup with a diameter of 3 and 5 mm, respectively. For sugar-induced memory, filter paper was soaked in 2 M sucrose solution, dried, and presented together with one of the odours (Supplementary Fig. 1c). Alternately, the control odour was paired with dried filter paper (Supplementary Fig. 1c). For thermo-activation with *dTRPA1*, flies were trained by being transferred from a background temperature of 24 °C to a pre-warmed tube in a climate box (30 °C) and presented with the trained odorant (Fig. 1c)<sup>10</sup>. Temperature was measured with a VC-960 digital multimeter (Votcraft). For unpaired thermo-activation with *dTRPA1*, flies were exposed to the pre-warmed tube either between or after the two odorants (Supplementary Fig. 1a). The restrictive temperature for the experiments with *UAS-shi<sup>ts1</sup>* was 32 °C. For memory retention, trained flies were kept in a vial with moistened filter paper. After a given retention time, the trained flies were allowed to choose between MCH and OCT for 2 min in a T-maze. A learning index was then calculated by taking the mean preference of the two reciprocally trained groups<sup>2</sup>. Half of the trained groups received reinforcement together with the first presented odour and the other half with the second odour to cancel the effect of the order of reinforcement. To control feeding motivation, flies were kept in a food vial for 30 min before training or test. For 24-h memory, flies were fed for 1 h after training.

For testing sugar preference, flies were placed in a cylindrical, infrared-illuminated arena, and given a choice between two halves of dried filter paper, one of which was soaked in 2 M sucrose<sup>28</sup>. The arena was video-recorded from above with a CMOS video camera (Firefly MV; Point Grey) at one frame per second, and the first 120 s were analysed. The performance index represents the difference in the number of flies in the two halves, divided by the total number of flies.

**Statistics.** Statistical analyses were performed with Prism5 software (GraphPad). Most tested groups did not violate the assumption of normal distribution and homogeneity of variance. All the data except the experiment in Fig. 1g were therefore analysed with parametric statistics: one-sample *t*-test or one-way analysis of variance followed by the planned pairwise multiple comparisons (Bonferroni). Because the data in Fig. 1g were significantly different from the normal distribution, non-parametric statistics (that is, Kruskal–Wallis test followed by Dunn's multiple pairwise comparison test) were applied. The significance level of statistical tests was set to 0.05.

**Histochemistry.** Immunolabelling was performed with a standard protocol<sup>10</sup>, with the exception of a fixation (0.6% glutaraldehyde in PBS for 30 min) and the following glutaraldehyde protocol for dopamine<sup>23</sup>. Fluorescence of *mCD8::GFP* and *mCD8::RFP* was detected without immunohistochemistry. Frontal optical sections of whole-mount brains were sampled with a confocal microscope (Olympus FV1000). To evaluate the effect of *R58E02-GAL80*, brains to be compared were scanned with comparable intensity and offset. Confocal stacks were analysed with Image-J (National Institutes of Health).

**In vivo calcium imaging.** Female flies of the genotype *w<sup>1118</sup>;UAS-GCaMP3/+;R58E02-GAL4/+* aged 1–2 days after eclosion were prepared essentially as described<sup>30</sup>, with the following modifications: the fly was briefly anaesthetized with CO<sub>2</sub>; the proboscis was left free, to enable ingestion (except in tarsal stimulation experiments, in which the proboscis was occluded with the glue); sucrose was replaced with ribose in the solution for bathing the head capsule during surgery<sup>37</sup>. At the end of the surgery, the brain was covered with a drop of the same solution supplemented with 1% agarose, so that the brain was embedded in a gel to limit motion artefacts. Time courses of fluorescence changes were recorded in a transverse section of the brain showing the projections of PAM neurons in the different levels of both MB medial lobes at a rate of two images per second. The terminals on the  $\gamma$  and  $\beta'$  lobes were clearly discernible, whereas the slice of the  $\beta$  terminals might contain some  $\beta'$  terminals. We therefore here use the label ' $\beta/\beta'$  terminals' collectively. Three types of stimulation were performed: a droplet of 8  $\mu$ l of mineral water, 1 M sucrose or 0.1 M caffeine solution in mineral water deposited on a plastic plate was brought within reachable distance of the fly for 5 s with the use of a micromanipulator. These concentrations were chosen because they elicit saturating responses in taste neurons in the subesophageal ganglion (SOG)<sup>37</sup>. The solutions were delivered in random order, and when sucrose was not the last solution tested, an additional sucrose response was measured at the end of the experiment as a positive control, which was not included in analyses.

Image analysis was performed essentially as described<sup>30</sup>. For each region of interest, the baseline ( $F_0$ ) was estimated as the mean fluorescence over the 10 s preceding the stimulus, and the mean response was calculated as the average of  $\Delta F/F_0$  during the period when the drop of solution was available. Responses from both hemispheres were averaged to yield the mean response of each fly, but for time courses (Fig. 4f) only one hemisphere was considered for each animal (six right, four left).

- Kume, K. *et al.* Dopamine is a regulator of arousal in the fruit fly. *J. Neurosci.* **25**, 7377–7384 (2005).
- Friggi-Grelin, F. *et al.* Targeted gene expression in *Drosophila* dopaminergic cells using regulatory sequences from tyrosine hydroxylase. *J. Neurobiol.* **54**, 618–627 (2003).
- Li, H., Chaney, S., Roberts, I. J., Forte, M. & Hirsh, J. Ectopic G-protein expression in dopamine and serotonin neurons blocks cocaine sensitization in *Drosophila melanogaster*. *Curr. Biol.* **10**, 211–214 (2000).
- Lee, T. & Luo, L. Mosaic analysis with a repressible cell marker for studies of gene function in neuronal morphogenesis. *Neuron* **22**, 451–461 (1999).
- Robinson, I. M., Ranjan, R. & Schwarz, T. L. Synaptotagmins I and IV promote transmitter release independently of Ca<sup>2+</sup> binding in the C<sub>2</sub>A domain. *Nature* **418**, 336–340 (2002).
- Cole, S. H. *et al.* Two functional but non-complementing *Drosophila* tyrosine decarboxylase genes: distinct roles for neural tyramine and octopamine in female fertility. *J. Biol. Chem.* **280**, 14948–14955 (2005).
- Marella, S. *et al.* Imaging taste responses in the fly brain reveals a functional map of taste category and behavior. *Neuron* **49**, 285–295 (2006).

# Protocadherins mediate dendritic self-avoidance in the mammalian nervous system

Julie L. Lefebvre<sup>1</sup>, Dimitar Kostadinov<sup>1</sup>, Weisheng V. Chen<sup>2</sup>, Tom Maniatis<sup>2</sup> & Joshua R. Sanes<sup>1</sup>

Dendritic arborizations of many neurons are patterned by a process called self-avoidance, in which branches arising from a single neuron repel each other<sup>1–7</sup>. By minimizing gaps and overlaps within the arborization, self-avoidance facilitates complete coverage of a neuron's territory by its neurites<sup>1–3</sup>. Remarkably, some neurons that display self-avoidance interact freely with other neurons of the same subtype, implying that they discriminate self from non-self. Here we demonstrate roles for the clustered protocadherins (Pcdhs) in dendritic self-avoidance and self/non-self discrimination. The *Pcdh* locus encodes 58 related cadherin-like transmembrane proteins, at least some of which exhibit isoform-specific homophilic adhesion in heterologous cells and are expressed stochastically and combinatorially in single neurons<sup>7–11</sup>. Deletion of all 22 *Pcdh* genes in the mouse  $\gamma$ -subcluster (*Pcdhg* genes) disrupts self-avoidance of dendrites in retinal starburst amacrine cells (SACs) and cerebellar Purkinje cells. Further genetic analysis of SACs showed that *Pcdhg* proteins act cell-autonomously during development, and that replacement of the 22 *Pcdhg* proteins with a single isoform restores self-avoidance. Moreover, expression of the same single isoform in all SACs decreases interactions among dendrites of neighbouring SACs (heteroneuronal interactions). These results suggest that homophilic *Pcdhg* interactions between sibling neurites (isoneuronal interactions) generate a repulsive signal that leads to self-avoidance. In this model, heteroneuronal interactions are normally permitted because dendrites seldom encounter a matched set of *Pcdhg* proteins unless they emanate from the same soma. In many respects, our results mirror those reported for *Dscam1* (Down syndrome cell adhesion molecule) in *Drosophila*: this complex gene encodes thousands of recognition molecules that exhibit stochastic expression and isoform-specific interactions, and mediate both self-avoidance and self/non-self discrimination<sup>4–7,12–15</sup>. Thus, although insect *Dscam* and vertebrate *Pcdh* proteins share no sequence homology, they seem to underlie similar strategies for endowing neurons with distinct molecular identities and patterning their arborizations.

The 58 genes of the mouse *Pcdh* locus are tandemly arranged in  $\alpha$ -,  $\beta$ - and  $\gamma$ -subclusters, called *Pcdha*, *Pcdhb* and *Pcdhg*, which encode 14, 22 and 22 cadherin-like proteins, respectively<sup>8</sup> (Fig. 1a). In the *Pcdha* and *Pcdhg* subclusters, single variable exons encoding extracellular, transmembrane and juxtamembrane domains are spliced to three constant exons, generating proteins with unique extracellular but common intracellular domains<sup>8</sup>. The complexity of this locus is reminiscent of that of *Dscam1*, which mediates self-avoidance in *Drosophila*<sup>4–7,15</sup>. Moreover, *Pcdh* genes, like *Dscam1*, exhibit stochastic expression, and both *Pcdhg* and *Dscam* proteins exhibit isoform-specific homotypic recognition<sup>13,14</sup>. In contrast, the two vertebrate *Dscams* are not complex genes, so although they mediate both repulsive and attractive interactions among neurons<sup>16–19</sup>, they are unlikely to underlie self/non-self discrimination. We therefore investigated roles of *Pcdh* genes in these processes.

Previous studies of mouse mutants lacking all 22 *Pcdhg* genes revealed that they are required for survival of multiple neuronal

types<sup>20–23</sup>. To seek roles of *Pcdh*s in self-avoidance, we focused on a retinal interneuron, the SAC, which expresses *Pcdhg* genes<sup>22</sup> and exhibits marked dendritic self-avoidance<sup>24</sup>. Radially symmetric SAC dendritic arborizations are confined to narrow planes within the inner plexiform (synaptic) layer; SACs have no axons. Dendrites of a single SAC seldom cross one another, yet dendrites of neighbouring SACs cross freely (Fig. 1b, c; Supplementary Fig. 1) and even form synapses with each other<sup>24,25</sup>, suggesting that they can distinguish 'self' from 'non-self'.

We used a conditional mutant (*Pcdhg*<sup>con3</sup>)<sup>22</sup> to bypass the neonatal lethality of constitutive *Pcdhg* mutants and employed Cre drivers that delete *Pcdhg* genes from all or subsets of retinal cells. We visualized individual neurons by infection with recombinant adeno-associated virus (rAAV) expressing a fluorescent protein (XFP; Fig. 1d, e), biolistic delivery of DNA encoding XFP, or intracellular injection of a fluorescent dye. We identified SACs, the sole cholinergic neurons in retina, with antibodies to choline acetyltransferase (ChAT), which also demonstrated the association of XFP-positive SAC dendrites with dendrites from other (XFP-negative) SACs (Supplementary Figs 1 and 2).

SAC morphology was profoundly altered in *Pcdhg* mutant retinas (*Pcdhg*<sup>con3/con3</sup>; *retina-cre*, called *Pcdhg*<sup>rko/rko</sup> here; see Methods for genotypes). Dendrites arising from a single SAC frequently crossed each other and sometimes formed loose bundles (Fig. 1f–i and Supplementary Fig. 1). Crossing frequency was increased several-fold in both proximal and distal regions of the arborization (Fig. 1j). These defects were highly specific, in that the diameter of SAC arborizations, the number of dendritic termini, the laminar targeting of SAC dendrites, and the mosaic arrangement of SAC bodies were all unaffected in *Pcdhg*<sup>rko/rko</sup> mutants (Fig. 1k, l and Supplementary Figs 1 and 2). Thus, *Pcdh*s are dispensable for many aspects of SAC morphogenesis but are required for their self-avoidance.

In the absence of *Pcdhg* genes, neurons of many types die in elevated numbers during the period of naturally occurring cell death<sup>20–23</sup>. Although SACs are largely spared in *Pcdhg* mutants<sup>22</sup>, their dendritic defects might be secondary to loss of other neurites with which they ordinarily interact. To test this possibility, we blocked apoptosis by deleting the *Bax* gene, which is required for naturally occurring and *Pcdhg*-dependent neuronal death<sup>22,23,26</sup>. SAC morphology was normal in *Bax*<sup>−/−</sup> mice, but self-avoidance defects persisted in *Bax*<sup>−/−</sup>; *Pcdhg*<sup>rko/rko</sup> double mutants (Supplementary Fig. 3).

We next asked whether *Pcdh*s are required for the development of SAC arborizations, or only for their maintenance. In wild-type neonates, SACs extended dendrites that branched profusely and contacted each other (Fig. 2a–c). By postnatal day (P)12, however, excess neurites and isoneuronal contacts were eliminated, resulting in a radial arborization with evenly spaced branches (Fig. 2d, and see ref. 24). Thus, self-avoidance arises rapidly following a short period of isoneuronal 'sampling'. In *Pcdhg*<sup>rko/rko</sup> mice, SACs were clearly aberrant by P3, exhibiting excessive crossing and tangling of neurites (Fig. 2e–g). Excess branches were subsequently eliminated, but

<sup>1</sup>Center for Brain Science and Department of Molecular and Cellular Biology, Harvard University, 52 Oxford Street, Cambridge, Massachusetts 02138, USA. <sup>2</sup>Department of Biochemistry and Molecular Biophysics, Columbia University Medical Center, 701 West 168th Street, New York, New York 10032, USA.



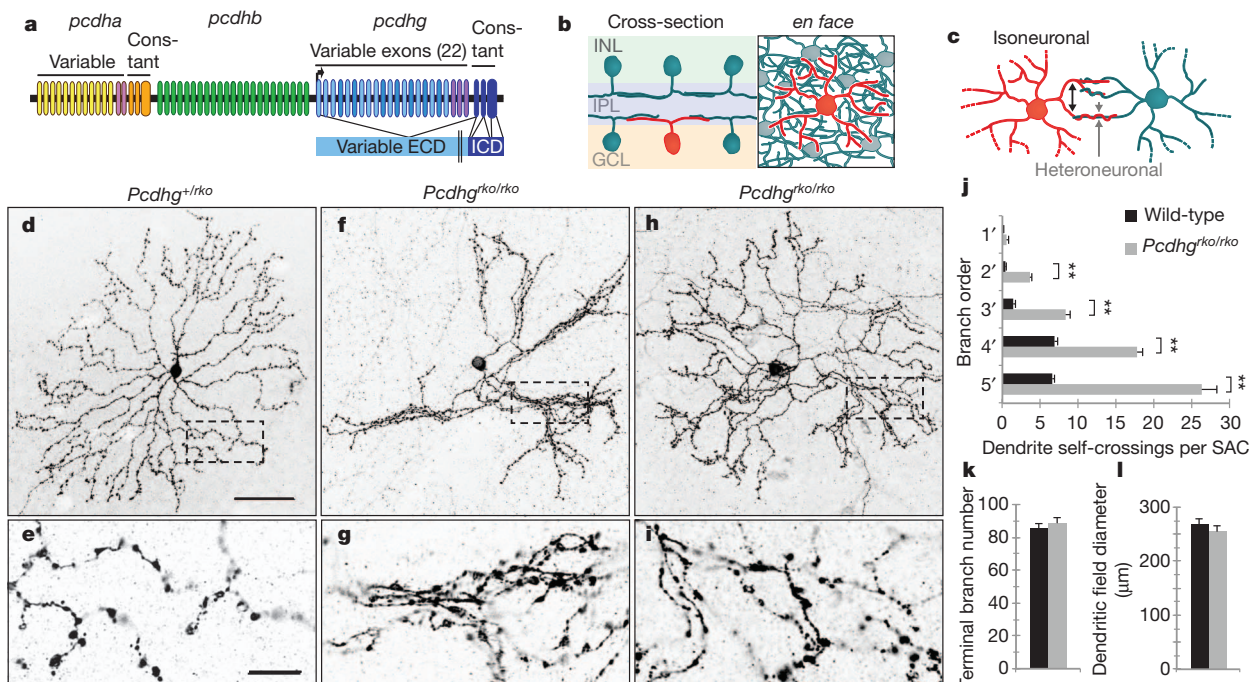
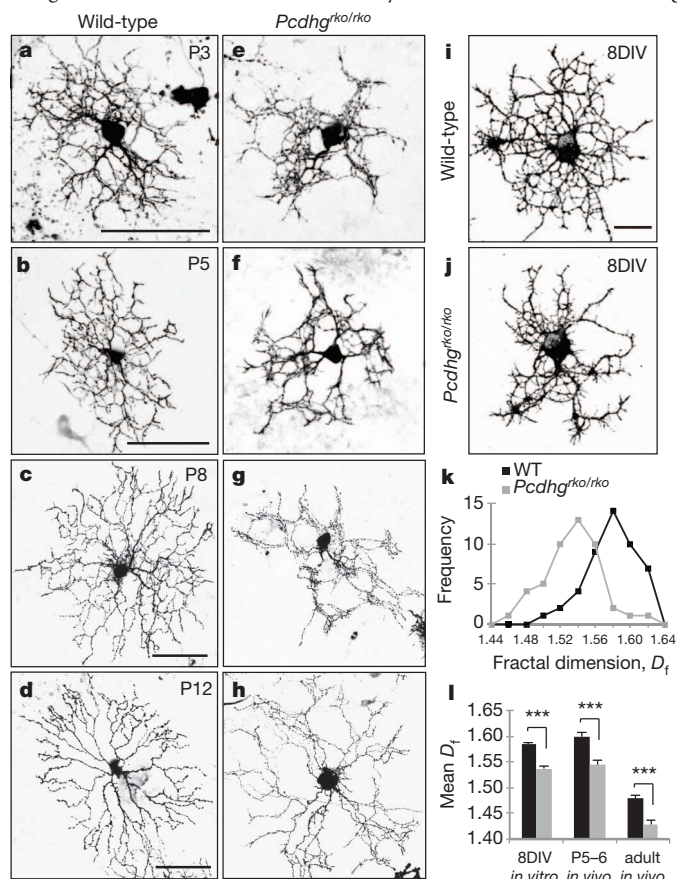


**Figure 1** | *Pcdhgs* are required for self-avoidance of SAC dendrites. **a**, *Pcdh* locus comprises *Pcdha*, *Pcdhb* and *Pcdhg* subclusters. *Pcdha* and *Pcdhg* isoforms are assembled by splicing of one variable exon encoding extracellular (ECD) and transmembrane domains to three constant exons encoding the intracellular domain (ICD). **b**, SACs are present in both the inner nuclear layer (INL) and the ganglion cell layer (GCL) and extend dendrites that form radially symmetrical arborizations confined to thin sublaminae in the inner plexiform layer (IPL). **c**, SAC dendrites avoid isoneuronal dendrites (red) but interact heteroneuronally with other SACs (blue), forming synapses on their dendrites. **d–i**, Morphology of a single SAC, labelled with membrane-Cherry, in the GCL in control and *Pcdhg*

mutant retinas. Wild-type SAC dendrites self-avoid. In *Pcdhg* mutants, self-avoidance defects include self-crossing and bundling of dendrites. Crossings are detected at 0.2 μm *x–y* resolution in single 0.8-μm optical sections (**e**, **g**, **i** show magnified views of boxed areas in **d**, **f**, **h**). Images with 0.2 μm *z* resolution are shown in Supplementary Fig. 1. **j**, SAC dendritic self-crossings in first–fifth order branches per SAC. Graph underestimates difference between genotypes because the most severely affected mutant SACs could not be scored. **k**, **l**, Number of terminal branches (**k**) and dendritic field diameter (**l**) do not differ between wild-type and mutant SACs. Panels **j–l** show means ± s.e.m.; *n* = 8 cells from 5–6 animals per genotype. Scale bars, 50 μm (**d**, **f**, **h**) and 10 μm (**e**, **g**, **i**).



whereas most crossing branches were eliminated in controls, many persisted in mutants (Fig. 2h). Thus, *Pcdhgs* may lead to self-avoidance by mediating repulsive interactions that bias the rearrangement process to selectively eliminate contacts among isoneuronal branches.

To initiate analysis of the mechanism by which *Pcdhgs* mediate self-avoidance, we next asked whether they act cell-autonomously. We selectively removed *Pcdhg* genes from SACs using a *Chat-Cre* line. In this case, *Pcdhg*-negative SACs were surrounded by *Pcdhg*-positive neurons of other types. We also deleted *Pcdhg* genes from individual SACs using a transgenic line that expressed tamoxifen-activated Cre recombinase in SACs; we activated Cre with a low dose of tamoxifen and introduced a Cre-dependent reporter to mark mutant SACs. In this case, *Pcdhg*-negative SACs were surrounded by *Pcdhg*-positive SACs. In both cases, SACs lacking *Pcdhg* genes exhibited striking self-avoidance defects (Supplementary Fig. 4). To test whether *Pcdhgs* can act in completely isolated SACs, we used fluorescence-activated cell sorting to purify SACs from a transgenic line in which

**Figure 2** | *Pcdhgs* pattern developing SAC dendrites in a cell-autonomous manner. **a–h**, SACs in developing wild-type and *Pcdhg* mutant retinas. Wild-type SACs extend fine, exuberant branches (P3, P5) that make transient intradendritic contacts (P5, P8); by P12, excess branches and isoneuronal contacts are eliminated. Dendrites of mutant SACs display excessive self-crossing and bundling by P3; by P12, excess branches are eliminated, but crossing dendrites remain. **i**, **j**, Cultured *Pcdhg* mutant SACs exhibit loss of symmetric growth and uneven distribution of neurites. **k**, Histogram of fractal dimensions (*D<sub>f</sub>*, metric for space-filling) for 47 wild-type (black) and 47 mutant (grey) SACs. Wild-type SAC in **i** has *D<sub>f</sub>* of 1.61 and mutant SAC in **j** has *D<sub>f</sub>* of 1.53. **l**, Mean *D<sub>f</sub>* for cultured SACs (*n* = 47 cells), SACs *in vivo* at P5 (*n* = 6) and adult (*n* = 9). **\*\*\****P* < 0.001. Error bars, s.e.m. Scale bars, 50 μm (**a–d**, also apply respectively to **e–h**) and 20 μm (**i**, **j**).



they are selectively labelled by an orange fluorescent protein (*Thy1-OPF3*) and cultured them at low density. Isolated SACs extended dendrites that formed radial, web-like arborizations (Fig. 2i), reminiscent of those observed at ~P5 *in vivo* (Fig. 2b). In contrast, SACs from *Pcdhg<sup>rko/rko</sup>*; *Thy1-OPF3* mice exhibited less symmetrical and unevenly spaced arborizations, reminiscent of those observed in *Pcdhg<sup>rko/rko</sup>* retinas at P5 (Fig. 2j and Supplementary Fig. 5). Analysis of the space-filling capacity of dendritic arborizations<sup>2,27</sup> (see Methods) revealed that defects *in vitro* were similar in magnitude to those *in vivo* (Fig. 2k,l). Thus, *Pcdhgs* do not depend on intercellular interactions to promote self-avoidance.

We next assessed the requirement for isoform diversity in *Pcdhg*-dependent self-avoidance. We used RT-PCR (PCR with reverse transcription) to survey expression of *Pcdhg* isoforms in whole retina, in amacrine generally and in SACs specifically. All 22 *Pcdhg* variants were expressed in each preparation, with no indication of decreased diversity in purified subpopulations (Supplementary Fig. 6). We then analysed a targeted mouse mutant, *Pcdhg<sup>tcko</sup>*, in which three

contiguous *Pcdhg* variable exons, C3–C5, had been deleted. Expression of the remaining 19 *Pcdhg* isoforms is unperturbed in this allele<sup>28</sup>. Because *Pcdhg<sup>tcko</sup>* homozygous mice die at birth<sup>28</sup>, we generated transheterozygous animals (*Pcdhg<sup>tcko/fcon3</sup>*; *retina-cre*) so that only retina lacks both copies of *Pcdhgc3-c5*. In these retinas, neuronal death was as prevalent as in those of *Pcdhg<sup>rko/rko</sup>* mice<sup>22,28</sup>, yet SACs exhibited normal self-avoidance (Fig. 3a, e).

In a complementary approach, we generated a line in which the single *PcdhgC3* isoform, fused to a fluorescent protein (mCherry), could be expressed in any cell in a Cre-dependent manner (*ROSA26-CAG::lox-Stop-lox-Pcdhgc3-mCherry* or *cC3-mCherry*). Thus, in *cC3-mCherry*; *Pcdhg<sup>rko/rko</sup>* mice, Cre both deletes all 22

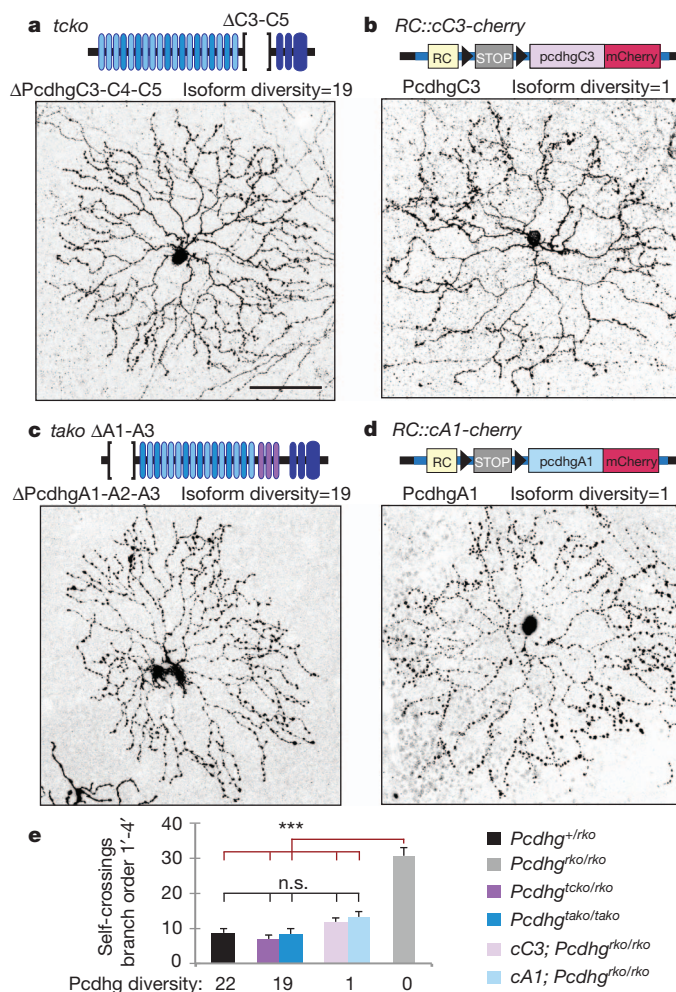


**Figure 3 | No single *Pcdhg* isoform is necessary and any isoform is sufficient for dendrite self-avoidance.** **a**, SACs lacking *Pcdhgc3-c5* (*pcdhg<sup>tcko/fcon3</sup>*; *retina-cre*) exhibit self-avoidance. **b**, Replacement of all 22 *Pcdhgs* by the *PcdhgC3* isoform, using the *RC::cC3-cherry* transgene, rescues SAC dendrite self-avoidance. **c**, SACs lacking *PcdhgA1-a3* (*pcdhg<sup>tako/tako</sup>*) exhibit self-avoidance. **d**, Replacement of all 22 *Pcdhgs* by the *PcdhgA1* isoform, using the *RC::cA1-cherry* transgene, rescues SAC dendrite self-avoidance. **e**, Compared to mutants lacking all 22 isoforms, self-crossings of SACs in retinas expressing 19 or 1 isoforms are restored to control levels. \*\*\**P* < 0.001; n.s., not significant. Data are mean  $\pm$  s.e.m., from 7 SACs from *pcdhg<sup>tcko/fcon3</sup>*; *retina-cre* retinas, 3 SACs from *pcdhg<sup>tako/tako</sup>*, and 9 from remaining genotypes. Scale bar in **a**, 50  $\mu$ m; applies to **b–d** also.

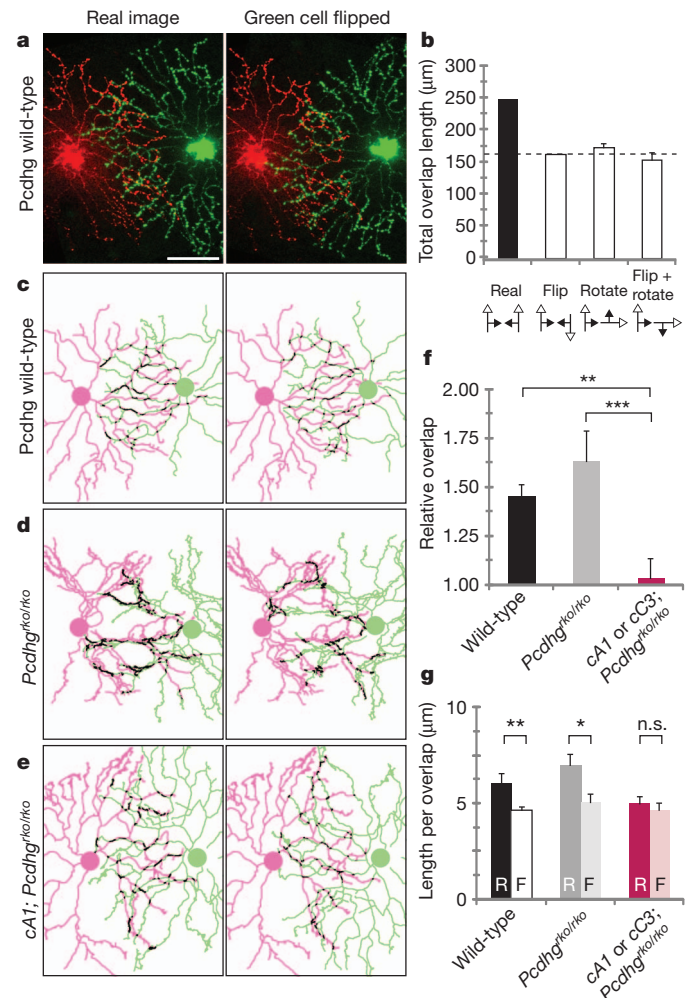


**Figure 4 | Reducing *Pcdhg* diversity disrupts heteroneuronal SAC interactions.** **a**, Two nearby SACs from a wild-type mouse injected with contrasting fluorescent dyes. Right panel shows image of the green SAC flipped vertically. **b**, Overlap between red and green cells in **a**. First two bars are derived from the two panels in **a**. The green cell was rotated in 45° steps or flipped and then rotated (manipulations indicated by symbols beneath graph); third and fourth bars show mean overlap  $\pm$  s.e.m. derived from these images (*n* = 7). All inversions and rotations decrease overlap, indicating that overlap in the real image is non-random. **c–e**, Tracings of SAC pairs, and versions flipped as in **a**, from wild-type (**c**), *Pcdhg<sup>rko/rko</sup>* (**d**) and *cA1; Pcdhg<sup>rko/rko</sup>* (**e**) mice. Overlap shown in black. **f**, Overlap between neighbouring cells, expressed as ratio between overlap measured in real and flipped images. Bars show mean  $\pm$  s.e.m. for 11, 9 and 8 pairs from wild-type, *Pcdhg<sup>rko/rko</sup>* and single isoform-expressing (*cA1; Pcdhg<sup>rko/rko</sup>* and *cC3; Pcdhg<sup>rko/rko</sup>*) animals. Expression of a single isoform in neighbouring SACs decreases their interaction. **g**, Mean length of overlapping segments between SAC pairs. R, real image; F, flipped image. \**P* = 0.05; \*\**P* < 0.05; \*\*\**P* < 0.01. Error bars, s.e.m.; n as in **f**. Scale bar in **a**, 50  $\mu$ m; applies to **c–e** also.



endogenous *Pcdhg* genes and activates the single *PcdhgC3*-mCherry isoform throughout the retina. Analysis of mCherry fluorescence confirmed Cre-dependent expression of the transgene in all retinal cells and appropriate localization of the fusion protein to cell membranes and synaptic layers (Supplementary Fig. 7). Expression of *PcdhgC3* alone rescued self-avoidance defects of *Pcdhg* mutants (Fig. 3b, e).

To test the possibility that only some isoforms are dispensable for self-avoidance, we analysed a second set of isoforms. We generated *Pcdhg<sup>tako</sup>*, which lacks the *Pcdhga1-a3* variable exons<sup>28</sup>, and a line that expresses *Pcdhga1-mCherry* in a Cre-dependent manner (*cA1-mCherry*). Results were similar to those for the C3–C5 group: self-avoidance persisted in the absence of *PcdhgA1–A3* and was rescued by replacement of all *Pcdhg* isoforms with *PcdhgA1* alone (Fig. 3c–e and Supplementary Fig. 7). From these results, we conclude that no single *Pcdhg* isoform is necessary but any single isoform is sufficient for dendritic self-avoidance.

Although *Pcdhg* isoform diversity is not required for isoneuronal self-avoidance, it may be required to ensure that dendrites of adjacent SACs do not avoid each other, which would prevent them from interacting. The ability to generate a SAC population expressing a single *Pcdhg* isoform (*Pcdhga1* or *Pcdhgc3*) enabled us to test this idea. We injected closely spaced pairs of SACs with different fluorophores (Fig. 4a) and measured the extent to which their dendrites overlapped. To determine whether this method reliably revealed interactions among SACs, we rotated, flipped or rotated and flipped the image of one of the cells, and recalculated overlap. Only the real image showed an overlap greater than that of the manipulated images (Fig. 4b). We then measured overlap for pairs of SACs from wild-type, mutant and single isoform-expressing mice, normalizing for intercellular distance by comparing overlap to the value calculated from the flipped image (Fig. 4c–e and Supplementary Fig. 8). Overlap was equivalent in wild-type and mutant retina, but significantly decreased in retinas expressing a single isoform (Fig. 4f); values for *Pcdhga1* and *Pcdhgc3* were similar (1.01 and 1.08). Likewise, the mean length of overlapping

segments was greater than expected for random overlap in wild-type and mutant but not in single isoform-expressing pairs (Fig. 4g). Thus, when all SACs express the same *Pcdhg* isoform, heteroneuronal dendrites avoid each other, just as isoneuronal dendrites do in control SACs. We conclude that isoform diversity enables SACs to distinguish isoneuronal from heteroneuronal dendrites.

Finally, we asked whether *Pcdhgs* mediate self-avoidance in areas other than retina. We examined cerebellar Purkinje cells, which have elaborate, planar dendritic arborizations known to exhibit self-avoidance<sup>3</sup> (Fig. 5a–c). Importantly, stochastic and combinatorial expression, which underlies the ability of *Drosophila Dscam1* to mediate self-avoidance<sup>4–6,12,14,15,29</sup>, has been documented for *Pcdhg* genes in Purkinje cells<sup>10</sup>. We selectively deleted *Pcdhg* genes from Purkinje neurons using an *L7-cre* transgene, marked cells with a vector that expresses fluorescent proteins in a Cre-dependent manner, and examined them at P15, P21 and at P35, after arborizations have matured<sup>30</sup>. Deletion of *Pcdhg* genes from Purkinje cells had no detectable effect on their survival, shape, size or branching pattern (Fig. 5d, e, h, i and Supplementary Fig. 9), but their arborizations were disorganized and dendrites often crossed over each other (Fig. 5f, g). Use of a Cre-dependent reporter revealed that deletion remained incomplete at P8, at which time Purkinje dendrite growth was already advanced (Supplementary Fig. 9). It is therefore possible that earlier deletion of *Pcdhg* genes would lead to a more dramatic effect. Nonetheless, these results demonstrate a role for *Pcdhg* genes in Purkinje cell self-avoidance.

In summary, although vertebrate *Pcdh* genes and *Drosophila Dscam1* are structurally unrelated, they have remarkable parallels: both encode numerous isoforms from a single locus, the isoforms are expressed stochastically and combinatorially, and the encoded proteins interact homophilically<sup>7,8,10–14</sup>. We have now shown that in mammalian neurons, *Pcdhgs*, like *Dscam1* (refs 4–6, 12), promote self-avoidance during development by a cell-autonomous mechanism. In addition, for both *Dscam1* and *Pcdhg* genes, diversity appears to

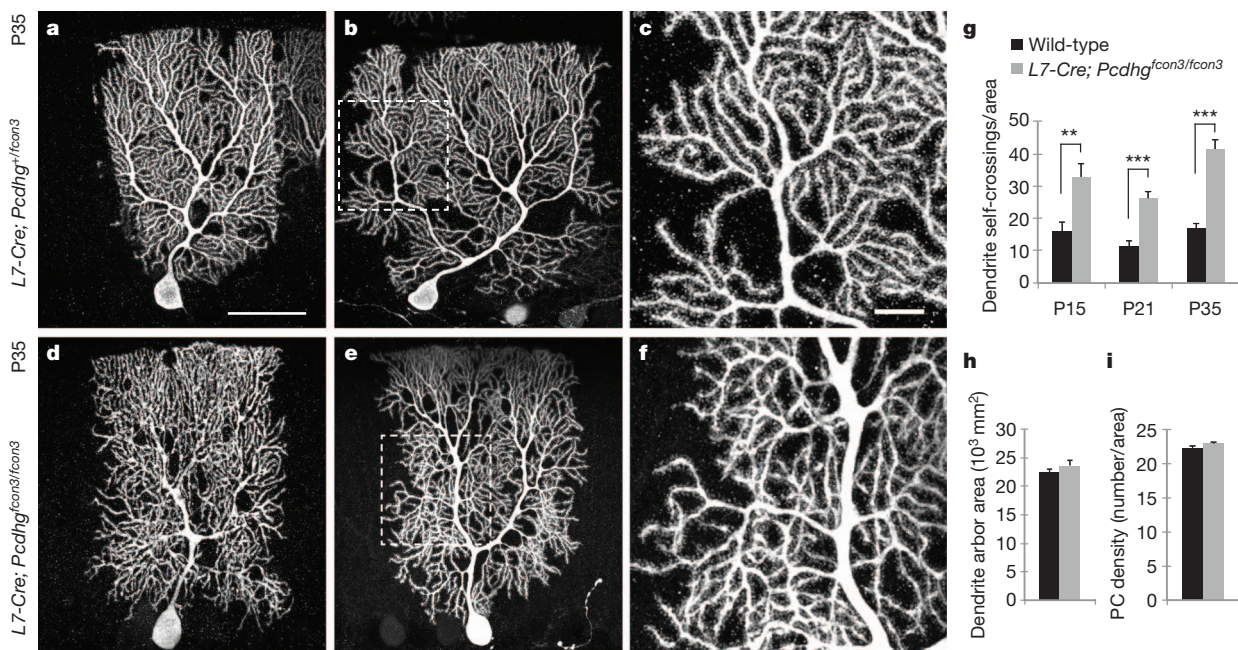


**Figure 5 | Purkinje cell dendrite self-avoidance requires *Pcdhgs*.** a–c, Control Purkinje cells (a, b) labelled with Cre-dependent AAV-XFP in *L7-cre* transgenic mouse. Self-avoidance is clear in high-magnification view in c (shows area boxed in b). d–f, Purkinje cells lacking *Pcdhgs* and labelled as in a–c have disorganized arborizations marked by frequent self-crossing defects. Panel f shows area boxed in e. g, Self-crossings detected in single confocal

z-sections of 7,225  $\mu\text{m}^2$  unit area from controls and mutants. \*\* $P < 0.01$ ; \*\*\* $P < 0.001$ ;  $n = 8, 15$  and 15 cells at P15, P21 and P35 respectively from  $\geq 3$  mice per genotype. h, i, Area of dendritic arborizations ( $n = 20$  cells) and cell density ( $> 40$  regions) do not differ between control and mutant Purkinje cells. Data show mean  $\pm$  s.e.m. Scale bars, 50  $\mu\text{m}$  (a, b, d, e) and 10  $\mu\text{m}$  (c, f).



underlie self/non-self discrimination, presumably because neighbouring neurons are unlikely to express the same isoforms and are therefore free to interact<sup>7,12,14,15,29</sup>. Thus, two phyla appear to have recruited different molecules to mediate similar, complex strategies for self-recognition during formation of neuronal arborizations. These parallels raise the question of why vertebrate and invertebrate nervous systems have invested heavily in mechanisms that promote self-avoidance. In principle, self-avoidance allows neurons to cover their receptive or projective fields maximally while retaining the ability to overlap those of neighbouring neurons<sup>1–3</sup>. However, to our knowledge, the effect of perturbing self-avoidance on circuit function has yet to be assessed in any system. We can now address this issue by electrophysiological analysis of SACs, Purkinje cells, and their synaptic targets in *Pcdhg* mutant mice.

## METHODS SUMMARY

Transgenic, knockout and knock-in mouse lines used for this study, as well as methods for marking cells are described in Methods. Identity of labelled SACs was confirmed by immunolabelling retinas for the cholinergic neuron-specific marker. Dendrite self-crossings were quantified by number of branch overlaps detected in single confocal planes.

**Full Methods** and any associated references are available in the online version of the paper.

Received 19 December 2011; accepted 7 June 2012.

Published online 29 July 2012.

- Kramer, A. P. & Kuwada, J. Y. Formation of the receptive fields of leech mechanosensory neurons during embryonic development. *J. Neurosci.* **3**, 2474–2486 (1983).
- Montague, P. R. & Friedlander, M. J. Expression of an intrinsic growth strategy by mammalian retinal neurons. *Proc. Natl Acad. Sci. USA* **86**, 7223–7227 (1989).
- Grueber, W. B. & Sagasti, A. Self-avoidance and tiling: mechanisms of dendrite and axon spacing. *Cold Spring Harb. Perspect. Biol.* **2**, a001750 (2010).
- Matthews, B. J. *et al.* Dendrite self-avoidance is controlled by Dscam. *Cell* **129**, 593–604 (2007).
- Soba, P. *et al.* *Drosophila* sensory neurons require Dscam for dendritic self-avoidance and proper dendritic field organization. *Neuron* **54**, 403–416 (2007).
- Hughes, M. E. *et al.* Homophilic Dscam interactions control complex dendrite morphogenesis. *Neuron* **54**, 417–427 (2007).
- Zipursky, S. L. & Sanes, J. R. Chemoaffinity revisited: dscams, protocadherins, and neural circuit assembly. *Cell* **143**, 343–353 (2010).
- Wu, Q. & Maniatis, T. A striking organization of a large family of human neural cadherin-like cell adhesion genes. *Cell* **97**, 779–790 (1999).
- Kohmura, N. *et al.* Diversity revealed by a novel family of cadherins expressed in neurons at a synaptic complex. *Neuron* **20**, 1137–1151 (1998).
- Kaneko, R. *et al.* Allelic gene regulation of *Pcdh-α* and *Pcdh-γ* clusters involving both monoallelic and biallelic expression in single Purkinje cells. *J. Biol. Chem.* **281**, 30551–30560 (2006).
- Schreiner, D. & Weiner, J. A. Combinatorial homophilic interaction between  $\gamma$ -protocadherin multimers greatly expands the molecular diversity of cell adhesion. *Proc. Natl Acad. Sci. USA* **107**, 14893–14898 (2010).
- Zhan, X. L. *et al.* Analysis of Dscam diversity in regulating axon guidance in *Drosophila* mushroom bodies. *Neuron* **43**, 673–686 (2004).
- Wojtowicz, W. M., Flanagan, J. J., Millard, S. S., Zipursky, S. L. & Clemens, J. C. Alternative splicing of *Drosophila* Dscam generates axon guidance receptors that exhibit isoform-specific homophilic binding. *Cell* **118**, 619–633 (2004).
- Neves, G., Zucker, J., Daly, M. & Chess, A. Stochastic yet biased expression of multiple Dscam splice variants by individual cells. *Nature Genet.* **36**, 240–246 (2004).
- Hattori, D. *et al.* Robust discrimination between self and non-self neurites requires thousands of Dscam1 isoforms. *Nature* **461**, 644–648 (2009).
- Yamagata, M. & Sanes, J. R. Dscam and Sidekick proteins direct lamina-specific synaptic connections in vertebrate retina. *Nature* **451**, 465–469 (2008).
- Fuerst, P. G., Koizumi, A., Masland, R. H. & Burgess, R. W. Neurite arborization and mosaicism in the mouse retina require DSCAM. *Nature* **451**, 470–474 (2008).
- Fuerst, P. G. *et al.* DSCAM and DSCAML1 function in self-avoidance in multiple cell types in the developing mouse retina. *Neuron* **64**, 484–497 (2009).
- Sanes, J. R. & Zipursky, S. L. Design principles of insect and vertebrate visual systems. *Neuron* **66**, 15–36 (2010).
- Wang, X. *et al.* Gamma protocadherins are required for survival of spinal interneurons. *Neuron* **36**, 843–854 (2002).
- Prasad, T., Wang, X., Gray, P. A. & Weiner, J. A. A differential developmental pattern of spinal interneuron apoptosis during synaptogenesis: insights from genetic analyses of the protocadherin- $\gamma$  gene cluster. *Development* **135**, 4153–4164 (2008).
- Lefebvre, J. L., Zhang, Y., Meister, M., Wang, X. & Sanes, J. R.  $\gamma$ -Protocadherins regulate neuronal survival but are dispensable for circuit formation in retina. *Development* **135**, 4141–4151 (2008).
- Weiner, J. A., Wang, X., Tapia, J. C. & Sanes, J. R. Gamma protocadherins are required for synaptic development in the spinal cord. *Proc. Natl Acad. Sci. USA* **102**, 8–14 (2005).
- Stacy, R. C. & Wong, R. O. Developmental relationship between cholinergic amacrine cell processes and ganglion cell dendrites of the mouse retina. *J. Comp. Neurol.* **456**, 154–166 (2003).
- Lee, S. & Zhou, Z. J. The synaptic mechanism of direction selectivity in distal processes of starburst amacrine cells. *Neuron* **51**, 787–799 (2006).
- White, F. A., Keller-Peck, C. R., Knudson, C. M., Korsmeyer, S. J. & Snider, W. D. Widespread elimination of naturally occurring neuronal death in Bax-deficient mice. *J. Neurosci.* **18**, 1428–1439 (1998).
- Jelinek, H. F. & Fernandez, E. Neurons and fractals: how reliable and useful are calculations of fractal dimensions? *J. Neurosci. Methods* **81**, 9–18 (1998).
- Chen, W. V. *et al.* Functional significance of isoform diversification in the protocadherin gamma gene cluster. *Neuron* (in the press).
- Wang, J. *et al.* Transmembrane/juxtamembrane domain-dependent Dscam distribution and function during mushroom body neuronal morphogenesis. *Neuron* **43**, 663–672 (2004).
- Kaneko, M. *et al.* Remodeling of monoplanar Purkinje cell dendrites during cerebellar circuit formation. *PLoS ONE* **6**, e20108 (2011).

**Supplementary Information** is linked to the online version of the paper at [www.nature.com/nature](http://www.nature.com/nature).

**Acknowledgements** We thank members of our laboratory for providing advice and reagents, including D. Cai and K. Cohen (rAAV), I.-J. Kim (*fst4*-line 1 mice) and M. Yamagata for modified Rosa-CAG targeting vector. We also thank B. Stevens (Children's Hospital) for advice on culture methods. This work was supported by grants from NIH to J.R.S. (R01NS029169 and R01EY022073) and T.M. (R01NS043915) and NARSAD Young Investigator Award to J.L.L.

**Author Contributions** J.L.L., D.K. and J.R.S. designed experiments and prepared the manuscript. J.L.L. and D.K. performed experiments and data analysis. J.R.S. supervised the project. W.V.C. and T.M. generated *Pcdhg*<sup>lako</sup> and *Pcdhg*<sup>lcko</sup> mice. All authors commented on the manuscript.

**Author Information** Reprints and permissions information is available at [www.nature.com/reprints](http://www.nature.com/reprints). The authors declare no competing financial interests. Readers are welcome to comment on the online version of this article at [www.nature.com/nature](http://www.nature.com/nature). Correspondence and requests for materials should be addressed to J.R.S. ([sanesj@mcb.harvard.edu](mailto:sanesj@mcb.harvard.edu)).

## METHODS

**Mouse strains.** The *Pcdhg*<sup>con3</sup> conditional mutant allele, in which the third constant exon is flanked by loxP sequences and which generates a functionally null allele following Cre recombination, was described previously<sup>21,22</sup>. Retina-specific *Chx10-cre*<sup>31</sup> and *Six3-cre* transgenic mice<sup>32</sup> were provided by C. Cepko (Harvard) and W. Klein (M.D. Anderson Cancer Center), respectively. *Bax*<sup>-/-</sup> mutants<sup>33</sup>, Purkinje-specific *L7Bac-cre* transgenic mice<sup>34</sup>, *Chat-cre*, in which the Cre recombinase gene was targeted to the endogenous ChAT gene<sup>35</sup>, and Rosa-CAG-LoxP-STOP-LoxP-tdTomato-WPRE reporter mice<sup>36</sup> were obtained from Jackson Laboratories. A line of BAC transgenic mice in which regulatory elements from the *fstl4* gene drive expression of CreER was generated as described in ref. 37. In this line, called line 1 to distinguish it from the line called 'BD' in ref. 37, CreER was expressed in SACs, as well as sparse other amacrine cells. We believe that expression reflects influences at the site of transgene integration rather than expression of *fstl4*. Thy1-OPF3 transgenic mice, in which Thy1 promoter and regulatory elements direct expression of Kusabira Orange (OPF) in SACs and subsets of retinal ganglion cells (RGCs), were described previously<sup>37</sup>. *Pcdhg*<sup>tko</sup> and *Pcdhg*<sup>tako</sup> mice were generated using standard gene targeting techniques<sup>28</sup>. Mice were maintained on a C57/B6J background. All experiments were carried out in accordance with protocols approved by the Harvard University Standing Committee on the Use of Animals in Research and Teaching.

**Generation of single *Pcdhg* isoform conditional knock-in mice.** *Pcdhga1* and *pdhgc3* full-length cDNAs were amplified from RNA isolated from P21 C57/BL6 mouse brain, and cloned in frame into pCMV-mCherry-N1 (Clontech). Linker sequence residing between the third constant exon and *gfp* in *Pcdhg*<sup>fusg</sup> knock-in mice and shown to produce functional *Pcdhg*-GFP fusion proteins *in vivo*<sup>20</sup> was subcloned into pCMV-*pdhga1/c3*-mCherry-N1. Targeting vector pRosa26-PAS<sup>38</sup> was modified as described in ref. 39 to include a CAG cassette (chicken  $\beta$ -actin promoter and CMV immediate-early enhancer), a Gateway RFA destination site (Invitrogen), a WPRE fragment (woodchuck hepatitis virus posttranscriptional element), and a STOP sequence was cloned from pBS302 (Addgene plasmid 11925). LoxP-STOP-loxP-*Pcdhga1/c3*-mCherry was recombined into pRosa26-CAG-Rfa-WPRE-FNF-iSceI, creating pRosa26-CAG-loxP-STOP-loxP-*Pcdhga1/c3*-mCherry-WPRE-FNF-iSceI targeting vectors. The iSceI-linearized vectors were electroporated into 129/B6 F1 hybrid ES cell line V6.5. G418-resistant, targeted ES clones were identified by PCR: 1.7 kb fragment amplified by 5'-Rosa-F: GGCGGACTGGCGGGACTA and 5'-CAG-R: CCAGGCGGGCC ATTTACCGTAAG; and 8.2 kb fragment amplified by 3'-Cherry-F: CTCCCCA CACGAGGACTACACCATC and 3'-Rosa-R: GCATTTTAAAGCATGAAAC TACAAC. ES cell transfections and blastocyst injections were performed by the Genome Modification Facility, Harvard University. Following germ-line transmission, the FRT-neo-FRT cassette was excised by crossing to mice that express Flp recombinase ubiquitously<sup>40</sup>. *Gt(Rosa)26Sor::CAG-loxP-STOP-loxP-Pcdhga1/c3-mCherry* conditional knock-in mice are called *cA1-mCherry* and *cC3-mCherry*.

**Labelling of neurons.** Plasmid encoding pAAV2/2-CAG-palmitoylation tag-mCherry-WPRE was used to generate recombinant AAV2/2 expressing membrane-tagged Cherry. To label SACs in retina expressing *cC3-mCherry* or *cA1-mCherry*, we used rAAV2/2-CBA-YC3.6-WPRE expressing a calcium sensor that includes cytosolic YFP and used here for visualization of neuronal morphology<sup>41</sup>. Recombinant AAV2/2-CAG-memb-mCherry and rAAV2/2-YC3.6 were prepared at the Harvard Gene Therapy Institute ((1–2) × 10<sup>12</sup> genome copies per ml). Optimal titres of (1–2) × 10<sup>9</sup> viral genome particles per ml for AAV2/2-CAG-memb-mCherry and 2 × 10<sup>10</sup> viral genome particles per ml for rAAV2/2-YC3.6 were prepared in phosphate-buffered saline (PBS, pH = 7.4). rAAV2/9 expressing GFP and mCherry were generated and provided by D. Cai and K. Cohen in our laboratory; high titre virus was produced at the University of Pennsylvania Vector Core.

To inject virus into eyes, adult mice were anaesthetized with ketamine/xylazine by intraperitoneal injection. A 30½G needle was used to make a small hole in the temporal eye, below the cornea, and 1.5 µl of rAAV virus was injected into the vitreous humour with a Hamilton syringe and 33G blunt-ended needle. Animals were killed and retinas were dissected 4–6 weeks following injection. For cerebellar virus infection, P1–P2 mice were anaesthetized with ice and a small puncture was made into the caudal-medial position of one cortical lobe; 1.5 µl of rAAV2/9-GFP; mCherry virus was injected with a Hamilton syringe and 33G blunt-ended needle. Mice were analysed 12–35 days after infection.

For biolistic transfection of SACs, gold particles (1.0 µm diameter, Bio-Rad) were coated with plasmids encoding tdTomato driven by CMV promoter<sup>24</sup>. Live retinas were dissected, transected with four radial incisions, flattened with photoreceptor side down, and mounted onto a nitrocellulose filter (Millipore). Gold particles were delivered using a Biolistics Helios Gene gun device (Bio-Rad), and retinas were cultured in Ames medium (Sigma) in an oxygenated incubator heated to 37 °C for 12–16 h.

To assess interactions between dendrites of neighbouring SACs, we injected pairs of cells with fluorescent dyes. Retinas from mice expressing OPF in SACs (Thy1-OPF3) were mounted RGC side up and perfused with Ames medium bubbled with 95%O<sub>2</sub>/5%CO<sub>2</sub> at 25 °C. OPF<sup>+</sup> SACs were visualized with epifluorescence, and impaled with high resistance electrodes (50 MΩ) filled with a K<sup>+</sup> based intracellular recording solution supplemented with 50 µM Alexa Fluor 568 (for targeting) and 200 µM of Alexa Fluor 488 or 647 (for filling, Invitrogen). Square voltage pulses of ~3 V were applied to SACs at 50 Hz using a BK Precision Model 3011B function generator. After filling one SAC, the electrode was replaced with a second containing the contrasting dye and the second cell was filled. Images of labelled SAC pairs in live retinas were acquired at 40× on a Zeiss LSM 510 confocal microscope.

**Tissue preparation and immunohistochemistry.** Mice were killed with intraperitoneal injection of Nembutal, and either enucleated immediately or transcardially perfused with Ringer's solution followed by 4% paraformaldehyde (PFA) in PBS. Eye cups were removed and fixed in 4% PFA on ice for 1 h, followed by dissection and post-fixation of retinas for an additional 30 min, then rinsed with PBS. Brains were post-fixed in 4% PFA at 4 °C overnight. Animal procedures were in compliance with the US National Institutes of Health Guide for the Care and Use of Laboratory Animals and approved by the Animal and Care and Use Program at Harvard University.

Whole-mount preparations and cryosections of retinas were performed as described<sup>22,42</sup>. Briefly, whole retinas were incubated for 1–2 h in blocking buffer (0.4% Triton-X, 4% normal donkey serum in PBS), then incubated for 6 days at 4 °C with primary antibodies. Sagittal 80 µm sections of cerebellum were obtained with a vibratome (Leica), incubated in blocking buffer, and with primary antibodies for 2 days at 4 °C. Following washing, retinas and brain sections were incubated for 3 h at room temperature with Alexa-conjugated secondary antibodies (Invitrogen or Jackson ImmunoResearch). Whole retinas were flattened with photoreceptor side down onto nitrocellulose filters. Retina flat-mounts and brain sections were mounted onto glass slides, covered with Vectashield (Vector) or Fluoromount G (Southern Biotech), and imaged on an Olympus FV1000 scanning confocal microscope. Antibodies used were as follows: chick and rabbit anti-GFP (Aves and Millipore); rabbit anti-DsRed (Clontech); goat anti-choline acetyltransferase (Millipore); guinea pig anti-vGluT3 (Millipore); rabbit anti-Calbindin (Swant); mouse anti-syntaxin HPC1 clone (Sigma); rabbit anti-cleaved caspase3 (Cell Signaling Technology). Nuclei were labelled with DAPI, Po-pro1, or NeuroTrace Nissl 435/455 (Invitrogen).

**SAC purification and culture.** To isolate and culture wild-type and *Pcdhg* mutant SACs *in vitro*, we crossed the *Thy1-OPF3* transgene, which selectively directs expression of Kusabira Orange (OPF) in SACs and subset of RGCs<sup>37</sup>, into *Pcdhg*<sup>con3</sup>; *Six3-cre* mice. Retinas from genotyped *Pcdhg*<sup>con3/fcon3</sup>; *Six3-cre*; *Thy1-OPF3* mutant and control P2 mice were dissociated using papain<sup>22</sup>. OPF<sup>+</sup> SACs were isolated by fluorescence activated cell sorting (FACS, MoFlo), plated onto poly-L-lysine-coated glass coverslips (Warner) and cultured for 7–9 days in RGC growth media modified from Meyer-Franke<sup>43</sup> in the following ways: (1) substitution of NS21<sup>44</sup> for B27, (2) substitution of N2 (Invitrogen) for Sato stock, (3) addition of TGF-β1 and TGF-β2 (2.5 ng ml<sup>-1</sup>; Peprotech), and (4) addition of mouse glia-conditioned medium (15%). One-third of media was exchanged with fresh media every three days. Cells were fixed with cold 4%PFA/4% sucrose for 15 min, and immunostained for syntaxin and calbindin to confirm SAC identity, and for GFP to confirm *Pcdhg*<sup>-/-</sup>; GFP<sup>-</sup> SACs from unrecombined *Pcdhg*-GFP<sup>+</sup> SACs due to variegated *Six3*-Cre activity in retina.

**Image analysis.** For best reproduction and clarity of SAC arborizations, maximized projections of confocal images were inverted and contrast-enhanced using Photoshop (Adobe Systems). For morphometric analysis of SACs, we used Fiji software and selected confocal image series of wild-type and *Pcdhg* mutant SACs situated in comparable retinal eccentricities. Self-crossings per dendritic branch order were quantified as number of branch overlaps detected in single confocal planes; crossings occurring distal to fifth branch order could not be quantified accurately owing to severity of defects in mutants. Dendritic field diameter was measured as the longest axis of arborization. In some cases, arborizations were re-imaged by oversampling using a 60× 1.45NA objective at x,y,z resolution of 47 × 47 × 131 µm and then subjected to deconvolution using Huygens software (<http://www.svi.nl/HuygensProfessional>).

For analysis of SAC density and mosaic regularity, confocal z-stacks of ChAT-labelled SACs through the GCL and INL were acquired at similar locations in central retina. Sample sizes were 4–5 areas (0.099 mm<sup>2</sup>) per animal, 2–4 animals per genotype. For each field, x–y coordinates of SAC arrays were obtained by manually marking centres of cells using Fiji and used to compute SAC density (number per mm<sup>2</sup>), packing factor<sup>45</sup>, and density recovery profiles (DRP)<sup>46</sup> with WinDRP software (<http://www.mpimf-heidelberg.mpg.de/~teuler/WinDRP/ReadMe.htm>).

To compare the space-filling and complexity of control and mutant SAC arborizations, we computed fractal dimensions,  $D_f$ , which provide a measure of how completely dendrites fill its area<sup>2,27,47,48</sup>. To calculate  $D_f$ , we applied the box-counting method as implemented in the FracLac 2.5 plug-in for ImageJ software (<http://rsb.info.nih.gov/ij/plugins/fraclac/FLHelp/Introduction.htm>; NIH). Confocal images of cultured mutant and control SACs were obtained at equivalent laser scanning parameters with a 60× oil immersion lens, and maximum projections and thresholded, binary images were processed using Image J. Box counts using a series of progressively smaller box sizes ( $d$ ) were scanned in a region of interest covering the SAC arborization, and the number of boxes intersected by pixels [ $k(d)$ ] were analysed; this computes  $D_f$ , which represents an inverse linear regression between  $\log[k(d)]$  and  $\log(d)$ .  $D_f$  ranges from 1.0 (straight line with a dimension of 1) to 2.0 (plane with a dimension of 2); a difference of 0.1 represents a doubling of complexity<sup>27</sup>.

For analysis of dendrite overlap between arborizations of neighbouring SACs, pairs with somata separated by 80–160  $\mu\text{m}$  were selected because their dendrites are known to interact<sup>25</sup>. Images were processed using Fiji or Photoshop software. To estimate the amount of dendritic overlap that would occur by chance if two SAC arborizations occupy the same territory, we flipped or rotated the image of one SAC, realigned cell body position, and merged images. This method was inspired by work on tiling of RGC dendrites<sup>49</sup>. We measured total overlapping pixels in real and flipped images, interpreting ratios of  $>1$  (real/flipped) as indicating non-random interactions between SACs.

Purkinje cell dendrite self-crossings detected in single confocal planes were counted in a 7,225  $\mu\text{m}^2$  region of interest assigned to middle of arborization. Purkinje arborization areas were measured using the convex-hull selection in Fiji. Calbindin-labelled Purkinje somata residing along a 635  $\mu\text{m}$  segment in lobules III–VI in single confocal planes were counted to measure Purkinje cell density.

Means were compared using the two-tailed Student's  $t$  test on condition of equivalent variances determined by  $F$ -test, or with the Mann–Whitney non-parametric test. Means of multiple samples were compared using ANOVA and posthoc Tukey test.

**RT-PCR of dissociated retina cells.** We used FACS to sort live cells from dissociated P7 whole retina, VC1.1<sup>+</sup> amacrine cells, and  $\text{OFP}^+$ ;Thy1.2<sup>−</sup> SACs cells, as described previously<sup>37,50</sup>. Amacrine cells were sorted from a live cell suspension of dissociated retinal cells using monoclonal VC1.1 antibody (200  $\mu\text{g ml}^{-1}$ , Sigma) and an anti-IgM secondary conjugated to phycoerythrin-Cy7 (Southern).  $\text{OFP}^+$  SACs were sorted from  $\text{OFP}^+$  RGCs by negative selection of Thy1.2-PE-Cy7 labelled RGCs. In each condition, 2,000 cells were sorted directly into RNA lysis buffer (Qiagen); RNA was purified and first strand cDNAs were generated with Superscript RT III (Invitrogen). Primers that uniquely detect the 22 Pcdhg variable exon-constant exon spliced transcripts were adapted from ref. 21, with modifications to avoid cross-hybridization. These primers, and others used to assess purity of the sorted population, are listed in Supplementary Table 1. PCR program used

is: 94 °C for 2 min; 30 cycles of 94 °C for 20 s, 56 °C for 30 s, 72 °C for 1 min; 72 °C for 7 min.

31. Rowan, S. & Cepko, C. L. Genetic analysis of the homeodomain transcription factor Chx10 in the retina using a novel multifunctional BAC transgenic mouse reporter. *Dev. Biol.* **271**, 388–402 (2004).
32. Furuta, Y., Lagutin, O., Hogan, B. L. & Oliver, G. C. Retina- and ventral forebrain-specific Cre recombinase activity in transgenic mice. *Genesis* **26**, 130–132 (2000).
33. Knudson, C. M., Tung, K. S., Tourtellotte, W. G., Brown, G. A. & Korsmeyer, S. J. Bax-deficient mice with lymphoid hyperplasia and male germ cell death. *Science* **270**, 96–99 (1995).
34. Zhang, X. M. *et al.* Highly restricted expression of Cre recombinase in cerebellar Purkinje cells. *Genesis* **40**, 45–51 (2004).
35. Rossi, J. *et al.* Melanocortin-4 receptors expressed by cholinergic neurons regulate energy balance and glucose homeostasis. *Cell Metab.* **13**, 195–204 (2011).
36. Madisen, L. *et al.* A robust and high-throughput Cre reporting and characterization system for the whole mouse brain. *Nature Neurosci.* **13**, 133–140 (2010).
37. Kay, J. N. *et al.* Retinal ganglion cells with distinct directional preferences differ in molecular identity, structure, and central projections. *J. Neurosci.* **31**, 7753–7762 (2011).
38. Srinivas, S. *et al.* Expression of green fluorescent protein in the ureteric bud of transgenic mice: a new tool for the analysis of ureteric bud morphogenesis. *Dev. Genet.* **24**, 241–251 (1999).
39. Yamagata, M. & Sanes, J. R. Transgenic strategy for identifying synaptic connections in mice by fluorescence complementation (GRASP). *Front. Mol. Neurosci.* **5**, 18 (2012).
40. Farley, F. W., Soriano, P., Steffen, L. S. & Dymecki, S. M. Widespread recombinase expression using FLP<sup>er</sup> (flipper) mice. *Genesis* **28**, 106–110 (2000).
41. Kuchibhotla, K. V. *et al.* A $\beta$  plaques lead to aberrant regulation of calcium homeostasis in vivo resulting in structural and functional disruption of neuronal networks. *Neuron* **59**, 214–225 (2008).
42. Hong, Y. K., Kim, I. J. & Sanes, J. R. Stereotyped axonal arbors of retinal ganglion cell subsets in the mouse superior colliculus. *J. Comp. Neurol.* **519**, 1691–1711 (2011).
43. Meyer-Franke, A., Kaplan, M. R., Pfrieger, F. W. & Barres, B. A. Characterization of the signaling interactions that promote the survival and growth of developing retinal ganglion cells in culture. *Neuron* **15**, 805–819 (1995).
44. Chen, Y. *et al.* NS21: re-defined and modified supplement B27 for neuronal cultures. *J. Neurosci. Methods* **171**, 239–247 (2008).
45. Whitney, I. E., Keeley, P. W., Raven, M. A. & Reese, B. E. Spatial patterning of cholinergic amacrine cells in the mouse retina. *J. Comp. Neurol.* **508**, 1–12 (2008).
46. Rodieck, R. W. The density recovery profile: a method for the analysis of points in the plane applicable to retinal studies. *Vis. Neurosci.* **6**, 95–111 (1991).
47. Montague, P. R. & Friedlander, M. J. Morphogenesis and territorial coverage by isolated mammalian retinal ganglion cells. *J. Neurosci.* **11**, 1440–1457 (1991).
48. Smith, T. G. Jr, Lange, G. D. & Marks, W. B. Fractal methods and results in cellular morphology—dimensions, lacunarity and multifractals. *J. Neurosci. Methods* **69**, 123–136 (1996).
49. Wässle, H., Peichl, L. & Boycott, B. B. Dendritic territories of cat retinal ganglion cells. *Nature* **292**, 344–345 (1981).
50. Kay, J. N., Voinescu, P. E., Chu, M. W. & Sanes, J. R. Neurod6 expression defines new retinal amacrine cell subtypes and regulates their fate. *Nature Neurosci.* **14**, 965–972 (2011).



# A restricted cell population propagates glioblastoma growth after chemotherapy

Jian Chen<sup>1</sup>, Yanjiao Li<sup>1</sup>, Tzong-Shiue Yu<sup>1,2†</sup>, Renée M. McKay<sup>1</sup>, Dennis K. Burns<sup>3</sup>, Steven G. Kernie<sup>1,2†</sup> & Luis F. Parada<sup>1</sup>

**Glioblastoma multiforme is the most common primary malignant brain tumour, with a median survival of about one year<sup>1</sup>. This poor prognosis is due to therapeutic resistance and tumour recurrence after surgical removal. Precisely how recurrence occurs is unknown. Using a genetically engineered mouse model of glioma, here we identify a subset of endogenous tumour cells that are the source of new tumour cells after the drug temozolomide (TMZ) is administered to transiently arrest tumour growth. A *nestin-ATK-IRES-GFP* (*Nes-ATK-GFP*) transgene that labels quiescent subventricular zone adult neural stem cells also labels a subset of endogenous glioma tumour cells. On arrest of tumour cell proliferation with TMZ, pulse-chase experiments demonstrate a tumour re-growth cell hierarchy originating with the *Nes-ATK-GFP* transgene subpopulation. Ablation of the GFP<sup>+</sup> cells with chronic ganciclovir administration significantly arrested tumour growth, and combined TMZ and ganciclovir treatment impeded tumour development. Thus, a relatively quiescent subset of endogenous glioma cells, with properties similar to those proposed for cancer stem cells, is responsible for sustaining long-term tumour growth through the production of transient populations of highly proliferative cells.**

We have extensively studied a series of mouse strains harbouring conditional alleles of the tumour suppressors *Nf1*, *p53* (also known as *Trp53*) and *Pten*, which spontaneously develop malignant gliomas with 100% penetrance, and have identified the source cells of these tumours as deriving from the subventricular zone (SVZ)<sup>2–4</sup>. Thus, we proposed that adult neural stem cells (NSCs) are the likely source of these tumours<sup>2</sup>. We wished to determine whether a *Nes-ATK-GFP* transgene<sup>5</sup>, originally devised to mark adult NSCs, would also mark endogenous glioma cells. Elements of the nestin gene can drive transgene expression specifically in adult NSCs<sup>2,5</sup> (Fig. 1a). The transgene also harbours a cassette containing a modified version of the herpes simplex virus (HSV) thymidine kinase ( $\Delta$ TK), allowing for temporally regulated ablation of dividing neural progenitors by systemic ganciclovir (GCV) administration, and an IRES-GFP cassette to mark *Nes-ATK*-expressing cells in the absence of GCV. The *Nes-ATK-GFP* transgenic mice showed the expected expression in both glial fibrillary acidic protein (GFAP)-positive adult NSCs and early doublecortin (DCX)-positive neural progenitor cells (NPCs) in the major adult NSC niche: the SVZ of the lateral ventricle (Fig. 1b, c). To validate that the GCV-activated *Nes-ATK-GFP* transgene could effectively eliminate endogenous neural stem/progenitor cells, 1-month-old transgenic mice were treated with GCV for 2 weeks. In control mice, the rostral migratory stream (RMS), formed by NPCs migrating from the SVZ to the olfactory bulb, is visualized by Nissl staining. In contrast, the RMS was severely diminished in *Nes-ATK-GFP* mice after GCV treatment (Fig. 1b, bottom). Consistent with this observation, DCX immunostaining indicated the absence of NPCs in the SVZ of GCV-treated *Nes-ATK-GFP* animals (Fig. 1c, bottom). Because, in the presence of GCV, HSV TK targets only proliferating cells, the GFAP<sup>+</sup>

NSCs that remained quiescent were unaffected, although they also express the transgene, as indicated by GFP (Fig. 1c, bottom). Thus, our *Nes-ATK-GFP* transgene is specifically expressed in SVZ quiescent

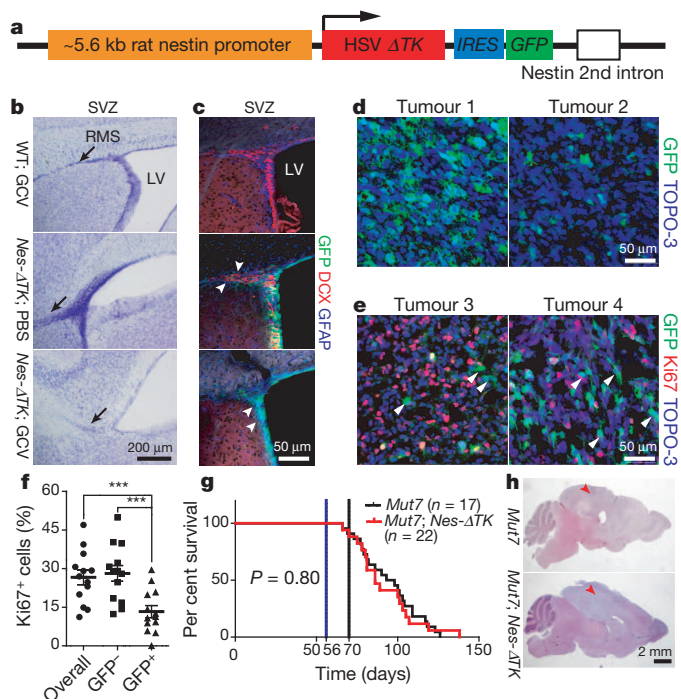


**Figure 1 | Characterization of the *Nes-ATK-GFP* transgene.** **a**, Diagram of the *Nes-ATK-GFP* transgene. **b**, **c**, GCV administration ablates NSCs in wild-type mice. **b**, Representative Nissl staining of the SVZ region in wild-type mice treated with GCV (WT; GCV), *Nes-ATK* transgenic mice treated with PBS (*Nes-ATK*; PBS) and *Nes-ATK* transgenic mice treated with GCV (*Nes-ATK*; GCV); black arrows indicate the stem cell RMS, which is greatly reduced in *Nes-ATK* mice treated with GCV. **c**, GFP (transgene), GFAP (quiescent NSCs) and DCX (committed neural progenitors) immunostaining of the SVZ stem cell niche. White arrowheads in middle panel (*Nes-ATK*; PBS) indicate DCX<sup>+</sup> cells more distal in the RMS. White arrowheads in bottom panel (*Nes-ATK*; GCV) indicate GFP<sup>+</sup>/GFAP<sup>+</sup> but DCX<sup>−</sup> quiescent NSCs. **d**, Representative GFP immunostaining in sections from two untreated gliomas of *Mut7*;*Nes-ATK* mice. From tumour to tumour, varying numbers of GFP<sup>+</sup> cells were observed. TOPO-3 stains nuclei. **e**, Representative GFP and Ki67 co-immunostaining in two untreated gliomas of *Mut7*;*Nes-ATK* mice. White arrowheads highlight GFP<sup>+</sup> but Ki67<sup>−</sup> cells, demonstrating that many transgene GFP<sup>+</sup> cells are quiescent. **f**, Percentage of Ki67<sup>+</sup> cells in GFP<sup>+</sup>, GFP<sup>−</sup>, and overall tumour population in gliomas from untreated *Mut7*;*Nes-ATK* mice. **g**, Kaplan–Meier survival curve of untreated *Mut7* and *Mut7*;*Nes-ATK* animals. No difference in per cent survival was observed. **h**, Representative haematoxylin and eosin staining of *Mut7* and *Mut7*;*Nes-ATK* brains without treatment. Infiltrative malignant gliomas are present in the cortex (red arrowhead) of both genotypes. \*\*\**P* < 0.001.

<sup>1</sup>Department of Developmental Biology & Kent Walderp Center for Basic Research on Nerve Growth and Regeneration, University of Texas Southwestern Medical Center, Dallas, Texas 75390-9133, USA.

<sup>2</sup>Department of Pediatrics, University of Texas Southwestern Medical Center, 5323 Harry Hines Boulevard, Dallas, Texas 75390, USA. <sup>3</sup>Department of Pathology, University of Texas Southwestern Medical Center, 5323 Harry Hines Boulevard, Dallas, Texas 75390, USA. <sup>†</sup>Present address: Department of Pathology and Cell Biology, Columbia University, New York, New York 10032, USA.

and proximal progenitor cells, and chronic GCV administration effectively blocks neurogenesis by ablating quiescent cells as they enter the cell cycle.

We bred the *Nes-ATK-GFP* transgene into *hGFAP-Cre;Nf1<sup>fl/+</sup>;P53<sup>fl/fl</sup>;Pten<sup>fl/+</sup>* (*Mut7*) glioma-prone mice<sup>3</sup>. *Mut7* mice develop malignant glioma, with full penetrance, by somatic deletion of three of the most frequently mutated tumour suppressors in glioblastoma multiforme: p53, NF1 and Pten<sup>6</sup>. All *Mut7;Nes-ATK-GFP* mice also developed gliomas and we observed only a subset of tumour cells expressing GFP (*Nes-ATK-GFP* positive; Fig. 1d, e). These cells also co-expressed the neural stem cell marker Sox2 (not shown). We next examined tumour cell proliferation and found that *Mut7;Nes-ATK-GFP* tumours exhibited a significant proportion of Ki67<sup>+</sup>/GFP<sup>+</sup> cells, and conversely, the subset of GFP<sup>+</sup> tumour cells rarely co-stained for Ki67 (Fig. 1e, f). These data indicate that most transgene GFP<sup>+</sup> tumour cells are relatively quiescent in comparison to a highly proliferative (Ki67<sup>+</sup>) subpopulation reminiscent of the SVZ, where GFP<sup>+</sup> stem cells are quiescent compared to GFP<sup>+</sup> progenitors (Fig. 1c). Furthermore, as in wild-type mice, in which the *Nes-ATK-GFP* transgene does not affect SVZ neurogenesis in the absence of GCV administration (Fig. 1b, c), introduction of the transgene into the *Mut7* genetic background did not affect tumour development or enhance survival (Fig. 1g). Like *Mut7* mice, *Mut7;Nes-ATK-GFP* mice developed malignant glioma with 100% penetrance and with similar kinetics (Fig. 1g, h).

TMZ is a DNA alkylating agent that is currently the primary chemotherapy administered to glioblastoma multiforme patients<sup>7</sup> as it has transient tumour growth-arrest properties. We found that TMZ eradicates proliferative cells in the endogenous murine gliomas. TMZ was administered over several days to tumour-bearing mice followed by BrdU injection 2 hours after final treatment, and the mice were killed 2 hours thereafter (Fig. 2a). The TMZ-treated mice showed a marked reduction of BrdU incorporation in both tumours and NSC niches (Fig. 2b, c). Similar to treated glioma patients after TMZ treatment, the murine tumours reinitiated cell division and growth. Thus, TMZ targets proliferating cells but tumour recurrence is inevitable. To examine the details of tumour recurrence, we traced the first wave of tumour cell proliferation after completion of the drug regimen in tumour-bearing mice by pulse chase using the BrdU analogues CldU and IdU. CldU and IdU were injected 1 day and 3 days, respectively, after the final TMZ injection (Fig. 2d). Given the variable but relatively low proportion of GFP<sup>+</sup> cells in all tumours (Fig. 1d, e), we reasoned that if cell proliferation reinitiated randomly in tumour cells after TMZ treatment, then the number of GFP<sup>+</sup> cells that would incorporate CldU and/or IdU should be low to insignificant. However, if renewed tumour cell proliferation was hierarchical and derived from the GFP<sup>+</sup> cells, a biased incorporation of nucleotide analogues into the relatively small GFP<sup>+</sup> cohort of tumour cells would result. Examination of tumour sections with immunohistochemistry revealed that the large majority of cells incorporating CldU and IdU after relatively short chases also contained GFP expression (Fig. 2e; GFP percentage in CldU<sup>+</sup> population = 77 ± 14, GFP percentage in IdU<sup>+</sup> population = 83 ± 10). Moreover, IdU<sup>+</sup> cells retained both GFP and CldU, indicating that after TMZ eradication of a majority of pre-existing proliferating tumour cells, the re-emergent population of proliferating cells derived from *Nes-ATK-GFP*-expressing cells and not from random tumour or other specific subsets of cells (Fig. 2e; CldU percentage in IdU<sup>+</sup> population = 86 ± 9). When the second, IdU, pulse was prolonged to a 7-day chase after the CldU pulse, most IdU cells double-labelled for CldU (85 ± 7%) but lost GFP expression (Supplementary Fig. 1a–c). Thus, as in the normal SVZ stem cell niche, over time the GFP-expressing glioma cell population gives rise to cells that progressively lose stem cell properties (that is, nestin expression and relative quiescence) and concomitantly shut down the *Nes-ATK-GFP* transgene (Supplementary Fig. 1c, d). Using endogenous lineage tracing of renewed cell division within tumours, we have identified the

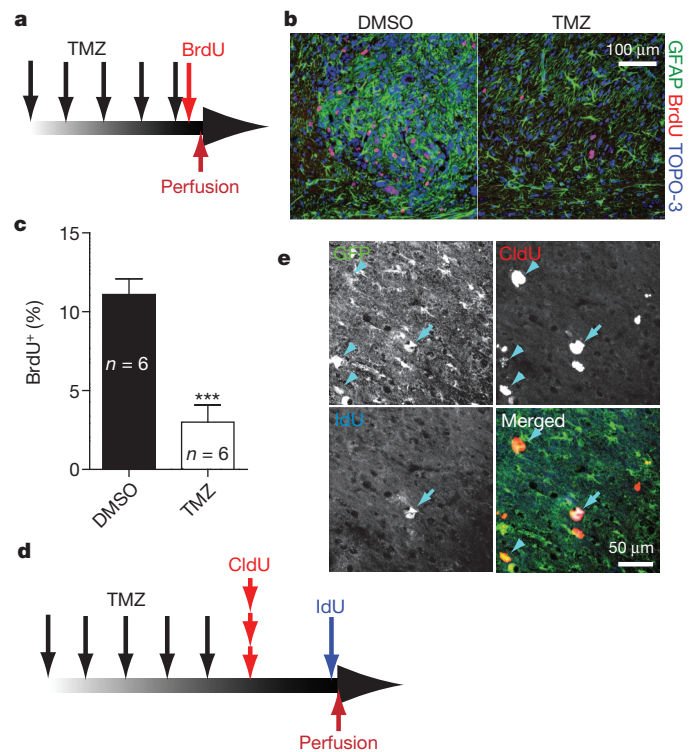


**Figure 2 | TMZ targets proliferating derivatives but not the GFP<sup>+</sup> quiescent cell population.** **a**, TMZ injection schema. *Mut7* mice were treated with TMZ for 5 days, injected with BrdU 2 h after the final TMZ treatment, and killed 2 h later for BrdU immunostaining. **b**, Representative GFAP/BrdU co-staining of glioma from DMSO- or TMZ-treated mice shows a marked reduction in the number of BrdU<sup>+</sup> cells. **c**, Quantification of the percentage of maximal BrdU<sup>+</sup> cells in gliomas from *Mut7* mice treated with or without TMZ showed a significant decrease in the TMZ-treated mice. Data are mean ± s.e.m.; *n* = 6 for each treatment; \*\*\**P* < 0.001, Student's *t*-test. **d**, **e**, *Nes-ATK*<sup>+</sup> cells are resistant to TMZ and produce new tumour cells. **d**, Schema of TMZ treatment and short-term labelling with BrdU analogues. *Mut7;Nes-ATK* mice were treated with TMZ for 5 days and then injected with the BrdU analogues CldU and IdU 1 and 3 days after the last TMZ treatment, respectively. **e**, Representative tumour section illustrating that repopulating tumour cells after TMZ treatment express the *Nes-ATK* transgene (GFP<sup>+</sup>); merged panel, CldU-incorporating (arrowhead) or IdU-incorporating (arrow) cells also express GFP driven by the *Nes-ATK* transgene. (Percentage of GFP<sup>+</sup> cells in the CldU<sup>+</sup> population = 77 ± 14; percentage of GFP<sup>+</sup> cells in the IdU<sup>+</sup> population = 83 ± 10; *n* = 5.) Note that the majority of CldU<sup>+</sup> cells and IdU<sup>+</sup> cells are positive for GFP expression, and also that the majority of IdU<sup>+</sup> cells are CldU<sup>+</sup>, indicating that the CldU<sup>+</sup> cells gave rise to the IdU<sup>+</sup> cells.

relatively quiescent *Nes-ATK-GFP*-expressing tumour cells as the primary source of proliferating and eventually non-dividing tumour cell derivatives (Supplementary Fig. 1c, d). In addition, the data show that in our endogenous glioma models, TMZ targets the proliferating derivatives but not the GFP<sup>+</sup> quiescent cells.

One prediction would be that eradication of the GFP<sup>+</sup> cells in the endogenous tumours should considerably decrease the emergence of new dividing tumour cells. We tested this prediction at two stages: early endogenous tumour development and advanced tumour development. First, *Mut7;Nes-ATK-GFP* mice were treated with GCV beginning at 8 weeks of age—the earliest time of detectable pre-tumorigenic anomalies<sup>3</sup>. To capture most quiescent GFP<sup>+</sup> cells in a dividing state, GCV treatment lasted for 10 weeks, requiring three osmotic mini-pump placement surgeries that unfortunately were accompanied by complications, resulting in considerable variance of drug delivery. Drug-delivery efficacy was qualitatively measured by examination of the normal stem cell niche response to drug (Fig. 1b, c) as manifested by residual RMS (Supplementary Fig. 2a). Accordingly, tumour incidence varied from mouse to mouse, with some perishing



early with large tumours. However, as a group, the GCV-treated cohort showed a clear survival advantage (Fig. 3a). After 10 weeks of treatment, the only surviving mice were among those treated with GCV (Supplementary Fig. 2b), and analysis of their brains revealed only low-grade lesions (Supplementary Fig. 2c). When GCV was effectively delivered, survival was substantially prolonged and tumour progression was severely impaired. Thus, elimination of *Nes-ATK-GFP*<sup>+</sup> cells at early/pre-tumorigenic stages prevents development of high-grade gliomas.

A second GCV regimen was started in 10-week-old tumour-bearing mice. Most 10-week-old *Mut7* mice do not show neurological symptoms, yet histological examination of large cohorts showed that all mice harbour astrocytomas of differing grades (Supplementary Fig. 3). We subjected 10-week-old *Mut7*;*Nes-ATK-GFP* or *Mut7* mice to GCV or saline for 2 months. GCV treatment of *Mut7*;*Nes-ATK-GFP* mice improved survival by approximately 30 days compared to saline

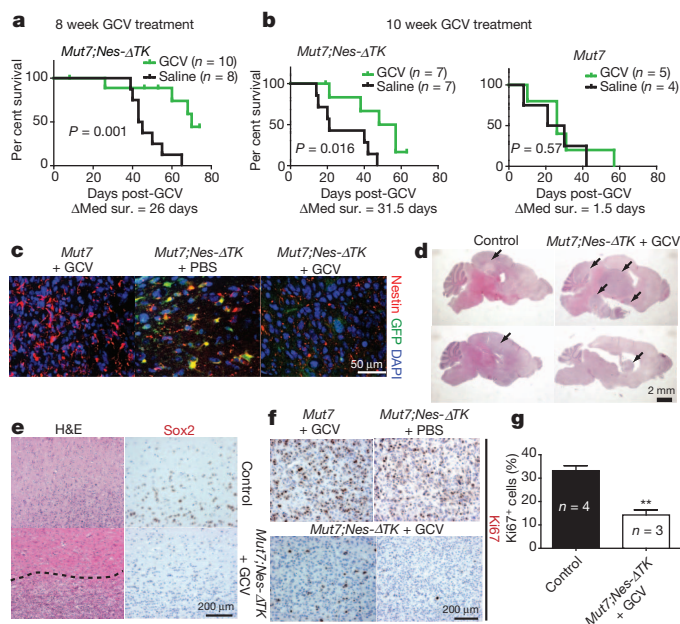


**Figure 3 | GCV treatment prolongs survival of *Mut7*;*Nes-ATK* mice.**

**a**, Kaplan–Meier curve of *Mut7*;*Nes-ATK* mice treated with saline or GCV for 10 weeks starting at 8 weeks of age showed a clear survival advantage for the GCV-treated mice ( $n = 10$  for GCV-treated;  $n = 8$  for saline-treated;  $P$  values determined using log-rank test).  $\Delta$ Med sur., change in median survival. **b**, Kaplan–Meier survival curves of *Mut7*;*Nes-ATK* (left) or *Mut7* (right) mice treated with GCV or saline for 2 months starting at 10 weeks of age. GCV treatment increased survival of *Mut7*;*Nes-ATK* mice compared to saline treatment but had no such effect on the *Mut7* mice.  $n = 5$ –7 for the GCV-treated mice;  $n = 4$ –7 for the saline-treated mice;  $P$  values determined using log-rank test. **c**, GFP/Neoslin co-immunostaining of gliomas from control (*Mut7* mice treated with GCV or *Mut7*;*Nes-ATK* mice treated with PBS) and GCV-treated *Mut7*;*Nes-ATK* mice. Elimination of GFP and Neoslin double-positive cells in the *Mut7*;*Nes-ATK* mice treated with GCV from 10 weeks. **d**, Representative haematoxylin and eosin staining of control and GCV-treated *Mut7*;*Nes-ATK* brains. The tumours in the GCV-treated *Mut7*;*Nes-ATK* mice are less infiltrative than in control. Tumours are indicated by black arrows. **e**, Representative haematoxylin and eosin (H&E) and Sox2 staining of tumour edges in control and GCV-treated *Mut7*;*Nes-ATK* tumours showing the GCV-treated tumours have a defined boundary (dotted line) and lack infiltrative Sox2<sup>+</sup> cells. **f**, **g**, GCV treatment decreases proliferation index in *Mut7*;*Nes-ATK* tumours. **f**, Representative Ki67 staining of control (top) or GCV-treated *Mut7*;*Nes-ATK* tumours (bottom) showing the marked decrease in proliferation in the GCV-treated *Mut7*;*Nes-ATK* tumours. **g**, Quantification of the percentage of Ki67<sup>+</sup> cells in tumour regions with highest number of proliferating cells in cortex. The percentage is significantly decreased in GCV-treated *Mut7*;*Nes-ATK* mice ( $n = 3$ ) versus control ( $n = 4$ ). Data are mean  $\pm$  s.e.m.; \*\* $P < 0.01$ , Student's  $t$ -test.

control, whereas neither treatment was effective in improving survival of *Mut7* mice (Fig. 3b). Consistent with this, GFP and endogenous nestin double immunostaining showed that GFP<sup>+</sup> cells were successfully eliminated in gliomas of *Mut7*;*Nes-ATK-GFP* mice after prolonged GCV treatment (Fig. 3c).

The residual tumours in these tumour-bearing *Mut7*;*Nes-ATK* mice treated with GCV beginning at 10 weeks of age did not have the classic glioma feature of invasiveness but instead were circumscribed with well-defined boundaries (Fig. 3d, e and Supplementary Fig. 2d, e). Although the *Mut7*;*Nes-ATK-GFP* transgene is only expressed in a subset of cells in the untreated tumour (Fig. 1e), tumours in GCV-treated *Mut7*;*Nes-ATK* mice showed a marked reduction of Ki67<sup>+</sup> cells and stem cell markers (Fig. 3e–g). These data further support the hypothesis that chronic GCV administration progressively ablates the relatively quiescent GFP<sup>+</sup> tumour cell population and the remaining GFP<sup>−</sup> tumour cells eventually exhaust their proliferative and infiltrative potential.

The HSV TK system has been widely used as a method to induce endogenous cell suicide. A potentially confounding phenomenon is the ‘bystander effect’, whereby HSV-TK-expressing cells not only commit suicide in the presence of GCV, but can also induce the death of neighbouring non-TK-expressing cells<sup>6</sup>. However, several NSC-specific HSV-TK-expressing transgenic mice have been reported and no bystander effect has been described<sup>8–11</sup>. To examine whether tumour development was appreciably impaired by the bystander effect, we turned to transplantation assays.

We first determined whether GCV treatment would also blunt *Mut7*;*Nes-ATK-GFP* tumour growth in a transplantation assay. Primary gliomas from *Mut7*;*Nes-ATK-GFP* and *Mut7* mice were dissociated and directly injected subcutaneously into nude mice in the presence of continuous GCV or saline treatment (Supplementary Fig. 4a). Neither GCV nor saline affected the tumour growth of *Mut7*-derived cells (Supplementary Fig. 4b). In contrast, similar to a previous report<sup>12</sup>, mice transplanted with *Mut7*;*Nes-ATK* tumour cells and then treated with GCV developed significantly smaller tumours that appeared to be poorly vascularized compared to saline-treated controls (Supplementary Fig. 4c–f). Thus, the *Mut7* tumour cells transplant efficiently in immunocompromised mice and, as in the endogenous setting (Fig. 3), GCV treatment severely impairs tumour development after transplantation. To test for the bystander effect, we transduced primary *Mut7* cells with a lentivirus harbouring either a control RFP cassette or an HSV TK cassette (Supplementary Fig. 5a). Mixed ratios of the two cell populations were injected subcutaneously into nude mice and allowed to seed tumours for 4 weeks, after which GCV was administered for 2 weeks (Supplementary Fig. 5b). The data indicate that the presence of a 10%, 20% or 50% initial ratio of TK-expressing tumour cells did not impair tumour development of the non-TK-expressing cells in the presence of GCV (Supplementary Fig. 5c, d). In the extreme case when equal numbers of TK<sup>+</sup> (10<sup>5</sup>) and TK<sup>−</sup> (10<sup>5</sup>) cells were injected compared to 10<sup>5</sup> TK<sup>−</sup> cells alone, tumour development was equivalent in both cohorts, demonstrating that GCV toxicity to 50% of the tumour cells did not extend into the TK<sup>−</sup> tumour cell population (Supplementary Fig. 5c, d). In our endogenous tumours, such a bystander effect would require the relatively rare GFP<sup>+</sup> tumour-propagating cells to be widely toxic in order to have a considerable paracrine effect on tumour properties. Instead, these studies indicate that GCV administration does not have an appreciable effect on cells outside those expressing the TK gene, consistent with other recently reported studies<sup>8–12</sup>. We conclude that eradication of the *Mut7*;*Nes-ATK-GFP* endogenous tumour cells through GCV treatment effectively disrupts the continued production of tumour cells, as predicted from the preceding data.

Despite effective depletion of GFP-expressing tumour-propagating cells with GCV treatment, a considerable residual tumour mass remained (Fig. 3d). We therefore attempted a therapeutic strategy to eliminate both the rapidly proliferating tumour cells and the quiescent



GFP<sup>+</sup> cells by sequentially administering TMZ and GCV (TMZ/GCV), respectively (Fig. 4a, b). Initially it seemed that this regimen did not prolong survival beyond that of GCV treatment alone (Fig. 4c). However, examination of the brains of the sequentially treated mice revealed only vestigial tumours in the dorsal brain that showed no transgene GFP expression, indicating effective depletion (Fig. 4d). The cellular density of the residual TMZ/GCV-treated tumours was lower than that of tumours at the beginning of treatment (10 weeks), indicating a statistically significant reduction in tumour bulk. This contrast was markedly enhanced when treated tumours were compared to untreated control tumours (Fig. 4e), which manifested in a spectrum of survival time from 12–16 weeks. Thus, the combined treatment had dramatic inhibitory effects on dorsal tumour growth in these mice.

We were puzzled that TMZ/GCV treatment did not significantly prolong survival beyond the GCV-only treated mice, in which residual circumscribed tumour mass remained (Fig. 3d, e and Supplementary Fig. 2d, e). Analysis of the TMZ/GCV-treated brains revealed that, despite the marked inhibition of original tumour growth, these mice developed novel tumours in the ventral brain region. Six out of seven TMZ/GCV-treated mice had tumours in the brainstem region, whereas gliomas in untreated *Mut7* mice and their remnants in the successfully treated mice are predominantly located in the dorsal/midbrain (Supplementary Fig. 6a). Examination of the TMZ/GCV-resistant hindbrain tumours revealed high endogenous nestin protein but no GFP expression (Supplementary Fig. 6b, c). We also searched

archived material and found that a small percentage of *Mut7* brains harboured both dorsal and ventral tumours that we now appreciate were independently arising and not extensions of the dorsal tumours. Appearance of ventral tumours in the presence of GCV indicates an inactive *Nes-ATK-GFP* transgene, and direct examination of untreated *Mut7*; *Nes-ATK-GFP* mice demonstrated that the *Nes-ATK-GFP* transgene was indeed silent (Supplementary Fig. 6b, e).

We next examined the expression of tumour markers in these hind-brain tumours. In contrast to typical *Mut7* or *Mut7*; *Nes-ATK-GFP* gliomas, all ventral tumours in the TMZ/GCV group showed low levels of endogenous GFAP but relatively high levels of S100B (Supplementary Fig. 6c and data not shown). Seven out of eleven tumours in the ventral and brain stem region of GCV-treated mice (GCV alone or TMZ and GCV) showed histopathological features of oligodendroglioma (Supplementary Fig. 7a–c), including high PDGFR- $\alpha$  levels (Supplementary Fig. 7d). This is in contrast to the pure astrocytic tumours typically observed in this mouse model in the absence of TMZ/GCV. Thus, these data indicate that the ventral tumours that become evident after TMZ/GCV treatment are oligoastrocytic, independently arising, and distinct from the dorsal tumours. Such tumours were recently described in *Mut3* mice<sup>13</sup>, and the source was reported to be oligodendroglial progenitors. We are currently further characterizing these tumours.

Our *Nes-ATK-GFP* transgene labels SVZ stem cells and, fortuitously, a specific subset of glioblastoma multiforme cells that possesses many features proposed for cancer stem cells (CSCs). The CSC hypothesis holds that some tumours are composed of a hierarchical cadre of cells of which only a subset retains both self-renewal and differentiation capacity<sup>14</sup>. In this model, only CSCs have the capacity to sustain tumour growth and are responsible for recurrence after therapy fails.

The current standard for evaluating whether solid tumours contain CSCs is an *ex vivo* limiting dilution tumorigenic transplantation assay into immunodeficient animals<sup>14</sup>. However, controversy regarding the presence and frequency of solid tumour CSCs remains, probably as a reflection of the variability that accompanies such assays<sup>15–18</sup>. Our study identifies a putative endogenous glioma stem cell located at the apex of a cellular hierarchy in tumour maintenance and recurrence after chemotherapy (Fig. 4a). Continued evaluation of these cells and their properties, including isolation and genetic lineage tracing, may yield important insights into novel therapeutic targets for this intractable disease.

## METHODS SUMMARY

**Mice.** All mice were maintained on a mixed 129SvJ/C57BL/6/B6CAB background. *Mut7* and *Mut7*; *Nes-ATK* mice were obtained by crossing male *hGFAP-Cre*; *P53*<sup>f/f</sup> mice with female *Nf1*<sup>f/f</sup>; *P53*<sup>f/f</sup>; *Pten*<sup>f/f</sup>; *Nes-ATK* mice. Genotyping for *Mut7* mice was performed as reported previously<sup>3</sup>.

**In vivo chemical administration.** Stock CldU (Sigma) and BrdU (Sigma) were dissolved in PBS at a concentration of 8.5 mg ml<sup>-1</sup> and 10 mg ml<sup>-1</sup>, respectively. 11.5 mg ml<sup>-1</sup> IdU (MP Biomedicals) solution was made fresh each time<sup>19</sup>. To label dividing cells, 5 ml kg<sup>-1</sup> stock solution was injected intraperitoneally each time according to the experimental design. GCV (Cytovene-IV, Roche Pharmaceuticals) treatment was performed as described<sup>5</sup>. For initial characterization of *Nes-ATK-GFP* mice, 1-month-old *Nes-ATK-GFP* or control mice were administered GCV (300 mg kg<sup>-1</sup> d<sup>-1</sup>) or PBS via osmotic mini-pump (Model 2002, 0.5  $\mu$ l h<sup>-1</sup>, Alzet) for 2 weeks. For treatment starting from 8 or 10 weeks, 150 mg kg<sup>-1</sup> d<sup>-1</sup> GCV or PBS was delivered through osmotic mini-pump (Model 2004, 0.25  $\mu$ l h<sup>-1</sup>, Alzet); pumps were surgically removed and replaced every 4 weeks based on the experimental requirement. TMZ (Sigma) was dissolved in DMSO and injected intraperitoneally at a dose of 82.5 mg kg<sup>-1</sup> d<sup>-1</sup> for 5 days. For the combinational therapy group, mice were first treated with TMZ for 5 days and then osmotic mini-pumps with GCV were implanted 2 days after the last TMZ injection.

**Histology and immunohistochemistry.** Mice were perfused and brains were processed as described earlier<sup>2</sup>. Paraffin brain haematoxylin and eosin sections (5  $\mu$ m) were reviewed by J.C. and D.K.B. independently. Tumour type and grades were determined by D.K.B. Fourteen-micrometre cryostat sections were used for GFP/CldU/IdU staining following reported methods<sup>19</sup>. Primary antibodies were

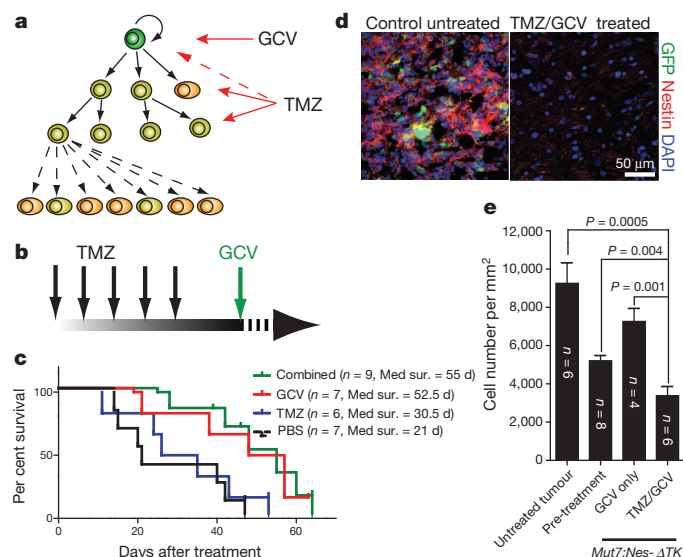


**Figure 4 | Combination treatment of TMZ and GCV inhibits glioma progression in cerebrum.** **a, b,** Therapeutic schema targeting both CSCs and their proliferating progeny. *Mut7*; *Nes-ATK* mice were treated with TMZ for 5 days, followed 2 days after by GCV. **c,** Kaplan–Meier survival curve of *Mut7*; *Nes-ATK* mice with different treatments. GCV-treated ( $n = 7$ ; median survival (Med sur.) = 52.5 days) and TMZ/GCV-treated ( $n = 9$ ; median survival = 52.5 days) *Mut7*; *Nes-ATK* mice had a similar survival advantage over TMZ-treated ( $n = 6$ ; median survival = 30.5 days) or PBS-treated ( $n = 7$ ; median survival = 21 days) mice.  $P$  values were determined using log-rank test. **d,** GFP and nestin double immunostaining of vestigial tumours in TMZ/GCV-treated *Mut7*; *Nes-ATK* mice (right) versus tumour in control (left) demonstrates depletion of CSCs as evidenced by lack of GFP expression. **e,** Maximal cell density in cortical tumours with different treatment regimens. Untreated *Mut7* mice ( $n = 6$ ) were used as control. Tumour density of 10-week-old non-symptomatic *Mut7* mice (pre-treatment) ( $n = 8$ ) was used as a reference starting point. Cell density was significantly lower in the TMZ/GCV-treated *Mut7*; *Nes-ATK* mice ( $n = 6$ ) compared to untreated tumours ( $P = 0.0005$ ), compared to tumours in pre-treatment mice ( $P = 0.004$ ), and compared to tumours from mice treated with GCV only ( $n = 4$ ). Data are mean  $\pm$  s.e.m.;  $P = 0.001$ , Student's  $t$ -test.

used against GFAP (DAKO, 1:2,000), Olig2 (Millipore, 1:1,000), Sox2 (Millipore, 1:5,000), nestin (BD Biosciences, 1:200), CD44 (BD Biosciences, 1: 75), GFP (Rockland, 1:200, Aves Lab, 1:500), BrdU/IdU (BD Biosciences, 1:100), BrdU/CldU (AbD Serotec, 1:500), Ki67 (Novacastra, 1:1,000), PDGFR- $\alpha$  (Santa Cruz, 1:200). Horseradish-peroxidase-based Vectastain ABC Kit (Vector Laboratories) or Cy2/Alexa-488, C3/Alexa555, Cy5-labelled secondary antibodies (Jackson Labs, Invitrogen) were used to visualize the primary antibody staining.

**Full Methods** and any associated references are available in the online version of the paper.

**Received 26 January 2011; accepted 7 June 2012.**

**Published online 1 August 2012.**

- Chen, J., McKay, R. M. & Parada, L. F. Malignant glioma: lessons from genomics, mouse models, and stem cells. *Cell* **149**, 36–47 (2012).
- Alcantara Llaguno, S. *et al.* Malignant astrocytomas originate from neural stem/progenitor cells in a somatic tumor suppressor mouse model. *Cancer Cell* **15**, 45–56 (2009).
- Kwon, C. H. *et al.* *Pten* haploinsufficiency accelerates formation of high grade astrocytomas. *Cancer Res.* **68**, 3286–3294 (2008).
- Zhu, Y. *et al.* Early inactivation of p53 tumor suppressor gene cooperating with NF1 loss induces malignant astrocytoma. *Cancer Cell* **8**, 119–130 (2005).
- Yu, T. S. *et al.* Traumatic brain injury-induced hippocampal neurogenesis requires activation of early nestin-expressing progenitors. *J. Neurosci.* **28**, 12901–12912 (2008).
- Ishii-Morita, H. *et al.* Mechanism of 'bystander effect' killing in the herpes simplex thymidine kinase gene therapy model of cancer treatment. *Gene Ther.* **4**, 244–251 (1997).
- Stupp, R. *et al.* Radiotherapy plus concomitant and adjuvant temozolomide for glioblastoma. *N. Engl. J. Med.* **352**, 987–996 (2005).
- Garcia, A. D. *et al.* GFAP-expressing progenitors are the principal source of constitutive neurogenesis in adult mouse forebrain. *Nature Neurosci.* **7**, 1233–1241 (2004).
- Deng, W. *et al.* Adult-born hippocampal dentate granule cells undergoing maturation modulate learning and memory in the brain. *J. Neurosci.* **29**, 13532–13542 (2009).
- Singer, B. H. *et al.* Compensatory network changes in the dentate gyrus restore long-term potentiation following ablation of neurogenesis in young-adult mice. *Proc. Natl Acad. Sci. USA* **108**, 5437–5442 (2011).
- Snyder, J. S. *et al.* Adult hippocampal neurogenesis buffers stress responses and depressive behaviour. *Nature* **476**, 458–461 (2011).
- Bao, S. *et al.* Stem cell-like glioma cells promote tumor angiogenesis through vascular endothelial growth factor. *Cancer Res.* **66**, 7843–7848 (2006).
- Liu, C. *et al.* Mosaic analysis with double markers reveals tumor cell of origin in glioma. *Cell* **146**, 209–221 (2011).
- Clarke, M. F. *et al.* Cancer stem cells—perspectives on current status and future directions: AACR Workshop on cancer stem cells. *Cancer Res.* **66**, 9339–9344 (2006).
- Boiko, A. D. *et al.* Human melanoma-initiating cells express neural crest nerve growth factor receptor CD271. *Nature* **466**, 133–137 (2010).
- Ishizawa, K. *et al.* Tumor-initiating cells are rare in many human tumors. *Cell Stem Cell* **7**, 279–282 (2010).
- Kelly, P. N. *et al.* Tumor growth need not be driven by rare cancer stem cells. *Science* **317**, 337 (2007).
- Quintana, E. *et al.* Efficient tumour formation by single human melanoma cells. *Nature* **456**, 593–598 (2008).
- Vega, C. J. & Peterson, D. A. Stem cell proliferative history in tissue revealed by temporal halogenated thymidine analog discrimination. *Nature Methods* **2**, 167–169 (2005).

**Supplementary Information** is linked to the online version of the paper at [www.nature.com/nature](http://www.nature.com/nature).

**Acknowledgements** The authors thank S. McKinnon, A. Deshaw, L. McClellan, S. Kennedy and P. Leake for technical assistance, and Parada laboratory members for helpful suggestions and discussion. CldU and IdU preparation and staining protocol was provided by D. A. Peterson at Rosalind Franklin University. This work was supported by grants awarded to S.G.K. (R01 NS048192-01) and to L.F.P. by the Goldhirsh Foundation, the James S. McDonnell Foundation (JSMF-220020206), Cancer Prevention Research Institute of Texas (RP 100782) and the National Institutes of Health (R01 CA131313). L.F.P. is an American Cancer Society Research Professor.

**Author Contributions** J.C. and Y.L. performed the experiments. T.-S.Y. and S.G.K. contributed vital reagents. J.C. and L.F.P. designed the experiments. J.C., R.M.M., D.K.B. and L.F.P. analysed the data. J.C., R.M.M. and L.F.P. wrote the paper.

**Author Information** Reprints and permissions information is available at [www.nature.com/reprints](http://www.nature.com/reprints). The authors declare no competing financial interests. Readers are welcome to comment on the online version of this article at [www.nature.com/nature](http://www.nature.com/nature). Correspondence and requests for materials should be addressed to L.F.P. ([luis.parada@utsouthwestern.edu](mailto:luis.parada@utsouthwestern.edu)).

## METHODS

**Mice.** All mouse experiments were approved by and performed according to the guidelines of the Institutional Animal Care and Use Committee of the University of Texas Southwestern Medical Center at Dallas. All mice were maintained on a mixed 129SvJ/C57BL/6/B6CAB background. *Mut7* and *Mut7;Nes-ΔTK* mice were obtained by crossing male *hGFAP-Cre;P53<sup>fl/fl</sup>* mice with female *NFI<sup>fl/fl</sup>;P53<sup>fl/fl</sup>;Pten<sup>fl/fl</sup>;Nes-ΔTK* mice. Genotyping for *Mut7* mice was performed as reported previously<sup>3</sup>.

**In vivo chemical administration.** Stock CldU (Sigma) and BrdU (Sigma) were dissolved in PBS at a concentration of 8.5 mg ml<sup>-1</sup> and 10 mg ml<sup>-1</sup>, respectively. 11.5 mg ml<sup>-1</sup> IdU (MP Biomedicals) solution was made fresh each time<sup>19</sup>. To label dividing cells, 5 ml kg<sup>-1</sup> stock solution was injected intraperitoneally each time according to the experimental design. GCV (Cytovene-IV, Roche Pharmaceuticals) treatment was performed as described<sup>5</sup>. For initial characterization of *Nes-ΔTK-GFP* mice, 1-month-old *Nes-ΔTK-GFP* or control mice were administered GCV (300 mg kg<sup>-1</sup> d<sup>-1</sup>) or PBS via osmotic mini-pump (Model 2002, 0.5 μl h<sup>-1</sup>, Alzet) for 2 weeks. For treatment starting from 8 or 10 weeks, 150 mg kg<sup>-1</sup> d<sup>-1</sup> GCV or PBS was delivered through osmotic mini-pump (Model 2004, 0.25 μl h<sup>-1</sup>, Alzet); pumps were surgically removed and replaced every 4 weeks based on the experimental requirement. TMZ (Sigma) was dissolved in DMSO and injected intraperitoneally at a dose of 82.5 mg kg<sup>-1</sup> d<sup>-1</sup> for 5 days. For the combinational therapy group, mice were first treated with TMZ for 5 days and then osmotic mini-pumps with GCV were implanted 2 days after the last TMZ injection.

**Histology and immunohistochemistry.** Mice were perfused and brains were processed as described earlier<sup>2</sup>. Paraffin brain haematoxylin and eosin sections (5 μm) were reviewed by J.C. and D.K.B. independently. Tumour type and grades were determined by D.K.B. Fourteen-micrometre cryostat sections were used for GFP/CldU/IdU staining following reported methods<sup>19</sup>. Primary antibodies were used against GFAP (DAKO, 1:2,000), Olig2 (Millipore, 1:1,000), Sox2 (Millipore, 1:5,000), nestin (BD Biosciences, 1:200), CD44 (BD Biosciences, 1: 75), GFP (Rockland, 1:200, Aves Lab, 1:500), BrdU/IdU (BD Biosciences, 1:100), BrdU/CldU (AbD Serotec, 1:500), Ki67 (Novacastra, 1:1,000), PDGFR-α (Santa Cruz, 1:200). Horseradish-peroxidase-based Vectastain ABC Kit (Vector Laboratories)

or Cy2/Alexa-488, C3/Alexa555, Cy5-labelled secondary antibodies (Jackson Labs, Invitrogen) were used to visualize the primary antibody staining. Images were taken using optical, fluorescence and confocal microscopy (Olympus and Carl Zeiss) and assembled in Adobe Illustrator (Adobe Systems Incorporated).

**TMZ, BrdU analogues and pulse-chase experiments.** To determine TMZ efficiency, 10- to 11-week-old *Mut7* mice were first injected intraperitoneally with 82.5 mg kg<sup>-1</sup> d<sup>-1</sup> TMZ for 5 days. 50 mg kg<sup>-1</sup> BrdU was injected 2 h after the final TMZ administration and mice were perfused 2 h after BrdU injection. The brain was then paraffin-processed and cut into 5-μm-thick slices. Haematoxylin and eosin staining was performed every 70 μm to identify tumour location. Adjacent tumour sections were selected for GFAP and BrdU co-immunostaining.

For the short-term CldU chase experiments, 10- to 11-week-old *Mut7;Nes-ΔTK* mice were first treated with TMZ for 5 days. A total of three doses of CldU were injected, with 2-h intervals, the day after the final TMZ injection. A single dose of IdU was then injected 3 days after the final TMZ injection. For the long-term CldU chase experiments, 10- to 11-week-old *Mut7;Nes-ΔTK* mice were first treated with TMZ for 5 days. CldU was injected 3 times a day, with 2-h intervals, for 3 days after the final TMZ injection. A single dose of IdU was then injected 7 days after the final TMZ injection. Mice were perfused 2 h after the IdU injection and the brains cryoprotected in 30% sucrose, embedded in OCT, and cut into 14-μm-thick frozen sections. GFAP and Ki67 co-immunostaining was performed every 140 μm to locate the tumour area. Adjacent sections were selected for GFP/CldU/IdU triple immunofluorescence staining.

**Quantification.** Because of the heterogeneous nature of the tumours, cell density, Ki67 index and BrdU<sup>+</sup> cell percentage were quantified using the highest staining area<sup>1</sup>. Briefly, staining was checked under low magnification and the highest staining area was identified. The area was viewed at ×200 in three continuous 5-μm-thick sections and positive cells counted using the measured parameters.

For quantification of GFP/CldU/IdU triple staining, tumour areas with at least one CldU<sup>+</sup> cell were selected, and an 8 μm Z-stack image was scanned and constructed using confocal microscopy (Olympus and Carl Zeiss). A total of ten different areas within each tumour was imaged and subjected to quantification.



# Defining the mode of tumour growth by clonal analysis

Gregory Driessens<sup>1</sup>, Benjamin Beck<sup>1</sup>, Amélie Caauwe<sup>1</sup>, Benjamin D. Simons<sup>2,3</sup> & Cédric Blanpain<sup>1,4</sup>

Recent studies using the isolation of a subpopulation of tumour cells followed by their transplantation into immunodeficient mice provide evidence that certain tumours<sup>1,2</sup>, including squamous skin tumours<sup>3–5</sup>, contain cells with high clonogenic potential that have been referred to as cancer stem cells (CSCs). Until now, CSC properties have only been investigated by transplantation assays, and their existence in unperturbed tumour growth is unproven. Here we make use of clonal analysis of squamous skin tumours using genetic lineage tracing to unravel the mode of tumour growth *in vivo* in its native environment. To this end, we used a genetic labelling strategy that allows individual tumour cells to be marked and traced over time at different stages of tumour progression. Surprisingly, we found that the majority of labelled tumour cells in benign papilloma have only limited proliferative potential, whereas a fraction has the capacity to persist long term, giving rise to progeny that occupy a significant part of the tumour. As well as confirming the presence of two distinct proliferative cell compartments within the papilloma, mirroring the composition, hierarchy and fate behaviour of normal tissue, quantitative analysis of clonal fate data indicates that the more persistent population has stem-cell-like characteristics and cycles twice per day, whereas the second represents a slower cycling transient population that gives rise to terminally differentiated tumour cells. Such behaviour is shown to be consistent with double-labelling experiments and detailed clonal fate characteristics. By contrast, measurements of clone size and proliferative potential in invasive squamous cell carcinoma show a different pattern of behaviour, consistent with geometric expansion of a single CSC population with limited potential for terminal differentiation. This study presents the first experimental evidence for the existence of CSCs during unperturbed solid tumour growth.

Different models have been proposed to explain tumour heterogeneity and growth<sup>1,6,7</sup>. In the stochastic model, all tumour cells are considered equipotent and only a fraction (due to genetic and/or epigenetic changes) will contribute to tumour growth. By contrast, in the CSC model, only a fraction of tumour cells have high clonogenic potential, and give rise to a predictable hierarchical mode of tumour growth. These two models of tumour growth are not mutually exclusive and competition may still arise in the hierarchical model. Until now, CSC properties have been demonstrated by the ability of a subpopulation of tumour cells to reform a tumour identical to the parental tumour on transplantation into immunodeficient mice. This 'gold standard' assay has some caveats as tumour cells are usually transplanted at a heterotopic site, embedded in Matrigel containing a cocktail of growth factors, into an allogenic or xenogenic immunocompromised host<sup>8</sup>. These studies clearly demonstrate the long-term renewal potential of cancer cells in these experimental conditions, but they do not necessarily reflect the physiological fate of these cells in their native environment<sup>1</sup>.

Here we sought to investigate the fate of individual tumour cells within their natural microenvironment in the early stage of squamous skin tumours. Chemical-induced carcinogenesis is the most commonly used tumour model in mice<sup>9,10</sup>. Although this model may only imperfectly mimic the occurrence of human skin cancers, it has proved to be

extremely useful in dissecting the different steps of tumour initiation, promotion and malignant progression, and has been instrumental in defining many paradigms in cancer biology relevant to human pathology<sup>9,11,12</sup>. In this protocol, mice are first treated with the carcinogen DMBA (7,12-dimethylbenz[ $\alpha$ ]anthracene) followed by continuous administration of the mitogen TPA (12-O-tetradecanoylphorbol-13-acetate). During the course of TPA administration, benign tumours, known as papilloma, appear (initiation) and grow steadily (promotion), with a fraction eventually progressing into invasive tumours. Papilloma are characterized by a skin excrescence that expands slowly and presents a stereotypical architecture similar to normal epidermis with a basal layer of proliferative tumour cells expressing K5/K14 and suprabasal layers of non-proliferative cells expressing K1/K10, which finally enucleate and form a stratum corneum structure (Fig. 1a). In contrast with normal homeostasis, in which the rate of cell production matches the rate of loss, during tumour growth this balance is shifted towards proliferation, with the diameter of the papilloma doubling in size every month (Supplementary Fig. 1). Although these tumours

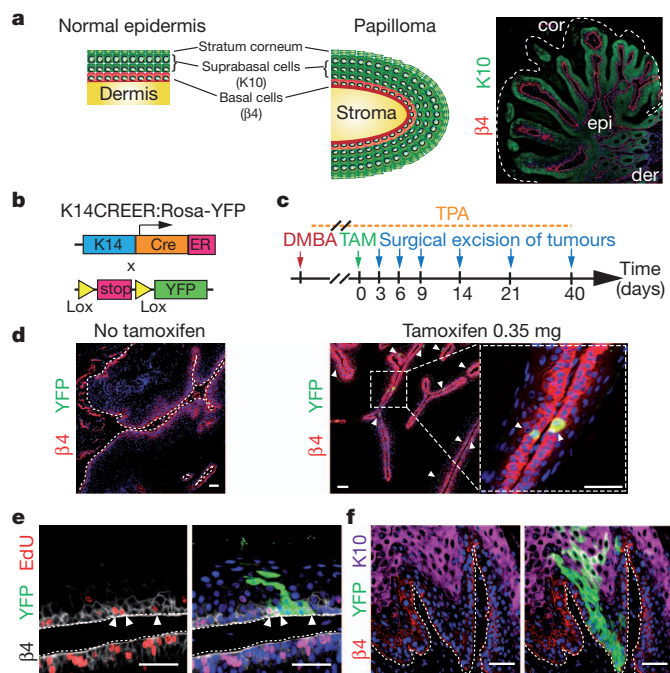


**Figure 1 | Genetic tracing of skin papilloma at clonal density.** **a**, Scheme of the stereotypical architecture of papilloma similar to normal epidermis. cor, stratum corneum; der, dermis; epi, epithelial cells. **b**, Scheme of genetic strategy to induce YFP expression in papilloma. ER, tamoxifen-responsive hormone-binding domain of the oestrogen receptor; K14, human keratin 14 promoter. **c**, Protocol of DMBA/TPA and tamoxifen (TAM) administration. **d**, Immunostainings for  $\beta 4$ -integrin ( $\beta 4$ ) and YFP in papilloma with or without TAM. **e**, Immunostaining for  $\beta 4$ -integrin, YFP and 5-ethynyl-2'-deoxyuridine (EdU) in a papilloma 6 days post-labelling. **f**, Immunostaining for  $\beta 4$  integrin, YFP and K10 in a papilloma 14 days post-labelling. Scale bars, 50  $\mu$ m.

<sup>1</sup>Université Libre de Bruxelles, IRIBHM, Brussels B-1070, Belgium. <sup>2</sup>Cavendish Laboratory, Department of Physics, J. J. Thomson Avenue, Cambridge CB3 0HE, UK. <sup>3</sup>The Wellcome Trust/Cancer Research UK Gurdon Institute, University of Cambridge, Tennis Court Road, Cambridge CB2 1QN, UK. <sup>4</sup>WELBIO, Brussels B-1070, Belgium.

contain a mass of amorphous material arising from the terminal differentiation of tumour cells, the proportion of differentiated cells remains relatively constant over time (Supplementary Fig. 1), indicating that tumours grow mostly through basal epithelial cell expansion.

These observations raise several important questions. Why is the growth of the papilloma relatively slow? Classical theories of tumour development often involve unbridled replication of the tumour-maintaining cell population, leading to geometric expansion of the tumour mass<sup>13</sup>. However, papilloma arise sporadically following DMBA/TPA treatment, after which they grow slowly, giving rise to a heterogeneous size distribution (Supplementary Fig. 1). Is the characteristic stem/progenitor cell hierarchy of normal tissue recapitulated in the tumour? Are proliferative tumour cells equipotent, or is the papilloma sustained by a distinct population of tumour cells with stem-cell-like properties? To address these questions, we used a quantitative lineage-tracing strategy that has proved successful in resolving cellular hierarchy and stem-cell fate in normal epithelial tissues<sup>14–19</sup>.

To mark individual tumour cells, we made use of an inducible genetic lineage tracing system (Fig. 1b). Following the administration of tamoxifen (TAM) to K14CREER/Rosa-YFP mice bearing skin tumours induced by DMBA/TPA treatment, we were able to label cells at clonal density within the papilloma (Fig. 1c). Titrating down the dose of TAM to 0.35 mg generated yellow fluorescent protein (YFP) expression in around 1% of basal tumour epithelial cells (Fig. 1d and Supplementary Fig. 2), a density that allows the fate of individual labelled cells to be traced over time. In the weeks following TAM administration, some YFP-labelled basal cells actively divided (Fig. 1e), and formed clones containing several basal cells as well as suprabasal cells that reach the top of the cornified layer (Fig. 1f), demonstrating that labelled tumour cells are capable of generating all cell types that comprise the tumour. Interestingly, the initial shape of the marked tumour clones is reminiscent of the column of marked cells (sometimes termed epidermal proliferative units) observed in the interfollicular epidermis during normal homeostasis<sup>14,15,20–22</sup>.

To gain further insight into the proliferative potential of labelled tumour cells, we first quantified the size and persistence of clones across a range of time points from 3 days up to 7 weeks post-labelling (Fig. 2a–c). Analysis of the junction between normal epidermis and papilloma excluded the possibility that tumour clones arise from cells coming from normal epidermis (Supplementary Fig. 3). Whereas the frequency of labelled tumour clones (number per sectional area) remained relatively constant during the first 2 weeks after TAM administration, this number had dropped by around 3 weeks, and by 7 weeks involved only 20% of the initial clones (Fig. 2b), indicating that only a fraction of proliferative tumour cells present long-term self-renewal potential. The near-absence of active caspase 3<sup>+</sup> cells in these tumours ( $0.28 \pm 0.03\%$  active caspase 3<sup>+</sup> tumour epithelial cells) indicates that clones were lost through differentiation rather than by apoptosis. (Supplementary Fig. 4). Of the clones that did survive at 7 weeks post-labelling, many were enormous, containing several hundreds to thousands of cells, and sometimes comprising an entire lobe of the tumour (Fig. 2a, c). These data indicate heterogeneity in the proliferative potential of tumour cells, and indicate that a fraction may conform to the CSC paradigm *in vivo* by massively contributing at the clonal level to tumour growth.

Although the stratified architecture is conserved in papilloma, its folded structure does not facilitate whole-mounting. Instead, clones can only be visualized through the acquisition of sectional data. As a result, total clone size could only be scored at single-cell resolution for individual clones by three-dimensional (3D) reconstruction using confocal analyses of serial (25  $\mu$ m) sections (Supplementary Fig. 5). Following this procedure, we scored a limited number of clones over a 7-week time course (Fig. 2c), from which several qualitative features emerged. First, single-cell clones, which account for some 50% of the total YFP-labelled clones at 3 days post-labelling, showed a decline only around day 9, indicating that the loss rate of terminally differentiated cells is relatively slow in comparison to the cell division rate.

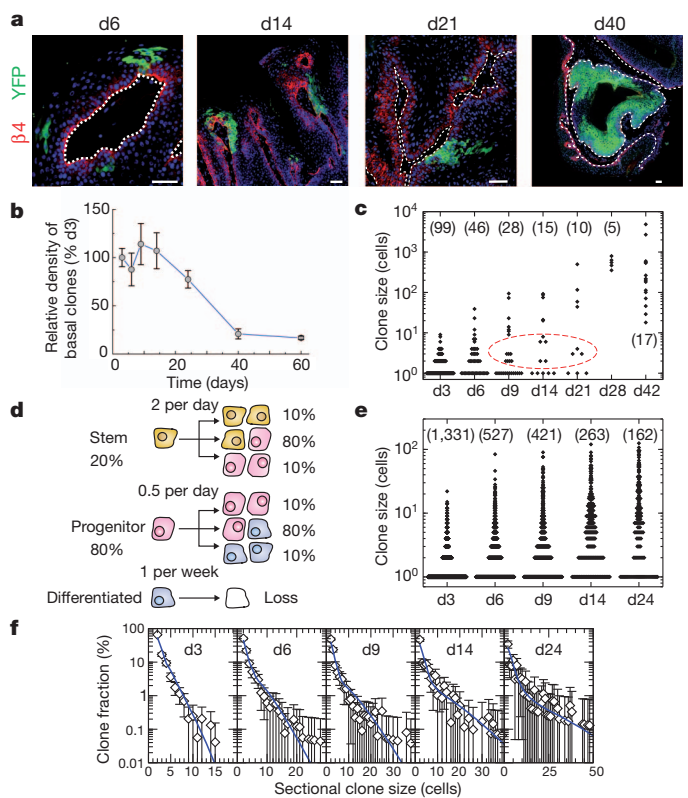


**Figure 2 | Quantitative clonal analysis in skin papilloma.**

**a**, Immunostainings for  $\beta 4$ -integrin and YFP in papilloma after TAM administration. **b**, Quantification of the relative density of basal clones over time ( $n = 666, 383, 328, 194, 162, 35$  and  $33$  clones from at least 5 different tumours at day 3, 6, 9, 14, 24, 40 and 60, respectively). **c**, Total size of clones derived from 3D serial reconstruction over time. The  $n$  value is shown. **d**, Tumour growth model showing the proliferative stem/progenitor cells. **e**, Clone sizes derived from single sections over time. The  $n$  value is shown. **f**, Fit of the hierarchical model (**d**) to the corresponding cumulative sectional clonal size distribution. Points show data (**e**) and the blue lines show the model prediction. Scale bars, 50  $\mu$ m. Error bars denote s.e.m.

Second, from the size distribution (Fig. 2c), there is further evidence of proliferative heterogeneity. Although the spectrum of clone sizes is broad and continuous at 3 days post-labelling (with clones of ten cells or more coexisting with clones of only two cells), by 9 days the distribution becomes bimodal (Fig. 2c). Of the clones involving multiple cells (and therefore derived from proliferative cells), a minority continue to grow and expand rapidly over the time course, whereas others generate clones with fewer than ten cells that become progressively lost. At 7 weeks post-labelling, clones still present significant heterogeneity in size ranging from dozens of cells to several thousands of cells (Fig. 2c).

Although data from the 3D reconstruction provides qualitative insight into the proliferative cell dynamics, to further resolve the properties of these populations, we turned to a quantitative analysis. Because acquisition of a large statistical ensemble of clone sizes from serial reconstruction is impractical, we used data from independent sections, which could be obtained in larger numbers. Fortunately, analysis of data from the 3D reconstruction revealed a robust quadratic relationship between sectional clone size,  $n_{2D}$ , and total clone size,  $n_{3D}$ , which allows the statistical distribution of the latter to be reliably reconstructed from the former (Supplementary Fig. 5 and Supplementary Information). This quadratic dependence,  $n_{3D} \approx n_{2D}^2/3$ , follows from the architecture of the tissue that constrains clones to grow laterally as cohesive ‘pancake-like’ structures once the clone has spanned the suprabasal cell layers.

Data from the serial reconstruction indicate that papilloma are sustained by a cellular hierarchy in which a minority population of



tumour cells with stem-cell-like properties gives rise to a more transient progenitor cell pool. Motivated by lineage-tracing studies of normal epidermis<sup>14,15,18</sup>, we propose that the progenitor cell population follows a stochastic pattern of fate in which cell division can lead to all three fate outcomes: two dividing cells, two non-dividing, and one dividing and one non-dividing (Fig. 2d). Further, we propose that the stem-cell-like population divides rapidly, leading to a similar pattern of stochastic fate involving self-renewal and the generation of progenitor cell progeny (Fig. 2d). With this model, we made use of the sectional clone size data (Fig. 2e) to fit the experimental parameters (for further details of the modelling scheme and fitting procedure, see Supplementary Information). This procedure is simplified considerably by the divergence in size of the progenitor- and stem-cell-derived clones, with the former dominating the distribution for smaller clone sizes and early time points, and the latter contributing substantially to the larger clone sizes and later time points. From the predicted dynamics, we obtain an excellent fit to the clone size distributions over the wide time course (Fig. 2f) if we suppose that the stem-cell-like population accounts for just 20% of the labelled tumour proliferative cells, and take both the progenitor and stem cell fates to be approximately balanced with some 80% of divisions leading to asymmetric fate outcome while the remaining 20% lead to either symmetrical duplication or differentiation, with equal probability (Fig. 2d). Moreover, the inferred stem-cell-like tumour cell division rate of twice per day is approximately four times larger than the progenitor cell division rate in the tumour, and an order of magnitude larger than the progenitor cell division rate in normal tissue. Finally, as expected from the analysis of the serial reconstruction, the loss rate of terminally differentiated cells is slow, at around once per week.

To test the predictions of the model, we performed a double-labelling nucleotide pulse-chase assay to estimate the proportion of cells that re-enter the cell cycle after 12 h. To this end, we first administered a pulse of 5-ethynyl-2'-deoxyuridine (EdU) to mice bearing papilloma, and administered 5-bromo-2-deoxyuridine (BrdU) 12 h later, and analysed double-labelled basal cells 4 h after that (Fig. 3a). Significantly, whereas virtually no double-positive cells can be found in normal epidermis on the edge of the tumour (Supplementary Fig. 6), around 17% of the basal tumour epithelial cells were BrdU-EdU double-positive (Fig. 3b), consistent with the predictions made by the analysis of the clonal fate data (Fig. 2d and Supplementary

Information). To challenge the model further, we looked for additional clonal fate characteristics that can be matched against the predicted dynamics. To fit the parameters of the model, we make use of the total clone size data without reference to the relative contribution of basal and suprabasal cells within the clones. To test the model, at 9 days post-labelling, we explored the clone size distribution disaggregated into basal and total cell contributions, focusing on the ensemble of basal clones (those with at least one cell that retains an attachment to the basal lamina) (Fig. 3c and Supplementary Fig. 7). With the same parameters, we found good agreement with the measured size distributions (Fig. 3d), lending further support to the findings.

To determine whether the transition from benign papilloma to malignant invasive squamous cell carcinoma (SCC) is accompanied by a change in the cellular hierarchy and proliferation dynamics, we combined a study of clonal fate with proliferation kinetics in invasive SCC arising from the spontaneous malignant transformation of papilloma in DMBA/TPA-treated mice. Whereas SCCs do not express keratins associated with epidermal differentiation (such as K10), evidence of terminal differentiation is visible in cell clusters known as keratin pearls (one of the pathognomonic features of skin SCCs), with a frequency that varies from tumour to tumour (Supplementary Fig. 8). Administration of 1 mg TAM to K14CREER/Rosa-YFP mice presenting invasive SCC induced YFP expression at clonal density ( $0.9 \pm 0.3$  clone per  $\text{mm}^2$ ) (Fig. 4a, b). From a confocal analysis of serial thick sections (Supplementary Fig. 9), we were able to score the total clone size at 9 days post-labelling, the time point for which we have the most comprehensive clonal data set in papilloma. The proportion of clones presenting signs of differentiation through the presence of keratin pearls is similar to the overall frequency of differentiated cells within tumours, indicating that the targeted clones are representative (Supplementary Fig. 8). Whereas clones showed significant heterogeneity in size (Fig. 4c–g), in contrast with papilloma, SCC also showed tumour-to-tumour variability, and the incidence of small clones was significantly diminished. Interestingly, all of the largest clones contained cells that contact the stroma and endothelial cells as well as cells that have lost their cohesion with the rest of the clone, and present signs of epithelial to mesenchymal transition with a fibroblastic-like morphology (Fig. 4d, e, h). Most cells within these clones present no sign of terminal differentiation despite having undergone many rounds of division (Fig. 4e), indicating that these clones are comprised of proliferative cells with a very low probability of terminal differentiation.

Consistent with the notion that most cells in invasive SCCs are proliferative, about 70% of cells in SCC are Ki67<sup>+</sup> and continuous administration of BrdU for 5 days labelled about 90% of undifferentiated cells in invasive SCCs (Fig. 4i–k and Supplementary Fig. 8). Although heterogeneity of clone size could reflect tumour cells with a range of proliferative potential, the exponential form of the cumulative clone size distribution of individual tumours (Supplementary Fig. 9) is equally consistent with a single equipotent proliferative cell population, biased towards symmetric self-renewal, with a broad distribution of cell cycle times (Supplementary Information). Within this paradigm, we estimate an average cell division time that varies between 1 and 2 days (according to the tumour). This figure is consistent with the results of a BrdU-EdU double-labelling assay, which revealed that, whereas 23% of SCC cells acquire BrdU or EdU expression following a short pulse, the frequency of double-labelled cells after 16 h chase was below 2% (Fig. 4l–n and Supplementary Information).

In summary, our data present the first attempt to dissect the mode of tumour growth using clonal analysis by lineage tracing in mice, and demonstrate for the first time the existence of tumour cells with stem-cell-like properties in an unperturbed solid tumour, consistent with the CSC paradigm. The neutral competition of tumour cells uncovered here in skin papilloma is reminiscent of the dynamics found in normal tissue and indicates that this hierarchical mode of tumour growth is mediated at the cellular level by stochastic cell fate decisions. This mode of tumour growth, involving the chance expansion and extinction of

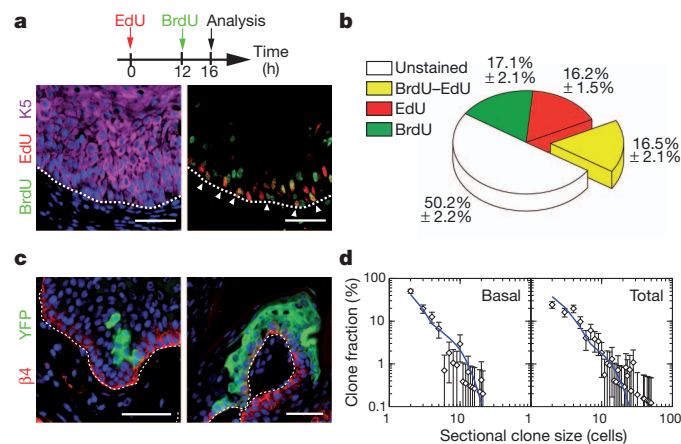


**Figure 3 | Challenging the stem/progenitor cell model in papilloma.**

**a**, Immunostaining for BrdU, EdU and K5 in papilloma from mice treated following the protocol schemed above. **b**, Quantification of the proportion of unlabelled cells, BrdU, EdU and EdU-BrdU double-labelled cells within the basal layer of papilloma ( $n = 5,512$  cells from 8 papilloma). **c**, Immunostaining for YFP and  $\beta 4$ -integrin on papilloma 9 days after TAM administration. **d**, Comparison between the model prediction (blue lines), with parameters defined in Fig. 2d and in the text, and the clone size distribution ( $n = 105$  clones from 7 tumours). Scale bars, 50  $\mu\text{m}$ . Error bars denote s.e.m.



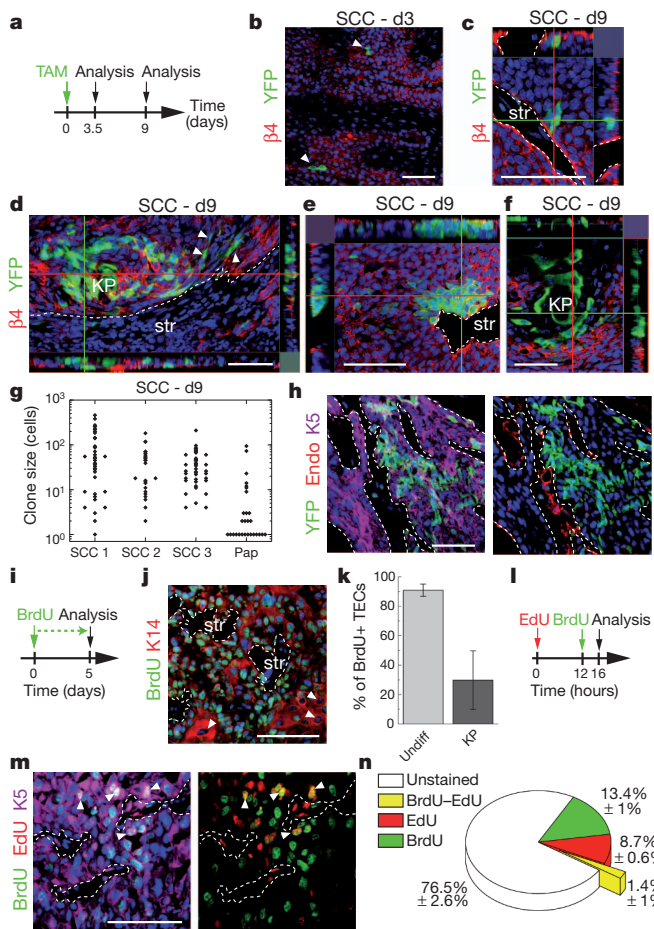


**Figure 4 | Quantitative clonal analysis of squamous cell carcinoma.**

**a**, Protocol of TAM administration and clonal analysis in SCC. **b**, Immunostaining for YFP and  $\beta 4$ -integrin in SCC 3 days after TAM administration. **c–f**, Same as in **b** 9 days after TAM administration. KP, keratin pearl; str, stroma. **g**, Total size of clones quantified from serial 30  $\mu$ m sections 9 days after TAM administration ( $n = 37, 25, 42$  and 28 clones in SCC 1, 2, 3 and papilloma (Pap), respectively). **h**, Immunostaining for YFP, K5 and endoglin (Endo) in SCC 9 days after TAM administration. **i**, Protocol of BrdU administration. **j**, Immunostaining for BrdU and K14 in SCC. **k**, Quantification of the BrdU<sup>+</sup> tumour epithelial cells (TECs) within SCC after 5 days of continuous BrdU administration ( $n = 676$  undifferentiated tumour cells and 282 KP cells). Error bars denote s.d. Undiff, undifferentiated. **l**, Protocol of BrdU and EdU administration. **m**, Immunostaining for BrdU, EdU and K5 in SCC from mice treated following the protocol shown in **l**. **n**, Quantification of the proportion of unmarked cells, BrdU, EdU and EdU–BrdU double-labelled cells within SCC ( $n = 9,010$  cells from 2 SCC). Scale bars, 50  $\mu$ m.

neighbouring clones, may explain the clonal heterogeneity found in many different tumours<sup>23</sup>. In future studies, it will be important to define the mechanisms regulating the balance between proliferation and differentiation during tumour progression, the influence of the external environment and other physical constraints on tumour expansion, and whether this stochastic mode of tumour progression also operates in other types of cancer.

## METHODS SUMMARY

Squamous skin tumours were induced by treating K14CREER/Rosa-YFP mice with the two-step DMBA/TPA chemical carcinogenesis protocol<sup>10</sup>. Clonal YFP expression in skin tumours was performed by administering 0.35 mg or 1 mg TAM to K14CREER/Rosa-YFP mice bearing benign or malignant skin tumours. Immunostainings were performed as described<sup>24</sup>. Quantification of the total clone size was determined by counting the number of YFP-positive cells in 3D reconstruction of the whole clone using serial thick sections analysed by confocal microscopy. Two-dimensional clone size was determined by counting the number

of YFP cells in a single tumour thin section and its relation to the total clone size was inferred using the algorithm defined in the main text and Supplementary Information. BrdU–EdU double-labelling approach was performed as described<sup>25</sup>. For further details see Supplementary Methods.

**Full Methods** and any associated references are available in the online version of the paper.

Received 26 February; accepted 22 June 2012.

Published online 1 August 2012.

- Shackleton, M., Quintana, E., Fearon, E. R. & Morrison, S. J. Heterogeneity in cancer: cancer stem cells versus clonal evolution. *Cell* **138**, 822–829 (2009).
- Lobo, N. A., Shimono, Y., Qian, D. & Clarke, M. F. The biology of cancer stem cells. *Annu. Rev. Cell. Dev. Biol.* **23**, 675–699 (2007).
- Malanchi, I. *et al.* Cutaneous cancer stem cell maintenance is dependent on  $\beta$ -catenin signalling. *Nature* **452**, 650–653 (2008).
- Beck, B. *et al.* A vascular niche and a VEGF–Nrp1 loop regulate the initiation and stemness of skin tumours. *Nature* **478**, 399–403 (2011).
- Schober, M. & Fuchs, E. Tumor-initiating stem cells of squamous cell carcinomas and their control by TGF- $\beta$  and integrin/focal adhesion kinase (FAK) signaling. *Proc. Natl Acad. Sci. USA* **108**, 10544–10549 (2011).
- Nowell, P. C. The clonal evolution of tumor cell populations. *Science* **194**, 23–28 (1976).
- Greaves, M. & Maley, C. C. Clonal evolution in cancer. *Nature* **481**, 306–313 (2012).
- Nguyen, L. V., Vanner, R., Dirks, P. & Eaves, C. J. Cancer stem cells: an evolving concept. *Nature Rev. Cancer* **12**, 133–143 (2012).
- Kemp, C. J. Multistep skin cancer in mice as a model to study the evolution of cancer cells. *Semin. Cancer Biol.* **15**, 460–473 (2005).
- Abel, E. L., Angel, J. M., Kiguchi, K. & DiGiovanni, J. Multi-stage chemical carcinogenesis in mouse skin: fundamentals and applications. *Nature Protocols* **4**, 1350–1362 (2009).
- Owens, D. M. & Watt, F. M. Contribution of stem cells and differentiated cells to epidermal tumours. *Nature Rev. Cancer* **3**, 444–451 (2003).
- Perez-Losada, J. & Balmain, A. Stem-cell hierarchy in skin cancer. *Nature Rev. Cancer* **3**, 434–443 (2003).
- Klein, C. A. Parallel progression of primary tumours and metastases. *Nature Rev. Cancer* **9**, 302–312 (2009).
- Clayton, E. *et al.* A single type of progenitor cell maintains normal epidermis. *Nature* **446**, 185–189 (2007).
- Doupé, D. P., Klein, A. M., Simons, B. D. & Jones, P. H. The ordered architecture of murine ear epidermis is maintained by progenitor cells with random fate. *Dev. Cell* **18**, 317–323 (2010).
- Lopez-Garcia, C., Klein, A. M., Simons, B. D. & Winton, D. J. Intestinal stem cell replacement follows a pattern of neutral drift. *Science* **330**, 822–825 (2010).
- Snippert, H. J. *et al.* Intestinal crypt homeostasis results from neutral competition between symmetrically dividing Lgr5 stem cells. *Cell* **143**, 134–144 (2010).
- Simons, B. D. & Clevers, H. Strategies for homeostatic stem cell self-renewal in adult tissues. *Cell* **145**, 851–862 (2011).
- Klein, A. M. & Simons, B. D. Universal patterns of stem cell fate in cycling adult tissues. *Development* **138**, 3103–3111 (2011).
- Ghazizadeh, S. & Taichman, L. B. Multiple classes of stem cells in cutaneous epithelium: a lineage analysis of adult mouse skin. *EMBO J.* **20**, 1215–1222 (2001).
- Potten, C. S. Cell replacement in epidermis (keratopoiesis) via discrete units of proliferation. *Int. Rev. Cytol.* **69**, 271–318 (1981).
- Mackenzie, I. C. Retroviral transduction of murine epidermal stem cells demonstrates clonal units of epidermal structure. *J. Invest. Dermatol.* **109**, 377–383 (1997).
- Marusyk, A. & Polyak, K. Tumor heterogeneity: causes and consequences. *Biochim. Biophys. Acta* **1805**, 105–117 (2010).
- Van Keymeulen, A. *et al.* Epidermal progenitors give rise to Merkel cells during embryonic development and adult homeostasis. *J. Cell Biol.* **187**, 91–100 (2009).
- Rocheteau, P., Gayraud-Morel, B., Siegl-Cachedenier, I., Blasco, M. A. & Tajbakhsh, S. A subpopulation of adult skeletal muscle stem cells retains all template DNA strands after cell division. *Cell* **148**, 112–125 (2012).

**Supplementary Information** is linked to the online version of the paper at [www.nature.com/nature](http://www.nature.com/nature).

**Acknowledgements** C.B. is investigator of WELBIO and chercheur qualifié of the FRS/FNRS. B.B. is chargé de recherche of the FRS/FNRS and G.D. is supported by the Brussels Region. This work was supported by the FNRS, the program d'excellence CIBLES of the Wallonia Region, a research grant from the Fondation Contre le Cancer, the ULB foundation and the fond Gaston Ithier, a starting grant of the European Research Council (ERC), and the EMBO Young Investigator Program. We thank F. Bollet-Quivogne and J.-M. Vanderwinden for their help with confocal imaging.

**Author Contributions** C.B., G.D., B.B. and B.D.S. designed the experiments and performed data analysis. G.D. and B.B. performed most of the experiments. A.C. provided technical support. C.B. and B.D.S. wrote the manuscript.

**Author Information** Reprints and permissions information is available at [www.nature.com/reprints](http://www.nature.com/reprints). The authors declare no competing financial interests. Readers are welcome to comment on the online version of this article at [www.nature.com/nature](http://www.nature.com/nature). Correspondence and requests for materials should be addressed to B.D.S. (bds10@cam.ac.uk) or C.B. (Cedric.Blanpain@ulb.ac.be).

## METHODS

**Skin tumour induction and clonal YFP expression.** K14CREER<sup>26</sup> and Rosa-YFP mice were obtained from JAX. Mouse colonies were maintained in a certified animal facility in accordance with European guidelines. Mice were treated with DMBA and TPA as previously described<sup>4,9</sup>. Briefly, mice were treated with DMBA at postnatal day 23, 25 and 27 with DMBA (9,10-dimethyl-1,2-benzanthracene) and then treated weekly for several weeks with TPA (12-O-tetradecanoylphorbol-13-acetate). 7-week-old mice were treated again twice with DMBA. 0.35 mg Tamoxifen (TAM) was administered intraperitoneally to K14CREER/Rosa-YFP mice bearing papilloma and 1 mg to mice bearing SCC. The tumours were surgically excised at different time points after TAM injection.

**Measurement of tumour growth.** Skin tumours were measured using a precision calliper allowing to discriminate size modifications >0.1 mm. Tumour surface was measured every week with the formula  $A = \pi(dD/2)$ , where  $d$  is the minor tumour axis and  $D$  is the major tumour axis.

**Histology, immunostaining and imaging.** Tissues were pre-fixed for 2–8 h in 4% paraformaldehyde (PAF) and washed in sucrose 30% solution to remove the excess of PAF before being embedded in OCT. Samples were sectioned serially in thin 6–7 µm or thick 25–30 µm sections using a CM3050S Leica cryostat (Leica Microsystems GmbH).

The following primary antibodies were used: anti-K5 (rabbit, 1:1,000, Covance), anti-β4 (rat, 1:200, BD), anti-K14 (chicken, 1:1,000, Covance), anti-GFP (rabbit, 1:1,000, Molecular Probes), anti-K10 (rabbit, 1:2,000, Covance), anti-active caspase 3 (rabbit, 1:600, R&D Systems), FITC (fluorescein isothiocyanate)-coupled anti-BrdU (mouse, 1:100, BD), EdU staining was performed following the manufacturer's instructions (Invitrogen). Sections were incubated in blocking buffer (PBS, normal donkey serum (NDS) 5%, BSA 1%, Triton 0.2% or 0.5% for thin and thick sections, respectively) for 1 h at room temperature. Primary antibodies were incubated in blocking buffer overnight at 4 °C. Sections were rinsed three times in PBS and incubated with secondary antibodies diluted at 1:400 for 1 h at room temperature for thin sections or overnight at 4 °C for thick sections. The following secondary antibodies were used: anti-rabbit, anti-rat, anti-chicken conjugated to AlexaFluor488 (Molecular Probes), to rhodamine Red-X (Jackson ImmunoResearch) or to Cy5 (Jackson ImmunoResearch). Nuclei were stained in Hoechst solution (1:1,000) and slides were mounted in DAKO mounting medium supplemented with 2.5% Dabco (Sigma). In all immunofluorescences, Hoechst nuclear staining is represented in blue.

Pictures were acquired using an Axio Imager M1 Microscope, AxioCamMR3 camera using Axiovision software (Carl Zeiss).

Confocal pictures were acquired using Zeiss LSM 510 or Zeiss LSM 780 confocal microscopes using Zen software. Images were median-filtered (3 to 3) and are represented as orthogonal projections of 20–65 optical sections in 0.3–1 µm increments rendered using Zen software.

**Analysis of clone size.** Total clone size was determined by counting the number of YFP-positive cells in 3D reconstruction of confocal analysis of the whole clone using serial thick sections.

2D clone size was determined by imaging 30 to 1,330 clones from at least 8 different tumours from different mice at each time point. 6–7 µm sections were analysed to number the cells and the total clone size was inferred after correction as described in the Supplementary Information. The density of basal clones was determined by quantifying the number of basal clones per area of tumour and corrected for the increase in the total surface during tumour growth.

**Proliferation assays.** To measure the kinetics of tumour cell proliferation, mice were treated with EdU (pulse) and chased for 12 h followed by BrdU administration and another chase of 4 h. Tissues were first stained for K5. Sections were then washed in PBS and fixed again in PAF 4%. After washing in PBS, tissues were incubated for 20 min in HCl 1 N at 37 °C, washed three times and incubated overnight with FITC-coupled anti-BrdU antibody (mouse, 1:100, BD). The tissues were washed in PBS the next day and the EdU staining was performed following the manufacturer's instructions (Invitrogen). Slides were mounted in DAKO mounting medium supplemented with 2.5% Dabco (Sigma).

**FACS quantification of YFP basal tumour cells.** 3 days after TAM administration to the K14CREER/Rosa-YFP mice bearing skin tumours, tumours were digested in collagenase I (Sigma) for 2 h at 37 °C on a rocking plate. Collagenase I activity was blocked by addition of EDTA (5 mM). After tumour digestion, cells were first incubated in PBS complemented with 30% FCS to block Fc receptors for 15 min at room temperature. Immunostaining was performed using phycoerythrin-conjugated anti-α6-integrin (clone GoH3; BD Pharmingen), allophycocyanin-Cy7-conjugated anti-Epcam (clone G8.8; Biolegend). YFP-positive tumour cells were quantified within the Epcam<sup>+</sup>/α6-integrin<sup>+</sup> population after forward scatter, side scatter selection and Hoechst dye exclusion. Fluorescence-activated cell sorting analysis was performed using BD LSR Fortessa and FACSDiva software (BD Biosciences).

**Theory.** See Supplementary Information.

26. Vasioukhin, V., Degenstein, L., Wise, B. & Fuchs, E. The magical touch: genome targeting in epidermal stem cells induced by tamoxifen application to mouse skin. *Proc. Natl Acad. Sci. USA* **96**, 8551–8556 (1999).

# NRT/PTR transporters are essential for translocation of glucosinolate defence compounds to seeds

Hussam Hassan Nour-Eldin<sup>1\*</sup>, Tonni Grube Andersen<sup>1\*</sup>, Meike Burow<sup>1</sup>, Svend Roesen Madsen<sup>1</sup>, Morten Egevang Jørgensen<sup>1</sup>, Carl Erik Olsen<sup>1</sup>, Ingo Dreyer<sup>2</sup>, Rainer Hedrich<sup>3</sup>, Dietmar Geiger<sup>3</sup> & Barbara Ann Halkier<sup>1</sup>

**In plants, transport processes are important for the reallocation of defence compounds to protect tissues of high value<sup>1</sup>, as demonstrated in the plant model *Arabidopsis*, in which the major defence compounds, glucosinolates<sup>2</sup>, are translocated to seeds on maturation<sup>3</sup>. The molecular basis for long-distance transport of glucosinolates and other defence compounds, however, remains unknown. Here we identify and characterize two members of the nitrate/peptide transporter family, GTR1 and GTR2, as high-affinity, proton-dependent glucosinolate-specific transporters. The *gtr1 gtr2* double mutant did not accumulate glucosinolates in seeds and had more than tenfold over-accumulation in source tissues such as leaves and silique walls, indicating that both plasma membrane-localized transporters are essential for long-distance transport of glucosinolates. We propose that GTR1 and GTR2 control the loading of glucosinolates from the apoplasm into the phloem. Identification of the glucosinolate transporters has agricultural potential as a means to control allocation of defence compounds in a tissue-specific manner.**

As sessile organisms, plants depend on their vast array of chemical weapons for defence against herbivores and pathogens. According to the optimal defence theory<sup>4</sup>, these defence compounds are metabolically costly to produce<sup>5</sup> and accumulate to highest levels in tissues that are most likely to be attacked<sup>6</sup>. Consequently, transport processes are of essential importance as plants seek to optimize cost expenses by reallocation of defence compounds to tissues of highest fitness value, as exemplified by a decrease in senescing vegetative tissues accompanied by an increase in reproductive tissues<sup>6–8</sup>. For humans, however, the presence of toxic defence compounds in edible tissues (for example, seeds or tubers) severely reduces the nutritional value of important crops<sup>9,10</sup>. Thus, the ability to control accumulation of such compounds in a tissue-specific manner has been a central target of plant biotechnology<sup>11,12</sup>. To provide molecular tools for improving the nutritional value of crops, we sought to identify proteins responsible for long-distance transport of plant defence compounds.

In the plant model *Arabidopsis thaliana*, the major defence compounds are methionine- and tryptophan-derived glucosinolates, which accumulate in all parts of the plant during vegetative development<sup>8</sup>. Upon senescence, a decrease in glucosinolate content in leaves coincides with accumulation to high levels in seeds<sup>8</sup>. As seeds are unable to synthesize glucosinolates, import of these defence compounds from other tissues must occur<sup>3</sup>, as supported by the detection of glucosinolates in the phloem sap<sup>13,14</sup> and the ability of <sup>14</sup>C-labelled glucosinolates to move from leaves to seeds<sup>13</sup>. Using a functional genomics approach<sup>15</sup>, 239 transport proteins from *Arabidopsis* were screened for uptake of 4-methylthiobutyl glucosinolate (4MTB; the most abundant seed glucosinolate in the *Arabidopsis* Col-0 ecotype<sup>8</sup>), and AT3G47960 was identified as being capable of transporting 4MTB into *Xenopus laevis* oocytes (Fig. 1a). AT3G47960 is a member of the

nitrate/peptide (NTR/PTR) transporter family (also known as proton-dependent oligopeptide transporters), which, although present across all kingdoms, is particularly prevalent in higher plants, with 53 family-member proteins in *Arabidopsis*. Phylogenetic analysis in *Arabidopsis* identified two closely related homologues, AT5G62680 and AT1G18880 (also known as NRT1.9; ref. 16), which share 80% and 60% amino acid similarity with AT3G47960, respectively (Fig. 1b). Both homologues and 14 other randomly selected *Arabidopsis* NRT/PTR family proteins were tested individually for uptake of 4MTB in *X. laevis* oocytes. Glucosinolate transport activity was associated with a specific subclade of *Arabidopsis* NRT/PTRs consisting of AT5G62680, AT1G18880, AT1G69860 and AT1G69870 (also known as NRT1.7; ref. 17), showing 75%, 17%, 7% and 3% uptake activity, respectively, compared with AT3G47960 (Supplementary Fig. 1). Phylogenetic analysis of the NRT/PTR family in ten species across the plant kingdom showed that AT3G47960 and AT5G62680 grouped in a subclade together with four homologues from *Arabidopsis lyrata* and *Carica papaya*, the only other glucosinolate-producing species included in the study (Fig. 1c and Supplementary Fig. 2). Interestingly, a polyphyly suggested that the glucosinolate transporters may have arisen from the low-affinity nitrate transporter AT1G18880, which also has weak glucosinolate transport activity (Supplementary Fig. 1). In *Arabidopsis*, the larger clade, which includes AT1G18880, AT1G27080 (also known as NRT1.6) and AT1G69870, may represent an evolutionary link between nitrate/peptide- and glucosinolate transporting NRT/PTRs. No other NRT/PTRs showed glucosinolate-transport activity, suggesting that this clade may have been the one with the most potential to evolve glucosinolate transporters. We named AT3G47960 and AT5G62680 *ARABIDOPSIS THALIANA* *GLUCOSINOLATE TRANSPORTER-1* (GTR1) and -2 (GTR2), respectively.

Biophysical characterization of GTR1 and GTR2 was performed using two-electrode voltage-clamp measurements in *X. laevis* oocytes. Application of 100  $\mu$ M of 4MTB, 4-methylsulphonylbutyl glucosinolate, 3-methylsulphonylpropyl glucosinolate or *p*-hydroxybenzyl (pOHb) glucosinolate resulted in comparable negative currents representing an influx of positive charge, with an apparent higher preference for 4MTB (Fig. 2a and Supplementary Fig. 3a). By contrast, uninjected oocytes did not respond to glucosinolates. GTR1 and GTR2 carried the largest 4MTB-induced currents with the highest extracellular proton concentration (Fig. 2b and Supplementary Fig. 3b). In addition, the current amplitude was unaffected by the presence or absence of Na<sup>+</sup>, K<sup>+</sup> or *N*-methyl-D-glucamine (NMDG<sup>+</sup>) in the buffer (Fig. 2c and Supplementary Fig. 3c), providing evidence for glucosinolate-proton co-transport rather than glucosinolate transport driven by other monovalent cations. Thus, combined with the fact that glucosinolates occur as monovalent organic anions (pK<sub>a</sub> value of sulphate moiety = -3) and that 4MTB by oocyte extract analyses is shown to be imported into oocytes, the observed negative currents show that GTR1 and GTR2 are

<sup>1</sup>VKR Research Centre for Pro-Active Plants and DynaMo Center of Excellence, Department of Plant and Environmental Sciences, Faculty of Science, University of Copenhagen, Thorvaldsensvej 40, 1871 Frederiksberg C, Denmark. <sup>2</sup>Centre for Plant Biotechnology and Genomics, Universidad Politécnica de Madrid, Campus de Montegancedo, Carretera M-40, E-28223 Pozuelo de Alarcón (Madrid), Spain. <sup>3</sup>Julius-von-Sachs Institute, Molecular Plant Physiology and Biophysics, University of Würzburg Julius-von-Sachs-Platz 2, D-97082 Würzburg, Germany.

\*These authors contributed equally to this work.



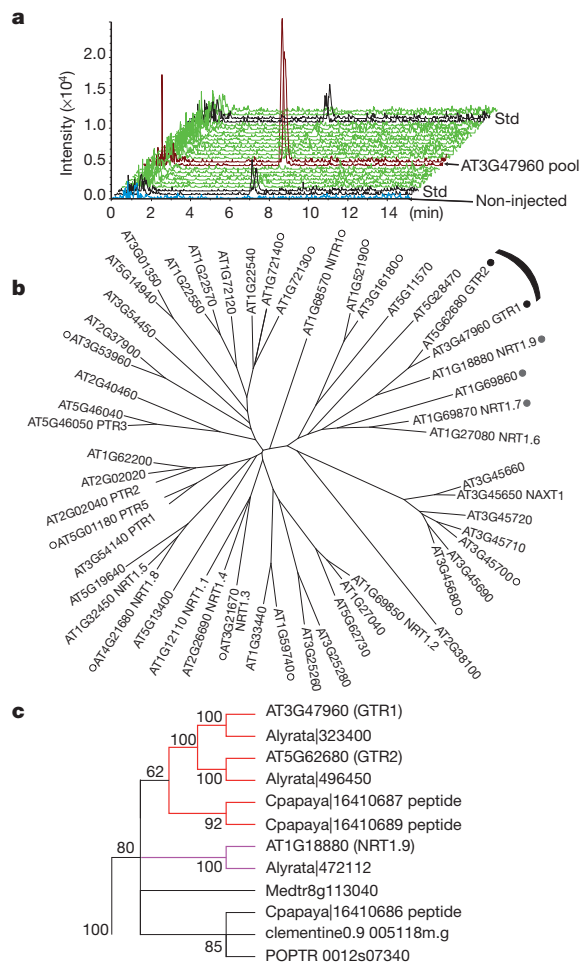


**Figure 1 | Identification of *Arabidopsis* transporters with glucosinolate uptake activity.** **a**, An *Arabidopsis* library consisting of 239 transporter complementary DNAs was screened for uptake of 4MTB glucosinolate in pools (ten cDNAs per pool) in *X. laevis* oocytes. Liquid chromatography–mass spectrometry (LC–MS) analysis of oocyte extracts is depicted as extracted ion chromatograms ( $m/z$  364) for desulphated 4MTB (see Supplementary Methods for details). Black indicates desulphated 4MTB standard (std), red indicates oocytes expressing a pool containing AT3G47960 (GTR1), green indicates a representative selection of other pools and blue indicates uninjected oocytes. **b**, Phylogenetic tree of the *Arabidopsis* NRT/PTR family. Shading of circles indicates relative glucosinolate uptake activity in *X. laevis* oocytes (see Supplementary Fig. 1); white circles indicate zero uptake and black circles indicate maximum uptake. Unmarked circles were not tested. **c**, Subset of a phylogenetic tree of 446 proteins belonging to the NRT/PTR family in ten plant species (see Supplementary Fig. 2 for full tree and description). Bootstrap test values (1,000 replicates) are shown next to branches. Red indicates predicted glucosinolate transport activity and lilac indicates predicted nitrate activity.

$H^+$ /glucosinolate co-transporters with a stoichiometry  $n_H > n_{\text{glucosinolate}}$  (for details about transport mechanism and stoichiometry please see Supplementary Discussion and Supplementary Fig. 3f–h). Plotting currents at  $-60$  mV as a function of increasing 4MTB concentrations yielded a saturation curve, which was best fitted by a Michaelis–Menten equation (Supplementary Fig. 3d, e) with apparent affinity constants towards 4MTB of  $20 \pm 1.2 \mu\text{M}$  for GTR1 and  $18.7 \pm 4.2 \mu\text{M}$  for GTR2 (data are s.e.m.). This categorizes both transporters as high-affinity  $H^+$ /glucosinolate symporters. Analysis of substrate specificity showed GTR-mediated glucosinolate uptake to be largely unaffected by varying the amino-acid-derived side chains (Fig. 2a and Supplementary Fig. 3a). In addition, the application of 10 mM sulphate, 10 mM glucose or 100  $\mu\text{M}$  desulphated 4MTB did not result in inward currents (Fig. 2d), indicating that the thioglucose and (Z)-N-hydroxyiminosulphate moieties common to all glucosinolates in combination have an essential role in

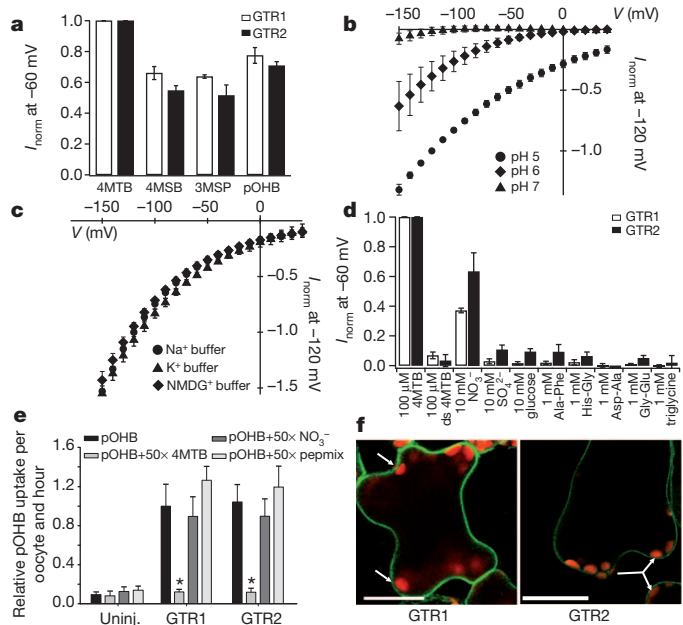


**Figure 2 | Biophysical and biochemical transport properties of GTRs.**

**a**, Quantification of glucosinolate-induced currents in oocytes expressing GTR1 or GTR2 on exposure to 100  $\mu\text{M}$  different glucosinolates at  $-60$  mV and pH 5. Currents were normalized to currents observed with 100  $\mu\text{M}$  4MTB (4-methylthiobutyl glucosinolate) at  $-60$  mV (error bars are s.d.;  $n = 4$ –5 oocytes). 4MSB, 4-methylsulphanylbutyl glucosinolate; 3MSP, 3-methylsulphanylpropyl glucosinolate; pOHB, *p*-hydroxybenzyl glucosinolate. **b**, pH dependence of GTR1-mediated glucosinolate transport. Currents induced by 1 mM 4MTB were measured at different membrane potentials at pH 5, 6 and 7. Data sets were normalized to currents induced at  $-120$  mV and pH 5 (error bars are s.d.;  $n = 4$  oocytes). **c**, GTR1-mediated 4MTB-induced currents at different membrane potentials and pH 5 in buffers exclusively containing  $K^+$ ,  $Na^+$  or NMDG $^+$  as monovalent cations in the bath solution. 4MTB-induced currents were normalized to the currents in the  $Na^+$ -based bath solution at  $-120$  mV (error bars are s.d.;  $n = 4$  oocytes). **d**, **e**, Substrate specificity of GTR1 and GTR2. **d**, Inward currents induced by potential substrates measured at  $-60$  mV and pH 5. Data sets were normalized to currents induced by 100  $\mu\text{M}$  4MTB at  $-60$  mV (error bars are s.d.;  $n = 5$  oocytes). Ds, desulphated. **e**, Relative GTR1- and GTR2-mediated uptake of 40  $\mu\text{M}$   $^{14}\text{C}$ -labelled p-OHB (40 nCi,  $2 \mu\text{Ci } \mu\text{mol}^{-1}$ ) in the presence or absence of 50-fold excess (2 mM) of potential substrates at pH 5. Uptake of pOHB by GTR1 with no competing substrates is set to 1 (error bars are s.d.;  $n = 10$  oocytes;  $*P < 0.05$ ). Pepmix, mixture of Ala-His, Gly-Leu, Asp-Ala, Gly-Gly-Gly and Met-Ala-Ser peptides (2 mM each; pH adjusted to 5); uninj., uninjected. **f**, Representative single-plane confocal imaging of 5-week-old leaves from stable *Arabidopsis* lines transformed with pGTR1(2 kb)–GTR1 (genomic fragment)–yellow fluorescent protein (YFP; Venus)–GTR1\_3' untranslated region (UTR; 0.3 kb) (seven independent lines) or pGTR2(2 kb)–GTR2 (genomic fragment)–mORANGE–GTR2\_3' UTR (0.3 kb) (22 independent lines). Representative mesophyll cells are shown for GTR1 and representative phloem-associated cells are shown for GTR2. Arrows indicate plasma-membrane localization. Scale bars, 25  $\mu\text{m}$ .

substrate recognition or binding. Exposure to 1 mM di- or tripeptides did not elicit currents, whereas 10 mM nitrate elicited currents of approximately half the magnitude compared with 100  $\mu\text{M}$  4MTB (Fig. 2d). Subsequently, competition assays in which GTR-mediated uptake of  $^{14}\text{C}$ -labelled pOHB was challenged with 50-fold excess unlabelled 4MTB, nitrate or a mixture of di- and tripeptides showed that only 4MTB inhibited the uptake of pOHB (Fig. 2e), suggesting that both proteins have high specificity towards glucosinolates.

Analysis of glucosinolate content of seeds from *gtr1* and *gtr2* single mutants (see Supplementary Fig. 4 for expression analyses of mutants) showed a  $48 \pm 11\%$  reduction in total glucosinolate levels in seeds of the *gtr2* mutant, whereas the glucosinolate seed content in the *gtr1* mutant was not significantly different than wild type ( $P > 0.05$ ) (Fig. 3a and Supplementary Fig. 5). Notably, the total glucosinolate

content of seeds from *gtr1 gtr2* double mutants was reduced to below detection limits. Molecular complementation of the *gtr1 gtr2* double mutant with either *GTR1* or *GTR2* restored glucosinolate accumulation in seeds (Supplementary Figs 4 and 5), demonstrating unequivocally that the decrease in glucosinolate accumulation in seeds of *gtr2* and *gtr1 gtr2* mutants was due to the absence of GTRs. The abolished accumulation of glucosinolates in seeds of *gtr1 gtr2* mutants was accompanied by >tenfold over-accumulation of methionine-derived glucosinolates in source tissues such as senescent leaves and silique walls (Fig. 3b, c). This strongly indicates a role for GTRs in the transport of glucosinolates from source tissues to seeds. Notably, tryptophan-derived glucosinolates, which were also eliminated from seeds of the *gtr1 gtr2* mutants (Fig. 3a), did not over-accumulate in source tissues (Fig. 3b, c). This suggests that tryptophan-derived glucosinolates in *Arabidopsis* may be subject to specific turnover or negative-feedback mechanisms<sup>18</sup>. Our data therefore show that GTR1 and GTR2 are crucial for the transport of both methionine- and tryptophan-derived glucosinolates to seeds.

The pH gradient dependency of the GTRs suggests a function in the import of glucosinolates into the cytosol, from either the apoplast or the vacuole. Confocal Z-stack images of GTR-fluorophore fusion proteins supported plasma membrane localization for both proteins in *Arabidopsis*, indicating transport from apoplast to cytosol (Fig. 2f, Supplementary Fig. 6 and Supplementary Movies 1–4). At the cellular level, the *GTR* genes showed vasculature-associated expression, with GTR2 primarily in veins and GTR1 also present in adjacent mesophyll cells in leaves (Fig. 4 and Supplementary Fig. 7). Together with the distinct reduction in seed glucosinolates and a threefold over-accumulation of methionine-derived glucosinolates in source tissues in *gtr2* but not in *gtr1* single mutants (Fig. 3a), these localization patterns suggest that GTR2 has a major role in apoplastic phloem-loading of glucosinolates. The expression of *GTR1* in mesophyll cells in leaves combined with the absence of a seed glucosinolate chemotype in the *gtr1* mutant suggests that GTR1 may primarily be involved in the distribution of glucosinolates within the leaf, potentially including import into the glucosinolate-rich S-cells located adjacent to the phloem (identified as large sulphur-rich cells characteristic of the *Brassicaceae*)<sup>19</sup>.

*In silico* expression analyses showed wound induction and co-regulation with jasmonate signalling pathway genes for *GTR1* but

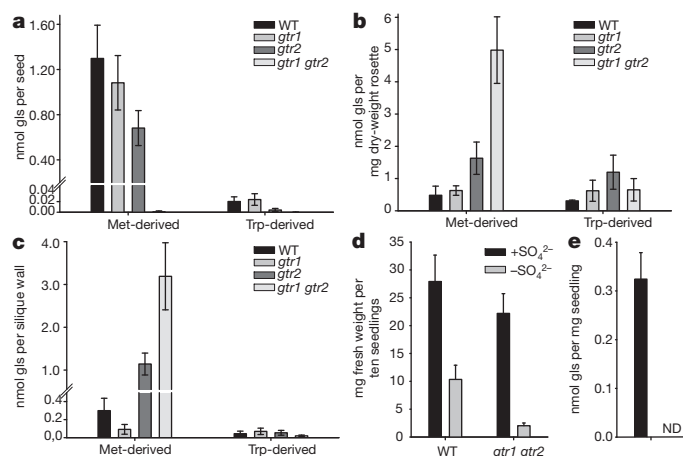


**Figure 3 | Glucosinolate analysis of *gtr1* and *gtr2* knockout mutants.** High-performance liquid chromatography (HPLC) analyses of total methionine- and tryptophan-derived glucosinolates (gls) in tissues from wilted wild type (WT), *gtr1* and *gtr2* single mutant and *gtr1 gtr2* double mutant plants. **a**, Content per seed (average of 20 seeds per plant). **b**, Content per entire rosette (mg dry weight). **c**, Content per set of silique walls (for **a**–**c**, error bars are s.d.;  $n = 6$ –8 plants). **d**, Fresh weight of pools of ten 10-day-old wild-type and *gtr1 gtr2* seedlings, respectively, grown in the presence or absence of sulphate (error bars are s.d.;  $n = 10$  pools). **e**, HPLC analysis of total glucosinolate content in pools of 10-day-old wild-type seedlings per mg fresh weight grown in the presence or absence of sulphate (error bars are s.d.;  $n = 10$  pools). ND, not determined.

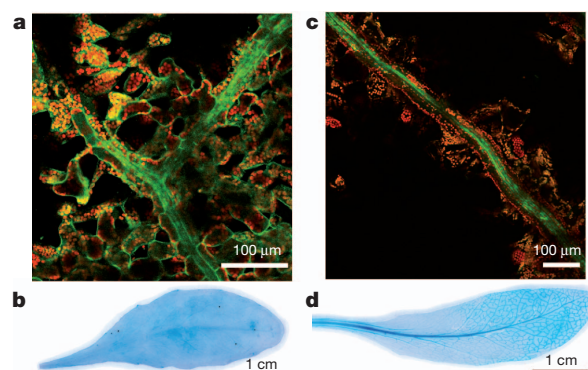


**Figure 4 | Localization of GTR1 and GTR2.** **a**, **c**, Representative confocal imaging of 5-week-old leaves from stable *Arabidopsis* lines expressing: **a**, pGTR1(2 kb)-GTR1(genomic fragment)-YFP(Venus)-GTR1\_3' UTR (0.3 kb) (seven independent lines) and **c**, pGTR2 (2 kb)-GTR2 (genomic fragment)-mORANGE-GTR2\_3' UTR (0.3 kb) (22 independent lines). **b**, **d**, Representative pictures of 6-week-old *Arabidopsis* rosette leaves expressing the  $\beta$ -glucuronidase (GUS) reporter gene under the control of 2 kb 5' regulatory sequences for *GTR1* (**b**) and *GTR2* (**d**), respectively. Six independent lines for each construct were analysed. No GUS activity was detected in wild-type plants (data not shown).

not *GTR2* (data not shown), suggesting a further role for *GTR1* in the transport of glucosinolates in response to stress<sup>20</sup>.

Among the oilseed crops dominating the world market at present, canola seeds (*Brassica napus*) stand out for their high levels of oil with excellent health-giving properties<sup>21</sup>, and a protein-rich seedcake ideal for animal feed<sup>22</sup>. However, wild-type *B. napus* seeds contain high concentrations of glucosinolates, which severely hinders the use of the seedcake in animal fodder<sup>23</sup>. Elimination of glucosinolates from *Arabidopsis* seeds by removing their transporters suggests transport engineering as a biotechnological approach for increasing the nutritional value of crops. Accordingly, several key traits of agricultural interest were investigated. Untargeted differential metabolite profiling of *Arabidopsis* seeds showed that 81 out of 184 analysed masses were abolished from *gtr1 gtr2* mutant seeds compared with wild type. Among these, 78 represented characteristic mass spectrometry fragmentation patterns of glucosinolates found in *Arabidopsis* Col-0 seeds<sup>24</sup> and only three masses represented other seed compounds of low abundance (Supplementary Table 1). Single *gtr1 gtr2* seeds weighed  $12 \pm 3\%$  less than wild-type seeds, with wild-type glucosinolate content accounting for approximately 20% of this weight difference (Supplementary Table 2). By comparison, total seed yield from *gtr1 gtr2* plants weighed  $26 \pm 8\%$  less than the yield from wild type. Thus, although elimination of *GTR1* and *GTR2* by transfer DNA mutagenesis seems to only weakly affect the composition of seed metabolites, the mutations were accompanied by a reduction in individual seed weight and total seed yield. The underlying cause for this reduction and its relevance from an agricultural perspective remain to be investigated. Furthermore, whereas no apparent morphological alterations were seen when *gtr1 gtr2* plants were grown on normal soil (data not shown), germination of wild type and *gtr1 gtr2* double mutants in the absence of a sulphur source showed a 2.7- and 11-fold reduction in fresh weight of 10-day-old seedlings, respectively, compared with growth in the presence of sulphur (Fig. 3d). In wild-type seedlings, this was accompanied by a reduction in total glucosinolate content below detection levels (Fig. 3e). Thus, particularly when facing nutrient scarcity, these experiments confirm that seed glucosinolates are catabolized on germination and can potentially serve as an important sulphur source<sup>25</sup>.

In conclusion, *GTR1* and *GTR2* are the first examples of high-affinity, proton-dependent symporters transporting defence compounds in plants with high specificity. A wild-type morphological phenotype of the *gtr1 gtr2* double mutant combined with a marked glucosinolate chemotype stands in contrast to the severe pleiotropic effects seen



for mutants of essential transporters of primary metabolites<sup>26,27</sup>. We therefore propose the glucosinolate transport pathway in *Arabidopsis* as an excellent model system for identifying critical barriers in the transport of metabolites along the source/sink route, including export from synthesizing cells, unloading and storage at sinks and reallocation in response to signalling cues. Moreover, the glucosinolate-free seeds of *gtr1 gtr2* mutants provide a unique tool for investigating the role of these sulphur-rich compounds in nutrient storage and defence.

The ability of the GTRs to transport glucosinolates, which has possibly arisen through neo-functionalization of NRT/PTR family members, assigns a new role to this large transport protein family in secondary metabolism. Considering the wide range of plant secondary metabolites and the fact that the large NRT/PTR family has a high level of diversification, contraction and expansion (Supplementary Fig. 2), we propose that the plant NRT/PTR family may contain other long-sought transporters of secondary metabolites. From an agricultural perspective, the retention of defence compounds in source tissues combined with their specific elimination from sinks provides a transport engineering strategy for solving the ancient agricultural challenge of specifically eliminating anti-nutritional metabolites from edible parts of crops while retaining their biological function in the rest of the plant.

## METHODS SUMMARY

**Identification and characterization of GTRs.** Identification and *in vitro* biochemical characterization of the GTRs was performed in *X. laevis* oocytes. Glucosinolate transport was measured by liquid chromatography–mass spectrometry (LC–MS) analyses of oocyte extracts and two-electrode voltage-clamp electrophysiological measurements.

**Generation of expression, complementation and reporter constructs.** All constructs were cloned and assembled using uracil-specific excision reagent (USER) cloning and USER fusion technologies<sup>28,29</sup>, and for all PCR reactions the USER-cloning-compatible proof-reading DNA polymerase PfuX7 was used<sup>30</sup>.

**In planta glucosinolate and metabolite analysis.** Glucosinolate and metabolite analysis was performed on representative lines from the F<sub>3</sub> generation for each genotype. Glucosinolates were analysed as desulphated glucosinolates by HPLC. Untargeted metabolite profiling of seeds was performed on methanol extracts using LC–MS and the MetAlign software package.

**Subcellular and cellular localization.** Stable *Arabidopsis* lines expressing the genomic fragment of each GTR fused to fluorophores and controlled by the endogenous regulatory elements were used. Localization was determined by confocal laser-scanning microscopy.

Received 24 March 2011; accepted 6 June 2012.

Published online 5 August 2012.

1. Feeny, P. in *Biochemical Interaction Between Plants and Insects* (eds Wallace, J. W. & Mansel, R. L.) 1–40 (Plenum, 1976).
2. Halkier, B. A. & Gershenzon, J. Biology and biochemistry of glucosinolates. *Annu. Rev. Plant Biol.* **57**, 303–333 (2006).
3. Nour-Eldin, H. & Halkier, B. Piecing together the transport pathway of aliphatic glucosinolates. *Phytochemistry Rev.* **8**, 53–67 (2009).
4. McKey, D. Adaptive patterns in alkaloid physiology. *Am. Nat.* **108**, 305–320 (1974).
5. Züst, T., Joseph, B., Shimizu, K. K., Kliebenstein, D. J. & Turnbull, L. A. Using knockout mutants to reveal the growth costs of defensive traits. *Proc. Biol. Sci.* **278**, 2598–2603 (2011).
6. Ohnmeiss, T. E. & Baldwin, I. T. Optimal defense theory predicts the ontogeny of an induced nicotine defense. *Ecology* **81**, 1765–1783 (2000).
7. Wink, M. Wounding-induced increase of quinolizidine alkaloid accumulation in lupin leaves. *Z. Naturforschung* **38**, 905–909 (1983).
8. Brown, P. D., Tokuhisa, J. G., Reichelt, M. & Gershenzon, J. Variation of glucosinolate accumulation among different organs and developmental stages of *Arabidopsis thaliana*. *Phytochemistry* **62**, 471–481 (2003).
9. Townsend, B. J. & Llewellyn, D. J. Reduced terpene levels in cottonseed add food to fiber. *Trends Biotechnol.* **25**, 239–241 (2007).
10. Mailer, R., McFadden, A., Ayton, J. & Redden, B. Anti-nutritional components, fibre, sinapine and glucosinolate content, in Australian canola (*Brassica napus* L.) meal. *J. Am. Oil Chem. Soc.* **85**, 937–944 (2008).
11. Wu, S. & Chappell, J. Metabolic engineering of natural products in plants; tools of the trade and challenges for the future. *Curr. Opin. Biotechnol.* **19**, 145–152 (2008).
12. Enneking, D. & Wink, M. in *Proceedings of the Third International Food Legumes Research Conference, Linking Research and Marketing Opportunities for Pulses in the 21st Century* (ed. Knight, R.) 671–683 (Kluwer, 2000).
13. Chen, S., Petersen, B. L., Olsen, C. E., Schulz, A. & Halkier, B. A. Long-distance phloem transport of glucosinolates in *Arabidopsis*. *Plant Physiol.* **127**, 194–201 (2001).

14. Ellerbrock, B. L., Kim, J. H. & Jander, G. Contribution of glucosinolate transport to *Arabidopsis* defense responses. *Plant Signal. Behav.* **2**, 282–283 (2007).
15. Nour-Eldin, H. H., Norholm, M. H. & Halkier, B. A. Screening for plant transporter function by expressing a normalized *Arabidopsis* full-length cDNA library in *Xenopus* oocytes. *Plant Methods* **2**, 17–25 (2006).
16. Wang, Y. Y. & Tsay, Y. F. *Arabidopsis* nitrate transporter NRT1.9 is important in phloem nitrate transport. *Plant Cell* **23**, 1945–1957 (2011).
17. Fan, S. C., Lin, C. S., Hsu, P. K., Lin, S. H. & Tsay, Y. F. The *Arabidopsis* nitrate transporter NRT1.7, expressed in phloem, is responsible for source-to-sink remobilization of nitrate. *Plant Cell* **21**, 2750–2761 (2009).
18. Bednarek, P. *et al.* A glucosinolate metabolism pathway in living plant cells mediates broad-spectrum antifungal defense. *Science* **323**, 101–106 (2009).
19. Koroleva, O. A. *et al.* Identification of a new glucosinolate-rich cell type in *Arabidopsis* flower stalk. *Plant Physiol.* **124**, 599–608 (2000).
20. Balbi, V. & Devoto, A. Jasmonate signalling network in *Arabidopsis thaliana*: crucial regulatory nodes and new physiological scenarios. *New Phytol.* **177**, 301–318 (2008).
21. Foster, R., Williamson, C. S. & Lunn, J. Culinary oils and their health effects. *Nutrition Bulletin* **34**, 4–47 (2009).
22. Snowden, R., Luhs, W. & Friedt, W. in *Genome Mapping and Molecular Breeding in Plants* (ed. Kole, C.) 55–114 (Springer, 2007).
23. Wittkop, B., Snowden, R. & Friedt, W. Status and perspectives of breeding for enhanced yield and quality of oilseed crops for Europe. *Euphytica* **170**, 131–140 (2009).
24. Clarke, D. B. Glucosinolates, structures and analysis in food. *Anal. Methods* **2**, 310–325 (2010).
25. Zhang, J. *et al.* Metabolite profiling of *Arabidopsis* seedlings in response to exogenous sinalbin and sulfur deficiency. *Phytochemistry* **72**, 1767–1778 (2011).
26. Gottwald, J. R., Krysan, P. J., Young, J. C., Evert, R. F. & Sussman, M. R. Genetic evidence for the *in planta* role of phloem-specific plasma membrane sucrose transporters. *Proc. Natl Acad. Sci. USA* **97**, 13979–13984 (2000).
27. Vert, G. *et al.* IRT1, an *Arabidopsis* transporter essential for iron uptake from the soil and for plant growth. *Plant Cell* **14**, 1223–1233 (2002).
28. Nour-Eldin, H. H., Hansen, B. G., Norholm, M. H. H., Jensen, J. K. & Halkier, B. A. Advancing uracil-excision based cloning towards an ideal technique for cloning PCR fragments. *Nucleic Acids Res.* **34**, e122 (2006).
29. Geu-Flores, F., Nour-Eldin, H. H., Nielsen, M. T. & Halkier, B. A. USER fusion: a rapid and efficient method for simultaneous fusion and cloning of multiple PCR products. *Nucleic Acids Res.* **35**, e55 (2007).
30. Norholm, M. A mutant Pfu DNA polymerase designed for advanced uracil-excision DNA engineering. *BMC Biotechnol.* **10**, 21–27 (2010).

**Supplementary Information** is linked to the online version of the paper at [www.nature.com/nature](http://www.nature.com/nature).

**Acknowledgements** We thank M. Palmgren, A. Schulz and D. Kliebenstein for comments on the manuscript and H. K. S. Jepsen, L. B. Møller and A. Kraus for technical assistance. We thank D. Klærke and technicians T. K. Soland, B. L. Christensen, M. Olsen and C. Derrer for providing *X. laevis* oocytes. We thank the Salk, Stanford, Plant Gene Expression Center (SSP) Consortium and the RIKEN Genome Science Center for providing full-length cDNAs. Imaging data were achieved at the Center for Advanced Bioimaging, University of Copenhagen. H.H.N.-E. was supported by the Danish Research Council for Technology and Production (FTP) grant 09-065827/274-08-0354. M.B. was supported by a Marie Curie fellowship (grant PIEF-GA-2008-221236). I.D. was supported by a Marie-Curie Career Integration Grant of the European Union (FP7-PEOPLE-2011-CIG No. 303674 (Regopoc)). D.G. was supported by the Deutsche Forschungsgemeinschaft grant GE2195/1-1 and R.H. by Deutsche Forschungsgemeinschaft grants within FOR 1061. B.A.H. is partner of The VKR Research Centre for Pro-Active Plants funded by the Villum Kann Rasmussen Foundation. Funding for DynaMo Center of Excellence is provided by the Danish National Research Foundation.

**Author Contributions** H.H.N.-E. identified the GTRs, designed the study, performed the phylogenetic analyses, contributed to biochemical characterization, data analysis, confocal localization experiments and analyses of metabolite profiling data and wrote the paper. T.G.A. performed the confocal localization experiments, generated and characterized glucosinolate in the *gtr* knockout mutants and contributed to biochemical characterization, study design and preparation of the manuscript. M.B. purified glucosinolates necessary for biochemical characterization and contributed to study design, data analysis and preparation of the manuscript. S.R.M. generated and analysed GTR-promoter- $\beta$ -glucuronidase lines, contributed to confocal localization experiments and performed germination experiments. M.E.J. performed metabolite profiling of seeds and analysed data and performed seed morphology and yield analyses. C.E.O. performed LC–MS analyses for the transporter library screen and for metabolite profiling. I.D. performed theoretical discussion on GTR kinetics. R.H. contributed to the study design and data analyses. D.G. performed the biophysical characterization of the GTR transport mechanism and contributed to the theoretical discussion on GTR kinetics, study design and preparation of the manuscript. B.A.H. contributed to and supervised the study design and contributed to data analyses and preparation of the manuscript. All authors discussed the results and commented on the manuscript.

**Author Information** Reprints and permissions information is available at [www.nature.com/reprints](http://www.nature.com/reprints). The authors declare competing financial interests: details are available in the online version of the paper. Readers are welcome to comment on the online version of this article at [www.nature.com/nature](http://www.nature.com/nature). Correspondence and requests for materials should be addressed to B.A.H. (bah@life.ku.dk).



# The protein kinase Pstol1 from traditional rice confers tolerance of phosphorus deficiency

Rico Gamuyao<sup>1</sup>, Joong Hyoun Chin<sup>1</sup>, Juan Pariasca-Tanaka<sup>2</sup>, Paolo Pesaresi<sup>3</sup>, Sheryl Catausan<sup>1</sup>, Cheryl Dalid<sup>1</sup>, Inez Slamet-Loedin<sup>1</sup>, Evelyn Mae Tecson-Mendoza<sup>4</sup>, Matthias Wissuwa<sup>2</sup> & Sigrid Heuer<sup>1</sup>

As an essential macroelement for all living cells, phosphorus is indispensable in agricultural production systems. Natural phosphorus reserves are limited<sup>1</sup>, and it is therefore important to develop phosphorus-efficient crops. A major quantitative trait locus for phosphorus-deficiency tolerance, *Pup1*, was identified in the traditional *aus*-type rice variety Kasalath about a decade ago<sup>2,3</sup>. However, its functional mechanism remained elusive<sup>4,5</sup> until the locus was sequenced, showing the presence of a *Pup1*-specific protein kinase gene<sup>6</sup>, which we have named phosphorus-starvation tolerance 1 (*PSTOL1*). This gene is absent from the rice reference genome and other phosphorus-starvation-intolerant modern varieties<sup>7,8</sup>. Here we show that overexpression of *PSTOL1* in such varieties significantly enhances grain yield in phosphorus-deficient soil. Further analyses show that *PSTOL1* acts as an enhancer of early root growth, thereby enabling plants to acquire more phosphorus and other nutrients. The absence of *PSTOL1* and other genes—for example, the submergence-tolerance gene *SUB1A*—from modern rice varieties underlines the importance

of conserving and exploring traditional germplasm. Introgression of this quantitative trait locus into locally adapted rice varieties in Asia and Africa is expected to considerably enhance productivity under low phosphorus conditions.

Phosphorus (P) is of unequivocal importance for the production of food crops, and the demand for P fertilizer is increasing worldwide. In Asia, where rice is the main and sometimes the only source of calories, 40% of the rice is produced in rain-fed systems, with little or no water control and frequent occurrence of floods, droughts and other calamities. In addition, 60% (29 Mha) of the rain-fed lowland rice is produced on poor and problem soils<sup>9,10</sup> (Fig. 1a) that are constrained by a multitude of abiotic stresses and are naturally low in phosphorus or P fixing. Rice yields are therefore low<sup>11</sup> and, not surprisingly, poverty in these regions is among the highest in the world (<http://www.ruralpovertyportal.org/web/guest/region>). A lack of resources or limited access to P fertilizer are some of the constraints for poor farmers. There is a high risk that the situation will be further aggravated given that phosphate rock, the source of P fertilizer, is a finite and non-renewable resource that is

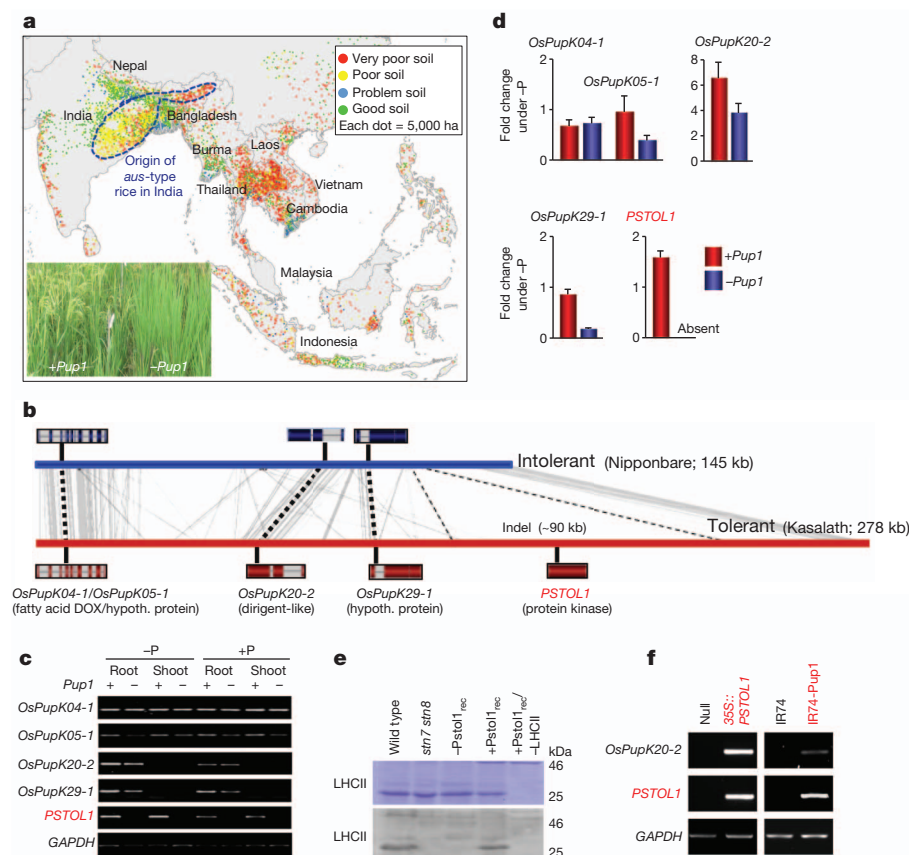


**Figure 1 | Origin of the donor variety Kasalath and *Pup1* candidate genes.** **a**, Problem soils in Asia and the origin of stress-tolerant *aus*-type rice varieties<sup>9,10,13</sup>. Inlay, breeding lines with and without the tolerant *Pup1* locus<sup>8</sup> under P-deficient field conditions. **b**, Relative position of *Pup1* candidate genes in Kasalath and the Nipponbare reference genome. *OsPupK05-1* is part of *OsPupK04-1* (refs 6, 8). DOX, dioxygenase. Hypoth., hypothetical. **c**, Semiquantitative RT-PCR analysis of *Pup1* candidate genes in contrasting Nipponbare NILs +*Pup1* and -*Pup1* grown in P-deficient soil +/- P fertilizer. Glyceraldehyde-3-phosphate dehydrogenase (GAPDH) was used as a control. **d**, qRT-PCR analysis of *Pup1* genes in roots of NILs (gene expression +P = 1). Error bars denote s.e.m. **e**, Top, gel stained with Coomassie blue. Bottom, phosphothreonine-specific immunoblot showing that recombinant Pstol1 protein restores phosphorylation of the light-harvesting complex II (LHCII) in the *Arabidopsis stn7 stn8* double mutant (lane 4). **f**, Semiquantitative RT-PCR analysis of *OsPupK20-2* in IR64 35S::*PSTOL1* plants and IR74-Pup1 NILs grown in +P hydroponics.

<sup>1</sup>International Rice Research Institute (IRRI), DAPO Box 7777 Metro, Manila 1301, Philippines. <sup>2</sup>Japan International Research Center for Agricultural Sciences (JIRCAS), 1-1 Ohwashi, Tsukuba 305-8686, Japan. <sup>3</sup>Dipartimento di Bioscienze, Università degli studi di Milano, 20133 Milano, Italy. <sup>4</sup>University of the Philippines, Los Baños, Laguna 4031, Philippines.

concentrated in only a few countries (Morocco, China and the USA), and mining costs are rising<sup>1,12</sup>. Apart from the need for long-term strategies to address this problem, the development of rice varieties with high productivity under low P and other stress conditions is a valid and necessary approach to improve yield and enhance food security in rice-dependent countries.

In recent years, a specific group of rice (*aus*-type varieties) that originates from a region in India with poor and problem soils<sup>9,10,13</sup> (Fig. 1a) has been recognized as a valuable source of tolerance genes. For instance, the donor of the submergence-tolerance gene *SUB1A* is an *aus*-type variety and rice breeding lines with this gene (Sub1 or 'scuba' rice) survive up to 2 weeks in flooded fields<sup>14,15</sup>. Likewise, tolerance of drought and heat<sup>16</sup>, in addition to other stresses, is present in such varieties. The *aus*-type variety Kasalath, which is tolerant of P deficiency, was identified about a decade ago, subsequently leading to the identification of a major quantitative trait locus (QTL) associated with P-deficiency tolerance<sup>17</sup>. At present, phosphorus uptake 1 (*Pup1*) is the only P-related QTL available for marker-assisted breeding programs, and tolerant *Pup1* breeding lines have proven effective in field trials<sup>7,8</sup> (Fig. 1a). Previous efforts to link *Pup1* with known P-uptake-related mechanisms showed that *Pup1* near-isogenic lines (NILs) had improved root growth under stress, but the underlying mechanisms remained enigmatic<sup>4</sup>, indicating that *Pup1* might act through a new mechanism or that the underlying gene may be missing in the reference genome.

Indeed, sequencing of the *Pup1* locus in Kasalath showed the presence of an ~90 kilobase transposon-rich insertion–deletion (indel) that is absent from the Nipponbare reference genome and other P-starvation-intolerant rice varieties<sup>6</sup> (Fig. 1b). A rice germplasm screen conducted with *Pup1*-specific molecular markers additionally showed that a gene located in the indel, the putative protein kinase gene *OsPupK46-2*, was most closely associated with tolerance of P deficiency and was highly conserved in stress-adapted rice accessions<sup>7,8</sup>.

To gain insight into the function of *Pup1* and to identify the major genetic determinant of P-deficiency tolerance, the protein kinase *OsPupK46-2* and four additional *Pup1* candidate genes<sup>8</sup> were short-listed from the initially predicted 68 *Pup1* gene models<sup>6</sup>. Gene expression was analysed by semiquantitative reverse transcriptase PCR (RT-PCR) and quantitative (q)RT-PCR analyses in contrasting NILs with (+*Pup1*) and without (–*Pup1*) the Kasalath *Pup1* locus. The data confirmed that *OsPupK46-2* was absent from the Nipponbare genome and showed that it was upregulated under P-deficient conditions (Fig. 1c, d). Expression of the other genes did not change under –P conditions (*OsPupK04-1*, *OsPupK05-1*, *OsPupK29-1*) or increased in both +*Pup1* and –*Pup1* NILs (*OsPupK20-2*) (Fig. 1c, d). Additional analyses subsequently showed that *OsPupK20-2*, which codes for a dirigent protein, is downstream of the protein kinase (see below). On the basis of these data and the probable role of protein kinases in the sensing and signalling of P homeostasis<sup>18,19</sup>, we considered *OsPupK46-2* the most obvious candidate gene and named it phosphorus-starvation tolerance 1 (*PSTOL1*).

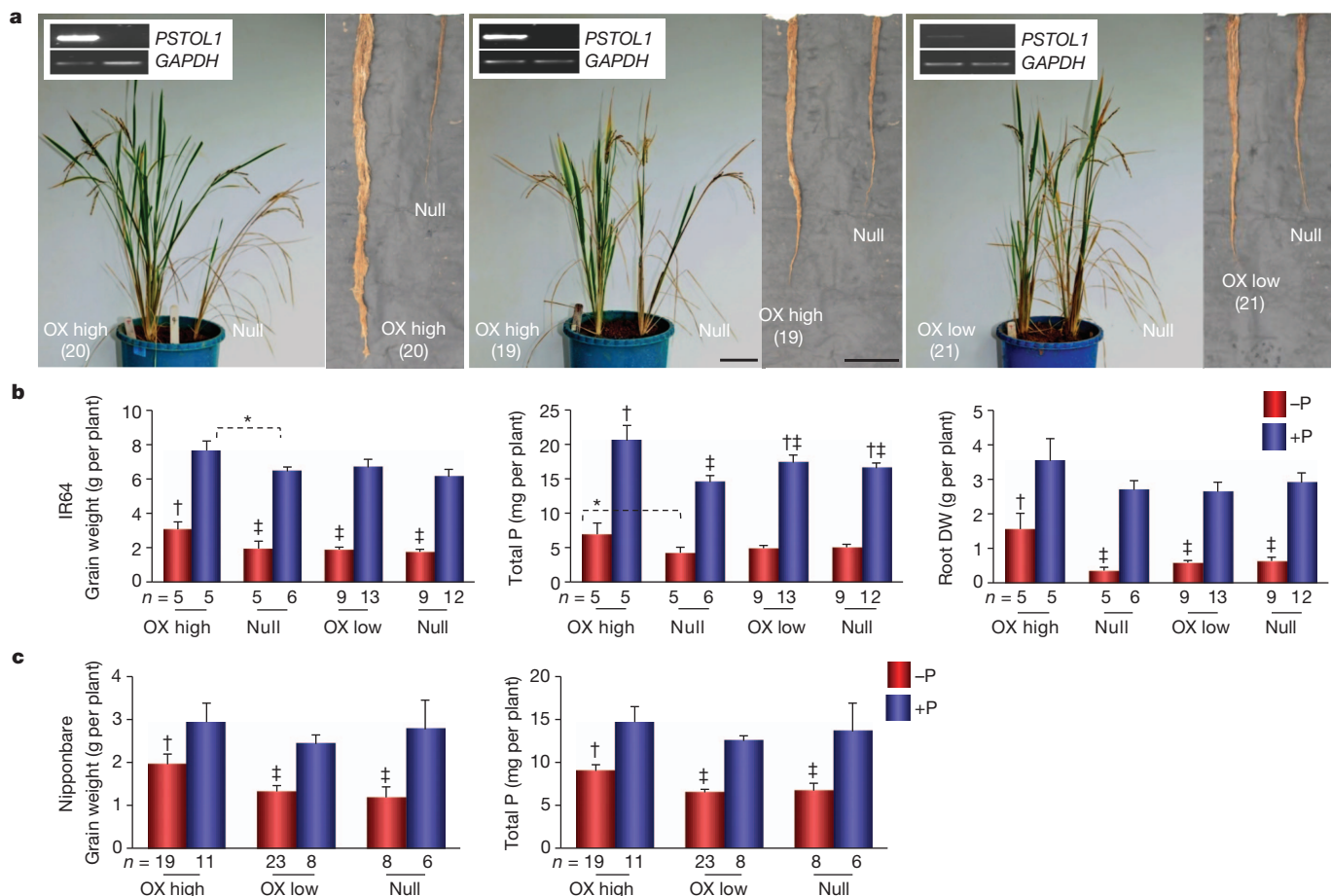


**Figure 2 | *PSTOL1* overexpression enhances tolerance of P deficiency.**

**a**, Representative IR64 35S::*PSTOL1* plants with high (OX high) and low (OX low) transgene expression of independent events (event numbers 20, 19 and 21) and corresponding null segregants at 8 weeks in P-deficient soil (root photos were taken after harvest). **b**, Grain weight, P content and root dry weight (DW) of IR64 transformants and nulls. *n* = number of plants. **c**, Grain weight and

total P content of Nipponbare transformants and nulls. Error bars indicate s.e.m. Significance ( $P < 0.05$ ) is indicated by † (analysis of variance and Tukey's honestly significant difference test) and asterisks (paired *t*-test). The mean with symbol † indicates significant difference from the mean with symbol ‡. The means with the same symbol (†‡ versus †‡) or with a common symbol († versus †‡; ‡ versus †‡) are not significantly different from each other. Scale bars, 10 cm.

Pstol1 shows the highest amino acid sequence similarity with serine/threonine receptor-like kinases of the LRK10L-2 subfamily, but lacks the amino-terminal extension typically present in this family<sup>20</sup>. This classifies Pstol1 as a receptor-like cytoplasmic kinase<sup>21</sup>. Interestingly, the conserved kinase domain is most similar to the *Arabidopsis* defence-related receptor-like kinases PR5K<sup>22</sup> (58%) and SNC4 (ref. 23; 57%) (Supplementary Figs 1–3). To assess whether Pstol1 is a functional protein kinase, an *in vitro* phosphorylation assay was performed using thylakoid membranes isolated from the *Arabidopsis thaliana* double mutant *stn7 stn8*, which is defective in STN7 and STN8 (also known as AT1G68830 and AT5G01920, respectively) serine/threonine protein kinases and therefore devoid of phosphorylation of the light-harvesting complex II<sup>24</sup>. The data show that recombinant Pstol1 protein restored phosphorylation of *stn7 stn8* thylakoids to almost wild-type levels (Fig. 1e), confirming that Pstol1 is a functional serine/threonine protein kinase.

To quantify the effect of Pstol1 on plant performance under low-P stress, we generated transgenic plants with constitutive overexpression of the full-length *PSTOL1* coding region (35S::PSTOL1). Two rice varieties (IR64 and Nipponbare) were used for this experiment, representing two distinct types of modern irrigated varieties (*indica* and *japonica*, respectively) that naturally lack the *PSTOL1* gene<sup>8</sup> (Supplementary Fig. 4). Phenotypic analyses conducted in two different

locations and P-deficient soil types (from fields that had not received P fertilizer for up to 40 years; –P) showed that high expression of the *PSTOL1* transgene enhanced grain yield by more than 60% under –P conditions in both varieties (Fig. 2a–c and Supplementary Fig. 5). Transgenic lines with low transgene expression were comparable to segregants without the transgene (null) that were used as controls. These data indicate that expression of *PSTOL1* above a certain threshold is required to confer tolerance of P deficiency. In both varieties, a significantly higher P content was observed in high *PSTOL1*-overexpressing lines (Fig. 2b, c). For the IR64 plants, we further confirmed that the superior performance of *PSTOL1* lines with high transgene expression was due to a higher root dry weight (Fig. 2a, b). The larger root system also enhanced the uptake of other nutrients, as nitrogen and potassium content were also higher in these lines (Supplementary Fig. 6). Subsequent phenotypic analyses of IR64 *PSTOL1*-overexpressing lines conducted in nutrient solution with high (100  $\mu$ M) and reduced (10  $\mu$ M) P concentrations showed that, under both P treatments, total root length and root surface area were significantly higher in transgenic seedlings (Fig. 3a, c). The same experiment was then repeated with two different contrasting *Pup1* NILs (IR64 and IR74, with (+) or without (–) *Pup1*) that were developed by marker-assisted introgression of the Kasalath *Pup1* locus<sup>8</sup>. In agreement with the above data, seedlings of +*Pup1* NILs

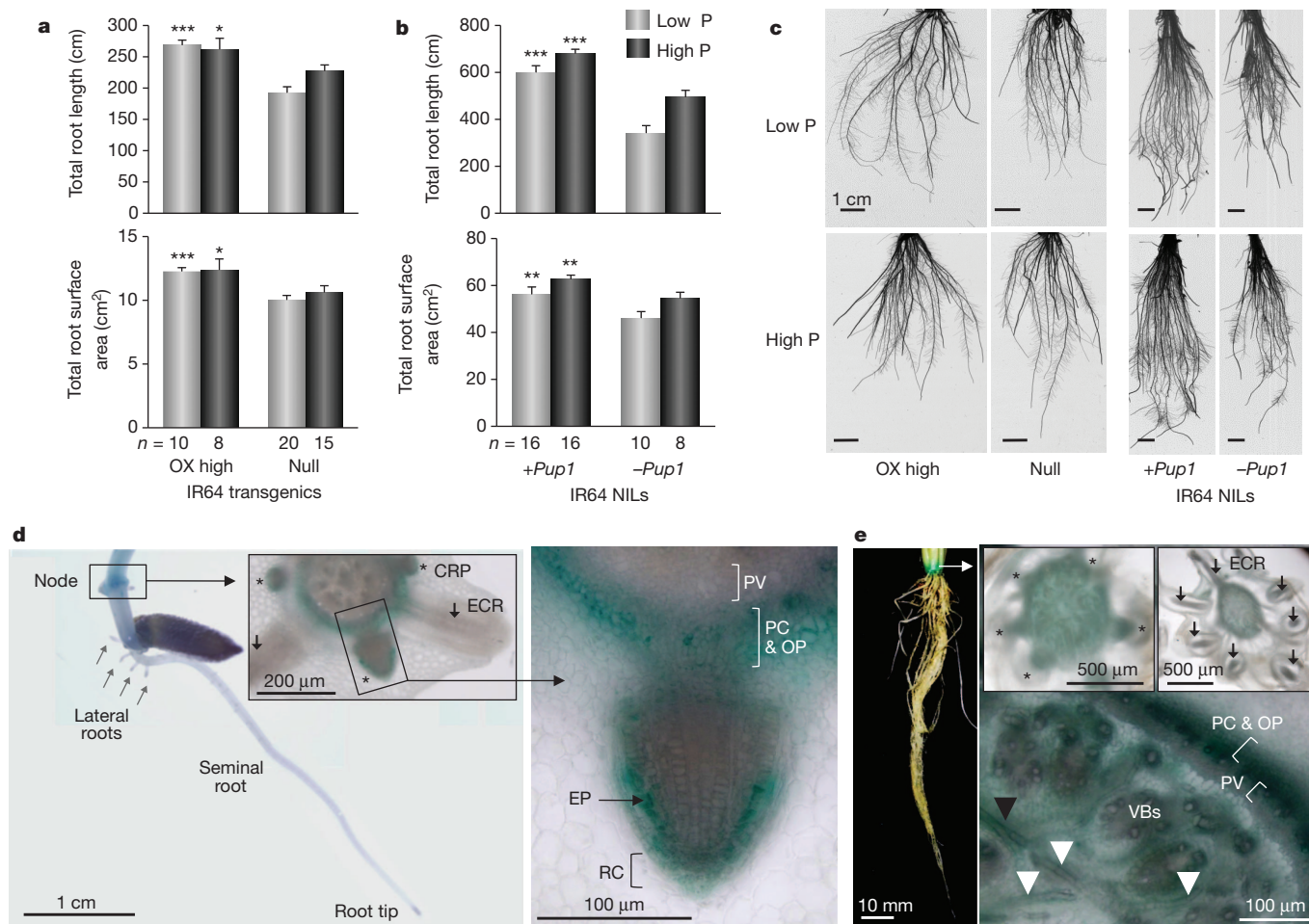


**Figure 3 | *PSTOL1* is an enhancer of root growth.** **a**, Total root length and surface area of IR64 35S::PSTOL1 plants (OX high; T2 no. 20) and corresponding nulls grown in high-P (100  $\mu$ M) and low-P (10  $\mu$ M) hydroponics solution for 15 days. **b**, Root data of sister NILs with and without *Pup1* grown under the same conditions for 21 days. Error bars indicate standard error. Significance was analysed by paired *t* test (95%). \*0.05 > *P*  $\geq$  0.01; \*\*0.01 > *P*  $\geq$  0.001; \*\*\**P* > 0.001. **c**, Representative root scans. Scale bars, 1 cm. **d**, GUS expression driven by the native *PSTOL1* promoter in young

IR64 seedlings is observed in parenchyma (PC) and outer parenchyma (OP) cells adjacent to the peripheral vascular (PV) cylinder of the coleoptilar node and in crown root primordia (CRP; indicated by asterisks), but not in emerging crown roots (ECR; arrows). RC, root cap. **e**, GUS staining in older plants (28 days after germination) is likewise seen in crown root primordia (asterisks) and additionally in cells surrounding vascular bundles (VBs), which are interconnected by nodal vascular anastomoses (arrowheads).



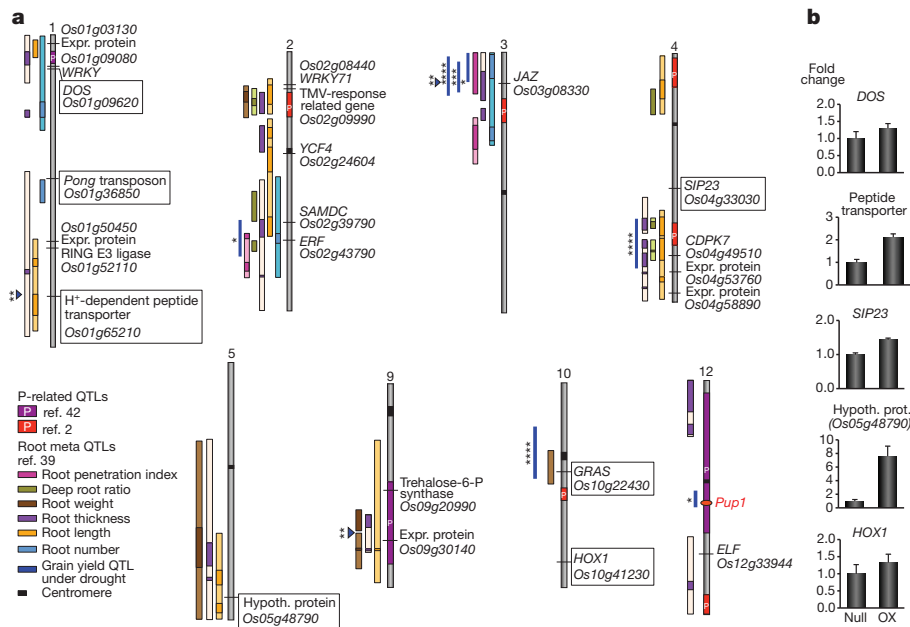


**Figure 4** | *PSTOL1* putative downstream genes co-localize with root and drought QTLs. **a**, Approximate chromosomal location of genes with constitutively higher (boxed) or lower (all other genes) expression in roots of 35S::*PSTOL1* transgenics. QTLs for P-deficiency tolerance are indicated in red and green on the chromosomes. Root-related meta-QTLs and QTLs for grain

showed significantly enhanced root growth under high and low P conditions (Fig. 3b, c and Supplementary Fig. 7). The finding that root growth was enhanced in *PSTOL1*-overexpressing lines as well as in *Pup1* introgression lines provides strong evidence that *PSTOL1* is indeed the major tolerance gene within the *Pup1* QTL and that this gene acts at least partially independently of P. In support of this, down-regulation of *PSTOL1* by RNA interference in Kasalath caused a significant reduction in plant number and root surface area, which negatively affected overall plant growth (Supplementary Fig. 8a–g).

To analyse the expression of *PSTOL1* during root development in more detail, we expressed the  $\beta$ -glucuronidase (GUS) reporter gene under the control of the native *PSTOL1* promoter in transgenic IR64 plants. Specific GUS staining was detected in stem nodes where, in rice, crown roots are formed that constitute the main root system (Fig. 3d, e). Within the nodes, GUS staining was restricted to crown root primordia and parenchymatic cells located outside of the peripheral vascular cylinder. This expression pattern is similar to that described for other root-development genes, namely *CROWN ROOTLESS 1* (also known as *AB200234*) and *RR2*, a cytokinin type-A-responsive regulator<sup>25,26</sup>. In older plants, GUS staining was additionally detected in the cells surrounding the nodal vascular anastomoses, which interconnect vascular bundles (Fig. 3e). No GUS staining was observed in older, emerging crown roots or in the initial (seminal) seedling root. Taken together, our data indicate that *PSTOL1* is a regulator of early crown root development and root growth in rice.

Because *Pstol1* is a protein kinase, it cannot directly regulate the expression of genes. However, regulation of transcription factors through phosphorylation has been well studied in the yeast P-starvation response system, which involves the transcription factor *PHO4* (ref. 18), as well as in two-component signalling systems that depend on membrane-bound histidine kinases<sup>27</sup>. To gain insight into the downstream responses of *Pstol1*, we conducted an Affymetrix gene-array analysis using root samples from soil-grown IR64 transgenic plants (high *PSTOL1* overexpression) and control plants. The data showed that known P-starvation genes were not differentially regulated in the transgenic plants (Supplementary Table 1). Similar results were obtained in a previous Agilent microarray analysis using

yield under drought are shown as colour-coded bars (see key). Centromeres are indicated in black. Expr., expressed. **b**, qRT-PCR analysis of upregulated genes in root samples of IR64 transgenics (OX) and null controls grown in +P hydroponics. References for the drought QTLs are \*ref. 37, \*\*ref. 38, \*\*\*ref. 40 and \*\*\*\*ref. 41.

*Pup1* NILs<sup>5</sup>. Instead, we identified 23 genes with constitutively (that is, independent of the P supply and developmental stage) higher or lower expression in the transgenic plants that are related to root growth and stress response (Supplementary Table 2). Interestingly, 21 of these differentially expressed genes co-localize with QTLs related to drought tolerance and root growth (Fig. 4a), providing further support for an important role of *Pup1/PSTOL1* during root development and stress tolerance. These findings are also supported by a *Pup1*-marker analysis that had shown high conservation of *PSTOL1* in drought-tolerant rice accessions<sup>7,8</sup>. In this context, we also determined that the *Pup1* dirigent gene (*OsPupK20-2*) is downstream of *PSTOL1*, as this gene was specifically induced in 35S::*PSTOL1* plants and in +*Pup1* NILs (Fig. 1f).

To assess whether the expression of the genes identified is indeed independent of P and/or soil-related factors, a qRT-PCR analysis of selected genes was conducted using root RNA samples of 35S::*PSTOL1* plants grown under high P conditions in hydroponics. Whereas the data were inconsistent for many of the downregulated genes (data not shown), higher expression was confirmed for six out of the seven genes that were specifically induced in 35S::*PSTOL1* roots (Fig. 4b). Among these are two genes coding for transcription factors; namely *HOX1*, a positive regulator of root cell differentiation<sup>28</sup>, and *DOS*, which was shown to delay leaf senescence in rice<sup>29</sup>. Altered expression of *HOX1* is well in agreement with a role for *PSTOL1* in root development. An association study further showed that a region on chromosome 1, where *DOS* and a gene coding for a WRKY-type transcription factor are located, was significantly associated with the presence of *PSTOL1* in a wider range of tolerant rice accessions (Supplementary Fig. 9). Interestingly, a putative peptide transporter was among the constitutively upregulated genes that might, in addition to P, improve the nitrogen status of the plants<sup>30</sup>.

In light of the need to increase rice production for a growing population despite potentially negative impacts of climate change and increasing scarcity of natural resources, it will be critically important to systematically explore traditional rice varieties in which high-value genes such as *PSTOL1* are preserved, and to enable breeders to efficiently use these genes in breeding programs.

## METHODS SUMMARY

**Pup1 candidate gene-expression analysis.** Expression of *Pup1* candidate genes was analysed by semiquantitative RT-PCR as described<sup>8</sup> and by qRT-PCR of root samples derived from 49-day-old plants of a set of Nipponbare NILs with and without the Kasalath *Pup1* introgression. Plants were grown in P-deficient and P-sufficient soil in Japan. Primer sequences for this and other experiments are provided in Supplementary Table 3.

**Protein kinase activity of Pstol1.** Recombinant Pstol1 protein was synthesized in *Escherichia coli* (strain BL21; pBAD-DEST49 expression vector, Invitrogen). Purified protein was incubated with isolated thylakoid membranes from the *Arabidopsis* double mutant *stin7stin8* defective in phosphorylating the light-harvesting complex II<sup>24</sup>.

**Transgenic 35S::PSTOL1 plants and Affymetrix analysis.** The *PSTOL1* coding sequence was cloned into the binary vector pMDC32 with the 35S promoter and used for *Agrobacterium*-mediated transformation of immature IR64 and Nipponbare embryos. Transgene copy number and expression level were determined by Southern blot analysis and RT-PCR, respectively. Independent transgenic lines (T1 and T2) were phenotyped at the International Rice Research Institute (the Philippines) and Japan International Research Center for Agricultural Sciences (Japan) in P-deficient soil +/− P fertilizer application (equivalent of 60 kg P<sub>2</sub>O<sub>5</sub> ha<sup>−1</sup>). For the Affymetrix gene-array analysis (line 20) root samples from IR64 35S::PSTOL1 plants and nulls grown in P-deficient soil +/− P fertilizer were used. Plants were at the reproductive/heading stage (−P treatment) and at mid-tillering (+P control treatment). Complementary RNA samples were analysed at ATLAS Biolabs GmbH (Germany) using GeneChip Operating System 1.4.

**Promoter::GUS analysis.** A 1,755 base pair genomic region upstream of the *PSTOL1* start ATG codon was amplified from the genomic DNA of +*Pup1* NILs using the primer pair oRG107/oRG109 (Supplementary Table 3) and cloned into the pMDC164 vector containing the gene coding for GUS. For GUS staining, IR64 transgenic T1 plants were germinated on Petri dishes in the dark at room temperature (26 °C) and monitored for GUS after 1 week and 4 weeks.

**Full Methods** and any associated references are available in the online version of the paper.

Received 23 November 2011; accepted 25 June 2012.

1. Van Kauwenbergh, S. J. *World Phosphate Rock Reserves and Resources* [http://www.ifdc.org/getdoc/56358fb1-fc9b-49ba-92fe-187dc08e9586/T-75\\_World\\_Phosphate\\_Rock\\_Reserves\\_and\\_Resources](http://www.ifdc.org/getdoc/56358fb1-fc9b-49ba-92fe-187dc08e9586/T-75_World_Phosphate_Rock_Reserves_and_Resources) (International Fertilizer Development Center, 2010).
2. Wissuwa, M., Yano, M. & Ae, N. Mapping of QTLs for phosphorus-deficiency tolerance in rice (*Oryza sativa* L.). *Theor. Appl. Genet.* **97**, 777–783 (1998).
3. Wissuwa, M. & Ae, N. Genotypic variation for tolerance to phosphorus deficiency in rice and the potential for its exploitation in rice improvement. *Plant Breed.* **120**, 43–48 (2001).
4. Wissuwa, M. Combining a modeling with a genetic approach in establishing associations between genetic and physiological effects in relation to phosphorus uptake. *Plant Soil* **269**, 57–68 (2005).
5. Pariasca-Tanaka, J., Satoh, K., Rose, T., Mauleon, R. & Wissuwa, M. Stress response versus stress tolerance: a transcriptome analysis of two rice lines contrasting in tolerance to phosphorus deficiency. *Rice* **2**, 167–185 (2009).
6. Heuer, S. *et al.* Comparative sequence analyses of the major quantitative trait locus *Phosphorus uptake 1* (*Pup1*) reveal a complex genetic structure. *Plant Biotechnol. J.* **7**, 456–471 (2009).
7. Chin, J. H. *et al.* Development and application of gene-based markers for the major rice QTL *Phosphorus uptake 1*. *Theor. Appl. Genet.* **120**, 1073–1086 (2010).
8. Chin, J. H. *et al.* Developing rice with high yield under phosphorus deficiency: *Pup1* sequence to application. *Plant Physiol.* **156**, 1202–1216 (2011).
9. Haefele, S. M. & Hijmans, R. J. In *Science, Technology, and Trade for Peace and Prosperity: Proceedings of the 26th International Rice Research Conference, New Delhi, India*. (eds Aggarwal P. K., Ladha J. K., Singh R. K., Devakumar C. & Hardy B.) International Rice Research Institute, Indian Council of Agricultural Research, and National Academy of Agricultural Sciences, Los Baños, Philippines, and New Delhi, India 297–308 (2007).
10. Haefele, S. M. & Hijmans, R. J. Soil quality in rainfed lowland rice. *Rice Today* **8**, 30–31 (2009).
11. Dawe, D., Pandey, S. & Nelson, A. In *Rice in the Global Economy. Strategic Research and Policy Issues for Food Security* (eds Pandey, S. *et al.*) 5–35 (International Rice Research Institute, 2010).

12. Cordell, D., Drangert, J. O. & White, S. The story of phosphorus: global food security and food for thought. *Glob. Environ. Change* **19**, 292–305 (2009).
13. Londo, J. P., Chiang, Y. C., Hung, K. H., Chiang, T. Y. & Schaal, B. A. Phylogeography of Asian wild rice, *Oryza rufipogon*, reveals multiple independent domestications of cultivated rice, *Oryza sativa*. *Proc. Natl Acad. Sci. USA* **103**, 9578–9583 (2006).
14. Xu, K. *et al.* *Sub1A* is an ethylene-responsive-factor-like gene that confers submergence tolerance to rice. *Nature* **442**, 705–708 (2006).
15. Manzanilla, D. O. *et al.* Submergence risks and farmers' preferences: implications for breeding *Sub1* rice in Southeast Asia. *Agric. Syst.* **104**, 335–347 (2011).
16. Gowda, V. R. P. *et al.* Water uptake dynamics under progressive drought stress in diverse accessions of the *Oryza* SNP panel of rice (*Oryza sativa*). *Func. Plant Bio.* **39**, 402–411 (2012).
17. Wissuwa, M., Wegner, J., Ae, N. & Yano, M. Substitution mapping of *Pup1*: a major QTL increasing phosphorus uptake of rice from a phosphorus-deficient soil. *Theor. Appl. Genet.* **105**, 890–897 (2002).
18. Gregory, P. D., Barbari, S. & Hörz, W. Transcriptional control of phosphate-regulated genes. *Food Technol. Biotechnol.* **38**, 295–303 (2000).
19. Yang, X. J. & Finnegan, P. M. Regulation of phosphate starvation responses in higher plants. *Ann. Bot. (Lond.)* **105**, 513–526 (2010).
20. Dardick, C., Chen, J., Richter, T., Ouyang, S. & Ronald, P. The rice kinase database. A phylogenomic database for the rice kinome. *Plant Physiol.* **143**, 579–586 (2007).
21. Vij, S., Giri, J., Dansana, P. K., Kapoor, S. & Tyagi, A. K. The receptor-like cytoplasmic kinase (*OsRLCK*) gene family in rice: organization, phylogenetic relationship, and expression during development and stress. *Mol. Plant* **1**, 732–750 (2008).
22. Wang, X., Zafian, P., Choudhary, M. & Lawton, M. The PR5K receptor protein kinase from *Arabidopsis thaliana* is structurally related to a family of plant defense proteins. *Proc. Natl Acad. Sci. USA* **93**, 2598–2602 (1996).
23. Bi, D., Cheng, Y. T., Li, X. & Zhang, Y. Activation of plant immune responses by a gain-of-function mutation in an atypical receptor-like kinase. *Plant Physiol.* **153**, 1771–1779 (2010).
24. Bonardi, V. *et al.* Photosystem II core phosphorylation and photosynthetic acclimation require two different protein kinases. *Nature* **437**, 1179–1182 (2005).
25. Inukai, Y. *et al.* *Crown rootless1*, which is essential for crown root formation in rice, is a target of an AUXIN RESPONSE FACTOR in auxin signaling. *Plant Cell* **17**, 1387–1396 (2005).
26. Zhao, Y., Hu, Y., Dai, M., Huang, L. & Zhou, D.-X. The WUSCHEL-related homeobox gene *WOX11* is required to activate shoot-borne crown root development in rice. *Plant Cell* **21**, 736–748 (2009).
27. Lohrmann, J. & Harter, K. Plant two-component signaling systems and the role of response regulators. *Plant Physiol.* **128**, 363–369 (2002).
28. Scarpella, E., Simons, E. J. & Meijer, A. J. Multiple regulatory elements contribute to the vascular-specific expression of the rice HD-Zip gene *Oshox1* in *Arabidopsis*. *Plant Cell Physiol.* **46**, 1400–1410 (2005).
29. Kong, Z., Li, M., Yang, W., Xu, W. & Xue, Y. A novel nuclear-localized CCH-type zinc finger protein, OsDOS, is involved in delaying leaf senescence in rice. *Plant Physiol.* **141**, 1376–1388 (2006).
30. Ouyang, J. *et al.* Identification and analysis of eight peptide transporter homologs in rice. *Plant Sci.* **179**, 374–382 (2010).

**Supplementary Information** is linked to the online version of the paper at [www.nature.com/nature](http://www.nature.com/nature).

**Acknowledgements** We would like to thank A. Cruz, E. Ramos and L. Olivo for technical and secretarial support, the staff at the transformation laboratory, F. Rossi for help with the Pstol1 kinase assay, M. Akutsu for help with the analysis of transgenic plants, and S. Haefele and his team for their support. We thank J. Prasetyono, M. Bustamam and S. Moeljopawiro for their long-term collaboration. This project has been primarily funded by the Generation Challenge Program (GCP) since 2005.

**Author Contributions** R.G. cloned and transformed the *PSTOL1* gene into IR64 and Nipponbare. R.G., J.P.T. and M.W. performed the phenotyping of transgenic plants. J.H.C. conducted the root meta-QTL analysis and J.H.C. and C.D. developed the IR64-Pup1 and IR74-Pup1 NILs. P.P. carried out the Pstol1 kinase assay. S.C. conducted the expression analysis of putative *PSTOL1* downstream genes. E.M.T.M. provided advice about the experiments and I.S.-L. provided technical support and infrastructure for rice transformation. R.G., M.W. and S.H. designed the experiments and wrote the manuscript.

**Author Information** GenBank protein accession numbers for *OsPupK04-1*, *OsPupK05-1*, *OsPupK20-2*, *OsPupK29-1* and *PSTOL1/OsPupK46-2* are BAH79993, BAH79994, BAK26565, BAH80018 and BAK26566, respectively. Reprints and permissions information is available at [www.nature.com/reprints](http://www.nature.com/reprints). The authors declare no competing financial interests. Readers are welcome to comment on the online version of this article at [www.nature.com/nature](http://www.nature.com/nature). Correspondence and requests for materials should be addressed to S.H. ([s.heuer@cgiar.org](mailto:s.heuer@cgiar.org)).

## METHODS

**qRT-PCR of *Pup1* candidate genes.** Seeds of NILs segregating for the *Pup1* locus (+*Pup1*, NILs 6-4, Y-4 and 14-4; -*Pup1*, NILs Y6, Y10 and Nipponbare)<sup>7,17</sup> were sown directly in pots filled with P-deficient and P-fixing andosol from a field located at Tsukuba, Japan, that had not received P fertilizer throughout its 40-year cropping history (-P). An equivalent of 60 kg P ha<sup>-1</sup> was applied for the control treatment (+P). Pots were initially watered every 2–3 days and afterwards the soil was kept near field capacity. The experiment was conducted in a completely randomized design with three replications and four plants per replicate pot. Root tissue samples were taken at 49 days after sowing. Total RNA was extracted using the RNeasy mini kit according to the instructions of the manufacturer (Qiagen) and treated with RNase-free DNase I (Qiagen). qRT-PCR was performed as described<sup>5</sup> with some modifications. Complementary DNA synthesis was conducted at 37 °C for 15 min followed by 5 s of 85 °C using 500 ng DNase-treated total RNA with PrimeScript RT reagent kit (Takara). qRT-PCR was performed with 10 ng reverse transcriptase template and SYBR Premix Ex Taq (Perfect Real Time; Takara). PCR cycle conditions were 94 °C for 10 s as the first denaturing step, followed by 40 cycles at 94 °C for 5 s, 55–60 °C for 10 s and 72 °C for 15 s, and a gradual increase in temperature from 55 °C to 96 °C during the dissociation stage to monitor the specificity of each primer pair. Rice 18S (also known as *RRN18*) was used as an internal control. For primer sequences, see Supplementary Table 3. Expression levels were calculated using the delta-delta comparison and expressed as fold changes under -P relative to expression under +P conditions (expression = 1).

**In vitro phosphorylation assay.** Seeds of *A. thaliana* ecotype Col-0 and of the *stn7stn8* double mutant were sown in plastic trays containing one portion of Techinc and one portion of Flox 6 soils and incubated for 3 days at 5 °C in the dark to break the dormancy. Plants were grown in a greenhouse under long-day conditions (16 h light and 8 h dark) for 4 weeks. Thylakoids were isolated from 4-week-old plants as described<sup>24</sup> in the presence of the phosphatase inhibitor sodium fluoride (10 mM). The coding sequence (CDS) of *PTSTOL1* (Pstol1<sub>rec</sub>) was expressed in the *E. coli* strain BL21 with a carboxy-terminal 6× His-tag. Pstol1<sub>rec</sub> was purified under denaturing conditions following a nickel-nitrilotriacetic acid batch purification procedure according to the instructions of the manufacturer (Qiagen). After protein precipitation in 10% trichloroacetic acid followed by three washing steps with absolute ethanol, around 500 µg of Pstol1<sub>rec</sub> protein was re-suspended in 500 µl 1% (w/v) lithium dodecyl sulphate, 12.5% (w/v) sucrose, 5 mM e-aminocaproic acid, 1 mM benzamide and 50 mM HEPES potassium hydroxide buffer, pH 7.8, as previously described<sup>31</sup>. Subsequently, Pstol1<sub>rec</sub> protein was boiled for 2 min at 100 °C and incubated for 15 min at 25 °C. Dithiothreitol (DTT; 75 mM final concentration) was then added and the solution was subjected to three freeze-thaw cycles (20 min at -20 °C, 20 min at -80 °C and 20 min at -20 °C, thawing in an ice-water bath, and 5 min at 25 °C). After completion of the three freeze-thawing cycles, octylglucopyranoside (1% (w/v) final concentration) was added and the solution was kept on ice for 15 min before potassium chloride (75 mM, final concentration) was added to precipitate the lithium dodecyl sulphate detergent. After centrifugation at 16,000g at 4 °C for 10 min, the supernatant containing the re-folded Pstol1<sub>rec</sub> in the presence of 1% (w/v) octylglucopyranoside was collected. Subsequently, 1 µl of kinase was incubated together with thylakoids corresponding to 5 µg of total chlorophyll. The phosphorylation reaction was performed in 50 µl total volume containing 0.06% (w/v) dodecyl-B-D-maltoside, 5 mM magnesium acetate, 5 mM DTT, 100 mM HEPES potassium hydroxide, pH 7.8, 200 mM ATP and 10 mM sodium fluoride at 37 °C for 2 h. The reaction mixture was loaded on an SDS-PAGE, and immunoblot analyses with phosphothreonine-specific antibodies (Cell Signaling) were performed as described<sup>32</sup>. A replicative SDS-PAGE was stained with Coomassie blue.

**Generation of 35S::PTSTOL1 transgenic plants.** The CDS of *PTSTOL1* was amplified from Kasalath genomic DNA using the primer pair oKas4603 and oKas4604 (all primer sequences are provided in Supplementary Table 3), cloned into pCR8/GW/TOPO TA cloning vector (Invitrogen) and sent for sequencing (Macrogen). Through LR clone recombination reaction (Invitrogen), the CDS was sub-cloned into the pMDC32 binary destination vector<sup>33</sup> containing the 35S promoter and NOS terminator (35S::PTSTOL1). The construct was sequenced using primer pairs amplifying the 35S promoter (oRG89) and the NOS-terminator (oSH07) with adjacent CDS, respectively. The correct sequence of *PTSTOL1* was re-confirmed by sequencing with the primer pair oKas4603 and oKas4604. Transformation of the construct into the *indica*-type IR64 and *japonica*-type Nipponbare rice varieties, which naturally lack the *PTSTOL1* gene, was mediated by the *Agrobacterium tumefaciens* strain LBA4404 according to a published protocol<sup>34</sup> with modifications (I.S.-L. *et al.*, in preparation). Transgenic plants were tested by genomic PCR in the T1 generation for the presence of the hygromycin phosphotransferase gene (*hpt*; primer pair oRG127 and oRG128) and the 35S

promoter with part of the CDS (primer pair oRG89 and oRG88). PCR was carried out in a total volume of 20 µl with the following conditions: 100 ng genomic DNA, primers (0.2 µM each of forward and reverse), 1× PCR buffer, 0.5 mM dNTP mix and 1.5 U iTaq DNA polymerase (Intron Biotechnology). The PCR cycle settings were 94 °C for 5 min, followed by 30 cycles of 94 °C for 30 s, Ta (55 °C for primer pair oRG127 and oRG128, 60 °C for primer pairs oRG88 and oRG89 and GAPDH forward (-F) and GAPDH reverse (-R) for 30 s, 72 °C for extension time (30 s for oRG127 and oRG128 and 45 s for oRG88 and oRG89 and GAPDH-F and GAPDH-R) and a final extension at 72 °C for 10 min. As a control, the GAPDH gene was amplified using the primer pair GAPDH-F and GAPDH-R. PCR products were separated by agarose gel electrophoresis and stained with SYBR Safe (Invitrogen). The copy number of the transgene in selected plants was determined by Southern blot analysis using genomic DNA digested with XbaI and SacI, respectively, and hybridized with a digoxigenin-labelled *hpt* probe. Plants with independent transformation events were selected for phenotypic analysis in the T1 generation (Supplementary Fig. 4).

**Phenotyping of 35S::PTSTOL1 plants.** T1 seeds from selected independent IR64 transgenic lines (Supplementary Fig. 4b) were pre-germinated in Petri dishes for 3 days in the dark at room temperature (26 °C) before seedlings were transferred into seedling trays. At 21 days after germination (DAG), transgenic plants and the corresponding null segregant were transferred into pots filled with P-deficient soil (P-Bray, 1.23 ± 0.30 mg kg<sup>-1</sup>; P-Olsen, 0.77 ± 0.46 mg kg<sup>-1</sup>) from Siniloan (Luzon, the Philippines). To control for pot-to-pot variation, one transgenic plant and one null segregant were always grown together in each pot. Each pot received the equivalent of 90 kg nitrogen ha<sup>-1</sup>, 40 kg potassium ha<sup>-1</sup> and 20 kg zinc ha<sup>-1</sup>. The equivalent of 60 kg P ha<sup>-1</sup> was applied only to the +P control treatment that was done in parallel. To mimic upland field conditions, plants grown under -P conditions were exposed to a dry-down treatment until leaf rolling at about 60 days after germination. Control pots were kept well watered but aerobic.

In an initial experiment, seven independent lines and the corresponding nulls were analysed (data not shown) and two lines (19 and 20) with high transgene expression and three lines (5, 14 and 21) with low transgene expression (Supplementary Figs 4 and 5) were selected for detailed analyses. A similar phenotyping experiment was conducted at the Japan International Research Center for Agricultural Sciences using independent T2 Nipponbare transgenic lines grown in well-watered (aerobic) P-deficient soil from Tsukuba (Japan) (Supplementary Fig. 4a). For the +P control, soil from a field that had regularly received P fertilizer was used and 60 kg P ha<sup>-1</sup> was additionally applied.

Macronutrients in roots, shoots and grains of IR64 transgenic plants and null controls were analysed by the Analytical Services Laboratory (ASL) at the International Rice Research Institute. The Kjeldahl method was used to determine the percentage of nitrogen, whereas a modified ASL nitric/perchloric acid digestion was done for inductively coupled plasma analysis of phosphorus and potassium.

**Semiquantitative RT-PCR analysis of transgene expression.** RT-PCR analysis of 35S::PTSTOL1 expression was conducted using leaf samples. Total RNA was extracted using Trizol (Invitrogen) or RNeasy mini kit (Qiagen) and DNA contaminations were removed with RNase-free DNase I (Promega or Qiagen). cDNA synthesis in the IR64 experiment was performed at 55 °C for 1 h in a 20 µl reaction with 1 µg RNA template, 2.5 µM oligo dT, 0.5 mM dNTP mix, 0.01 M DTT, 1× first-strand buffer and 200 U of Superscript III RT (Invitrogen). For the Nipponbare experiment, 500 ng RNA template was used for cDNA synthesis in a total volume of 10 µl using PrimeScript RT reagent kit (Takara) at 37 °C for 15 min and then 85 °C for 5 s. For standard PCR analyses, 0.5–1 µl cDNA was used as template for amplification of the transgene with iTaq DNA polymerase (Intron Biotechnology) or Takara Taq (Takara) using gene-specific primers (0.2 µM each of oKas4603 and oKas4604; Supplementary Table 3). *GAPDH* was used as a positive control.

**Root scan of IR64 35S::PTSTOL1 T2 plants and *Pup1* NILs grown in hydroponics.** Seeds of the IR64 T2 transgenic line 20 and seeds of IR64-*Pup1* and IR74-*Pup1* NILs<sup>8</sup> were pre-germinated in Petri dishes in the dark at room temperature. After 3 days, germinated seeds were transferred to Yoshida culture solution<sup>35</sup> with 100 µM and 10 µM NaH<sub>2</sub>PO<sub>4</sub>, respectively. The solution was replaced every 3 days. Total root length and root surface area of seedlings (11–21 DAG) were measured using WinRhizo (MAC STD1600; Regent Instruments). Each root system was evenly spread out and scanned at least twice to obtain average values. Each experiment was reproduced at least once. Null controls and NILs without *Pup1* were always grown and analysed in parallel.

**PTSTOL1 promoter:GUS IR64 transgenic plants.** The 1,755 base pair promoter of *PTSTOL1* was amplified from the genomic DNA of +*Pup1* NILs using the primer pair oRG107 and oRG109 (Supplementary Table 3), cloned into the pCR8/GW/TOPO TA cloning vector (Invitrogen) and sent for sequencing (Macrogen). The promoter fragment was sub-cloned into a pMDC164 binary destination vector<sup>31</sup>



through LR clonase recombination reaction (Invitrogen). The final construct contained the *GUS* gene driven by the *PSTOL1* promoter, which was confirmed using the forward primer oRG120, sequencing from the 3' end of the promoter extending to the CDS of the *GUS* gene. The construct was transformed into IR64 using the same protocol as described above. Transformed T0 plants were identified by genomic PCR using oRG120 and oRG134, also verifying the fusion of the *PSTOL1* promoter with the *GUS* gene. PCR conditions were the same as described above. For expression analyses, 1-week-old T1 seedlings grown in Petri dishes at room temperature in the dark were incubated in GUS staining solution according to the protocol<sup>36</sup>. Samples were stored in 70% ethanol before embedding in agarose for sectioning (200 µm) and brightfield microscopy (Olympus BX53 with attached Olympus DP70 camera).

**Affymetrix gene-expression analysis.** For microarray analyses, root samples of IR64 35S::PSTOL1 and the corresponding null segregants were collected from T1 plants of line 20 grown in pots with P-deficient soil under stress (–P; dry-down) and control (+ P fertilizer; well-watered aerobic) conditions. Plants grown under control conditions were sampled at the four-tiller stage at 33 DAG. The stress treatment delayed development, and plants were collected at the heading stage when plants had developed two to four tillers. For all treatments, samples of two biological replicates were analysed. Total root RNA was extracted using Trizol according to the instructions from the manufacturer (Invitrogen), with modifications. The RNA was re-precipitated by adding 2.5× volume absolute ethanol and one-tenth volume 3M NaOAc, pH 5.2, washed twice (70% and 100% ethanol), air-dried and dissolved in RNase-free water before treatment with RNase-free DNase I (Promega). cRNA synthesis and labelling, hybridization and data analysis with the GeneChip operating system 1.4 were performed by ATLAS Biolabs GmbH using Affymetrix GeneChip rice genome arrays. Identification of genes with differential expression between transgenics and nulls and between P treatments was restricted to probe-set IDs with consistent data in both replicates. For the identification of genes with lower expression in transgenic plants compared with nulls, all IDs 'present' (expressed) in the nulls were used. For the identification of genes with higher expression, all IDs present in transgenic plants were used. Genes classified as 'constitutively' changed in the transgenics showed significantly ( $P < 0.05$ ) altered expression in all data sets.

**Expression analysis and physical location of putative *PSTOL1* downstream genes.** For qRT-PCR analysis of the genes identified in the Affymetrix study, roots from IR64 35S::PSTOL1 T2 and null control plants grown hydroponically in Yoshida culture solution with 100 µM P were collected at 49 DAG. Total RNA extracted with Trizol (Invitrogen) was treated with RNase-free DNase I (Promega) and cDNA synthesis was performed with Transcriptor First Strand cDNA Synthesis Kit (Roche) using 1 µg DNase-treated RNA. qRT-PCR was conducted with LightCycler 480 SYBR Green I Master (Roche) using 0.5 µl cDNA template with the following PCR conditions: 94 °C for 5 min, 40 cycles at 94 °C for 10 s, 55 °C for 5 s and 72 °C for 20 s. Primer sequences are provided in Supplementary Table 3. *GAPDH* was used as an internal control. Expression levels were calculated using the delta-delta comparison and expressed as fold change relative to the expression in null controls (expression = 1). The physical location of genes was derived from the Rice Genome Browser (<http://rice.plantbiology.msu.edu/cgi-bin/gbrowse/rice/>) and the physical position of drought tolerance and meta-QTLs for roots and drought was derived from published data<sup>2,37–42</sup>. The data were manually summarized and graphically illustrated.

**Association analysis.** A total of 79 rice varieties with different *Pup1* haplotypes<sup>8</sup> were genotyped with 379 single-nucleotide polymorphism (SNP) markers using the RiceOPA2.1 BeadXpress platform<sup>43</sup> and analysed using structure<sup>44</sup> to identify co-ancestry subgroups. The optimum number of populations ( $K$ ) was selected by testing for  $K = 1$  to  $K = 8$  using ten independent runs of 10,000 burn-in runs followed by 100,000 iterations with a model allowing for admixture and correlated allele frequencies<sup>45</sup>.  $K = 6$  provided the best distinction and two subgroups with the most contrasting *Pup1* haplotypes (Kasalath type, +*Pup1*; Nipponbare type, –*Pup1*) were selected for further analysis. SNP markers located within the putative

*PSTOL1* downstream genes (Fig. 4) are not present in the 379 SNP set and markers located within approximately 1 megabase distance from the genes were therefore used for analysis of allelic associations with *PSTOL1* using TASSEL 3.0<sup>46</sup> (Supplementary Fig. 9). Rice accessions included in this study were: Kas group, Kasalath, AUS196, AUS257, Dular, IR84144-11-12, Lemont and Vandana; Nip group, Bala, CT6510-24-1-2, IR 42, IR64, IR66424-1-2-1-5, IR73678-6-9-B, IR 74, IR74371-46-1-1, K36-5-1-1BB, Nipponbare, PM-36 and Vary Lava 701.

**RNA interference (RNAi) transgenic plants.** A 322 bp fragment specific to the *PSTOL1* gene was amplified using the primer pair oSH07 and oSH08 and cloned into pENTR/D-TOPO vector (Invitrogen). The cloned fragment was transferred into pANDA RNAi vector<sup>47</sup> through LR clonase recombination reaction (Invitrogen). The RNAi construct was transformed into the *Pup1* donor variety Kasalath using the rice-transformation protocol described above. Six RNAi lines (T2 and T3 generation) were selected on the basis of semiquantitative RT-PCR showing downregulation of *PSTOL1* in roots using the oSH07 and oSH08 primer pair as described above. To verify whether the RNAi cassette is active, the expression of the *GUS* linker between the sense and antisense sequence<sup>47</sup> of the cloned *PSTOL1* fragment was determined. Selected RNAi lines were grown in hydroponics culture solution and in P-deficient soil and phenotyped (see supplementary Fig. 8). Wild-type Kasalath and null segregants were analysed in parallel.

- Haldup, A., Naver, H. & Scheller, H. V. The interaction between plastocyanin and photosystem I is inefficient in transgenic *Arabidopsis* plants lacking the PSI-N subunit of photosystem I. *Plant J.* **17**, 689–698 (1999).
- Pribil, M., Pesaresi, P., Hertle, A., Barbato, R. & Leister, D. Role of plastid protein phosphatase TAP38 in LHCII dephosphorylation and thylakoid electron flow. *PLoS Biol.* **8**, e1000288 (2010).
- Curtis, M. D. & Grossniklaus, U. A Gateway cloning vector set for high throughput functional analysis of genes in planta. *Plant Physiol.* **133**, 462–469 (2003).
- Hiei, Y., Ishida, Y., Kasaoka, K. & Komari, T. Improved frequency of transformation in rice and maize by treatment of immature embryos with centrifugation and heat prior to infection with *Agrobacterium tumefaciens*. *Plant Cell Tissue Org.* **87**, 233–243 (2006).
- Yoshida, S., Forno, D. A., Cock, J. H. & Gomez, K. A. *Laboratory Manual for Physiological Studies of Rice* 2nd edn 1–70 (International Rice Research Institute, 1972).
- Jefferson, R. A., Kavanagh, T. A. & Bevan, M. W. GUS fusions:  $\beta$ -glucuronidase as a sensitive and versatile gene fusion marker in higher plants. *EMBO J.* **6**, 3901–3907 (1987).
- Bernier, J., Kumar, A., Ramaiah, V., Spaner, D. & Atlin, G. A large-effect QTL for grain yield under reproductive-stage drought stress in upland rice. *Crop Sci.* **47**, 507–518 (2007).
- Bimpong, I. K. et al. Determination of genetic variability for physiological traits related to drought tolerance in African rice (*Oryza glaberrima*). *J. Plant Breed. Crop Sci.* **3**, 60–67 (2011).
- Courtois, B. et al. Rice root architecture: meta-analysis from a drought QTL database. *Rice* **2**, 115–128 (2009).
- Gomez, M. S. et al. Mapping QTLs linked to physio-morphological and plant production traits under drought stress in rice (*Oryza sativa* L.) in the target environment. *Am. J. Biochem. Biotechnol.* **2**, 161–169 (2006).
- Lanceras, J. C., Pantuwan, G., Jongdee, B. & Toojinda, T. Quantitative trait loci associated with drought tolerance at reproductive stage in rice. *Plant Physiol.* **135**, 384–399 (2004).
- Ni, J. J., Wu, P., Senadhira, D. & Huang, N. Mapping QTLs for phosphorus deficiency tolerance in rice (*Oryza sativa* L.). *Theor. Appl. Genet.* **97**, 1361–1369 (1998).
- Thomson, M. J. et al. High-throughput single nucleotide polymorphism genotyping for breeding applications in rice using the BeadXpress platform. *Mol. Breed.* **29**, 875–886 (2011).
- Pritchard, J. K., Stephens, M. & Donnelly, P. Inference of population structure using multilocus genotype data. *Genetics* **155**, 945–959 (2000).
- Falush, D., Stephens, M. & Pritchard, J. K. Inference of population structure using multilocus genotype data: linked loci and correlated allele frequencies. *Genetics* **164**, 1567–1587 (2003).
- Bradbury, P. J. et al. TASSEL: software for association mapping of complex traits in diverse samples. *Bioinformatics* **23**, 2633–2635 (2007).
- Miki, D. & Shimamoto, K. Simple RNAi vectors for stable and transient suppression of gene function in rice. *Plant Cell Physiol.* **45**, 490–495 (2004).

# The human CST complex is a terminator of telomerase activity

Liuh-Yow Chen<sup>1</sup>, Sophie Redon<sup>1</sup> & Joachim Lingner<sup>1</sup>

The lengths of human telomeres, which protect chromosome ends from degradation and end fusions<sup>1,2</sup>, are crucial determinants of cell lifespan<sup>3</sup>. During embryogenesis and in cancer, the telomerase enzyme counteracts telomeric DNA shortening. As shown in cancer cells, human telomerase binds the shelterin component TPP1 at telomeres<sup>4,5</sup> during the S phase of the cell cycle, and adds ~60 nucleotides in a single round of extension<sup>6</sup>, after which telomerase is turned off by unknown mechanisms. Here we show that the human CST (CTC1, STN1 and TEN1) complex, previously implicated in telomere protection and DNA metabolism<sup>7–11</sup>, inhibits telomerase activity through primer sequestration and physical interaction with the protection of telomeres 1 (POT1)–TPP1 telomerase processivity factor<sup>12,13</sup>. CST competes with POT1–TPP1 for telomeric DNA, and CST–telomeric-DNA binding increases during late S/G2 phase only on telomerase action, coinciding with telomerase shut-off. Depletion of CST allows excessive telomerase activity, promoting telomere elongation. We propose that through binding of the telomerase-extended telomere, CST limits telomerase action at individual telomeres to approximately one binding and extension event per cell cycle. Our findings define the sequence of events that occur to first enable and then terminate telomerase-mediated telomere elongation.

In budding yeast, a trimeric complex, CST, composed of Cdc13, Stn1 and Ten1, associates with the telomeric 3' overhang, modulating telomere protection and replication<sup>14–17</sup>. Homologues of Stn1 and Ten1 have recently been identified in other fungi, plants and mammals<sup>7,9,18</sup>. In addition, CTC1 (conserved telomere maintenance component 1) also referred to as AAF-132 ( $\alpha$ -accessory factor)<sup>8</sup>, a protein that forms a trimeric 'CST' complex with STN1 and TEN1, was identified; however, CTC1 bears little sequence similarity with Cdc13. Like budding yeast CST components, those of human CST contain putative OB-fold domains involved in binding single-stranded DNA and promoting protein interactions. Human CST was detected at telomeres with suggested roles in protecting telomeres from eliciting a DNA damage response. In addition, human CTC1 and STN1 stimulate DNA polymerase  $\alpha$ -primase, increasing its affinity for template DNA<sup>8</sup>, and as such have been implicated in assisting DNA replication at telomeres and possibly other special DNA sequences throughout the genome<sup>7,9–11</sup>. In order to identify roles of CST in telomere length control, we transduced the telomerase-positive HT1080 fibrosarcoma cell line with retroviral vectors expressing small hairpin (sh)RNAs targeting the messenger RNAs of the three CST subunits (Fig. 1a–c) and propagated pools of cells for up to 100 days. Depletion of any of the three CST components caused steady telomere elongation (Fig. 1a–c), whereas the control shRNA against green fluorescent protein (GFP) had no notable effect on telomere length. Thus, CST is required for telomere length homeostasis in telomerase-positive cells limiting telomere lengthening.

In order to corroborate the effects of CST on telomerase, we expressed amino-terminal (amino acids 1–701) and carboxy-terminal (amino acids 844–1217) CTC1 fragments (whose protein interactions

are characterized further below) after stable retroviral transduction in telomerase-positive HT1080 cells and in telomerase-negative primary lung fibroblasts (HLF). CTC1(1–701) expression caused a progressive reduction in telomere length in HT1080 cells (Supplementary Fig. 1a), while it had no notable effect on the telomere shortening rate in HLF cells (Supplementary Fig. 1b). This indicates that CTC1(1–701) interferes with telomere lengthening by telomerase. In contrast, CTC1(844–1217) promoted robust and continuous telomere elongation in HT1080 cells (Supplementary Fig. 1a), which was abolished upon addition of the telomerase inhibitor BIBR1532 (ref. 19) to the medium (Fig. 1d). In HLF cells, CTC1(844–1217) slightly accelerated the telomere shortening rate (Supplementary Fig. 1b). The opposing

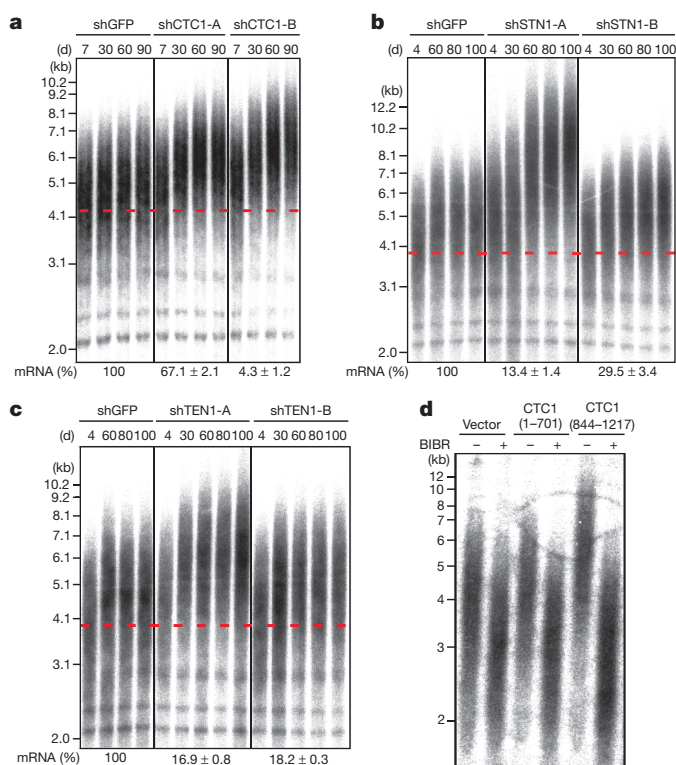


**Figure 1 | The CST complex limits telomere elongation in human cancer cells.** **a–c**, Telomere lengths of HT1080 cells stably expressing the indicated shRNAs (suffixes -A and -B refer to different shRNAs) were determined by in-gel hybridization of restriction digested DNA extracted from cells described after indicated times in culture. The dashed lines indicate the peak intensity of telomere length signals of the GFP shRNA expressing cells at the first time point. Relative mRNA levels of CTC1, STN1 and TEN1 (indicated below the panels) were determined by real-time RT-PCR (mean ± s.e.;  $n = 3$ ). **d**, Telomere length analysis of HT1080 cells stably expressing vector, CTC1(1–701) and CTC1(844–1217) grown in the absence or presence of BIBR1532 (BIBR; 10  $\mu$ M) for 25 days.

<sup>1</sup>Swiss Institute for Experimental Cancer Research (ISREC), School of Life Sciences, Frontiers in Genetics National Center of Competence in Research, Ecole Polytechnique Fédérale de Lausanne (EPFL), Station 19, 1015 Lausanne, Switzerland.

effects of CTC1 domains on telomere length in telomerase-positive HT1080 versus telomerase-negative HLF cells and the abolition of telomere elongation upon addition of BIBR1532 strongly support the notion that CST mediates its effects on telomere length by regulating telomerase.

Recombinant human CTC1, STN1 and TEN1 were co-expressed in HEK293E cells and the trimeric CST complex was purified (Fig. 2a). Single-stranded telomeric DNA binding was analysed by electrophoretic mobility shift assay (EMSA; Fig. 2b–g, Supplementary Figs 2, 3). Because of a dissociation half-life of roughly 12 h with G-strand (TTAGGG-repeat containing) oligonucleotides (Supplementary Fig. 3), complexes were incubated for 24 h at 4 °C in order to approach equilibrium before EMSA. CST bound with nanomolar affinity to 18-mer and longer G-strand oligonucleotides, but not the 12-mer G-strand (Fig. 2b, c, Supplementary Fig. 2a). For C-strand oligonucleotides, efficient binding by CST required considerably longer oligonucleotide lengths (>36 nucleotides) and the binding constants remained higher (Fig. 2d, Supplementary Fig. 2b). In competition experiments in which increasing amounts of unlabelled competitor DNA were added to the binding reactions (Fig. 2e–g), G-strand oligonucleotide binding by CST was tight and specific, whereas C-strand oligonucleotide binding was readily competed with non-telomeric sequences. The dissociation half-life of CST in complex with (TTAGGG)<sub>10</sub> was 680 min whereas it was less than 1 min with (CCCTAA)<sub>10</sub> (Supplementary Fig. 3). Thus, CST has specificity for the telomeric G-strand sequence. However, preferred binding of the G- versus the C-strand decreased with oligonucleotide length, in accordance with published data<sup>7</sup>. CTC1 alone failed to bind single-stranded DNA and purified STN1–TEN1 complex failed to show DNA binding by EMSA (Supplementary Fig. 4), suggesting that

the formation of a trimeric CST complex is required for single-strand DNA binding.

To investigate whether CST regulates telomerase activity, we extracted telomerase from HEK293T cells that overexpress the core components of telomerase, human TERT and human TR (ref. 20). Direct telomerase assays (DTAs) were carried out, in which elongated products are detected owing to the incorporation of radioisotope-labelled nucleotides in the elongated primers (Fig. 3). Substrate primer concentration was in vast excess (>1,000 fold) over telomerase to ensure that the reaction products were due to processive primer extension and not due to rebinding of already extended products. Time course experiments demonstrated that reaction end points had not been reached during the course of the experiments (Supplementary Fig. 5). Addition of increasing amounts (0–250 nM) of CST to a telomerase assay with primers TS or (TTAGGG)<sub>2</sub> did not markedly influence the telomerase reaction (Fig. 3a, two left panels). Neither of these primers is bound by CST in its non-extended form (Fig. 2, Supplementary Fig. 2c). On the other hand, when using oligonucleotides containing three or eight telomeric repeats, both of which bind CST, telomerase activity was diminished (Fig. 3a, two right panels). With the highest concentration of CST, telomerase activity was reduced to 11% when using (TTAGGG)<sub>8</sub> as a substrate. Thus, CST represses telomerase activity upon primer binding, presumably by sequestering the 3' end of the substrate.

Telomere extension is stimulated by the POT1–TPP1 telomerase processivity factor<sup>12,13</sup>. We expressed, purified and characterized recombinant POT1–TPP1 from HEK293E (Supplementary Fig. 6). POT1–TPP1 increased telomerase processivity, as evinced by the longer extension products seen in the direct telomerase assays<sup>12</sup>

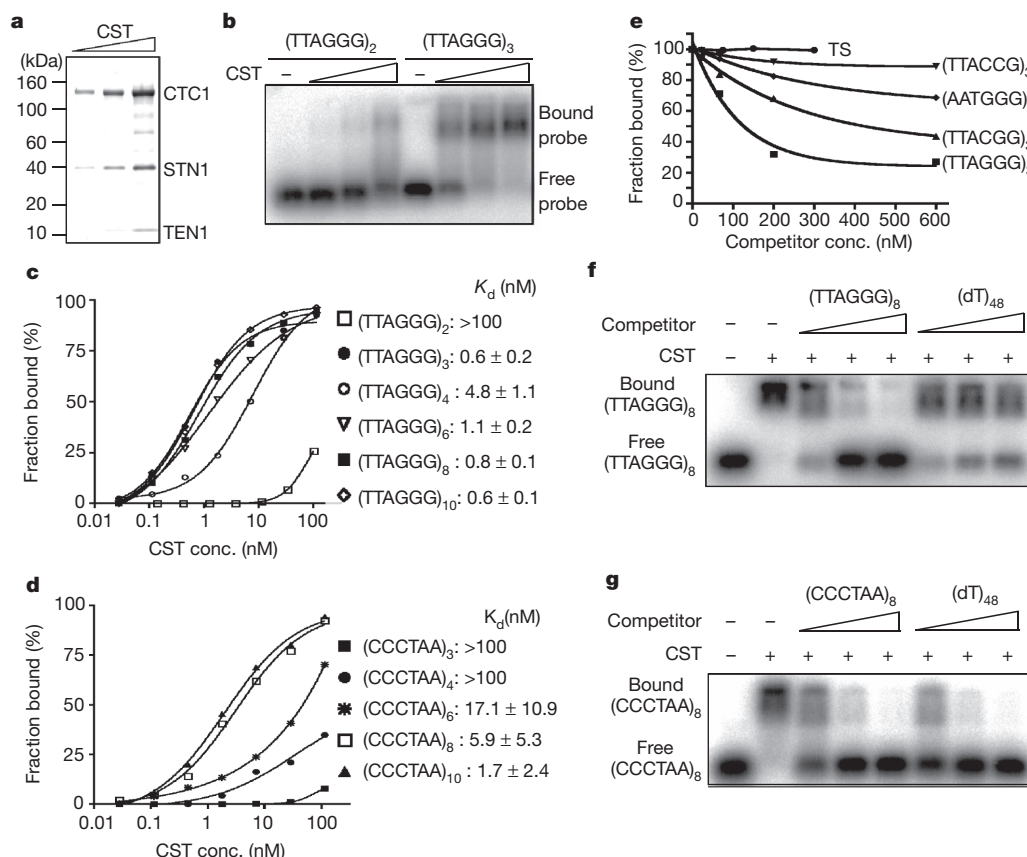


**Figure 2 | Sequence-specific binding of CST to the human telomere G-stranded sequences.** **a**, Coomassie blue staining of purified CST (2.5, 5 and 10  $\mu$ l) separated on SDS-PAGE. **b**, DNA binding of CST analysed by EMSA on agarose gels. Indicated probes were incubated with increasing amounts of CST (0, 5, 20 and 100 nM). **c**, **d**, Equilibrium binding curves of CST. Dissociation constants ( $K_d$ ) are indicated (mean  $\pm$  s.d.;  $n = 2-3$ ). **e**, Competition

experiment. 2 nM [<sup>32</sup>P]-labelled (TTAGGG)<sub>3</sub> was incubated with 100 nM of CST in the absence or presence of indicated unlabelled competitor oligonucleotides. TS oligonucleotide is 5'-AATCCGTCGAGCAGAGTT-3'. **f**, **g**, Competition binding of CST bound to [<sup>32</sup>P]-labelled (TTAGGG)<sub>8</sub> or (CCCTAA)<sub>8</sub> (1 nM) as in **e** with unlabelled competitor oligonucleotides (0, 20, 200, 1,000 nM).



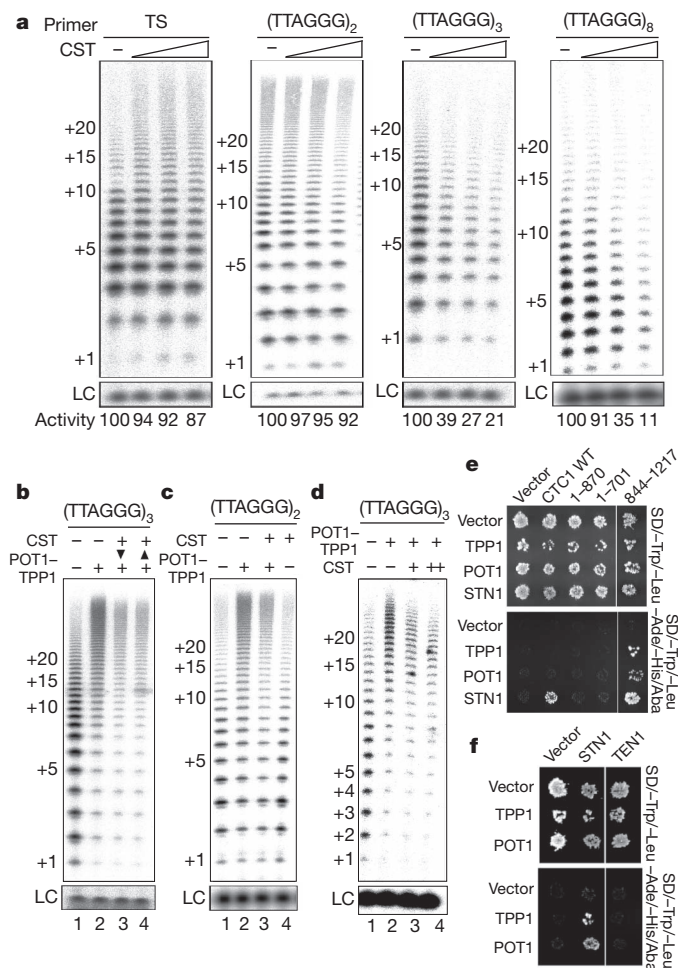


**Figure 3 | CST inhibits telomerase activity *in vitro*.** **a**, Direct telomerase assay (DTA) with CST. Indicated primers (20 nM) were pre-incubated with increasing concentration of CST (0, 63, 125, and 250 nM) for 30 min before DTA. Relative amount of activity is indicated (bottom). LC, loading control. Numbers on the left of each panel indicate the number of telomeric repeats added. **b**, DTA with CST and POT1-TPP1 using (TTAGGG)<sub>3</sub> (20 nM) pre-incubated with saturating amount of CST (250 nM, lane 3) or POT1-TPP1 (150 nM, lane 4) for 20 min, followed by addition of POT1-TPP1 (150 nM, lanes 2 and 3) or CST (250 nM, lane 4) for 20 min before DTA. In lane 3 (down-triangle), CST was added before POT1-TPP1. In lane 4 (up-triangle), POT1-TPP1 was added before CST. **c**, DTA with CST and POT1-TPP1 using (TTAGGG)<sub>2</sub> (10 nM) pre-mixed with CST (100 nM) and/or POT1-TPP1 (60 nM) for 30 min before DTA. **d**, DTA with CST and POT1-TPP1 on beads. Biotinylated-(TTAGGG)<sub>3</sub> primer (20 nM) pre-incubated with POT1-TPP1 (160 nM, lanes 2–4) was immobilized on streptavidin-coated beads and unbound POT1-TPP1 was washed off. DTA was performed in the absence (lanes 1, 2) or presence of CST (lane 3: 85 nM, lane 4: 170 nM). Relative DNA synthesis levels in lanes 2–4 are: lane 2, 100%; lane 3, 54%; lane 4, 38%. **e**, **f**, Yeast two-hybrid assay for interactions of CST and POT1-TPP1. Diploid yeast cells expressing indicated bait (across top of panel) and prey (left side of panel) proteins were grown on SD (synthetic dextrose-containing minimal medium)/–Trp/–Leu agar plates. Protein interactions were detected by replica-plating on SD/–Trp/–Leu/–His/–Ade/–Aba (aureobasidin A) agar plates.

(Fig. 3b, c, compare lanes 1 and 2). Further addition of CST to the POT1-TPP1-containing telomerase reaction with (TTAGGG)<sub>3</sub> as primer reduced the amount of reaction product without affecting product lengths (Fig. 3b, compare lane 2 to lanes 3 and 4). This effect was independent of whether POT1-TPP1 or CST was pre-incubated for 30 min with the primer before the addition of the other complex and telomerase (Fig. 3b, lanes 3 and 4). CST, when added second, did not promote the release of POT1-TPP1 from the primer and POT1-TPP1 did not promote the release of CST (Supplementary Fig. 7). To

further test whether CST-dependent telomerase inhibition in the context of POT1-TPP1 requires primer binding by CST, as seen in reactions lacking POT1-TPP1, we tested the (TTAGGG)<sub>2</sub> substrate which does not bind CST. Strikingly and in contrast with what was seen in the absence of POT1-TPP1, CST clearly repressed telomerase in the presence of POT1-TPP1 with (TTAGGG)<sub>2</sub> as primer (Fig. 3c). Together, these data suggest that CST interferes with POT1-TPP1-dependent telomerase activity even without substrate pre-binding of CST.

The telomerase reactions in Fig. 3b and 3c involved excess amounts of POT1-TPP1 over the primer substrate. The free POT1-TPP1 may bind during the reaction to freshly synthesized telomeric repeats and contribute to the observed enhancement of telomerase processivity. Therefore, the inhibitory effects of CST on POT1-TPP1-dependent telomerase activity could be the result of reducing the binding of POT1-TPP1 to the newly elongated products. We therefore tested interference of CST with POT1-TPP1 that was pre-bound to substrate primer in the absence of free POT1-TPP1. 5'-biotinylated (TTAGGG)<sub>3</sub> was immobilized on streptavidin beads and incubated with an excess of POT1-TPP1. Unbound protein was washed away and telomerase fraction was added in the presence or the absence of CST (Fig. 3d). Addition of CST again reduced product accumulation (62% reduction in lane 4 compared to lane 2 in Fig. 3d) even though in this experiment free POT1-TPP1 was absent. Taken together, these data reveal that CST inhibits telomerase through two mechanisms: first, it inhibits telomerase when directly binding the primer substrate. Second, it restricts the stimulation of telomerase by POT1-TPP1, possibly through physical interaction between CST and POT1-TPP1. We searched for physical interactions between POT1-TPP1 and CST in two-hybrid assays in yeast and in co-immunoprecipitation experiments in HEK293T cells (Fig. 3e, f, Supplementary Fig. 8). These experiments uncovered and delineated physical interactions between CTC1 and TPP1, CTC1 and POT1, and STN1 and TPP1.

In order to better understand telomerase inhibition by CST at telomeres *in vivo*, we investigated its association with telomeres in cells by chromatin immunoprecipitation (ChIP) of formaldehyde-crosslinked chromatin. For this, Myc-tagged CTC1 was expressed in HT1080 cells and the amounts of telomeric DNA co-immunoprecipitated with the anti-Myc antibody were determined by dot-blot hybridization (Fig. 4a–g). CTC1-Myc was specifically associated with telomeric DNA but not Alu-repeat-containing DNA (Fig. 4b and Supplementary Fig. 9). shRNA-mediated depletion of either TPP1 or POT1 led to an increase of telomeric DNA found in association with CTC1 (Fig. 4a–c), indicating that POT1-TPP1 and CST compete for telomeric DNA binding *in vivo*. To investigate telomeric association of CST during the cell cycle, we synchronized Myc-tagged CTC1-expressing and vector control HT1080 cells with a double-thymidine block in early S phase and released them from the block by thymidine removal. Cell cycle progression was monitored by flow cytometry (Supplementary Fig. 10). Telomere association of CTC1-Myc was detectable by ChIP in all stages of the cell cycle with a steady enhancement during late S phase and early G2 (Fig. 4d, e), correlating with the period in the cell cycle when telomerase is shut off. This suggested that CST binding to telomeres increases after their extension by telomerase in order to restrict telomere lengthening. This model infers that telomerase inhibition should abolish increased telomere association of CTC1-Myc in late S/G2 phase. This prediction was tested by inhibiting telomerase in synchronized cells with BIBR1532, which indeed abolished increased association of CTC1-Myc with telomeres in late S/G2 (Fig. 4f, g). Thus CST most probably binds to the telomeric 3' overhang upon its extension by telomerase.

In human cells undergoing homeostatic telomere length maintenance, roughly 60 nucleotides are added in a processive manner to each telomere by a single binding and extension event<sup>6,21</sup>. Processive addition is thought to be mediated by POT1-TPP1 (refs 12, 13). How is telomere elongation restricted to one extension event in order to avoid stochastic overelongation? We propose here that CST restricts

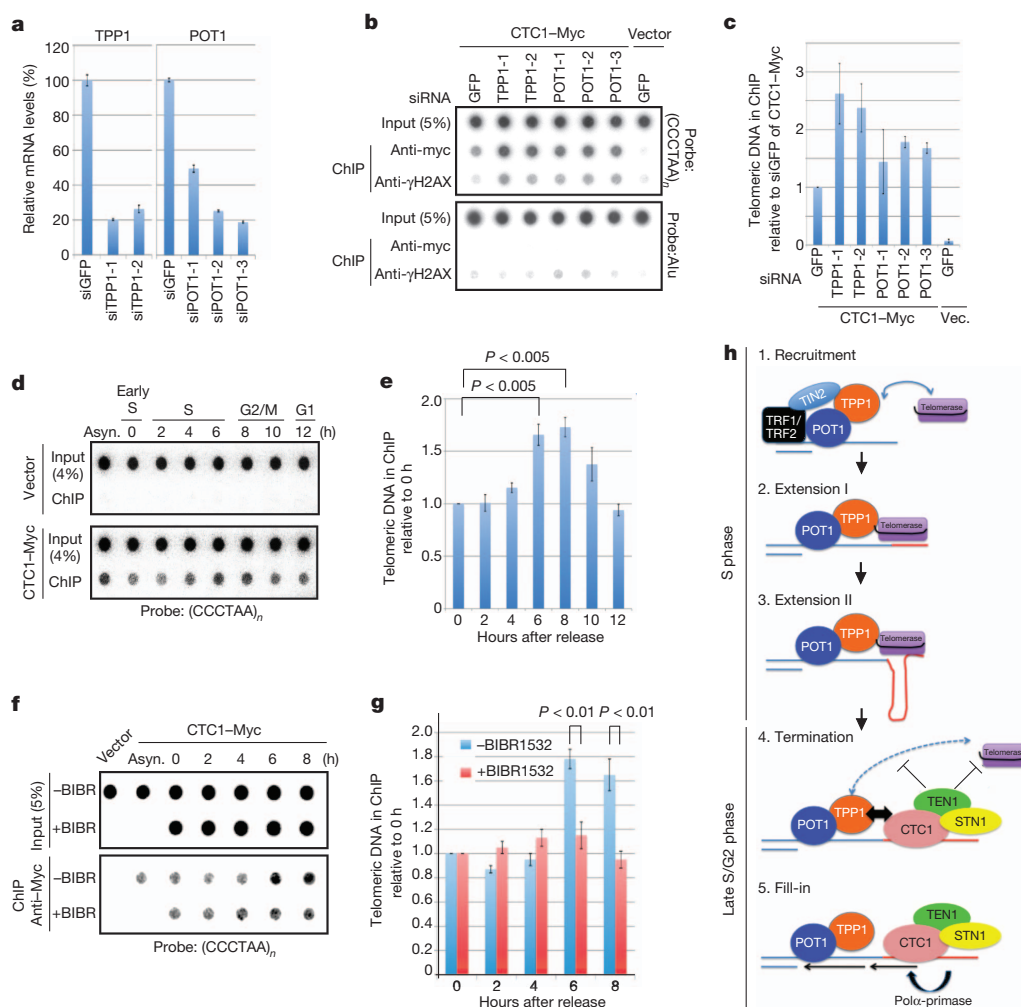


**Figure 4 | Cell cycle regulated telomeric association of CST.** **a–c**, Telomeric association of CTC1 upon POT1–TPP1 depletion. HT1080 cells stably expressing vector or CTC1–Myc were transfected with indicated small interfering (si)RNAs. Suffixes -1, -2 and -3 refer to different siRNA sequences. **a**, mRNA levels of TPP1 and POT1 determined by real-time RT–PCR (mean  $\pm$  s.e.;  $n = 3$ ). **b**, ChIP using anti-Myc or anti- $\gamma$ H2AX antibodies. **c**, Relative levels of telomeric DNA associated with CTC1–Myc (mean  $\pm$  s.d.;  $n = 2$ ) upon quantification of **b**. **d–g**, Telomeric association of CST during the cell cycle. Cells were synchronized in early S phase by double-thymidine block

and released. BIBR1532 (10  $\mu$ M) was added to inhibit telomerase (**f**). Asyn., asynchronous cells. **e**, **g**, Quantification (mean  $\pm$  s.d.;  $n = 3$ , Student's *t*-test). **h**, Model for roles of CST in telomerase regulation. 1, TIN2–TPP1 recruits telomerase and POT1–TPP1 (2, 3) promotes processive telomere elongation. 4, CST binds to the telomerase-extended telomere 3' end suppressing telomerase access. CST also inhibits the telomerase-stimulatory functions of POT1–TPP1 upon binding. 5, CST promotes fill-in synthesis of the C-strand stimulating DNA polymerase  $\alpha$ -primase.

telomerase-mediated telomere extension to a single binding and extension event (Fig. 4h). First, we have shown in cells that CST restricts telomere length through inhibition of telomerase (Fig. 1). Second, we have demonstrated *in vitro* that telomerase inhibition by CST involves the tight binding of the telomeric G-strand substrate in addition to the inhibition of the telomerase-stimulator POT1–TPP1 (Figs 2 and 3). The latter most probably involves direct physical interactions of CST with POT1–TPP1 (Fig. 3e, f; Supplementary Fig. 8). In addition, CST and POT1–TPP1 compete for binding of the telomeric DNA substrate (Fig. 4a–c). Third, and in accordance with CST acting in telomere replication after telomerase, we have shown that CST binding at telomeres increases steadily during S phase with a peak at S/G2 (Fig. 4d, e). Significantly, this increased binding strictly depends on active telomerase, indicating that CST binds to the newly extended overhangs (Fig. 4f, g).

Specific binding of CST to the telomerase-extended telomeric 3' overhangs may terminate telomerase-mediated telomere elongation. In addition, it may prepare fill-in synthesis of the C-strand by lagging strand polymerases (Fig. 4h). Human CST subunits stimulate DNA polymerase  $\alpha$ -primase<sup>8</sup>, and CST from *Saccharomyces cerevisiae* has also been implicated in fill-in synthesis of the telomerase-extended

telomeres<sup>16,17</sup>. This CST-mediated switch from telomere elongation to fill-in synthesis, functioning autonomously at single chromosome ends, can ensure that every telomere is extended by telomerase once and only once during every cell cycle.

## METHODS SUMMARY

shRNAs were expressed from retroviral vectors. Recombinant CST complex and POT1–TPP1 were expressed in HEK293E cells and purified. For EMSA, DNA substrates were labelled at their 5' ends with <sup>32</sup>P. Complexes were separated on 2.5% agarose or 6% polyacrylamide gels. Direct telomerase assays were done at 30 °C for 30 min in the presence of [ $\alpha$ -<sup>32</sup>P]-labelled dGTP and unlabelled dTTP and dATP. For ChIP, cells were fixed with 1% formaldehyde for 30 min at room temperature. The Matchmaker Gold Yeast Two-Hybrid system (Clontech) was used according to the manufacturer's instructions.

**Full Methods** and any associated references are available in the online version of the paper.

Received 17 November 2011; accepted 29 May 2012.

Published online 4 July 2012.

1. Jain, D. & Cooper, J. P. Telomeric strategies: means to an end. *Annu. Rev. Genet.* **44**, 243–269 (2010).

2. de Lange, T. How telomeres solve the end-protection problem. *Science* **326**, 948–952 (2009).
3. Bodnar, A. G. *et al.* Extension of life-span by introduction of telomerase into normal human cells. *Science* **279**, 349–352 (1998).
4. Abreu, E. *et al.* TIN2-tethered TPP1 recruits human telomerase to telomeres *in vivo*. *Mol. Cell. Biol.* **30**, 2971–2982 (2010).
5. Xin, H. *et al.* TPP1 is a homologue of ciliate TEBP- $\beta$  and interacts with POT1 to recruit telomerase. *Nature* **445**, 559–562 (2007).
6. Zhao, Y. *et al.* Processive and distributive extension of human telomeres by telomerase under homeostatic and nonequilibrium conditions. *Mol. Cell* **42**, 297–307 (2011).
7. Miyake, Y. *et al.* RPA-like mammalian Ctc1-Stn1-Ten1 complex binds to single-stranded DNA and protects telomeres independently of the Pot1 pathway. *Mol. Cell* **36**, 193–206 (2009).
8. Casteel, D. E. *et al.* A DNA polymerase- $\alpha$  primase cofactor with homology to replication protein A-32 regulates DNA replication in mammalian cells. *J. Biol. Chem.* **284**, 5807–5818 (2009).
9. Surovtseva, Y. V. *et al.* Conserved telomere maintenance component 1 interacts with STN1 and maintains chromosome ends in higher eukaryotes. *Mol. Cell* **36**, 207–218 (2009).
10. Nakaoka, H., Nishiyama, A., Saito, M. & Ishikawa, F. *Xenopus laevis* Ctc1-Stn1-Ten1 (x CST) protein complex is involved in priming DNA synthesis on single-stranded DNA template in *Xenopus* egg extract. *J. Biol. Chem.* **287**, 619–627 (2012).
11. Gu, P. *et al.* CTC1 deletion results in defective telomere replication, leading to catastrophic telomere loss and stem cell exhaustion. *EMBO J.* **31**, 2309–2321 (2012).
12. Wang, F. *et al.* The POT1–TPP1 telomere complex is a telomerase processivity factor. *Nature* **445**, 506–510 (2007).
13. Latrick, C. M. & Cech, T. R. POT1–TPP1 enhances telomerase processivity by slowing primer dissociation and aiding translocation. *EMBO J.* **29**, 924–933 (2010).
14. Gao, H., Cervantes, R. B., Mandell, E. K., Otero, J. H. & Lundblad, V. RPA-like proteins mediate yeast telomere function. *Nature Struct. Mol. Biol.* **14**, 208–214 (2007).
15. Pennock, E., Buckley, K. & Lundblad, V. Cdc13 delivers separate complexes to the telomere for end protection and replication. *Cell* **104**, 387–396 (2001).
16. Qi, H. & Zakian, V. A. The *Saccharomyces* telomere-binding protein Cdc13p interacts with both the catalytic subunit of DNA polymerase  $\alpha$  and the telomerase-associated Est1 protein. *Genes Dev.* **14**, 1777–1788 (2000).
17. Grossi, S., Puglisi, A., Dmitriev, P. V., Lopes, M. & Shore, D. Pol12, the B subunit of DNA polymerase  $\alpha$ , functions in both telomere capping and length regulation. *Genes Dev.* **18**, 992–1006 (2004).
18. Martin, V., Du, L. L., Rozenzhak, S. & Russell, P. Protection of telomeres by a conserved Stn1-Ten1 complex. *Proc. Natl Acad. Sci. US* **104**, 14038–14043 (2007).
19. Damm, K. *et al.* A highly selective telomerase inhibitor limiting human cancer cell proliferation. *EMBO J.* **20**, 6958–6968 (2001).
20. Cristofari, G. & Lingner, J. Telomere length homeostasis requires that telomerase levels are limiting. *EMBO J.* **25**, 565–574 (2006).
21. Zhao, Y. *et al.* Telomere extension occurs at most chromosome ends and is uncoupled from fill-in in human cancer cells. *Cell* **138**, 463–475 (2009).

**Supplementary Information** is linked to the online version of the paper at [www.nature.com/nature](http://www.nature.com/nature).

**Acknowledgements** We thank P. Reichenbach, K. Ong and S. Feuerhahn for technical help, the PCF-EPFL core facility for protein expression and J. Cooper for discussion. Research in the laboratory of J.L. was supported by the Swiss National Science Foundation, a European Research Council advanced investigator grant (grant agreement no. 232812), the Swiss Cancer League and EPFL.

**Author Contributions** L.-Y.C. performed most experiments, S.R. contributed to ChIP assays, L.-Y.C. and J.L. designed the study and wrote the paper.

**Author Information** Reprints and permissions information is available at [www.nature.com/reprints](http://www.nature.com/reprints). The authors declare no competing financial interests. Readers are welcome to comment on the online version of this article at [www.nature.com/nature](http://www.nature.com/nature). Correspondence and requests for materials should be addressed to J.L. ([joachim.lingner@epfl.ch](mailto:joachim.lingner@epfl.ch)).



## METHODS

**Protein and shRNA expression vectors.** cDNAs were subcloned into pcDNA6 (Invitrogen) and retroviral-based pCL vectors for expression of V5- and Flag- or Myc-tagged proteins, respectively. For HEK293E expression and purification of protein complexes, cDNAs of Flag-tagged CTC1, STN1, (His)<sub>6</sub>-tagged TEN1, Flag-tagged POT1, and TPP1 were cloned into pEAK8 vector behind the EF1- $\alpha$  promoter. A TEV protease site was engineered in between the Flag tag and the start site of the ORFs. TPP1 used in the study contains the residues 87–544 as described<sup>12,13</sup> with additional mutations (W527R, A528K) that were designed to prevent co-purification of other endogenous shelterin components by disrupting the TPP1–TIN2 interaction (L.-Y.C. and J.L., unpublished data). For shRNA expression, oligonucleotide duplexes containing targeting sequences were cloned into pCL-mU6 retroviral vector. The oligonucleotide sequences for control (GFP) and CST targeting were 5'-CACAAAGCTGGAGTACAAC-3' (shGFP), 5'-GGCGTCTCTCTGGATGAAA-3' (shCTC1-A), 5'-GCCAGCTGCCAACTCAAT-3' (shCTC1-B), 5'-GGACTGCCAGAAACCAAT-3' (shSTN1-A), 5'-GGGAA TGGGATTGGCATA-3' (shSTN1-B), 5'-GGCGGCAGCCAGTAGGAAA-3' (shTEN1-A), and 5'-GCCTGTCTGGAGCTCGAA-3' (shTEN1-B). The oligonucleotide sequences of GFP, TPP1 and POT1 siRNAs were 5'-CACA AGCUGGAGUACAACU-3' (GFP), 5'-CCAAGACUUAUGAUGUUCAGAA-3' (TPP1-1), 5'-GUGGUACCAGCAUCAGCCUU-3' (TPP1-2), 5'-GCUAUCU GCUACAAUACUU-3' (POT1-1), 5'-GUACUAGAAGCUAUCUCA-3' (POT1-2), 5'-GGGUGGUACAUAUUGUCAAU-3' (POT1-3).

**Real-time PCR and data analysis.** To generate cDNA, total RNA was isolated using the RNeasy kit (Qiagen) followed by reverse transcription using the iScript cDNA synthesis kit (Bio-rad). Real-time PCR was performed using the Power SYBR Green Mix (Applied Biosystems) on the Applied Biosystems 7900HT Real-Time PCR System. The oligonucleotide sequences for Real-time PCR were 5'-CTGGCTCCTCTCCCTACTTG-3' + 5'-TGATTTCCCTGTTGCCACAAT-3' (CTC1), 5'-GACCTGCACAGAAAGATCCA-3' + 5'-AAGTGACAGCCCTTC TCCAT-3' (STN1), 5'-GCTCCCTGTACATCGTCCTC-3' + 5'-CAACAAGG GCAGGTTTCATC-3' (TEN1), 5'-GATATTGTCGCTTTCACAGGC-3' + 5'-GAAGTGCAGGATGATAGGG-3' (POT1), 5'-GCTCAATGCTGTGCA TCTCT-3' + 5'-TGAGGAAGGAGAGAGAGGCTA-3' (TPP1), 5'-TCCCTGGA GAAGAGCTACGA-3' + 5'-AGCACTGTGTTGGCGTACAG-3' ( $\beta$ -actin).

**Mammalian expression and purification of recombinant protein complexes.** Protein expression was carried out upon transient co-transfection of the plasmids into HEK293E cells for 72 h. The cells were then harvested and lysed with NETN buffer (40 mM Tris-HCl, pH 8.0, 100 mM NaCl, 1 mM EDTA, 0.5% NP40) supplemented with protease inhibitor cocktail (Roche), and centrifuged at 15,000g at 4 °C for 20 min. For CST purification, the supernatant supplemented with 10 mM of imidazole was first applied to a HisTrap column (GE). After washing with NETN, elution was proceeded with 250 mM imidazole, 20 mM Tris-HCl, pH 7.5. The eluate was 10 times diluted with BC75 (20 mM Tris-HCl, pH 8.0, 75 mM NaCl, 0.2 mM EDTA, 0.5 mM DTT, 10% glycerol) and applied to a HiTrap Heparin column (GE), washed with BC150 (20 mM Tris-HCl, pH 8.0, 150 mM NaCl, 0.2 mM EDTA, 0.5 mM DTT, 10% glycerol) and eluted with BC650 (20 mM Tris-HCl, pH 8.0, 650 mM NaCl, 0.2 mM EDTA, 0.5 mM DTT, 10% glycerol). Equal volume of NETN was then added to the eluate for purification by anti-Flag M2 affinity gel (Sigma) and the CST complex was eluted with Flag peptide (200  $\mu$ M) into storage buffer (20 mM Tris-HCl, pH 8.0, 50 mM NaCl, 0.5 mM EDTA, 0.25% NP-40, 10% glycerol). The purified CST complex was uniform without aggregation in sucrose gradient sedimentation analysis. The fraction of protein complex active in DNA binding was determined in titration experiments using (TTAGGG)<sub>3</sub> oligonucleotide as the substrate. The purified complex was consistently about 65–70% active. The proteins in the Coomassie blue stained gel shown in Fig. 2a comprised full-length CTC1, STN1 and TEN1 (~95%), truncated CTC1 (~3%) and HSP70 (~2%).

For STN1/TEN1 purification, the supernatant supplemented with 10 mM of imidazole was first applied to a HisTrap column (GE). After wash with NETN, elution was proceeded with 250 mM imidazole, 20 mM Tris-HCl, pH 7.5. The eluate was 10 times diluted with BC75 and applied to a tandem HiTrap Heparin-HiTrap Q Sepharose column. The HiTrap Q Sepharose column was then washed with BC75 and eluted with BC150. The protein was concentrated with Centricon (Millipore) into PBS supplemented with 10% glycerol.

For POT1–TPP1 purification, anti-Flag M2 affinity gel (Sigma) was added to the supernatant and incubated at 4 °C for 4 h, followed by wash with NETN buffer and PBS. The POT1–TPP1 complex was then eluted by TEV protease cleavage at 4 °C for 5 h into PBS supplemented with 10% glycerol, and TEV protease (Invitrogen) was removed by Ni-NTA agarose (Qiagen). To minimize association of HSP70 during purification, 1 mM ATP and 3 mM MgCl<sub>2</sub> were included in the wash before final elution. The concentrations of the protein complexes were determined by Coomassie blue staining on SDS–PAGE gels using BSA as a standard. The purified

protein complexes were subjected to mass spectrometric analysis and showed no detectable cross contamination of the CST and STN1/TEN1 complexes with endogenous POT1–TPP1 and vice versa. In addition, the purified POT1–TPP1 was free of any of the shelterin components other than POT1–TPP1.

**Electromobility shift assay.** Reactions containing indicated concentration of [<sup>32</sup>P]-labelled oligonucleotide primers, proteins, 50 mM Tris-HCl, pH 8.0, 50 mM NaCl, 1 mM DTT, 5% glycerol were incubated at 4 °C (various times) before electrophoretic analysis on 6% polyacrylamide gels or 2.5% agarose gels with 0.5 $\times$  TBE buffer at 150 V for 1.5 h. Gels were dried and analysed on a Phosphorimager (FLA-3000, FujiFilm) and radioactivity on the gels was quantified using the Aida Image Analyzer. To determine equilibrium dissociation constants ( $K_d$ ), reactions containing trace amounts (<50 pM) of [<sup>32</sup>P]-labelled oligonucleotide primer were incubated at 4 °C for 20–24 h before electrophoresis as described above. Data analysis was performed on GraphPad Prism. Theoretical binding curves were fitted to the data to obtain the  $K_d$  ( $Y = B_{\max} \times X / (K_d + X)$ ), where  $Y$  is the fraction bound,  $B_{\max}$  is the maximal binding,  $X$  is the protein concentration, and  $K_d$  is the apparent equilibrium constant).

**Telomere length analysis.** For genomic DNA isolation, cells were lysed in buffer containing 10 mM Tris-HCl, pH 8.0, 100 mM NaCl, 0.5% SDS, 1 mM EDTA, 250  $\mu$ g ml<sup>-1</sup> proteinase K (Roche) and 10  $\mu$ g ml<sup>-1</sup> RNase A and incubated at 50 °C overnight. Genomic DNA was prepared by phenol-chloroform extraction, followed by ethanol precipitation. After restriction digestion with *RsaI* and *HinfI*, DNA samples were resolved on 0.6% agarose gels for in-gel hybridization and analysed as previously described<sup>20</sup>.

**Direct telomerase activity assay.** Direct telomerase activity assay was performed as previous described<sup>22</sup> with minor modifications. In brief, telomerase reactions were carried out in 20  $\mu$ l at 30 °C for 30 min and contained 2  $\mu$ g of super-telomerase extract, 50 mM Tris-HCl, pH 8.0, 50 mM KCl, 1 mM spermidine, 1 mM MgCl<sub>2</sub>, 5 mM  $\beta$ -mercaptoethanol, 500  $\mu$ M dATP, 500  $\mu$ M dTTP, 3  $\mu$ M dGTP, 20  $\mu$ Ci of [ $\alpha$ -<sup>32</sup>P]-dGTP (3,000 Ci mmol<sup>-1</sup>), and 20 or 10 nM of 5'-biotinylated oligonucleotide primers as indicated in Fig. 3a–d. Reactions were stopped by addition of 10  $\mu$ l of 250 mM EDTA with trace amounts of 5'-[<sup>32</sup>P]-labelled and 3'-biotinylated 10- or 15-mer oligonucleotide as recovery control. After purification by streptavidin-conjugated magnetic beads (Dynabeads M-280, Invitrogen), the samples were resolved on 10% polyacrylamide-urea gels.

**Chromatin immunoprecipitation.** Cells were first fixed with 1% formaldehyde for 30 min at room temperature, incubated in PBS/glycine (200 mM) for 15 min and then harvested by scraping in PBS/glycine for centrifugation at 380g for 10 min. Cell pellets were resuspended in swelling buffer (25 mM Hepes, pH 7.9, 0.25% Triton X-100, 10 mM KCl, 1.5 mM MgCl<sub>2</sub>, 1 mM EDTA, 1 mM DTT + protease inhibitor cocktail) and incubated on ice for 10 min, and then centrifuged at 1,500g for 5 min. Samples were resuspended in sonication buffer (50 mM Hepes, pH 7.9, 150 mM NaCl, 1 mM EDTA, 0.1% sodium deoxycholate, 0.1% SDS, 1% Triton X-100 + protease inhibitor cocktail) and subjected to sonication for 40 min using Bioruptor (Diagenode). After centrifugation at 15,800g for 15 min, the supernatant was mixed with 20  $\mu$ g of sheared bacterial DNA (Sigma) and 5  $\mu$ g of anti-Myc 9E10 antibody, and incubated at 4 °C overnight. Subsequently, antibodies were captured by incubation with 20  $\mu$ l of protein G sepharose (GE Healthcare) at 4 °C for 2 h, followed by washing in sequence with buffers WA (20 mM Tris-HCl, pH 8.0, 1 mM EDTA, 0.1% SDS, 1% Triton X-100, 150 mM NaCl), WB (20 mM Tris-HCl, pH 8.0, 1 mM EDTA, 0.1% SDS, 1% Triton X-100, 500 mM NaCl), WC (20 mM Tris-HCl, pH 8.0, 1 mM EDTA, 0.5% NP40, 0.5% sodium deoxycholate, 250 mM LiCl) and TE (10 mM Tris-HCl, pH 8.0, 1 mM EDTA). Elution of the immunoprecipitate was carried out with 3  $\times$  150  $\mu$ l of elution buffer (1% SDS, 0.1 M NaHCO<sub>3</sub>, 5  $\mu$ g of proteinase K), followed by overnight incubation at 65 °C to reverse crosslinking. The eluate was mixed with 20  $\mu$ l of 1 M Tris-HCl, pH 6.8 and 10  $\mu$ g of RNase A for 1 h at 37 °C. Phenol-chloroform extraction, followed by ethanol precipitation was carried out to extract DNA for dot-blot assay as described<sup>20</sup>.

**Co-immunoprecipitation.** Cell lysates for co-immunoprecipitation experiments were prepared in NETN buffer (40 mM Tris-HCl, pH 8.0, 100 mM NaCl, 1 mM EDTA, 0.5% NP-40) supplemented with protease inhibitor cocktail (Sigma). Immunoprecipitation was performed with anti-Flag M2 affinity gel (Sigma) at 4 °C for 4–6 h. After wash with NETN, specific immuno-precipitates were eluted by Flag peptide (200  $\mu$ g ml<sup>-1</sup>) for SDS–PAGE and analysed on western blots using the indicated antibodies.

**Cell culture, stable cell line generation, and cell synchronization.** All human cells were maintained at 37 °C with 5% CO<sub>2</sub> in Dulbecco's Modified Eagle's Medium supplemented with 10% FCS and penicillin/streptomycin. Stable cell lines for wild type and truncated mutants of CTC1 and shRNA expression were generated by viral transduction and puromycin selection (1  $\mu$ g ml<sup>-1</sup>). For cell cycle synchronization in early S phase, HT1080 cells were treated twice with

thymidine (2.5 mM) for twelve hours with an eleven-hour interval in fresh medium between the thymidine treatments.

**Yeast two-hybrid assay.** The assay was performed using the Matchmaker Gold Yeast Two-Hybrid system (Clontech) according to the instruction manual. In brief, the plasmids for expression of bait and prey proteins were generated by subcloning of the cDNAs into pGBKT7 DNA-BD and pGADT7 AD vectors, respectively. Yeast mating was set up using the Y2H Gold yeast strain carrying a bait plasmid and the Y187 yeast strain carrying a prey plasmid, and diploid cells

expressing both bait and prey proteins were then selected to grow on SD/–Leu/–Trp agar plates. To test for protein interaction, replica-plating of diploid cells on SD/–Leu/–Trp/–Ade/–His/AbA (aureobasidin A) agar plates was performed to determine the expression of three reporter genes *ADE2*, *HIS3* and *AURI-C*.

22. Cristofari, G. *et al.* Low- to high-throughput analysis of telomerase modulators with Telospot. *Nature Methods* **4**, 851–853 (2007).